Advanced Photonic Crystals for Efficient Light-Trapping in Photocatalytic Applications

Siew Yee Lim

A thesis submitted for the degree of Doctor of Philosophy

The University of Adelaide

School of Chemical Engineering and Advanced Materials

September 2020

Table of Contents

Abstract

Despite advances in solar technologies, there is still a growing and urgent demand for light-harnessing materials that enable efficient utilisation of solar energy for solar-to-fuel conversion and environmental remediation applications. Existing photocatalytic technologies present inherent limitations to achieve these goals due to wide energy bandgap and poor electrochemical properties of conventional materials. A combination of fundamental and applied materials science, nanotechnology, chemistry, photonics and applied physics offers a way forward for developing new light-confining photocatalyst platforms with improved capabilities, versatilities, cost-effectiveness and sustainability to address global energy and environmental issues.

This thesis presents the development of rationally engineered composite photocatalyst platforms based on nanoporous anodic alumina photonic crystals (NAA-PCs) and photoactive materials. The fabrication of these photocatalytic systems with enhanced performances is achieved through structural engineering and chemical modification of NAA-PCs. Various forms of NAA-PCs were produced by pulse-like anodisation strategies with a view to optimising optical properties to harness light–matter interactions at the nanoscale efficiently, within high-irradiance spectral regions. The essential photocatalytic properties of these PC structures, well-defined energy bandgap capable of photogeneration of charge carriers, were provided by chemical functionalisation, using photoactive layers of titanium dioxide (TiO_2) deposited onto the inner surface of NAA-PCs through sol-gel method. Photocatalytic performances of photo-active NAA-PCs as well as photocatalytic enhancements associated with distinct forms of light–matter interactions were demonstrated through photodegradation of model organics such as methylene blue, methyl orange, rhodamine B and 4-chlorophenol, under simulated solar light irradiation conditions. Photocatalytic enhancements associated with slow photons, light confinement, and plasmonic effects in noble metal nanostructures with and without NAA-PCs were also analysed.

This thesis demonstrated that: (i) high-quality nanoporous anodic alumina gradient-index filters (NAA-GIFs) and hybrid NAA-PCs can be developed with tunable optical properties across the UV-visible-NIR spectrum, (ii) various forms of photo-active NAA-PCs with and without noble metal nanostructures are found to have superior

performances to benchmark photocatalyst materials in many cases due to "slow photon" effect and light confinement, and (iii) 2D gold nanodot plasmonic single-lattices show outstanding performances due to efficient utilisation of solar energy at high-irradiance spectral regions and harnessing plasmonic light-matter interactions. The studies completed in this thesis advance both fundamental understanding and applied knowledge on the photocatalytic performance of chemically-modified NAA-PCs with optimised structural, optical, chemical and photocatalytic properties. These advanced materials could potentially be integrated into fully functional and marketable real-life photocatalytic devices for addressing global energy challenges and environmental pollution remediation.

Preface

This thesis is submitted as a "thesis by publications" in accordance to the "Specifications for Thesis 2020" of The University of Adelaide. A complete list of publications are listed as follow.

Journal Covers
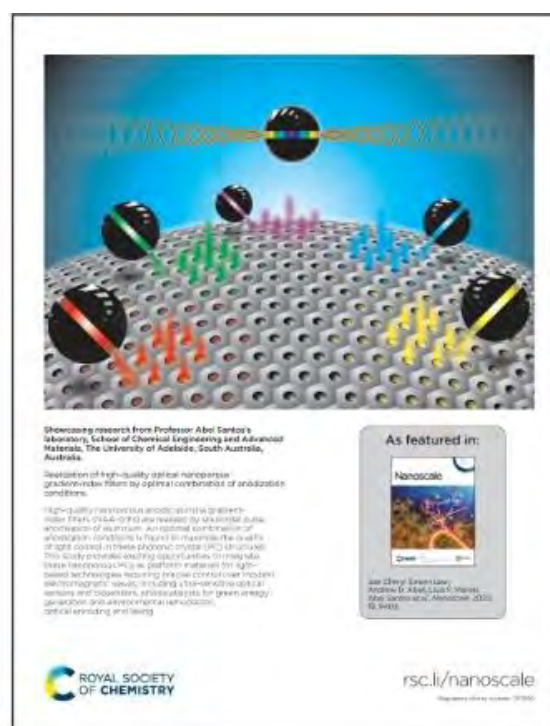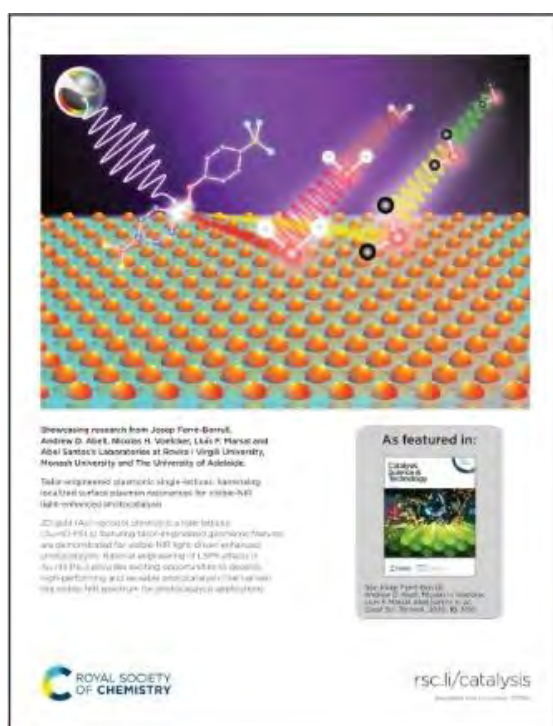
List of Publications

1. **S.Y. Lim**, C.S. Law, L. Liu, M. Markovic, C. Hedrich, R.H. Blick, A.D. Abell, R. Zierold, and A. Santos, *Electrochemical engineering of nanoporous materials for photocatalysis: fundamentals, advances, and perspectives*. Catalysts, 2019. **9**(12): p. 988. **(IF 3.444)**

2. **S.Y. Lim**, C.S. Law, L.F. Marsal, and A. Santos, *Engineering of hybrid nanoporous anodic alumina photonic crystals by heterogeneous pulse anodization*. Scientific Reports, 2018. **8**(1): p. 9455. **(IF 4.122)**

3. **S.Y. Lim**, C.S. Law, M. Markovic, J.K. Kirby, A.D. Abell, and A. Santos, *Engineering the slow photon effect in photoactive nanoporous anodic alumina gradient-index filters for photocatalysis*. ACS Applied Materials and Interfaces, 2018. **10**(28): p. 24124–24136. **(IF 8.456)**

4. **S.Y. Lim**, C.S. Law, M. Markovic, L.F. Marsal, N.H. Voelcker, A.D. Abell, and A. Santos, *Rational management of photons for enhanced photocatalysis in structurally-colored nanoporous anodic alumina photonic crystals*. ACS Applied Energy Materials, 2019. **2**(2): p. 1169–1184. **(IF 4.671)**

5. **S.Y. Lim**, C.S. Law, L. Liu, M. Markovic, A.D. Abell, and A. Santos, *Integrating surface plasmon resonance and slow photon effects in nanoporous anodic alumina photonic crystals for photocatalysis*. Catalysis Science & Technology, 2019. **9**(12): p. 3158–3176. **(IF 5.726)**

6. **S.Y. Lim**, C.S. Law, F. Bertó-Roselló, L. Liu, M. Markovic, J. Ferré-Borrull, A.D. Abell, N.H. Voelcker, L.F. Marsal, and A. Santos, *Tailor-engineered plasmonic single-lattices: harnessing localized surface plasmon resonances for visible–NIR light-enhanced photocatalysis*. Catalysis Science & Technology, 2020. **10**(10): p. 3195–3211. **(IF 5.726) Journal Cover**

7. **S.Y. Lim**, C.S. Law, L. Jiang, L. K. Acosta, A. Bachhuka, L.F. Marsal, A.D. Abell, and A. Santos, *Elucidating alcohol additives effect on mild pulse anodization by forbidden light propagation in nanoporous anodic alumina gradient-index filters*. Electrochimica Acta (under revision). **(IF 5.383)**

8. C.S. Law, **S.Y. Lim**, A.D. Abell, N.H. Voelcker, and A. Santos, *Nanoporous anodic alumina photonic crystals for optical chemo- and biosensing: fundamentals, advances, and perspectives*. Nanomaterials, 2018. **8**(10): p. 788. **(IF 4.034)**

9. C.S. Law, **S.Y. Lim**, R.M. Macalincag, A.D. Abell, and A. Santos, *Light-confining nanoporous anodic alumina microcavities by apodized stepwise pulse anodization*. ACS Applied Nano Materials, 2018. **1**(9): p. 4418–4434. **(IF NA) New Journal**

10. C.S. Law, **S.Y. Lim**, A.D. Abell, and A. Santos, *Real-time binding monitoring between human blood proteins and heavy metal ions in nanoporous anodic alumina photonic crystals*. Analytical Chemistry, 2018. **90**(16): p. 10039–10048. **(IF 6.350)**

11. C.S. Law, **S.Y. Lim**, A.D. Abell, L.F. Marsal, and A. Santos, *Structural tailoring of nanoporous anodic alumina optical microcavities for enhanced resonant recirculation of light*. Nanoscale, 2018. **10**(29): p. 14139–14152. **(IF 6.970)**

12. C.S. Law, **S.Y. Lim**, L. Liu, A.D. Abell, L.F. Marsal, and A. Santos, *Realization of high-quality optical nanoporous gradient-index filters by optimal combination*

of anodization conditions. Nanoscale, 2020. **12**(17): p. 9404–9415. **(IF 6.970)**
Journal Cover

13. C.S. Law, **<u>S.Y. Lim</u>**, and A. Santos, *On the precise tuning of optical filtering features in nanoporous anodic alumina distributed Bragg reflectors*. Scientific Reports, 2018. **8**(1): p. 4642. **(IF 4.122)**

14. L. Liu, **<u>S.Y. Lim</u>**, C.S. Law, B. Jin, A.D. Abell, G. Ni, and A. Santos, *Light-confining semiconductor nanoporous anodic alumina optical microcavities for photocatalysis*. Journal of Materials Chemistry A, 2019. **7**(39): p. 22514–22529. **(IF 10.733)**

15. L. Liu, **<u>S.Y. Lim</u>**, C.S. Law, L. K. Acosta, B. Jin, A.D. Abell, L.F. Marsal, G. Ni, and A. Santos, *Optical engineering of nanoporous photonic crystals by Gaussian-like pulse anodization*. ACS Applied Nano Materials (submitted) **(IF NA) New Journal**

16. C. Eckstein, C.S. Law, **<u>S.Y. Lim</u>**, S. Kaur, T. Kumeria, J. Ferré-Borrull, A.D. Abell, L.F. Marsal, and A. Santos, *Nanoporous photonic crystals with tailored surface chemistry for ionic copper sensing*. Journal of Materials Chemistry C, 2019. **7**(39): p. 12278–12289. **(IF 6.641)**

Conference Proceedings

1. **<u>S.Y. Lim</u>**, C.S. Law, and A. Santos, *Surface modification of nanoporous anodic alumina photonic crystals for photocatalytic applications*. in *Nanophotonics Australasia 2017*. 2018. International Society for Optics and Photonics.

2. **<u>S.Y. Lim</u>**, C.S. Law, and A. Santos, *Enhanced visible light photocatalysis in titanium dioxide-functionalized nanoporous anodic alumina photonic crystals*. in *Solid-State Lighting 2018*. 2018. Optical Society of America.

3. C.S. Law, **<u>S.Y. Lim</u>**, and A. Santos, *Fine tuning of transmission features in nanoporous anodic alumina distributed Bragg reflectors*. in *Nanophotonics Australasia 2017*. 2018. International Society for Optics and Photonics.

Conference Presentations

1. **<u>S.Y. Lim</u>**, C.S. Law, and A. Santos, Surface modification of nanoporous anodic alumina photonic crystals for photocatalytic applications, SPIE Nanophotonics Australasia 2017, Melbourne, December 2017 (Poster Presentation).

2. **<u>S.Y. Lim</u>**, C.S. Law, and A. Santos, Enhanced visible light photocatalysis in titanium dioxide-functionalized nanoporous anodic alumina photonic crystals, OSA Light, Energy and the Environment Congress 2018, Singapore, November 2018 (Poster Presentation).

Invited Seminar Presentations

1. **<u>S.Y. Lim</u>**, Engineering the slow photon effect in nanoporous photonic crystals for photocatalysis, IPAS Seminar, University of Adelaide, Adelaide, June 2019 (Oral Presentation).

HDR Thesis Declaration

I certify that this work contains no material which has been accepted for the award of any other degree or diploma in my name, in any university or other tertiary institution and, to the best of my knowledge and belief, contains no material previously published or written by another person, except where due reference has been made in the text. In addition, I certify that no part of this work will, in the future, be used in a submission in my name, for any other degree or diploma in any university or other tertiary institution without the prior approval of The University of Adelaide and where applicable, any partner institution responsible for the joint-award of this degree.

I acknowledge that copyright of published works contained within this thesis resides with the copyright holder(s) of those works.

I also give permission for the digital version of my thesis to be made available on the web, via the University's digital research repository, the Library Search and also through web search engines, unless permission has been granted by the University to restrict access for a period of time.

I acknowledge the support I have received for my research through the provision of an Australian Government Research Training Program Scholarship.

Signature : __   ___

Name   : Siew Yee Lim   Date: 25th August 2020

Acknowledgements

I would like to express my deepest appreciation to both of my supervisors, Dr. Abel Santos and Prof. Andrew D. Abell, for aiding me to have a smooth-sailing PhD journey. To Abel, my principal supervisor, to whom I am indebted for his patient guidance, enthusiastic encouragement and useful critiques as well as assistance in keeping my progress on schedule during my PhD study. With his guidance, support and continuous optimism, I did not encounter many hardships and have built my professionalism throughout my PhD candidature. No words can express how appreciative I am towards him. He is not only a supervisor and a mentor, but also a friend and someone I will always respect and find when I have any troubles. To Andrew, my co-supervisor, I would like to express my very great appreciation to him for his valuable, constructive and always wise suggestions on manuscripts as well as support in providing facilities when I needed. I could not express how thankful I am to both of them for their invaluable knowledge, encouragement and guidance.

Assistance provided by my colleagues is greatly appreciated, particularly to Dr. Cheryl Suwen Law, for her guidance and willingness to help in practical work and understanding of theoretical concepts. I am also very thankful to The University of Adelaide for providing me an opportunity to study my PhD in this university with a scholarship. I wish to acknowledge School of Chemical Engineering and Advanced Materials, Adelaide Microscopy, and Institute for Photonics and Advanced Sensing for the facilities.

Finally, my deep and sincere gratitude to my family for their continuous and unparalleled love, encouragement and support. I express my warmest gratitude to them for giving me the opportunities and experiences that have made me who I am. It is also pleasure to thank my friends for their company and support.

Chapter 1

INTRODUCTION

1. Introduction

1.1 Introductory Background

Solar light is one of the most promising green energy resources, capably of providing enough energy to address emerging global challenges such as energy shortage, climate change and environmental pollution. Among other light-harvesting processes, heterogeneous photocatalysis — henceforth "photocatalysis"— is a light-driven process involving a photoactive material (e.g., semiconductor) with a well-defined energy bandgap that is capable of degrading environmental contaminants [1,2], purifying air [3], producing clean hydrogen fuel [4,5], reducing carbon dioxide [6] and synthesising organics [7,8]. However, conventional photocatalyst materials harness incident solar energy poorly due to inherent constraints such as wide energy bandgap and poor electrochemical properties [9]. Thus, there is a growing demand for high efficiency, inexpensive and robust photocatalyst materials that can maximise the efficiency of photocatalytic reactions for future breakthrough technologies.

At the nanoscale, every photon is precious. A detailed understanding of the fundamentals and engineering of light–matter interactions at the nanoscale along, in combination with smart chemical and structural designs of photocatalysts, makes it possible to maximise photocatalytic efficiencies by rational management of incident photons. Photocatalysis can be significantly enhanced by judiciously utilising various forms of light–matter interactions, including localised surface plasmon resonance (LSPR) effects in noble metal nanoparticles [8] and photonic effects in photonic crystal (PC) structures [10,11]. For example, PC structures can enhance and maximise light–matter interactions for photocatalysis by trapping, controlling and manipulating the propagation of light (i.e. photons) of specific energies and wavelengths via Bragg diffraction, light confinement, multiple scattering and "slow photon" effect. PC structures feature characteristic photonic stopbands (PSBs) – range of wavelengths within with light propagation is forbidden within the PC structure – which can be tailor-engineered by the geometric features and chemical composition of PC structures. Nanoporous PCs also provide high specific surface area, enhanced utilisation of incoming photons and efficient mass transport of ionic and molecular species involved in photocatalytic reactions. These advantages can be precisely engineered to harness photons for enhanced photocatalytic performances in semiconductor PC structures.

Semiconductor inverse opal PC photocatalysts show improvements in photocatalytic performances when compared to benchmark photocatalyst materials [12,13]. Photocatalytic enhancements are mainly due to the localisation of slow photons near the edges of the PCs' PSB, creating light-trapping and confinement capabilities that can be utilised to enhance the efficiency of light-driven reactions. The performance of semiconductor inverse opal photocatalysts can also be significantly enhanced by chemical modification of these PC structure with semiconducting oxides [14], and through decoration with noble metal nanoparticles for LSPR effect [15]. Despite these advantages, such PC structures present several inherent drawbacks, including long fabrication process (> 24 h), restriction to 3D nanostructures and formation of structural defects [11,16].

Alternatives include electrochemically engineered nanoporous materials (EENMs). These structures provide promising photocatalyst PC platforms due to their versatile, highly controllable and self-organised nanoporous structure [17,18]. Advances in electrochemical oxidation – anodisation – of valve metals such as aluminium and titanium provide new opportunities to precisely modulate and engineer the effective medium of semiconductor oxides to harness light–matter interactions for photocatalysis. In particular, nanoporous anodic alumina (NAA) present a unique set of physical and chemical properties, including chemical resistance, thermal stability, mechanical robustness, optoelectronic properties and large specific surface area [18], all of which are essential prerequisites to develop high-performance photocatalytic systems. The versatile pore geometry and fabrication process of NAA allows production of various PC structures, including Fabry-Pérot interferometers, gradient-index filters and distributed Bragg reflectors. Despite all the advantages as promising photocatalyst PC platforms, the wide energy bandgap (7.0–9.5 eV) of NAA prevents NAA-PCs to be directly used for photocatalysis. This intrinsic drawback can be easily overcome by chemical modification of NAA-PCs, in particular with photoactive material with well-defined energy bandgap. This provides new opportunities to endow these photonic platforms with desired photocatalytic properties to overcome the intrinsic limitations of currently available photocatalysts.

This PhD thesis addresses the urgent demand for photocatalytic systems that provide simplicity, cost-competitiveness, mechanical robustness and high efficiency of photocatalytic activities for addressing emerging global challenges such as

environmental pollution. Despite significant advances in this field, more extensive fundamental research must be carried out to maximise applications of solar energy for various real-life photocatalytic applications. This thesis focuses on the structural optimisation and chemical modification of NAA-PCs, and their use in photocatalysis to tailor-engineer advanced photocatalytic platforms for efficient light-harvesting performances with broad applicability in environmental and energy fields.

1.2 Objectives of Thesis

The aim of this thesis is to develop inexpensive and robust chemically-modified NAA-PCs with optimised structural and photocatalytic properties essential for improving performances of existing photocatalytic materials.

The associated objectives of the thesis are to:

1. Design and engineer nanoporous anodic alumina photonic crystals (NAA-PCs) with different nanoarchitectures with optimised structural and optical properties.
2. Endow NAA-PCs with photocatalytic properties through chemical modifications (i.e. sol-gel method, noble metal sputtering).
3. Assess reproducibility, stability and photocatalytic performances of chemically modified NAA-PCs as photocatalytic platforms in the photodegradation of model organic pollutants in aqueous environment.
4. Fundamentally understand photocatalytic enhancement associated with slow photons, light confinement and plasmonic effects.

1.3 Scope and Structure of Thesis

Chapter 2 reviews recent advances of electrochemically engineered nanoporous materials (EENMs) for photocatalysis. This chapter provides a detailed overview on fabrication, chemical modification and structural engineering of EENMs for photocatalytic platforms. The key factors influencing photocatalysis and relevant literature about the recent applications of non-structurally and structurally EENMs for photocatalysis are also included in this chapter.

Chapter 3 reports the fabrication of hybrid NAA-PCs (Hy-NAA-PCs) composed of distributed Bragg reflectors (DBRs) and apodised gradient-index filters (APO-GIFs) embedded within the same PC structures by heterogeneous pulse anodisation (HPA). This chapter also demonstrates the tunability of the optical properties of these PC structures across the UV–visible–NIR spectrum by modifying various anodisation parameters.

Chapter 4 explores the fabrication of high-quality, light-forbidding propagation of NAA-GIFs by selective addition of alcohol type and concentration into the anodising acid electrolyte. The effect of type and concentration of alcohol additive on the electrochemical, structural, chemical and optical features NAA-GIFs are comprehensively analysed. Systematic assessment of the characteristic PSB of NAA-GIFs fabricated by sinusoidal pulse anodisation under mild conditions makes it possible to determine the most optimal alcohol modification conditions to maximise forbidden light propagation in NAA-GIFs in the form of well-resolved, narrow, intense, high-quality PSBs.

Chapter 5 explores for the first time light-trapping capabilities of NAA-GIFs functionalised with layers of semiconducting oxide – titanium dioxide (TiO_2) – to improve the efficiency of photocatalytic reactions by "slow photon" effect. The optical properties of pristine and TiO_2-NAA-GIFs as a function of anodisation parameters and aqueous media are investigated. The photocatalytic capability of these chemically-modified NAA-GIFs in the photodegradation of various organic dyes is also demonstrated, revealing that TiO_2-NAA-GIFs outperform conventional photocatalyst materials.

Chapter 6 presents enhanced photocatalytic capability of a different nanoarchitecture of TiO_2-functionalised NAA-PCs (i.e. TiO_2-NAA-DBRs) by "slow photon" effect. Through a systematic modification of anodisation parameters and aqueous media, the resulting optical and chemical properties of pristine and chemically-modified NAA-

DBRs are examined. Applicability and performance of TiO_2-NAA-DBRs as photocatalyst platforms is assessed by monitoring the photodegradation of various organic dyes and pesticides. The effect of additive concentration and assessment of reusability of these chemically-modified NAA-DBRs are also assessed, including comparison of photocatalytic performances with representative benchmark photocatalyst materials.

Chapter 7 investigates the coupling effect of surface plasmon resonance and "slow photons" in enhancing the photocatalytic reactions of gold-coated titania-functionalised NAA-DBRs (Au-TiO_2-NAA-DBRs). The effect of anodisation parameters, noble metal deposition time and type of noble metal (i.e. gold – Au, silver – Ag) on the optical and photocatalytic properties of chemically-modified NAA-DBRs are investigated. This chapter also compares the photocatalytic performances of Ag-TiO_2-NAA-DBRs with benchmark photocatalyst materials.

Chapter 8 explores a better understanding of LSPR effect for visible-NIR light driven photocatalysis by developing a photocatalytic platform material composed of 2D gold nanodot plasmonic single-lattices (Au-nD-PSLs). The geometric and optical features of these Au-nD-PSLs are demonstrated to be tuneable and optimisable by manipulation of Au deposition time and sizes of nanopatterned aluminium templates fabricated by different anodisation conditions. The photocatalytic and recyclability performances of Au-nD-PSLs are investigated by monitoring the photodegradation of various organic dyes with a systematic modification of the geometric features, type of noble metal nanodots and presence of underlying semiconducting substrates. Fundamental understanding of photocatalytic enhancements associated with LSPR effect in Au-nD-PSLs is demonstrated by analysing finite-difference time-domain (FDTD) simulations. The photocatalytic performances of these Au-nD-PSLs are compared with benchmark photocatalyst materials.

Chapter 9 summarises the recent advances in structural engineering and chemical modification of NAA-PCs as well as their applicability as photocatalyst platforms for photocatalysis, providing a future outlook in this exciting and dynamic research field.

1.4 References

1. J.H. Carey, J. Lawrence, and H.M. Tosine, *Photodechlorination of PCB's in the presence of titanium dioxide in aqueous suspensions*. Bulletin of Environmental Contamination and Toxicology, 1976. **16**(6): p. 697–701.

2. N.K. Gupta, Y. Ghaffari, S. Kim, J. Bae, K.S. Kim, and M. Saifuddin, *Photocatalytic degradation of organic pollutants over MFe_3O_4 (M = Co, Ni, Cu, Zn) nanoparticles at neutral pH*. Scientific Reports, 2020. **10**: p. 4942.

3. J. Zhao, and X. Yang, *Photocatalytic oxidation for indoor air purification: a literature review*. Building and Environment, 2003. **38**(5): p. 645–654.

4. A. Fujishima, and K. Honda, *Electrochemical photolysis of water at a semiconductor electrode*. Nature, 1972. **238**(5358): p. 37–38.

5. K. Maeda, *Photocatalytic water splitting using semiconductor particles: history and recent developments*. Journal of Photochemistry and Photobiology C: Photochemistry Reviews, 2011. **12**(4): p. 237–268.

6. Y. Izumi, *Recent advances in the photocatalytic conversion of carbon dioxide to fuels with water and/or hydrogen using solar energy and beyond*. Coordination Chemistry Reviews, 2013. **257**(1): p. 171–186.

7. Y. Shiraishi, and T. Hirai, *Selective organic transformations on titanium oxide-based photocatalysts*. Journal of Photochemistry and Photobiology C: Photochemistry Reviews, 2008. **9**(4): p. 157–170.

8. C. Wang, and D. Astruc, *Nanogold plasmonic photocatalysis for organic synthesis and clean energy conversion*. Chemical Society Reviews, 2014. **43**(20): p. 7188–7216.

9. X. Chen, and S.S. Mao, *Titanium dioxide nanomaterials: synthesis, properties, modifications, and applications*. Chemical Reviews, 2007. **107**(7): p. 2891–2959.

10. J. Liu, H. Zhao, M. Wu, B.V.D. Schueren, Y. Li, O. Deparis, J. Ye, G.A. Ozin, T. Hasan, and B.-L. Su, *Slow photons for photocatalysis and photovoltaics*. Advanced Materials, 2017. **29**(17): p. 1605349.

11. V. Likodimos, *Photonic crystal-assisted visible light activated TiO_2 photocatalysis*. Applied Catalysis B: Environmental, 2018. **230**: p. 269–303.

12. X. Zheng, S. Meng, J. Chen, J. Wang, J. Xian, Y. Shao, X. Fu, and D. Li, *Titanium dioxide photonic crystals with enhanced photocatalytic activity: matching photonic band gaps of TiO_2 to the absorption peaks of dyes*. The Journal of Physical Chemistry C, 2013. **117**(41): p. 21263–21273.

13. S. Meng, D. Li, P. Wang, X. Zheng, J. Wang, J. Chen, J. Fang, and X. Fu, *Probing photonic effect on photocatalytic degradation of dyes based on 3D inverse opal ZnO photonic crystal*. RSC Advances, 2013. **3**(38): p. 17021–17028.

14. Z. Geng, Y. Zhang, X. Yuan, M. Huo, Y. Zhao, Y. Lu, and Y. Qiu, *Incorporation of Cu_2O nanocrystals into TiO_2 photonic crystal for enhanced UV–visible light driven photocatalysis*. Journal of Alloys and Compounds, 2015. **644**: p. 734–741.

15. S. Meng, D. Li, X. Fu, and X. Fu, *Integrating photonic bandgaps with surface plasmon resonance for the enhancement of visible-light photocatalytic performance*. Journal of Materials Chemistry A, 2015. **3**(46): p. 23501–23511.

16. M. Curti, J. Schneider, D.W. Bahnemann, and C.B. Mendive, *Inverse opal photonic crystals as a strategy to improve photocatalysis: underexplored questions*. The Journal of Physical Chemistry Letters, 2015. **6**(19): p. 3903–3910.

17. X. Zhou, N. Liu, and Patrik Schmuki, *Photocatalysis with TiO_2 nanotubes: "colorful" reactivity and designing site-specific photocatalytic centers into TiO_2 nanotubes*. ACS Catalysis, 2017. **7**(5): p. 3210–3235.

18. A. Santos, *Nanoporous anodic alumina photonic crystals: fundamentals, developments and perspectives*. Journal of Materials Chemistry C, 2017. **5**(23): p. 5581–5599.

Chapter 2

LITERATURE REVIEW

2. Literature Review

This chapter is presented as published review article by **<u>S.Y. Lim</u>**, C.S. Law, L. Liu, M. Markovic, C. Hedrich, R.H. Blick, A.D. Abell, R. Zierold, and A. Santos, *Electrochemical engineering of nanoporous materials for photocatalysis: fundamentals, advances, and perspectives*. Catalysts, 2019. **9**(12): p. 988.

Statement of Authorship

Title of Paper	Electrochemical Engineering of Nanoporous Materials for Photocatalysis: Fundamentals, Advances, and Perspectives
Publication Status	☑ Published ☐ Accepted for Publication ☐ Submitted for Publication ☐ Unpublished and Unsubmitted work written in manuscript style
Publication Details	S.Y. Lim, C.S. Law, L. Liu, M. Markovic, C. Hedrich, R.H. Blick, A.D. Abell, R. Zierold, and A. Santos, *Electrochemical engineering of nanoporous materials for photocatalysis: fundamentals, advances, and perspectives.* Catalysts, 2019. **9**(12): p. 988.

Principal Author

Name of Principal Author (Candidate)	Siew Yee Lim
Contribution to the Paper	Wrote the manuscript under the supervision of Abel Santos and Andrew D. Abell.
Overall percentage (%)	60
Certification:	This paper reports on original research I conducted during the period of my Higher Degree by Research candidature and is not subject to any obligations or contractual agreements with a third party that would constrain its inclusion in this thesis. I am the primary author of this paper.
Signature	Date 10/06/2020

Co-Author Contributions

By signing the Statement of Authorship, each author certifies that:

    i.   the candidate's stated contribution to the publication is accurate (as detailed above);

    ii.   permission is granted for the candidate in include the publication in the thesis; and

    iii.   the sum of all co-author contributions is equal to 100% less the candidate's stated contribution.

Name of Co-Author	Cheryl Suwen Law
Contribution to the Paper	Aided in constructing the manuscript. Give consent to Siew Yee Lim to present this paper for examination towards the Doctorate of Philosophy.
Signature	Date 15/06/2020

Name of Co-Author	Lina Liu
Contribution to the Paper	Aided in the evaluation of final version of manuscript. Give consent to Siew Yee Lim to present this paper for examination towards the Doctorate of Philosophy.
Signature	Date 10/06/2020

Name of Co-Author	Marijana Markovic
Contribution to the Paper	Aided in the evaluation of final version of manuscript. Give consent to Siew Yee Lim to present this paper for examination towards the Doctorate of Philosophy.

Signature		Date	11/06/20

Name of Co-Author	Carina Hedrich
Contribution to the Paper	Aided in the evaluation of final version of manuscript. Give consent to Siew Yee Lim to present this paper for examination towards the Doctorate of Philosophy.

Signature		Date	10|06|2020

Name of Co-Author	Robert H. Blick
Contribution to the Paper	Aided in the evaluation of final version of manuscript. Give consent to Siew Yee Lim to present this paper for examination towards the Doctorate of Philosophy.

Signature		Date	10. June 2020

Name of Co-Author	Andrew D. Abell
Contribution to the Paper	Aided in the evaluation of final version of manuscript. Give consent to Siew Yee Lim to present this paper for examination towards the Doctorate of Philosophy.

Signature		Date	10/06/2020

Name of Co-Author	Robert Zierold
Contribution to the Paper	Aided in the evaluation of final version of manuscript. Give consent to Siew Yee Lim to present this paper for examination towards the Doctorate of Philosophy.

Signature		Date	10/06/2020

Name of Co-Author	Abel Santos		
Contribution to the Paper	Acted as a primary supervisor for the candidate, and aided in developing, revising and evaluating the manuscript for submission. Give consent to Siew Yee Lim to present this paper for examination towards the Doctorate of Philosophy.		
Signature		Date	11/06/2020

24

Electrochemical Engineering of Nanoporous Materials for Photocatalysis: Fundamentals, Advances, and Perspectives

Siew Yee Lim [1,2,3], Cheryl Suwen Law [1,2,3], Lina Liu [1,4,5], Marijana Markovic [1,6], Carina Hedrich [7], Robert H. Blick [7], Andrew D. Abell [2,3,8], Robert Zierold [7,*] and Abel Santos [1,2,3,*]

[1] School of Chemical Engineering and Advanced Materials, The University of Adelaide, Adelaide, SA 5005, Australia; siewyee.lim@adelaide.edu.au (S.Y.L.); suwen.law@adelaide.edu.au (C.S.L.); lina.liu@adelaide.edu.au (L.L.); marijana.markovic@adelaide.edu.au (M.M.)
[2] Institute for Photonics and Advanced Sensing (IPAS), The University of Adelaide, Adelaide, SA 5005, Australia; andrew.abell@adelaide.edu.au
[3] ARC Centre of Excellence for Nanoscale BioPhotonics (CNBP), The University of Adelaide, Adelaide, SA 5005, Australia
[4] School of Chemistry and Chemical Engineering, Ningxia University, Yinchuan 750021, China
[5] State Key Laboratory of High-Efficiency Utilization of Coal and Green Chemical Engineering, Ningxia University, Yinchuan 750021, China
[6] School of Agriculture Food and Wine, The University of Adelaide, Adelaide, SA 5064, Australia
[7] Center for Hybrid Nanostructures, Universität Hamburg, 22761 Hamburg, Germany; chedrich@physnet.uni-hamburg.de (C.H.); rblick@chyn.uni-hamburg.de (R.H.B.)
[8] Department of Chemistry, The University of Adelaide, Adelaide, SA 5005, Australia
* Correspondence: rzierold@physnet.uni-hamburg.de (R.Z.); abel.santos@adelaide.edu.au (A.S.); Tel.: +49-40-42838-1594 (R.Z.); Tel.: +61-8-8313-1535 (A.S.)

check for updates

Abstract: Photocatalysis comprises a variety of light-driven processes in which solar energy is converted into green chemical energy to drive reactions such as water splitting for hydrogen energy generation, degradation of environmental pollutants, CO_2 reduction and NH_3 production. Electrochemically engineered nanoporous materials are attractive photocatalyst platforms for a plethora of applications due to their large effective surface area, highly controllable and tuneable light-harvesting capabilities, efficient charge carrier separation and enhanced diffusion of reactive species. Such tailor-made nanoporous substrates with rational chemical and structural designs provide new exciting opportunities to develop advanced optical semiconductor structures capable of performing precise and versatile control over light–matter interactions to harness electromagnetic waves with unprecedented high efficiency and selectivity for photocatalysis. This review introduces fundamental developments and recent advances of electrochemically engineered nanoporous materials and their application as platforms for photocatalysis, with a final prospective outlook about this dynamic field.

Keywords: photocatalysis; nanoporous materials; anodization; chemical modification; structural engineering; optical nanostructures

1. Introduction

Solar light is one of the most promising green energy resources, which can theoretically provide more than enough energy to address emerging global challenges such as climate change

and environmental pollution. Heterogeneous photocatalysis—henceforth "photocatalysis"—is a light-driven process in which photons (light–electromagnetic waves) interact with atoms (matter–semiconductor) to generate electron–hole (e^-/h^+) pairs (charge carriers) that produce free radicals able to undergo secondary reactions. Photocatalytic processes involve a photoactive material (e.g., semiconductor, noble metal) with a well-defined energy bandgap [1]. When the energy of the incoming photons is higher than the energy bandgap of the platform material, electrons and holes are generated in the material's conduction and valence bands, respectively [1]. e^-/h^+ pairs can subsequently produce non-selective free radicals (i.e., ·OH radicals) on the surface of the material upon reaction with red-ox species in the surrounding media, enabling secondary chemical reaction paths for different applications, including energy generation and environmental remediation. This light-driven process can either be carried out under open-circuit conditions (i.e., photocatalysis) or under applied electrochemical bias (i.e., photo-electrocatalysis). The seminal study demonstrating clean hydrogen (H_2) fuel generation by water splitting on titanium dioxide (TiO_2) under UV light irradiation by Fujishima and Honda in 1972 stimulated intensive research activity in this field [2]. Currently, photocatalysis comprises a wide range of light-driven chemical reactions, including degradation of pollutants [3,4], air purification [5,6], clean H_2 energy generation [7,8], carbon dioxide (CO_2) reduction [9,10], ammonia (NH_3) production [11,12] and organic synthesis [13,14]. However, conventional photocatalyst materials have inherent constraints such as low photon-to-electron conversion rates due to limited utilization of high-irradiance solar spectral regions (e.g., ~43% visible) and low effective surface area [15]. Therefore, fundamental understanding and engineering of light–matter interactions at the nanoscale along with smart chemical and structural designs of photocatalysts can provide new paths to maximize the efficiency of photocatalytic reactions for future breakthrough technologies.

Typically, in order to enhance photocatalytic reactions and achieve maximum photocatalytic efficiencies, the structure of the photocatalyst platform is engineered to a high specific surface area to increase the number of active sites for red-ox reactions. Such adaptation is often achieved by engineering photocatalysts in the form of nanoparticle-based systems, which are either suspended in the reaction media or compacted into a photoelectrode [16]. However, nanoparticulate systems are susceptible to aggregation, poor electronic properties caused by band bending, photobleaching, feature structural defects and have high charge carrier recombination rates [15]. Furthermore, practical use of nanoparticulate systems in photocatalysis has environmental and health regulatory challenges (i.e., uncertainty about the fate and toxicity of nanomaterials), which prevent the bench-to-field translation of this technology. Although photocatalysts in the form of thin films can overcome the drawbacks associated with nanoparticulate systems due to their robustness and integrability into fixed-bed photocatalytic reactors, these photocatalyst systems often show a reduced efficiency compared to their nanoparticle counterparts due to their low surface area, which allows only one species (either e^- or h^+) to be available for reaction [17]. Significant efforts have been devoted to enhance performance of photocatalyst platforms by modifying their crystal structure [18,19], decoration with nanoparticles [20,21], co-deposition via sol-gel [22–25], atomic layer deposition [26,27], physical vapor [28,29] as well as electrochemical deposition [30,31], and doping [32,33]. The efficiency of photocatalysts can also be enhanced by engineering their structure at the nanoscale in the form of nanoporous photonic crystals (PC), which provide high specific surface area, enhanced utilization of incoming photons, and efficient mass transport of ionic and molecular species involved in photocatalytic reactions [22–25,34–43]. Inverse opal PC photocatalysts feature a characteristic photonic stopband (PSB) that can be engineered with precision across the spectral regions to harvest incoming photons from high-irradiance spectral regions [39–43]. Although these PC structures have been extensively explored as platform material for photocatalysis, they present several inherent drawbacks, including long fabrication process (>24 h), restriction to 3D nanostructures, constraints to small domain areas and formation of structural defects [44].

Among other alternatives, electrochemically engineered nanoporous materials (EENMs) are promising photocatalyst platforms due to their versatile, highly controllable and self-organized

nanoporous structure [18–38]. Advances in electrochemical oxidation (anodization) of valve metals such as aluminium and titanium enable new opportunities to precisely modulate and engineer the effective medium of semiconductor oxides to harness light–matter interactions for photocatalysis. Nanoporous anodic films can be produced with well-defined straight cylindrical nanopores or nanotubes as well as other advanced PC structures [45,46]. EENMs can also be produced with a unique set of physical and chemical properties, including chemical resistance, thermal stability, mechanical robustness, optoelectronic properties and large specific surface area, all of which are essential prerequisites to achieve high-performance photocatalytic devices [37,45]. In this context, this review provides a comprehensive perspective on recent advances in non-structurally and structurally engineered nanoporous photocatalyst materials produced by anodization (Figure 1). Electrochemical fabrication processes are first introduced, followed by a detailed description of chemical and structural modifications used to enhance the photocatalytic efficiency of these systems. We also provide an overview of the current state of the photocatalytic capabilities of electrochemically engineered nanoporous materials. Finally, this review concludes with a general overview and a prospective outlook on future trends in this field.
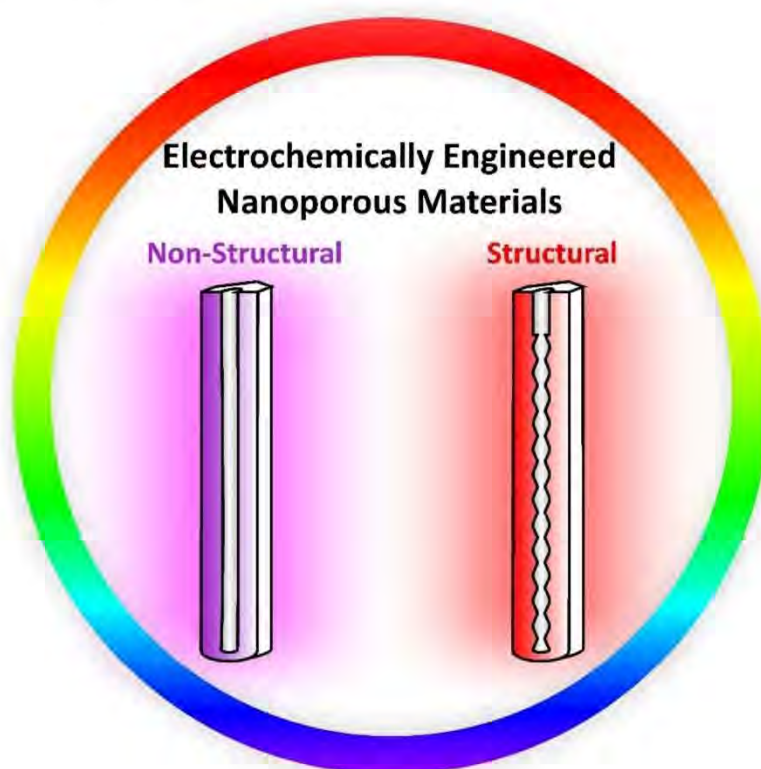

Figure 1. Electrochemically engineered nanoporous materials as photoactive platforms featuring non-structural and structural modifications to control light–matter interaction for photocatalysis.

2. Electrochemical Engineering of Nanoporous Materials

Anodization is an electrochemically driven oxidation process traditionally employed in the metal finishing industry to decorate metal surfaces and to protect them from corrosion [47]. During anodization, a passive layer of anodic metal oxide is produced on the metal surface, the morphology of which can either be nanoporous or compact non-porous. The ground-breaking discovery of self-organized nanoporous anodic alumina (Al_2O_3) in 1995 [48] stimulated an intensive research activity in anodization of valve metals (i.e., Al, Ti, Fe, W, Zr, Nb, Hf, V and Co) [49–68].

Anodization of valve metals is generally performed in a temperature-controlled electrochemical cell, in which two electrodes (i.e., anode = valve metal (M) and cathode = platinum (Pt)) are submerged in an electrolyte (Figure 2a) [69]. When the cell is externally supplied either by constant potential (i.e.,

potentiostatic oxidation) or by constant current (i.e., galvanostatic oxidation), an oxidation reaction $M \rightarrow M^{z+} + z\,e^-$ is initiated. Depending on the main anodization parameters (i.e., voltage/current, temperature and electrolyte), three possible reactions exist: (i) the metal is continuously dissolved to produce M^{z+} ions (soluble anodic oxide); (ii) M^{z+} ions react with O^{2-} from H_2O in the electrolyte and form compact non-porous oxide (MO) (non-soluble anodic oxide); and (iii) competition between formation and dissolution of oxide occurs, leading to the formation of nanoporous MO structures (partially soluble anodic oxide). Under specific experimental conditions for certain valve metals, (iv) disorganized rapid growth of bundles of nanopores/nanotubes, and (v) formation of thick self-organized mesoporous structures can occur.
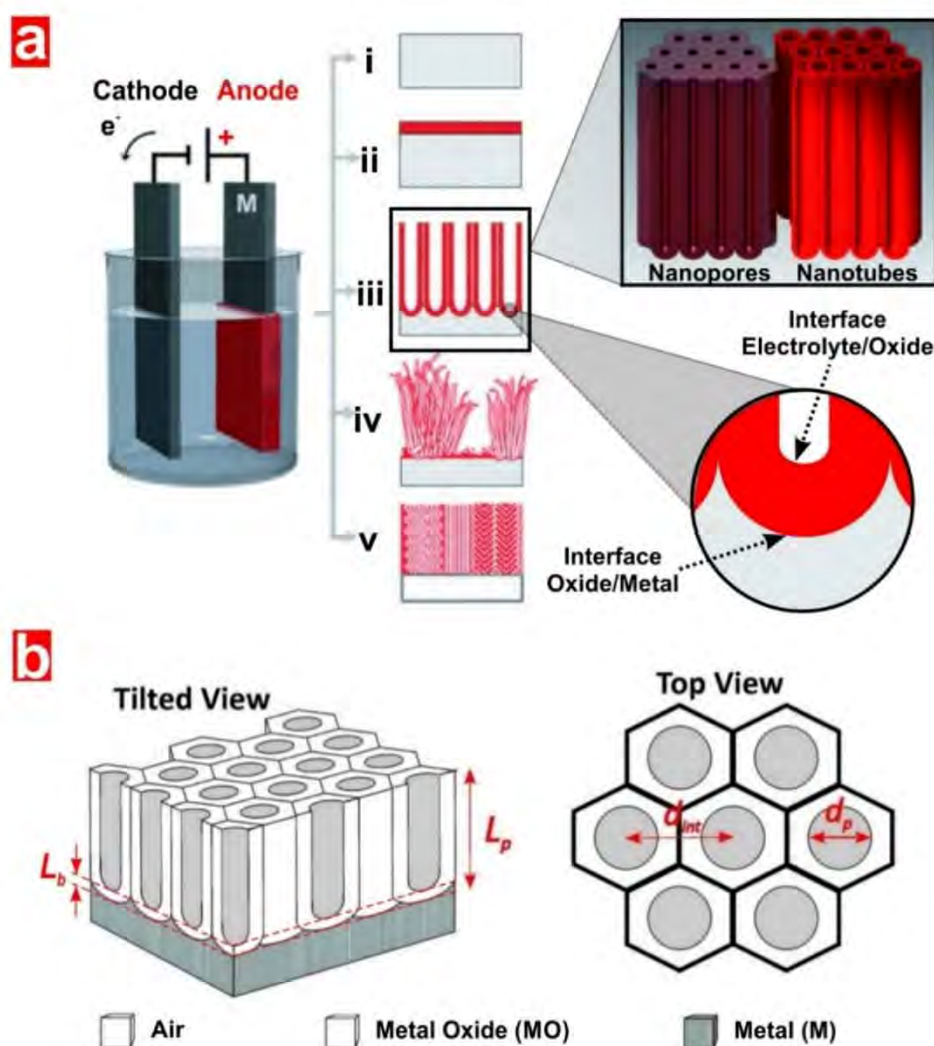
Figure 2. Fabrication of electrochemically engineered nanoporous materials (EENMs). (**a**) Schematic diagram illustrating the electrochemical anodization process, details of the oxide barrier layer located at the bottom tip of the nanostructures and possible anodic morphologies: (**i**) metal electropolishing; (**ii**) formation of compact anodic oxides; (**iii**) self-organized oxides (nanopores or nanotubes); (**iv**) rapid (disorganized) oxide nanotube formation; and (**v**) ordered nanoporous layers. Reproduced from [69], with copyright permission from Wiley-VCH Verlag GmbH & Co. KGaA, Weinheim, 2011. (**b**) Structural and geometric features of EENMs produced by anodization with tilted view of an EENM (left) (L_p–nanopore length and L_b–barrier layer thickness) and top view of EENMs (right) (d_{int}–interpore distance and d_p–nanopore diameter). Reproduced from [70], with copyright permission from MDPI, 2018.

Anodization is a highly versatile 3D nanofabrication approach, which can be applied to multiple metal substrates. Fabrication of nanoporous anodic alumina (NAA) structures by electrochemical oxidation of aluminium is the most developed anodization technology as compared to other metal oxides due to its controllability and well-defined nanoporous geometry [45]. However, there is a significant progress in anodization of other valve metals such as Ti, Fe, W, Zr, Nb, Hf, V and Co. Efforts have been made to develop Ti anodization technology due to the high stability against photo-corrosion and excellent optoelectronic properties for photocatalysis of anodic titanium dioxide (TiO_2) structures [16,37,69]. Anodization of valve metals under suitable conditions can result in anodic films featuring ordered nanopores or nanotubes with high aspect ratio. Figure 2b shows a graphic definition of the structural features of nanopore/nanotube geometry such as diameter (d_p), pore length (L_p), interpore distance (d_{int}) and barrier layer thickness (L_b). These characteristics can be precisely engineered by controlled manipulation of the anodization parameters [70]. The most representative examples of the self-organizing anodization conditions (i.e., voltage (V), temperature (T), electrolyte type) and main structural features (i.e., d_p) for multiple valve metals are summarized in Table 1. These studies demonstrate the fabrication of highly controllable nanoporous or nanotubular structures of various metal oxides through simple modification of the anodization parameters. For most of the valve metals, the presence of fluoride (F-) ions in the acid electrolyte is key in the formation of nanoporous or nanotubular structures due to the high chemical stability of their anodic oxides.

Table 1. Summary of self-organizing conditions and structural features of nanopores or nanotubes obtained by anodization of various valve metals.

Ref.	Valve Metal	Electrolyte Type	T (°C)	V (V)	d_p (nm)
[49,50]	Al	Diluted H_2SO_4	0–5	25–40	25–30
[48,51]		Diluted $C_2H_2O_4$	0–8	40–140	30–50
[52]		Diluted H_3PO_4	0–1	195	500
[53]	Ti	Buffered neutral electrolyte with F^- salts	20	20	100
[54,55]		Organic solvent with F^- salts	20	60	120–150
[56,57]		Cl^--containing electrolyte	4–20	10–60	15–40
[58,59]		Ethylene glycol with F^- salts and H_2O	20	30–50	38–174
[60,61]	Fe	Ethylene glycol with NH_4F and H_2O	20	20–100	50–110
[62]	Zr	Ethylene glycol with NH_4F and H_2O	20	20–100	70–120
[57]	W	Cl^--containing electrolyte	4	50–80	30–50
[63]		Diluted NaF	20	20–60	100
[64]	Nb	Diluted H_3PO_4 with HF	20	1–5	8–12
[65]		Glycerol with NH_4F and H_2O	20	20–60	50
[66]	Hf	Diluted H_2SO_4 with HF	20	10–60	15–90
[67]	V	$[BF_4]^-$ or $[TiF_6]^{2-}$-based electrolyte	20	40–300	10–30
[68]	Co	Ethylene glycol with NH_4F and H_2O	0	50	100

3. Chemical Modification of Electrochemically Engineered Nanoporous Materials

The chemical structure of EENMs is often modified with different entities (e.g., metals, quantum dots, semiconductor oxide films, conducting polymers, chalcogenides) to tune their optical, electrical and chemical properties to achieve desired functionalities and performances for specific photocatalytic and photo-electrocatalytic applications [37,69,71].

3.1. Doping

The chemical composition of EENMs can be altered by doping or bandgap engineering to enhance their performance in photocatalysis. Doping involves the introduction of secondary electronically active species into the crystal lattice of EENMs in order to modify the electrical conductivity and narrow the optical bandgap of the anodic oxide [72,73]. The intermediate states introduced from the doping elements (i.e., dopants) are required to be considerably close to the band edges (i.e., conduction or valence bands) of the anodic oxide for successful modification. The relative positions of

29

dopants to the band edges of the intrinsic photocatalyst material can be estimated by the density of states (DOS) calculations [16,37]. Strategies to dope the chemical composition of EENMs include the implantation of non-metal (C, N, B and F) [33,74–77] and metal (Cu and lanthanides) [78,79] elements, which are introduced by thermal treatment (annealing) in the gas atmosphere of the dopant element, co-sputtering or sputtering in dopant atmosphere, treatment in solution or melt of dopant, and high-energy ion implantation [69].

The most widespread doping approach is N-doping via ion implantation, which has been demonstrated to be particularly successful to incorporate nitrogen-containing species into as-produced TiO_2 nanotube structures at low-to-medium doping levels (1×10^{16} ions cm^{-2}) [75,80]. However, this doping method is limited by the short ion penetration depth, recrystallization requirement and inhomogeneous dopant distribution across the inner and top surface of EENMs [37,81,82]. Despite these constraints, well-defined buried junctions can be created into the inner surface of EENMs by rational utilization of the implantation profiles [80].

A particular straightforward doping approach to modify the chemical structure of EENMs in-situ the anodization process is using a metal alloy as a substrate. The alloy can either be prepared by arc melting or by co-sputtering of the pure valve metal and dopant metal [37]. Alloys can then be anodized to produce metal-doped EENMs. For instance, TiO_2 nanotubular structures doped with N [83], W [84,85], Mo [4], Nb [7], Ta [86], Ru [87,88] and noble metal [89] fabricated by anodization of different alloy substrates have been demonstrated. These electrochemically synthesized doped anodic oxides have shown improved open-circuit photocatalytic (OCP) and photo-electrochemical (PEC) activities. Enhancement effects have been ascribed to modification of the band- or surface-state distribution, increase in conductivity, functionality as a co-catalyst or localized surface plasmon resonance (LSPR). Although considerable efforts have gone into solution-based doping approaches (i.e., ion incorporation from the anodization electrolyte during anodization) for P [90] and N [91], efforts targeting N-doping are questionable due to XPS peaks located at 400 eV (adsorbed species), which were mostly obtained for nitrogen and unclarified electronic coupling of the doping species [69]. Though doping the structure of EENMs with non-metal and metal elements can be a suitable approach to increase the photocatalytic activity of these anodic oxides, the overall conversion efficiencies are often limited by thermal instability, decrease in charge carrier lifetime and unreliability of bandgap engineering [92]. Recent studies have demonstrated that visible light photo-response of EENMs for photocatalysis can be further enhanced by co-doping with a suitable combination of metals and/or non-metals [3,93,94]. For example, Yan et al. demonstrated enhanced photocatalytic and PEC properties under visible light irradiation by the synergetic effect in TiO_2 nanotubes co-doped with N and S (Figure 3a) [3]. These TiO_2 nanostructures were prepared by a combination of two-step anodization and treatment with thiourea and calcination under vacuum at 500 °C for 3 h.

Reduction or annealing treatment under atmospheric pressure of TiO_2-based EENMs can result in self-doping of TiO_2 nanotubes by the formation of Ti^{3+}/Ov (oxygen vacancy) lattice defects [37]. Ti^{3+} formation is beneficial to improve visible light photoresponse, increasing conductivity for improved charge separation and formation of surface states that facilitate charge transfer. This approach has been demonstrated as an optimal means of improving photocatalytic and PEC performances in reduced TiO_2 nanotubes [8,95,96]. Liu et al. showed that TiO_2 nanotubes exposed to high-pressure hydrogen treatment can produce reduced (black) TiO_2 nanotubes for OCP photocatalytic H_2 evolution without the need of co-catalysts (Figure 3b) [8]. Ion implantation of H and N into reduced TiO_2 nanotubes can further enhance noble metal-free photocatalytic H_2 generation by co-catalytic effect [97,98]. Despite the advantages of Ti^{3+}, the surface states of Ti^{3+} are less stable and can readily be oxidized by air. Nevertheless, it has been reported that Ti^{3+} states in anatase can stabilize these configurations [99].
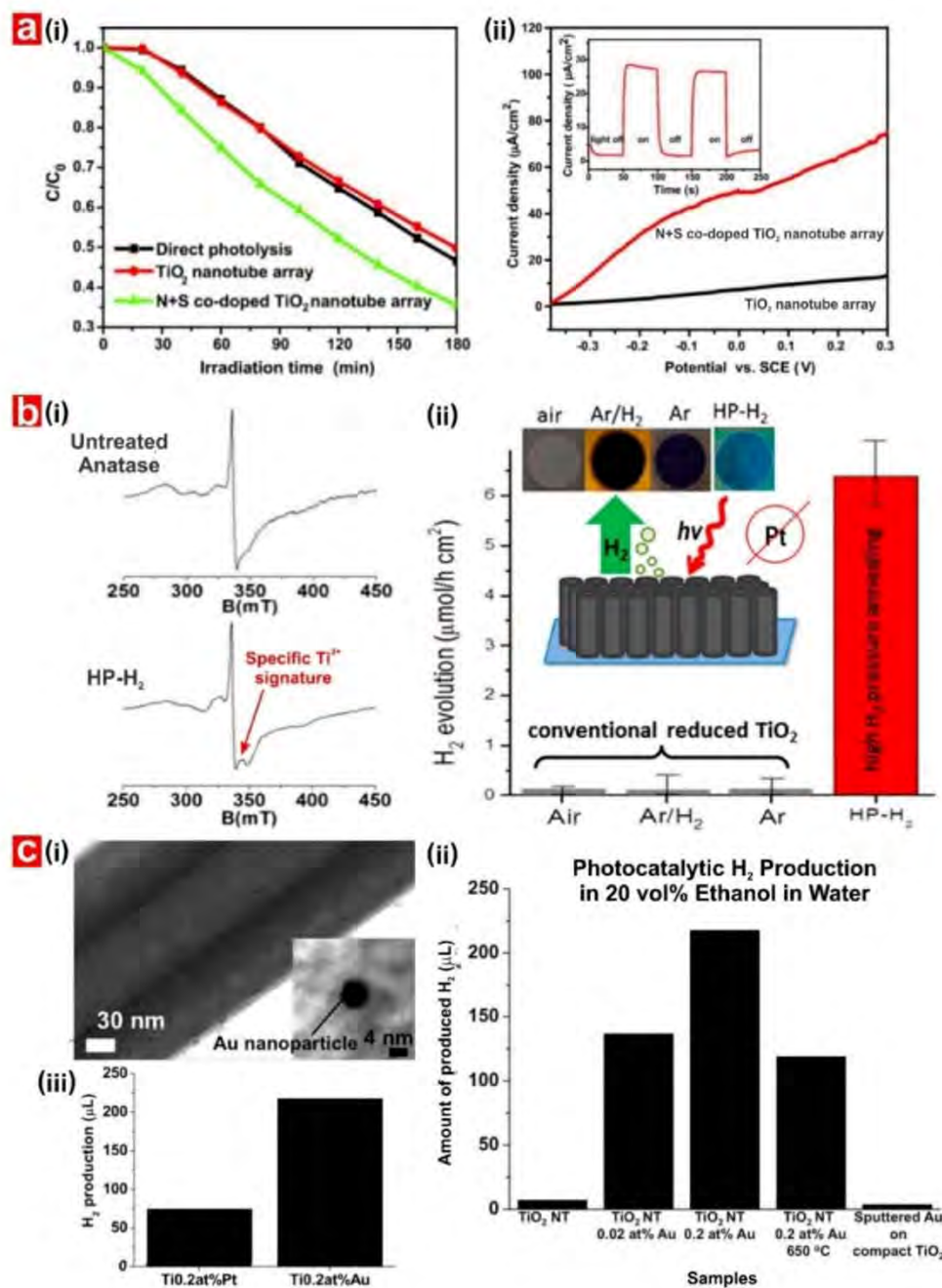
Figure 3. Examples of applicability of chemically-modified TiO$_2$ nanotubes in photocatalytic and photo-electrocatalytic applications. (**a**) (**i**) Photodegradation kinetics of methylene blue (MB) and (**ii**) photo-electrochemical properties for pristine and N, S co-doped TiO$_2$ nanotubes under visible light irradiation. Reproduced from [3], with copyright permission from Elsevier B.V., 2011. (**b**) (**i**) EPR spectra for anatase and hydrogenated anatase TiO$_2$ nanotubes and (**ii**) noble metal-free photocatalytic H$_2$ generation under open circuit conditions in methanol/water (50/50 vol%) using TiO$_2$ nanotubes heat-treated in different atmospheres (air at 450 °C; Ar at 500 °C; Ar/H$_2$ at 500 °C; HP-H$_2$, heat treatment in H$_2$ at 20 bar at 500 °C). Reproduced from [37], with copyright permission from American Chemical Society, 2017. (**c**) (**i**) TEM image of self-decorated nanotubes formed by anodizing a Ti-Au alloy (0.2 at-% Au); (**ii**) photocatalytic H$_2$ production activities for different Ti-Au alloys and reference samples in 20 vol% ethanol in water; and (**iii**) photocatalytic H$_2$ evolution with different types of noble metal on TiO$_2$ nanotubes. Reproduced from [20], with copyright permission from Wiley-VCH Verlag GmbH & Co. KGaA, Weinheim, 2013.

3.2. Physical Vapour Deposition (PVD)

Physical vapour deposition (PVD) is an atomistic deposition process in which atoms or molecules of material are physically vaporized and transported through a vacuum or low pressure gaseous (or plasma) environment to form a thin film on the surface of EENMs by condensation [100]. Although PVD produces a non-conformal coating of deposited materials on EENMs, the deposition process is relatively inexpensive. PVD is typically used to deposit films elements, alloys and compounds with thicknesses in the range of a few nano-s to micrometres. PVD is categorized into five main categories, including electron beam evaporation, molecular beam epitaxy, pulsed laser deposition, sputtering and thermal deposition [101]. Ag, Au, Pt, W, Mo, Ni, Cu, semiconductor oxides and quantum dots are often deposited into nanoporous materials by thermal evaporation [102], sputter deposition [21,28,29,89,103–105] or pulsed laser deposition [106] to improve photocatalytic and PEC performances by extending the lifetime of photogenerated charge carriers, narrowing the bandgap or by integrating LSPR effects. Nanoporous materials, such as NAA, can also be used as templates to produce various nanostructured materials (i.e., nanorods, nanowires and nanotubes) in combination with PVD processes. The resulting nanostructures have broad applicability in photocatalysis and the NAA templates can either be selectively removed or kept after the deposition process [101].

3.3. Electrochemical Deposition (ECD)

Electrochemical deposition (ECD)—commonly known as electrodeposition—is compared to the other deposition techniques a relatively simple and inexpensive deposition method where a solid coating on the surface of conductive EENMs is produced from ionic electrolytes under current/voltage-driven electrochemical reduction reactions [107]. Although ECD is limited by low deposition rate and single use of host template, this process is cost-effective, environmentally friendly and can be performed in any wet chemistry laboratory [72,101,107]. Various metals [35,108], oxides [30,109,110] and sulphides [31] can be electrodeposited to enhance the properties of EENMs for photocatalysis applications, including conductivity, chemical stability, PEC and photocatalytic properties [71].

3.4. Atomic Layer Deposition (ALD)

Atomic layer deposition (ALD) is a chemical gas phase technique used to deposit thin layers of materials such as oxides, nitrides, phosphates, sulphides and metals onto the entire surface of EENMs [111]. By this approach, the inner surface of EENMs is coated with atomic layers of an arbitrary material by repeating cyclic exposures to precursors and reactants, and purging. This method enables the precise control over the thickness and composition of the deposited film at the atomic scale, allowing the formation of homogeneous monolayers of the deposited material over large surfaces and high aspect ratios [112]. Nevertheless, the slow deposition rate, challenges in theoretical modelling of reactions and film growth, and potential cross-contamination of thin films by residual precursors can limit the application of ALD [113,114]. Despite these limitations, the ALD-assisted modification of EENMs has demonstrated excellent photocatalytic activities in degrading organic pollutants and OCP and PEC H_2 evolution [26,115–117].

3.5. Sol-Gel Chemistry

The sol-gel method is a wet chemical deposition technique involving three main steps: (i) hydrolysis and partial condensation of a precursor by dip or spin coating; (ii) gel formation by polycondensation; and (iii) solvent evaporation and gel drying [118,119]. The sol-gel process can be used to fabricate films with high specific surface area and rich surface chemistry that allows for functionalization under low synthesis temperature, controllable reaction conditions and simple equipment [120]. Nevertheless, thin films produced by this method have some drawbacks, including expensive production cost, limited thickness controllability and poor mechanical properties [121]. Despite these drawbacks, the sol-gel method has been extensively used to tune the surface chemistry of the nanoporous materials.

For instance, sol-gel derived synthesized coatings based on TiO_2 and WO_3 have been used to modify the inner surface of NAA-based structures to attain photocatalytic activity to effectively photodegrade organic pollutants under UV or visible light irradiation [22–25,122].

3.6. Decoration with Nanoparticles

The inner and/or outer surfaces of nanoporous materials are often decorated with metal-, semiconductor- and polymer-based nanoparticles to improve their photocatalytic properties by: (i) heterojunction formation and sensitization to change surface band bending (metal clusters or other semiconductors), (ii) suitable surface mediators for enhanced charge carrier transfer (co-catalytic effects), and (iii) LSPR effects for electromagnetic field enhancements around metal nanoparticles to achieve efficient light-harvesting properties [37].

The surface of EENMs can be decorated with noble metal nanoparticles (i.e., Au, Ag, Pt, Pd and mixtures) by PVD [21,89,123,124], photoreduction method [36] or chemical reduction techniques [125]. This approach makes it possible to achieve co-catalytic effects to enhance photocatalytic reactions such as OCP or PEC H_2 evolution and degradation of pollutants. Furthermore, EENMs can also be decorated with noble metal particles by anodization of low concentrations of valve metal–noble metal alloys [20,29,124]. This method provides a controllable distribution of particles over the surfaces of the EENMs with very uniform and defined particle diameters for efficient photocatalysis. Lee et al. demonstrated the in-situ formation of Au nanoclusters on TiO_2 nanotubes grown by anodizing Ti–Au alloys (Figure 3c) [20]. The homogeneous distribution of Au clusters with a typical particle size of ~5–7 nm was achieved. Cluster spacing can be controlled by the Au concentration within the alloy and the anodization time. The remarkable enhancement in H_2 evolution from ethanol solution was achieved by these noble metal-decorated TiO_2 nanotubular structures, with an H_2 production rate ~30 times faster than that of bare TiO_2 nanotubes and ~50 times more efficient than compact (flat) TiO_2 films decorated with the same number of Au clusters. Although Pt-decorated TiO_2 nanotubes can be produced by anodization of Ti–Pt alloys, poor photocatalytic H_2 generation was obtained due to the poisoning effect [20]. However, this study demonstrated that this decoration technique can be readily transferrable to other noble metals and alloys.

High photocatalytic rates have also been reported for EENMs decorated with semiconductor nanoparticles (i.e., CuO, Fe_2O_3, ZnO, Bi_2O_3, ZnTe or NiO). These hybrid structures were produced by slow hydrolysis of precursors [126], dip coating [127], chemical vapor deposition [128] and electrodeposition [30,109,110,129]. Enhanced photocatalytic performances were attributed to heterojunction formation, increase in surface area and/or possible charge injection from the electronic states of decorated nanoparticles. Nevertheless, careful considerations on the long-term stability of these composite nanoporous materials are required since some of these materials are susceptible to electrolytic corrosion, photo corrosion and instability under an applied voltage. Other common narrow bandgap semiconductors such as Bi_2S_3, PbS, ZnS, CdS and CdSe in the form of various nanostructures (i.e., nanoparticles, nanoclusters or quantum dots) can also be deposited on the inner surface of EENMs by successive ionic layer adsorption and reaction (SILAR) [130–132] as well as electrodeposition [31,131,133] methods. These composite photocatalyst materials provide enhanced photocatalytic and photo-electrocatalytic performances. More recent works have decorated EENMs with C60 [134], graphene [135], Ag/AgCl [136], AgBr [137] and BiOI [138] for enhanced photocatalysis. These studies demonstrate that photocatalytic enhancements in these composite photocatalyst materials are associated with different effects such as redox capability of Ag halogenides, effective charge transportation of C60 or graphene, or strong visible light absorption of BiOI. Note, not only inorganic compounds but also organic monolayers such as silanes and phosphonates deposited on the surfaces of EENMs have been investigated for photocatalytic applications [37].

4. Structural Engineering of Nanoporous Materials

In 1987, Yablonovitch and John demonstrated the concept of photonic crystals (PCs), which are multi-dimensional periodically structured materials that can control the propagation of electromagnetic waves across their structure [139,140]. Since these pioneering studies, many theoretical concepts and technological applications of PCs in the field of sensing [141–150], photocatalysis [22–25,34–36,38–43] and dye-sensitized solar cells [151–153] have been demonstrated. PCs feature regularly distributed variations of dielectric constant, and thus the refractive index, in a 1D, 2D or 3D fashion [45]. PCs feature a characteristic photonic stopband (PSB) which corresponds to a wavelength range within which incoming photons are not allowed to propagate through the PC's structure. This light–matter interaction can be tailor-made engineered by the geometric features and chemical composition of the PC structures, enabling different forms of light control such as Bragg diffraction, multiple scattering, light confinement and slow photon (SP) effect. This approach provides new opportunities to enhance light–dielectric interactions for photocatalysis by confining, controlling and manipulating the propagation of incident photons of specific energies or wavelengths [139,154,155].

Bragg diffraction forbids the propagation of photons within the PSB wavelength range, while multiple scattering increases trapping of photons propagating at wavelengths that are away from the PC's PSB. The SP effect slows down the group velocity of photons at the frequency edges of the PSBs. SPs generated on the red and blue edges of the PSB are primarily localized in the high and low dielectric parts of the PCs, respectively, increasing the lifetime of photons and the overall light absorption of the PC structure at specific spectral regions. In general, PC structures can be mechanistically described as an optical effective medium, in which the macroscopic optical properties of the composite PCs can be represented by model approximations such as Bruggeman, Drude, Looyenga–Landau–Lifshiftz, Lorentz–Lorenz and Maxwell Garnett [45]. For instance, the macroscopic optical properties of the composite NAA-PCs (i.e., air and alumina) can be estimated by averaging the properties of individual components (i.e., effective refractive index, effective dielectric constant) through effective medium approximation. In recent years, advances in nanofabrication technology have made it possible to develop conceptual PC structures. The most widespread techniques used to synthesize PCs are lithography and dry etching, vertical selective oxidation, wet chemical etching, fibre-pulling, embossing, self-organization and anodization [156]. Of all nanofabrication approaches, anodization has been demonstrated as a suitable method to fabricate EENM-based multi-dimensional PC structures with finely engineered geometric and optical properties. These PCs provide large surface area, versatility, scalable production, high throughput and resolution, making them attractive platform materials for a broad range of light-based technologies. However, the fabrication of EENMs by anodization still faces challenges. For instance, anodization of valve metals such as Fe, Zr, W, Nb, Hf, V and Co are limited to straight nanotubular structures produced under constant potential and F-containing electrolytes [16,157].

Recent developments in anodization technology have demonstrated approaches to overcome these constraints, enabling the production of a plethora of PC structures through rationally designed anodization conditions to effectively translate electric field variations into in-depth porosity modulations. NAA produced by anodization of aluminium is the most researched EENM in the development of PC structures. Forms of NAA-PC structures include Fabry–Pérot interferometers (NAA-FPIs) [141–143], distributed Bragg reflectors (NAA-DBRs) [144–146], gradient index filters (NAA-GIFs) [147–149], optical microcavities (NAA-µCVs) [158–160], apodized DBRs and GIFs (Apo-NAA-DBRs and Apo-NAA-GIFs) [161–163], bandpass filters (NAA-BPFs) [164] and linear variable bandpass filters (NAA-LVBPFs) [165]. The architecture and geometric features of NAA-PCs can be engineered with precision by pulse-like anodization under mild anodization conditions (i.e., low anodization voltage/current density and moderate acid electrolyte temperatures). Rationally designed anodization profiles along with optimal anodization conditions (i.e., the level of anodizing current density/voltage, type, concentration and temperature of acidic electrolyte) allow for engineering the effective medium of NAA in-depth during anodization. For instance, NAA-FPIs feature straight cylindrical nanopores

with a homogeneous distribution of effective refractive index in-depth and are produced by constant voltage/current density anodization [141–143]. NAA-DBRs feature a stepwise distribution of effective refractive index between low and high values, which can be generated by stepwise pulse anodization (STPA) approach [144–146]. NAA-GIFs have a sinusoidal modulation of porosity and can be synthesized by sinusoidal pulse anodization (SPA) [147–149]. NAA-μCVs are composed of a physical cavity layer sandwiched between two highly reflective mirrors, typically NAA-DBRs or NAA-GIFs, which can also be produced by different anodization approaches [158–160]. Several studies have successfully demonstrated the application of apodization functions to anodization profiles by modifying the anodization amplitude throughout time to produce apodized NAA-DBRs and NAA-GIFs [161–163].

NAA-BPFs can be produced by pseudo-stepwise pulse anodization (PSPA). Such PC structures allow for the transmission of light at certain bands of wavelengths in a selective manner while forbidding the propagation of photons of certain energies [164]. NAA-LVBPFs can be produced by the combination of SPA and selective chemical etching, where the effective medium of these EENM-based PC structures is engineered perpendicularly to the nanopores' growth direction [165]. Some detailed review articles describing the fundamental concepts, representative examples and realization of NAA-PCs are provided in [45,70].

TiO_2 nanotubes are the most representative example of TiO_2-based PCs, which are composed of self-ordered straight arrays of nanotubes. Distinct TiO_2-PC morphologies have also been fabricated by manipulating the anodization voltage or water content in the electrolyte, including hierarchical nanotubes [34–36,151], periodically structured nanotubes [46,150,152,164,165], bilayered nanotubes [153] and aperiodically structured nanotubes [166]. Hierarchical nanotubes with PC properties can be fabricated by manipulating the anodization voltage through sequential anodization steps [34–36]. The morphology of hierarchical top and bottom layers of TiO_2 nanotubes can be finely tuned between nanoring/nanotube, nanopore/nanotube and nanohole-nanocave/nanotube morphologies.

3D periodically structured TiO_2 nanotubes with broadband omnidirectional photonic stopbands can be prepared by periodic current pulse anodization, where the currents are alternated between high and low current density values [46,150,152,164,165]. A bilayered TiO_2 PC structure featuring dense arrays of smooth-walled nanotubes and a periodic structure along axial direction can be obtained by periodic current pulse anodization followed by heat treatment and a single constant current anodization step [153]. Aperiodic TiO_2 nanotube PCs with a gradually decreasing lattice constant (in an arithmetic sequence) can be synthesized by time-decreasing current density pulse anodization [166]. These TiO_2 PCs have demonstrated their applicability in a variety of applications, including sensing [150], photonics [46,164,165], dye-sensitized solar cells [151–153], photovoltaics [166] and PEC H_2 evolution [34–36], to name a few. Some excellent review articles introducing fundamental concepts and realization of TiO_2 nanotube structures are provided in [16,37,69].

Figure 4 shows schematic illustrations of representative NAA- and TiO_2-based PCs fabricated by anodization of aluminium and titanium substrates, including SEM images, anodization profiles and characteristic PSBs of these EENM-based PC materials. Figure 4a presents schematics of various nanostructures of EENM-based PC including (i) NAA in the form of NAA-DBRs, NAA-GIFs and NAA-μCVs, and (ii) TiO_2 in the form of bilayer TiO_2-PCs, aperiodic TiO_2-PCs and periodic TiO_2-PCs. Figure 4b presents the geometric and optical features as well as the anodization profile employed to fabricate (i) NAA-μCVs and (ii) periodic TiO_2-PCs. NAA-μCVs composed of a physical cavity layer sandwiched between two highly reflective mirrors (i.e., NAA-GIFs) were fabricated by sinusoidal pulse anodization and feature a resonance band within the characteristic PSB (Figure 4b(i)). Periodic TiO_2-PCs featuring small voids around each stack interface and broad PSBs over the entire visible spectrum were obtained under current pulse anodization (Figure 4b(ii)).

Although anodization of valve metals such as Fe, Zr, W, Nb, Hf, V and Co has been demonstrated successfully, the production of PC structures based on the anodic oxides of these valve metals remains challenging [16,57,60–68,157]. The development of advanced PC structures with precisely controlled

optical properties is still limited. Therefore, future developments in anodization of these valve metals to fabricate PCs will be essential to spread the applicability of EENMs across many technological disciplines, including photocatalysis and photovoltaics.
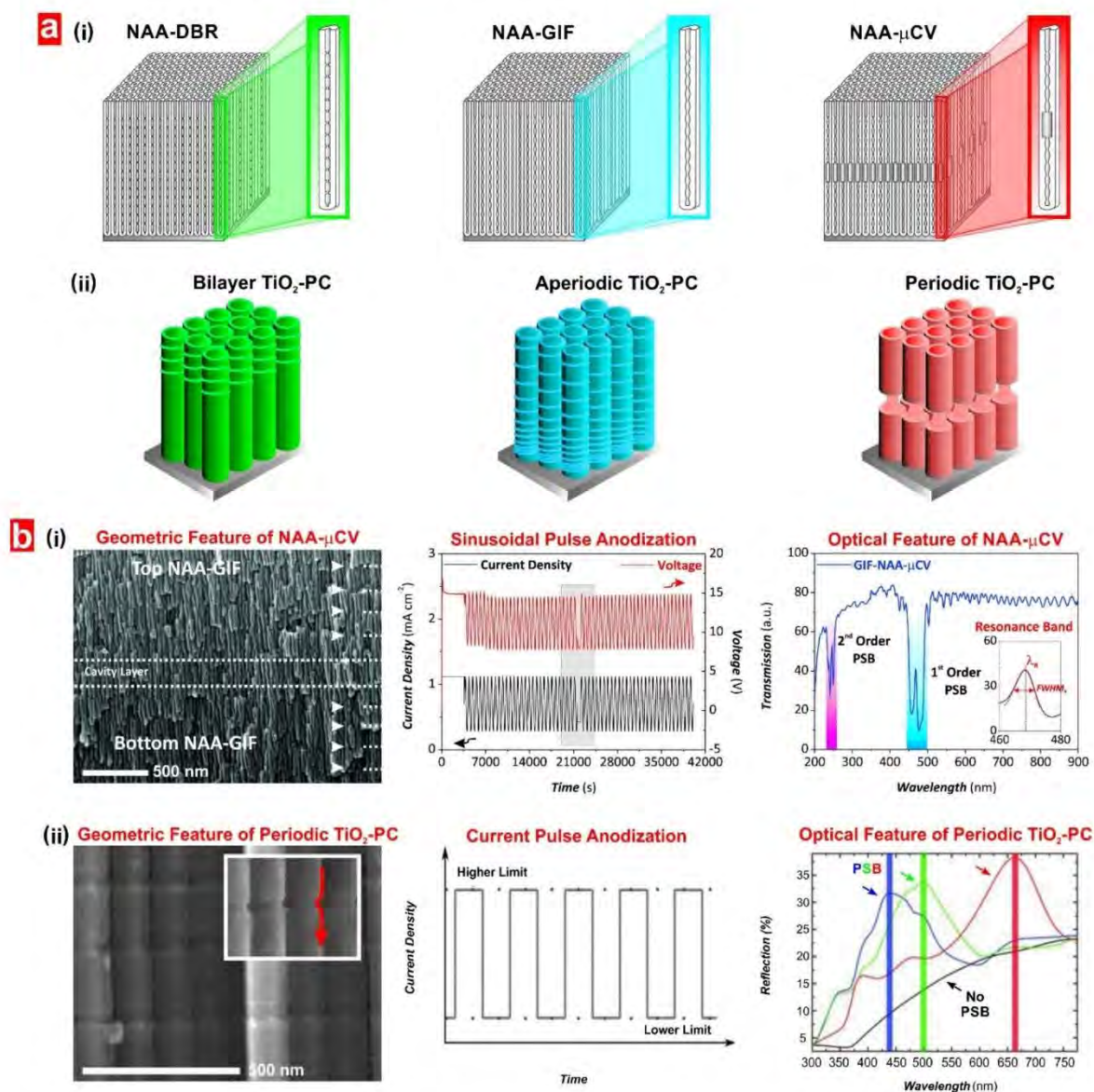

Figure 4. Structural engineering of electrochemically engineered nanoporous materials (EENMs) by anodization. (**a**) Schematics showing examples of (**i**) nanoporous anodic alumina photonic crystals (NAA-PCs) (i.e., NAA-DBR—NAA distributed Bragg reflector; NAA-GIF–NAA gradient-index filter; NAA-μCV–NAA optical microcavity), and (**ii**) TiO$_2$ photonic crystals (TiO$_2$-PCs) (i.e., bilayer, aperiodic and periodic). (**b**) Representative SEM images (left), anodization profile (center) and photonic stopbands (PSBs) (right) of (**i**) NAA-μCV and (**ii**) periodic TiO$_2$-PCs. Reproduced from [160], with copyright permission from the Royal Society of Chemistry, 2018, and [164], with copyright permission from Wiley-VCH Verlag GmbH & Co. KGaA, Weinheim, 2011, respectively.

5. Electrochemically Engineered Nanoporous Materials for Photocatalysis

EENMs have been devised as platform materials for photocatalysis due to their unique physical, chemical, electrical and optical properties. EENMs can be used under open-circuit conditions or as a photoanode together with an inert or catalytic cathode such as Pt, C and others. The effective

medium, surface chemistry and crystallinity of EENMs can be precisely engineered for enhanced photocatalytic applications, including open-circuit dye degradation, and OCP and PEC H_2 generation. In many cases, photocatalytic performances of EENMs are superior to those of benchmark photocatalyst nanoparticles due to different phenomena, including an increase in effective surface area, enhanced orthogonal carrier separation, the formation of electronic junctions and optimized geometry and crystallinity [37]. This section summarizes the most important factors affecting the photocatalytic activity of EENMs and gives a brief overview of current efforts towards EENM-based photocatalytic and photo-electrocatalytic systems.

5.1. Key Factors Influencing Photocatalysis

A common factor influencing the photocatalytic performance of EENMs is the crystal structure (i.e., polymorph and facets). EENMs fabricated by anodization are amorphous in nature but their crystalline structure can be modified by post-annealing treatment. Crystallinity affects the conductivity of the anodic oxide and lifetime of charge carriers in the structure of the photocatalyst material. For instance, annealing TiO_2 nanotube structures in air with increasing annealing temperature >300 °C results in better photocatalytic activities due to the formation of anatase crystals and the higher crystallinity degree of TiO_2 [18]. When TiO_2 nanotubes are annealed at 650 °C, anatase–rutile crystal junctions are formed, enhancing photocatalytic degradation of pollutants and OCP H_2 evolution under solar light or UV laser illumination due to band offsets and increment in light absorption. However, careful control over annealing temperature and oxidizing conditions (i.e., in O_2) is required since these conditions may deteriorate the nanostructures or lead to the formation of other crystal structures that might detrimentally affect photocatalytic performances [37]. Exposure of different crystal planes of crystalline structures also influences the photocatalytic activity of EENMs in photocatalysis due to the intrinsically different energetic nature between distinct planes and the formation of microjunctions. Lee et al. observed photocatalytic enhancements in anatase TiO_2 nanotubes featuring predominantly highly energetic {001} facets (i.e., TNT-11 fabricated at an anodization time of 11 h) using the photocatalytic degradation of Rhodamine B as an indicator [19]. Enhancements were attributed to these high energetic facets, which provide sites to boost the production of active oxygen species such as $\cdot OH$, $\cdot O_2^-$ and H_2O_2 upon UV irradiation (Figure 5a).

The structural features of EENMs play a key role in enhancing photocatalysis. In general, a strong increase in photocatalytic degradation kinetics of organic pollutants can be observed with increasing nanopore length, which is attributed to an enhanced light absorption efficiency and a specific surface area increase (Figure 5b) [18,22,37]. Other geometric features influencing the photocatalytic performance of EENMs are the nanopore/nanotube diameter, surface features and sidewall roughness [37]. EENMs in the form of PC structures provide other approaches to further enhance the utilization of light for further boosting photocatalytic or PEC reactions. [22–25,39–43]. The chemical structure of EENMs can be intrinsically or extrinsically modified to improve their photocatalytic performance by formation of heterojunctions to change surface band bending, creation of suitable surface states for efficient charge exchange, integration of co-catalytic effects for photocatalytic and PEC reactions, incorporation of LSPR effects to concentrate electromagnetic fields in the vicinity of metal particles for more efficient light-harvesting, and increasing specific surface area [37]. These phenomena are strongly dependent on the elements or materials incorporated into the structure of EENMs and the type of treatment applied. For instance, OCP H_2 evolution by TiO_2 nanotubes can only be significantly enhanced with the presence of co-catalysts such as Pt nanoparticles and by exposure of the EENM to activating treatments such as H_2-annealing and ion-implantation. On the other hand, the conductivity of TiO_2 nanotubes can be adjusted to attain optimal PEC activities by doping their structure with visible-light transition metals (i.e., Nb, Ta, Ru, etc.) or exposure to reductive treatments (Figure 5c).

5.2. Non-Structurally Engineered Nanoporous Materials Produced by Anodization

TiO_2 nanotubes produced by anodization of Ti substrates have been extensively employed for photocatalysis, especially for the conversion of sunlight green energy (H_2 gas), photodegradation of harmful environmental organic pollutants, and photosynthesis organic compounds and photocatalytic-based biomedical applications. TiO_2 is regarded as the benchmark photocatalytic material due to its low cost, high photostability, strong chemical resistance and excellent electronic properties [16,37,69]. Anodization of Ti substrates under specific conditions results in hexagonally ordered TiO_2 nanotube arrays, which grow perpendicularly to the surface of the underlying Ti substrate. From a photocatalysis point-of-view, TiO_2-based nanotubular structures provide several advantages, including an increase in specific surface area, efficient orthogonal charge carrier separation and formation of well-defined electronic gradients.
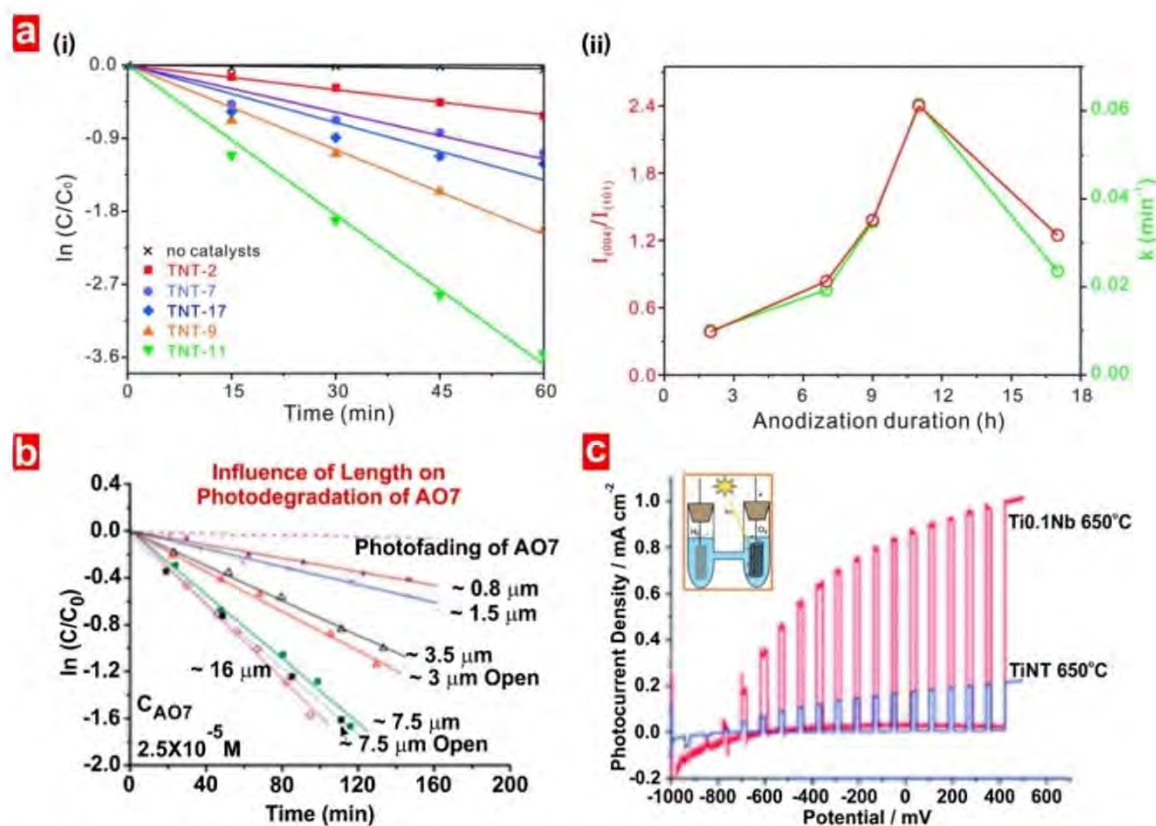

Figure 5. Examples of key factors that influence the photocatalytic activity of TiO_2 nanotubes. (**a**) (**i**) Photocatalytic degradation kinetics for Rhodamine B by TiO_2 nanotubes fabricated with different anodization time, and (**ii**) (red) (004/101) facets intensity ratios and (green) photocatalytic rate constants as a function of anodization time. Reproduced from [19], with copyright permission from the Royal Society of Chemistry (RSC) on behalf of the Centre National de la Recherche Scientifique and the RSC, 2016. (**b**) Influence of TiO_2 nanotube layer thickness on the photocatalytic degradation of AO7. Reproduced from [37], with copyright permission from American Chemical Society, 2017. (**c**) Photocurrent transients as a function of applied potential for TiO_2 and Ti0.1Nb nanotubes annealed at 650 °C demonstrating the water splitting performance in 1 M KOH under AM 1.5 condition. Reproduced from [7], with copyright permission from the Royal Society of Chemistry, 2011.

Already pristine TiO_2 nanotubes perform relatively fast photodegradation of various organic pollutants in water such as herbicides [167,168], pharmaceutical compounds [169,170], organochlorine compounds [171,172], cosmetic compounds [170] and azo or organic dyes [4,19]. Some of these processes have been assessed for real-life photocatalytic applications, using water matrices with

three different common water constituents (i.e., bicarbonate ions, phosphate ions and natural organic matters) [168,169]. Similarly, pristine TiO_2 nanotubes were shown to have excellent photocatalytic capabilities in the decomposition of gaseous volatile organic compounds such as acetylaldehyde [5], methane [6], hexane [27] and toluene [173]. Despite having demonstrated excellent photocatalytic performances in degrading organic pollutants in air and water, the average ratio of the efficacy of TiO_2 over the benchmark photocatalyst form of TiO_2–P25 TiO_2 nanoparticles–was only ~1 and 1.5 for air and water, respectively [174]. Numerous studies have performed chemical modifications of as-produced TiO_2 nanotubes, either intrinsically or extrinsically by anodization of alloy substrates [84,85,89], doping [33,76–79,91,94], reduction treatments [95,96], ALD [26,115,116], electrodeposition [110] and decoration with nanoparticles [21,89,124–138]. These TiO_2-based nanotubular structures have shown superior photocatalytic activities over pristine TiO_2 nanotubes for the degradation of various organic pollutants in water, particularly organic and azo dyes. For instance, Sopha et al. deposited uniform TiO_2 coatings by ALD within TiO_2 nanotube layers fabricated by anodization for photocatalysis (Figure 6a) [26]. An efficient charge carrier separation and high surface area were achieved for TiO_2 nanotubes (i.e., the thickness of anodic film ~5 μm and a diameter of nanotubes ~230 nm), with an optimal ALD TiO_2 coating thickness of ~11 nm.

The photocatalytic performance of ALD TiO_2 coated TiO_2 nanotubes (i.e., TNT with 200 cycles of ALD) was also found to be superior to their uncoated or TiO_2 nanoparticle-decorated counterparts by 72% and 88%, respectively, in degrading methylene blue under 365 nm UV light illumination. TiO_2 nanotubes modified with P, W, Mn, Pt, TiO_2, Bi_2S_3 and lanthanides by doping, anodization of alloy substrates, decoration with quantum dots and ALD have also shown successful photocatalytic degradation of gaseous pollutants (i.e., toluene, hexane) [27,79,90,130,175] and the photoreduction of Cr^{6+} [176]. In many of these cases, doped TiO_2 nanotubes achieved better photocatalytic performance than their pristine analogues. Despite the advantages of chemically modified TiO_2 nanotubes for photocatalysis, the addition of coating onto TiO_2 nanotubes may not necessarily have the same beneficial effect for the photocatalytic degradation of organic pollutants in air and water. For instance, Sopha et al. have reported that ALD TiO_2 coatings in TiO_2 nanotube layers do not enhance the photocatalytic degradation of hexane in air due to a reduction of active surface area (Figure 6b) [27]. Several studies have explored the application of TiO_2 nanotubes for photocatalytic conversion of CO_2 into CH_4 (in a wet gas phase) or CH_3OH (in liquid H_2O) in the presence of H_2O [177,178], including modified TiO_2 nanotube crystal structures with dopants [9] and decoration with co-catalyst nanoparticles [9,30,179] under UV, UV-visible and solar sunlight irradiation conditions.

For example, Varghese et al. developed N-doped TiO_2 nanotubes decorated with Pt and/or Cu co-catalyst nanoparticles to photo-reduce CO_2 with H_2O vapour under outdoor sunlight irradiation (Figure 6c) [9]. Strategies to enhance photocatalytic CO_2 conversion rates in TiO_2 nanotubular structures include (i) employing high specific surface area of TiO_2 nanotubes with a wall thickness thin enough to facilitate efficient transportation of photogenerated charge carriers to surface species; (ii) introducing N dopants to modify TiO_2 bandgap for absorbing and utilizing visible light; and (iii) distributing co-catalyst nanoparticles on nanotubes to efficiently adsorb reactants and aid redox reactions. Upon natural sunlight irradiation, a very high hydrocarbon production rate of ~111 ppm cm^{-2} h^{-1} was achieved, which is at least 20 times higher than those reported for Pt/TiO_2 under UV illumination. Nevertheless, conversion of CO_2 to useful fuels is still kinetically hindered by the energetically disadvantageous nature of the two electron transfer steps involved in the conversion process.

Chemically modified TiO_2 nanotubes have also been widely investigated for their potential in photocatalytic [20,28,29,97–99,103,117,123] and photo-electrocatalytic [7,31,74,86–88,109] water splitting to generate clean H_2. TiO_2 nanotubes split water efficiently as photoanodes in a photo-electrochemical setting with an ideal electrode (such as Pt) for "slow" cathodic H_2 evolution reaction under voltage bias [179]. Photoanodes based on TiO_2 nanotubes have been reported to be more promising than nanoparticulate layers due to their well-defined geometry and incorporation with co-catalysts (i.e., CuO and NiO) [31,109] or dopants (i.e., Nb, Ru, C and Ta) [7,74,86–88]. Particularly

promising results regarding the modification of TiO_2 nanotubes for water splitting have been reported by Roy et al. [87] and Yoo et al [88]. TiO_2 nanotubes were synthesized by anodizing low concentration Ti-Ru alloys, where Ru in TiO_2 can either act as a dopant for PEC water splitting or be present as RuO_2 to act as a co-catalyst for O_2 evolution. In PEC experiments, Roy et al. successfully demonstrated very high light-to-H_2 conversion efficiencies of an almost six-fold increase for intrinsically Ru-doped TiO_2 nanotubes in comparison with undoped TiO_2 nanotubes in terms of photocurrent density (Figure 6d) [89]. While TiO_2 can be used as a platform material to perform the photocatalytic synthesis of organics, the high selectivity required for organic synthesis is often not reached due to the non-selective character of generated free radicals (e.g., ·OH radicals) upon light irradiation [37]. However, modification of the electronic properties and nanoporous geometry of TiO_2 can steer carrier energies and lifetimes to overcome this inherent constraint [13,14]. Recently, Tripathy et al. demonstrated modification of crystal structures (i.e., anatase or rutile) and/or incorporation of Ru dopant into TiO_2 nanotubes for photocatalytic oxidation of toluene under 325 nm UV light illumination (Figure 6e) [13]. A significant change in the main reaction product (i.e., benzoic acid versus benzaldehyde) can be achieved, where certain undesired reaction pathways can be completely shut down due to the change in the electronic properties by Ru doping. Ru states prevent the formation of intermediate superoxide radicals, switching the reaction product from toluene to benzoic acid. The geometric features of TiO_2 nanotubes also show higher selectivity than that of nanoparticle-based layers, indicating that the combination of nanoarchitecture and tailor-engineered electronic bands of photocatalyst materials are a promising approach for achieving high selectivity in organic synthesis.

Nanotubular TiO_2 structures also provide new opportunities to induce chain scission in functional organic monolayers (i.e., silanes and phosphonates) for drug delivery applications [180–182]. When exposed to UV light, scission of organic chains occurs on anchoring groups, leaving the inorganic section of these molecules attached to the surface of TiO_2 nanotubes. As-produced and Fe_3O_4 nanoparticle-decorated TiO_2 nanotubes have also shown potential for photocatalytic killing of cancer cells under UV light irradiation [182,183]. Faraji et al. have shown that TiO_2 nanotubes modified with Ag/Benzene have effective sterilization effects by degrading a resilient bacterium such as Escherichia coli (E. coli) under UV and visible light irradiation due to LSPR effect and efficient charge separation (Figure 6f) [184].

Other pristine and chemically modified oxide nanotubes such as ZrO_2 [185], WO_3 [186,187] and Co_3O_4 [68] have also been investigated for various photocatalytic and photo-electrocatalytic applications, including degradation of organic pollutants, water splitting and CO_2 reduction, due to their favorable band-edge positions, superior chemical stability, and low cost. Although NAA is an electronic insulator with a wide energy bandgap (i.e., 8.0–9.5 eV), the inner surface of this EENM can be modified with semiconductor materials for photocatalysis. Several studies have demonstrated successful photocatalytic applications of semiconductor-modified NAA-based platforms, including CO_2 reduction [10] and photodegradation of organic pollutants [122,188].
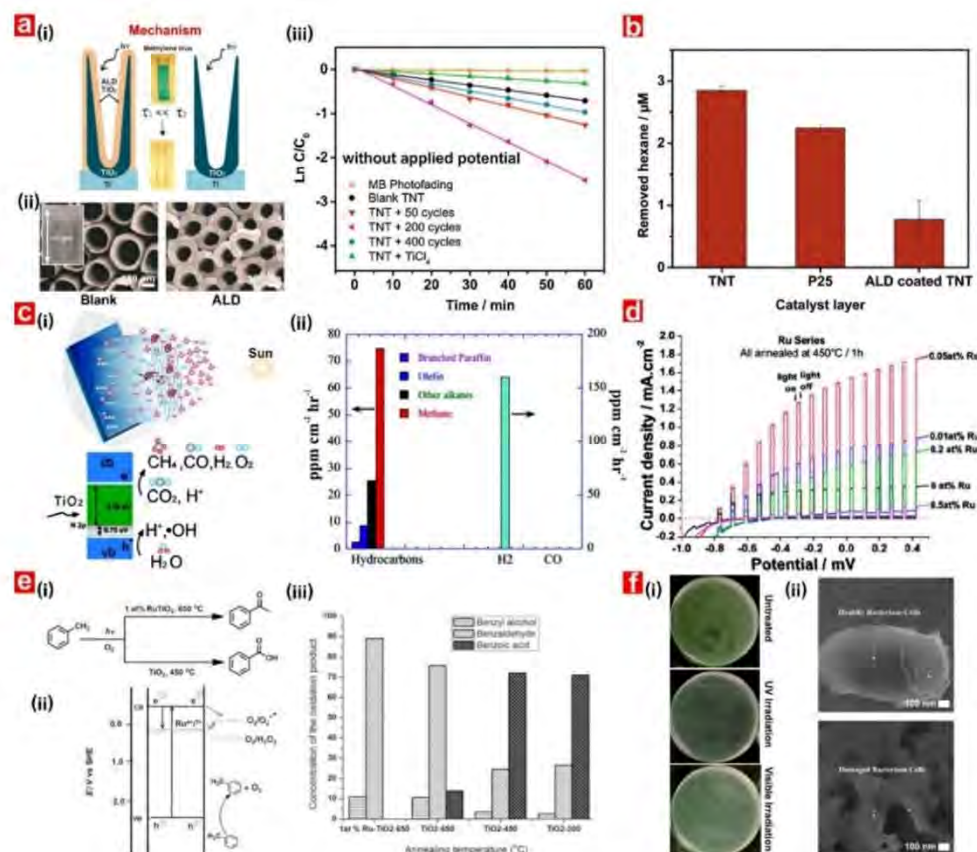
40

Figure 6. Applicability of non-structural electrochemical engineered nanoporous materials (EENMs) in photocatalytic and photoelectrochemical applications. (**a**) (**i**) Photocatalytic degradation mechanism for methylene blue by TiO_2 nanotubes coated with TiO_2 layers via ALD; (**ii**) SEM images of pristine and ALD TiO_2 coated TiO_2 nanotubes; and (**iii**) photocatalytic degradation rates of MB for blank, ALD TiO_2 coated TiO_2 nanotubes (50, 200 and 400 cycles) and TiO_2 nanoparticle-decorated TiO_2 nanotubes ($TiCl_4$) under UV light illumination. Reproduced from [26], with copyright permission from Elsevier Ltd., 2017. (**b**) Photocatalytic removal of hexane in air for three different TiO_2-based photocatalysts under UV light illumination. Reproduced from [27], with copyright permission from Elsevier B.V., 2018. (**c**) (**i**) Schematic illustration of sunlight-driven photocatalytic CO_2 reduction using N-doped TiO_2 nanotubes surface-loaded with Cu and/or Pt co-catalyst nanoparticles; (**ii**) Product evolution rates from N-doped TiO_2 nanotubes annealed at 600 °C and surface loaded with 52% Cu and 48% Pt nanoparticles. Reproduced from [9], with copyright permission from American Chemical Society, 2009. (**d**) Photo-electrochemical water splitting: photocurrent transient vs. potential curves in 1 M KOH solution using an Ag/AgCl reference electrode under AM 1.5 illumination for different Ru substrate contents (0%–1.2%) TiO_2 nanotubes annealed at 450 °C for 1 h. Reproduced from [87], with copyright permission from American Chemical Society, 2011. (**e**) Tuning reaction selectivity: (**i**) illustration of different photocatalytic pathways on TiO_2 nanotubes, (**ii**) illustration of the band position during toluene oxidation on pristine and Ru-doped TiO_2 nanotubes under UV irradiation; and (**iii**) product distribution from the oxidation of toluene after 4 h UV exposure of pristine and Ru-doped TiO_2 nanotubes. Reproduced from [13], with copyright permission from Wiley-VCH Verlag GmbH & Co. KGaA, Weinheim, 2014. (**f**) (**i**) Digital images of bacteria colony counting (dilution: 10-4) showing the antibacterial activity of Ag/benzene modified TiO_2 nanotubes in different irradiation conditions after 1 h; and (**ii**) SEM images of bacteria cell before (top) and after (bottom) exposure to Ag/benzene modified TiO_2 nanotubes under visible light irradiation. Reproduced from [184], with copyright permission from the Royal Society of Chemistry (RSC) on behalf of the Centre National de la Recherche Scientifique and the RSC, 2018.

5.3. Structurally Engineered Nanoporous Materials Produced by Anodization

Although various structurally engineered forms of TiO_2-PCs have been synthesized by anodization [34–36,46,150–153,164–166], only pristine and noble metal (i.e., Ag or Au) decorated hierarchical nanotubes have been investigated for clean H_2 energy generation via PEC water splitting [34–36]. Zhang et al. developed hierarchical TiO_2 nanotubes by varying the voltage during a two-step constant anodization for PEC water splitting (Figure 7a) [34]. Hierarchical TiO_2 nanotube arrays were composed of a periodically organized nanoporous layer on top of a uniform nanotube array, in which the top nanoporous structure served as a PC to enhance optical absorption of the overall photocatalyst platform. Of all the hierarchical TiO_2 structures assessed in this study (i.e., nanoring (top)/nanotube (bottom), nanopore (top)/nanotube (bottom) and nanohole-nanocave (top)/nanotube (bottom)), the nanopore (top)/nanotube (bottom) configuration achieved the highest photocurrent density value (i.e., $1.59\,mA\,cm^{-2}$ at 1.23 V vs RHE) under AM 1.5G illumination. Lian et al. prepared Ag quantum dots-modified hierarchical TiO_2 nanostructures (i.e., nanoring (top)/nanotube (bottom)) utilizing a similar fabrication method for PEC H_2 evolution under visible light irradiation [35]. A high photocatalytic H_2 evolution rate (i.e., $124.5\,\mu mol\,cm^{-2}\,h^{-1}$) was achieved, which was attributed to synergetic effects of Ag and the hierarchical PC structure. This smart design makes it possible to harness strong LSPR effect and anti-shielding effect of ultrafine Ag quantum dots within the same photocatalyst platform (Figure 7b).

Zhang et al. developed TiO_2 nanotube-based PCs by voltage variation during the second anodization step flowing a stepwise profile between high and low voltage to compensate for the loss of electric field intensity [36]. This fabrication approach improves periodicity and uniformity of the nanoporous top layer of hierarchical TiO_2 nanostructures, which are critical factors for the formation of an effective PC structure with well-resolved photonic stopband (PSB). Nanoring (top)/nanotube (bottom) hierarchical TiO_2 structures feature well-defined PSBs, which can be finely tuned across high-irradiance spectral regions for enhanced photocatalytic and PEC performances [34].
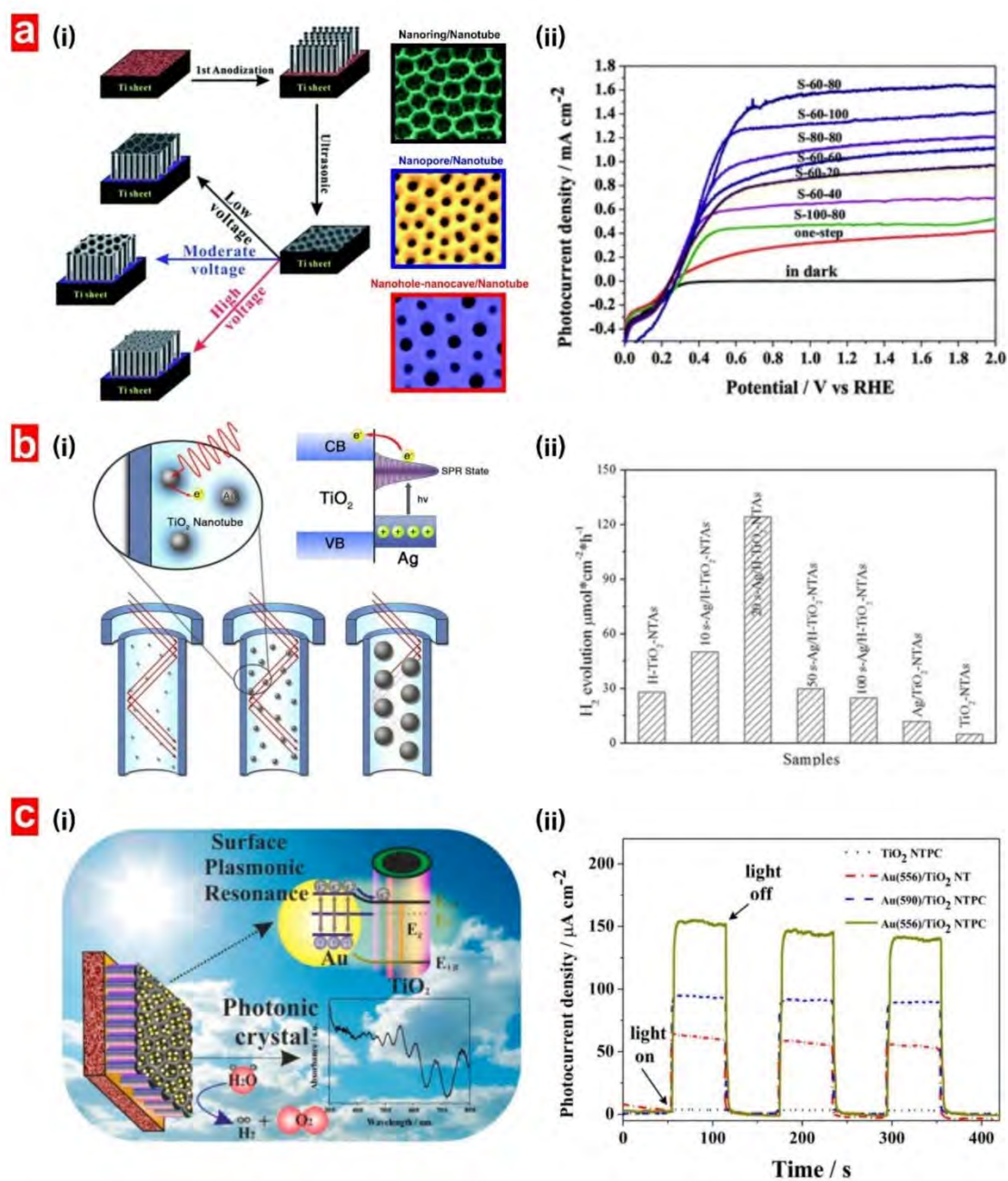
Figure 7. Examples of applicability of pristine and noble metal-decorated hierarchical TiO_2-PCs in photoelectrochemical (PEC) H_2 evolution. (**a**) (**i**) Two-step anodization process (left) and SEM images of various top layer nanostructures (right) of hierarchical TiO_2-PCs, and (**ii**) PEC water splitting performances in terms of linear-sweep voltammograms collected with a scan rate of 5 mV s^{-1} in dark and under illumination for various hierarchical TiO_2-PCs. Reproduced from [34], with copyright permission from the Royal Society of Chemistry, 2012. (**b**) (**i**) Light penetration mechanism in Ag nanocrystal-loaded hierarchical TiO_2-PCs, and (**ii**) PEC H_2 production rate by various TiO_2-based photocatalyst platforms under visible light irradiation. Reproduced from [35], with copyright permission from Scientific Reports, 2015. (**c**) (**i**) Summary of Au-decorated hierarchical TiO_2-PCs for PEC water splitting, and (**ii**) amperometric *I-t* curve at an applied potential of 1.23 V vs RHE under visible light illumination with 60 s light on/off cycles. Reproduced from [36], with copyright permission from American Chemical Society, 2013.

Furthermore, Zhang et al. assembled 20 nm Au nanocrystals onto these PC structures and achieved a photocurrent density of ~150 µA cm^{-2} at 1.23 V vs RHE, which is the highest value reported to date in

hybrid plasmonic Au/TiO_2 system for PEC water splitting under visible light irradiation (Figure 7c) [36]. This significant enhancement was ascribed to match the SPR absorption to the PSB of the PC structure, where the PC structure can localize, trap and provide multiple passes for plasmonically active photons generated around the Au nanocrystals. Thus, the average photon path length is increased and results in an enhanced SPR intensity of the Au nanocrystals for efficient PEC water splitting.

Despite providing outstanding light-harvesting capabilities, NAA-based PC structures produced by anodization of aluminium cannot be used for photocatalysis applications due to the high energy bandgap of alumina. However, recent studies have demonstrated promising results in the development of photocatalysts PCs based on surface-modified NAA-PCs. Lim et al. have explored for the first time the capabilities of NAA-GIFs functionalized with TiO_2 (TiO_2-NAA-GIFs) to enhance photon-to-electron conversion rates and improve photocatalytic reactions by "slow photon" effect (Figure 8) [22].
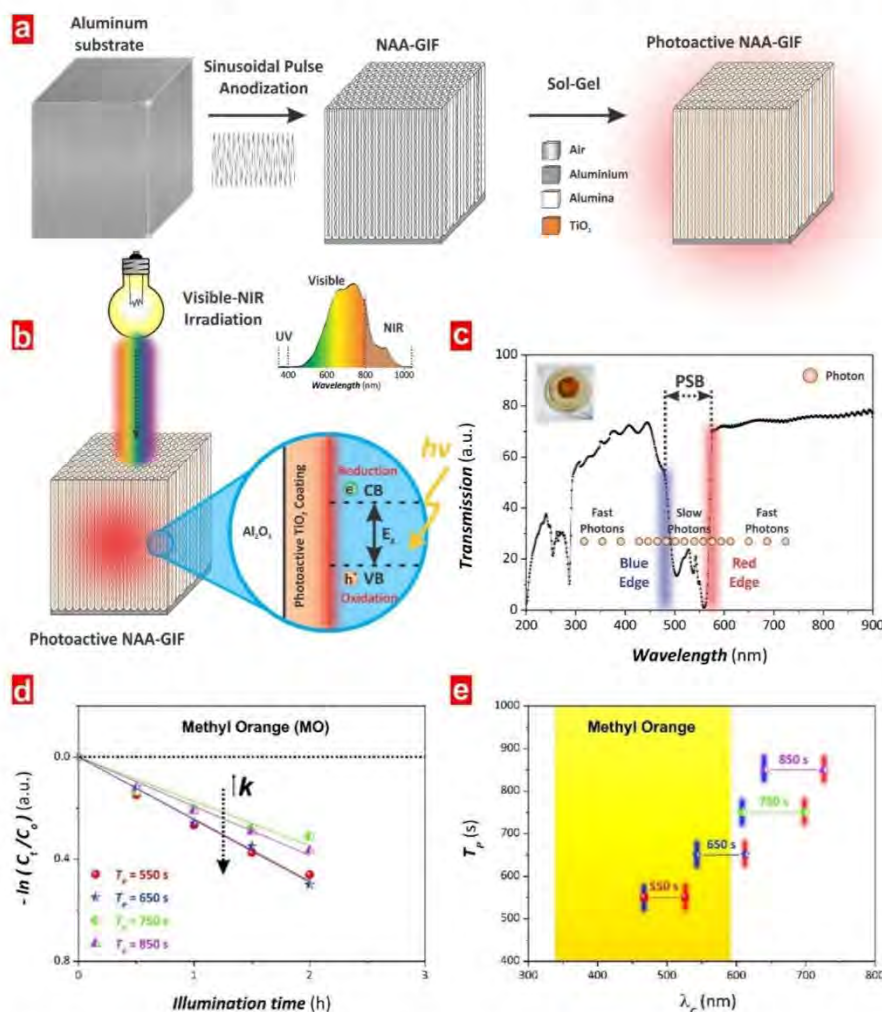

Figure 8. Applicability of TiO_2-NAA-GIFs in photocatalytic degradation of organics. (**a**) Schematic representation of the fabrication process of TiO_2-NAA-GIFs; (**b**) schematic showing the utilization of TiO_2-NAA-GIFs in photocatalysis under controlled visible–NIR irradiation conditions; (**c**) transmission spectrum of a representative TiO_2-NAA-GIFs showing the blue and red edges of the PSB, where photons at the blue and red edges of the PSB slow down their group velocity after interacting with the PC structure; (**d**) photocatalytic degradation kinetics for methyl orange (MO) by TiO_2-NAA-GIFs fabricated with varying anodization period (T_P) under controlled irradiation conditions; and (**e**) relative position of the blue and red edges of the characteristic PSB of TiO_2-NAA-GIFs produced with various T_P and the absorbance band of MO. Reproduced from [22], with copyright permission from American Chemical Society, 2018.

NAA-GIFs were fabricated by sinusoidal pulse anodization and functionalized with photoactive layers of TiO_2 through the sol-gel method. The photocatalytic performance of TiO_2-NAA-GIFs was assessed by studying the photodegradation of three model organic dyes (i.e., methyl orange–MO, methylene blue–MB and rhodamine B–RhoB) with well-defined absorption bands across different spectral regions under visible–NIR irradiation conditions. TiO_2-NAA-GIFs achieved high photocatalytic performances (k) in the degradation of MO, RhoB and MB (i.e., $k_{MO} = 0.25$ h^{-1}, $k_{RhoB} = 0.39$ h^{-1} and $k_{MB} = 2.10$ h^{-1}). These NAA-based PCs outperformed other forms of semiconductor photocatalysts such as pristine TiO_2 nanotubes, 3D TiO_2 PCs and P25 nanoparticles under simulated solar light irradiation. Performance enhancements were ascribed to the "slow photon" effect, where a group of incoming photons propagate with strongly reduced group velocity and are localized in high (i.e., photocatalysts) and low (i.e., dye and pores) dielectric parts of the red and blue edges of the PSB of these PC structures, respectively. Slow photons collected by the underlying NAA-GIF structure can be efficiently utilized by the photoactive TiO_2 layer to generate extra e$^-$/h$^+$ pairs and increase photon-to-electron conversion rates. Spectral alignment of the characteristic PSBs of TiO_2-NAA-GIFs to the specific absorption bands of the organic dyes was demonstrated to significantly enhance the photodegradation rate of these organic dyes.

Lim et al. have also prepared NAA-DBRs and functionalized with photoactive TiO_2 layers for assessing their photocatalytic performance associated with "slow photon" effect in the degradation of model organics under visible–NIR irradiation conditions (Figure 9) [23]. These TiO_2-NAA-DBRs achieved better photocatalytic performances (i.e., $k_{MO} = 0.32$ h^{-1}, $k_{RhoB} = 0.35$ h^{-1} and $k_{MB} = 3.04$ h^{-1}) than those of TiO_2-NAA-GIFs. The measured enhanced performances were attributed to a better light collection associated with the broader and more intense characteristic PSB of NAA-DBR structures fabricated by stepwise pulse anodization (STPA). Real-life application of TiO_2-NAA-DBRs to degrade resilient organochlorine compounds such as 4-chlorophenol in various environmental matrices and the reusability of these composite PC structures over five cycles were also demonstrated [23].
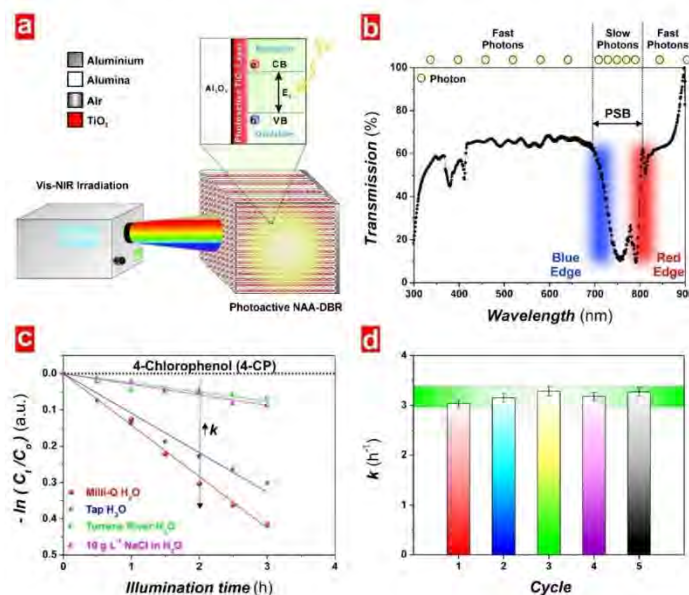

Figure 9. Applicability of TiO_2-NAA-DBRs in photocatalytic degradation of organics. (**a**) Schematic of setup used to assess the photocatalytic performance of TiO_2-NAA-DBR under visible–NIR irradiation conditions; (**b**) representative transmission spectrum of NAA-DBRs showing details of the characteristic PSB with its blue and red edges denoting reduced group velocity of photons across these spectral regions; (**c**) photocatalytic degradation kinetics of 4-chlorophenol (4-CP) in different aqueous matrices by TiO_2-NAA-DBR under controlled irradiation conditions; and (**d**) reusability test of TiO_2-NAA-DBRs on the photodegradation of methylene blue (MB) under simulated solar light irradiation. Reproduced from [23], with copyright permission from American Chemical Society, 2019.

45

Liu et al. have recently fabricated TiO$_2$-NAA-μCVs by a combination of rationally designed sinusoidal pulse anodization and the sol-gel method and explored their applicability in photodegradation of the model organic dyes (i.e., MO, RhoB and MB) under visible–NIR irradiation conditions (Figure 10) [24]. Unlike the optical phenomena (i.e., "slow photon" effect) of other NAA-PC-based photocatalyst platforms (i.e., TiO$_2$-NAA-GIFs and TiO$_2$-NAA-DBRs) used to enhance the photocatalytic reactions, photocatalytic enhancements in TiO$_2$-NAA-μCVs are attributed to a highly efficient recirculation and confinement of incoming photons with energies within the resonance band of these PC structures.
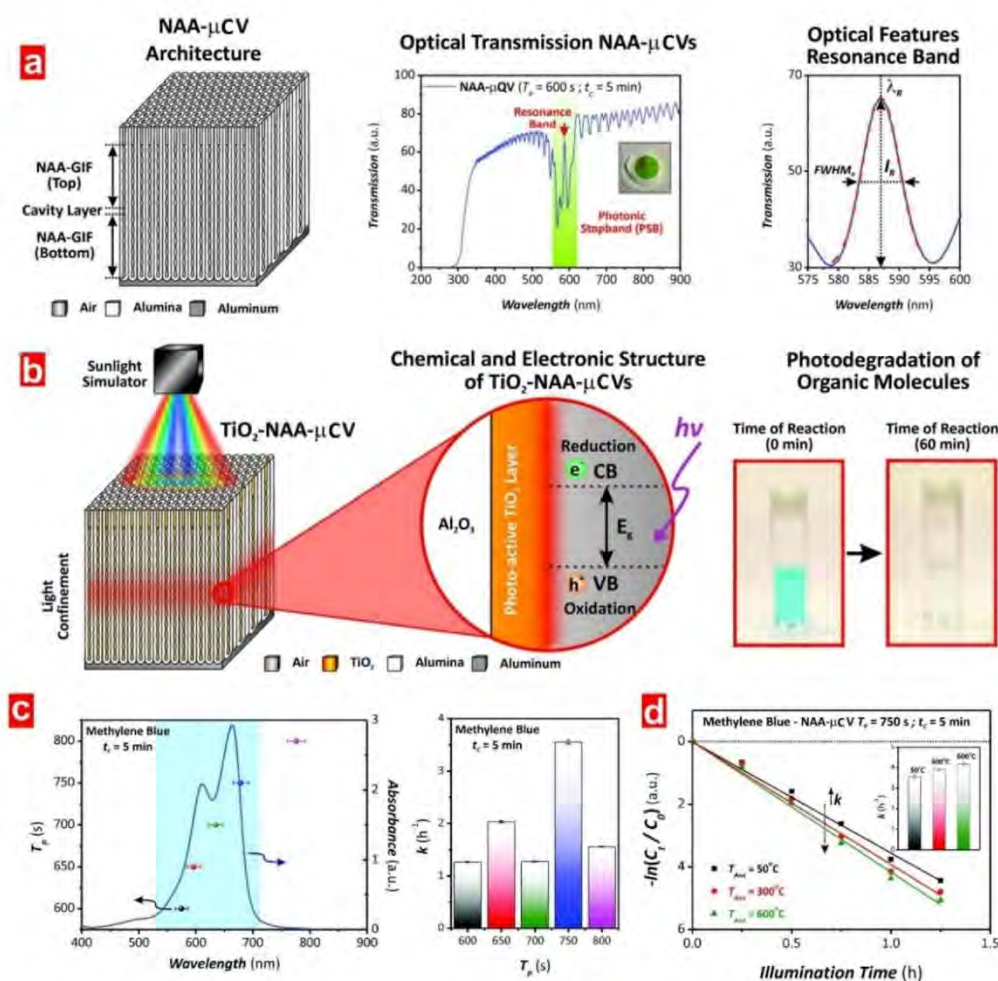

Figure 10. Applicability of TiO$_2$-NAA-μCVs in photocatalytic degradation of organics. (**a**) Illustration of the architecture of NAA-μCVs and representative transmission spectrum of a NAA-μCV with a magnified view of the resonance band and a graphical description of its optical features; (**b**) schematic showing the photocatalytic activity of TiO$_2$-NAA-μCVs under controlled visible-NIR irradiation conditions (left) and digital pictures showing the color change in MB from blue to transparent due to the successful photodegradation of MB by TiO$_2$-NAA-μCVs after 1h (right); (**c**) relative position between the resonance band of TiO$_2$-NAA-μCVs fabricated with varying anodization period (T_P) and the absorbance spectrum of methylene blue (MB) (left) and values of kinetic constants (k) for TiO$_2$-NAA-μCVs fabricated with various T_P (right); and (**d**) photocatalytic degradation kinetics of MB by representative TiO$_2$-NAA-μCVs annealed at different temperatures (T_{Ann}) and inset showing k values of these composite PC structures. Reproduced from [24], with copyright permission from the Royal Society of Chemistry, 2019.

This optical effect extends the lifetime of incident electromagnetic waves within the microcavity structure, thus increasing the probability of photon-to-semiconductor interactions and speeding up

photocatalytic reactions due to an increased generation of charge carriers. Photocatalytic enhancements in TiO$_2$-NAA-µCVs were found to strongly rely on the relative position between the resonance band of these NAA-PCs and the absorbance band of organic dyes, and on the light confinement quality. These composite PC structures have shown outstanding photocatalytic performances (i.e., $k_{MO} = 0.77$ h^{-1}, $k_{RhoB} = 1.34$ h^{-1} and $k_{MB} = 3.55$ h^{-1}) and demonstrated superior photocatalytic activities to other NAA-PC-based and TiO$_2$-PC-based photocatalyst platforms.

The effect of the crystallographic phase of TiO$_2$ (i.e., amorphous, anatase and rutile) modified by annealing treatment (i.e., 50, 300 and 600 °C) on the photocatalytic degradation of MB by TiO$_2$-NAA-µCVs was also investigated. TiO$_2$-NAA-µCVs featuring the rutile phase outperformed their counterparts containing amorphous and anatase phases of TiO$_2$ due to the higher tendency to trap holes and electrons for photocatalytic reactions. Lim et al. developed hybrid Au-TiO$_2$-NAA-DBRs photocatalyst platforms integrating slow photons and LSPR effects in the same photocatalyst platforms (Figure 11) [25]. Au films were deposited on the top surfaces of TiO$_2$-NAA-DBRs, and photocatalytic degradation of the MB molecules under visible–NIR illumination was used as reference reaction to assess enhancements associated with slow photon–LSPR coupling effects. However, this study demonstrated that photocatalytic enhancements are more strongly determined by "slow photon" effect than by LSPR effect due to the localized nature of generated surface plasmons on the top surface of the composite PC structures. Note, the obtained results revealed that these optical phenomena must be finely coupled in order to improve the design of noble metal-NAA-based photoactive PCs.
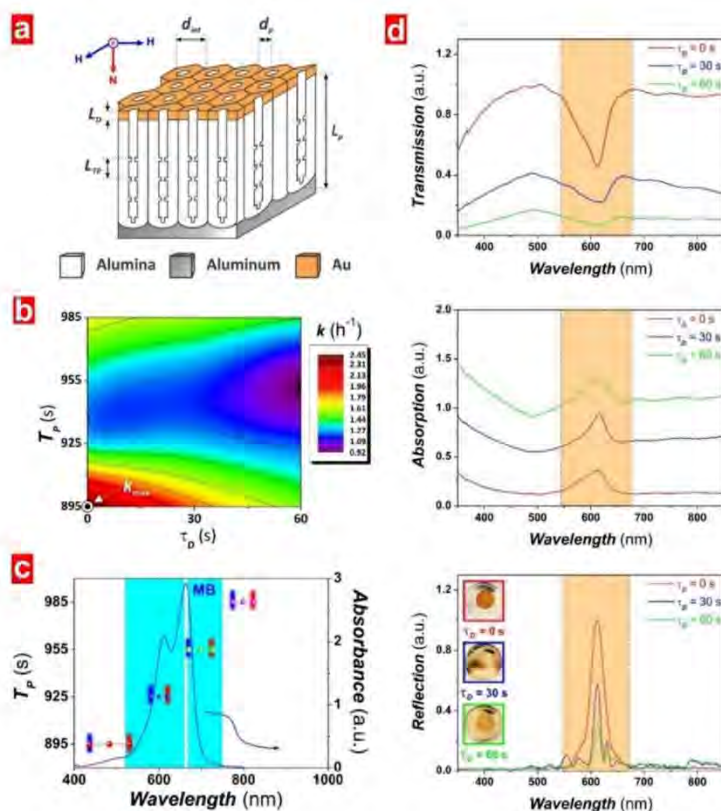
Figure 11. Applicability of Au-TiO$_2$-NAA-DBRs in photocatalytic degradation of organics. (**a**) Illustration describing the geometric features of Au-coated NAA-DBRs (i.e., total pore length–L_p, interpore distance–d_{int}; pore diameter–d_p; period length–L_{TP}; Au thickness–L_D); (**b**) representative contour plot showing the combined effect of anodization period (T_P) and Au deposition time (τ_D) on k values for photodegradation of MB by Au-TiO$_2$-NAA-DBRs; (**c**) representative relative position of the blue and red edges of the characteristic PSB of Au-TiO$_2$-NAA-DBRs produced with various T_P and the absorbance band of MB; and (**d**) optical characterization of a representative Au-TiO$_2$-NAA-DBR demonstrating localized position of the Au layer in the composite PC photocatalyst platform. Reproduced from [25], with copyright permission from the Royal Society of Chemistry, 2019.

6. Conclusions

This review provides a comprehensive overview of fundamental aspects and recent progress in EENMs as photocatalyst platforms for photocatalytic and photo-electrocatalytic applications. Over the past ten years, the potential of these nanoporous materials in pollution degradation and hydrogen evolution has been demonstrated. EENMs provide many advantages to drive photocatalytic reactions efficiently, including highly defined tailor-made self-organized nanoporous structures, outstanding control over light to harness electromagnetic waves and efficient management of charge carrier separation.

The structure of EENMs can be precisely tailored in various types of photonic crystal by anodization—an inexpensive, simple and fully scalable nanofabrication approach. These PC structures provide new opportunities to harvest incident photons by different optical phenomena such as strong localization, trapping, slowing and recirculation. The optimal structural and chemical design of EENMs makes it possible to significantly enhance photon-to-electron conversion rates for several photocatalytic applications. However, more systematic experimental investigations will be needed to fully develop this technology for high performance, real-life photocatalytic applications. Furthermore, the ability to modify EENMs by a broad range of chemical and physical methods can endow these materials with desirable properties to achieve unprecedented performances by rational design and integration of

optical and electronic structures. There remain fundamental questions regarding the optimal design of photonic and electronic band structures that can maximize the performance of hybrid semiconductor PC structures. The use of new crystalline structures, geometric features and chemical composition of EENMs, including modification of the inner surface with advanced carbonaceous materials, will be crucial aspects to overcome existing constraints in photocatalysis technology. The existing studies shown throughout this review demonstrate that EENMs have promising potential for a broad range of photocatalytic and photo-electrocatalytic applications. The photocatalytic performance and selectivity of these unique materials are found in many cases to be superior to existing photocatalysts such as nanoparticulate systems and inverted opals. Therefore, it is expected that future developments in EENMs might pave the way to new and exciting opportunities to expand the applicability of this technology across classic photocatalysis fields such as pollution remediation and hydrogen generation and cutting edge applications such as CO_2 reduction, highly selective organic synthesis, biomedical devices and self-cleaning surfaces.

Conflicts of Interest: The authors declare no conflict of interest.

References

1. Fox, M.A.; Dulay, M.T. Heterogeneous photocatalysis. *Chem. Rev.* **1993**, *93*, 341–357. [CrossRef]
2. Fujishima, A.; Honda, K. Electrochemical photolysis of water at a semiconductor electrode. *Nature* **1972**, *238*, 37–38. [CrossRef] [PubMed]
3. Yan, G.; Zhang, M.; Hou, J.; Yang, J. Photoelectrochemical and photocatalytic properties of N+S co-doped TiO_2 nanotube array films under visible light irradiation. *Mater. Chem. Phys.* **2011**, *129*, 553–557. [CrossRef]
4. Agarwal, P.; Paramasivam, I.; Shrestha, N.K.; Schmuki, P. MoO_3 in self-organized TiO_2 nanotubes for enhanced photocatalytic activity. *Chem. Asian J.* **2010**, *5*, 66–69. [CrossRef] [PubMed]
5. Liu, Z.; Zhang, X.; Nishimoto, S.; Murakami, T.; Fujishima, A. Efficient photocatalytic degradation of gaseous acetaldehyde by highly ordered TiO_2 nanotube arrays. *Environ. Sci. Technol.* **2008**, *42*, 8547–8551. [CrossRef] [PubMed]
6. In, S.; Nielsen, M.G.; Vesborg, P.C.K.; Hou, Y.; Abrams, B.L.; Henriksen, T.R.; Hansen, O.; Chorkendorff, I. Photocatalytic methane decomposition over vertically aligned transparent TiO_2 nanotube arrays. *Chem. Commun.* **2011**, *47*, 2613–2615. [CrossRef] [PubMed]
7. Das, C.; Roy, P.; Yang, M.; Jha, H.; Schmuki, P. Nb doped TiO_2 nanotubes for enhanced photoelectrochemical water-splitting. *Nanoscale* **2011**, *3*, 3094–3096. [CrossRef]
8. Liu, N.; Schneider, C.; Freitag, D.; Hartmann, M.; Venkatesan, U.; Müller, J.; Spiecker, E.; Schmuki, P. Black TiO_2 nanotubes: Cocatalyst-free open-circuit hydrogen generation. *Nano Lett.* **2014**, *14*, 3309–3313. [CrossRef]
9. Varghese, O.K.; Paulose, M.; LaTempa, T.J.; Grimes, C.A. High-rate solar photocatalytic conversion of CO_2 and water vapor to hydrocarbon fuels. *Nano Lett.* **2009**, *9*, 731–737. [CrossRef]
10. Kandy, M.M.; Gaikar, V.G. Photocatalytic reduction of CO_2 using CdS nanorods on porous anodic alumina support. *Mater. Res. Bull.* **2018**, *102*, 440–449. [CrossRef]
11. Hirakawa, H.; Hashimoto, M.; Shiraishi, Y.; Hirai, T. Photocatalytic conversion of nitrogen to ammonia with water on surface oxygen vacancies of titanium dioxide. *J. Am. Chem. Soc.* **2017**, *140*, 10929–10936. [CrossRef] [PubMed]
12. Yang, J.; Guo, Y.; Jiang, R.; Qin, F.; Zhang, H.; Lu, W.; Wang, J.; Yu, J.C. High-efficiency "working-in-tandem" nitrogen photofixation achieved by assembling plasmonic gold nanocrystals on ultrathin Titania nanosheets. *J. Am. Chem. Soc.* **2018**, *140*, 8497–8508. [CrossRef] [PubMed]
13. Tripathy, J.; Lee, K.; Schmuki, P. Tuning the selectivity of photocatalytic synthetic reactions using modified TiO_2 nanotubes. *Angew. Chem. Int. Ed.* **2014**, *53*, 12605–12608.

14. Paramasivam, I.; Avhale, A.; Inayat, A.; Boesmann, A.; Schmuki, P.; Schwieger, W. MFI-type (ZSM-5) zeolite-filled TiO$_2$ nanotubes for enhanced photocatalytic activity. *Nanotechnology* **2009**, *20*, 225607. [CrossRef]

15. Qu, Y.; Duan, X. Progress, challenge and perspective of heterogeneous photocatalysts. *Chem. Soc. Rev.* **2013**, *42*, 2568–2580. [CrossRef]

16. Paramasivam, I.; Jha, H.; Liu, N.; Schmuki, P. A review of photocatalysis using self-organized TiO$_2$ nanotubes and other ordered oxide nanostructures. *Small* **2012**, *8*, 3073–3103. [CrossRef]

17. Molina-Reyes, J.; Romero-Moran, A.; Uribe-Vargas, H.; Lopez-Ruiz, B.; Sanchez-Salas, J.L.; Ortega, E.; Ponce, A.; Morales-Sanchez, A.; Lopez-Huerta, F.; Zuñiga-Islas, C. Study on the photocatalytic activity of titanium dioxide nanostructures: Nanoparticles, nanotubes and ultra-thin films. *Catal. Today* **2020**, *341*, 2–12. [CrossRef]

18. Liu, N.; Paramasivam, I.; Yang, M.; Schmuki, P. Some critical factors for photocatalysis on self-organized TiO$_2$ nanotubes. *J. Solid State Electrochem.* **2012**, *16*, 3499–3504. [CrossRef]

19. Lee, H.; Park, T.-H.; Jang, D.-J. Preparation of anatase TiO$_2$ nanotube arrays dominated by highly reactive facets via anodization for high photocatalytic performances. *New J. Chem.* **2016**, *40*, 8737–8744. [CrossRef]

20. Lee, K.; Hahn, R.; Altomare, M.; Selli, E.; Schmuki, P. Intrinsic Au decoration of growing TiO$_2$ nanotubes and formation of a high-efficiency photocatalyst for H$_2$ production. *Adv. Mater.* **2013**, *25*, 6133–6137. [CrossRef]

21. Paramasivam, I.; Macak, J.M.; Schmuki, P. Photocatalytic activity of TiO$_2$ nanotube layers loaded with Ag and Au nanoparticles. *Electrochem. Commun.* **2008**, *10*, 71–75. [CrossRef]

22. Lim, S.Y.; Law, C.S.; Markovic, M.; Kirby, J.K.; Abell, A.D.; Santos, A. Engineering the slow photon effect in photoactive nanoporous anodic alumina gradient-index filters for photocatalysis. *ACS Appl. Mater. Interfaces* **2018**, *10*, 24124–24136. [CrossRef] [PubMed]

23. Lim, S.Y.; Law, C.S.; Markovic, M.; Marsal, L.F.; Voelcker, N.H.; Abell, A.D.; Santos, A. Rational management of photons for enhanced photocatalysis in structurally-colored nanoporous anodic alumina photonic crystals. *ACS Appl. Energy Mater.* **2019**, *2*, 1169–1184. [CrossRef]

24. Liu, L.; Lim, S.Y.; Law, C.S.; Jin, B.; Abell, A.D.; Ni, G.; Santos, A. Light-confining semiconductor nanoporous anodic alumina optical microcavities for photocatalysis. *J. Mater. Chem. A* **2019**, *7*, 22514–22529. [CrossRef]

25. Lim, S.Y.; Law, C.S.; Liu, L.; Markovic, M.; Abell, A.D.; Santos, A. Integrating surface plasmon resonance and slow photon effects in nanoporous anodic alumina photonic crystals for photocatalysis. *Catal. Sci. Technol.* **2019**, *9*, 3158–3176. [CrossRef]

26. Sopha, H.; Krbal, M.; Ng, S.; Prikryl, J.; Zazpe, R.; Yam, F.K.; Macak, J.M. Highly efficient photoelectrochemical and photocatalytic anodic TiO$_2$ nanotube layers with additional TiO$_2$ coating. *Appl. Mater. Today* **2017**, *9*, 104–110. [CrossRef]

27. Sopha, H.; Baudys, M.; Krbal, M.; Zazpe, R.; Prikryl, J.; Krysa, J.; Macak, J.M. Scaling up anodic TiO$_2$ nanotube layers for gas phase photocatalysis. *Electrochem. Commun.* **2018**, *97*, 91–95. [CrossRef]

28. Nguyen, N.T.; Altomare, M.; Yoo, J.E.; Schmuki, P. Efficient photocatalytic H$_2$ evolution: Controlled dewetting-dealloying to fabricate site-selective high-activity nanoporous Au particles on highly ordered TiO$_2$ nanotube arrays. *Adv. Mater.* **2015**, *27*, 3208–3215. [CrossRef]

29. Hejazi, S.; Altomare, M.; Mohajernia, S.; Schmuki, P. Composition gradients in sputtered Ti-Au alloys: Site-selective Au decoration of anodic TiO$_2$ nanotubes for photocatalytic H$_2$ evolution. *ACS Appl. Nano Mater.* **2019**, *2*, 4018–4025. [CrossRef]

30. Zhang, L.; Cao, H.; Pen, Q.; Wu, L.; Hou, G.; Tang, Y.; Zheng, G. Embedded CuO nanoparticles@TiO$_2$-nanotube arrays for photoelectrocatalytic reduction of CO$_2$ to methanol. *Electrochim. Acta* **2018**, *283*, 1507–1513. [CrossRef]

31. Banerjee, S.; Mohapatra, S.K.; Das, P.P.; Misra, M. Synthesis of coupled semiconductor by filling 1D TiO$_2$ nanotubes with CdS. *Chem. Mater.* **2008**, *20*, 6784–6791. [CrossRef]

32. Tsui, L.-K.; Xu, Y.; Dawidowski, D.; Cafiso, D.; Zangari, G. Efficient water oxidation kinetics and enhanced electron transport in Li-doped TiO$_2$ nanotube photoanodes. *J. Mater. Chem. A* **2016**, *4*, 19070–19077.

33. Le, P.H.; Hieu, L.T.; Lam, T.-N.; Hang, N.T.N.; Truong, N.V.; Tuyen, L.T.C.; Phong, P.T.; Leu, J. Enhanced photocatalytic performance of nitrogen-doped TiO$_2$ nanotube arrays using a simple annealing process. *Micromachines* **2018**, *9*, 618. [CrossRef] [PubMed]

34. Zhang, Z.; Wang, P. Optimization of photoelectrochemical water splitting performance on hierarchical TiO$_2$ nanotube arrays. *Energy Environ. Sci.* **2012**, *5*, 6506–6512. [CrossRef]

35. Lian, Z.; Wang, W.; Xiao, S.; Li, X.; Cui, Y.; Zhang, D.; Li, G.; Li, H. Plasmonic silver quantum dots coupled with hierarchical TiO₂ nanotube arrays photoelectrodes for efficient visible-light photoelectrocatalytic hydrogen evolution. *Sci. Rep.* **2015**, *5*, 10461. [CrossRef]

36. Zhang, Z.; Zhang, L.; Hedhili, M.N.; Zhang, H.; Wang, P. Plasmonic gold nanocrystals coupled with photonic crystal seamlessly on TiO₂ nanotube photoelectrodes for efficient visible light photoelectrochemical water splitting. *Nano Lett.* **2013**, *13*, 14–20. [CrossRef]

37. Zhou, X.; Liu, N.; Schmuki, P. Photocatalysis with TiO₂ nanotubes: "colorful" reactivity and designing site-specific photocatalytic centers into TiO₂ nanotubes. *ACS Catal.* **2017**, *7*, 3210–3235. [CrossRef]

38. Chiarello, G.L.; Zuliani, A.; Ceresoli, D.; Martinazzo, R.; Selli, E. Exploiting the photonic crystal properties of TiO₂ nanotube arrays to enhance photocatalytic hydrogen production. *ACS Catal.* **2016**, *6*, 1345–1353. [CrossRef]

39. Zheng, X.; Meng, S.; Chen, J.; Wang, J.; Xian, J.; Shao, Y.; Fu, X.; Li, D. Titanium dioxide photonic crystals with enhanced photocatalytic activity: Matching photonic band gaps of TiO₂ to the absorption peaks of dyes. *J. Phys. Chem. C* **2013**, *117*, 21263–21273. [CrossRef]

40. Zhang, L.; Baumanis, C.; Robben, L.; Kandiel, T.; Bahnemann, D. Bi₂WO₆ inverse opals: Facile fabrication and efficient visible-light driven photocatalytic and photoelectrochemical water-splitting activity. *Small* **2011**, *7*, 2714–2720. [CrossRef]

41. Li, X.; Zhen, X.; Meng, S.; Xian, J.; Shao, Y.; Fu, X.; Li, D. Structuring β-Ga₂O₃ photonic crystal photocatalyst for efficient degradation of organic pollutants. *Environ. Sci. Technol.* **2013**, *47*, 9911–9917. [CrossRef]

42. Meng, S.; Li, D.; Wang, P.; Zheng, X.; Wang, J.; Chen, J.; Fang, J.; Fu, X. Probing photonic effect on photocatalytic degradation of dyes based on 3D inverse opal ZnO photonic crystal. *RSC Adv.* **2013**, *3*, 17021–17028. [CrossRef]

43. Meng, S.; Li, D.; Fu, X.; Fu, X. Integrating photonic bandgaps with surface plasmon resonance for the enhancement of visible-light photocatalytic performance. *J. Mater. Chem. A* **2015**, *3*, 23501–23511. [CrossRef]

44. Curti, M.; Schneider, J.; Bahnemann, D.W.; Mendive, C.B. Inverse opal photonic crystals as a strategy to improve photocatalysis: Underexplored questions. *J. Phys. Chem. Lett.* **2015**, *6*, 3903–3910. [CrossRef] [PubMed]

45. Santos, A. Nanoporous anodic alumina photonic crystals: Fundamentals, developments and perspectives. *J. Mater. Chem. C* **2017**, *5*, 5581–5599. [CrossRef]

46. Ermolaev, G.A.; Kushnir, S.E.; Sapoletova, N.A.; Napolskii, K.S. Titania photonic crystals with precise photonic band gap position via anodizing with voltage versus optical path length modulation. *Nanomaterials* **2019**, *9*, 651. [CrossRef] [PubMed]

47. Diggle, J.W.; Downie, T.C.; Goulding, C.W. Anodic oxide films on aluminum. *Chem. Rev.* **1969**, *69*, 365–405. [CrossRef]

48. Masuda, H.; Fukuda, K. Ordered metal nanohole arrays made by a two-step replication of honeycomb structures of anodic alumina. *Science* **1995**, *268*, 1466–1468. [CrossRef]

49. Masuda, H.; Hasegawa, F.; Ono, S. Self-ordering of cell arrangement of anodic porous alumina formed in sulfuric acid solution. *J. Electrochem. Soc.* **1997**, *144*, L127–L130. [CrossRef]

50. Schwirn, K.; Lee, W.; Hillebrand, R.; Steinhart, M.; Nielsch, K.; Gösele, U. Self-ordered anodic aluminium oxide formed by H₂SO₄ hard anodization. *ACS Nano* **2008**, *2*, 302–310. [CrossRef]

51. Lee, W.; Ji, R.; Gösele, U.; Nielsch, K. Fast fabrication of long-range ordered porous alumina membranes by hard anodization. *Nat. Mater.* **2006**, *5*, 741–747. [CrossRef] [PubMed]

52. Masuda, H.; Yada, K.; Osaka, A. Self-ordering of cell configuration of anodic porous alumina with large-size pores in phosphoric acid solution. *Jpn. J. Appl. Phys.* **1998**, *37*, L1340–L1342. [CrossRef]

53. Macak, J.M.; Sirotna, K.; Schmuki, P. Self-organized porous titanium dioxide prepared in Na₂SO₄/NaF electrolytes. *Electrochim. Acta* **2005**, *50*, 3679–3684. [CrossRef]

54. Yoriya, S.; Paulose, M.; Varghese, O.K.; Mor, G.K.; Grimes, C.A. Fabrication of vertically oriented TiO₂ nanotube arrays using dimethyl sulfoxide electrolytes. *J. Phys. Chem. C* **2007**, *111*, 13770–13776. [CrossRef]

55. Paulose, M.; Prakasam, H.E.; Varghese, O.K.; Peng, L.; Popat, K.C.; Mor, G.K.; Desai, T.A.; Grimes, C.A. TiO₂ nanotube arrays of 1000 μm length by anodization of titanium foil: Phenol red diffusion. *J. Phys. Chem. C* **2007**, *111*, 14992–14997. [CrossRef]

56. Allam, N.K.; Grimes, C.A. Formation of vertically oriented TiO₂ nanotube arrays using a fluoride free HCl aqueous electrolyte. *J. Phys. Chem. C* **2007**, *111*, 13028–13032. [CrossRef]

57. Hahn, R.; Macak, J.M.; Schmuki, P. Rapid anodic growth of TiO_2 and WO_3 nanotubes in fluoride free electrolytes. *Electrochem. Commun.* **2007**, *9*, 947–952. [CrossRef]

58. Macak, J.M.; Albu, S.P.; Schmuki, P. Towards ideal hexagonal self-ordering of TiO_2 nanotubes. *Phys. Stat. Sol. (RRL)* **2007**, *1*, 181–183. [CrossRef]

59. Shin, Y.; Lee, S. Self-organized regular arrays of anodic TiO_2 nanotubes. *Nano Lett.* **2008**, *8*, 3171–3173. [CrossRef]

60. Mohapatra, S.K.; John, S.E.; Banerjee, S.; Misra, M. Water photooxidation by smooth and ultrathin α-Fe_2O_3 nanotube arrays. *Chem. Mater.* **2009**, *21*, 3048–3055. [CrossRef]

61. Albu, S.P.; Ghicov, A.; Schmuki, P. High aspect ratio, self-ordered iron oxide nanopores formed by anodization of Fe in ethylene glycol/NH_4F electrolytes. *Phys. Stat. Sol. (RRL)* **2009**, *3*, 64–66. [CrossRef]

62. Berger, S.; Jakubka, F.; Schmuki, P. Formation of hexagonally ordered nanoporous anodic zirconia. *Electrochem. Commun.* **2008**, *10*, 1916–1919. [CrossRef]

63. Tsuchiya, H.; Macak, J.M.; Sieber, I.; Taveira, L.; Ghicov, A.; Sirotna, K.; Schmuki, P. Self-organized porous WO_3 formed in NaF electrolytes. *Electrochem. Commun.* **2005**, *7*, 295–298. [CrossRef]

64. Choi, J.; Lim, J.H.; Lee, S.C.; Chang, J.H.; Kim, K.J.; Cho, M.A. Porous niobium oxide films prepared by anodization in HF/H_3PO_4. *Electrochim. Acta* **2006**, *51*, 5502–5507. [CrossRef]

65. Wei, W.; Lee, K.; Shaw, S.; Schmuki, P. Anodic formation of high aspect ratio, self-ordered Nb_2O_5 nanotubes. *Chem. Commun.* **2012**, *48*, 4244–4246. [CrossRef] [PubMed]

66. Berger, S.; Jakubka, F.; Schmuki, P. Self-ordered hexagonal nanoporous hafnium oxide and transition to aligned HfO_2 nanotube layers. *Electrochem. Solid-State Lett.* **2009**, *12*, K45–K48. [CrossRef]

67. Yang, Y.; Albu, S.P.; Kim, D.; Schmuki, P. Enabling the anodic growth of highly ordered V_2O_5 nanoporous/nanotubular structures. *Angew. Chem. Int. Ed.* **2011**, *50*, 9071–9075. [CrossRef]

68. Shen, Q.; Chen, Z.; Huang, X.; Liu, M.; Zhao, G. High-yield and selective photoelectrocatalytic reduction of CO_2 to formate by metallic copper decorated Co_3O_4 nanotube arrays. *Environ. Sci. Technol.* **2015**, *45*, 5828–5835. [CrossRef]

69. Roy, P.; Berger, S.; Schmuki, P. TiO_2 nanotubes: Synthesis and applications. *Angew. Chem. Int. Ed.* **2011**, *50*, 2904–2939. [CrossRef]

70. Law, C.S.; Lim, S.Y.; Abell, A.D.; Voelcker, N.H.; Santos, A. Nanoporous anodic alumina photonic crystals for optical chemo- and biosensing: Fundamentals, advances, and perspectives. *Nanomaterials* **2018**, *8*, 788. [CrossRef]

71. Macak, J.M. Self-organized anodic TiO_2 nanotubes: Functionalities and applications due to a secondary material. In *Electrochemically Engineered Nanoporous Materials: Methods, Properties and Applications*, 1st ed.; Losic, D., Santos, A., Eds.; Springer International Publishing: Cham, Switzerland, 2015; Volume 220, pp. 65–92. ISBN 978-3-319-20346-1.

72. Nah, Y.-C.; Paramasivam, I.; Schmuki, P. Doped TiO_2 and TiO_2 nanotubes: Synthesis and applications. *ChemPhysChem* **2010**, *11*, 2698–2713. [CrossRef] [PubMed]

73. Di Valentin, C.; Finazzi, E.; Pacchioni, G.; Selloni, A.; Livraghi, S.; Paganini, M.C.; Giamello, E. N-doped TiO_2: Theory and experiment. *Chem. Phys.* **2007**, *339*, 44–56. [CrossRef]

74. Park, J.H.; Kim, S.; Bard, A.J. Novel carbon-doped TiO_2 nanotube arrays with high aspect ratios for efficient solar water splitting. *Nano Lett.* **2006**, *6*, 24–28. [CrossRef] [PubMed]

75. Ghicov, A.; Macak, J.M.; Tsuchiya, H.; Kunze, J.; Haeublein, V.; Frey, L.; Schmuki, P. Ion implantation and annealing for an efficient N-doping of TiO_2 nanotubes. *Nano Lett.* **2006**, *6*, 1080–1082. [CrossRef]

76. Siuzdak, K.; Szkoda, M.; Lisowska-Oleksiak, A.; Grochowska, K.; Karczewski, J.; Ryl, J. Thin layer of ordered boron-doped TiO_2 nanotubes fabricated in a novel type of electrolyte and characterized by remarkably improved photoactivity. *Appl. Surf. Sci.* **2015**, *357*, 942–950. [CrossRef]

77. Xue, C.; Hu, S.; Chang, Q.; Li, Y.; Liu, X.; Yang, J. Fluoride doped $SrTiO_3$/TiO_2 nanotube arrays with a double layer walled structure for enhanced photocatalytic properties and bioactivity. *RSC Adv.* **2017**, *7*, 49759–49768. [CrossRef]

78. Momeni, M.M.; Ghayeb, Y.; Ghonchegi, Z. Fabrication and characterization of copper doped TiO_2 nanotube arrays by in situ electrochemical method as efficient visible-light photocatalyst. *Ceram. Int.* **2015**, *41*, 8735–8741. [CrossRef]

79. Mazierski, P.; Lisowski, W.; Grzyb, T.; Winiarski, M.J.; Klimczuk, T.; Mikolajczyk, A.; Flisikowski, J.; Hirsch, A.; Kolakowska, A.; Puzyn, T.; et al. Enhanced photocatalytic properties of lanthanide-TiO$_2$ nanotubes: An experimental and theoretical study. *Appl. Catal. B Environ.* **2017**, *205*, 376–385. [CrossRef]

80. Ghicov, A.; Macak, J.M.; Tsuchiya, H.; Kunze, J.; Haeublein, V.; Kleber, S.; Schmuki, P. TiO$_2$ nanotube layers. Dose effects during nitrogen doping by ion implantation. *Chem. Phys. Lett.* **2006**, *419*, 426–429. [CrossRef]

81. Kobayashi, N.; Tanoue, H. Nitrogen ion implantation into ZrN thin films. *Nucl. Instrum. Methods Phys. Res.* **1989**, *39*, 746–749. [CrossRef]

82. Tsujide, T.; Nojiri, M.; Kitagawa, H. Formation of silicon nitride compound layers by high-dose nitrogen implantation. *Appl. Phys.* **1980**, *51*, 1605–1610. [CrossRef]

83. Kim, D.; Fujimoto, S.; Schmuki, P.; Tsuchiya, H. Nitrogen doped anodic TiO$_2$ nanotubes grown from nitrogen-containing Ti alloys. *Electrochem. Commun.* **2008**, *10*, 910–913. [CrossRef]

84. Paramasivam, I.; Nah, Y.-C.; Das, C.; Shrestha, N.K.; Schmuki, P. WO$_3$/TiO$_2$ nanotubes with strongly enhanced photocatalytic activity. *Chem. Eur. J.* **2010**, *16*, 8993–8997. [CrossRef] [PubMed]

85. Das, C.; Paramasivam, I.; Liu, N.; Schmuki, P. Photoelectrochemical and photocatalytic activity of tungsten doped TiO$_2$ nanotube layers in the near visible region. *Electrochim. Acta* **2011**, *56*, 10557–10561. [CrossRef]

86. Altomare, M.; Lee, K.; Killian, M.S.; Selli, E.; Schmuki, P. Ta-doped TiO$_2$ nanotubes for enhanced solar-light photoelectrochemical water splitting. *Chem. Eur. J.* **2013**, *19*, 5841–5844. [CrossRef]

87. Roy, P.; Das, C.; Lee, K.; Hahn, R.; Ruff, T.; Moll, M.; Schmuki, P. Oxide nanotubes on Ti-Ru alloys: Strongly enhanced and stable photoelectrochemical activity for water splitting. *J. Am. Chem. Soc.* **2011**, *133*, 5629–5631. [CrossRef]

88. Yoo, H.; Choi, Y.W.; Choi, J. Ruthenium oxide-doped TiO$_2$ nanotubes by single-step anodization for water-oxidation applications. *J. ChemCatChem* **2015**, *7*, 643–647. [CrossRef]

89. Enachi, M.; Guix, M.; Braniste, T.; Postolache, V.; Ciobanu, V.; Ursaki, V.; Schmidt, O.G.; Tiginyanu, I. Photocatalytic properties of TiO$_2$ nanotubes doped with Ag, Au and Pt or covered by Ag, Au and Pt nanodots. *Surf. Eng. Appl. Electrochem.* **2015**, *51*, 3–8. [CrossRef]

90. Nakata, K.; Liu, B.; Ishikawa, Y.; Sakai, M.; Saito, H.; Ochiai, T.; Sakai, H.; Murakami, T.; Abe, M.; Takagi, K.; et al. Fabrication and photocatalytic properties of TiO$_2$ nanotube arrays modified with phosphate. *Chem. Lett.* **2011**, *40*, 1107–1109. [CrossRef]

91. Su, Y.; Zhang, X.; Zhou, M.; Han, S.; Lei, L. Preparation of high efficient photoelectrode of N-F-codoped TiO$_2$ nanotubes. *J. Photochem. Photobiol. A* **2008**, *194*, 152–160. [CrossRef]

92. Zhang, F.; Wang, X.; Liu, H.; Liu, C.; Wan, Y.; Long, Y.; Cai, Z. Recent advances and applications of semiconductor photocatalytic technology. *Appl. Sci.* **2019**, *9*, 2489. [CrossRef]

93. Lu, D.; Zhang, M.; Zhang, Z.; Li, Q.; Wang, X.; Yang, J. Self-organized vanadium and nitrogen co-doped titania nanotube arrays with enhanced photocatalytic reduction of CO$_2$ into CH$_4$. *Nanoscale Res. Lett.* **2014**, *9*, 272. [CrossRef] [PubMed]

94. Zhang, M.; Lu, D.; Yan, G.; Wu, J.; Yang, J. Fabrication of Mo+N-codoped TiO$_2$ nanotube arrays by anodization and sputtering for visible light-induced photoelectrochemical and photocatalytic properties. *J. Nanomater.* **2013**, *12*, 156.

95. Yang, Y.; Hoffmann, M.R. Synthesis and stabilization of blue-black TiO$_2$ nanotube arrays for electrochemical oxidant generation and wastewater treatment. *Environ. Sci. Technol.* **2016**, *50*, 11888–11894. [CrossRef] [PubMed]

96. Cho, K.; Lee, S.; Kim, H.; Kim, H.-E.; Son, A.; Kim, E.-J.; Li, M.; Qiang, Z.; Hong, S.W. Effects of reactive oxidants generation and capacitance on photoelectrochemical water disinfection with self-doped titanium dioxide nanotube arrays. *Appl. Catal. B Environ.* **2019**, *257*, 117910. [CrossRef]

97. Liu, N.; Haeublein, V.; Zhou, X.; Venkatesan, U.; Hartmann, M.; MacKovic, M.; Nakajima, T.; Spiecker, E.; Osvet, A.; Frey, L.; et al. "Black" TiO$_2$ nanotubes formed by high-energy proton implantation show noble-metal-co-catalyst free photocatalytic H$_2$-evolution. *Nano Lett.* **2015**, *15*, 6815–6820. [CrossRef]

98. Zhou, X.; Häublein, V.; Liu, N.; Nguyen, N.T.; Zolnhofer, E.M.; Tsuchiya, H.; Killian, M.S.; Meyer, K.; Frey, L.; Schmuki, P. TiO$_2$ nanotubes: Nitrogen-ion implantation at low dose provides noble-metal-free photocatalytic H$_2$-evolution activity. *Angew. Chem. Int. Ed.* **2016**, *55*, 3763–3767. [CrossRef]

99. Liu, N.; Zhou, X.; Nguyen, N.T.; Peters, K.; Zoller, F.; Hwang, I.; Schneider, C.; Miehlich, M.E.; Freitag, D.; Meyer, K.; et al. Black magic in gray titania: Noble-metal-free photocatalytic H$_2$ evolution from hydrogenated anatase. *ChemSusChem* **2017**, *10*, 62–67. [CrossRef]

100. Mattox, D.M. *Handbook of Physical Vapor Deposition (PVD) Processing*, 2nd ed.; William Andrew: Cambridge, MA, USA, 2010; pp. 1–24. ISBN 978-0-8155-2037-5.

101. Lee, W.; Park, S.-J. Porous anodic aluminum oxide: Anodization and templated synthesis of functional nanostructures. *Chem. Rev.* **2014**, *114*, 7487–7556. [CrossRef]

102. Lai, C.W.; Sreekantan, S. Photoelectrochemical response studies of W deposited TiO_2 nanotubes via thermal evaporation technique. *J. Exp. Nanosci.* **2014**, *9*, 728–738. [CrossRef]

103. Zhou, X.; Licklederer, M.; Schmuki, P. Thin MoS_2 on TiO_2 nanotube layers: An efficient co-catalyst/harvesting system for photocatalytic H_2 evolution. *Electrochem. Commun.* **2016**, *73*, 33–37. [CrossRef]

104. Chung, C.K.; Tu, K.T.; Chang, C.Y.; Peng, Y.C. Fabrication of thin-film spherical anodic alumina oxide templates using a superimposed nano-micro structure. *Surf. Coat. Technol.* **2019**, *361*, 170–175. [CrossRef]

105. Spanu, D.; Recchia, S.; Mohajernia, S.; Tomanex, O.; Kment, S.; Zboril, R.; Schmuki, P.; Altomare, M. Templated dewetting-alloying of NiCu bilayers on TiO_2 nanotubes enables efficient noble-metal-free photocatalytic H_2 evolution. *ACS Catal.* **2018**, *8*, 5298–5305. [CrossRef]

106. Bjelajac, A.; Djokic, V.; Petrovic, R.; Socol, G.; Mihailescu, I.N.; Florea, I.; Ersen, O.; Janackovic, D. Visible light-harvesting of TiO_2 nanotubes array by pulsed laser deposition CdS. *Appl. Surf. Sci.* **2014**, *309*, 225–230. [CrossRef]

107. Nasirpouri, F. Fundamentals and principles of electrode-position. In *Electrodeposition of Nanostructured Materials*; Springer International Publishing: Cham, Switzerland, 2017; Volume 62, pp. 75–121. ISBN 978-3-319-44920-3.

108. Yliniemi, K.; Nguyen, N.T.; Mohajemia, S.; Liu, N.; Wilson, B.P.; Schmuki, P.; Lundström, M. A direct synthesis of platinum/nickel co-catalysts on titanium dioxide nanotube surface from hydrometallurgical-type process streams. *J. Clean. Prod.* **2018**, *201*, 39–48. [CrossRef]

109. Li, Y.; Yu, H.; Zhang, C.; Fu, L.; Li, G.; Shao, Z.; Yi, B. Electrodeposition of Ni oxide on TiO_2 nanotube arrays for enhancing visible light photoelectrochemical water splitting. *J. Electroanal. Chem.* **2013**, *688*, 228–231. [CrossRef]

110. Xiao, F.-X.; Hung, S.-F.; Tao, H.B.; Miao, J.; Yang, H.B.; Liu, B. Spatially branched hierarchical ZnO nanorod-TiO_2 nanotube array heterostructures for versatile photocatalytic and photoelectrocatalytic applications: Towards intimate integration of 1D-1D hybrid nanostructures. *Nanoscale* **2014**, *6*, 14950–14961. [CrossRef]

111. Muneshwar, T.; Miao, M.; Borujeny, E.R.; Cadien, K. Atomic layer deposition: Fundamentals, practice and challenges. In *Handbook of Thin Film Deposition*, 4th ed.; Seshan, K., Schepis, D., Eds.; William Andrew: Cambridge, MA, USA, 2018; pp. 359–373. ISBN 978-0-12-812311-9.

112. Elam, J.; Routkevitch, D.; Mardilovich, P.; George, S. Conformal coating on ultrahigh-aspect-ratio nanopores of anodic alumina by atomic layer deposition. *Chem. Mater.* **2003**, *15*, 3507–3517. [CrossRef]

113. Johnson, R.W.; Hultqvist, A.; Bent, S.F. A brief review of atomic layer deposition: From fundamentals to applications. *Mater. Today* **2014**, *17*, 236–246. [CrossRef]

114. Leskelä, M.; Ritala, M. Atomic layer deposition chemistry: Recent developments and future challenges. *Angew. Chem. Int. Ed.* **2003**, *42*, 5548–5554. [CrossRef]

115. Turkevych, I.; Kosar, S.; Pihosh, Y.; Mawatari, K.; Kitamori, T.; Ye, J.; Shimamura, K. Synergetic effect between TiO_2 and ubiquitous metal oxides on photocatalytic activity of composite nanostructures. *J. Ceram. Soc. Jpn.* **2014**, *122*, 393–397. [CrossRef]

116. Ng, S.; Krbal, M.; Zaxpe, R.; Prikryl, J.; Charvot, J.; Dvořák, F.; Strizik, L.; Slang, S.; Sopha, H.; Kosto, Y.; et al. $MoSe_xO_y$-coated 1D TiO_2 nanotube layers: Efficient interface for light-driven applications. *Adv. Mater. Interfaces* **2018**, *5*, 1701146. [CrossRef]

117. Yoo, J.; Zazpe, R.; Cha, G.; Prikryl, J.; Hwang, I.; Macak, J.M.; Schmuki, P. Uniform ALD deposition of Pt nanoparticles within 1D anodic TiO_2 nanotubes for photocatalytic H_2 generation. *Electrochem. Commun.* **2018**, *86*, 6–11. [CrossRef]

118. Danks, A.; Hall, S.; Schnepp, Z. The evolution of 'sol-gel' chemistry as a technique for materials synthesis. *Mater. Horiz.* **2016**, *3*, 91–112. [CrossRef]

119. Owens, G.J.; Singh, R.K.; Foroutan, F.; Alqaysi, M.; Han, C.-M.; Mahapatra, C.; Kim, H.-W.; Knowles, J.C. Sol-gel based materials for biomedical applications. *Prog. Mater. Sci.* **2016**, *77*, 1–79. [CrossRef]

120. Figueira, R.; Silva, C.J.; Pereira, E. Organic-inorganic hybrid sol-gel coatings for metal corrosion protection: A review of recent progress. *J. Coat. Technol. Res.* **2015**, *12*, 1–35. [CrossRef]

121. Clark Wooten, M.K.; Koganti, V.R.; Zhou, S.; Rankin, S.E.; Knutson, B.L. Synthesis and nanofiltration membrane performance of oriented mesoporous silica thin films on macroporous supports. *ACS Appl. Mater. Inter.* **2016**, *8*, 21806–21815. [CrossRef]

122. Qu, X.; Xie, D.; Gao, L.; Cao, L.; Du, F. Synthesis and characterization of TiO_2/WO_3 composite nanotubes for photocatalytic applications. *J. Mater. Sci.* **2015**, *50*, 21–27. [CrossRef]

123. Nguyen, N.T.; Ozkan, S.; Hejazi, S.; Denisov, N.; Tomanec, O.; Zboril, R.; Schmuki, P. Providing significantly enhanced photocatalytic H_2 generation using porous PtPdAg alloy nanoparticles on spaced TiO_2 nanotubes. *Int. J. Hydrog. Energy* **2019**, *44*, 22962–22971. [CrossRef]

124. Sanabria-Arenas, B.E.; Mazare, A.; Yoo, J.; Nguyen, N.T.; Hejazi, S.; Bian, H.; Diamanti, M.V.; Pedeferri, M.P.; Schmuki, P. Intrinsic AuPt-alloy particles decorated on TiO_2 nanotubes provide enhanced photocatalytic degradation. *Electrochim. Acta* **2018**, *292*, 865–870. [CrossRef]

125. Hu, Z.; Chen, D.; Zhan, X.; Wang, F.; Qin, L.; Huang, Y. Synthesis of Ag-loaded $SrTiO_3/TiO_2$ heterostructure nanotube arrays for enhanced photocatalytic performances. *Appl. Phys. A* **2017**, *123*, 399. [CrossRef]

126. Kontos, A.I.; Likodimos, V.; Stergiopoulos, T.; Tsoukleris, D.S.; Falaras, P.; Rabias, I.; Papavassiliou, G.; Kim, D.; Kunze, J.; Schmuki, P. Self-organized anodic TiO_2 nanotube arrays functionalized by iron oxide nanoparticles. *Chem. Mater.* **2009**, *21*, 662–672. [CrossRef]

127. Zhao, X.; Liu, H.; Qu, J. Photoelectrocatalytic degradation of organic contaminants at Bi_2O_3/TiO_2 nanotube array electrode. *Appl. Surf. Sci.* **2011**, *257*, 4621–4624. [CrossRef]

128. Yang, H.Y.; Yu, S.F.; Lau, S.P.; Zhang, X.; Sun, D.D.; Jun, G. Direct growth of ZnO nanocrystals onto the surface of porous TiO_2 nanotube arrays for highly efficient and recyclable photocatalysts. *Small* **2009**, *5*, 2260–2264. [CrossRef]

129. Liu, Y.; Zhang, X.; Liu, R.; Yang, R.; Liu, C.; Cai, Q. Fabrication and photocatalytic activity of high-efficiency visible-light-responsive photocatalyst $ZnTe/TiO_2$ nanotube arrays. *J. Solid State Chem.* **2011**, *184*, 684–689. [CrossRef]

130. Mazierski, P.; Nadolna, J.; Nowaczyk, G.; Lisowski, W.; Winiarski, M.J.; Klimczuk, T.; Kobylański, M.P.; Jurga, S.; Zaleska-Medynska, A. Highly visible-light-photoactive heterojunction based on TiO_2 nanotubes decorated by Pt nanoparticles and Bi_2S_3 quantum dots. *J. Phys. Chem. C* **2017**, *121*, 17215–17225. [CrossRef]

131. Kang, Q.; Liu, S.; Yang, L.; Cai, Q.; Grimes, C.A. Fabrication of PbS nanoparticle-sensitized TiO_2 nanotube arrays and their photoelectrochemical properties. *ACS Appl. Mater. Interfaces* **2011**, *3*, 746–749. [CrossRef]

132. Zhang, M.; Gong, Z.; Tao, J.; Wang, X.; Wang, Z.; Yang, L.; He, G.; Lv, J.; Wang, P.; Fing, Z.; et al. Effect of ZnS layers on optical properties of prepared CdS/TiO_2 nanotube arrays for photocatalyst. *J. Nanoparticle Res.* **2017**, *19*, 120. [CrossRef]

133. Yang, L.; Luo, S.; Liu, R.; Cai, Q.; Xiao, Y.; Liu, S.; Su, F.; Wen, L. Fabrication of CdSe nanoparticles sensitized long TiO_2 nanotube arrays for photocatalytic degradation of anthracene-9-carboxylic acid under green monochromatic light. *J. Phys. Chem. C* **2010**, *114*, 4783–4789. [CrossRef]

134. Lin, J.; Zong, R.; Zhou, M.; Zhu, Y. Photoelectric catalytic degradation of methylene blue by C60-modified TiO_2 nanotube array. *Appl. Catal. B* **2009**, *89*, 425–431. [CrossRef]

135. Liu, C.; Teng, Y.; Liu, R.; Luo, S.; Tang, Y.; Chen, L.; Cai, Q. Fabrication of graphene films on TiO_2 nanotube arrays for photocatalytic application. *Carbon* **2011**, *49*, 5312–5320. [CrossRef]

136. Yu, J.; Dai, G.; Huang, B. Fabrication and characterization of visible-light-driven plasmonic photocatalyst $Ag/AgCl/TiO_2$ nanotube arrays. *J. Phys. Chem. C* **2009**, *113*, 16394–16401. [CrossRef]

137. Shrestha, N.K.; Yang, M.; Paramasivam, I.; Schmuki, P. Visible-light-induced photocatalysis using self-organized TiO_2 nanotubes decorated with AgBr deposits. *Semicond. Sci. Technol.* **2011**, *26*, 092002. [CrossRef]

138. Liu, J.; Ruan, L.; Adeloju, S.B.; Wu, Y. $BiOI/TiO_2$ nanotube arrays, a unique flake-tube structured p-n junction with remarkable visible-light photoelectrocatalytic performance and stability. *Dalton Trans.* **2014**, *43*, 1706–1715. [CrossRef] [PubMed]

139. Yablonovitch, E. Inhibited spontaneous emission in solid-state physics and electronics. *Phys. Rev. Lett.* **1987**, *58*, 2059–2062. [CrossRef]

140. John, S. Strong localization of photons in certain disordered dielectric superlattices. *Phys. Rev. Lett.* **1987**, *58*, 2486–2489. [CrossRef]

141. Santos, A.; Kumeria, T.; Losic, D. Optically optimized photoluminescent and interferometric biosensors based on nanoporous anodic alumina: A comparison. *Anal. Chem.* **2013**, *85*, 7904–7911. [CrossRef]

55

142. Law, C.S.; Sylvia, G.M.; Nemati, M.; Yu, J.; Losic, D.; Abell, A.D.; Santos, A. Engineering of surface chemistry for enhanced sensitivity in nanoporous interferometric sensing platforms. *ACS Appl. Mater. Interfaces* **2017**, *9*, 8929–8940. [CrossRef]

143. Law, C.S.; Lim, S.Y.; Abell, A.D.; Santos, A. Real-time binding monitoring between human blood proteins and heavy metal ions in nanoporous anodic alumina photonic crystals. *Anal. Chem.* **2018**, *90*, 10039–10048. [CrossRef]

144. Kumeria, T.; Santos, A.; Rahman, M.M.; Ferré-Borrull, J.; Marsal, L.F.; Losic, D. Advanced structural engineering of nanoporous photonic structures: Tailoring nanopore architecture to enhance sensing properties. *ACS Photonics* **2014**, *1*, 1298–1306. [CrossRef]

145. Chen, Y.; Santos, A.; Wang, Y.; Kumeria, T.; Ho, D.; Li, J.; Wang, C.; Losic, D. Rational design of photonic dust from nanoporous anodic alumina films: A versatile photonic nanotool for visual sensing. *Sci. Rep.* **2015**, *5*, 12893. [CrossRef] [PubMed]

146. Chen, Y.; Santos, A.; Wang, Y.; Kumeria, T.; Li, J.; Wang, C.; Losic, D. Biomimetic nanoporous anodic alumina distributed Bragg reflectors in the form of films and microsized particles for sensing applications. *ACS Appl. Mater. Interfaces* **2015**, *7*, 19816–19824. [CrossRef] [PubMed]

147. Kumeria, T.; Rahman, M.M.; Santos, A.; Ferré-Borrull, J.; Marsal, L.F.; Losic, D. Nanoporous anodic alumina rugate filters for sensing of ionic mercury: Toward environmental point-of-analysis systems. *ACS Appl. Mater. Interfaces* **2014**, *6*, 12971–12978. [CrossRef] [PubMed]

148. Santos, A.; Yoo, J.H.; Rohatgi, C.V.; Kumeria, T.; Wang, Y.; Losic, D. Realisation and advanced engineering of true optical rugate filters based on nanoporous anodic alumina by sinusoidal pulse anodisation. *Nanoscale* **2016**, *8*, 1360–1373. [CrossRef]

149. Eckstein, C.; Law, C.S.; Lim, S.Y.; Kaur, S.; Kumeria, T.; Ferré-Borrull, J.; Abell, A.D.; Marsal, L.F.; Santos, A. Nanoporous photonic crystals with tailored surface chemistry for ionic copper sensing. *J. Mater. Chem. C* **2019**, *7*, 12278–12289. [CrossRef]

150. Wang, G.; Wang, J.; An, Y.; Wang, C. Anodization fabrication of 3D TiO$_2$ photonic crystals and their application for chemical sensors. *Supperlattice Microst.* **2016**, *100*, 290–295. [CrossRef]

151. Ye, M.; Xin, X.; Lin, C.; Lin, Z. High efficiency dye-sensitized solar cells based on hierarchically structured nanotubes. *Nano Lett.* **2011**, *11*, 3214–3220. [CrossRef]

152. Guo, M.; Xie, K.; Lin, J.; Yong, Z.; Yip, C.T.; Zhou, L.; Wang, Y.; Huang, H. Design and coupling of multifunctional TiO$_2$ nanotube photonic crystal to nanocrystalline titania layer as semi-transparent photoanode for due-sensitized solar cell. *Energy Environ. Sci.* **2012**, *5*, 9881–9888. [CrossRef]

153. Yip, C.T.; Huang, H.; Zhou, L.; Xie, K.; Wang, Y.; Feng, T.; Li, J.; Tam, W.Y. Direct and seamless coupling of TiO$_2$ nanotube photonic crystal to dye-sensitized solar cell: A single-step approach. *Adv. Mater.* **2011**, *23*, 5624–5628. [CrossRef]

154. Wijnhoven, J.E.G.J.; Vos, W.L. Preparation of photonic crystals made of air spheres in Titania. *Science* **1998**, *281*, 802–804. [CrossRef]

155. Liu, J.; Zhao, H.; Wu, M.; Van der Schueren, B.; Li, Y.; Deparis, O.; Ye, J.; Ozin, G.A.; Hasan, T.; Su, B.-L. Slow photons for photocatalysis and photovoltaics. *Adv. Mater.* **2017**, *29*, 1605349. [CrossRef]

156. Santos, A.; Deen, M.J.; Marsal, L.F. Low-cost fabrication technologies for nanostructures: State-of-the-art and potential. *Nanotechnology* **2015**, *26*, 042001. [CrossRef]

157. Dai, X.-C.; Hou, S.; Huang, M.-H.; Li, Y.-B.; Li, T.; Xiao, F.-X. Electrochemically anodized one-dimensional semiconductors: A fruitful platform for solar energy conversion. *J. Phys. Energy* **2019**, *1*, 022002. [CrossRef]

158. Wang, Y.; Chen, Y.; Kumeria, T.; Ding, F.; Evdokiou, A.; Losic, D.; Santos, A. Facile synthesis of optical microcavities by a rationally designed anodization approach: Tailoring photonic signals by nanopore structure. *ACS Appl. Mater. Interfaces* **2015**, *7*, 9879–9888. [CrossRef]

159. Law, C.S.; Lim, S.Y.; Macalincag, R.M.; Abell, A.D.; Santos, A. Light-confining nanoporous anodic alumina microcavities by apodized stepwise pulse anodization. *ACS Appl. Nano Mater.* **2018**, *1*, 4418–4434. [CrossRef]

160. Law, C.S.; Lim, S.Y.; Abell, A.D.; Marsal, L.F.; Santos, A. Structural tailoring of nanoporous anodic alumina optical microcavities for enhanced resonant recirculation of light. *Nanoscale* **2018**, *10*, 14139–14152. [CrossRef]

161. Law, C.S.; Lim, S.Y.; Santos, A. On the precise tuning of optical filtering features in nanoporous anodic alumina distributed Bragg reflectors. *Sci. Rep.* **2018**, *8*, 4642. [CrossRef]

162. Santos, A.; Law, C.S.; Lei, D.W.C.; Pereira, T.; Losic, D. Fine tuning of optical signals in nanoporous anodic alumina photonic crystals by apodized sinusoidal pulse anodisation. *Nanoscale* **2016**, *8*, 18360–18375. [CrossRef]

163. Lim, S.Y.; Law, C.S.; Marsal, L.F.; Santos, A. Engineering of hybrid nanoporous anodic alumina photonic crystals by heterogeneous pulse anodization. *Sci. Rep.* **2018**, *8*, 9455. [CrossRef]

164. Lin, J.; Liu, K.; Chen, X. Synthesis of periodically structured Titania nanotube films and their potential for photonic applications. *Small* **2011**, *7*, 1784–1789. [CrossRef]

165. Sapoletova, N.A.; Kushnir, S.E.; Napolskii, K.S. Anodic titanium oxide photonic crystals prepared by novel cyclic anodizing with voltage versus charge modulation. *Electrochem. Commun.* **2018**, *91*, 5–9. [CrossRef]

166. Guo, M.; Xie, K.; Wang, Y.; Zhou, L.; Huang, H. Aperiodic TiO_2 nanotube photonic crystal: Full-visible-spectrum solar light harvesting in photovoltaic devices. *Sci. Rep.* **2014**, *4*, 6442. [CrossRef] [PubMed]

167. Suhaimy, S.H.M.; Lai, C.W.; Tajuddin, H.A.; Samsudin, E.M.; Johan, M.R. Impact of TiO_2 nanotubes' morphology on the photocatalytic degradation of simazine pollutant. *Materials* **2018**, *11*, 2066. [CrossRef]

168. Ye, Y.; Bruning, H.; Liu, W.; Rijnaarts, H.; Yntema, D. Effect of dissolved natural organic matter on the photocatalytic micropollutant removal performance of TiO_2 nanotube array. *J. Photochem. Photobiol. A* **2019**, *371*, 216–222. [CrossRef]

169. Ye, Y.; Feng, Y.; Bruning, H.; Yntema, D.; Rijnaarts, H.H.M. Photocatalytic degradation of metoprolol by TiO_2 nanotube arrays and UV-LED: Effects of catalyst properties, operational parameters, commonly present water constituents, and photo-induced reactive species. *Appl. Catal. B Environ.* **2018**, *220*, 171–181. [CrossRef]

170. Gomes, J.; Lincho, J.; Domingues, E.; Gmurek, M.; Mazierski, P.; Zaleska-Medynska, A.; Klimczuk, T.; Quinta-Ferreira, R.M.; Martins, R.C. TiO_2 nanotube arrays-based reactor for photocatalytic oxidation of paraben mixtures in ultrapure water: Effects of photocatalyst properties, operational parameters and light source. *Sci. Total Environ.* **2019**, *689*, 79–89. [CrossRef]

171. Wang, N.; Li, X.; Wang, Y.; Quan, X.; Chen, G. Evaluation of bias potential enhanced photocatalytic degradation of 4-chlorophenol with TiO_2 nanotube fabricated by anodic oxidation method. *Chem. Eng. J.* **2009**, *146*, 30–35. [CrossRef]

172. Quan, X.; Ruan, X.; Zhao, H.; Chen, S.; Zhao, Y. Photoelectrocatalytic degradation of pentachlorophenol in aqueous solution using a TiO_2 nanotube film electrode. *Environ. Pollut.* **2007**, *147*, 409–414. [CrossRef]

173. Arenas, B.E.S.; Strini, A.; Schiavi, L.; Bassi, A.L.; Russo, V.; Curto, B.D.; Diamanti, M.V.; Pedeferri, M. Photocatalytic activity of nanotubular TiO_2 films obtained by anodic oxidation: A comparison in gas and liquid phase. *Materials* **2018**, *11*, 488. [CrossRef]

174. Pichat, P. Are TiO_2 nanotubes worth using in photocatalytic purification of air and water? *Molecules* **2014**, *19*, 15075–15087. [CrossRef]

175. Nevárez-Martínez, M.C.; Kobylánski, M.P.; Mazierski, P.; Wółkiewicz, J.; Trykowski, G.; Malankowska, A.; Kozak, M.; Espinoza-Montero, P.J.; Zaleska-Medynska, A. Self-organized TiO_2-MnO_2 nanotube arrays for efficient photocatalytic degradation of toluene. *Molecules* **2017**, *22*, 564. [CrossRef] [PubMed]

176. Yang, L.; Xiao, Y.; Liu, S.; Li, Y.; Cai, Q.; Luo, S.; Zeng, G. Photocatalytic reduction of Cr(VI) on WO_3 doped long TiO_2 nanotube arrays in the presence of citric acid. *Appl. Catal. B Environ.* **2010**, *94*, 142–149. [CrossRef]

177. Schulte, K.L.; DeSario, P.A.; Gray, K.A. Effect of crystal phase composition on the reductive and oxidative abilities of TiO_2 nanotubes under UV and visible light. *Appl. Catal. B Environ.* **2010**, *97*, 354–360. [CrossRef]

178. Kar, P.; Zeng, S.; Zhang, Y.; Vahidzadeh, E.; Manuel, A.; Kisslinger, R.; Alam, K.M.; Thakur, U.K.; Mahdi, N.; Kumar, P.; et al. High rate CO_2 photoreduction using flame annealed TiO_2 nanotubes. *Appl. Catal. B Environ.* **2019**, *243*, 522–536. [CrossRef]

179. Lee, K.; Mazare, A.; Schmuki, P. One-dimensional titanium dioxide nanomaterials: Nanotubes. *Chem. Rev.* **2014**, *114*, 9385–9454. [CrossRef]

180. Song, Y.Y.; Roy, P.; Paramasivam, I.; Schmuki, P. Voltage-induced payload release and wettability control on TiO_2 and TiO_2 nanotubes. *Angew. Chem. Int. Ed.* **2010**, *49*, 351–354. [CrossRef]

181. Song, Y.; Schmidt-stein, F.; Bauer, S.; Schmuki, P. Amphiphilic TiO_2 nanotube arrays: An actively controllable drug delivery system. *J. Am. Chem. Soc.* **2009**, *131*, 4230–4232. [CrossRef]

182. Shrestha, N.K.; Macak, J.M.; Schmidt-Stein, F.; Hahn, R.; Mierke, C.T.; Fabry, B.; Schmuki, P. Magnetically guided Titania nanotubes for site-selective photocatalysis and drug release. *Angew. Chem. Int. Ed.* **2009**, *48*, 969–972. [CrossRef]

183. Kalbacova, M.; Macak, J.M.; Schmidt-Stein, F.; Mierke, C.T.; Schmuki, P. TiO$_2$ nanotubes: Photocatalyst for cancer cell killing. *Phys. Stat. Sol. (RRL)* **2008**, *2*, 194–196. [CrossRef]

184. Faraji, M.; Mohaghegh, N.; Abedini, A. TiO$_2$ nanotubes/Ti Plates modified by silver-benzene with enhanced photocatalytic antibacterial properties. *New J. Chem.* **2018**, *42*, 2058–2066. [CrossRef]

185. Jiang, W.; He, J.; Zhong, J.; Lu, J.; Yuan, S.; Liang, B. Preparation and photocatalytic performance of ZrO$_2$ nanotubes fabricated with anodization process. *Appl. Surf. Sci.* **2014**, *307*, 407–413. [CrossRef]

186. Cristino, V.; Caramori, S.; Argazzi, R.; Meda, L.; Marra, G.L.; Bignozzi, C.A. Efficient photoelectrochemical water splitting by anodically grown WO$_3$ electrodes. *Langmuir* **2011**, *27*, 7276–7284. [CrossRef] [PubMed]

187. Lai, C.W.; Hamid, S.B.A.; Sreekantan, S. A novel solar driven photocatalyst: Well-aligned anodic WO$_3$ nanotubes. *Int. J. Photoenergy* **2013**, *2013*, 745301. [CrossRef]

188. Liu, Y.; Meng, H.; Yu, X.; Zhu, Y.; Zhang, Y. Photocatalytic film of BiOCl honeycomb array from anodic aluminium oxide template. *Mater. Technol. Adv. Func. Mater.* **2015**, *30*, A84–A88. [CrossRef]
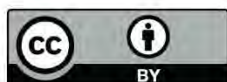
Chapter 3

ENGINEERING OF HYBRID NANOPOROUS
ANODIC ALUMINA PHOTONIC CRYSTALS
BY HETEROGENEOUS PULSE
ANODISATION

3. Engineering of Hybrid Nanoporous Anodic Alumina Photonic Crystals by Heterogeneous Pulse Anodisation

3.1 Introduction, Significance and Commentary

Fabrication of nanoporous anodic alumina photonic crystals (NAA-PCs) with advanced nanoarchitectures to control light–matter interactions for a variety of applications remains challenging. This study explores a heterogeneous pulse anodisation (HPA) approach to fabricate hybrid PCs (Hy-NAA-PCs) composed of different combinations of distributed Bragg reflectors (DBRs) and apodised gradient-index filters (APO-GIFs) in a single PC structure. The highly controllable optical properties (i.e. number, position and bandwidth of photonic stopband – PSB) of Hy-NAA-PCs produced using this versatile advanced nanofabrication method opens new opportunities to develop innovative photonic nanostructures with implications in many fields such as sensing, photonics and photocatalysis.

3.2 Publication

This chapter is presented as published journal article by **S.Y. Lim**, C.S. Law, L.F. Marsal, and A. Santos, *Engineering of hybrid nanoporous anodic alumina photonic crystals by heterogeneous pulse anodization*. Scientific Reports, 2018. **8**(1): p. 9455.

Statement of Authorship

Title of Paper	Engineering of Hybrid Nanoporous Anodic Alumina Photonic Crystals by Heterogeneous Pulse Anodization
Publication Status	☑ Published ☐ Accepted for Publication ☐ Submitted for Publication ☐ Unpublished and Unsubmitted work written in manuscript style
Publication Details	S.Y. Lim, C.S. Law, L.F. Marsal, and A. Santos, *Engineering of hybrid nanoporous anodic alumina photonic crystals by heterogeneous pulse anodization.* Scientific Reports, 2018. **8**(1): p. 9455.

Principal Author

Name of Principal Author (Candidate)	Siew Yee Lim		
Contribution to the Paper	Performed the experiment, processed and analysed the data and wrote the manuscript under the supervision of Abel Santos.		
Overall percentage (%)	70		
Certification:	This paper reports on original research I conducted during the period of my Higher Degree by Research candidature and is not subject to any obligations or contractual agreements with a third party that would constrain its inclusion in this thesis. I am the primary author of this paper.		
Signature		Date	10/06/2020

Co-Author Contributions

By signing the Statement of Authorship, each author certifies that:

    i.   the candidate's stated contribution to the publication is accurate (as detailed above);

    ii.   permission is granted for the candidate in include the publication in the thesis; and

    iii.   the sum of all co-author contributions is equal to 100% less the candidate's stated contribution.

Name of Co-Author	Cheryl Suwen Law		
Contribution to the Paper	Aided in performing the experiment. Give consent to Siew Yee Lim to present this paper for examination towards the Doctorate of Philosophy.		
Signature		Date	15/06/2020

Name of Co-Author	Lluís F. Marsal		
Contribution to the Paper	Aided in the evaluation of final version of manuscript. Give consent to Siew Yee Lim to present this paper for examination towards the Doctorate of Philosophy.		
Signature		Date	10/06/2020

Name of Co-Author	Abel Santos		
Contribution to the Paper	Acted as a primary supervisor for the candidate, and aided in developing, revising and evaluating the manuscript for submission. Give consent to Siew Yee Lim to present this paper for examination towards the Doctorate of Philosophy.		
Signature		Date	11/06/2020

SCIENTIFIC REPORTS

Engineering of Hybrid Nanoporous Anodic Alumina Photonic Crystals by Heterogeneous Pulse Anodization

Siew Yee Lim[1,2,3], Cheryl Suwen Law[1,2,3], Lluís F. Marsal [4] & Abel Santos[1,2,3]

In this study, we present an advanced nanofabrication approach, so-called 'heterogeneous pulse anodization' (HPA), in which galvanostatic stepwise and apodized sinusoidal pulse anodizations are combined in a single process. This novel anodization method enables the precise optical engineering of the characteristic photonic stopbands (PSBs) of nanoporous anodic alumina photonic crystals (NAA-PCs). The resulting structures are hybrid PCs (Hy-NAA-PCs) composed of distributed Bragg reflectors (DBRs) and apodized gradient-index filters (APO-GIFs) embedded within the same PC structure. The modification of various anodization parameters such as anodization period, relative and total anodization time, structural arrangement of PCs within Hy-NAA-PCs, and pore widening time allows the fine-tuning of the PSBs' features (i.e. number, position and bandwidth of central wavelength) across the spectral regions. The effects of these fabrication parameters are systematically assessed, revealing that the positions of the characteristic transmission bands of Hy-NAA-PCs are highly controllable. Our study provides a comprehensive rationale towards the development of unique Hy-NAA-PCs with controllable optical properties, which could open new opportunities for a plethora of applications.

Photonic crystals (PCs) are periodic optical nanostructures that can control the propagation of light by modifying the motion of incoming photons when these travel across the PC's structure[1-5]. These structures feature a dimensional variation in refractive index, which can be arranged a 1D, 2D or 3D fashion[6]. PCs are extensively used in a broad range of applications, including telecommunications[7,8], quantum computing[9,10], energy and water remediation[11-17], medical imaging[18,19], and metal coloring[20]. The unique optical and electronic properties of PCs make them ideal platforms for a plethora of applications since these structures can behave as an effective medium and display photonic stopbands (PSBs) in different regions of the spectrum to control light–matter interactions at the nanoscale with precision[21].

'Hybrid' PC structures can be defined as the combination of several individual PCs within a single complex PC structure, the spectrum of which corresponds to the combination of the spectra of each individual PC composing the hybrid structure. Hybrid PCs allow the generation of advanced systems to control light across the spectral regions with versatility, featuring different PSBs with flexible characteristics (e.g. combination of narrow and broad PSBs) for specific applications such as light filtering, sensing, etc. PCs can be synthesized by multiple fabrication methods, including lithography and dry etching[22-24], vertical selective oxidation[25], fibre-pulling[26], embossing[27], and self-organization[28,29]. However, the generation of hybrid PCs by these techniques remains challenging. Among alternative fabrication methods, anodization–electrochemical oxidation of metals–has been recently demonstrated as a suitable technique to fabricate complex metal oxide nanoporous PC structures since this cost-competitive, precise, and industrially scalable method enables the generation of PCs with high degree of regularity, flexibility, optimal resolution, and high aspect ratio[30,31].

[1]School of Chemical Engineering, The University of Adelaide, 5005, Adelaide, Australia. [2]Institute for Photonics and Advanced Sensing (IPAS), The University of Adelaide, 5005, Adelaide, Australia. [3]ARC Centre of Excellence for Nanoscale BioPhotonics (CNBP), The University of Adelaide, 5005, Adelaide, Australia. [4]Department of Electronic, Electric, and Automatics Engineering, Universitat Rovira i Virgili, 43007, Tarragona, Spain. Correspondence and requests for materials should be addressed to L.F.M. (email: lluis.marsal@urv.cat) or A.S. (email: abel.santos@adelaide.edu.au)

The intrinsic relationship between the fabrication parameters and the nanoporous structure of the resulting anodic oxide films enables the synthesis of multiple PC structures, including optical microcavities[32], Fabry-Pérot interferometers[33] bandpass filters[34], distributed Bragg reflectors[20,35], and gradient-index filters[36]. Of all the nanoporous anodic oxides produced by anodization of metals, nanoporous anodic alumina (NAA) produced by anodization of aluminum offers a unique platform material to generate complex PCs with versatile optical properties due to its excellent physical and chemical properties, highly controllable and flexible pore geometry, chemical resistance, thermal stability, mechanical robustness, non-cytotoxicity, and optoelectronic properties[37]. However, the generation of complex NAA-PCs poses some challenges due to the presence of the oxide barrier layer at the bottom tip of the nanopores, which prevents the diffusion of ionic species (e.g. Al^{3+}, O^{2-}, OH^-, etc.) from and to the bulk electrolyte and regulates the transfer of electrons from anode to cathode during anodization[38–42]. Although pioneering studies demonstrated that this inherent drawback can be overcome through pulse-like anodization approaches switching the regime between mild and hard conditions[43–47], the low controllability of hard anodization (i.e. fast oxide growth rate, heat generation, low porosity level, etc.) has limited the applicability of this approach to synthesize complex NAA-PCs[38].

Recently, some studies by us and others have demonstrated that pulse-like anodization under mild conditions enables a more controllable approach to generate a wide range of NAA-PCs (e.g. distributed Bragg reflectors (DBR)[20], optical microcavities[32], gradient-index filters (GIFs)[36], and apodized gradient-index filters (APO-GIFs)[48]). The utilization of rationally designed anodization profiles (i.e. apodized-sinusoidal, pseudo-sinusoidal, sinusoidal, sawtooth-like, and pseudo-stepwise) under suitable anodization conditions makes it possible to directly translate anodizing current density or voltage pulses into porosity modulations with precision, overcoming the inherent limitations of anodization for the in-depth engineering of the NAA's PSB. In particular, we have recently proved that stacked NAA-bandpass filters, which consist of layers of NAA produced with different pseudo-stepwise pulse anodization periods, lead to the generation of NAA-PCs with unprecedented broad transmission bands across the UV-visible-NIR spectrum[34]. We also envisage this nanofabrication concept for the generation of hybrid nanoporous anodic alumina photonic crystals (Hy-NAA-PCs) with unique optical properties.

Herein, we present a novel nanofabrication approach that enables the production of Hy-NAA-PCs composed of different combinations of DBRs and APO-GIFs in a single PC structure. This one-step anodization method ('heterogeneous pulse anodization'–HPA) is a combination of logarithmic negative apodized sinusoidal and stepwise pulse anodizations under mild conditions to attain a better controllability over the porosity and growth rate of the anodic oxide (Fig. 1). We systematically assess the effects of the fabrication parameters (i.e. anodization period, relative and total anodization time, pore widening time, and arrangement of PC structures) over the optical properties of Hy-NAA-PCs, including the position and bandwidth of the characteristic PSBs and interferometric colors. These Hy-NAA-PCs are fabricated with either two or three individual PCs featuring different geometries, demonstrating that the number, the position, and the bandwidth of the characteristic PSBs for each PC embedded within the hybrid PC structures can be precisely engineered to produce a set of unique Hy-NAA-PCs with outstanding optical properties.

Results and Discussion

Fabrication and Structural Characterization of Hy-NAA-PCs.
Figure 1 displays schematic representations of the structure of NAA-DBRs and APO-NAA-GIFs, which are the basic unit PC structures used in our study to create Hy-NAA-PCs by HPA. As these reveal, NAA-DBRs feature a stepwise modulation of the pore diameter in depth that follows with precision the stepwise current density profile applied during the stepwise pulse anodization (STPA) process (Fig. 1a). In the case of APO-NAA-GIFs, the nanoporous structure is composed of stacked layers of NAA featuring a sinusoidally modified porosity in depth produced during apodized sinusoidal pulse anodization (ASPA), where the higher the anodization current density the higher the level of porosity following a logarithmic negative apodization function with time-dependent current density amplitude (Fig. 1b). These fabrication methods allow the precise engineering of the effective medium of NAA in depth to tune the features of the PSB (i.e. position of central wavelength and full width at half maximum) across the spectral regions with precision, as demonstrated in previous studies (Fig. 1c,d)[20,48]. Figure 1e,f show representative transmission spectra of NAA-DBRs and APO-NAA-GIFs, where the former shows a much broader characteristic PSB than that of the latter PC, which displays a characteristically well-resolved and narrow PSB. As demonstrated in previous studies, the position of the characteristic PSB (λ_{PSB}) of these PCs can be precisely positioned across the spectral regions, from UV to IR, by modifying the anodization period (i.e. time between consecutive anodization pulses–T_P)[20,48]. Figure S1 (Supporting Information) shows the dependency of λ_{PSB} with T_P for NAA-DBRs and APO-NAA-GIFs, which was found to follow a linear trend in both cases. Although λ_{PSB} is red-shifted with T_P for NAA-DBRs and APO-NAA-GIFs, the former type of NAA-PC shows a slightly stronger dependency with T_P as denoted by the slopes of the fitting lines (i.e. 0.62 ± 0.02 and 0.42 ± 0.01 nm s^{-1} for NAA-DBRs and APO-NAA-GIFs, respectively). Another interesting observation is that at $T_P > 1150$ s, the position of the PSB of NAA-DBRs is at longer wavelengths than that of their APO-NAA-GIFs counterparts produced with the same anodization period. This trend is opposite at $T_P > 1150$ s, where APO-NAA-GIFs feature λ_{PSB} at longer wavelengths than that of NAA-DBRs for any T_P.

Figure 2a displays a conceptual illustration of Hy-NAA-PCs, where NAA-DBRs and APO-NAA-GIFs are combined into the same PC structure by HPA process. In this versatile top-down nanofabrication approach, the anodization profile can be modified to exchange the arrangement of the individual PC structures within the Hy-NAA-PC at will as well as to modify the number and characteristics of these PCs to control light in a versatile fashion for specific applications. In our study, we developed and assessed two types of Hy-NAA-PCs: i) Bi-Hy-NAA-PCs, composed of two individual NAA-PCs (Fig. 2a), and ii) Tri-Hy-NAA-PCs, formed by the generation of three individual NAA-PCs (Fig. 2b). As Fig. 2c,d show, the transmission spectrum of Hy-NAA-PCs
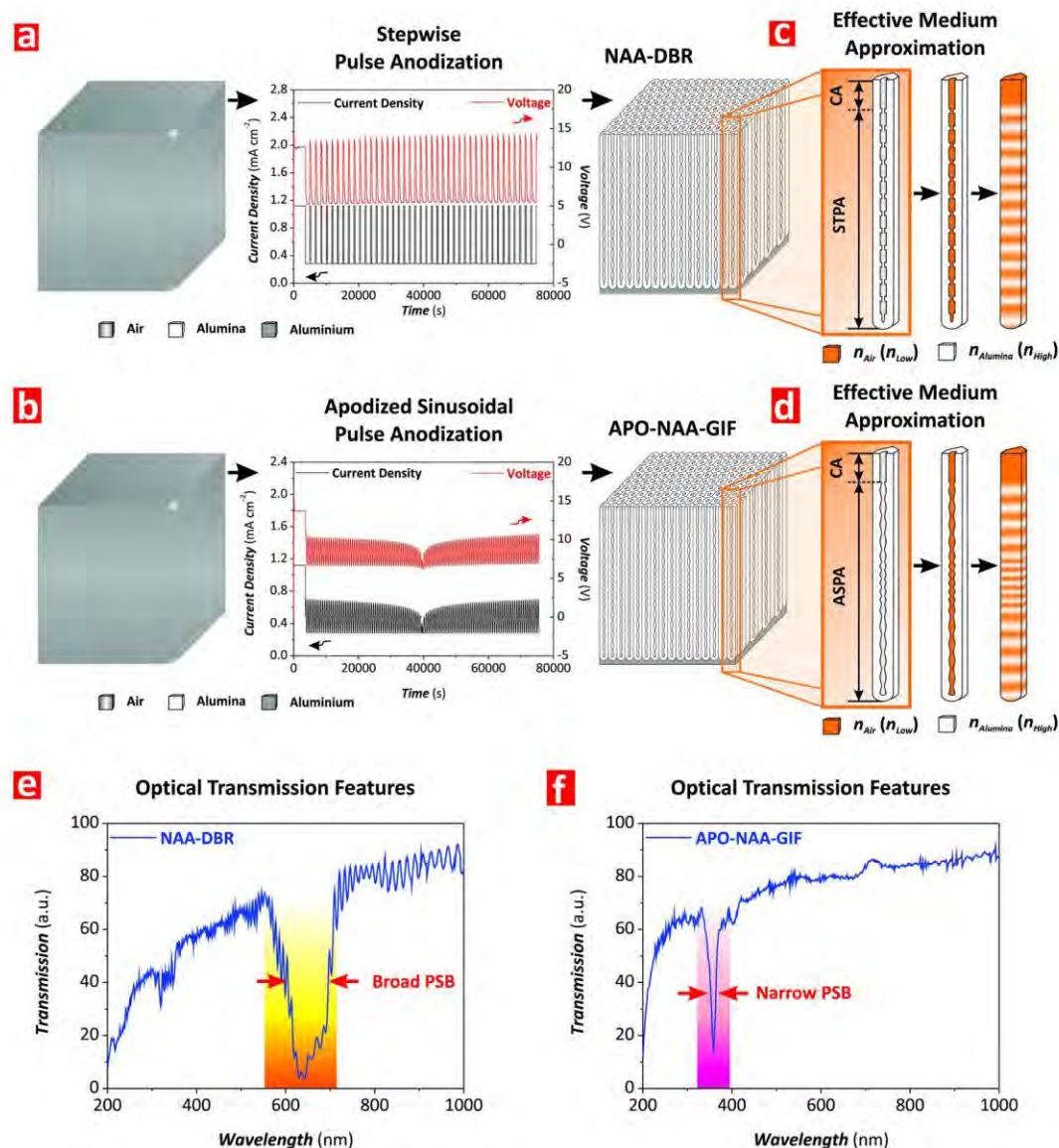
Figure 1. Fabrication of NAA-DBRs and APO-NAA-GIFs by stepwise pulse anodization (STPA) and apodized sinusoidal pulse anodization (ASPA), respectively. (**a,b**) Schematics illustrating the STPA and ASPA processes, representative anodization profiles, and nanoporous structure of NAA-DBRs and APO-NAA-GIFs, respectively. (**c,d**) Graphical correlation between nanopore geometry and distribution of refractive index in the structure of NAA-DBRs and APO-NAA-GIFs, respectively (Note: n_{Air} (n_{Low}) and $n_{Alumina}$ (n_{High}) are the refractive indices of air and alumina). (**e,f**) Representative transmission spectra showing the features of the photonic stopband (PSB) of NAA-DBRs and APO-NAA-GIFs, respectively.

can be approximated to the resulting combination of the spectra of each individual NAA-PCs embedded within the hybrid PC structure.

Figure 3 compiles a set of representative FEG-SEM images illustrating the structure of Hy-NAA-PCs. As these images reveal, Hy-NAA-PCs feature a random distribution of nanopores across their top surface, which have an as-produced diameter (d_p) of 10 ± 2 nm (i.e. $t_{pw} = 0$ min) and that is enlarged up to 20 ± 3 nm after 6 min of pore widening treatment (Fig. 3a). Cross-sectional FEG-SEM images demonstrate that the nanopore diameter in Hy-NAA-PCs is modulated in depth following the HPA current density profile (Fig. 3b,c), where each individual PC structure can be discerned.

Effect of Structural Arrangement on the Optical Properties of Bi-Hy-NAA-PCs. The structure of Bi-Hy-NAA-PCs is composed of two individual NAA-PCs: one NAA-DBR and one APO-NAA-GIF, in which these can be alternately arranged as the top or bottom structures (Fig. 2a). First, we fabricated two types of Bi-Hy-NAA-PCs featuring two configurations to study the effect of the arrangement of the NAA-DBR and APO-NAA-GIF on the optical properties of Bi-Hy-NAA-PCs and assess the capabilities of our HPA approach (Table 1): i) Bi-Hy-NAA-PCs, where the APO-NAA-GIF is located at the top of the hybrid NAA-PC structure and
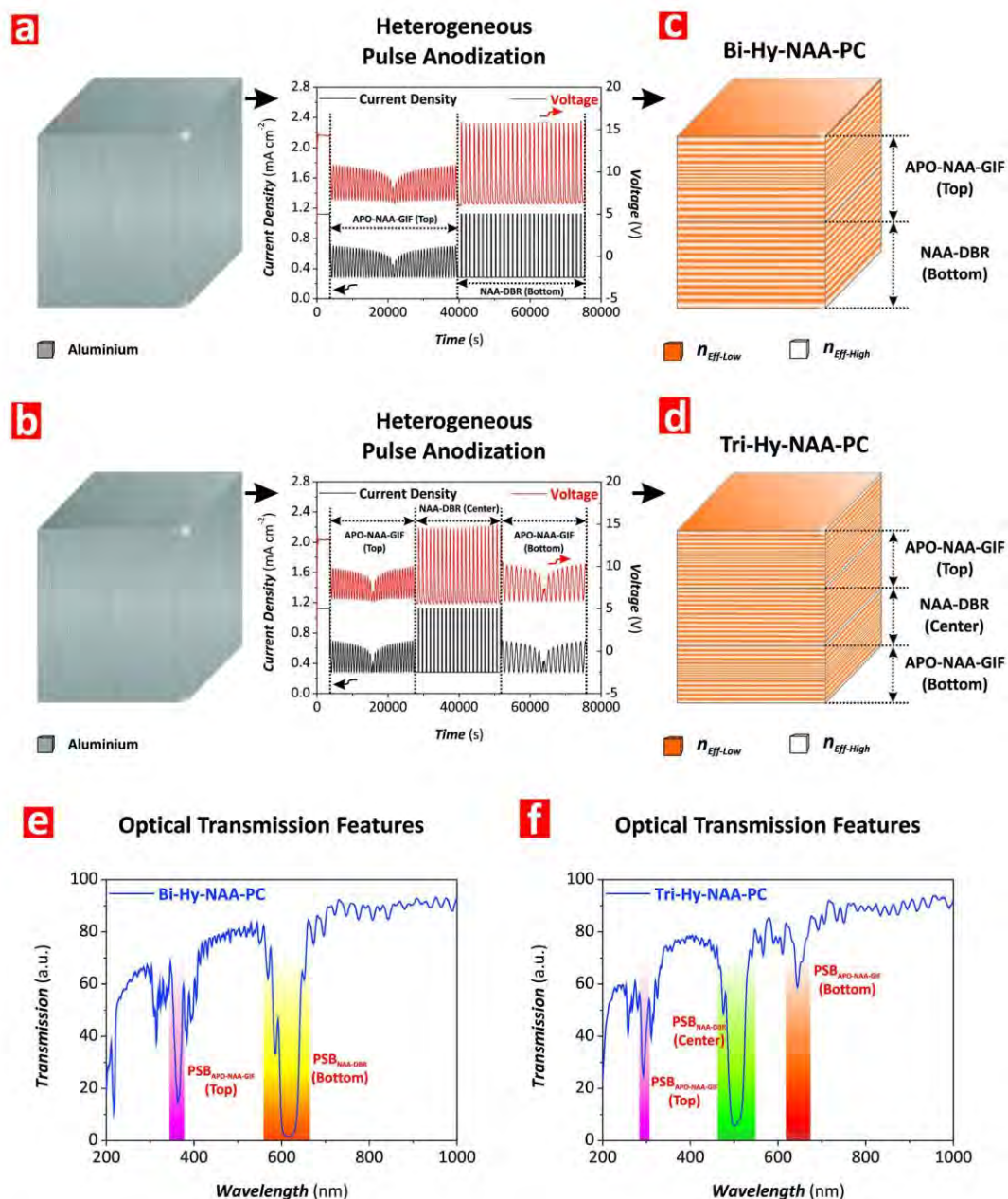
65

Figure 2. Fabrication of Bi- and Tri-Hy-NAA-PCs by heterogeneous pulse anodization (HPA). (**a,b**) Schematics illustrating the HPA processes used to produce Bi- and Tri-Hy-NAA-PCs with representative anodization profiles, respectively. (**c,d**) Schematic illustration of the distribution of effective refractive index in depth for Bi- and Tri-Hy-NAA-PCs, respectively (Note: $n_{Eff-Low}$ and $n_{Eff-High}$ are the low and high effective refractive indices, respectively). (**e,f**) Representative transmission spectra showing the features of the photonic stopbands (PSBs) of NAA-DBRs and APO-NAA-GIFs embedded within the structure of Bi- and Tri-Hy-NAA-PCs, respectively.

the NAA-DBR is located at its bottom, and ii) Inv-Bi-Hy-NAA-PCs with an inverted configuration, in which the NAA-DBR is located at the top and the APO-NAA-GIF at the bottom of the PC structure.

Figure 4a,b display representative anodization profiles used to produce the Bi-Hy-NAA-PCs and Inv-Bi-Hy-NAA-PCs analyzed in our study. NAA-DBRs were fabricated with $T_P = 1200\,s$ (i.e. $t_{min} = 960\,s$ and $t_{max} = 240\,s$) and 30 pulses (i.e. relative anodization time = 10 h), and APO-NAA-GIFs with $T_P = 800\,s$, $J_{Offset} = 0.280\,mA\,cm^{-2}$, $\Delta A_J = 0.210\,mA\,cm^{-2}$ and 45 pulses (i.e. relative anodization time = 10 h). Note that to avoid overlapping of PSBs, using Figure S1 as a reference, the fabrication conditions were selected so the PSB of NAA-DBRs and APO-NAA-GIFs were located at ~700 nm and ~450 nm, respectively.

The relative (i.e. time or number of pulses used to produce each individual PC structure) and total anodization times were fixed to 10 and 20 h, respectively, in both types of Hy-NAA-PCs. HPA is a continuous top-down fabrication process controlled by the diffusion of ionic species (e.g. Al^{3+}, O^{2-}, OH^{-}) along the nanopores and the
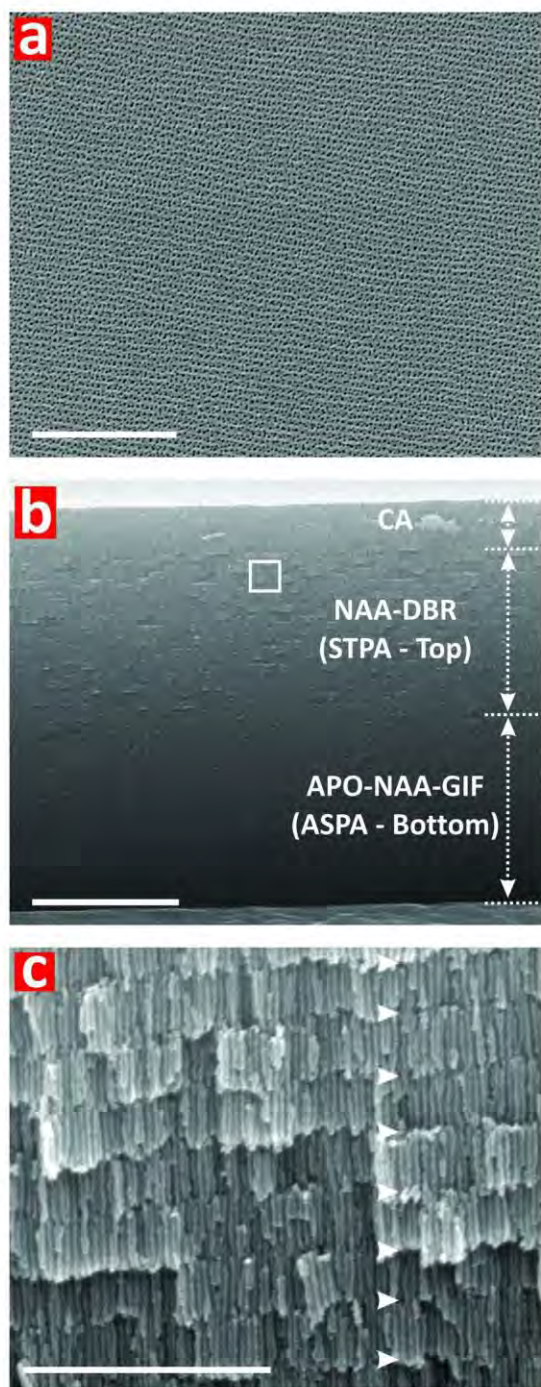
Figure 3. Structural characterization of Bi- and Tri-Hy-NAA-PCs produced by heterogeneous pulse anodization (HPA). (**a**) Top FEG-SEM image of a Bi-Hy-NAA-PC combining one NAA-DBR on its top and one APO-NAA-GIF on its bottom produced by HPA and $t_{pw} = 6$ min (scale bar = 1 μm). (**b**) Cross-sectional FEG-SEM image showing the different parts of the Bi-Hy-NAA-PC (Note: CA = constant anodization) (scale bar = 5 μm). (**c**) Magnified view of white rectangle shown in (**b**) revealing the modulation of pore diameter in depth, where white arrowheads denote the period length (i.e. distance between consecutive pulses in the structure of the Bi-Hy-NAA-PC) (scale bar = 1 μm).

oxide barrier layer. However, the anodization conditions used in our study make it possible the direct translation of current density pulses (input) into porosity changes in depth, as denoted by the anodization voltage (output), enabling the precise and versatile engineering of the nanoporous structure of NAA (Fig. 4c,d).

Figure 4e,f show representative transmission spectra of Bi-Hy-NAA-PCs and Inv-Bi-Hy-NAA-PCs fabricated with the above-mentioned characteristics as a function of the pore widening time (t_{pw}). In both cases, these NAA-PCs display two types of PSB at $t_{pw} = 0$ min, one broad PSB with λ_{PSB} at ~700 nm and one narrow PSB

Type	Top PC Structure $t_{An\text{-}Top}$ (h)–T_p (s)	Bottom PC Structure $t_{An\text{-}Bottom}$ (h)–T_P (s)	t_{An} (h)
Bi-Hy-NAA-PC	APO-NAA-GIF 10 h–800 s	NAA-DBR 10 h–1200 s	20 h
Inv-Bi-Hy-NAA-PC	NAA-DBR 10 h–1200 s	APO-NAA-GIF 10 h–800 s	20 h
Bi-Hy-NAA-PC	APO-NAA-GIF 7.5 h–800 s	NAA-DBR 7.5 h–1200 s	15 h
Bi-Hy-NAA-PC	APO-NAA-GIF 5 h–800 s	NAA-DBR 5 h–1200 s	10 h

Table 1. Summary table compiling the structural arrangement and fabrication conditions for each Bi-Hy-NAA-PC structure assessed in this study.

with λ_{PSB} at ~450 nm, which correspond to the NAA-DBR (PSB$_{NAA\text{-}DBR}$) and the APO-NAA-GIF PC structures (PSB$_{APO\text{-}NAA\text{-}GIF}$), respectively. It is observed that the position of the two characteristic PSBs undergoes a blue shift with increasing t_{pw}, which is in good agreement with previous studies reported elsewhere[48,49]. For instance, at $t_{pw} = 0$ min, λ_{PSB} for the APO-NAA-GIF structure in Bi-Hy-NAA-PCs and Inv-Bi-NAA-PCs was 449 ± 1 and 452 ± 1 nm, respectively, which is certainly close to the value estimated from Figure S1 (~450 nm). This observation is confirmed for the NAA-DBR structure too, which central wavelength was positioned at 692 ± 1 and 660 ± 1 nm in Bi-Hy-NAA-PCs and Inv-Bi-NAA-PCs, respectively (estimated value ~700 nm). These observations demonstrate that the position of the PSB$_{NAA\text{-}DBR}$ and PSB$_{APO\text{-}NAA\text{-}GIF}$ is practically independent on the arrangement of these PCs within the structure of Hy-NAA-PCs during the HPA process but highly dependent on the anodization period (NAA-DBR–$T_p = 1200$ s and APO-NAA-GIF–$T_p = 800$ s).

As these graphs reveal, the position of PSB$_{NAA\text{-}DBR}$ and PSB$_{APO\text{-}NAA\text{-}GIF}$ in Bi-Hy-NAA-PCs and Inv-Bi-NAA-PCs can be linearly tuned by a pore widening treatment. Linear fittings showing the dependence of λ_{PSB} with t_{pw} for each individual PC structure reveal that in Bi-Hy-NAA-PCs λ_{PSB} is blue-shifted with t_{pw} at similar rates (i.e. -14 ± 1 and -13 ± 2 nm min^{-1} for PSB$_{APO\text{-}NAA\text{-}GIF}$ and PSB$_{NAA\text{-}DBR}$, respectively). However, in the case of Inv-Bi-Hy-NAA-PCs, the position of the central wavelength of the NAA-DBR located at the top part was observed to change at slightly higher rate than its non-inverted counterpart (i.e. -22 ± 1 and -11 ± 2 nm min^{-1} for PSB$_{NAA\text{-}DBR}$ and PSB$_{APO\text{-}NAA\text{-}GIF}$, respectively) (Figure S2–Supporting Information). The analysis of the full width at half maximum (FWHM) of the PSB$_{NAA\text{-}DBR}$ and PSB$_{APO\text{-}NAA\text{-}GIF}$ for Bi-Hy-NAA-PCs and Inv-Bi-Hy-NAA-PCs reveals that, as expected, the FWHM of the PSB of NAA-DBRs are fairly wider than that of the APO-NAA-GIFs. Furthermore, in general, it is observed that the transmission bands are broader for Inv-Bi-Hy-NAA-PCs than those of Bi-Hy-NAA-PCs with increasing t_{pw}. For example, in the case of Bi-Hy-NAA-PCs, the FWHM$_{APO\text{-}NAA\text{-}GIF}$ and FWHM$_{NAA\text{-}DBR}$ for t_{pw} 0 and 6 min were measured to be 8 ± 1 and 18 ± 1 nm, and 20 ± 1 and 54 ± 1 nm, respectively. However, for Inv-Bi-Hy-NAA-PCs, the values of FWHM$_{APO\text{-}NAA\text{-}GIF}$ and FWHM$_{NAA\text{-}DBR}$ for t_{pw} 0 and 6 min were 10 ± 1 and 29 ± 1 nm, and 30 ± 1 and 160 ± 1 nm, respectively.

The arrangement of individual PC structures from Bi-Hy-NAA-PCs to Inv-Bi-Hy-NAA-PCs produced an increment of FWHM of 23 and 49% for the APO-NAA-GIF at $t_{pw} = 0$ and 6 min, and 34 and 66% for the NAA-DBR. Therefore, our analysis reveals that, while the interchange of individual PCs within the structure of Bi-Hy-NAA-PCs has not significant effect on the position of the PSBs, it significantly affects the FWHM of the PSBs.

Figure 4e,f compile digital images of Bi-Hy-NAA-PCs and Inv-Bi-Hy-NAA-PCs as a function of t_{pw}, showing that these PCs display vivid interferometric colors across the UV-visible-NIR spectrum. In good agreement with our observations about the effect of the arrangement of individual PC structures on the λ_{PSB} and FWHM of Hy-NAA-PCs, it is observed that the interferometric color at a fixed t_{pw} is slightly blue shifted in Inv-Bi-Hy-NAA-PCs as compared to their reference Bi-Hy-NAA-PCs (e.g. green and orange colors for the former and latter at $t_{pw} = 6$ min, respectively). This result can be ascribed to the broader and more intense PSB of the NAA-DBR embedded in the structure of Inv-Bi-Hy-NAA-PCs, which is the main contributor to the efficient reflection of light (i.e. color) from Bi-Hy-NAA-PCs.

Effect of Relative and Total Anodization Times on the Optical Properties of Bi-Hy-NAA-PCs.

As mentioned above, the structure of Bi-Hy-NAA-PCs is composed of two individual PCs, with one APO-NAA-GIF and one NAA-DBR located at the top and bottom of the hybrid photonic structure, respectively. As shown in the previous section, these NAA-PCs were fabricated at fixed relative anodization time (t_{An}) or number of pulses and anodization period, which were set at $t_{An\text{-}Top} = 10$ h (or 45 pulses) and $T_p = 800$ s for the APO-NAA-GIF, and at $t_{An\text{-}Bottom} = 10$ h (or 30 pulses) and $T_p = 1200$ s for the NAA-DBR, respectively. HPA is a versatile nanofabrication approach that can be used to engineer the characteristic features of each individual PC within Hy-NAA-PCs. To gain insight into the capabilities of HPA, we assessed the effect of the relative anodization times (i.e. $t_{An\text{-}Top}$ and $t_{An\text{-}Bottom}$) and the total anodization time (t_{An}) on the optical properties (i.e. λ_{PSB}, FWHM, and interferometric color) of Bi-Hy-NAA-PCs by systematic modification of these fabrication parameters. Table 1 summarizes the set of $t_{An\text{-}Top}$, $t_{An\text{-}Bottom}$, and t_{An} values used in our study, the transmission spectra of which are shown in Figure S3 (Supporting Information).

Figure 5 shows the effect of t_{An} (from 10 to 20 h) on the λ_{PSB}, FWHM, and interferometric color of the Bi-Hy-NAA-PCs produced at $t_{An\text{-}Top} = t_{An\text{-}Bottom}$ (from 5 to 10 h) and different pore widening times (from 0 to 6 min). Figure 5a displays the dependency of λ_{PSB} for the APO-NAA-GIF and NAA-DBR in the structure of
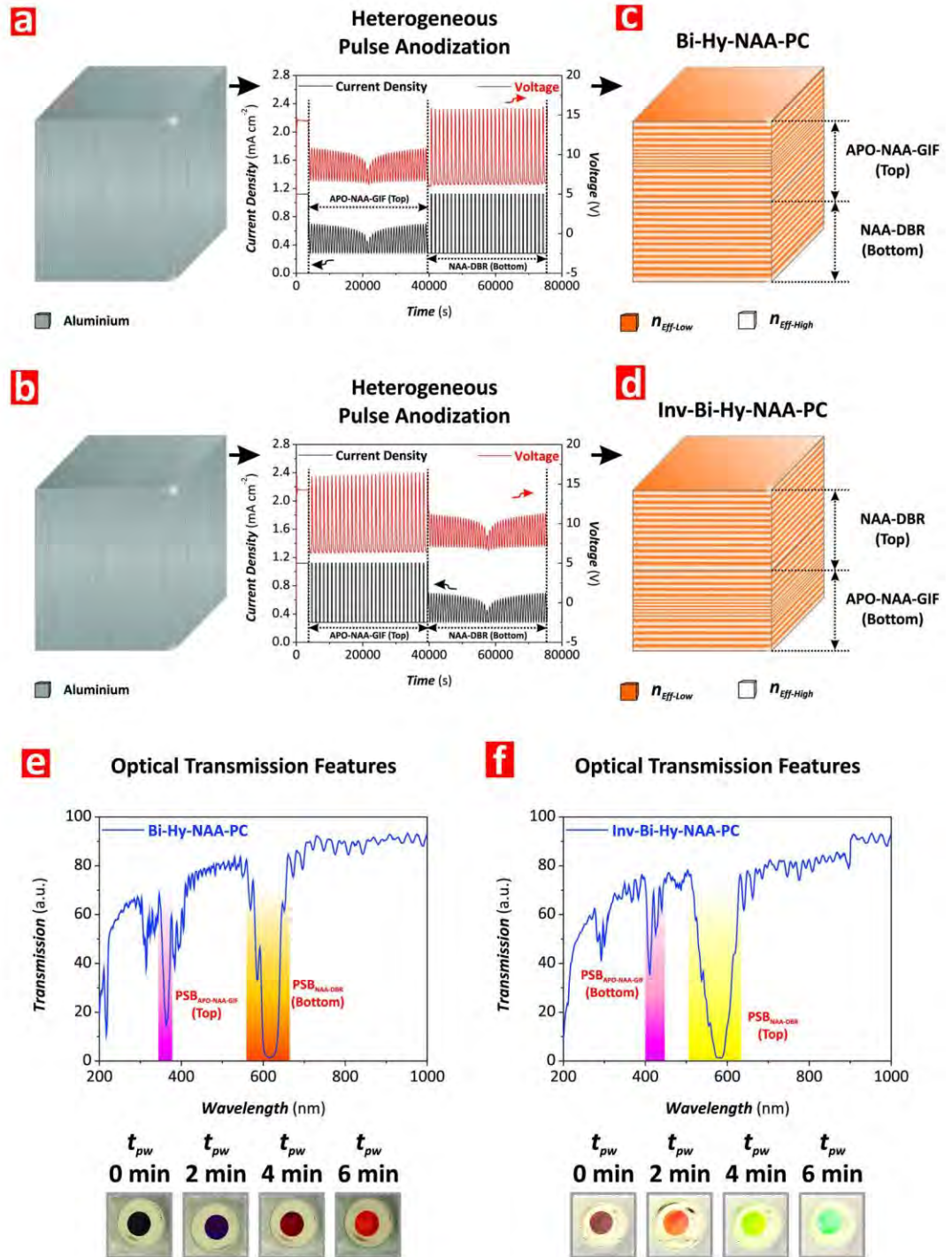
68

Figure 4. Fabrication of Bi- and Inv-Bi-Hy-NAA-PCs by heterogeneous pulse anodization (HPA). (**a,b**) Schematics illustrating the HPA processes used to produce Bi- and Inv-Bi-Hy-NAA-PCs with representative anodization profiles, respectively. (**c,d**) Schematic illustration of the distribution of effective refractive index in depth for Bi- and Inv-Bi-Hy-NAA-PCs, respectively. (**e,f**) Representative transmission spectra showing the features of the photonic stopbands (PSBs) of NAA-DBRs and APO-NAA-GIFs embedded within the structure of Bi- and Inv-Bi-Hy-NAA-PCs and digital pictures showing the interferometric color displayed by these PC structures as a function of t_{pw}, respectively.

Bi-Hy-NAA-PCs as a function of t_{An} and t_{pw}. It is observed that, in the case of the NAA-DBR structure, λ_{PSB} undergoes a blue shift as t_{An} is reduced from 20 to 10 h (i.e. $t_{An-Top} = t_{An-Bottom} = 10$ and 5 h, respectively).

This blue shift is observed to be more significant as t_{pw} increases from 0 to 6 min. However, this trend is not observable in the case of the APO-NAA-GIF structure, which shows no statistically significant changes in λ_{PSB} with t_{An}. In good agreement with previous results, λ_{PSB} undergoes a blue shift with t_{pw}, which was found
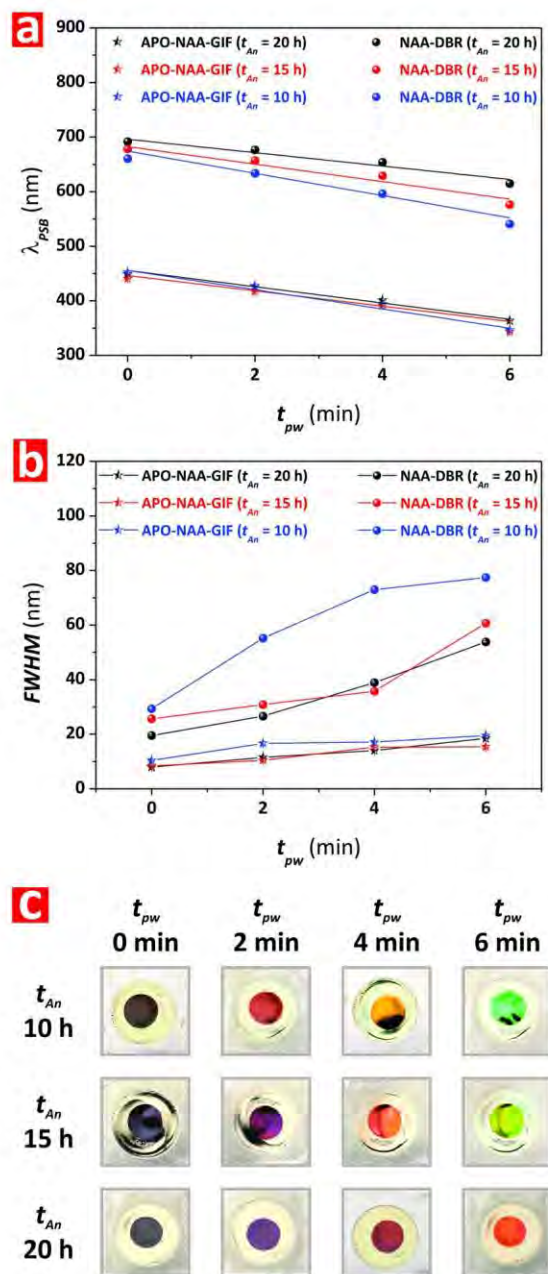
69

Figure 5. Effect of total anodization time (t_{An}) and pore widening time (t_{pw}) on the optical features (position of central wavelength–λ_{PSB}, full-width at half maximum–FWHM, and interferometric color) of Bi-Hy-NAA-PCs. (**a**) Effect of t_{An} and t_{pw} on λ_{PSB}. (**b**) Effect of t_{An} and t_{pw} on FWHM. (**c**) Effect of t_{An} and t_{pw} on interferometric color.

to be statistically the same at any t_{An}. Figure 5b shows the dependency of the FWHM of the PSB$_{APO-NAA-GIF}$ and PSB$_{NAA-DBR}$ structures in Bi-Hy-NAA-PCs as a function of t_{An} and t_{pw}. At first glance, it is verified that the longer t_{pw} the wider FWHM in both the APO-NAA-GIF and NAA-DBR structure, although it is worth noting that this effect is much more significant for the latter individual PC structure. Another aspect to note is that the FWHM shows similar behavior for both PCs at t_{An} = 15 and 20 h. However, a reduction of t_{An} down to 10 h results in a significant enlargement of the FWHM of the PSB$_{NAA-DBR}$. This increment is also observed in the case of the APO-NAA-GIF, although in a less significant manner than that of its NAA-DBR counterpart.

As far as the interferometric color of these Bi-Hy-NAA-PCs is concerned, Fig. 5c compiles a set of digital pictures of these NAA-based PCs, in which it is observed that a reduction of the total anodization time results in a slight blue shift in the interferometric color displayed by these PCs, which is in good agreement with our analysis performed in Fig. 5a. For instance, at t_{pw} = 0 min all the samples are transparent, indicating that the PSB is located in the NIR region of the spectrum. At t_{pw} = 2 min, those Bi-Hy-NAA-PCs produced at t_{An} = 10 h display red color, while those produced at 15 and 20 h are still transparent. At t_{pw} = 4 min, Bi-Hy-NAA-PCs produced at t_{An} = 10,
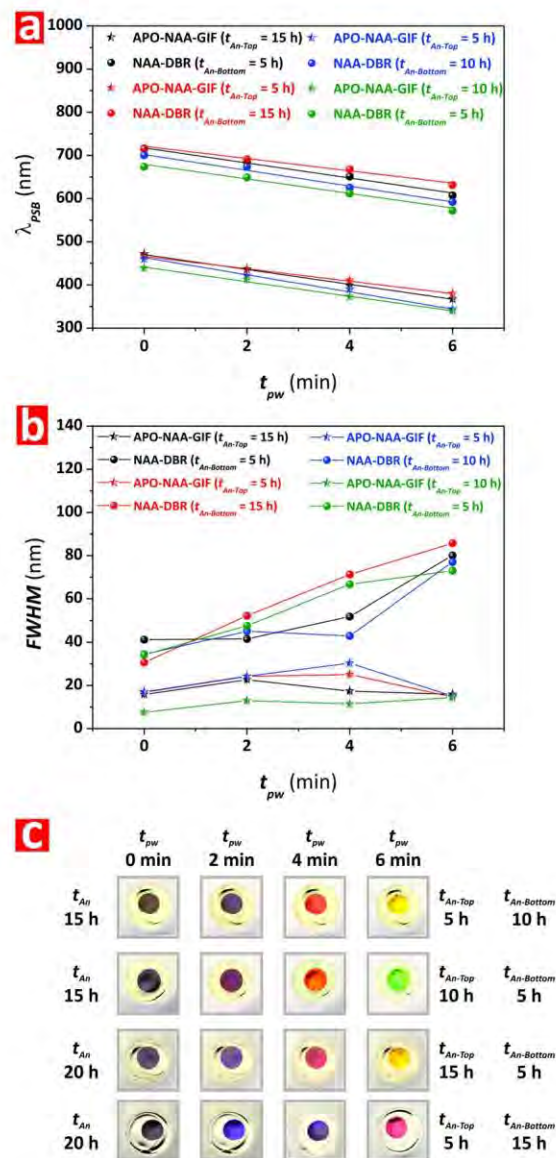
Figure 6. Effect of relative anodization time ($t_{An\text{-}Top}$ and $t_{An\text{-}Bottom}$) and pore widening time (t_{pw}) on the optical features (position of central wavelength–λ_{PSB}, full-width at half maximum–FWHM, and interferometric color) of Bi-Hy-NAA-PCs. (**a**) Effect of $t_{An\text{-}Top}$, $t_{An\text{-}Bottom}$, and t_{pw} on λ_{PSB}. (**b**) Effect of $t_{An\text{-}Top}$, $t_{An\text{-}Bottom}$, and t_{pw} on FWHM. (**c**) Effect of $t_{An\text{-}Top}$, $t_{An\text{-}Bottom}$, and t_{pw} on interferometric color.

15, and 20 h display gold, orange-red, and red color, respectively, denoting a slight blue shift in color as a result of the anodization time.

To gain further insights into the effect of the relative anodization time (i.e. time or number of pulses used to fabricate each of the individual PC structures of Bi-Hy-NAA-PCs–$t_{An\text{-}Top}$ for APO-NAA-GIF and $t_{An\text{-}Bottom}$ for NAA-DBR), we modified these parameters systematically while keeping the total anodization time (t_{An}) constant. We assessed four Bi-Hy-NAA-PCs produced with the following values of $t_{An\text{-}Top}$, $t_{An\text{-}Bottom}$, and t_{An}: i) $t_{An\text{-}Top} = 15\,h$, $t_{An\text{-}Bottom} = 5\,h$, and $t_{An} = 20\,h$; ii) $t_{An\text{-}Top} = 5\,h$, $t_{An\text{-}Bottom} = 15\,h$, and $t_{An} = 20\,h$; iii) $t_{An\text{-}Top} = 5\,h$, $t_{An\text{-}Bottom} = 10\,h$, and $t_{An} = 15\,h$; and iv) $t_{An\text{-}Top} = 10\,h$, $t_{An\text{-}Bottom} = 5\,h$, and $t_{An} = 15\,h$.

Figure 6a summarizes the effect of these fabrication parameters in combination with t_{pw} on the position of the characteristic PSB of these Bi-Hy-NAA-PCs. As a rule, it is observed that the PSB$_{NAA\text{-}DBR}$ undergoes a slight blue shift when t_{An} is reduced from 20 to 15 h, which is further enhanced when the relative anodization time used to produce the NAA-DBR ($t_{An\text{-}Bottom}$) is reduced from 15 to 5 h and from 10 to 5 h, and t_{pw} increased. This trend is also observed in the case of the APO-NAA-GIF structure, although the magnitude of the blue shift with both the relative and total anodization time are less significant than that observed for the NAA-DBR structure.

Figure 6b shows the effect of the relative and total anodization times combined with t_{pw} on the FWHM of the APO-NAA-GIF and NAA-DBR structures of Bi-Hy-NAA-PCs. Although it is not possible to find any consistent pattern of the effect of $t_{An\text{-}Top}$, $t_{An\text{-}Bottom}$, and t_{An} on the FWHM, it can be clearly observed that, likewise in previous

71

cases, extended pore widening times lead to an enlargement of the FWHM of the $PSB_{NAA-DBR}$. The FWHM of the $PSB_{APO-NAA-GIF}$ is much narrower than that of its NAA-DBR counterpart at any t_{An-Top}, $t_{An-Bottom}$, t_{An}, and t_{pw}, and it is also confirmed that it increases with t_{pw} up to 4 min. A slight decrement of FWHM is observed from $t_{pw} = 4$ to 6 min, which might be associated with over etching of the APO-NAA-GIF structure.

Finally, Fig. 6c compiles a set of representative digital pictures of Bi-Hy-NAA-PCs as a function of t_{An-Top}, $t_{An-Bottom}$, t_{An}, and t_{pw}. The qualitative analysis of these pictures reveals that, as shown in Fig. 6a, the reduction of t_{An} leads to a slight blue shift as denoted by the interferometric color of Bi-Hy-NAA-PCs when the $PSB_{NAA-DBR}$ is located within the visible range of the spectrum. This shift is much more evident when the relative anodization time used to produce the NAA-DBR structure ($t_{An-Bottom}$) is reduced since, as mentioned above, the interferometric color is predominantly established by the PSB of the NAA-DBR. For example, at $t_{An} = 15$ h and $t_{pw} = 6$ min, Bi-Hy-NAA-PCs display yellow and green color at $t_{An-Bottom}$ 10 and 5 h, respectively. This is also confirmed at $t_{An} = 20$ h and $t_{pw} = 6$ min, when Bi-Hy-NAA-PCs display red and orange-yellow color at $t_{An-Bottom}$ 20 and 15 h, respectively.

Effect of Structural Arrangement and Relative Anodization Time on the Optical Properties of Tri-Hy-NAA-PCs.

To further demonstrate the versatility of the HPA technique to fabricate hybrid PC structures, we produced a set of Tri-Hy-NAA-PCs featuring three individual PCs in the form of APO-NAA-GIFs and NAA-DBRs. First, we analyzed the effect of the arrangement of the individual PCs on the optical properties of Tri-Hy-NAA-PCs. To this end, we fabricated two types of Tri-Hy-NAA-PCs at constant $t_{An} = 20$ h: Type-1) one structure composed of a NAA-DBR produced with $T_P = 1000$ s and $t_{An-Center} = 6.67$ h (~22 pulses–central structure) sandwiched between two APO-NAA-GIFs produced with $T_P = 700$ s and $t_{An-Top} = 6.67$ h (~34 pulses–top structure) and $T_P = 1300$ s and $t_{An-Bottom} = 6.67$ h (~18 pulses–bottom structure), and Type-2) another structure composed of an APO-NAA-GIF produced with $T_P = 1100$ s and $t_{An-Center} = 6.67$ h (~22 pulses–central structure) sandwiched between two NAA-DBRs produced with $T_P = 900$ s and $t_{An-Top} = 6.67$ h (~27 pulses–top structure), and $T_P = 1200$ s and $t_{An-Bottom} = 6.67$ h (~20 pulses–bottom structure).

Figure 7a and b show representative anodization profiles used to produce these Tri-Hy-NAA-PCs by HPA and schematic illustrations of their structure (Fig. 7c and d). The transmission spectrum of the Type-1 hybrid PC structure displays three PSBs, the features of which are established by each individual PC structure composing the Tri-Hy-NAA-PC (Fig. 7e). However, it must be noted that the Type-2 Tri-Hy-NAA-PC structure composed of two NAA-DBRs and one APO-NAA-GIF did not show the characteristic PSB of the APO-NAA-GIF (Fig. 7f).

Figure 8 summarizes the dependency of λ_{PSB} and FWHM of the individual PCs composing the structure of Type-1 and Type-2 Tri-Hy-NAA-PCs with t_{pw}. It is clearly observed that the λ_{PSB} of these PCs embedded in the structure of Tri-Hy-NAA-PCs follows a linear trend with t_{pw}, where it is blue-shifted with the pore widening process (Fig. 8a). The relative position of the three characteristic PSBs of the Type-1 Tri-Hy-NAA-PC evolves in a similar way with t_{pw}, keeping an equidistant position across the spectrum according to the design of the fabrication conditions for each individual PC structure. Although the PSB of the central APO-NAA-GIF is vanished from the spectrum of the Type-2 Tri-Hy-NAA-PC, the PSBs of the top and bottom NAA-DBRs follow the same trend with t_{pw} than that observed for the Type-1. Figure 8b shows how the FWHM of these Tri-Hy-NAA-PCs varies with t_{pw}. This reveals that, for the Type-1 Tri-Hy-NAA-PC structure, the FWHM of the NAA-DBRs are broader than those of the APO-NAA-GIFs, although this difference is reduced as compared to that shown in Bi-Hy-NAA-PCs. Finally, Fig. 8c compiles digital pictures of these Tri-Hy-NAA-PCs. These images reveal that, while the interferometric color displayed by the Type-1 structure is clearly established by the PSB of the central NAA-DBR, the Type-2 structure shows a complex pattern of colors, which result from the combination of the bands of the two NAA-DBRs embedded into its structure. In both cases, the interferometric color is blue-shifted with t_{pw}.

As mentioned above, the PSB of the APO-NAA-GIF structure of the Type-2 Tri-Hy-NAA-PC, which was embedded between two NAA-DBRs, was found to vanish from the transmission spectrum of these PCs. To establish optimal fabrication conditions to overcome this limitation so Tri-Hy-NAA-PCs show the three characteristic PSBs in their transmission spectrum, we fabricated a set of Type-1 and Type-2 Tri-Hy-NAA-PCs by systematically modifying the relative anodization times (t_{An-Top}, $t_{An-Center}$, and $t_{An-Bottom}$) while keeping constant the total anodization time (t_{An}).

These conditions are summarized in Table 2 and the obtained result shown in Fig. 9 and Figure S4 (Supporting Information). Figure 9a,b show the dependency of λ_{PSB} for the different individual PCs composing the structure of Type-1 and Type-2 Tri-Hy-NAA-PCs as a function of t_{An-Top}, $t_{An-Centre}$, $t_{An-Bottom}$, and t_{pw}, respectively. It is verified that, likewise in previous cases, λ_{PSB} undergoes a blue shift with t_{pw}. In the case of Type-1 (Fig. 9a), it is demonstrated that the position of the characteristic PSBs of the APO-NAA-GIFs located at the top and bottom of the Tri-Hy-NAA-PC structures is red-shifted when the relative anodization time (t_{An-Top} and $t_{An-Bottom}$) is increased from 5 to 7.5 h. In contrast, the λ_{PSB} of the central NAA-DBR is red-shifted with decreasing relative anodization time ($t_{An-Center}$)–from 10 to 5 h, which is in good agreement with the general trend observed in other NAA-based PC structures. Figure 9b shows the obtained results for the Type-2 Tri-Hy-NAA-PCs. From our analysis, we found that the minimum relative anodization time for the central APO-NAA-GIF structure to show its characteristic PSB in the transmission spectrum was $t_{An-Center} = 10$ h. The hybrid PC structure produced at $t_{An-Centre} = 5$ h did not show characteristic PSB for the APO-NAA-GIF structure. The λ_{PSB} of the bottom NAA-DBR reveal that a significant red shift occurs when the relative anodization time used to produce this PC ($t_{An-Bottom}$) is increased from 5 to 7.5 h. In contrast, we observed a slight blue shift in the position of the PSB of the top NAA-DBR structure when t_{An-Top} is increased from 5 to 7.5 h, which is in good agreement with previous observations.

Figure 9c shows the evolution of the FWHM of the PSBs of each individual PC forming the structure of Type-1 Tri-Hy-NAA-PCs as a function of the relative anodization time and t_{pw}. This graph shows that the FWHM of the central NAA-DBR structure is enlarged with decreasing relative anodization time, when $t_{An-Center}$ is reduced
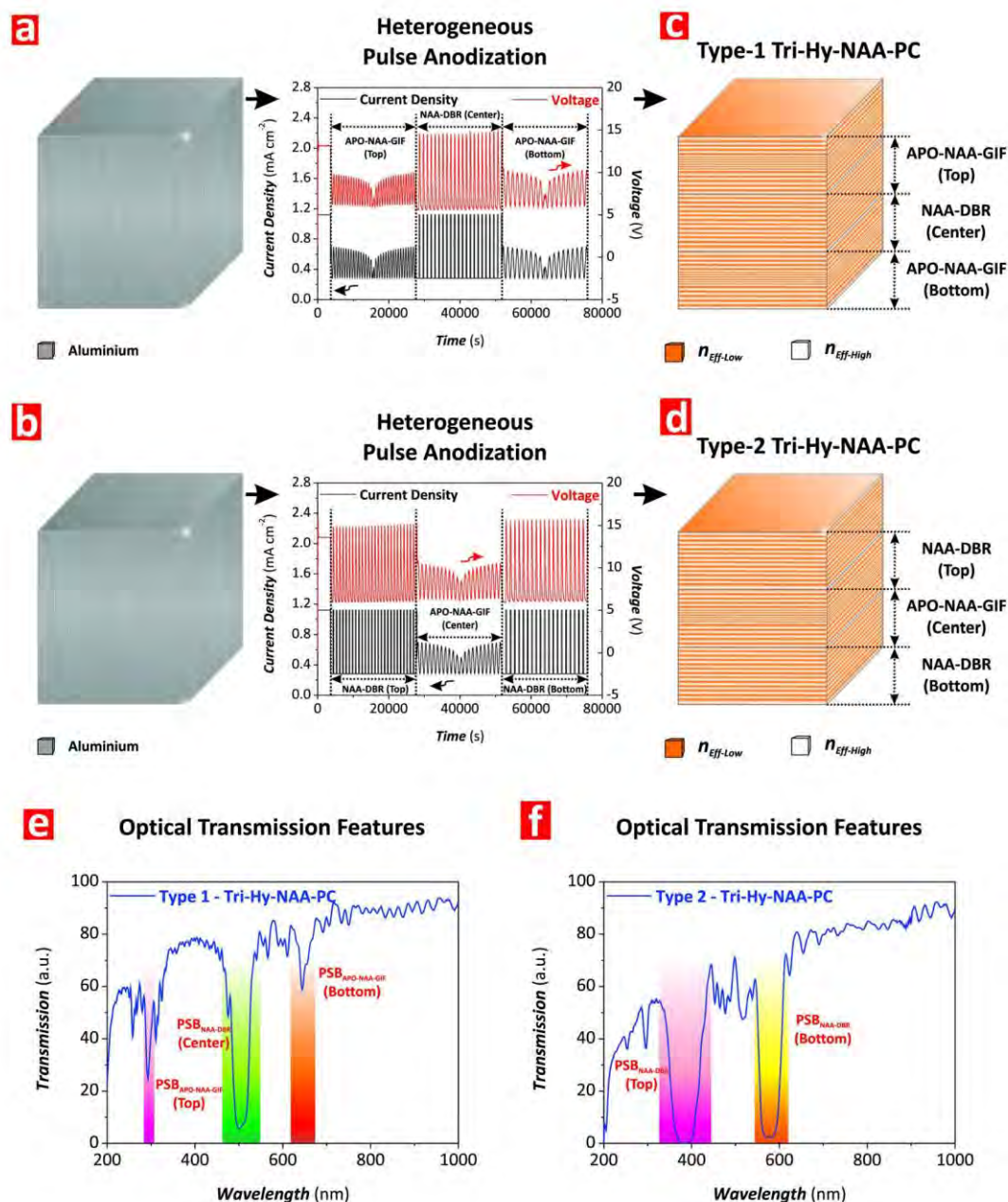
72

Figure 7. Fabrication of Type 1 and Type 2 Tri-Hy-NAA-PCs by heterogeneous pulse anodization (HPA). (**a,b**) Schematics illustrating the HPA processes used to produce Type 1 and Type 2 Tri-Hy-NAA-PCs with representative anodization profiles, respectively. (**c,d**) Schematic illustration of the distribution of effective refractive index in depth for Type 1 and Type 2 Tri-Hy-NAA-PCs, respectively. (**e,f**) Representative transmission spectra showing the features of the photonic stopbands (PSBs) of NAA-DBRs and APO-NAA-GIFs embedded within the structure of Type 1 and Type 2 Tri-Hy-NAA-PCs, respectively.

from 10 to 5 h. In the same way than in other NAA-based PCs, a pore widening treatment also enlarges the FWHM. This analysis reveals that, in the case of the top APO-NAA-GIF structure, the FWHM increases as $t_{An\text{-}Top}$ is extended from 5 to 7.5 h. It is also observed that a pore widening treatment increases slightly the FWHM of this PC structure, although in a much less significant manner than in the case of the central NAA-DBR. In contrast, $t_{An\text{-}Bottom}$ did not have any significant effect on the FWHM for the bottom APO-NAA-GIF structure up to $t_{pw} = 2$ min. However, at $t_{pw} > 2$ min, the FWHM is enlarged with decreasing relative anodization time from 7.5 to 5 h. Likewise in previous Hy-NAA-PCs, the FWHM of the PSB of the central NAA-DBR was found to be broader than that of its APO-NAA-GIFs counterparts. Figure 9d depicts the FWHM of the PSBs of the individual PCs composing the structure of Type-2 Tri-Hy-NAA-PCs. As expected, the FWHM of the NAA-DBRs' PSB is significantly broader than that of the APO-NAA-GIF, and it is enlarged with t_{pw}. Overall, the FWHM is broader at shorter relative anodization times, for both top and bottom NAA-DBRs. Furthermore, this analysis reveals
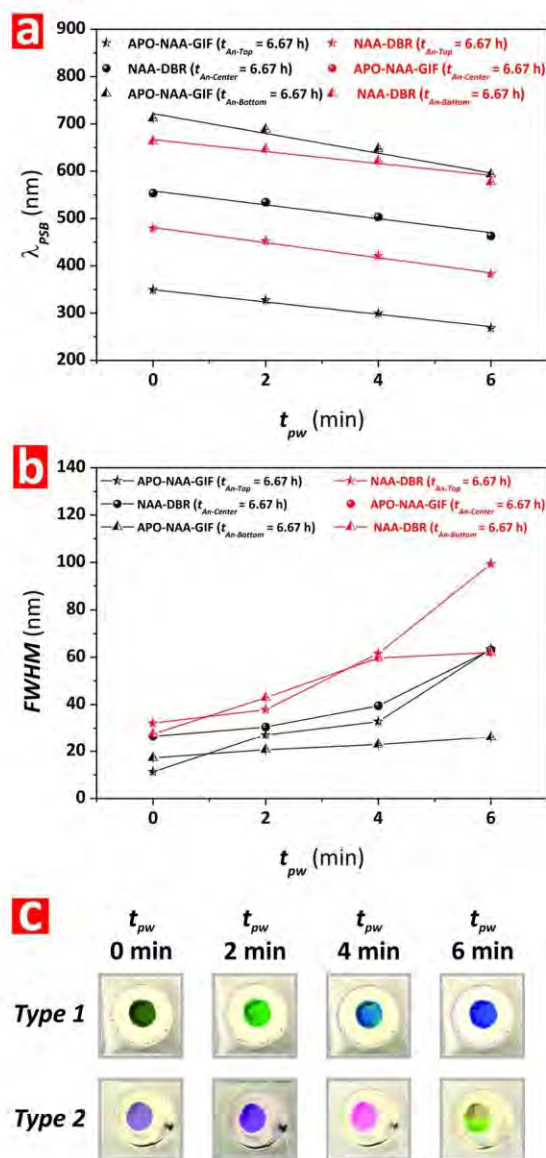
73

Figure 8. Effect of type of individual PC arrangement and pore widening time (t_{pw}) on the optical features (position of central wavelength–λ_{PSB}, full-width at half maximum–FWHM, and interferometric color) of Type 1 and Type 2 Tri-Hy-NAA-PCs. (**a**) Effect of structural arrangement and t_{pw} on λ_{PSB}. (**b**) Effect of structural arrangement and t_{pw} on FWHM. (**c**) Effect of structural arrangement and t_{pw} on interferometric color.

that the FWHM of the top NAA-DBR is wider than that of its counterpart located at the bottom of the Type-2 Tri-Hy-NAA-PCs.

Figure 9e and f compile digital pictures of the Type-1 and Type-2 Tri-Hy-NAA-PCs assessed in our study. These images denote that the Type-1 Tri-Hy-NAA-PCs (i.e. APO-NAA-GIF top, NAA-DBR center, and APO-NAA-GIF bottom) display clearly defined interferometric colors, which correspond to the position of the PSB of the central NAA-DBR. It is observed that the interferometric color displayed by these PCs undergoes a blue shift when the relative anodization time ($t_{An-Center}$) is increased from 5 to 10 h. This blue shift is further enhanced with t_{pw}. On the contrary, Type-2 Tri-Hy-NAA-PCs display complex color patterns, which are associated with the position of the PSBs of the two NAA-DBRs embedded in their structure. However, it is also observed that these PCs display well-defined colors when the λ_{PSB} of one of the NAA-DBRs is in the NIR or UV regions. For instance, the color of the samples produced with $t_{An-Top} = t_{An-Bottom} = 7.5$ h at $t_{pw} = 6$ min is green while it turns into orange-yellow when t_{An-Top} and $t_{An-Bottom}$ are set to 5 h. It is worthwhile noting that at $t_{pw} = 6$ min the PSB of the top NAA-DBR structure is in the UV region of the spectrum and therefore it has no significant contribution to the overall interferometric color of the Tri-Hy-NAA-PC, which is determined by the PSB of the bottom NAA-DBR.

To conclude, this study has presented the first realization of hybrid nanoporous anodic alumina photonic crystals (Hy-NAA-PCs) fabricated by a heterogeneous pulse anodization. This versatile nanofabrication approach enables the precise engineering of the effective medium of NAA in depth to create a set of Hy-NAA-PCs featuring

Type	Top PC Structure $t_{An\text{-}Top}$ (h)–T_P (s)	Center PC Structure $t_{An\text{-}Center}$ (h)–T_P (s)	Bottom PC Structure $t_{An\text{-}Bottom}$ (h)–T_P (s)	t_{An} (h)
Type 1	APO-NAA-GIF 6.67 h–700 s	NAA-DBR 6.67 h–1000 s	APO-NAA-GIF 6.67 h–1300 s	20 h
Type 2	NAA-DBR 6.67 h–900 s	APO-NAA-GIF 6.67 h–1100 s	NAA-DBR 6.67 h–1200 s	20 h
Type 1	APO-NAA-GIF 7.5 h–700 s	NAA-DBR 5 h–1000 s	APO-NAA-GIF 7.5 h–1300 s	20 h
Type 1	APO-NAA-GIF 5 h–700 s	NAA-DBR 10 h–1000 s	APO-NAA-GIF 5 h–1300 s	20 h
Type 2	NAA-DBR 7.5 h–900 s	APO-NAA-GIF 5 h–1100 s	NAA-DBR 7.5 h–1200 s	20 h
Type 2	NAA-DBR 5 h–900 s	APO-NAA-GIF 10 h–1100 s	NAA-DBR 5 h–1200 s	20 h

Table 2. Summary table compiling the structural arrangement and fabrication conditions for each Tri-Hy-NAA-PC structure assessed in this study.
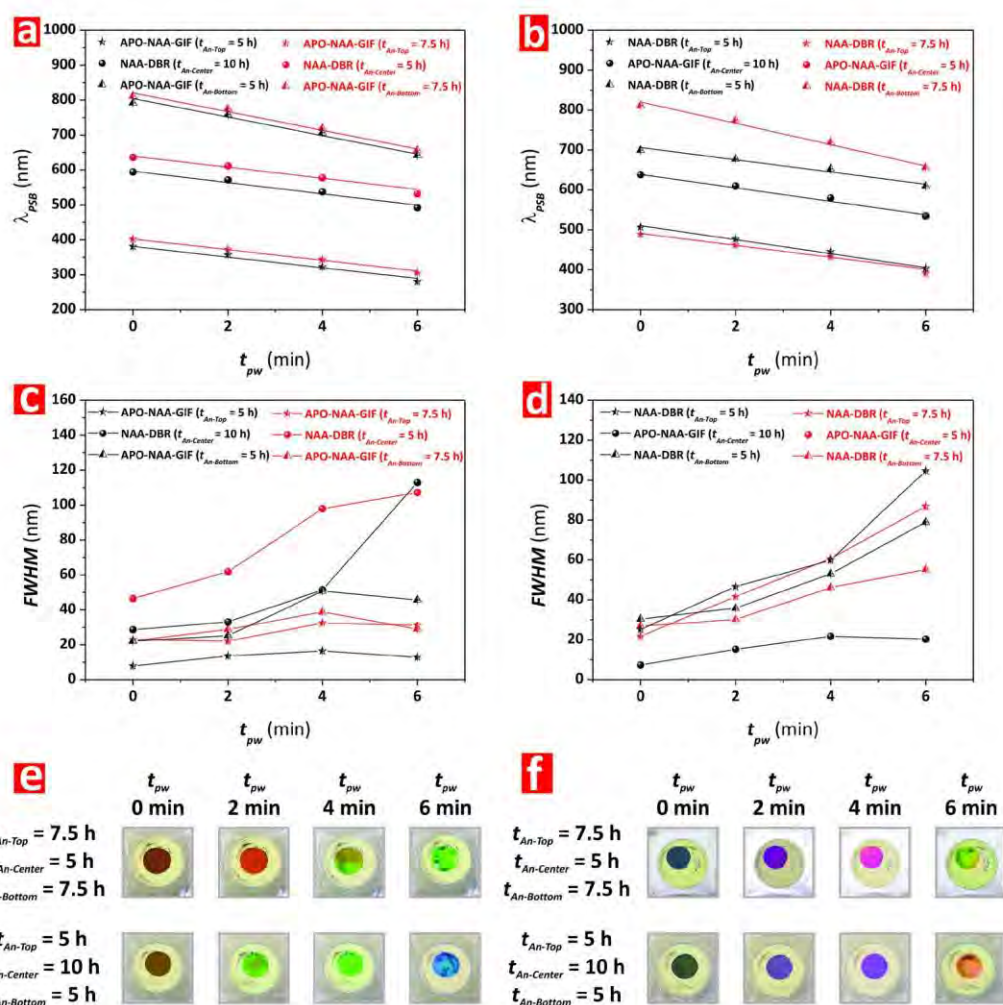
Figure 9. Effect of relative anodization time ($t_{An\text{-}Top}$, $t_{An\text{-}Center}$, and $t_{An\text{-}Bottom}$) and pore widening time (t_{pw}) on the optical features (position of central wavelength–λ_{PSB}, full-width at half maximum–FWHM, and interferometric color) of Type 1 and Type 2 Tri-Hy-NAA-PCs. (**a,b**) Effect of $t_{An\text{-}Top}$, $t_{An\text{-}Bottom}$, and t_{pw} on λ_{PSB} of Type 1 and Type 2 Tri-Hy-NAA-PCs, respectively. (**c,d**) Effect of $t_{An\text{-}Top}$, $t_{An\text{-}Bottom}$, and t_{pw} on FWHM of Type 1 and Type 2 Tri-Hy-NAA-PCs, respectively. (**e,f**) Effect of $t_{An\text{-}Top}$, $t_{An\text{-}Bottom}$, and t_{pw} on interferometric color of Type 1 and Type 2 Tri-Hy-NAA-PCs, respectively.

photonic stopbands with precisely engineered features (i.e. number, position, and width) that can be readily tuned across the spectral regions by various anodization parameters. The effects of the anodization period, the relative and total anodization times, the pore widening time, and the arrangement of structures on the optical properties

of Hy-NAA-PCs have been established by systematically modifying these parameters and assessing the optical properties of Bi- and Tri-Hy-NAA-PCs. The analysis of the optical properties of Bi- and Tri-Hy-NAA-PCs has revealed that the position of characteristic transmission bands is primarily dependent on the anodization period and the pore widening time, although the relative and total anodization times and the exchange of structures also have impact on these optical features. The assessment of the interferometric colors displayed by the Hy-NAA-PCs has revealed that this optical property is mainly established by the PSBs of the NAA-DBRs composing the structure of Bi- and Tri-Hy-NAA-PCs. Furthermore, we observed that the FWHM of the different individual PCs embedded in the structure of Hy-NAA-PCs follows the characteristics of their mono-structural counterparts, where NAA-DBRs and APO-NAA-GIFs display broad and narrow PSBs, respectively.

In summary, this study has established the first comprehensive rationale for the fabrication of complex photonic crystal structures based on NAA-PCs using a newly developed anodization approach. This versatile nanofabrication method opens new opportunities to develop innovative photonic nanostructures with implications in many fields such as sensing and photonics.

Methods

Materials.   High purity (99.9997%) aluminum (Al) foils with thicknesses of 0.32 mm were purchased from Goodfellow Cambridge Ltd. (UK) and used to produce Hy-NAA-PCs by HPA process. Sulfuric acid (H_2SO_4), phosphoric acid (H_3PO_4), hydrochloric acid (HCl), copper (II) chloride ($CuCl_2$), and ethanol (EtOH–C_2H_5OH) were supplied by Sigma-Aldrich (Australia) and used as received, without additional purification steps. Ultrapure Mili-Q® water (18.2 MΩ cm) was used for the preparation of aqueous solutions in this study.

Fabrication of Hy-NAA-PCs by HPA.   Hy-NAA-PCs were produced by a HPA under galvanostatic mode combining stepwise pulse anodization (STPA)[20] and apodized sinusoidal pulse anodization (ASPA)[48]. Briefly, before anodization, 1.5 × 1.5 cm Al substrates were cleaned in ethanol and water for 15 min each under sonication, dried under air stream, and electropolished in a mixture of EtOH and $HClO_4$ 4:1 (v:v) at 20 V and 5 °C for 3 min to achieve a cleaned mirror-like finishing surface prior to anodization. The electropolished Al substrates were anodized in a 1.1 M aqueous H_2SO_4 solution, in which 25 v% EtOH was added to prevent the solution from freezing at temperatures below 0 °C[50,51]. HPA was performed in a single step, starting with a constant anodization stage for 1 h at −1 °C at a constant current density of 1.120 mA cm^{-2} to achieve a homogeneous pore growth rate of anodic oxide before switching the anodization mode to HPA. The anodization profile was subsequently set into various arrangements of STPA and ASPA modes, depending on the number and order of structures composing the Hy-NAA-PCs to be produced. The HPA profiles were generated by a custom-designed Labview®-based software following the equations for STPA and ASPA.

For ASPA, the anodization current density was pulsed in a logarithmic negative apodized sinusoidal fashion given by Equation 1:

$$J(t) = A(t)_J \cdot \left[sin\left(\frac{2\pi}{T_P} t \right) + 1 \right] + J_{Offset} \tag{1}$$

where $J(t)$ is the current density at a given time t, T_P is the anodization period, t_{An} is the total anodization time at ASPA, and $A(t)_J$ is the current density amplitude as a function of time t given by Equations 2 and 3:

For $t \leq t_{An}/2$,

$$A(t)_J = A_{max} + \left(\frac{A_{min} - A_{max}}{log\left(\frac{t_{An}}{2} + 10 \right) - 1} \right) \cdot (log(t + 10) - 1) \tag{2}$$

For $t > t_{An}/2$,

$$A(t)_J = \left(\frac{A_{max} - A_{min}}{log(t_{An} + 10) - log\left(\frac{t_{An}}{2} + 10 \right)} \right) \times \left(log(t + 10) - log\left(\frac{t_{An}}{2} + 10 \right) \right) + A_{min} \tag{3}$$

Note that the current density offset (J_{offset}) and the minimum (A_{min}) and maximum amplitude (A_{max}) current density amplitudes were set to 0.280 mA cm^{-2}, and 0.000 and 0.210 mA cm^{-2}, respectively.

In STPA, the anodization current density was sequentially pulse between high ($J_{max} = 1.120$ mA cm^{-2}) and low ($J_{min} = J_{offset} = 0.280$ mA cm^{-2}) current density values in a stepwise fashion. The number of anodization pulses (N_P) set was defined by Equation 4, in which the pulse period (T_P) is given by Equation 5:

$$N_P = \frac{t_{An}}{T_P} \tag{4}$$

$$T_P = t_{max} + t_{min} \tag{5}$$

where t_{An} is the total anodization time at STPA, and t_{max} and t_{min} are the time for maximum and minimum current density pulses, respectively. Note that the time ratio for t_{max} and t_{min} (t_{max}:t_{min}) was set to 1:4 for each anodization period.

76

We assessed the capabilities of HPA to produce Hy-NAA-PCs with well-defined optical properties by modifying the arrangement of individual PC structures and their features through different fabrication parameters such as the total and relative anodization times, the anodization period, and the structural arrangement. Tables 1 and 2 summarize the fabrication conditions used to produce Bi- and Tri-Hy-NAA-PCs in our study. After anodization, the remaining Al substrate in Hy-NAA-PCs was selectively dissolved by wet chemical etching in a saturated solution of HCl–CuCl$_2$ using a 5 mm diameter circular window Viton^{TM} mask. The nanoporous structure of Hy-NAA-PCs was subsequently widened by a wet chemical etching treatment in an aqueous H$_3$PO$_4$ (5 *wt %*) solution at 35 °C under controlled time (t_{pw}), from 0 to 6 min with an interval (Δt_{pw}) of 2 min.

Optical characterization. The transmission spectra of Hy-NAA-PCs fabricated by HPA under different anodization conditions were acquired at normal incidence (i.e. $\theta = 0°$) from 200 to 900 nm with a resolution of 1 nm using a UV-visible-NIR spectrometer (Cary 300, Agilent, USA). Digital images of Hy-NAA-PCs displaying interferometric colors were acquired by a Canon EOS 700D digital camera equipped with a Tamron 90 mm F2.8 VC USD macro mount lens with autofocus feature under natural light illumination.

Structural characterization. The geometric features of Bi- and Tri-Hy-NAA-PCs were characterized by field emission gun scanning electron microscopy (FEG-SEM FEI Quanta 450). These FEG-SEM images were analyzed by ImageJ (public domain program developed at the RSB of the NIH)[52].

References

1. Song, B.-S., Noda, S., Asano, T. & Akahane, Y. Ultra-high-Q photonic double-heterostructure nanocavity. *Nat. Mater.* **4**, 207–210 (2005).
2. Noda, S., Chutinan, A. & Imada, M. Trapping and emission of photons by a single defect in a photonic bandgap structure. *Nature* **407**, 608–610 (2000).
3. Akahane, Y., Asano, T., Song, B.-S. & Noda, S. High-Q photonic nanocavity in a two-dimensional photonic crystal. *Nature* **425**, 944–947 (2003).
4. Noda, S., Tomoda, K., Yamamoto, N. & Chutinan, A. Full three-dimensional photonic bandgap crystals at near-infrared vavelengths. *Science* **289**, 604–606 (2000).
5. López, C. Materials aspects of photonic crystals. *Adv. Mater.* **15**, 1679–1704 (2003).
6. Brzózka, A., Brudzisz, A., Hnida, K. & Sulka, G. D. Chemical and structural modifications of nanoporous alumina and its optical Properties. In *Electrochemically Engineered Nanoporous Materials: Methods, Properties and Applications*, 1st ed.; Santos, A., Losic, D., Eds.; Springer International Publishing: Cham, Switzerland, Volume 220, pp. 219-288 (2015).
7. Matsui, T., Sakamoto, T., Tsujikawa, K., Tomita, S. & Tsubokawa, M. Single-mode photonic crystal fiber design with ultralarge effective area and low bending loss for ultrahigh-speed wdm transmission. *J. Lightwave Technol.* **29**, 511–515 (2011).
8. Takahashi, S. *et al.* Giant optical rotation in a three-dimensional semiconductor chiral photonic crystal. *Opt. Express* **21**, 29905–29913 (2013).
9. Yoshie, T. *et al.* Vacuum rabi splitting with a single quantum dot in a photonic crystal nanocavity. *Nature* **432**, 200–203 (2004).
10. Hennessy, K. *et al.* Quantum nature of a strongly coupled single quantum dot–cavity system. *Nature* **445**, 896–899 (2007).
11. Liu, J. *et al.* Hierarchically macro-/mesoporous Ti—Si oxides photonic crystal with highly efficient photocatalytic capability. *Environ. Sci. Technol.* **43**, 9425–9431 (2009).
12. Zheng, X. *et al.* Titanium dioxide photonic crystals with enhanced photocatalytic activity: matching photonic band gaps of TiO$_2$ to the absorption peaks of dyes. *J. Phys. Chem. C* **117**, 21263–21273 (2013).
13. Li, X. *et al.* Ga doped ZnO photonic crystals with enhanced photocatalytic cctivity and its reaction mechanism. *Appl. Catal. B. Environ.* **195**, 29–38 (2016).
14. Chiarello, G. L., Zuliani, A., Ceresoli, D., Martinazzo, R. & Selli, E. Exploiting the photonic crystal properties of TiO$_2$ nanotube arrays to enhance photocatalytic hydrogen production. *ACS Catal.* **6**, 1345–1353 (2016).
15. Yip, C. T. *et al.* Direct and seamless coupling of TiO$_2$ nanotube photonic crystal to dye-sensitized solar cell: A single-step approach. *Adv. Mater.* **23**, 5624–5628 (2011).
16. Guo, M. *et al.* Design and coupling of multifunctional TiO$_2$ nanotube photonic crystal to nanocrystalline titania layer as semi-transparent photoanode for dye-sensitized solar cell. *Energy Environ. Sci.* **5**, 9881–9888 (2012).
17. Guo, M., Xie, K., Wang, Y., Zhou, L. & Huang, H. Aperiodic TiO$_2$ nanotube photonic crystal: Full-visible-spectrum solar light harvesting in photovoltaic devices. *Sci Rep.* **4**, 6442 (2014).
18. Mosk, A. P., Lagendijk, A., Lerosey, G. & Fink, M. Controlling waves in space and time for imaging and focusing in complex media. *Nat. Photonics* **6**, 283–292 (2012).
19. Yuan, L. & Herman, P. R. Laser scanning holographic lithography for flexible 3D fabrication of multi-scale integrated nano-structures and optical biosensors. *Sci. Rep.* **6**, 22294 (2016).
20. Chen, Y. *et al.* On the generation of interferometric colors in high purity and technical grade aluminum: an alternative green process for metal finishing industry. *Electrochim. Acta* **174**, 672–681 (2015).
21. Santos, A. Nanoporous anodic alumina photonic crystals: fundamentals, developments and perspectives. *J. Mater. Chem. C* **5**, 5581–5599 (2017).
22. Gerard, J. M., Izraël, A., Marzin, J. Y., Padjen, R. & Ladan, F. R. Photonic bandgap of two-dimensional dielectric crystals. *Solid State Electron.* **37**, 1341–1344 (1994).
23. Charlton, M. D. B., Roberts, S. W. & Parker, G. J. Guided mode analysis, and fabrication of a 2-dimensional visible photonic band structure confined within a planar semiconductor waveguide. *Mater. Sci. Eng. B* **49**, 155–165 (1997).
24. Yi-Yan, A., Wilkinson, C. & Laybourn, P. Two-dimensional grating unit cell demultiplexer for thin-film optical waveguides. *IEEE J. Quantum Electron.* **16**, 1089–1092 (1980).
25. Dallesasse, J. M., Holonyak, N., Sugg, A. R., Richard, T. A. & El-Zein, N. Hydrolyzation oxidation of AlxGa1−xAs-AlAs-GaAs quantum well heterostructures and superlattices. *Appl. Phys. Lett.* **57**, 2844–2846 (1990).
26. Tonucci, R. J., Justus, B. L., Campillo, A. J. & Ford, C. E. Nanochannel array glass. *Science* **258**, 783–785 (1992).
27. Scott, B., Karteri, P., Xiao-Mei, Z. & George, W. Soft lithography and microfabrication. *Phys. World* **11**, 31–36 (1998).
28. Holland, B. T., Blanford, C. F. & Stein, A. Synthesis of macroporous minerals with highly ordered three-dimensional arrays of spheroidal voids. *Science* **281**, 538–540 (1998).
29. Lawandy, N. M., Balachandran, R. M., Gomes, A. S. L. & Sauvain, E. Laser action in strongly scattering media. *Nature* **368**, 436–438 (1994).
30. Wehrspohn, R. B. *et al.* Electrochemically-Prepared 2D and 3D Photonic Crystals. In *Photonic Crystals: Advances in Design, Fabrication, and Characterization*, 1st ed.; Busch, K., Lölkes, S., Wehrspohn, R.B., Föll, H., Eds.; Wiley-VCH Verlag GmbH & Co. KGaA: Weinheim, Germany, pp. 63–84 2006.

77

31. Santos, A., Deen, M. J. & Marsal, L. F. Low-cost fabrication technologies for nanostructures: state-of-the-art and potential. *Nanotechnology* **26**, 042001 (2015).
32. Wang, Y. *et al.* Facile synthesis of optical microcavities by a rationally designed anodization approach: tailoring photonic signals by nanopore structure. *ACS Appl. Mater. Interfaces* **7**, 9879–9888 (2015).
33. Santos, A. *et al.* Tunable Fabry-Pérot interferometer based on nanoporous anodic alumina for optical biosensing purposes. *Nanoscale Res. Lett.* **7**, 370 (2012).
34. Santos, A., Pereira, T., Law, C. S. & Losic, D. Rational engineering of nanoporous anodic alumina optical bandpass filters. *Nanoscale* **8**, 14846–14857 (2016).
35. Chen, Y. *et al.* Biomimetic nanoporous anodic alumina distributed Bragg reflectors in the form of films and microsized particles for sensing applications. *ACS Appl. Mater. Interfaces* **7**, 19816–19824 (2015).
36. Santos, A. *et al.* Realisation and advanced engineering of true optical rugate filters based on nanoporous anodic alumina by sinusoidal pulse anodisation. *Nanoscale* **8**, 1360–1373 (2016).
37. Lee, W. & Park, S.-J. Porous anodic aluminum oxide: anodization and templated synthesis of functional nanostructures. *Chem. Rev.* **114**, 7487–7556 (2014).
38. Law, C. S., Santos, A., Nemati, M. & Losic, D. Structural engineering of nanoporous anodic alumina photonic crystals by sawtooth-like pulse anodization. *ACS Appl. Mater. Interfaces* **8**, 13542–13554 (2016).
39. Masuda, H. & Fukuda, K. Ordered metal nanohole arrays made by a two-step replication of honeycomb structures of anodic alumina. *Science* **268**, 1466–1468 (1995).
40. Masuda, H., Hasegwa, F. & Ono, S. Self-ordering of cell arrangement of anodic porous alumina formed in sulfuric acid solution. *J. Electrochem. Soc.* **144**, L127–L130 (1997).
41. Hideki, M., Kouichi, Y. & Atsushi, O. Self-ordering of cell configuration of anodic porous alumina with large-size pores in phosphoric acid solution. *Jpn. J. Appl. Phys.* **37**, L1340–L1342 (1998).
42. Nielsch, K., Choi, J., Schwirn, K., Wehrspohn, R. B. & Gösele, U. Self-ordering regimes of porous alumina: the 10 porosity rule. *Nano Lett.* **2**, 677–680 (2002).
43. Lee, W., Ji, R., Gösele, U. & Nielsch, K. Fast fabrication of long-range ordered porous alumina membranes by hard anodization. *Nat. Mater.* **5**, 741–747 (2006).
44. Schwirn, K. *et al.* Self-ordered anodic aluminum oxide formed by H_2SO_4 hard anodization. *ACS Nano* **2**, 302–310 (2008).
45. Lee, W., Kim, J.-C. & Gösele, U. Spontaneous current oscillations during hard anodization of aluminum under potentiostatic conditions. *Adv. Funct. Mater.* **20**, 21–27 (2010).
46. Lee, W. *et al.* Structural engineering of nanoporous anodic aluminium oxide by pulse anodization of aluminium. *Nat. Nanotechn.* **3**, 234–239 (2008).
47. Yi, L., Zhiyuan, L., Xing, H., Yisen, L. & Yi, C. Formation and microstructures of unique nanoporous AAO films fabricated by high voltage anodization. *J. Mater. Chem.* **21**, 9661–9666 (2011).
48. Santos, A., Law, C. S., Chin Lei, D. W., Pereira, T. & Losic, D. Fine tuning of optical signals in nanoporous anodic alumina photonic crystals by apodized sinusoidal pulse anodisation. *Nanoscale* **8**, 18360–18375 (2016).
49. Rahman, M. M., Marsal, L. F., Pallarès, J. & Ferré-Borrull, J. Tuning the photonic stop bands of nanoporous anodic alumina-based distributed Bragg reflectors by pore widening. *ACS Appl. Mater. Interfaces* **5**, 13375–13381 (2013).
50. Santos, A., Formentín, P., Ferré-Borrull, J., Pallarès, J. & Marsal, L. F. Nanoporous anodic alumina bbtained without protective oxide layer by hard anodization. *Mater. Lett.* **67**, 296–299 (2012).
51. Wang, Y., Santos, A., Evdokiou, A. & Losic, D. Rational design of ultra-short anodic alumina nanotubes by short-time pulse anodization. *Electrochim. Acta* **154**, 379–386 (2015).
52. Abràmoff, M. D., Magalhaes, P. J. & Ram, S. J. Image processing with ImageJ. *Biophotonics Inter.* **11**, 36–42 (2004).

Acknowledgements

Author Contributions

Ms. Siew Yee Lim carried out the experimental part of this work assisted by Ms. Cheryl Suwen Law. Dr. Abel Santos conceived the idea and designed the experimental part of this work in collaboration with Prof. Lluis F. Marsal. The obtained results were discussed and analyzed by all the authors. The final version of the manuscript was written through contributions of all the authors. All the authors have given approval to the final version of the manuscript.

Additional Information

Supplementary information accompanies this paper at https://doi.org/10.1038/s41598-018-27775-6.

Competing Interests: The authors declare no competing interests.

Publisher's note: Springer Nature remains neutral with regard to jurisdictional claims in published maps and institutional affiliations.

78

Supporting

Information

Engineering of Hybrid Nanoporous Anodic Alumina Photonic Crystals by Heterogeneous Pulse Anodization

Siew Yee Lim [1,2,3], Cheryl Suwen Law [1,2,3], Lluís F. Marsal[4], and Abel Santos [1,2,3,]*

[1]School of Chemical Engineering, The University of Adelaide, Adelaide, SA 5005, Australia
[2]Institute for Photonics and Advanced Sensing (IPAS), The University of Adelaide, 5005 Adelaide, Australia
[3]ARC Centre of Excellence for Nanoscale BioPhotonics (CNBP), The University of Adelaide, 5005 Adelaide, Australia
[4]Department of Electronic, Electric, and Automatics Engineering, Universitat Rovira i Virgili, Avda, Països Catalans 26, Tarragona 43007, Spain

*E-Mail: abel.santos@adelaide.edu.au
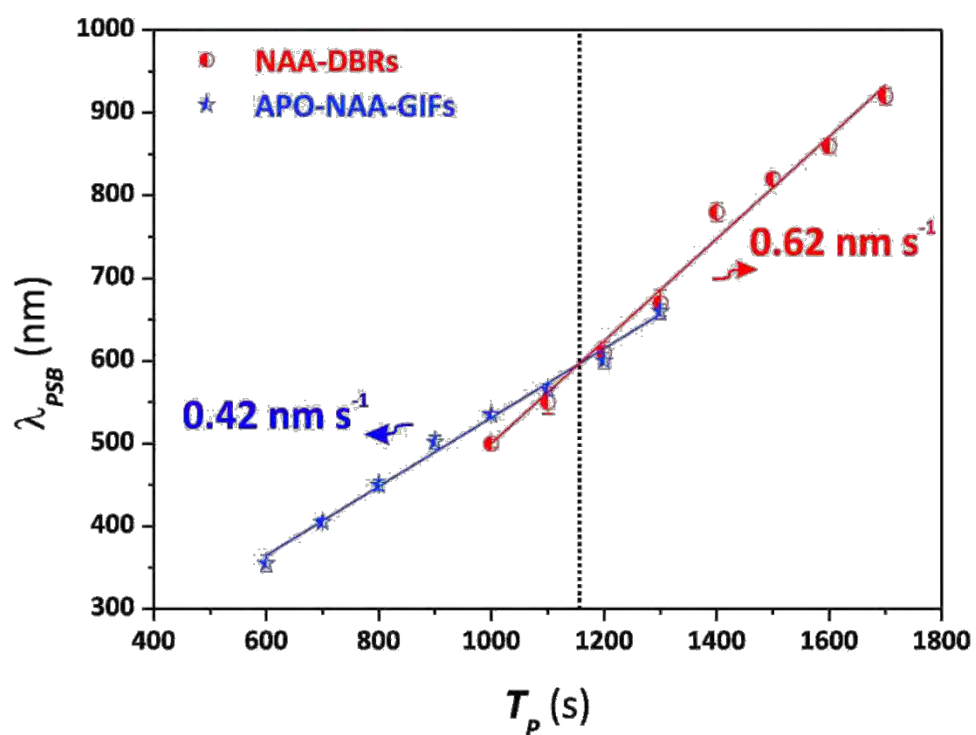
Figure S1. Dependency of λ_{PSB} with T_P for NAA-DBRs and APO-NAA-GIFs and corresponding linear fittings.
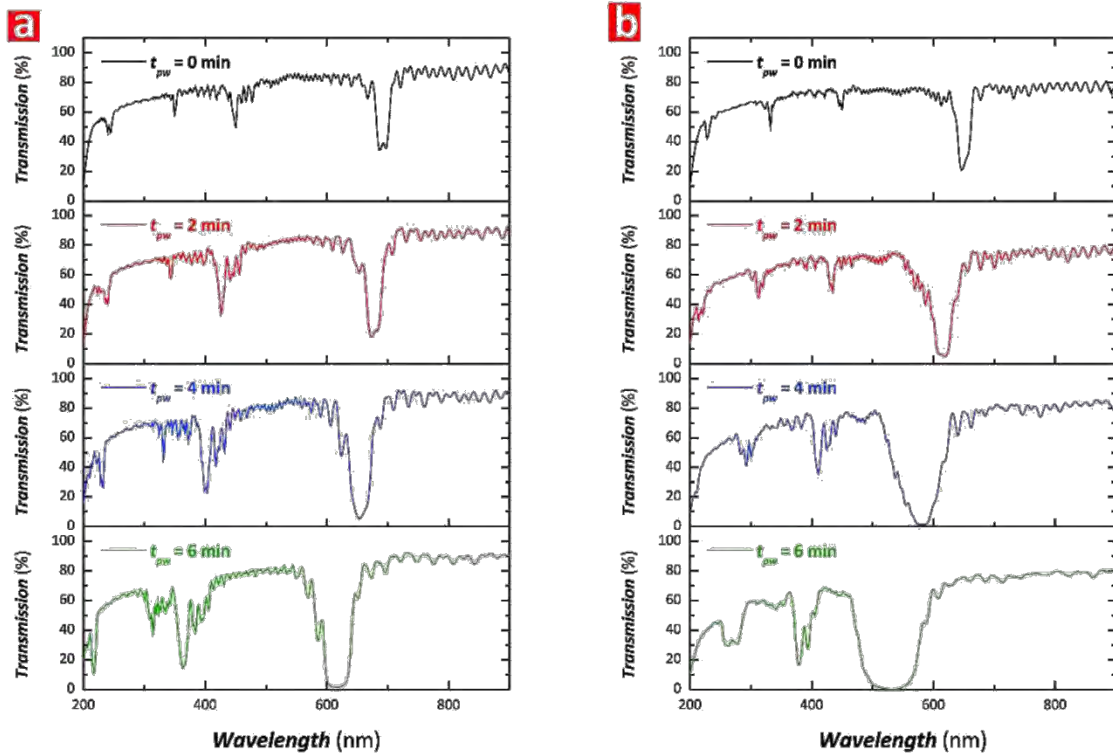
Figure S2. Transmission spectra as a function of t_{pw} for a) Bi-Hy-NAA-PC produced with a top APO-NAA-GIF (t_{An-Top} = 10 h and T_P = 800 s) and a bottom NAA-DBR ($t_{An-Bottom}$ = 10 h and T_P = 1200 s), and b) Inv-Bi-Hy-NAA-PC produced with a top NAA-DBR ($t_{An-Bottom}$ = 10 h and T_P = 1200 s) and a bottom APO-NAA-GIF (t_{An-Top} = 10 h and T_P = 800 s).
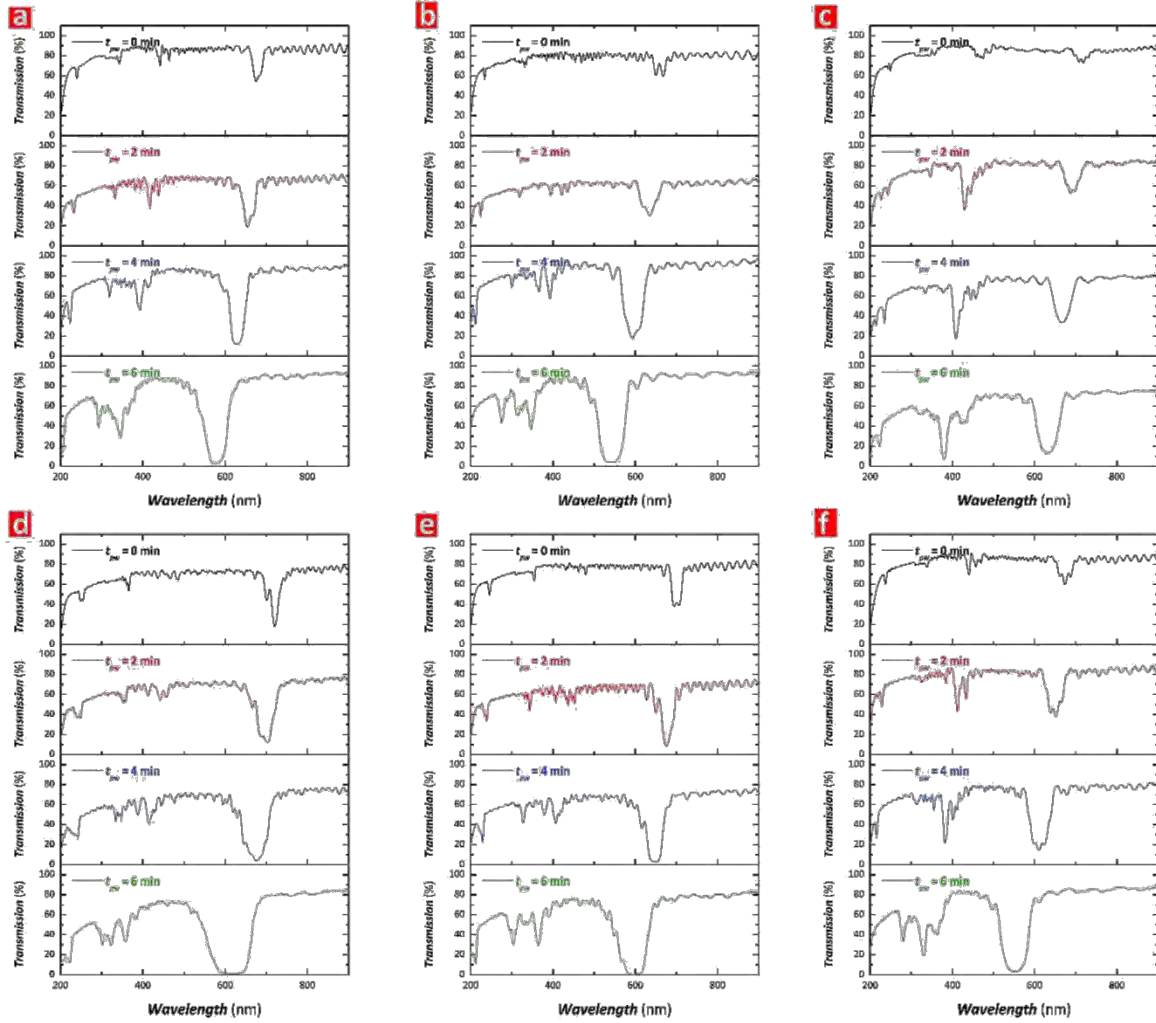
Figure S3. Transmission spectra as a function of t_{pw} for a) Bi-Hy-NAA-PC produced with a top APO-NAA-GIF ($t_{An\text{-}Top}$ = 7.5 h and T_P = 800 s) and a bottom NAA-DBR ($t_{An\text{-}Bottom}$ = 7.5 h and T_P = 1200 s), b) Bi-Hy-NAA-PC produced with a top APO-NAA-GIF ($t_{An\text{-}Top}$ = 5 h and T_P = 800 s) and a bottom NAA-DBR ($t_{An\text{-}Bottom}$ = 5 h and T_P = 1200 s), c) Bi-Hy-NAA-PC produced with a top APO-NAA-GIF ($t_{An\text{-}Top}$ = 15 h and T_P = 800 s) and a bottom NAA-DBR ($t_{An\text{-}Bottom}$ = 5 h and T_P = 1200 s), d) Bi-Hy-NAA-PC produced with a top APO-NAA-GIF ($t_{An\text{-}Top}$ = 5 h and T_P = 800 s) and a bottom NAA-DBR ($t_{An\text{-}Bottom}$ = 15 h and T_P = 1200 s), e) Bi-Hy-NAA-PC produced with a top APO-NAA-GIF ($t_{An\text{-}Top}$ = 5 h and T_P = 800 s) and a bottom NAA-DBR ($t_{An\text{-}Bottom}$ = 10 h and T_P = 1200 s), and f) Bi-Hy-NAA-PC produced with a top APO-NAA-GIF ($t_{An\text{-}Top}$ = 10 h and T_P = 800 s) and a bottom NAA-DBR ($t_{An\text{-}Bottom}$ = 5 h and T_P = 1200 s).
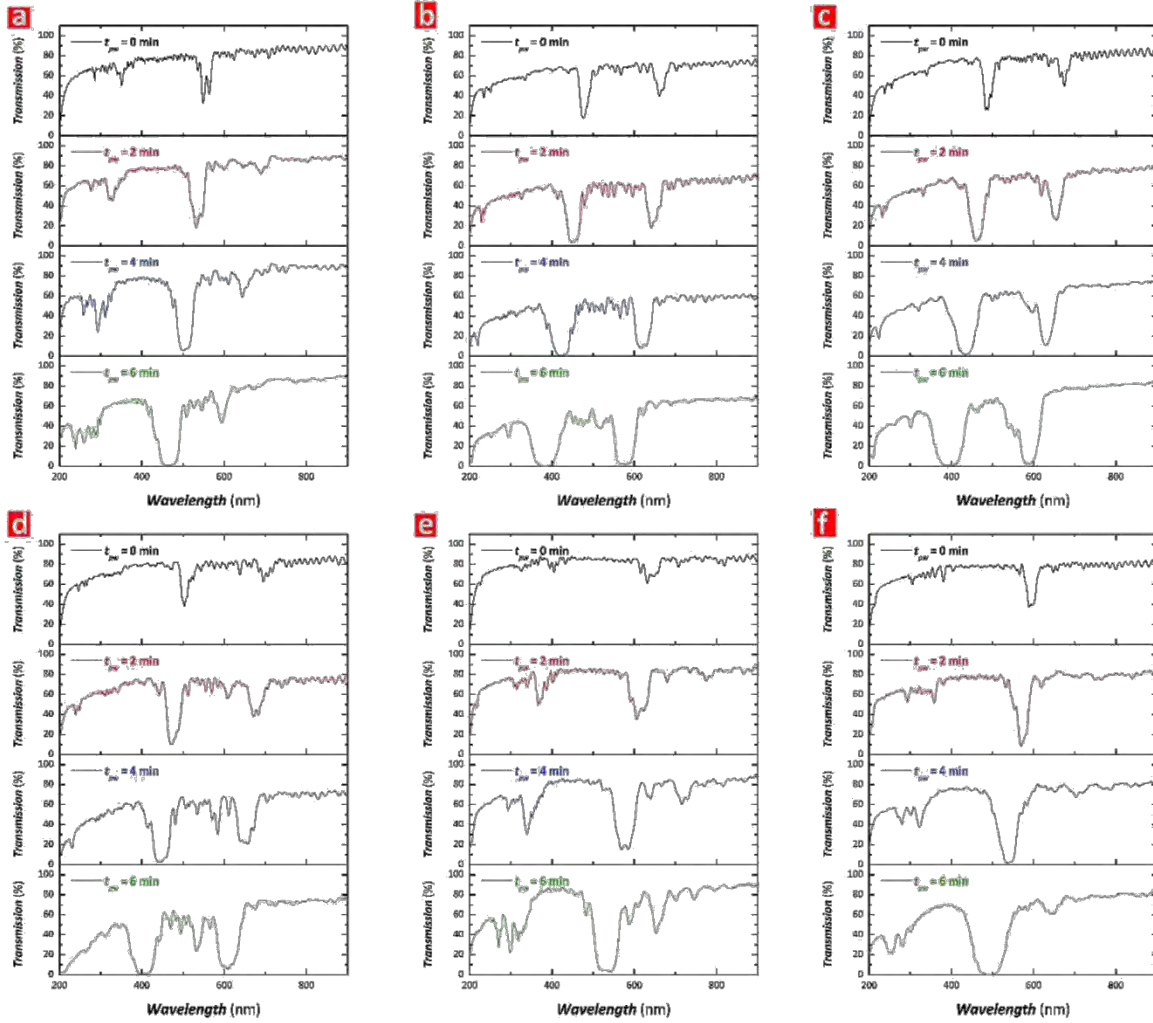
Figure S4. Transmission spectra as a function of t_{pw} for a) Tri-Hy-NAA-PC produced with a top APO-NAA-GIF (t_{An-Top} = 6.67 h and T_P = 700 s), a central NAA-DBR ($t_{An-Center}$ = 6.67 h and T_P = 1200 s), and bottom APO-NAA-GIF ($t_{An-Bottom}$ = 6.67 h and T_P = 1300 s), b) Tri-Hy-NAA-PC produced with a top NAA-DBR (t_{An-Top} = 6.67 h and T_P = 900 s), a central APO-NAA-GIF ($t_{An-Center}$ = 6.67 h and T_P = 1100 s), and bottom NAA-DBR ($t_{An-Bottom}$ = 6.67 h and T_P = 1200 s), c) Tri-Hy-NAA-PC produced with a top NAA-DBR (t_{An-Top} = 7.5 h and T_P = 900 s), a central APO-NAA-GIF ($t_{An-Center}$ = 5 h and T_P = 1100 s), and bottom NAA-DBR ($t_{An-Bottom}$ = 7.5 h and T_P = 1200 s), d) Tri-Hy-NAA-PC produced with a top NAA-DBR (t_{An-Top} = 5 h and T_P = 900 s), a central APO-NAA-GIF ($t_{An-Center}$ = 10 h and T_P = 1100 s), and bottom NAA-DBR ($t_{An-Bottom}$ = 5 h and T_P = 1200 s), e) Tri-Hy-NAA-PC produced with a top APO-NAA-GIF (t_{An-Top} = 7.5 h and T_P = 700 s), a central NAA-DBR ($t_{An-Center}$ = 5 h and T_P = 1200 s), and bottom APO-NAA-GIF ($t_{An-Bottom}$ = 7.5 h and T_P = 1300 s), and Tri-Hy-NAA-PC produced with a top APO-NAA-GIF (t_{An-Top} = 5 h and T_P = 700 s), a central NAA-DBR ($t_{An-Center}$ = 10 h and T_P = 1200 s), and bottom APO-NAA-GIF ($t_{An-Bottom}$ = 5 h and T_P = 1300 s).

Chapter 4

ELUCIDATING ALCOHOL ADDITIVES
EFFECT ON MILD PULSE ANODIZATION
BY FORBIDDEN LIGHT PROPAGATION IN
NANOPOROUS ANODIC ALUMINA
GRADIENT-INDEX FILTERS

4. Elucidating Alcohol Additives Effect on Mild Pulse Anodization by Forbidden Light Propagation in Nanoporous Anodic Alumina Gradient-Index Filters

4.1 Introduction, Significance and Commentary

High-quality, forbidden light propagation in NAA-based photonic crystals enables the detection of small changes in the refractive index of the surroundings, making them desired platforms for various high-precision photonic applications. This study demonstrates enhancements of quality of light-forbidding propagation in NAA-GIFs produced by sinusoidal pulse anodisation in modified alcohol-containing acid electrolytes. Comprehensive electrochemical, structural, optical and chemical analyses of NAA-GIFs reveal that a suitable selection of type and concentration of alcohol additive is critical in determining the quality of light forbidden propagation in NAA-GIFs. Sulphuric acid electrolyte modified with 40 v % methanol is found to be the most optimal condition to produce NAA-GIFs with high quality factors (i.e. approximately 32 to 54% quality enhancement compared to that of other alcohol additives), enabling future developments of high-quality NAA-based PC technologies for optical sensors, photocatalysts, lasing structures and other photonic devices.

4.2 Publication

This chapter is presented as published journal article by **<u>S.Y. Lim</u>**, C.S. Law, L. Jiang, L. K. Acosta, A. Bachhuka, L.F. Marsal, A.D. Abell, and A. Santos, *Elucidating alcohol additives effect on mild pulse anodization by forbidden light propagation in nanoporous anodic alumina gradient-index filters*. Electrochimica Acta (under revision).

Statement of Authorship

Title of Paper	Elucidating Alcohol Additives Effect on Mild Pulse Anodization by Forbidden Light Propagation in Nanoporous Anodic Alumina Gradient-Index Filters
Publication Status	☐ Published ☐ Accepted for Publication ☑ Submitted for Publication ☐ Unpublished and Unsubmitted work written in manuscript style
Publication Details	S.Y. Lim, C.S. Law, L. Jiang, L. K. Acosta, A. Bachhuka, L.F. Marsal, A.D. Abell, and A. Santos, *Elucidating alcohol additives effect on mild pulse anodization by forbidden light propagation in nanoporous anodic alumina gradient-index filters.* Electrochimica Acta (under revision).

Principal Author

Name of Principal Author (Candidate)	Siew Yee Lim		
Contribution to the Paper	Performed the experiment, processed and analysed the data and wrote the manuscript under the supervision of Abel Santos and Andrew D. Abell.		
Overall percentage (%)	40		
Certification:	This paper reports on original research I conducted during the period of my Higher Degree by Research candidature and is not subject to any obligations or contractual agreements with a third party that would constrain its inclusion in this thesis. I am the primary author of this paper.		
Signature		Date	10/06/2020

Co-Author Contributions

By signing the Statement of Authorship, each author certifies that:

     i.   the candidate's stated contribution to the publication is accurate (as detailed above);

     ii.   permission is granted for the candidate in include the publication in the thesis; and

     iii.   the sum of all co-author contributions is equal to 100% less the candidate's stated contribution.

Name of Co-Author	Cheryl Suwen Law		
Contribution to the Paper	Aided in performing the experiment, and processed and analysed the data. Equal contribution with Siew Yee Lim and give consent to her to present this paper for examination towards the Doctorate of Philosophy.		
Signature		Date	15/06/2020

Name of Co-Author	Lin Jiang		
Contribution to the Paper	Aided in performing the experiment. Give consent to Siew Yee Lim to present this paper for examination towards the Doctorate of Philosophy.		
Signature		Date	10/06/2020

Name of Co-Author	Laura K. Acosta		
Contribution to the Paper	Aided in the evaluation of final version of manuscript. Give consent to Siew Yee Lim to present this paper for examination towards the Doctorate of Philosophy.		
Signature		Date	11/06/2020

Name of Co-Author	Akash Bachhuka		
Contribution to the Paper	Aided in performing the characterisation part of the experiment. Give consent to Siew Yee Lim to present this paper for examination towards the Doctorate of Philosophy.		
Signature		Date	04/08/2020

Name of Co-Author	Lluís F. Marsal		
Contribution to the Paper	Aided in the evaluation of final version of manuscript. Give consent to Siew Yee Lim to present this paper for examination towards the Doctorate of Philosophy.		
Signature		Date	10/06/2020

Name of Co-Author	Andrew D. Abell		
Contribution to the Paper	Acted as a co-supervisor for the candidate, and aided in revising and evaluating the manuscript for submission. Give consent to Siew Yee Lim to present this paper for examination towards the Doctorate of Philosophy.		
Signature		Date	10/06/2020

Name of Co-Author	Abel Santos		
Contribution to the Paper	Acted as a primary supervisor for the candidate, and aided in developing, revising and evaluating the manuscript for submission. Give consent to Siew Yee Lim to present this paper for examination towards the Doctorate of Philosophy.		
Signature		Date	11/06/2020

Elucidating Alcohol Additives Effect on Mild Pulse Anodization by Forbidden Light Propagation in Nanoporous Anodic Alumina Gradient-Index Filters

Siew Yee Lim[‡,a,b,c], Cheryl Suwen Law[‡,,b,c], Lin Jiang[a], Laura K. Acosta[a,d], Akash Bachhuka[e], Lluís F. Marsal[d], Andrew D. Abell[b,c,f] and Abel Santos[*,a,b,c]*

[a]School of Chemical Engineering and Advanced Materials, The University of Adelaide, 5005 South Australia, Australia.
[b]Institute for Photonics and Advanced Sensing, The University of Adelaide, 5005 South Australia, Australia.
[c]ARC Centre of Excellence for Nanoscale BioPhotonics, The University of Adelaide, 5005 South Australia, Australia.
[d]Department of Electronic, Electric, and Automatics Engineering, Rovira i Virgili University, 43007 Tarragona, Spain.
[e]Future Industries Institute, University of South Australia, 5095 South Australia, Australia.
[f]Department of Chemistry, The University of Adelaide, 5005 South Australia, Australia.

[*]E-mails: suwen.law@adelaide.edu.au ; abel.santos@adelaide.edu.au
[‡]Equal Contribution.

Abstract: A comprehensive study on structural and optical engineering of high-quality nanoporous anodic alumina gradient-index filters (NAA–GIFs) by selective addition of alcohols to the anodizing acid electrolyte is presented. Analysis of the combined effect of type (methanol, ethanol, isopropanol, and ethylene glycol) and concentration (from 10 to 70 v %) of alcohol additives in sulfuric acid electrolyte on the optical features of the characteristic photonic stopband (PSB) of NAA–GIFs – central wavelength, full width at half maximum, intensity, and quality factor – allow us to elucidate the most optimal fabrication conditions to produce high-quality NAA–GIFs by sinusoidal pulse anodization under mild conditions. Comprehensive electrochemical, structural, optical, and chemical analyses demonstrate that a suitable selection of type and concentration of alcohol additive is critical in controlling the quality of forbidden light propagation within these photonic crystal (PC) structures. Particularly, NAA–GIFs produced by sinusoidal pulse anodization in sulfuric acid electrolyte modified with 40 v % methanol achieve an outstanding quality factor of ~58 (32–54 % superior than that of other alcohol additives). Our findings indicate that a combination of anodic oxide growth rate and suppressing-dissolution efficiencies, mildly branched nanoporous structure, and incorporation of carbon-containing impurities into the structure of NAA–GIFs are critical factors in enhancing light-forbidding quality of these NAA-based PCs. Our results advance understanding of structural engineering of NAA–PCs by dynamic modification of the input anodization profile under optimal electrolyte conditions.

Keywords: Nanoporous Anodic Alumina, Gradient-Index Filter, Anodization, Alcohol Additive, Quality Factor

1. Introduction

Nanoporous anodic alumina (NAA) produced by electrochemical oxidation of aluminum – henceforth "anodization" – is a versatile platform material due to its chemical resistance, thermal stability, mechanical robustness, optical properties, and highly controllable and versatile nanopore geometry [1–3]. Formation of NAA by anodization – a top–down nanofabrication approach – relies on an electrochemical equilibrium between two main electric field-assisted reactions occurring across the oxide barrier layer at each nanopore bottom tip: i) oxidation of aluminum at the metal/oxide interface, and ii) dissolution of alumina at the oxide/electrolyte interface [4]. Under steady mild anodization conditions, both formation and dissolution of alumina (Al_2O_3) across the oxide barrier layer are balanced, and nanopore growth is practically constant [5,6]. However, upon dynamic alteration of the anodizing input current density/voltage this electrochemical equilibrium undergoes a recovery stage, during which both reactions evolve to counterbalance the electric field perturbation by adjusting the thickness of the oxide barrier layer. This process can lead to both formation of well-defined nanopore modulations [7,8] or tree-like nanoporous structures [9,10], depending on whether anodization is performed within or outside self-organization regime, the magnitude of the electric field perturbation, and other anodization conditions such as electrolyte temperature and its concentration. As such, dynamic alterations of the input electric field can be judiciously harnessed to engineer the structure of NAA with precisely tailored properties for specific applications. Of all these, NAA-based photonic crystals (NAA–PCs) produced by pulse-like anodization – periodic variation of anodizing input current density/voltage throughout time – are ideal platform materials for light-based technologies such as lasing, sensing, photocatalysis, and optical encoding. The nanoporous structure of NAA provides a tunable effective medium composed of air and alumina, the architecture of which can be precisely modulated in depth by distinct forms of pulse-like anodization [11]. NAA–PCs selectively allow and forbid the

2

propagation of incoming photons of specific wavelengths or energies when incident electromagnetic waves travel across their structure. The characteristic photonic stopband (PSB) of NAA–PCs determines the wavelength range within which propagation of photons is inhibited. The PSB's features – central wavelength, full width at half maximum, intensity, and quality factor – can be finely engineered by pulse-like anodization to harness different forms of light–matter interactions across the UV–visible–NIR spectrum such as diffraction, reflection, refraction, transmission, emission, confinement and recirculation of electromagnetic waves [12]. Examples of NAA–PCs include gradient-index filters (NAA–GIFs) [13–19], optical microcavities [20–22], Fabry-Pérot interferometers [23–25], distributed Bragg reflectors [26–28], bandpass filters [29,30], heterogeneous PCs [31], and photonically encoded tags [32]. Of all these, NAA–GIFs are a class of NAA–PCs with smooth, periodic modulation of refractive index, which is optically translated into a characteristically well-resolved and narrow PSB – $\sim\pi/4$ narrower than that of their analogous quarter-wave distributed Bragg reflectors. The narrow line-width of NAA–GIFs' PSB with suppressed higher-order harmonics and sidelobes makes them suitable components for various high-precision light-filtering applications [33,34]. This optical feature also provides NAA–GIFs with high sensitivity and responsiveness to changes in the refractive index of the medium within their nanopores, making them ideal optical platforms for sensing and biosensing technologies [35–37]. To date, various sinusoidal pulse anodization strategies under mild conditions have been devised to achieve high-quality control of light in NAA–GIFs, including apodization of anodization profiles [13], implementation of voltage–period compensation modes [14–16], and optimization of anodization conditions [17–19]. Despite these advances, fabrication of high-quality NAA–PCs by mild pulse anodization remains challenging. NAA–PCs suffer from two main intrinsic constraints: i) a low refractive index contrast air–alumina ($n_{air} \sim 1.00$ RIU and $n_{alumina} \sim 1.5$–2.3 RIU), and ii) progressive chemical etching of NAA during anodization, which leads to an

3

unbalanced distribution of optical thickness along NAA stacks composing the structure of NAA–PCs. Therefore, more fundamental studies should be performed to elucidate suitable anodization conditions that enable both high refractive index contrast and chemical etching suppression of NAA during pulse anodization.

Addition of alcohols to the anodizing acid electrolyte was originally devised to prevent the anodizing electrolyte from freezing at sub-zero temperatures, enhance dissipation of Joule heat at the nanopore bottom tip, and facilitate uniform growth of the anodic film under hard anodization regime – high anodizing voltage/current density [38–43]. Studies using alcohol additives to produce NAA films under steady mild anodization conditions focused on assessing their impact on the geometric features of nanopores and the Coulombic efficiency of anodization under these conditions [44,45]. Herein, the effect of alcohol additives on the structural, chemical, and optical properties of NAA–GIFs produced by sinusoidal pulse anodization under mild conditions is elucidated (**Fig. 1a**). Comprehensive analysis of key physical and chemical features of NAA–GIFs and output electrochemical signals allow us to determine the interplay between type (methanol, ethanol, isopropanol, and ethylene glycol) and concentration (10–70 v %) of alcohol additive in engineering the structure of these NAA-based PCs (**Figs. 1b and c**). Systematic assessment of the characteristic PSB of NAA–GIFs makes it possible to determine the most optimal alcohol modification conditions to maximize forbidden light propagation within NAA–GIFs in the form of well-resolved, narrow, intense, high-quality PSBs (**Fig. 1d**).

2. Experimental Section

2.1. Materials. High purity (99.9997%), 0.32 mm thick aluminum (Al) foils were supplied by Goodfellow Cambridge Ltd. (UK). Perchloric acid ($HClO_4$), copper (II) chloride ($CuCl_2$), hydrochloric acid (HCl), and ethylene glycol (EGOH, $(CH_2OH)_2$) were purchased from Sigma-Aldrich (Australia). Sulfuric acid (H_2SO_4), methanol (MetOH, CH_3OH), isopropanol (IPA,

4

CH₃CHOHCH₃), and ethanol (EtOH, C₂H₅OH) were purchased from ChemSupply (Australia). All chemicals were used as received, without purification. All aqueous solutions used in this study were prepared in ultrapure Milli–Q® water (18.2 MΩ cm).

2.2. Fabrication of NAA–GIFs. NAA–GIFs were fabricated by sinusoidal pulse anodization (SPA) under current density control, using aqueous solutions of H_2SO_4 as anodizing acid electrolyte [46]. Before anodization, 1.5×1.5 cm square Al chips were sequentially sonicated in ethanol and water for 15 min each, dried under air stream, and electropolished in a 4:1 (*v:v*) EtOH:HClO₄ electrolyte at 20 V and 5 °C for 3 min to smooth the surface of Al. Electropolished Al chips were anodized in an electrochemical reactor with controlled electrolyte temperature (T_{an}) fixed at –2 °C and ~300 rpm stirring rate, using 1 M H_2SO_4 as acid electrolyte. The composition of the acid electrolyte was systematically modified with four alcohol additives (i.e. MetOH, EtOH, IPA, and EGOH) at varying concentration (i.e. *[Alcohol]* from 10 to 70 v % with *Δ[Alcohol]* = 10 v %) to investigate the combined effect of alcohol additive type and concentration on the electrochemical, chemical, structural, and optical features of NAA–GIFs. The fabrication process started with a 10 min anodization step at a constant current density of 1.120 mA cm⁻² to create a thin nanoporous oxide layer and achieve homogeneous nanopore growth before SPA. The anodization process was then switched to SPA mode, throughout which the input current density was sinusoidally pulsed between high (J_{max} = 1.120 mA cm⁻²) and low ($J_{min} = J_{offset}$ = 0.280 mA cm⁻²) values at fixed current density amplitude (A_J = 0.420 mA cm⁻²) and anodization period (T_P = 494 s) – time between consecutive sinusoidal pulses (**Fig. 1a**). Current density–time SPA profiles were generated by a custom-designed LabVIEW®-based software according to **Eq. 1**, using Keithley 2400C and 2612B sourcemeters (Keithley Instruments, USA):

$$J(t) = A_J \times \left[sin\left(\frac{2\pi}{T_P} \times t\right) + 1 \right] + J_{offset} \tag{1}$$

5

where $J(t)$ is the current density at a given time t as a function of A_J, T_P, and J_{offset}.

After anodization, NAA–GIFs were thoroughly washed in ultrapure Milli-Q® water under sonication for ~15–30 min to remove physiosorbed alcohol molecules.

2.3. Optical Characterization of NAA–GIFs. Prior to optical characterization, a circular transparent window of ~5 mm in diameter was created on the backside of NAA–GIFs by selectively etching the remaining Al substrate in a saturated HCl–CuCl$_2$ solution, using a Viton® etching mask. Transmission spectra of NAA–GIFs were acquired at normal incidence (i.e. $\theta = 0°$) in a UV–visible spectrometer (Cary 300, Agilent, USA), from 200 to 800 nm with a resolution of 1 nm and 5 nm slit. Transmission spectra of NAA–GIFs were processed in OriginPro 8.5® to quantify the features of the characteristic PSB (i.e. central wavelength position – λ_{PSB}, full width at half maximum – $FWHM_{PSB}$, intensity – I_{PSB}, and quality factor – Q_{PSB}) from Gaussian fittings, using the upper lobe of the PSB as a baseline (y_0) – graphical definition shown in **Fig. 1d**. The quality factor of NAA–GIFs' PSB – ratio of central wavelength position to its full width at half maximum – was used as the reference figure of merit to assess the quality of light-forbidding properties of NAA–GIFs according to **Eq. 2**:

$$Q_{PSB} = \frac{\lambda_{PSB}}{FWHM_{PSB}} \tag{2}$$

Digital images of the best performing NAA–GIFs were acquired by a Canon EOS 700D digital camera equipped with a Tamron 90 mm F2.8 VC USD macro mount lens under natural illumination, using a black card as a background. The effective refractive index (n_{eff}) of NAA as a function of $[MetOH]$ (from 10 to 70 v % with $\Delta[MetOH] = 10$ v %) was characterized by measuring the effective optical thickness (OT_{eff}) of a set of NAA thin films produced at $J_{max} = 1.120$ mA cm^{-2} and $J_{min} = 0.280$ mA cm^{-2}. NAA films were fabricated at $T_{an} = -2$ °C and $[H_2SO_4] = 1.0$ M but with varying concentration of alcohol additive and input current density, for a fixed total charge density of 5 C cm^{-2}. Reflection spectra at varying angle of incidence (θ

6

= 15º, 25º, 35º, and 45º) were acquired in a system comprising a variable-angle reflection stage (RSS–VA, Ocean Optics, USA), a tungsten light source (LS–1LL, Ocean Optics, USA), and a miniature visible optical fiber spectrometer (FLAME–T–VIS–NIR–ES, Ocean Optics, USA). White light was shinned over NAA films at a given angle of incidence and with a spot size of ~2 mm in diameter. Reflected light was collected and guided to the miniature spectrometer by two optical fibers (QP200–2–UV–VIS, Ocean Optics, USA). Reflection spectra were collected from 400 to 900 nm with an integration time of 10 ms and 20 average measurements. OT_{eff} was estimated by applying Fast Fourier transform (FFT) to reflection spectra of these NAA films in IgorPro® (Wavemerics, USA) according to **Eq. 3**:

$$OT_{eff} = 2n_{eff}L_P \cos \theta \qquad (3)$$

where L_P is the physical thickness of the NAA film established from FEG-SEM image analysis, and θ is the angle of incidence.

2.4. Structural and Chemical Characterization of NAA–GIFs. The structural features of NAA–GIFs were characterized by field emission gun scanning electron microscopy (FEG-SEM FEI Quanta 450). The geometric features of NAA–GIFs were established by analyzing top and cross-sectional view FEG-SEM images in ImageJ software [47]. Nanopore density per unit of cross-section along the nanopore length (ρ_P) was calculated from representative 1.4 × 1.4 μm^2 cross-sectional view FEG-SEM images at steps of 35 nm, using ImageJ's plugin 'Plot Profile'. After anodization, chemical composition of representative NAA–GIFs was analyzed by energy-dispersive X-ray (EDX) spectroscopy during FEG-SEM characterization, and by X-ray photoelectron spectroscopy (XPS) using a Kratos Axis Ultra DLD spectrophotometer with a monochromatic Al radiation source was operated at 10 kV and 20 mA to record all XPS spectra over 0–1000 eV at a pass energy of 120 eV and resolution of 0.5 eV. Internal flood gun was used to reduce sample charging during irradiation. Survey spectra were then processed to quantify atomic percentage of the elements present on NAA films. Neutral C1s carbon peak at

7

a binding energy of 285.0 eV was used as a reference to correct all other binding energies. All spectra were quantified using casaXPS software.

3. Results and Discussion

3.1. Fabrication and Structural Characterization of NAA–GIFs.

Fig. 2 shows representative anodization profiles, and top and cross-sectional view FEG-SEM images of NAA–GIFs produced at fixed T_P = 494 s, T_{an} = –2 °C, and $[H_2SO_4]$ = 1 M acid electrolyte modified with varying concentration of methanol ($[MetOH]$ = 10, 50, and 70 v %). It is apparent from these anodization profiles that the output voltage follows closely the input current density under the anodization conditions used in this study – highly concentrated sulfuric acid electrolyte at low temperature (**Fig. 2a**). **Figs. A.1–A.4** (**Appendix A**) compile all the anodization profiles of NAA–GIFs produced using different type and concentration of alcohol additives (MetOH, EtOH, IPA, and EGOH, from 10 to 70 v %). These profiles further confirm the direct translation of sinusoidal input current density pulses into sinusoidal output voltage pulses. Qualitative analysis of cross-sectional view FEG-SEM images shown in **Fig. 2b** reveals that the period length (L_{TP}) – distance between consecutive stacks of NAA generated by each sinusoidal pulse – increases with $[MetOH]$, from 10 to 70 v %, as denoted by the distance between white arrowheads and dotted lines in these images. It is also apparent from top view FEG-SEM images shown in **Fig. 2c** that the nanopore diameter (D_P) decreases with concentration of alcohol additive. For instance, L_{TP} and D_P for NAA–GIFs fabricated with $[MetOH]$ = 10, 50, and 70 v % were measured to be 130 ± 7, 151 ± 13, and 152 ± 8 nm, and 11 ± 2, 10 ± 2 and, 5 ± 2 nm, respectively. This preliminary analysis suggests that increasing concentration of alcohol additive, in this case MetOH, increases the growth rate of NAA and minimizes its dissolution at fixed sinusoidal input current density pulses, and acid electrolyte concentration and temperature. Interestingly, further qualitative analysis of magnified cross-sectional FEG-SEM images shown in **Fig. 3a** demonstrates that both nanopore morphology

8

and geometry evolve with MetOH concentration. At low *[MetOH]*, nanopores feature wider diameter, high tortuosity, and a tree-like branched structure, which is generated during the transition from high to low input current density within each sinusoidal pulse. When alcohol additive concentration in the electrolyte is increased, nanopore diameter is reduced, period length increases, and nanopores become straighter with a slight modulation of diameter induced by the sinusoidal input current density. This observation is consistent for other types of alcohol additives (**Fig. A.5 – Appendix A**). These results are further validated by analyzing the nanopore density per unit of cross-section (ρ_P) along the length of nanopores in the cross-sectional FEG-SEM images shown in **Fig. 2b**. It is apparent from this image analysis that ρ_P decreases with *[MetOH]* (**Fig. 3b**), with average values of $31 \pm 3, 27 \pm 2,$ and 19 ± 1 nanopores μm^{-1} of cross-section for NAA–GIFs produced by SPA in 1 M H_2SO_4 modified with *[MetOH]* = 10, 50, and 70 v %, respectively. These graphs also reveal that ρ_P maxima for *[MetOH]* = 10 and 50 v % (black and red arrows in **Fig. 3b**) are consistent with the interfaces between NAA stacks denoted by white arrowheads and dotted lines in **Fig. 2b**. Increment of ρ_P in these cross-sectional regions is attributable to nanopore splitting and branching induced by the reduction of the input current density, and the concomitant alteration of the electrochemical equilibrium across the oxide barrier layer **[7,8]**. In contrast, it is found that ρ_P remains practically constant with an almost negligible deviation ($\pm$ one nanopore per cross-sectional μm) at *[MetOH]* = 70 v %, indicating the effective suppression of nanopore branching with the dynamic sinusoidal change in input current density at that concentration of alcohol additive.

Analysis of the anodization profiles shown in **Figs. A.1–A.4 (Appendix A)** was performed in order to elucidate the effect of alcohol additives on the main electrochemical parameters in the sinusoidal output voltage. It is found that the minimum (V_{min}) and maximum (V_{max}) voltages, and the voltage amplitude ($A_V = V_{max} - V_{min}$) of the sinusoidal output voltage – graphically described in **Fig. 1a** – increase exponentially with increasing alcohol concentration, from 10 to

9

70 v %, for all alcohol additives (**Fig. A.6 and Table A.1 – Appendix A**). Qualitative assessment of V_{min} and V_{max} with *[Alcohol]* shown in **Figs. 4a and b** indicates that at a fixed input total charge density (Q) of 0.346 C cm^{-2} – integrated current density throughout time for one sinusoidal pulse – these electrochemical parameters increase with *[Alcohol]* following the order EGOH > MetOH > EtOH > IPA. Analysis of growth rates (R_V) of V_{min} and V_{max} per unit of concentration of alcohol additive summarized in **Fig. 4c** reveals that for MetOH, EtOH, and IPA additives, V_{max} grows faster than V_{min} with *[Alcohol]*, with R_V values of 0.21 ± 0.01, 0.13 ± 0.01, and 0.05 ± 0.01 V v %$^{-1}$ for V_{min}, and 0.26 ± 0.02, 0.22 ± 0.01, and 0.10 ± 0.01 V v %$^{-1}$ for V_{max}, respectively. However, the growth rate for V_{min} and V_{max} are statistically equivalent for EGOH additive, with values of 0.36 ± 0.01, and 0.35 ± 0.01 V v %$^{-1}$, respectively. These observations are in good agreement with previous studies analyzing the effect of alcohol additives on NAA produced under steady mild anodization conditions in sulfuric acid electrolyte **[44,45]**. Rise in output voltage upon increment of alcohol additive concentration at constant input current density was attributed to changes in the dielectric constant, viscosity, and conductivity of the acid electrolyte. It was also pointed that addition of alcohol additive does not affect the growth rate of the anodic film, but it minimizes its progressive dissolution in the acid electrolyte during anodization **[45]**. As such, the Coulombic efficiency of the anodization process – weight ratio between produced oxide and consumed aluminum – increases with concentration of alcohol additive. However, our observations indicate that further insights are needed to fully understand the effect of type and concentration of alcohol additives on the structure of NAA under a dynamic input current density profiles.

3.3. Correlation between Electrochemical Output and Structure of NAA–GIFs. To better understand the effect of alcohol additive type and concentration on the structural features of NAA–GIFs, we performed comprehensive FEG-SEM image analysis to determine the period length (L_{TP}) and nanopore diameter (D_P) of NAA–GIFs produced with MetOH, EtOH, IPA,

10

and EGOH at varying alcohol additive concentration, from 10 to 70 v % (**Figs. A.7–A.10 –**

Appendix A). **Fig. 5** and **Table A.2 (Appendix A)** demonstrate that, upon application of

sinusoidal current density pulses of 0.346 C cm^{-2}, L_{TP} in NAA–GIFs increases linearly with

[Alcohol] at rates of 0.38 ± 0.07, 0.52 ± 0.20, 0.46 ± 0.07, and 2.11 ± 1.15 nm v %$^{-1}$ for MetOH,

EtOH, IPA, and EGOH, respectively. It is also found that D_P is progressively reduced with

[Alcohol] (**Figs. 5a–d**), showing a weak linear correlation measured to be -0.06 ± 0.03, $0.02 \pm$

0.07, -0.04 ± 0.04, and -0.13 ± 0.15 nm v %$^{-1}$ for MetOH, EtOH, IPA, and EGOH,

respectively. It is apparent from analysis of D_P that addition of alcohol additives minimizes the

dissolution rate of the resulting anodic film during the anodization process, which is in good

agreement with previous observations [44,45]. However, in contrast to NAA films produced

under a constant input current density, analysis of L_{TP} indicates that addition of alcohol

additives to the acid electrolyte significantly alters the growth rate of the anodic film under

dynamic input current density conditions. This result is further validated by analyzing the effect

of alcohol additives on the position of the characteristic PSB of NAA–GIFs (λ_{PSB}), which is

found to red-shift with increasing *[Alcohol]* for all additives used in this study (*vide infra*). It

is generally accepted that, under a constant anodizing input current density, modification of the

acid electrolyte with alcohol additives does not affect the growth rate of anodic oxide [45].

However, we have previously demonstrated that addition of ethanol coolant to sulfuric acid

electrolyte enhances the formation of anodic alumina nanotubes by stepwise mild–hard pulse

anodization [48]. Increasing nanotube formation efficiency with concentration of EtOH was

attributed to enhanced structural inner–outer nanopore wall modulations, which consequently

facilitates structural cleavage of nanotubes along the anodic oxide film. Upon application of

mild sinusoidal current density pulses, the electrochemical equilibrium between formation and

dissolution of alumina across the oxide barrier layer is never fully achieved due to the dynamic

change in input current density throughout time. Analysis of V_{min} and V_{max} reveals an alcohol

11

additive concentration-dependent pattern, in which V_{max} increases at a faster rate than V_{min} with *[Alcohol]* for fixed high and low input current density levels, respectively. Therefore, it can be inferred that, under dynamic input current density conditions and increasing concentration of alcohol additive, the electrochemical equilibrium across the oxide barrier layer is altered in such a way that the overall growth rate of the anodic oxide film increases. Although a comprehensive mechanistic chemical–electrochemical model will require further investigations, it is apparent that the electric field-driven dissolution of anodic oxide is reduced in favor of its formation during this process, and that the anodic oxide grows faster during the J_{max} section of the input current density with *[Alcohol]*, as indicated by the faster growth rate of V_{max}, and analysis of nanopore geometry and morphology evolution. However, increment of period length during the V_{max} section of the output voltage, and the concomitant reduction of nanopore branching and increment of nanopore wall thickness with the concentration of alcohol additive (**Fig. 5e**) cannot be entirely attributed to the dissolution suppression effect of alcohol additives. Other factors such as the relative concentration of electrolytic species in the anodizing electrolyte, incorporation of impurities from the acid electrolyte into the anodic oxide, and their influence in the electrochemical equilibrium across the oxide barrier layer must be considered. Formation and dissolution of anodic oxide at the nanopore bottom tips can be described by the elementary reactions summarized in **Eqs. 4–9**:

(i) Anodic oxide formation at the aluminum/alumina interface:

$$Al \rightarrow Al^{3+}_{(ox)} + 3e^- \tag{4}$$

$$2Al^{3+}_{(ox)} + 3O^{2-}_{(ox)} \rightarrow Al_2O_3 \tag{5}$$

$$2Al^{3+}_{(ox)} + 3HO^-_{(ox)} \rightarrow Al_2O_3 + 3H^+_{(aq)} \tag{6}$$

(ii) Anodic oxide dissolution at the alumina/electrolyte interface:

$$Al_2O_3 + 6H^+_{(aq)} \rightarrow 2Al^{3+}_{(aq)} + 3H_2O_{(liq)} \tag{7}$$

$$3O^{2-}_{(ox)} \rightarrow O_{2(gas)} + 4e^- \tag{8}$$

12

$$2H_2O_{(liq)} \rightarrow O^{2-}_{(ox)} + OH^-_{(ox)} + 3H^+_{(aq)} \tag{9}$$

Generation and inward migration of Al^{3+} ions from the Al metal into the anodic oxide are determined by the electric field applied across the oxide barrier layer, which is constant at a given input current density value under mild conditions [1]. In contrast, the effective concentration of water molecules decreases with increasing concentration of alcohol additive. As such, local generation of OH^-, H^+, and O^{2-} species by heterolytic dissociation of water molecules at the alumina/electrolyte interface – supply of anions for formation and dissolution of Al_2O_3 – decreases with [Alcohol] (**Eq. 9**). Conversely, more OH^- ions are available in the electrolyte to react with inwardly migrated Al^{3+} cations to form Al_2O_3 (**Eq. 7**) and its hydroxyl forms (e.g. $Al(OH)_3$ and $Al(OH_2)_6^{3+}$) [49]. Therefore, it is possible to infer that the electric field-driven dissolution of anodic oxide is effectively reduced (**Eq. 7**), while its formation rate increases with increasing [Alcohol]. This would, in part, explain the observed increment of the oxide barrier layer thickness, reduction of nanopore diameter and branching, and overall anodic oxide growth rate increment with increasing [Alcohol].

3.4. Effect of Alcohol Additive Type and Concentration on the Optical Properties of NAA–GIFs. The characteristic PSB of NAA–GIFs is the optical feature that determines the quality of forbidden light propagation within these PC structures. Assessment of the features of the characteristic PSB (i.e. λ_{PSB}, $FWHM_{PSB}$, I_{PSB}, and Q_{PSB}) of NAA–GIFs produced with varying type and concentration of alcohol additive (i.e. MetOH, EtOH, IPA, and EGOH, from 10 to 70 v % with $\Delta[Alcohol] = 10$ v %) can serve as a figure of merit to characterize the impact of electrochemical conditions on the structural and optical properties of NAA-based PCs [19]. Therefore, key optical parameters were quantified from Gaussian fittings applied to the PSB in the optical transmission spectra of NAA–GIFs (**Figs. A.11–A.14 – Appendix A**). **Figs. 6a–d** summarize the dependence of λ_{PSB}, $FWHM_{PSB}$, I_{PSB}, and Q_{PSB} with [Alcohol] for NAA–GIFs fabricated by SPA in 1 M H_2SO_4 electrolyte modified with MetOH, EtOH, IPA, and EGOH,

respectively. The position of the central wavelength of NAA–GIFs' PSB (λ_{PSB}) is critically determined by L_{TP} and D_P, where λ_{PSB} red-shifts with longer L_{TP} and smaller D_P, according to the effective optical thickness of each NAA stack within the NAA–GIF structure [46]. As such, $\Delta\lambda_{PSB}$ is can be harnessed as an indicator to identify and quantify synergistic effects between the anodic oxide growth rate and dissolution-suppressing efficiencies for a given alcohol additive. Analysis of the effect of type and concentration of alcohol additive on λ_{PSB} indicates that the PSB of NAA–GIFs red-shifts – shift toward longer wavelength – its position linearly with increasing *[Alcohol]* for all additives, from an initial average λ_{PSB} of 474 ± 7 nm at *[Alcohol]* = 10 v %. This is in good agreement with FEG-SEM image analysis, in which L_{TP} increases and D_P decreases with *[Alcohol]*. However, it has been demonstrated that L_{TP} is the most critical parameters in determining λ_{PSB} in NAA-based PC structures [46]. Analysis of ratio of spectral shift rate to period length rate for alcohol additive unit, defined by **Eq. 10**, is estimated to be 4.3 ± 0.1, 2.8 ± 0.2, 1.4 ± 0.1, and 1.0 ± 0.6 nm v %$^{-1}$ for MetOH, EtOH, IPA, and EGOH, respectively.

$$R_{\Delta\lambda_{PSB}/\Delta L_{TP}} = \frac{\Delta\lambda_{PSB}/\Delta[Alcohol]}{\Delta L_{TP}/\Delta[Alcohol]} \tag{10}$$

Previous studies using the same anodization conditions at fixed 25 v % concentration of EtOH additive have reported $R_{\Delta\lambda_{PSB}/\Delta L_{TP}}$ values of ~3.3, ~2.5, ~3.4, and ~3.4 for sinusoidal [46], pseudo-stepwise [30], stepwise [26], and sawtooth pulses [50], respectively. Comparative analysis reveals that the type of alcohol additive is critical in determining the efficiency of pulse-like anodization to translate structural modulations of L_{TP} into λ_{PSB} shifts, where MetOH is found to be the most efficient alcohol additive to achieve broad spectral tunability of the PSB with a $R_{\Delta\lambda_{PSB}/\Delta L_{TP}}$ value of ~4.3. $FWHM_{PSB}$ is a critical factor in determining the quality of forbidden light propagation in NAA–GIFs, as indicated by **Eq. 2**. It is apparent from **Figs. 6a–d** that $FWHM_{PSB}$ decreases initially with *[Alcohol]* until it reaches a minimum value, beyond which $FWHM_{PSB}$ increases with *[Alcohol]*. The narrowest $FWHM_{PSB}$ in NAA–GIFs produced

14

with MetOH, EtOH, IPA, and EGOH were 9.5 ± 0.4 nm at 40 v %, 15.7 ± 0.6 nm at 30 v %, 17.5 ± 0.7 nm at 40 v %, and 14.1 ± 0.6 nm at 50 v %, respectively. A well-resolved, intense PSB is a desirable optical feature particularly critical for specific photonic applications requiring high light-filtering efficiency and sensitivity. Assessment of I_{PSB} in **Figs. 6a–d** indicates that forbidden light propagation is more efficient in NAA–GIFs fabricated with MetOH, EtOH, IPA, and EGOH at *[Alcohol]* = 40, 20–40, 20–40, and 40–50 v %, with average I_{PSB} values of 63 ± 3, 50 ± 2, 50 ± 2, and 46 ± 2 % in optical transmission units, respectively. Quality factor is the figure of merit that dictates how good a PC structure is in forbidding propagation of electromagnetic waves across its structure. **Figs. 6a–d** reveal that Q_{PSB} in NAA–GIFs fabricated by SPA in 1 M H_2SO_4 electrolyte relies strongly on the type and concentration of alcohol additive. It is demonstrated that Q_{PSB} is maximum at *[Alcohol]* = 40, 30, 40, and 50 v % for NAA–GIFs produced in MetOH, EtOH, IPA, and EGOH additives, with values of 58 ± 2, 32 ± 1, 27 ± 1, and 40 ± 2, respectively. Therefore, MetOH is the most effective alcohol additive to fabricate high-quality NAA–GIFs, with a 32–54 % superior quality than that of EtOH, IPA, and EGOH. Interestingly, this optical property is also translated into the characteristic interferometric color displayed by NAA–GIFs. Digital images of the best performing NAA–GIFs shown in **Figs. 6a–d** insets demonstrate that, while NAA–GIFs produced in EtOH and IPA are transparent (lowest Q_{PSB}), their counterparts fabricated in MetOH and EGOH (highest Q_{PSB}) display vivid green interferometric color, which corresponds to the position of the central wavelength of their characteristic PSB within the ~550 nm region of the visible spectrum. **Table 1** summarizes the electrochemical, structural, and optical parameters of the best performing NAA–GIFs in terms of Q_{PSB} for each alcohol additive assessed in this study. These results demonstrate that 1 M H_2SO_4 electrolyte modified with 40 v % of MetOH is the most optimal condition to fabricate NAA–GIFs with well-resolved, intense, narrow PSBs. Interplay analysis between electrochemical, structural, and optical

15

parameters suggests that a moderate balance between growth rate and dissolution-suppressing efficiencies across the oxide barrier layer, along with a mildly branched nanoporous structure can enhance the quality of PSBs in NAA-based PCs. These results also demonstrate that MetOH is the most efficient alcohol additive in improving the translation of input current density pulses into suitable modulations of nanopore geometry and morphology to enhance light–matter interactions in NAA–GIFs. However, further insights into the impact of alcohol additives on the chemical composition of NAA–GIFs are needed to further elucidate how these specific anodization conditions may alter the intrinsic optical properties of NAA–GIFs.

3.5. Effect of Alcohol Additive Type and Concentration on the Chemical Composition of NAA–GIFs. NAA features a concentrically distributed chemical composition with decreasing concentration of impurities from the outer nanopore wall – surface exposed to acid electrolyte – to the inner cell boundary, which is composed of Al_2O_3 in its pure form (**Fig. 7a**) [51–53]. Type, concentration, and distribution of anionic impurities incorporated into the structure of NAA during anodization rely intrinsically on input anodizing current density/voltage, and electrolyte type and its temperature and concentration [1]. NAA–PCs fabricated in 1 M H_2SO_4 at –2 °C under the current density conditions used in this study contain ~2–7 % of S atoms, which are associated with incorporated sulfate anion impurities (SO_4^{2-}) through inward migration from the acid electrolyte [22]. Although previous studies analyzed the effect of alcohol additives on structural features and Coulombic efficiency of NAA films fabricated under steady anodization conditions [40,44,45,54], to the best of our knowledge, the effect of alcohol additives on the chemical composition of NAA has not been studied in detail. To gain further insight into the potential effect of chemical composition on quality enhancement of forbidden light propagation in NAA–GIFs, we analyzed the elemental composition of these NAA-based PC structures using EDX and XPS analyses. Since the concentration of H_2SO_4 was kept constant at 1 M in all acid electrolytes, any change in chemical composition should be

16

attributable to carbon-containing impurities incorporated from alcohol additives in the electrolyte. Chen *et al.* did not observe any carbon-containing impurities in the chemical structure of NAA films produced in 0.2 M phosphoric acid electrolyte modified with 75 wt % polyethylene glycol [39]. However, EDX elemental map analysis shown in **Fig. 7b** indicates that NAA–GIFs produced in 1 M H_2SO_4 modified with 40 v % MetOH have a significant percentage of carbon atoms. Qualitative elemental analysis also suggests that Al, O, and C atoms are homogenously and densely distributed across structure of nanopores, while S atoms are preferentially accumulated within the nanopore walls (**Fig. 7b**). **Fig. 7c** shows quantitative XPS elemental analysis of a set of NAA–GIFs fabricated with varying concentration of methanol additive, from 10 to 70 v % (XPS spectra summarized in **Figs. A.15 and A.16 – Appendix A**). It is apparent from that graph that percentages of Al, O, and C atoms follow an alcohol concentration-dependent pattern, in which the relative percentages of O and Al atoms are inversely correlated with that of C. In contrast, the amount of S atoms remains stable at an average percentage of 1.9 ± 0.2 % S for any *[MetOH]*. Concentration of C atoms is found to initially increase with *[MetOH]*, from 10 to 40 v %, reaching a maximum of 32.9 ± 3.3 at 40 v %, and then decrease with increasing *[MetOH]*, from 40 to 70 v %. This analysis would suggest that, conversely to that of S atoms, the incorporation mechanism of carbon impurities is concentration-dependent, altering – to a greater extent than S atoms – the intrinsic local coordination environment of Al and O in the structure of Al_2O_3 by diffusing within its network during anodization [55]. Comparative chemical analysis between EDX and XPS results reveals an analogous distribution pattern between relative percentages of Al, O, C, and S (**Fig. A.17 – Appendix A**). However, relative percentages of Al, O, and S by EDX are higher than those obtained by XPS, while that of C is found to be higher in XPS than in EDX. XPS is a surface analysis technique with a penetration depth of ~10 nm, while EDX provides a deeper penetration distance of ~1 μm. Therefore, it is possible to infer that C-based impurities are

17

more abundant within the outer nanopore wall and decrease more significantly than S-containing impurities from the outer nanopore wall to the inner cell boundary. Impurities incorporated into NAA from the acid electrolyte during anodization are known to burn during annealing – thermal treatment – in an oxygen-containing environment [56,57]. **Fig. 7d** shows the relative percentage of C in a representative NAA–GIF produced with *[MetOH]* = 40 v % before and after annealing at 800 °C for 1 h under air atmosphere. It is found that the relative percentages of C and S atoms decrease (from 32.9 ± 3.3 % and 1.7 ± 0.2 % to 23.9 ± 2.1 % and 0.6 ± 0.1 % for C and S, respectively), while those of Al and O increase with this annealing (from 17.4 ± 2.0 % and 48.0 ± 2.5 % to 25.0 ± 2.3 % and 50.6 ± 1 % for Al and O, respectively). High-resolution XPS analysis was performed to determine the nature of carbon species incorporated into the structure of NAA during anodization. This analysis indicates that C species are mainly associated with C–H or C–C bonds at ~285.0 eV (~65 %) and C–O bonds at ~286.0 eV (~22 %), which are characteristically associated with organic materials such as alcohols and polymers [58]. Therefore, although further investigations will be needed to establish the incorporation mechanism of C atoms from alcohol-containing electrolytes, these analyses allow us to infer that C atoms are incorporated into NAA–GIFs in the form of impurities, and that their diffusion within the onion-like structure of Al_2O_3 is more effective and deeper than that of S impurities. XPS elemental analysis was further extended to other alcohol additive species. **Fig. 7d** summarizes the relative percentage of C atoms in the best performing NAA–GIFs produced with 40, 30, 40, and 50 v % MetOH, EtOH, IPA, and EGOH, respectively. These NAA–GIFs contained a relative percentage of C atoms of 32.9 ± 3.3, 21.0 ± 2.0, 20.2 ± 2, and 27.3 ± 3.0 %, respectively. MetOH (CH_3OH), EtOH (CH_3CH_2OH), and IPA ($CH_3CHOHCH_3$) are monohydric alcohols with one, two, and three carbon atoms, respectively, while EGOH ($HOCH_2CH_2OH$) is a dihydric alcohol with two carbon atoms in its structure. It is apparent from this elemental analysis that the amount of carbon-containing

18

105

impurities incorporated into the structure of NAA–GIFs from monohydric additive alcohols relies on the number of carbon atoms in their structure, where the lower the number of C atoms the more efficient the incorporation is. These results also indicate that, at a given number of carbon atoms, the incorporation of carbon from a dihydric alcohol such as EGOH is more effective than that of a monohydric alcohol with two carbons such as EtOH. Interestingly, the amount of carbon content also correlates with Q_{PSB} of these NAA–GIFs following the order MetOH > EGOH > EtOH > IPA.

3.6. Effect of Alcohol Additive Type and Concentration on the Effective and Intrinsic Optical Properties of NAA–GIFs.

The effective and intrinsic refractive indexes of NAA (n_{eff} and n_{int}) – critical factors in determining its optical properties – rely intrinsically on anodizing current density/voltage and acid electrolyte composition. For example, Fan *et al.* reported an n_{eff} of ~1.66 RIU for NAA films produced in 0.3 M oxalic electrolyte at 40 V, while Law *et al.* estimated the effective refractive index of NAA films produced in 1 M H_2SO_4 modified with 25 v % EtOH to be ~2.3 and ~1.8 RIU at $J = 1.120$ and 0.280 mA cm^{-2}, respectively [59,19]. **Fig. 8a** shows the dependence of n_{eff} in representative NAA thin films produced with varying concentration of *[MetOH]*, from 10 to 70 v % with $\Delta[MetOH] = 10$ v %, at $J_{max} = 1.120$ mA cm^{-2} and $J_{min} = 0.280$ mA cm^{-2}. This graph demonstrates that n_{eff} increases with *[MetOH]* for both J_{max} and J_{min}, where $n_{eff\text{-}Jmax}$ is higher than $n_{eff\text{-}Jmin}$ at any *[MetOH]*, following a logarithmic trend of $n_{eff\text{-}Jmax} = 0.4 \times \ln([MetOH] + 52.4)$ and $n_{eff\text{-}Jmin} = 0.4 \times \ln([MetOH] + 46.1)$. Comparative analysis between effective refractive index contrast, defined as $\Delta n_{eff} = n_{eff\text{-}Jmax} - n_{eff\text{-}Jmin}$, and Q_{PSB} in NAA–GIFs produced with varying concentration of methanol additive reveals an interesting correlation, in which this optical parameter is maximum at higher Δn_{eff} (i.e. 0.18 ± 0.03 RIU at 40 v %, **Fig. 8b**). Higher refractive index contrast within NAA stacks forming the structure of NAA–GIFs maximizes the efficiency of light-forbidding properties of these PC structures, which would in part explain why NAA–GIFs produced in *[MetOH]* = 40

19

v % achieve the highest Q_{PSB} value [46]. Further analysis was performed to determine the intrinsic optical properties of NAA–GIFs. **Fig. 8c** shows that the porosity (P) – measured by FEG-SEM image analysis – of the NAA films used in **Fig. 8a**, decreases linearly with increasing concentration of MetOH additive and input current density (representative top view FEG-SEM images of NAA films shown in **Fig. A.18 – Appendix A**). Optically, NAA–GIFs are a 1D composite material consisting of air-filled nanopores featuring a sinusoidally modified porosity in depth. Therefore, the effective refractive index of NAA–GIFs can be described by effective medium approximation (EMA) models, by which the macroscopic properties composite materials are estimated by averaging the properties of their individual constituents – air and alumina [60]. Of all EMA models, the Looyenga–Landau–Lifshitz (LLL) has been demonstrated to be a suitable approximation to estimate the effective refractive index of NAA–GIFs [46] according to **Eq. 11**:

$$n_{eff}^{2/3} = f_{Al_2O_3} \times n_{int}^{2/3} + f_{air} \times n_{air}^{2/3} \tag{11}$$

where f_{Al2O3} and f_{air} are the volume fractions of alumina and air estimated by FEG-SEM image analysis, respectively.

Analysis of the intrinsic refractive index of alumina (n_{int}) obtained from the adapted LLL–EMA model shown in **Eq. 11** indicates that this optical parameter increases with increasing *[MetOH]*, for both J_{max} and J_{min} (**Fig. 8d**). It is apparent that $n_{int–Jmax}$ is higher than $n_{int–Jmin}$ at any *[MetOH]*, where the latter increases from 2.07 ± 0.02 RIU at 10 v % to 2.15 ± 0.03 RIU at 70 v % and the former from 1.77 ± 0.01 RIU at 10 v % to 1.95 ± 0.02 RIU at 70 v %. It is also found that dependence of $n_{int–Jmin}$ with *[MetOH]* is stronger than that of $n_{int–Jmax}$, with logarithmic trends of $n_{int-Jmin} = 0.4 \times \ln([MetOH] + 92.2)$ and $n_{int-Jmax} = 0.4 \times \ln([MetOH] + 236.6)$. Surprisingly, these results suggest that, in contrast to S-based impurities [61], carbon impurities incorporated from alcohol additives in the acid electrolyte increase the intrinsic refractive index of NAA. To summarize, fundamental analysis of the chemical structure of NAA–GIFs produced in 1 M

20

H₂SO₄ modified with 10–70 v % mono and dihydric alcohols indicates that the incorporation of carbon-containing impurities plays a significant role in determining the optical properties of these NAA-based PC structures. To our knowledge, this is the first demonstration of incorporated carbon-containing impurities into the structure of NAA. However, further in-depth investigations will be needed to establish a comprehensive chemical–electrochemical mechanistic model for this impurity-incorporation process.

4. Conclusions

This study provides novel insights into the fabrication of high-quality nanoporous anodic alumina gradient-index filters by sinusoidal pulse anodization in alcohol-containing sulfuric acid electrolyte. Systematic modification of type and concentration of alcohol additive (i.e. four mono and dihydric alcohols, with concentrations ranging from 10 to 70 v %) have allowed us to determine the most optimal conditions to enhance the light-forbidding properties of NAA–GIFs. Comprehensive electrochemical, structural, optical, and chemical analyses have elucidated the interplay of these parameters in determining the quality of forbidden light propagation in NAA–GIFs, using their quality factor as a reference figure of merit to identify quality enhancements. Our results indicate that sulfuric acid electrolyte modified with 40 v % methanol is the most optimal condition to fabricate NAA–GIFs with well-resolved, intense, narrow photonic stopbands – 48–84 % narrower and 19–29 % more intense than that of other alcohol additives. Elemental chemical analysis of NAA–GIFs has revealed incorporation of carbon-containing impurities from alcohol-modified electrolytes into the structure of NAA–GIFs. However, a comprehensive mechanistic impurity-incorporation model will require further investigations. Interplay analysis between electrochemical, structural, optical, and chemical composition parameters suggests that moderate nanopore branching and suppressing-dissolution efficiencies along with incorporation of carbon-containing impurities and enhanced

21

effective refractive index contrast between NAA stacks maximize the quality of forbidden light propagation in NAA–GIFs.

Our results provide a better understanding of the impact of alcohol additives on the physical and chemical properties of NAA-based photonic crystals engineered by pulse-like anodization under mild conditions, generating new exciting opportunities to further spread the applicability of this technology across disciplines such as high-power photonics, optical sensing, photocatalysis and optoelectronics.

Appendix A

Supporting information including anodization profiles, summary of main electrochemical parameters, FEG-SEM images showing nanopore evolution, transmission spectra of NAA–GIFs, and XPS spectra, and tables summarizing fittings for main electrochemical parameters and geometric features with concentration and type of alcohol additives.

References

[1] W. Lee, J.S. Park, Porous anodic aluminum oxide: anodization and templated synthesis of functional nanostructures, Chem. Rev. 114 (2014) 7487. https://doi.org/10.1021/cr500002z

22

[2] G.D. Sulka, Highly ordered anodic porous alumina formation by self-organized anodizing, in: A. Eftekhari (Ed.), Nanostructured Materials in Electrochemistry, Vol. 1, Ch. 1, Wiley-VCH Verlag Gmbh&Co. KGaA, Weinheim, 2008, p. 1.

[3] D. Losic, A. Santos (Eds.), Nanoporous Alumina: Fabrication, Structure, Properties and Applications, Springer International Publishing, Swetzerland, 2015.

[4] A. Santos, T. Kumeria, D. Losic, Nanoporous anodic alumina: a versatile platform for optical biosensors, Materials 7 (2014) 4297. https://doi:10.3390/ma7064297

[5] H. Masuda, K. Fukuda, Ordered metal nanohole arrays made by a two-step replication of honeycomb structures of anodic alumina, Science 268 (1995) 1466. https://doi.org/110.1126/science.268.5216.1466

[6] A.P. Li, F. Müller, A. Birner, K. Nielsch, U. Gösele, Hexagonal pore arrays with a 50–420 nm interpore distance formed by self-organization in anodic alumina, J. Appl. Phys. 84 (1998) 6023. https://doi.org/10.1063/1.368911

[7] W. Cheng, M. Steinhart, U. Gösele. R.B. Wehrspohn, Tree-like alumina nanopores generated in a non-steady-state anodization, J. Mater. Chem. 17 (2007) 3493. https://doi.org/10.1039/B709618F

[8] R.C. Furneaux, W.R. Rigby, A.P. Davidson, The formation of controlled-porosity membranes from anodically oxidized aluminium, Nature 337 (1989) 47. https://doi.org/10.1038/337147a0

[11] A. Santos, Nanoporous anodic alumina photonic crystals: fundamentals, developments and perspectives, J. Mater. Chem. C 5 (2017) 5581. https://doi.org/10.1039/C6TC05555A

[12] C.S. Law, S.Y. Lim, A.D. Abell, N.H. Voelcker, A. Santos, A. Nanoporous anodic alumina photonic crystals for optical chemo- and biosensing: fundamentals, advances, and perspectives, Nanomaterials 8 (2018) 788. https://doi.org/10.3390/nano8100788

23

[13] A. Santos, C.S. Law, D.W.C. Lei, T. Pereira, D. Losic, Fine tuning of optical signals in nanoporous anodic alumina photonic crystals by apodized sinusoidal pulse anodisation, Nanoscale 8 (2016) 18360. https://doi.org/10.1039/C6NR06796D

[14] G.L. Shang, G.T. Fei, Y. Zhang, P. Yan, S.H. Xu, L.D. Zhang, Preparation of narrow photonic bandgaps located in the near infrared region and their applications in ethanol gas sensing , J. Mater. Chem. C 1 (2013) 5285. https://doi.org/10.1039/C3TC30782D

[15] G. Shang, G. Fei, Y. Li, L. Zhang, Influence of dielectrics with light absorption on the photonic bandgap of porous alumina photonic crystals, Nano Res. 9 (2016) 703. https://doi.org/10.1007/s12274-015-0949-x

[16] S.E. Kushnir, T.Y. Pchelyakova, K.S. Napolskii, Anodizing with voltage versus optical path length modulation: a new tool for the preparation of photonic structures, J. Mater Chem. C 6 (2018) 12192. https://doi.org/10.1039/C8TC04246B

[17] L.K. Acosta, F. Bertó-Roselló, E. Xifre-Perez, A. Santos, J. Ferré-Borrull, L.F. Marsal, Stacked nanoporous anodic alumina gradient-index filters with tunable multispectral photonic stopbands as sensing platforms, ACS Appl. Mater. Interfaces 11 (2018) 3360. https://doi.org/10.1021/acsami.8b19411

[18] P. Yan, G.T. Fei, G.L. Shang, B. Wu, L.D. Zhang, Fabrication of one-dimensional alumina photonic crystals with a narrow band gap and their application to high-sensitivity sensors, J. Mater. Chem. C 1 (2013) 1659. https://doi.org/10.1039/C2TC00396A

[19] C.S. Law, S.Y. Lim, L. Liu, A.D. Abell, L.F. Marsal, A. Santos, Realization of high-quality optical nanoporous gradient-index filters by optimal combination of anodization conditions, Nanoscale 12 (2020) 9404. https://doi.org/10.1039/C9NR10526C

[20] C.S. Law, S.Y. Lim, R.M. Macalincag, A.D. Abell, A. Santos, Light-confining nanoporous anodic alumina microcavities by apodized stepwise pulse anodization, ACS Appl. Nano Mater. 1 (2018) 4418. https://doi.org/10.1021/acsanm.8b00494

[21] C.S. Law, S.Y. Lim, A.D. Abell, L.F. Marsal, A. Santos, Structural tailoring of nanoporous anodic alumina optical microcavities for enhanced resonant recirculation of light, Nanoscale 10 (2018) 14139. https://doi.org/10.1039/C8NR04263B

[22] L. Liu, S.Y. Lim, C.S. Law, B. Jin, A.D. Abell, G. Ni, A. Santos, Light-confining semiconductor nanoporous anodic alumina optical microcavities for photocatalysis, J. Mater. Chem. A 7 (2019) 22514. https://doi.org/10.1039/C9TA08585H

[23] C.S. Law, G.M. Sylvia, M. Nemati, J. Yu, D. Losic, A.D. Abell, A. Santos, Engineering of Surface Chemistry for Enhanced Sensitivity in Nanoporous Interferometric Sensing Platforms, ACS Appl. Mater. Interfaces 9 (2017) 8929. https://doi.org/10.1021/acsami.7b01116

[24] C.S. Law, S.Y. Lim, A.D. Abell, A. Santos, Real-time binding monitoring between human blood proteins and heavy metal ions in nanoporous anodic alumina photonic crystals, Anal. Chem. 90 (2018) 10039. https://doi.org/10.1021/acs.analchem.8b02732

[25] C. Eckstein, C.S. Law, S.Y. Lim, S. Kaur, T. Kumeria, J. Ferré-Borrull, A.D. Abell, L.F. Marsal, A. Santos, Nanoporous photonic crystals with tailored surface chemistry for ionic copper sensing, J. Mater. Chem. C 7 (2019) 12278. https://doi.org/10.1039/c9tc04438h

[26] S.Y. Lim, C.S. Law, M. Markovic, L.F. Marsal, N.H. Voelcker, A.D. Abell, A. Santos, Rational management of photons for enhanced photocatalysis in structurally-colored nanoporous anodic alumina photonic crystals, ACS Appl. Energy Mater. 2 (2019) 1169. https://doi.org/10.1021/acsaem.8b01721

[27] C.S. Law, S.Y. Lim, A. Santos, On the precise tuning of optical filtering features in nanoporous anodic alumina distributed Bragg reflectors, Sci. Rep. 1 (2018) 4642. https://doi.org/10.1038/s41598-018-22895-5

25

[28] J. Ferré-Borrull, M.M. Rahman, J. Pallarès, L.F. Marsal, Tuning nanoporous anodic alumina distributed-Bragg reflectors with the number of anodization cycles and the anodization temperature, Nanoscale Res. Lett. 9 (2014) 416. https://doi.org/10.1186/1556-276X-9-416

[29] Sukarno, C.S. Law, A. Santos, Realisation and optical engineering of linear variable bandpass filters in nanoporous anodic alumina photonic crystals, Nanoscale 8 (2017) 7451. https://doi.org/10.1039/C7NR02115A

[30] A. Santos, T. Pereira, C.S. Law, D. Losic, Rational engineering of nanoporous anodic alumina optical bandpass filters, Nanoscale 8 (2016) 14846. https://doi.org/10.1039/C6NR03490J

[31] S.Y. Lim, C. S. Law, L.F. Marsal, A. Santos, Engineering of hybrid nanoporous anodic alumina photonic crystals by heterogeneous pulse anodization, Sci. Rep. 8 (2018) 9455. https://doi.org/10.1038/s41598-018-27775-6

[32] A. Santos, C.S. Law, T. Pereira, D. Losic, Nanoporous hard data: optical encoding of information within nanoporous anodic alumina photonic crystals, Nanoscale 8 (2016) 8091. https://doi.org/10.1039/C6NR01068G

[33] E. Lorenzo, C. J. Oton, N.E. Capuj, M. Ghulinyan, D. Navarro-Urrios, Z. Gaburro, L. Pavesi, Porous silicon-based rugate filters, Appl. Opt. 44 (2005) 5415. https://doi.org/10.1364/AO.44.005415

[34] A.C. van Popta, M.M. Hawkeye, J.C. Sit, M.J. Brett, Gradient-index narrow-bandpass filter fabricated with glancing-angle deposition, Opt. Lett. 29 (2004) 2545. https://doi.org/10.1364/OL.29.002545

[35] Y. Shang, X. Wang, E. Xu, C. Tong, J. Wu, Optical ammonia gas sensor based on a porous silicon rugate filter coated with polymer-supported dye, Anal. Chim. Acta 685 (2011) 58. https://doi.org/10.1016/j.aca.2010.11.008

[36] S. Li, D. Hu, J. Huang, L. Cai, Optical sensing nanostructures for porous silicon rugate filters, Nanoscale Res. Lett. 7 (2012) 79. https://doi.org/10.1186/1556-276X-7-79

[37] M. Nemati, A. Santos, C.S. Law, D. Losic, Assessment of binding affinity between drugs and human serum albumin using nanoporous anodic alumina photonic crystals, Anal. Chem., 88 (2016) 5971. https://doi.org/10.1021/acs.analchem.6b00993

[38] Y. Li, M. Zheng, L. Ma, W. Shen, Fabrication of highly ordered nanoporous alumina films by stable high-field anodization, Nanotechnol. 17 (2006) 5101. https://doi.org/10.1088/0957-4484/17/20/010

[39] W. Chen, J.-S. Wu, X.-H. Xia, Porous anodic alumina with continuously manipulated pore/cell size, ACS Nano 2 (2008) 959. https://doi.org/10.1021/nn700389j

[40] L. Zaraska, G.D. Sulka, M. Jaskuła, The effect of n-alcohols on porous anodic alumina formed by self-organized two-step anodizing of aluminum in phosphoric acid, Surf. Coat. Technol. 204 (2010) 1729. https://doi.org/10.1016/j.surfcoat.2009.10.051

[41] J. Martin, C.V. Manzano, O. Caballero-Calero, M. Martin-González, High-aspect-ratio and highly ordered 15-nm porous alumina templates, ACS Appl. Mater. Interfaces 5 (2013) 72. https://doi.org/10.1021/am3020718

[42] M. Norek, M. Dopierała, W.J. Stępniowski, Ethanol influence on arrangement and geometrical parameters of aluminum concaves prepared in a modified hard anodization for fabrication of highly ordered nanoporous alumina, J. Electroanal. Chem. 750 (2015) 79. https://doi.org/10.1016/j.jelechem.2015.05.024

[43] M. Norek, W.J. Stępniowski, D. Siemiaszko, Effect of ethylene glycol on morphology of anodic alumina prepared in hard anodization, J. Electroanal. Chem. 762 (2016) 20. https://doi.org/10.1016/j.jelechem.2015.12.026

27

[44] H. Asoh, M. Matsumoto, H. Hashimoto, Effects of ethanol on the efficiency of the formation of anodic alumina in sulfuric acid, Surf. Coat. Technol. 378 (2019) 124947. https://doi.org/10.1016/j.surfcoat.2019.124947

[45] M. Matsumoto, H. Hashimoto, H. Asoh, Formation efficiency of anodic porous alumina in sulfuric acid containing alcohol: comparison of the effects of monohydric and polyhydric alcohols as additives. J. Electrochem. Soc. 67 (2020) 041504. https://doi.org/10.1149/1945-7111/ab741c

[46] A. Santos, J.H. Yoo, C.V. Rohatgi, T. Kumeria, Y. Wang, D. Losic, Realisation and advanced engineering of true optical rugate filters based on nanoporous anodic alumina by sinusoidal pulse anodisation, Nanoscale 8 (2016) 1360. https://doi.org/10.1039/C5NR05462A

[47] M.D. Abràmoff, P.J. Magalhaes, S. J. Ram, Image processing with ImageJ, Biophotonics Int. 11 (2004) 36.

[48] Y. Wang, A. Santos, A. Evdokiou, D. Losic, Rational design of ultra-short anodic alumina nanotubes by short-time pulse anodization, Electrochim. Acta 154 (2015) 379. https://doi.org/10.1016/j.electacta.2014.12.056

[49] M. Noormohammadi, Z.S. Arani, A. Ramazani, M.A. Kashi, S. Abbasimofrad, Super-fast fabrication of self-ordered nanoporous anodic alumina membranes by ultra-hard anodization, Electrochim. Acta (2020) 136766. https://doi.org/10.1016/j.electacta.2020.136766

[50] C.S. Law, A. Santos, M. Nemati, D. Losic, Rational engineering of nanoporous anodic alumina photonic crystals by sawtooth-like pulse anodization, ACS Appl. Mater. Interfaces 8 (2016) 13542. https://doi.org/10.1021/acsami.6b03900

[51] Y. Yamamoto, N. Baba, S. Tajima, Coloured materials and photoluminescence centres in anodic film on aluminium, Science 289 (1981) 572. https://doi.org/10.1038/289572a0

[52] H. Han, S.J. Park, J.S. Jang, H. Ryu, K.J. Kim, S. Baik, W. Lee, In situ determination of the pore opening point during wet-chemical etching of the barrier layer of porous anodic

28

aluminum oxide: nonuniform impurity distribution in anodic oxide, ACS Appl. Mater. Interfaces 5 (2013) 3441. https://doi.org/10.1021/am400520d

[53] J. Choi, Y. Luo, R.B. Wehrspohn, R. Hillebrand, J. Schilling, U. Gösele, Perfect two-dimensional porous alumina photonic crystals with duplex oxide layers, J. Appl. Phys. 94 (2003) 4757. https://doi.org/10.1063/1.1609033

[54] L. Yi, L. Zhiyuan, H. Xing, L. Yisen, C. Yi, Investigation of intrinsic mechanisms of aluminium anodization processes by analyzing the current density, RSC Adv. 2 (2012) 5164. https://doi.org/10.1039/C2RA01050J

[55] I. Farnan, R. Dupree, A.J. Forty, Y. S. Jeong, G. Thompson, G.C. Wood, Structural information about amorphous anodic alumina from ^{27}Al MAS NMR, Philos. Mag. Lett. 59 (1989) 189. https://doi.org/10.1080/09500838908206342

[56] X.L. Xu, M.J. Zheng, S. Wu, W.Z. Shen, Effects of high-temperature annealing on structural and optical properties of highly ordered porous alumina membranes, Appl. Phys. Lett. 85 (2004) 4364. https://doi.org/10.1063/1.1815072

[57] G.S. Huang, X.L. Wu, G.G. Siu, P.K. Chu, On the origin of light emission from porous anodic alumina formed in sulfuric acid, Solid State Commun. 137 (2006) 621. https://doi.org/10.1016/j.ssc.2006.01.005

[58] M.M. Chechimi, M.L. Abel, J.F. Watts, R.P. Digby, Surface chemical and thermodynamic properties of γ-glycidoxy-propyltrimethoxysilane-treated alumina: an XPS and IGC study, J. Mater. Chem. 11 (2001) 533.

[59] D.H. Fan, G.Q. Ding, W.Z. Shen, M.J. Zheng, Anion impurities in porous alumina membranes: existence and functionality, Microporous Mesoporous Mater. 100 (2007) 154. https://doi.org/10.1016/j.micromeso.2006.10.025

29

[60] W. Theiβ, S. Henkel, M. Arntzen, Connecting microscopic and macroscopic properties of porous media: choosing appropriate effective medium concepts, Thin Solid Films 255 (1995) 177. https://doi.org/10.1016/0040-6090(94)05649-X

[61] I. Míguez–Bacho, S. Rodríguez–López, A. Climent–Font, D. Fichou, M. Vázquez, M. Hernández–Vélez, Variation of the refractive index by means of sulfate anion incorporation into nanoporous anodic aluminum oxide films, Microporous Mesoporous Mater. 225 (2016) 192–197. https://doi.org/10.1016/j.micromeso.2015.12.011

1
2
3
4
5
6
7
8
9
10
11
12
13
14
15
16
17
18
19
20
21
22
23
24
25
26
27
28
29
30
31
32
33
34
35
36
37
38
39
40
41
42
43
44
45
46
47
48
49
50
51
52
53
54
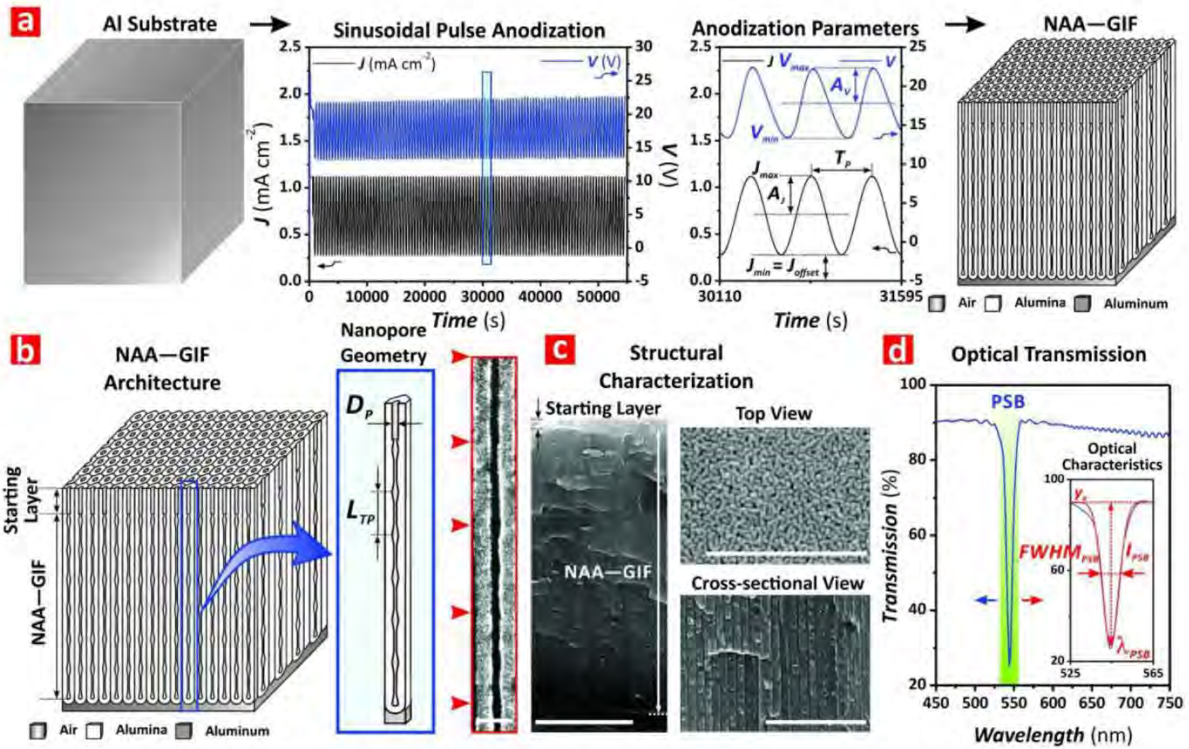55
56
57
58
59
60
61
62
63
64
65

30

FIGURES

Fig. 1 Fabrication, architecture, and optical features of nanoporous anodic alumina gradient-index filters (NAA–GIFs) produced by sinusoidal pulse anodization (SPA) in sulfuric acid electrolyte modified with alcohol additives. (a) Schematic of NAA–GIFs fabrication by SPA, with aluminum substrate (left), representative SPA profile under current density control conditions (center–left), including a graphical definition of the anodization and electrochemical parameters (magnified view of blue rectangle: anodization period – T_P, current density amplitude – A_J, current density offset – J_{offset}, current density minimum or offset – $J_{min} = J_{offset}$, current density maximum – J_{max}, voltage amplitude – A_V, minimum voltage – V_{min}, and maximum voltage – V_{max}) (center–right), and idealized structure of NAA–GIFs featuring sinusoidally modulated nanopores (right). (b) Illustration showing details of the structure of NAA–GIFs with a graphical definition of the main geometric features, including nanopore diameter – D_P and period length – L_{TP}. (c) Representative top and cross-sectional view FEG-SEM images of a NAA–GIF: nanopore magnified view with red arrowheads denoting nanopore modulations (scale bar = 100 nm; left) and full view (scale bar = 5 μm; left), top view (scale bar = 300 nm; right–top), and magnified cross-sectional view (scale bar = 500 nm; right–bottom) (NB: NAA–GIF fabricated at A_J = 0.420 mA cm^{-2}, $J_{offset} = J_{min}$ = 0.280 mA cm^{-2}, J_{max} = 1.120 mA cm^{-2}, and T_P = 494 s in 1 M H$_2$SO$_4$ electrolyte containing 70 v % ethylene glycol (EGOH) at –2 °C for 20 h). (d) Representative optical transmission spectrum of a NAA–GIF showing details of its photonic stopband (PSB): full view of PSB with arrows denoting blue- and red-shift directions in the position of characteristic PSB, respectively, and magnified view of PSB with graphical description of optical characteristics of PSB (inset) including position of central wavelength – λ_{PSB}, full width at half maximum – $FWHM_{PSB}$, intensity – I_{PSB}, and baseline – y_0 (NB: NAA–GIF fabricated at A_J = 0.420 mA cm^{-2}, $J_{offset} = J_{min}$ = 0.280 mA cm^{-2}, J_{max} = 1.120 mA cm^{-2} and T_P = 494 s in 1 M H$_2$SO$_4$ electrolyte containing 40 v % MetOH at –2 °C for 20 h).

31
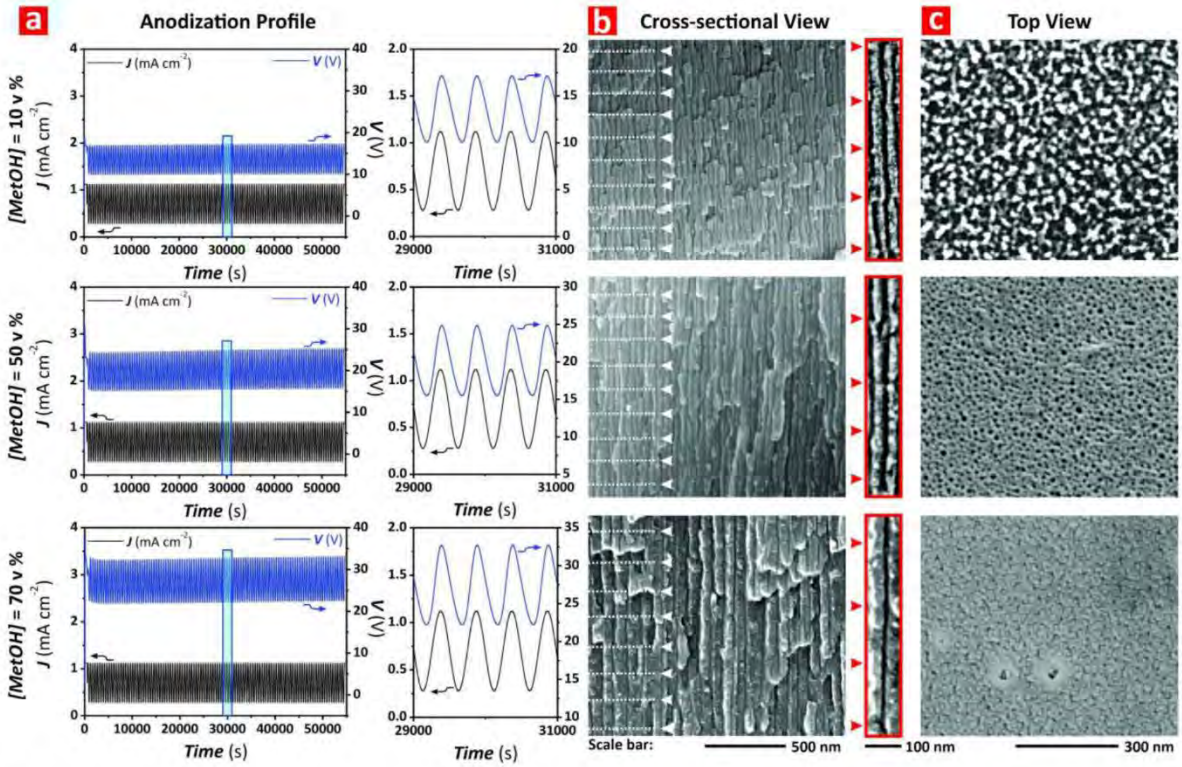
Fig. 2 Electrochemical and structural engineering of NAA–GIFs by SPA in acid electrolytes modified with alcohol additives. (a) Representative full-view sinusoidal pulse anodization profiles (left) and magnified views of blue rectangles (right) showing details of precise translation of sinusoidal input current density into sinusoidal output voltage pulses for NAA–GIFs fabricated in 1 M H_2SO_4 electrolyte modified with *[MetOH]* = 10, 50, and 70 v % . (b) Full (left) and magnified cross-sectional (right), and (c) top view FEG-SEM images showing details of the nanoporous structure of NAA–GIFs produced by the anodization profiles shown in (a) (NB: white and red arrowheads and white dotted lines denote interfaces between anodization periods or period length – L_{TP}).
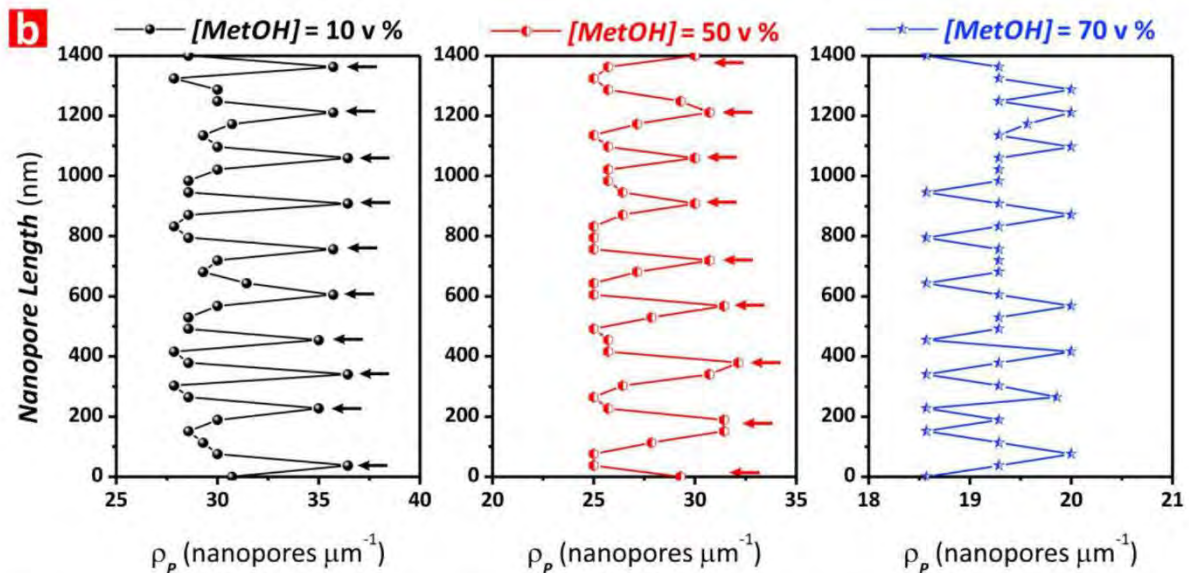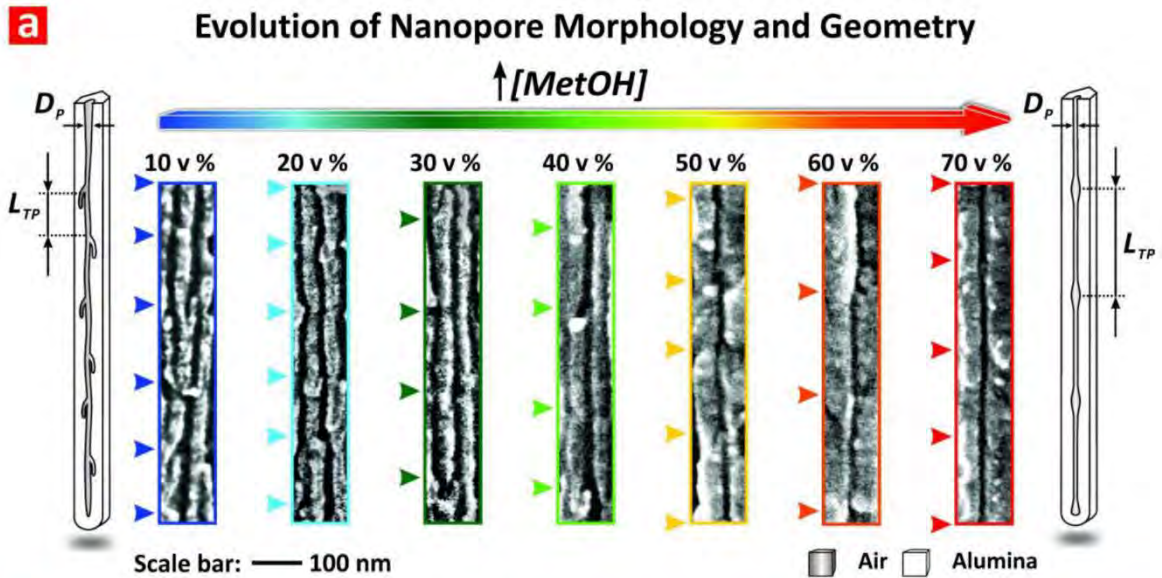
Fig. 3 Evolution of nanopore morphology in NAA–GIFs produced by SPA in acid electrolytes modified with alcohol additives. (a) Representative high-resolution cross-sectional view FEG-SEM images showing details of nanopore morphology with *[MetOH]*, from 10 to 70 v %, and schematics showing the idealized nanopore morphology at low (left) and high (right) concentration of alcohol additive in the acid electrolyte (NB: color arrowheads indicate interfaces between stacks of NAA with modulated porosity defined as period length – L_{TP}). (b) Nanopore density per unit length of cross-section (ρ_P) along the length of nanopores in the cross-sectional FEG-SEM images shown in **Fig. 2b** for NAA–GIFs produced with *[MetOH]* = 10, 50, and 70 v % (NB: black and red arrows denote areas with ρ_P maxima, which correspond to interfaces between structural periods).

33
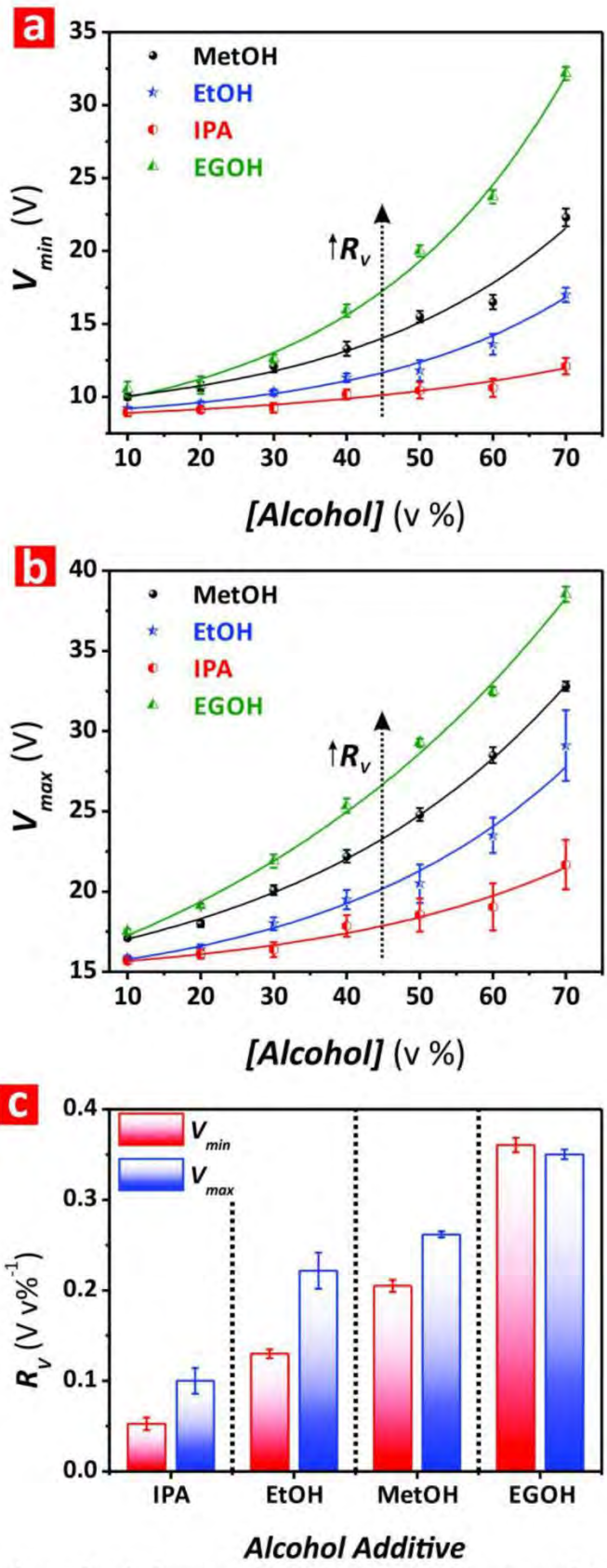
Fig. 4 Analysis of main electrochemical parameters (V_{min}, V_{max}, and R_V) measured from the anodization profiles used to fabricate NAA–GIFs by SPA at varying concentration of alcohol additives, from 10 to 70 v % with an increment of 10 v %. (a) Dependence of V_{min} with *[Alcohol]* for MetOH, EtOH, IPA, and EGOH additives. (b) Dependence of V_{max} with *[Alcohol]* for MetOH, EtOH, IPA, and EGOH additives. (c) Bar chart summarizing the values of R_V for V_{min} and V_{max} for MetOH, EtOH, IPA, and EGOH additives.
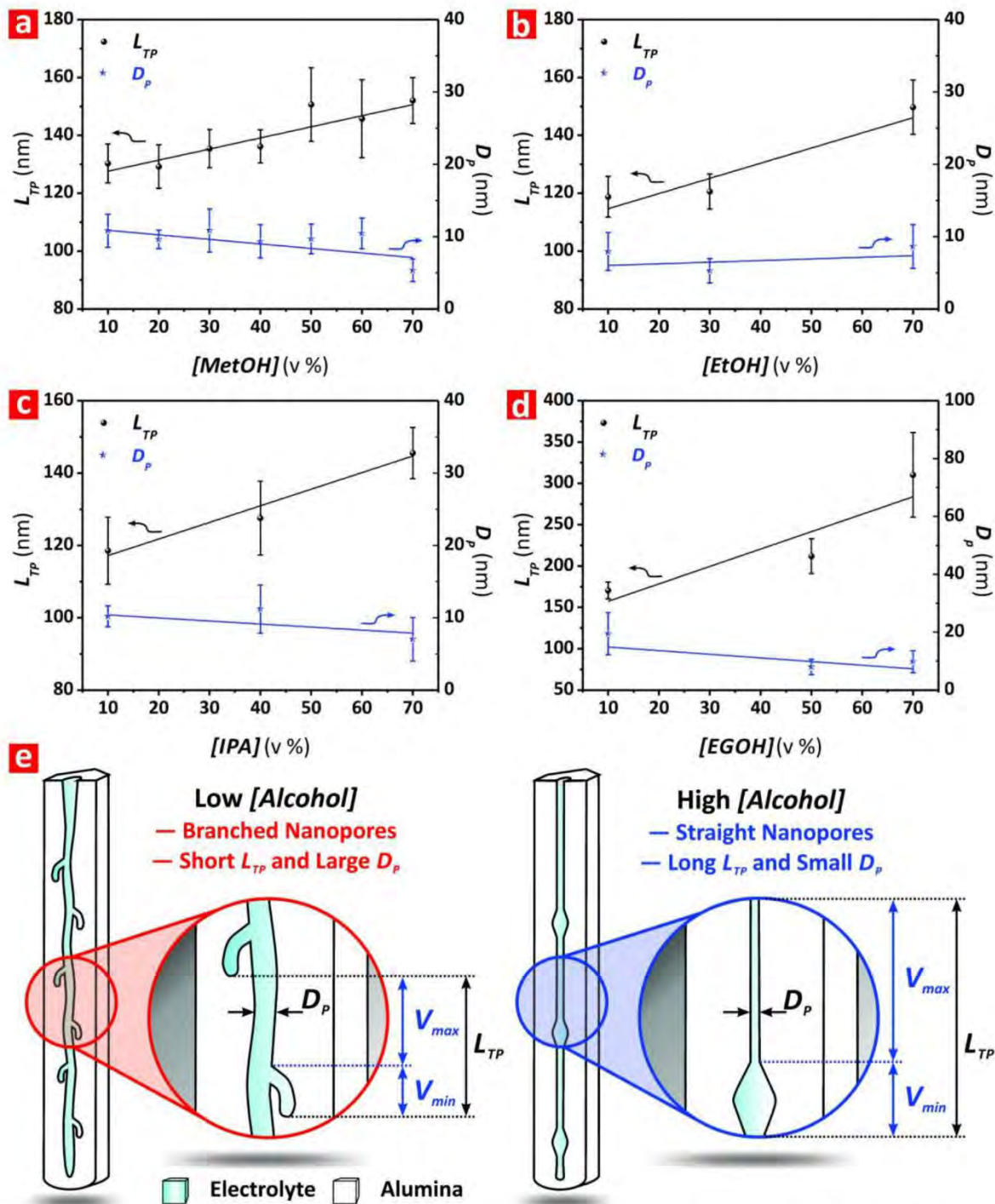
Fig. 5 Dependence of geometric features (period length – L_{TP} and nanopore diameter – D_P) and morphology of nanopores on type and concentration of alcohol additive, from 10 to 70 v %, in NAA–GIFs produced by SPA in 1 M H_2SO_4 modified with: (a) MetOH, (b) EtOH, (c) IPA, and (d) EGOH, and (e) schematic of idealized geometric and morphological transition of nanopores in NAA–GIFs with increasing concentration of alcohol additive and varying electrochemical sinusoidal output voltage (V_{min} and V_{max}).

35
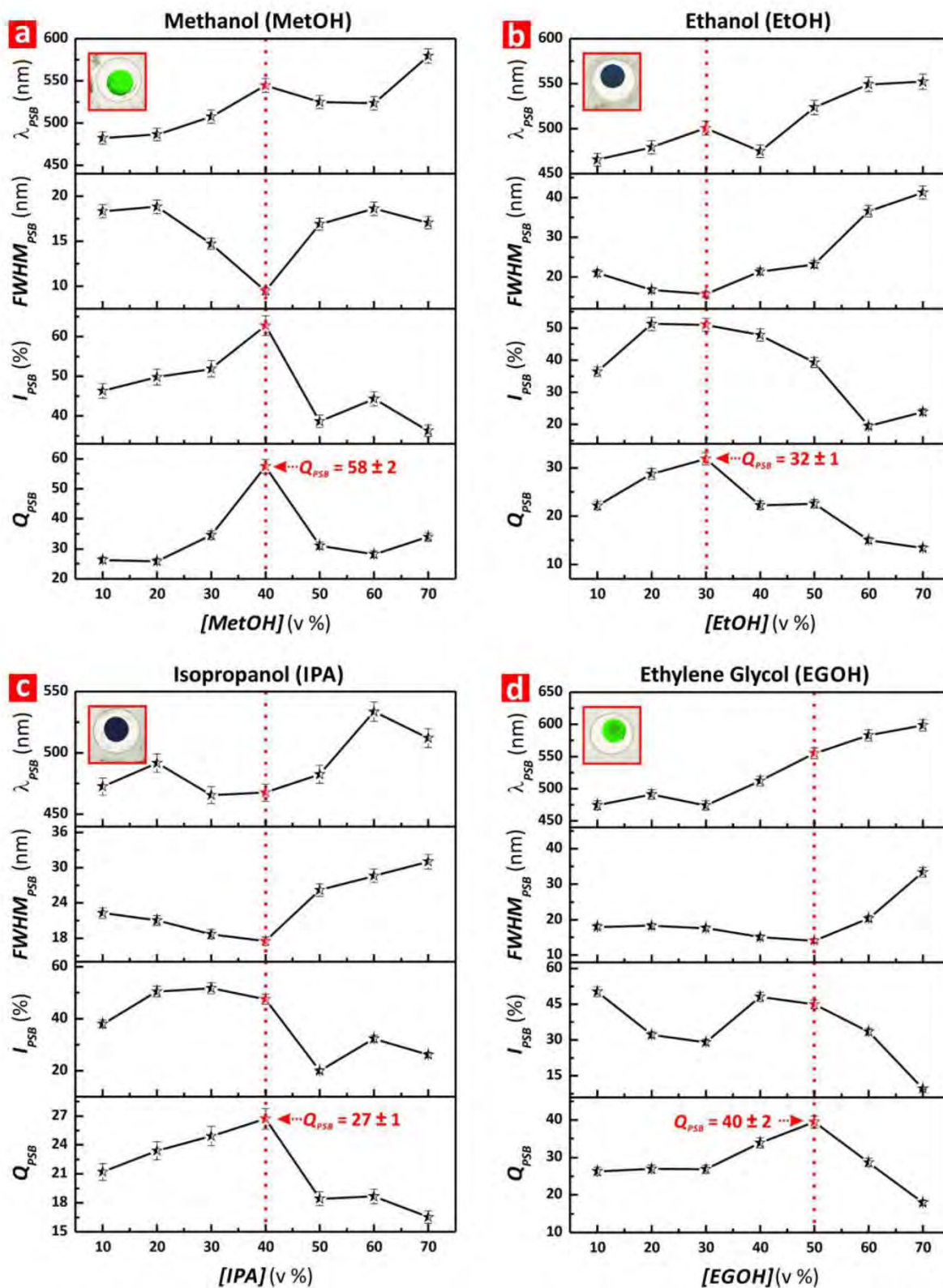
Fig. 6 Effect of alcohol additive type and concentration on the optical features of the PSB (position of central wavelength – λ_{PSB}, full width at half maximum – $FWHM_{PSB}$, intensity – I_{PSB}, and quality factor – Q_{PSB}) of NAA–GIFs produced by SPA in 1 M H_2SO_4 electrolyte (NB: red dotted vertical lines denote the optimal concentration for each type of alcohol that provides the maximum quality factor of the PSB, and insets show digital pictures of these NAA–GIFs): (a) MetOH, (b) EtOH, (c) IPA, and (d) EGOH.
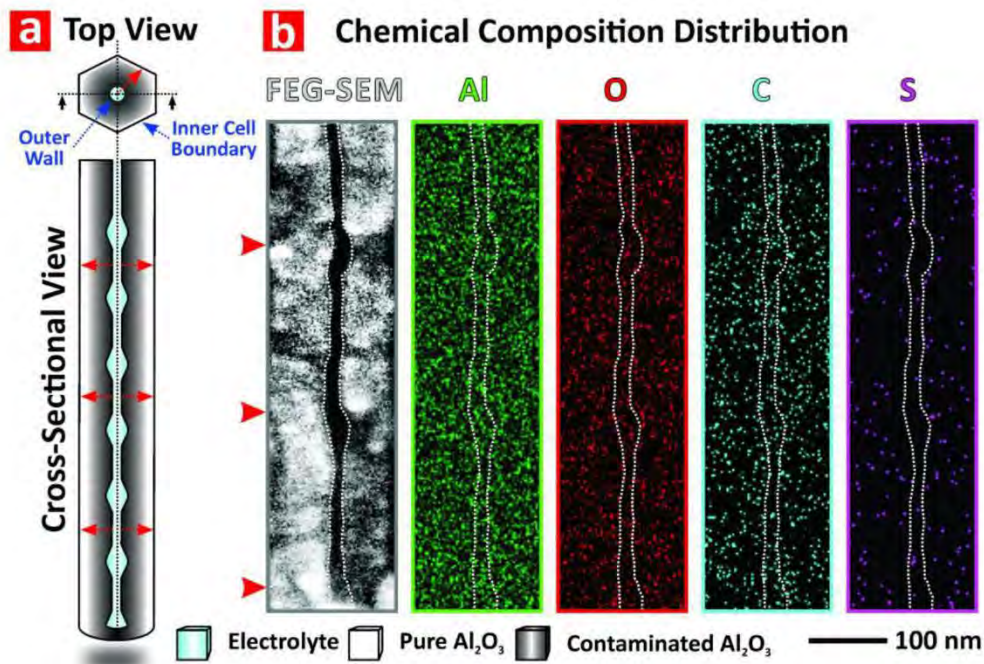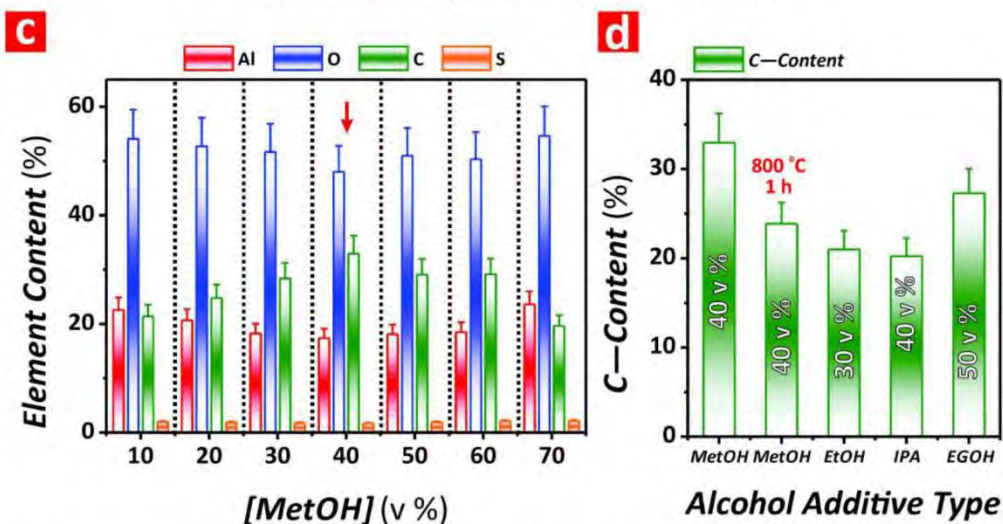
Fig. 7 Chemical composition analysis of NAA–GIFs fabricated by SPA in 1 M H_2SO_4 modified with alcohol additives. (a) Top and cross-sectional schematics of the nanopore structure of NAA–GIFs showing a concentric distribution of impurities with decreasing concentration from the outer nanopore wall (i.e. surface exposed to acid electrolyte) to the inner cell boundary (i.e. pure alumina – Al_2O_3) (NB: red arrows denote the direction at which the concentration of impurities decreases). (b) EDX elemental composition distribution of a representative NAA–GIF produced by SPA in 1 M H_2SO_4 modified with 40 v % methanol with (from left to right): magnified cross-sectional FEG-SEM image with red arrowheads denoting nanopore modulations, and distribution of aluminum – Al, oxygen – O, carbon – C, and sulfur – S (NB: white dotted lines represent nanopore boundaries from FEG-SEM image). (c) XPS elemental composition quantification of NAA–GIFs with *[MetOH]*, from 10 to 70 v % with *Δ[MetOH]* = 10 v %, and relative percentages of Al, O, C, and S (red arrow denotes the best performing NAA–GIFs in terms of Q_{PSB}). (d) C–content percentages of the best performing NAA–GIFs produced in MetOH (40 % v at room temperature and at 800 ºC for 1 h), EtOH (30 % v), IPA (40 % v), and EGOH (50 % v) (right).

37
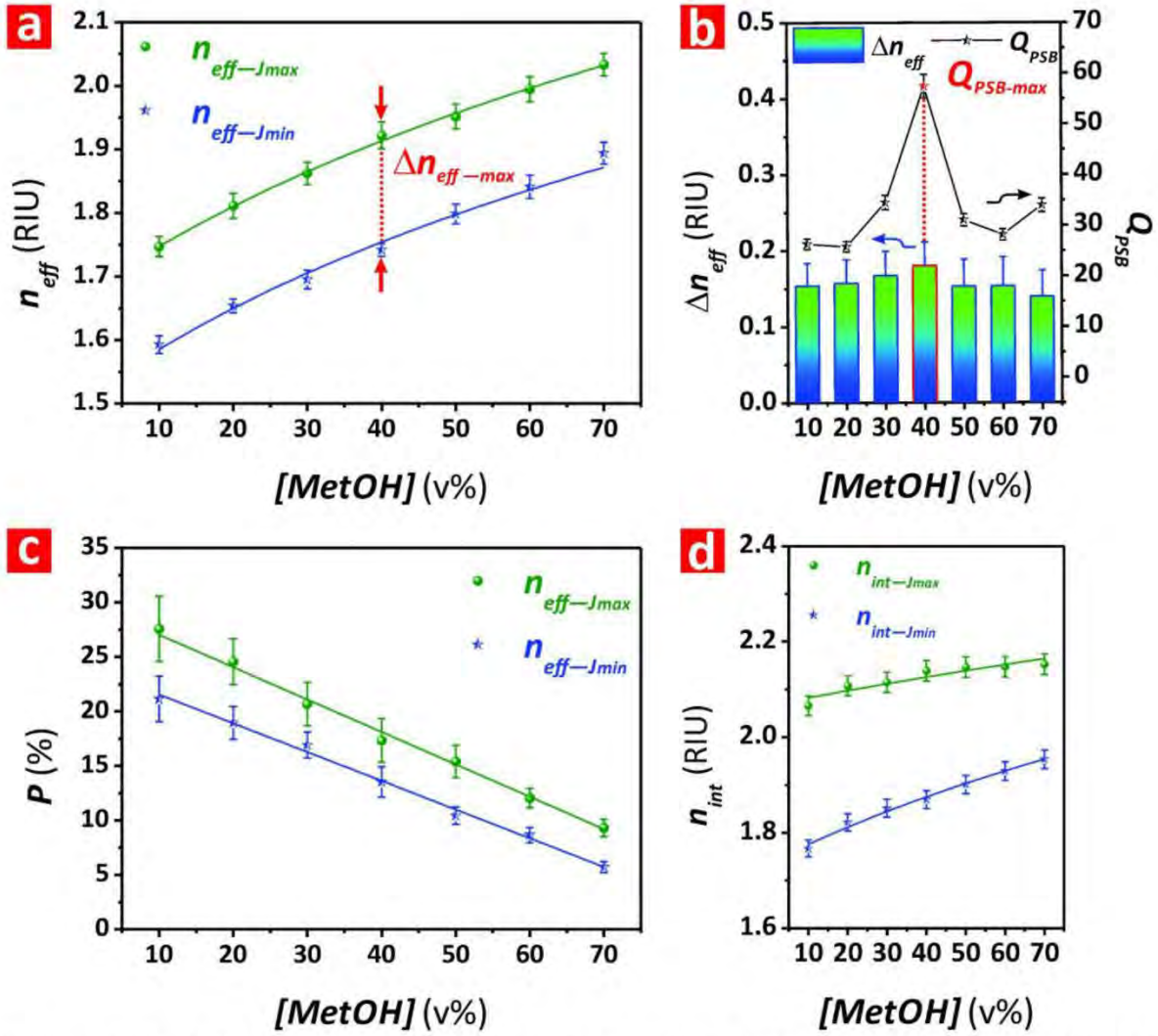
Fig. 8 Analysis of effective and intrinsic optical properties of NAA–GIFs fabricated by SPA in 1 M H$_2$SO$_4$ modified with alcohol additives. (a) Quantification of effective refractive index dependence with input current density at J_{max} and J_{min} ($n_{eff-Jmax}$ and $n_{eff-Jmin}$) and $[MetOH]$, from 10 to 70 v % with $\Delta[MetOH]$ = 10 v % (NB: red arrows and dotted line denote the maximum effective refractive index contrast defined as $\Delta n_{eff} = n_{eff-Jmax} - n_{eff-Jmin}$). (b) Correlation between effective refractive index contrast ($\Delta n_{eff} = n_{eff-Jmax} - n_{eff-Jmin}$) and quality factor of PSB (Q_{PSB}) with $[MetOH]$ in NAA–GIFs. (c) Dependence of porosity (P) of NAA thin films with $[MetOH]$, from 10 to 70 v % with $\Delta[MetOH]$ = 10 v %, and input current density at J_{max} and J_{min}. (d) Quantification of intrinsic refractive index dependence with input current density at J_{max} and J_{min} ($n_{int-Jmax}$ and $n_{int-Jmin}$) and $[MetOH]$, from 10 to 70 v % with $\Delta[MetOH]$ = 10 v %.

38

TABLES

Table 1. Summary of alcohol additive type (MetOH, EtOH, IPA, and EGOH) and concentration (*[Alcohol]*) conditions, and electrochemical, (minimum voltage – V_{min}, maximum voltage – V_{max}, and voltage amplitude – A_V), geometric (period length – L_{TP} and nanopore diameter – D_P), and optical features (position of central wavelength – λ_{PSB}, full width at half maximum – $FWHM_{PSB}$, intensity – I_{PSB}, and quality factor – Q_{PSB}) of the best performing light-forbidding NAA–GIFs fabricated by SPA in alcohol-modified 1 M H_2SO_4 electrolyte.

Parameters		*Alcohol Additive*			
		MetOH	**EtOH**	**IPA**	**EGOH**
Electrolyte	*[Alcohol]* (v %)	40	30	40	50
Electrochemical	V_{min} (V)	13.3 ± 0.1	10.3 ± 0.2	10.2 ± 0.3	20.0 ± 0.2
	V_{max} (V)	22.2 ± 0.4	18.0 ± 0.4	17.9 ± 0.7	29.3 ± 0.3
	A_V (V)	4.4 ± 0.1	3.8 ± 0.1	3.8 ± 0.2	4.6 ± 0.1
Geometric	L_{TP} (nm)	136 ± 6	121 ± 6	127 ± 10	192 ± 11
	D_P (nm)	9 ± 2	5 ± 2	11 ± 3	8 ± 3
Optical	λ_{PSB} (nm)	544 ± 8	501 ± 8	468 ± 7	555 ± 8
	$FWHM_{PSB}$ (nm)	9.5 ± 0.4	15.7 ± 0.6	17.5 ± 0.7	14.1 ± 0.6
	I_{PSB} (%)	63 ± 3	51 ± 2	48 ± 2	45 ± 2
	Q_{PSB}	58 ± 2	32 ± 1	27 ± 1	40 ± 2

39

Appendix A

Electronic Supplementary Information

Elucidating Alcohol Additives Effect on Mild Pulse Anodization by Forbidden Light Propagation in Nanoporous Anodic Alumina Gradient-Index Filters

Siew Yee Lim[a,b,c], Cheryl Suwen Law[*a,b,c], Lin Jiang[a] , Laura K. Acosta[a,d], Akash Bachhuka[e], Lluís F. Marsal[d], Andrew D. Abell[b,c,e] and Abel Santos[*a,b,c]

[a]School of Chemical Engineering and Advanced Materials, The University of Adelaide, 5005 South Australia, Australia.
[b]Institute for Photonics and Advanced Sensing, The University of Adelaide, 5005 South Australia, Australia.
[c]ARC Centre of Excellence for Nanoscale BioPhotonics, The University of Adelaide, 5005 South Australia, Australia.
[d]Department of Electronic, Electric, and Automatics Engineering, Rovira i Virgili University, 43007 Tarragona, Spain.
[e]Future Industries Institute, The University of South Australia, 5095 South Australia, Australia.
[f]Department of Chemistry, The University of Adelaide, 5005 South Australia, Australia.

*E-mails: suwen.law@adelaide.edu.au ; abel.santos@adelaide.edu.au
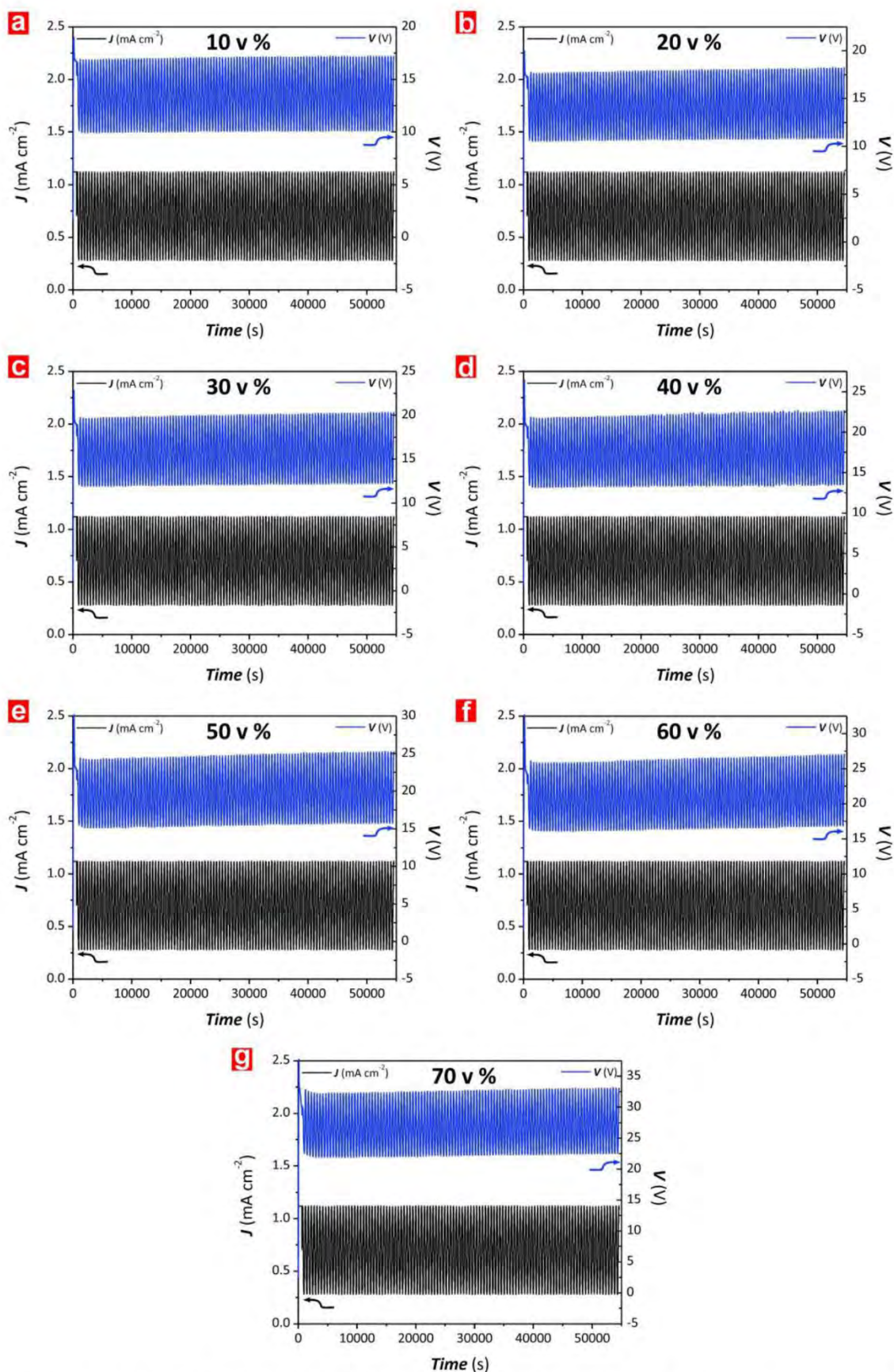
Fig. A.1. Sinusoidal pulse anodization (SPA) profiles used to fabricate NAA–GIFs under current density control conditions in 1 M H_2SO_4 electrolyte with varying methanol (MetOH) concentration: (a) 10 v %, (b) 20 v %, (c) 30 v %, (d) 40 v %, (e) 50 v %, (f) 60 v %, and (g) 70 v %.
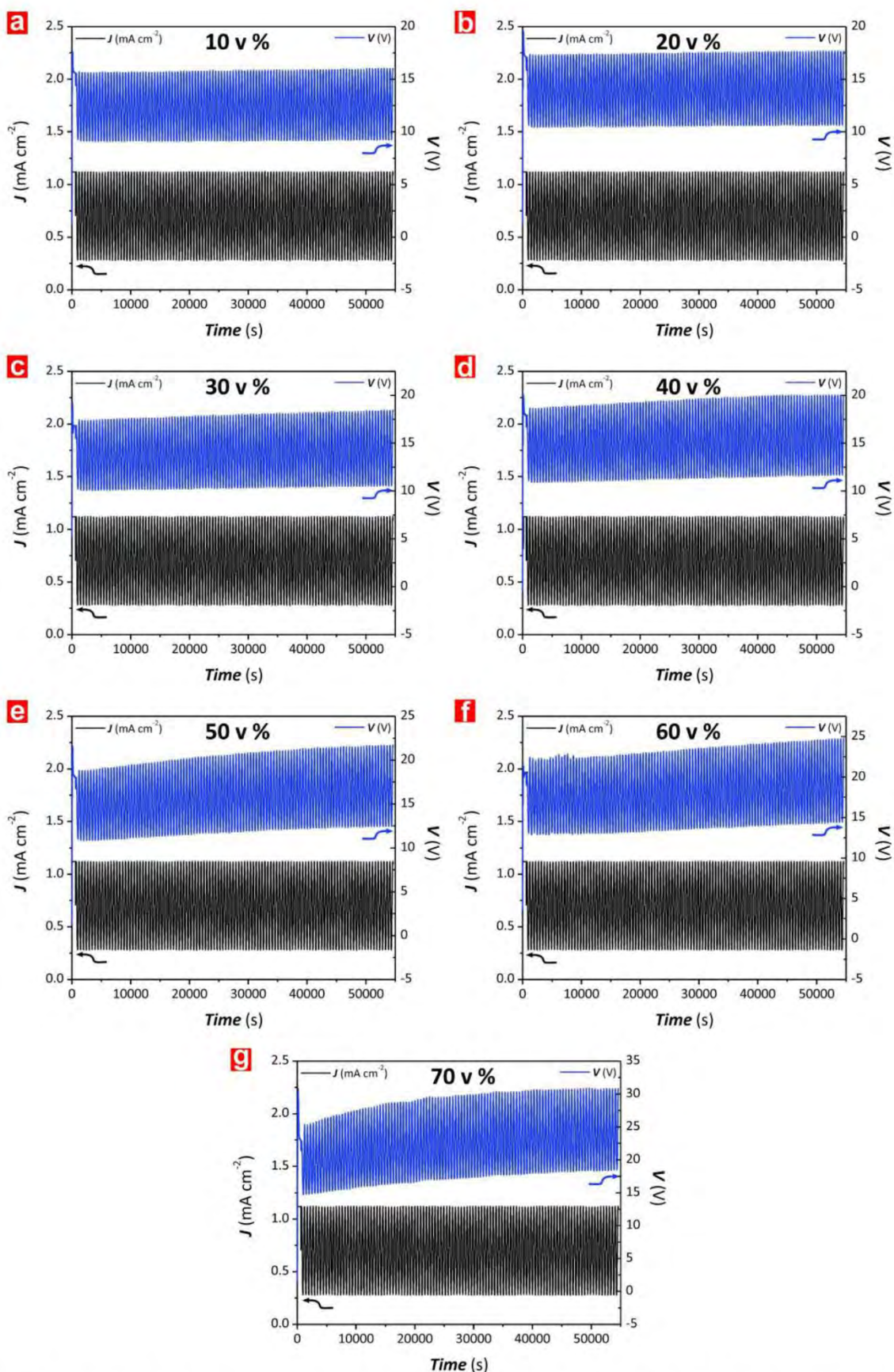
Fig. A.2. Sinusoidal pulse anodization (SPA) profiles used to fabricate NAA–GIFs under current density control conditions in 1 M H$_2$SO$_4$ electrolyte with varying ethanol (EtOH) concentration: (a) 10 v %, (b) 20 v %, (c) 30 v %, (d) 40 v %, (e) 50 v %, (f) 60 v %, and (g) 70 v %.

A-3
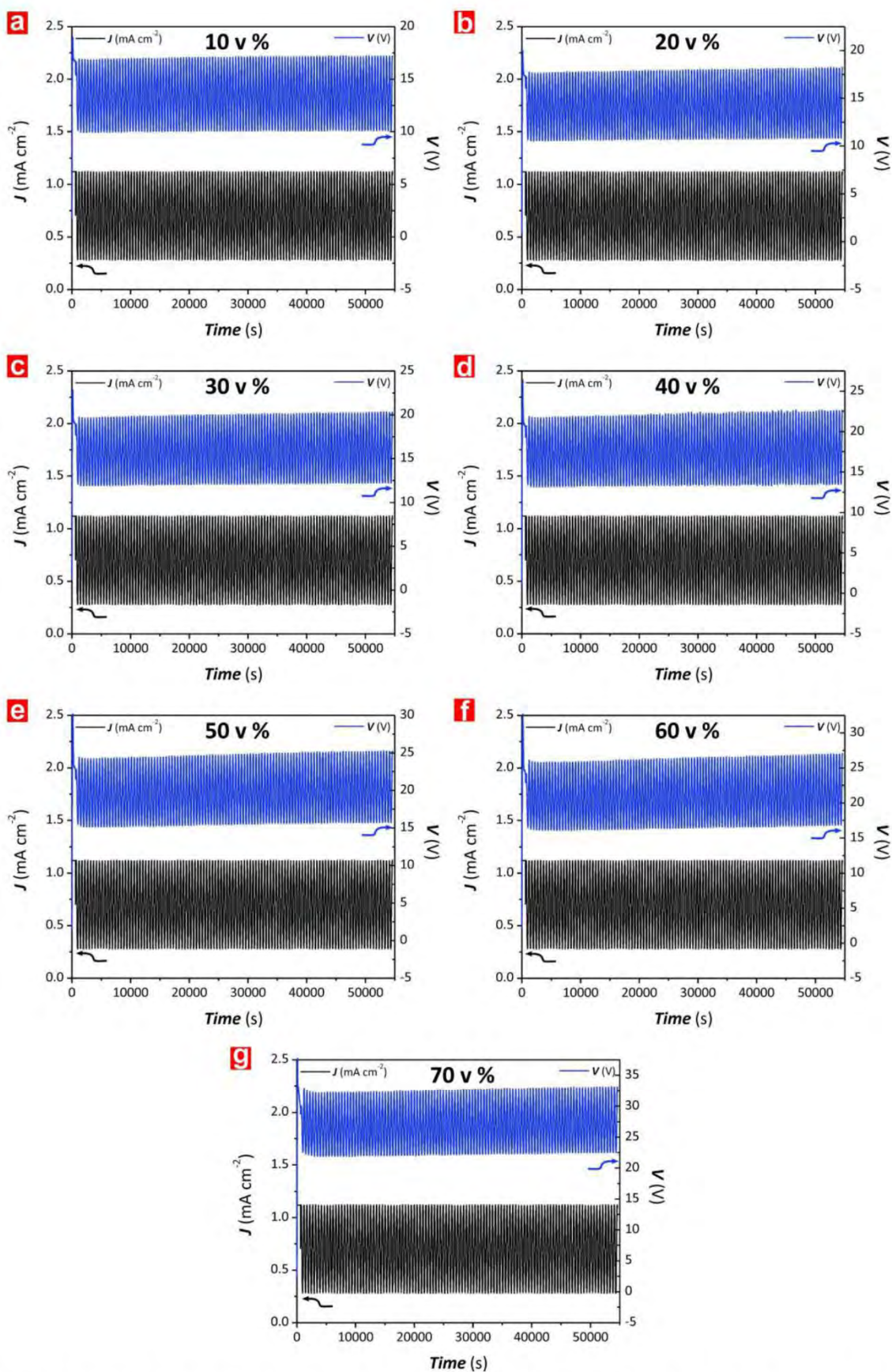
Fig. A.3. Sinusoidal pulse anodization (SPA) profiles used to fabricate NAA–GIFs under current density control conditions in 1 M H$_2$SO$_4$ electrolyte with varying isopropanol (IPA) concentration: (a) 10 v %, (b) 20 v %, (c) 30 v %, (d) 40 v %, (e) 50 v %, (f) 60 v %, and (g) 70 v %.
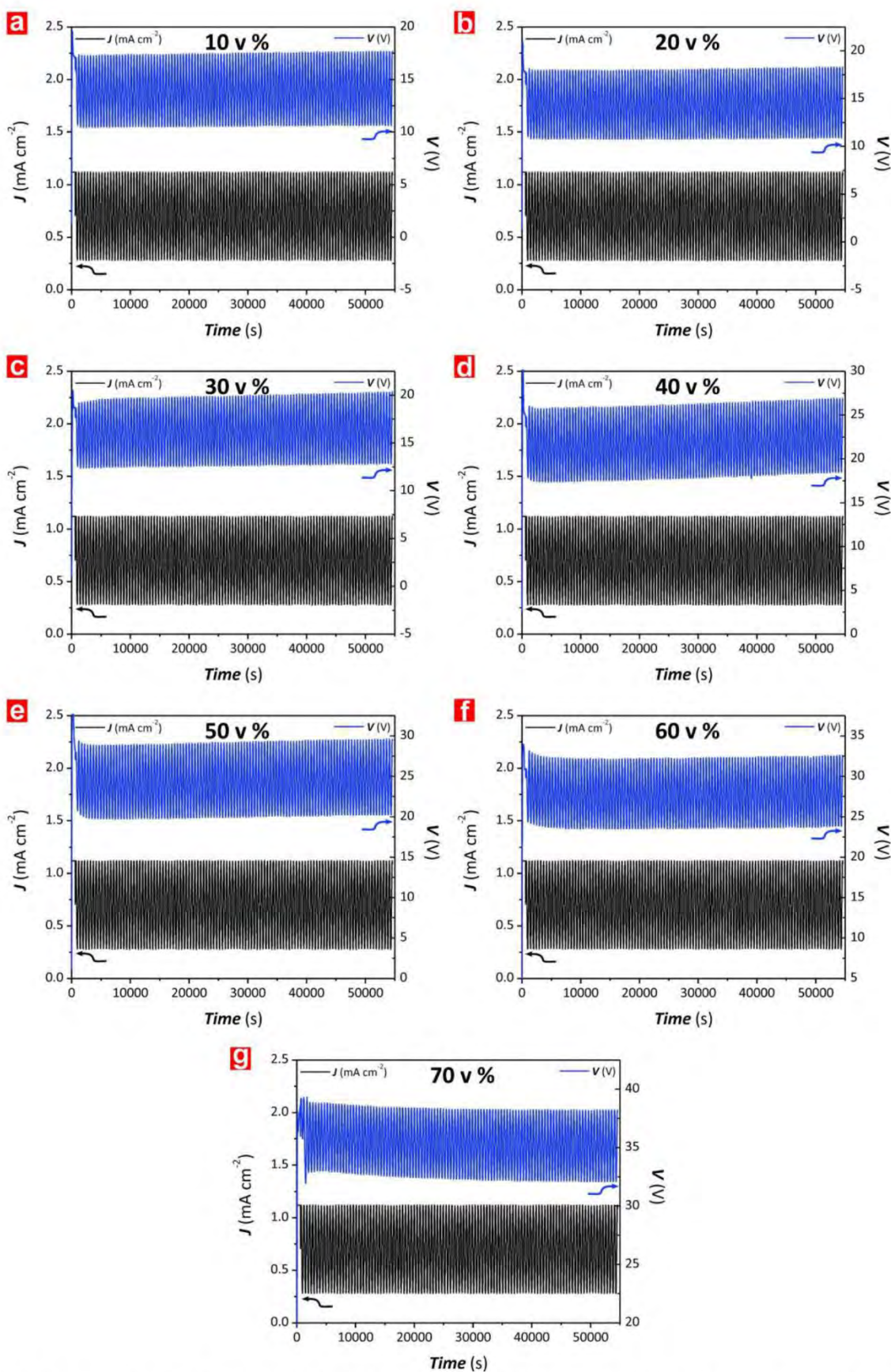
Fig. A.4. Sinusoidal pulse anodization (SPA) profiles used to fabricate NAA–GIFs under current density control conditions in 1 M H_2SO_4 electrolyte with varying ethylene glycol (EGOH) concentration: (a) 10 v %, (b) 20 v %, (c) 30 v %, (d) 40 v %, (e) 50 v %, (f) 60 v %, and (g) 70 v %.
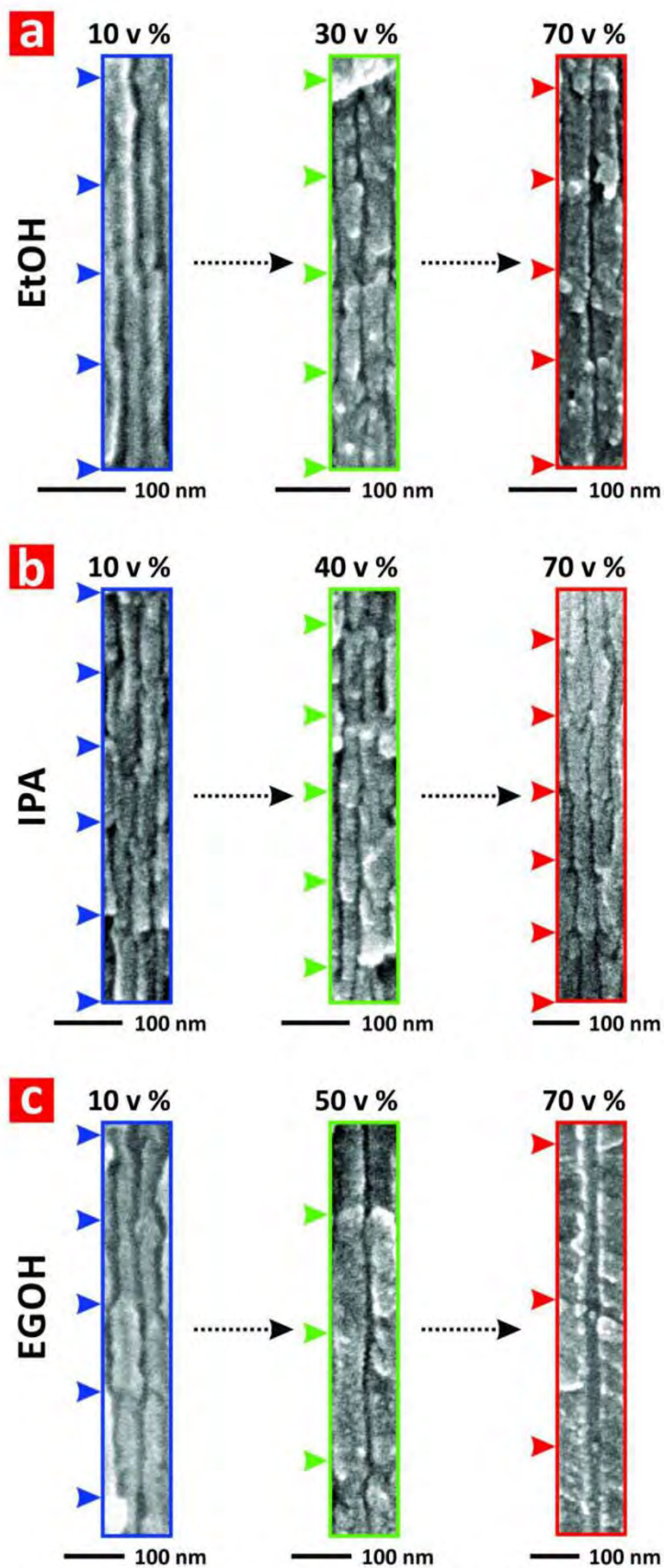
Fig. A.5. Representative high-resolution cross-sectional view FEG-SEM images showing details of nanopore morphology and geometry evolution with *[Alcohol]* for: (a) EtOH at 10, 30, and 70 v %, (b) IPA at 10, 40, and 70 v %, and (c) EGOH at 10, 50, and 70 v % (NB: color arrowheads indicate interfaces between stacks of NAA with modulated porosity defined as period length $- L_{TP}$).
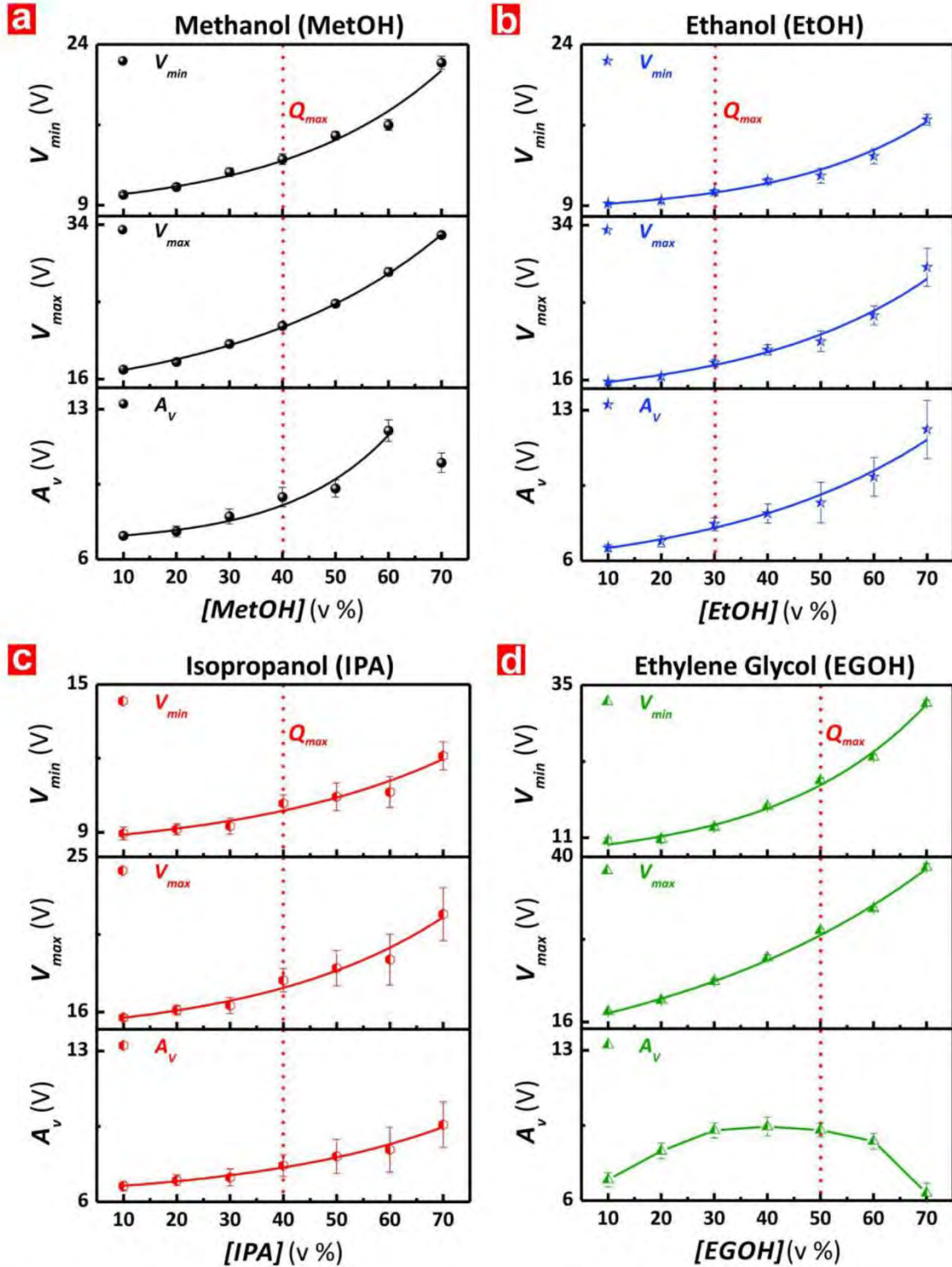
Fig. A.6. Analysis of main electrochemical parameters (V_{min}, V_{max}, and A_V) measured from the anodization profiles shown in Figs. A.1–A.4 for NAA–GIFs fabricated by SPA with varying concentration of alcohol additives (i.e. from 10 to 70 v % with an increment of 10 v %): (a) MetOH, (b) EtOH, (c) IPA, and (d) EGOH (NB: red dotted vertical line denotes the electrochemical parameters at which the quality factor of the photonic stopband (PSB) of NAA–GIFs is maximum – Q_{max}).
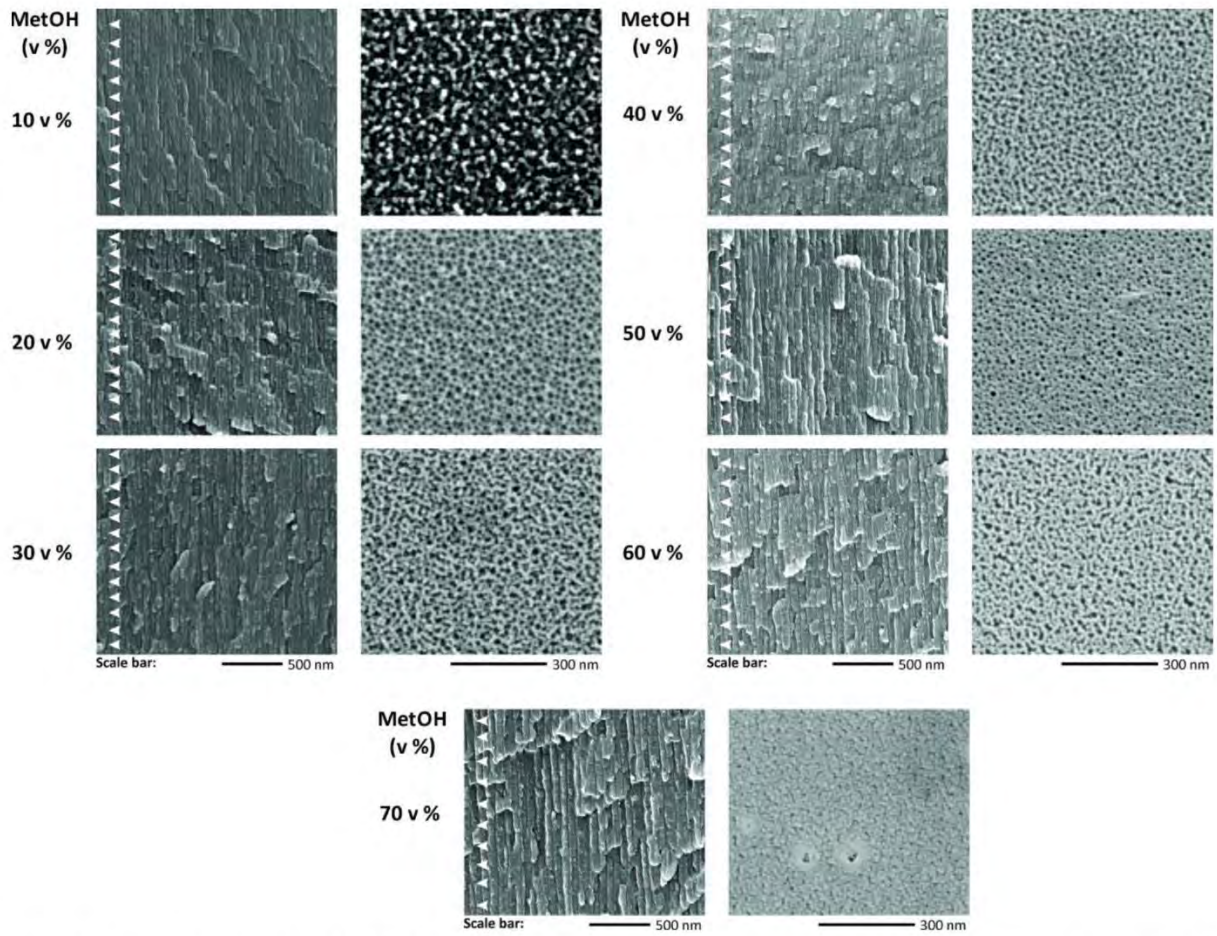
Fig. A.7. FEG-SEM images of NAA–GIFs produced with varying concentration of MetOH: cross-sectional view (left; scale bar = 500 nm), and top view (right; scale bar = 300 nm) (NB: white arrowheads denote the period length – L_{TP} within the structure of NAA–GIFs).

EtOH (v %)

10 v %

30 v %

70 v %

Scale bar: ———— 500 nm   ———— 300 nm
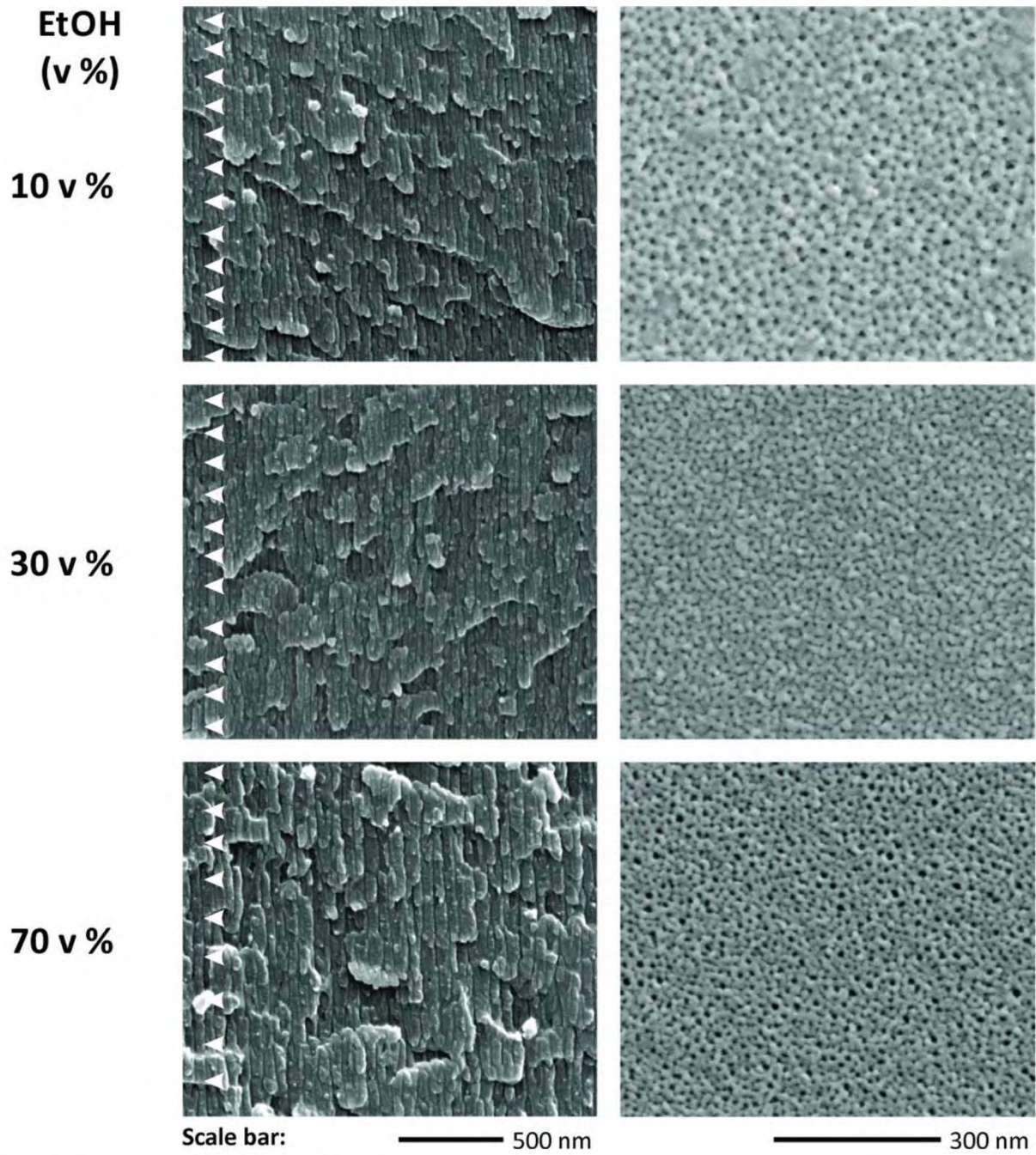
Fig. A.8. FEG-SEM images of NAA–GIFs produced with varying concentration of EtOH: cross-sectional view (left; scale bar = 500 nm), and top view (right; scale bar = 300 nm) (NB: white arrowheads denote the period length – L_{TP} within the structure of NAA–GIFs).

IPA (v %)

10 v %

40 v %

70 v %

Scale bar: ———— 500 nm ———— 300 nm
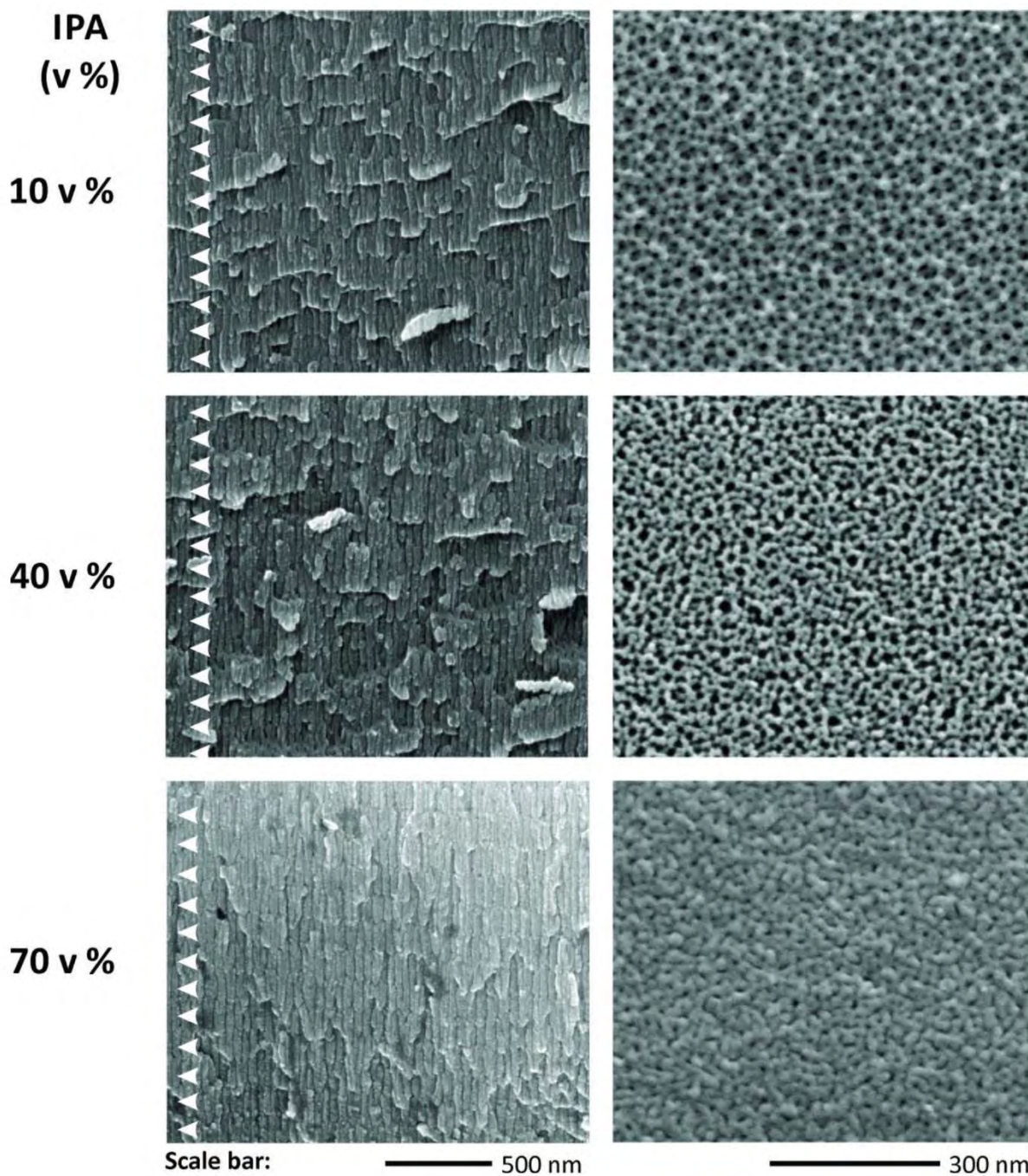
Fig. A.9. FEG-SEM images of NAA–GIFs produced with varying concentration of IPA: cross-sectional view (left; scale bar = 500 nm), and top view (right; scale bar = 300 nm) (NB: white arrowheads denote the period length – L_{TP} within the structure of NAA–GIFs).

A-10
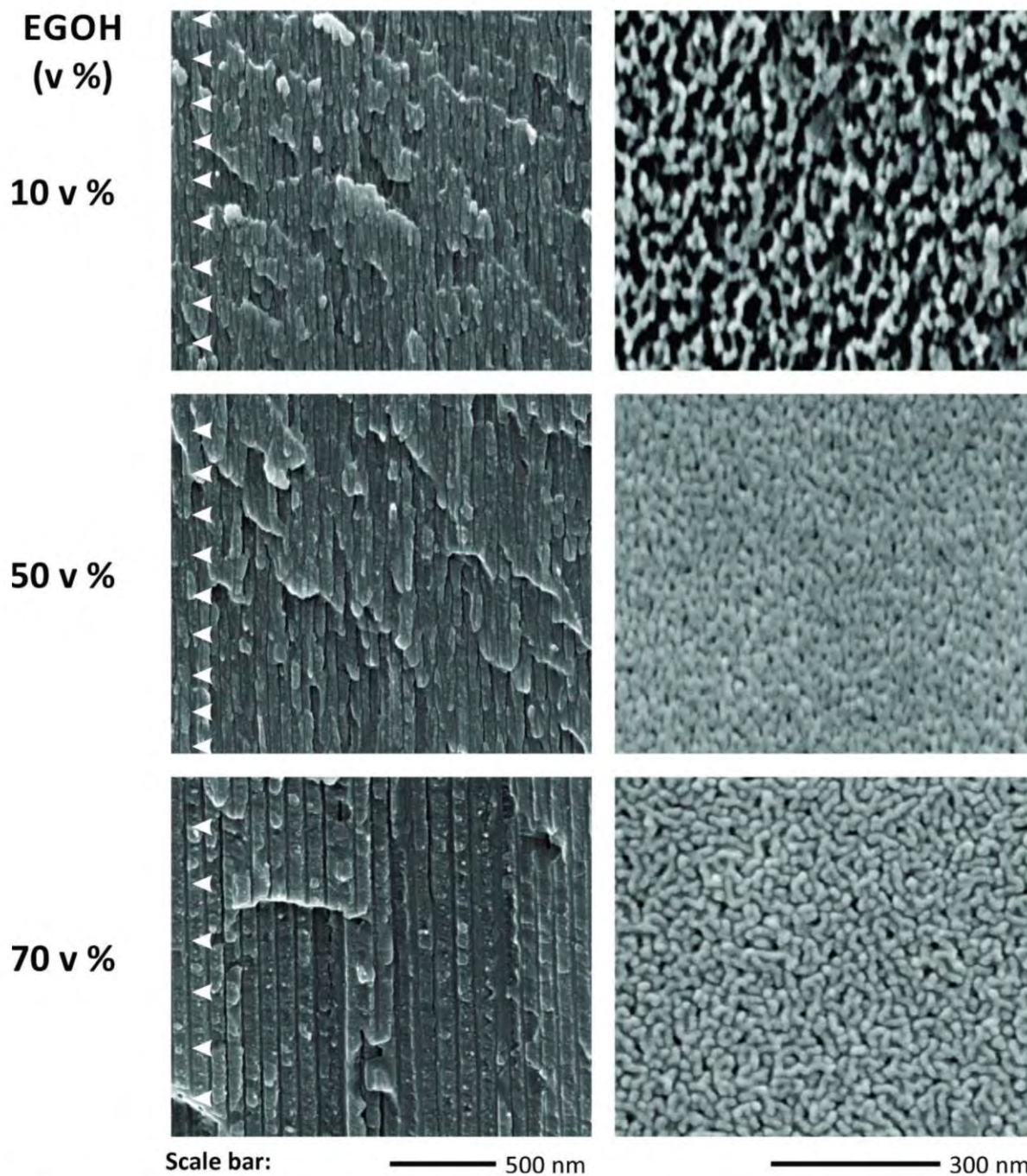
Fig. A.10. FEG-SEM images of NAA–GIFs produced with varying concentration of EGOH: cross-sectional view (left; scale bar = 500 nm), and top view (right; scale bar = 300 nm) (NB: white arrowheads denote the period length – L_{TP} within the structure of NAA–GIFs).
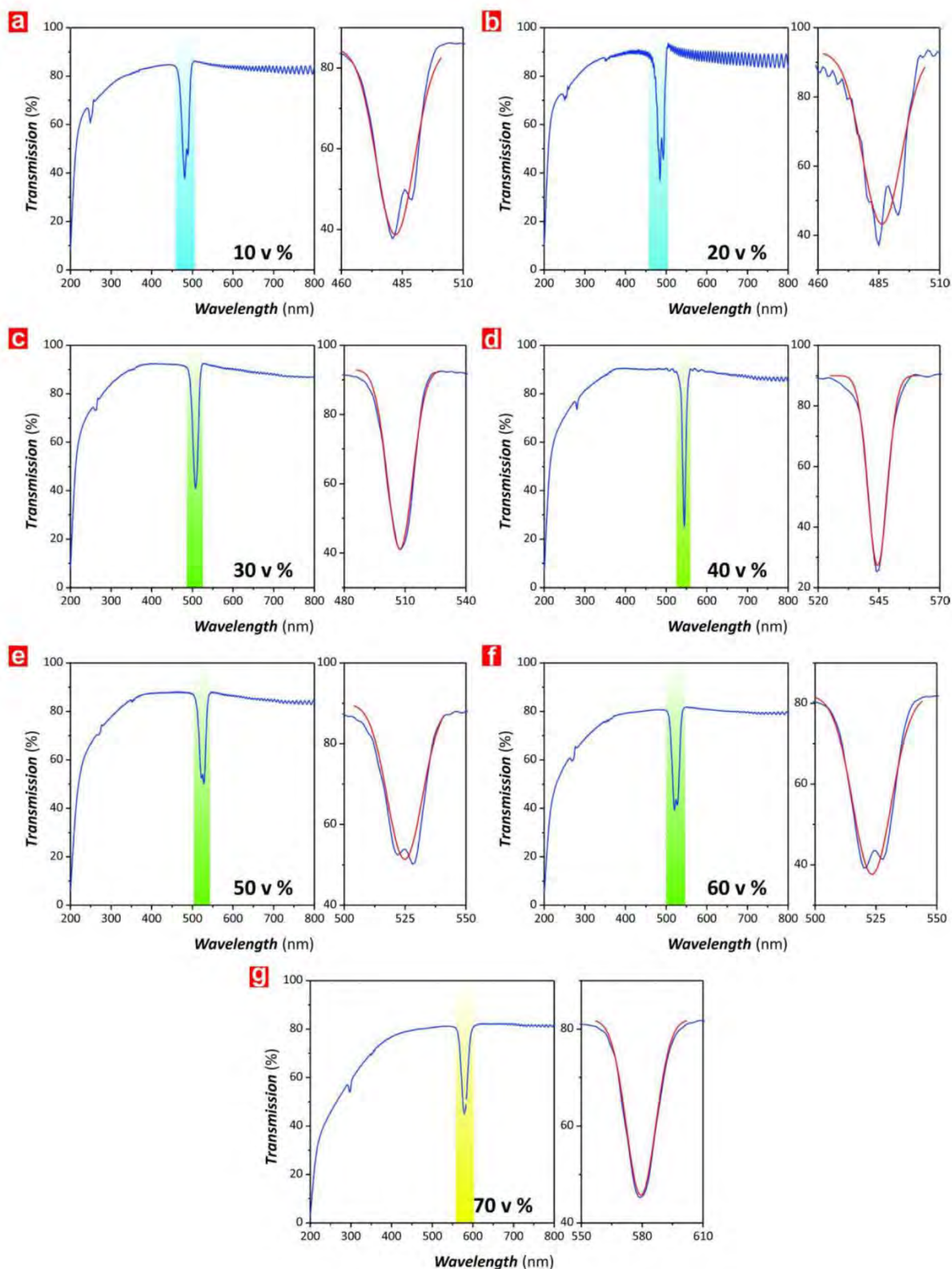
Fig. A.11. Full-view transmission spectra and magnified views of the characteristic PSB of NAA–GIFs produced by SPA with varying concentration of MetOH: (a) 10 v %, (b) 20 v %, (c) 30 v %, (d) 40 v %, (e) 50 v %, (f) 60 v %, and (g) 70 v %.
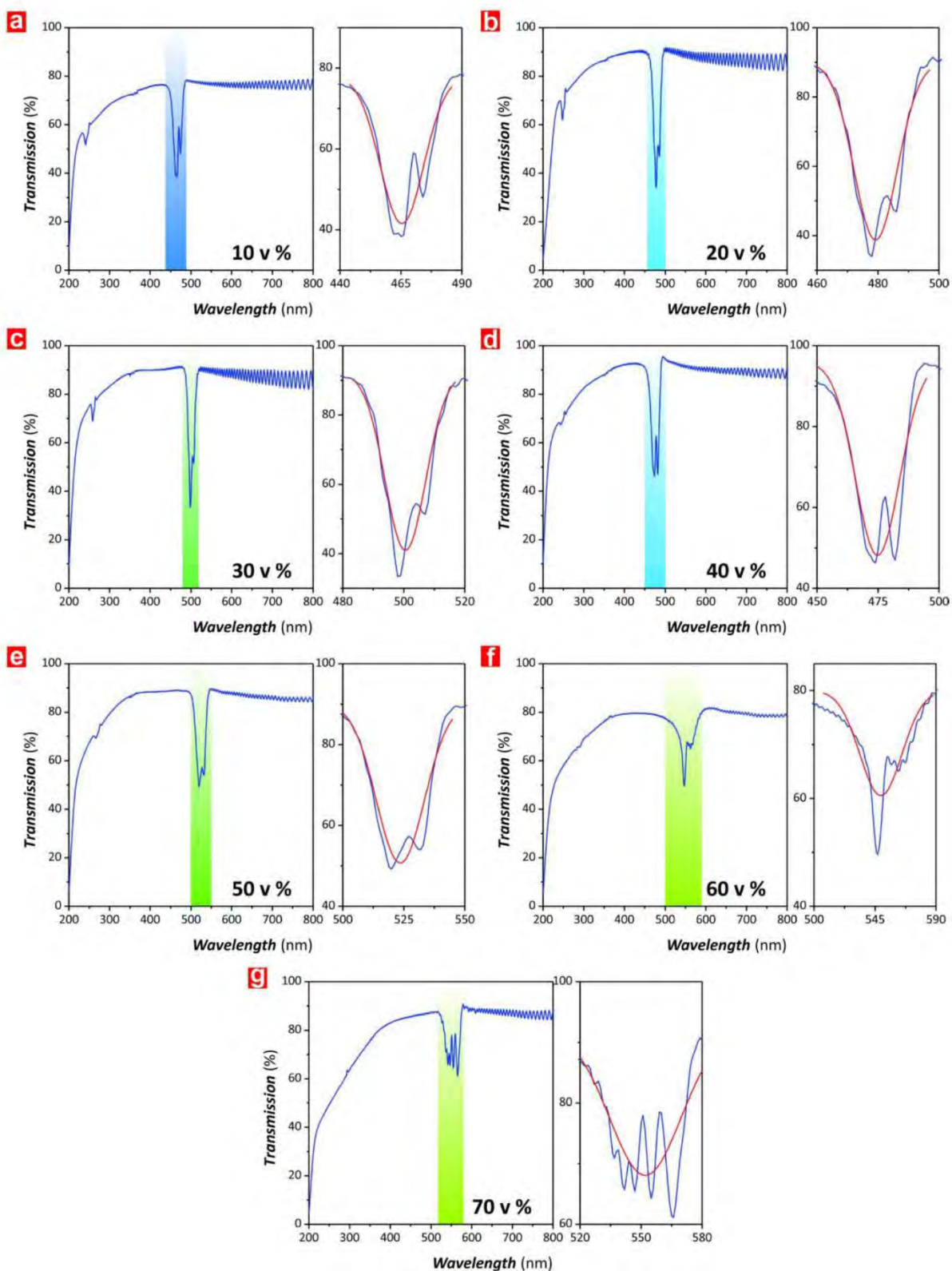
Fig. A.12. Full-view transmission spectra and magnified views of the characteristic PSB of NAA–GIFs produced by SPA with varying concentration of EtOH: (a) 10 v %, (b) 20 v %, (c) 30 v %, (d) 40 v %, (e) 50 v %, (f) 60 v %, and (g) 70 v %.
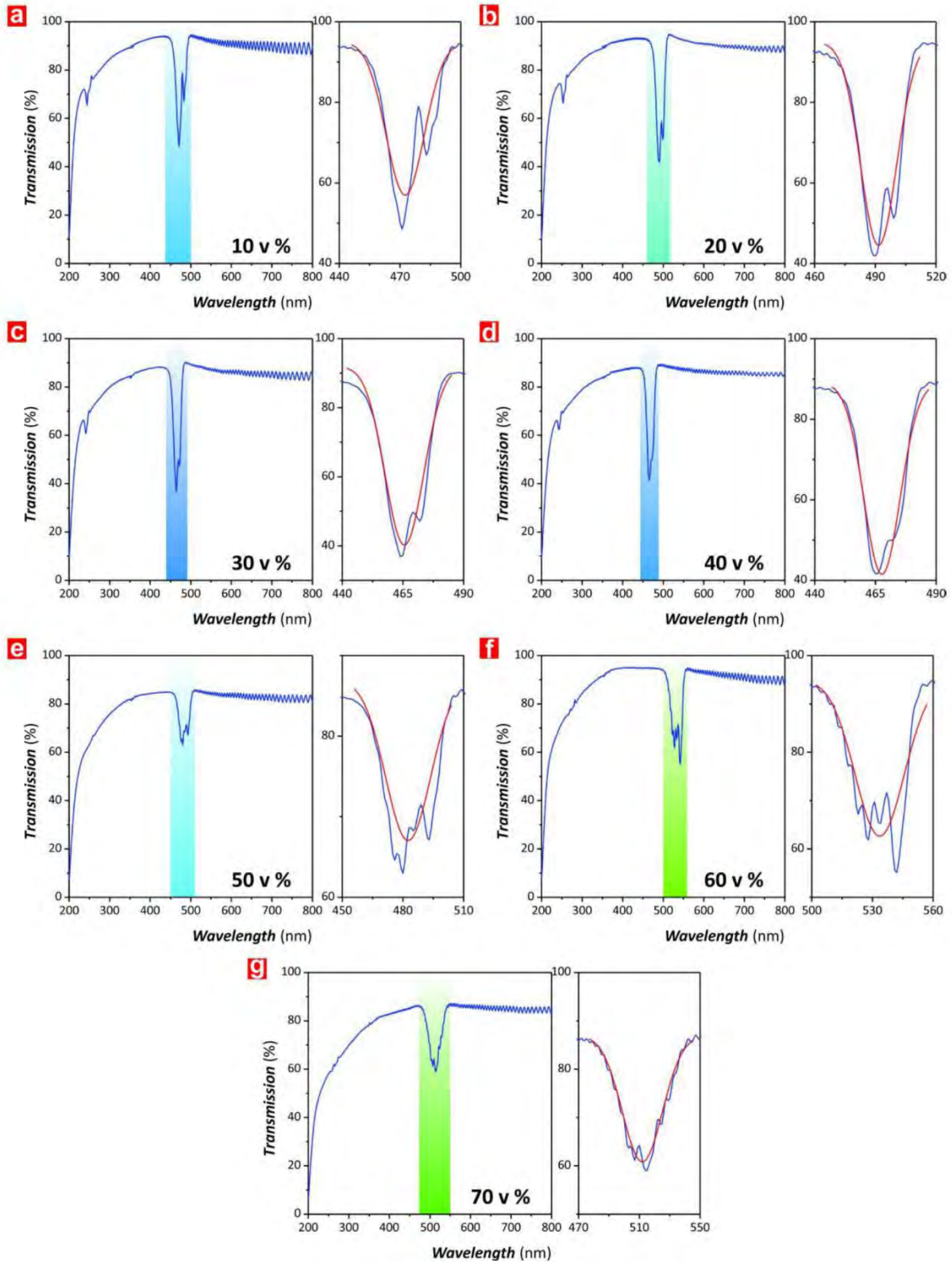
Fig. A.13. Full-view transmission spectra and magnified views of the characteristic PSB of NAA–GIFs produced by SPA with varying concentration of IPA: (a) 10 v %, (b) 20 v %, (c) 30 v %, (d) 40 v %, (e) 50 v %, (f) 60 v %, and (g) 70 v %.
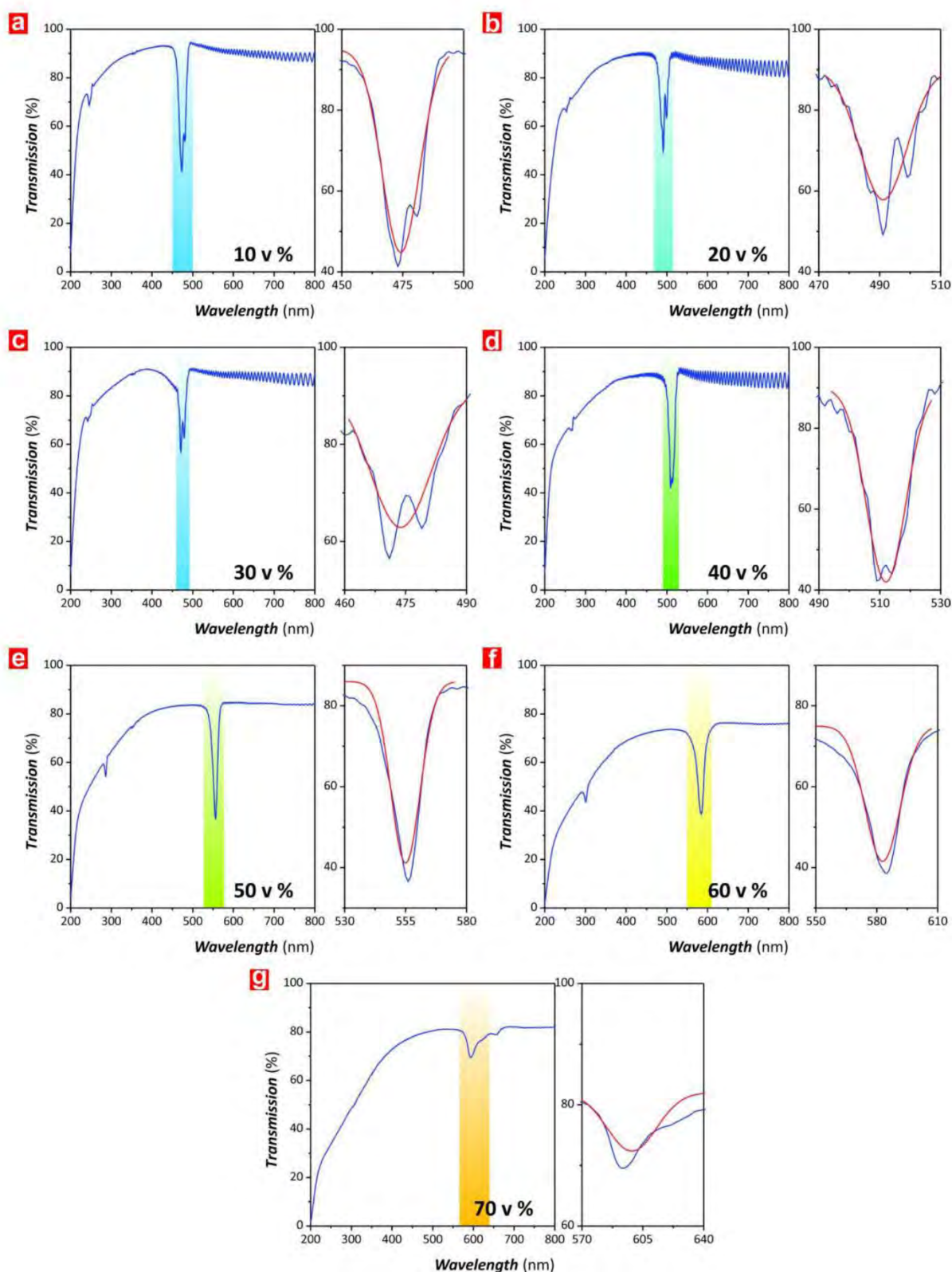
Fig. A.14. Full-view transmission spectra and magnified views of the characteristic PSB of NAA–GIFs produced by SPA with varying concentration of EGOH: (a) 10 v %, (b) 20 v %, (c) 30 v %, (d) 40 v %, (e) 50 v %, (f) 60 v %, and (g) 70 v %.
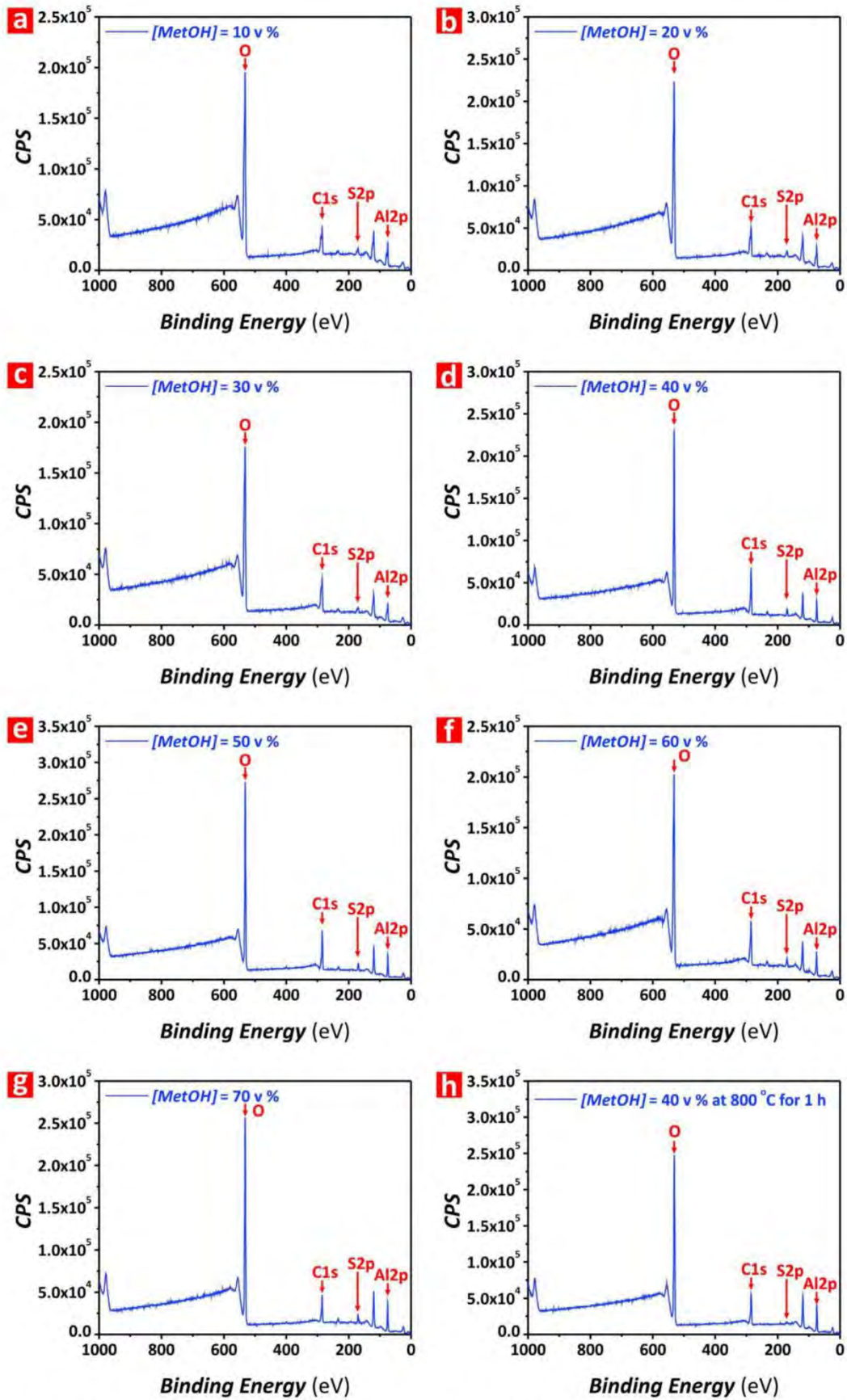
Fig. A.15. XPS spectra analysis of NAA–GIFs produced by SPA with varying concentration of MetOH: (a) 10 v %, (b) 20 v %, (c) 30 v %, (d) 40 v %, (e) 50 v %, (f) 60 v %, (g) 70 v %, and (h) 40 v % at 800 ∘C for 1 h (NB: aluminum – Al; oxygen – O; sulfur – S; carbon – C).
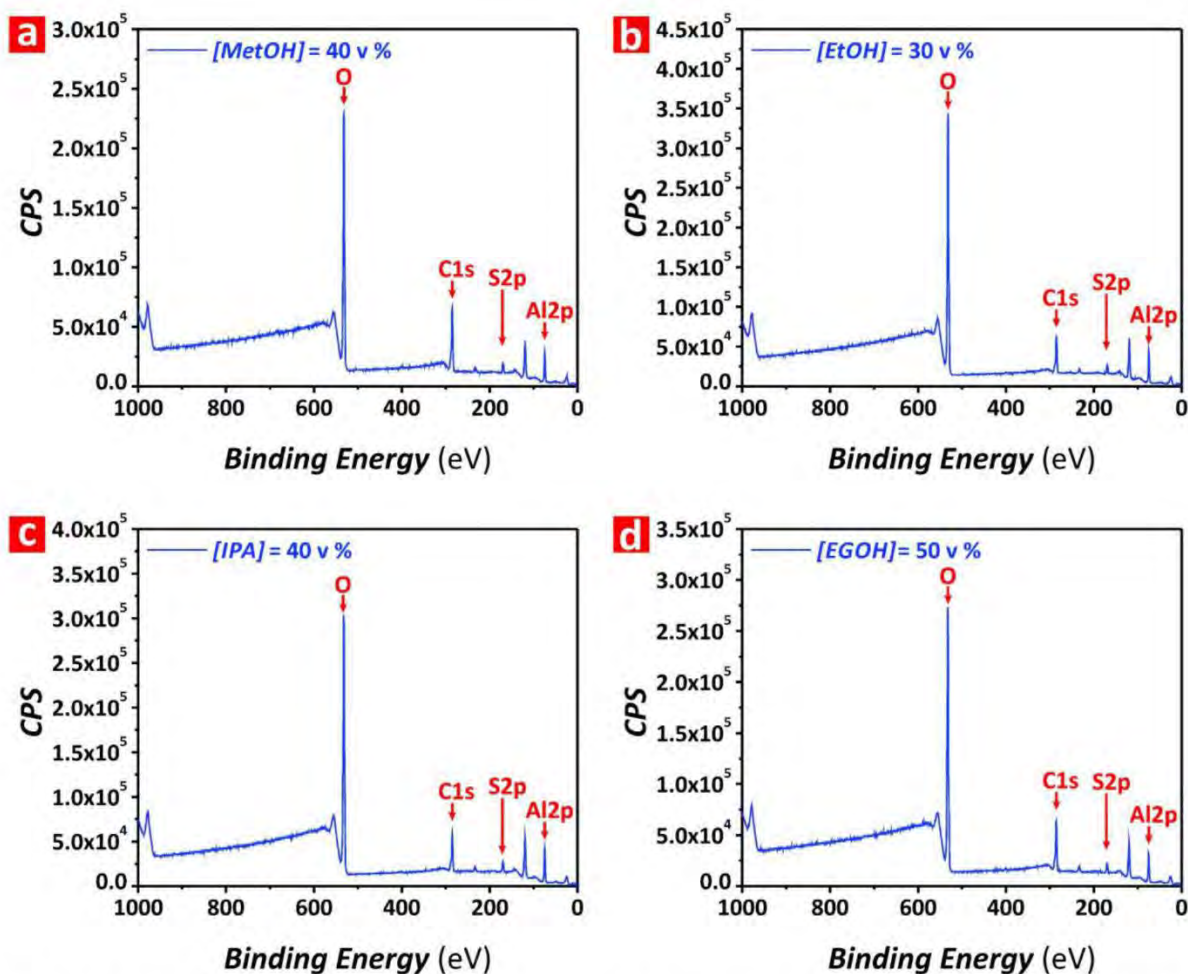
Fig. A.16. XPS spectra analysis of best performing NAA–GIFs produced by SPA with: (a) 40 v % MetOH, (b) 30 v % EtOH, (c) 40 v % IPA, and (d) 50 v % EGOH (NB: aluminum – Al; oxygen – O; sulfur – S; carbon – C).
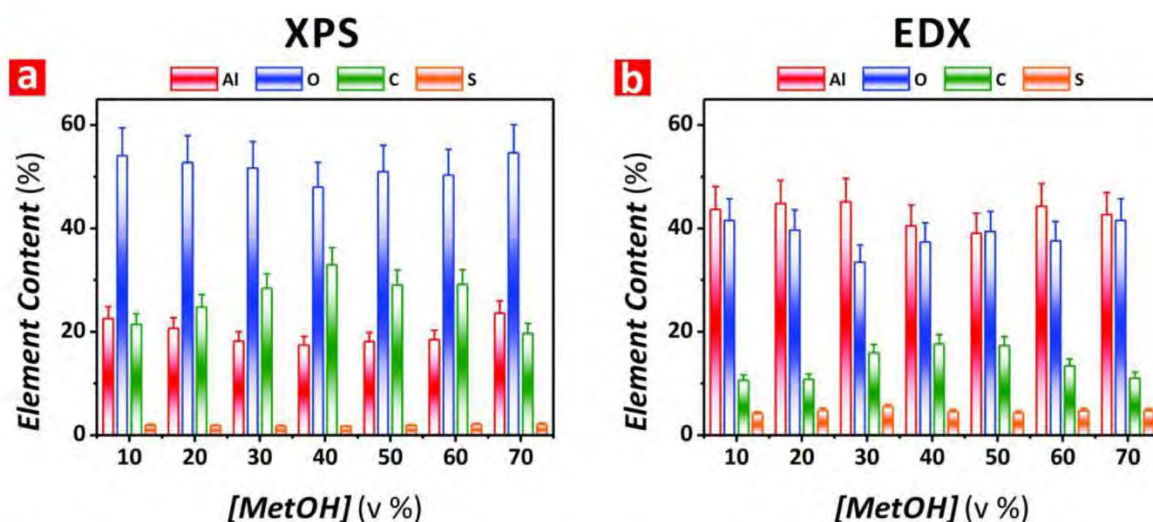
Fig. A.17. Comparative XPS (a) and EDX (b) elemental composition quantification of NAA–GIFs with [MetOH], from 10 to 70 v % with Δ[MetOH] = 10 v %, and relative percentages of Al, O, C, and S (NB: aluminum – Al; oxygen – O; sulfur – S; carbon – C).
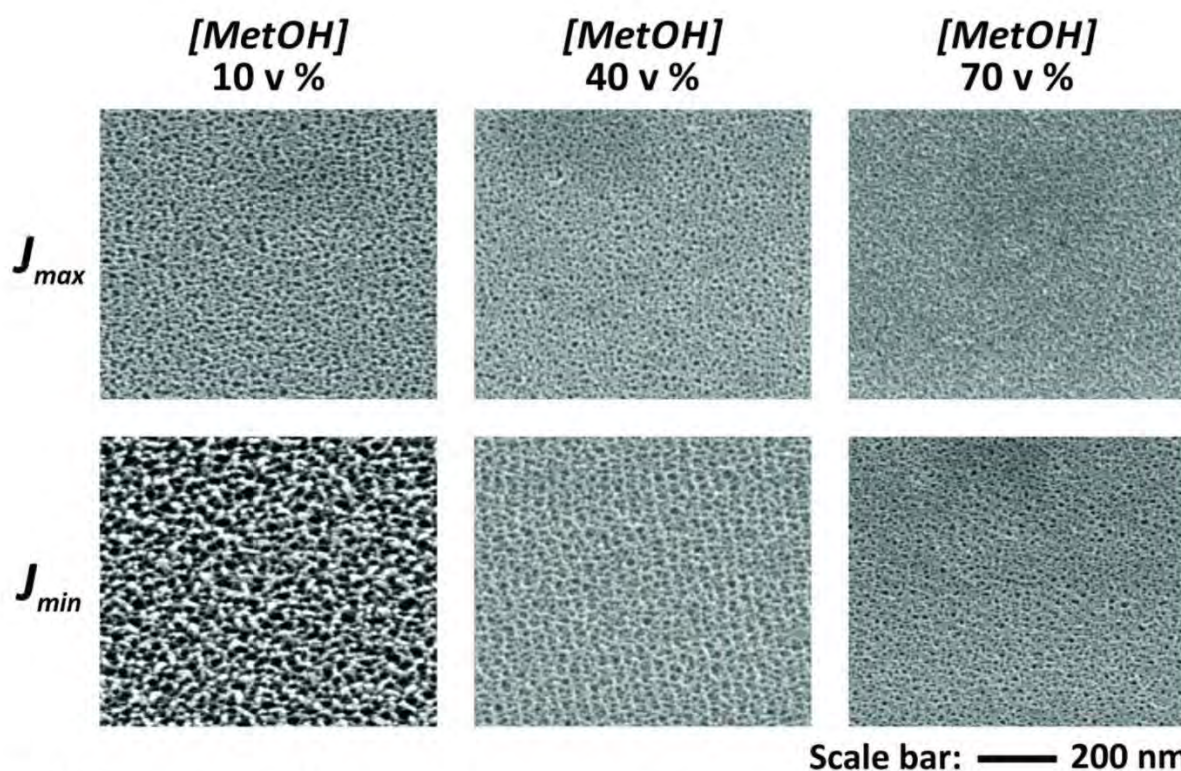
Fig. A.18. Top view FEG-SEM images of representative NAA thin films used to estimate the porosity, and effective and intrinsic refractive indexes of NAA–GIFs as a function of *[MetOH]* (NB: NAA thin films produced at J_{max} = 1.120 mA cm^{-2} and J_{min} = 0.280 mA cm^{-2} with *[MetOH]* = 10, 40, and 70 v %).

Table A.1. Summary of dependence of electrochemical parameters (minimum voltage – V_{min}, maximum voltage – V_{max} and voltage amplitude – A_v) with the concentration of alcohol additive (MetOH, EtOH, IPA and EGOH, from *[alcohol]* = 10 to 70 v%) for NAA–GIFs produced by SPA in 1 M H$_2$SO$_4$.

Alcohol Additive	Electrochemical Parameter	Fitting	R^2
MetOH	V_{min}	$V_{min} = 8.2 + 1.3 \cdot e^{0.033 \cdot [alcohol]}$	0.9841
	V_{max}	$V_{max} = 12.8 + 3.3 \cdot e^{0.026 \cdot [alcohol]}$	0.9984
	A_v	$A_v = 6.7 + 0.22 \cdot e^{0.052 \cdot [alcohol]}$	0.9641
EtOH	V_{min}	$V_{min} = 8.2 + 0.7 \cdot e^{0.037 \cdot [alcohol]}$	0.9885
	V_{max}	$V_{max} = 13.3 + 1.8 \cdot e^{0.030 \cdot [alcohol]}$	0.9756
	A_v	$A_v = 5.1 + 1.12 \cdot e^{0.025 \cdot [alcohol]}$	0.9723
IPA	V_{min}	$V_{min} = 8.1 + 0.7 \cdot e^{0.026 \cdot [alcohol]}$	0.9298
	V_{max}	$V_{max} = 14.4 + 1.0 \cdot e^{0.029 \cdot [alcohol]}$	0.9558
	A_v	$A_v = 6.1 + 0.5 \cdot e^{0.026 \cdot [alcohol]}$	0.9765
EGOH	V_{min}	$V_{min} = 7.0 + 2.1 \cdot e^{0.035 \cdot [alcohol]}$	0.9991
	V_{max}	$V_{max} = 6.7 + 8.8 \cdot e^{0.018 \cdot [alcohol]}$	0.9945
	A_v	–	–

Table A.2. Summary of dependence of geometric features (period length – L_{TP} and pore diameter – D_P) with the concentration of alcohol additive (MetOH, EtOH, IPA and EGOH, from *[alcohol]* = 10 to 70 v %) for NAA–GIFs produced by SPA in 1 M H_2SO_4.

Alcohol Additive	Geometric Features	Fitting	R^2
MetOH	L_{TP}	$L_{TP} = 0.38 \cdot [alcohol] + 123.8$	0.8488
	D_P	$D_P = -0.06 \cdot [alcohol] + 11.5$	0.3866
EtOH	L_{TP}	$L_{TP} = 0.52 \cdot [alcohol] + 109.4$	0.7442
	D_P	$D_P = 0.02 \cdot [alcohol] + 5.8$	0.8236
IPA	L_{TP}	$L_{TP} = 0.46 \cdot [alcohol] + 112.6$	0.9504
	D_P	$D_P = -0.04 \cdot [alcohol] + 10.8$	0.1200
EGOH	L_{TP}	$L_{TP} = 2.11 \cdot [alcohol] + 136.2$	0.5437
	D_P	$D_P = -0.13 \cdot [alcohol] + 16.2$	0.1930

A-19

Chapter 5

ENGINEERING THE SLOW PHOTON
EFFECT IN PHOTOACTIVE NANOPOROUS
ANODIC ALUMINA GRADIENT-INDEX
FILTERS FOR PHOTOCATALYSIS

5. Engineering the Slow Photon Effect in Photoactive Nanoporous Anodic Alumina Gradient-Index Filters for Photocatalysis

5.1 Introduction, Significance and Commentary

The large energy bandgap of conventional photocatalyst materials constrains their application for photocatalysis. Therefore, engineering light–matter interactions at the nanoscale with rational design of photocatalyst platforms is essential to overcome these limitations. This chapter presents a rationally designed photocatalyst material based on a titanium dioxide-functionalised nanoporous anodic alumina gradient-index filter (TiO$_2$-NAA-GIFs) as a platform to achieve enhanced photocatalytic performances by "slow photon" effect. NAA-GIFs were fabricated by sinusoidal pulse anodisation and subsequently functionalised with photoactive layers of TiO$_2$ through sol-gel method. This study demonstrates that the photocatalytic performance of TiO$_2$-NAA-GIFs is enhanced by "slow photon" effect, in which the photodegradation of three model organic dyes (i.e. methyl orange, Rhodamine B and methylene blue) with well-defined absorption bands across different spectral regions under simulated irradiation conditions were used as the enhancement indicator. These systems outperformed benchmark photocatalyst platforms, demonstrating promising potential for engineering high-performing photocatalytic materials for efficient photocatalysis with broad applicability.

5.2 Publication

This chapter is presented as published journal article by **S.Y. Lim**, C.S. Law, M. Markovic, J.K. Kirby, A.D. Abell, and A. Santos, *Engineering the slow photon effect in photoactive nanoporous anodic alumina gradient-index filters for photocatalysis*. ACS Applied Materials and Interfaces, 2018. **10**(28): p. 24124-24136.

Statement of Authorship

Title of Paper	Engineering the Slow Photon Effect in Photoactive Nanoporous Anodic Alumina Gradient-Index Filters for Photocatalysis
Publication Status	☑ Published ☐ Accepted for Publication ☐ Submitted for Publication ☐ Unpublished and Unsubmitted work written in manuscript style
Publication Details	S.Y. Lim, C.S. Law, M. Markovic, J.K. Kirby, A.D. Abell, and A. Santos, *Engineering the slow photon effect in photoactive nanoporous anodic alumina gradient-index filters for photocatalysis*. ACS Applied Materials and Interfaces, 2018. **10**(28): p. 24124-24136.

Principal Author

Name of Principal Author (Candidate)	Siew Yee Lim
Contribution to the Paper	Performed the experiment, processed and analysed the data and wrote the manuscript under the supervisions of Abel Santos and Andrew D. Abell.
Overall percentage (%)	70
Certification:	This paper reports on original research I conducted during the period of my Higher Degree by Research candidature and is not subject to any obligations or contractual agreements with a third party that would constrain its inclusion in this thesis. I am the primary author of this paper.
Signature		Date	10/06/2020

Co-Author Contributions

By signing the Statement of Authorship, each author certifies that:

   i.   the candidate's stated contribution to the publication is accurate (as detailed above);

   ii.   permission is granted for the candidate in include the publication in the thesis; and

   iii. the sum of all co-author contributions is equal to 100% less the candidate's stated contribution.

Name of Co-Author	Cheryl Suwen Law
Contribution to the Paper	Aided in performing the experiment. Give consent to Siew Yee Lim to present this paper for examination towards the Doctorate of Philosophy.
Signature		Date	15/06/2020

Name of Co-Author	Marijana Markovic		
Contribution to the Paper	Aided in the evaluation of final version of manuscript. Give consent to Siew Yee Lim to present this paper for examination towards the Doctorate of Philosophy.		
Signature		Date	11/06/20

Name of Co-Author	Jason K. Kirby		
Contribution to the Paper	Aided in the evaluation of final version of manuscript. Give consent to Siew Yee Lim to present this paper for examination towards the Doctorate of Philosophy.		
Signature		Date	10/06/2020

Name of Co-Author	Andrew D. Abell		
Contribution to the Paper	Acted as a co-supervisor for the candidate, and aided in revising and evaluating the manuscript for submission. Give consent to Siew Yee Lim to present this paper for examination towards the Doctorate of Philosophy.		
Signature		Date	10/06/2020

Name of Co-Author	Abel Santos		
Contribution to the Paper	Acted as a primary supervisor for the candidate, and aided in developing, revising and evaluating the manuscript for submission. Give consent to Siew Yee Lim to present this paper for examination towards the Doctorate of Philosophy.		
Signature		Date	11/06/2020

Engineering the Slow Photon Effect in Photoactive Nanoporous Anodic Alumina Gradient-Index Filters for Photocatalysis

Siew Yee Lim,[†,‡,§] Cheryl Suwen Law,[†,‡,§] Marijana Markovic,[∥,⊥] Jason K. Kirby,[⊥] Andrew D. Abell,*[,‡,§,#] and Abel Santos*[,†,‡,§]

[†]School of Chemical Engineering, The University of Adelaide, Adelaide, South Australia 5005, Australia

[‡]Institute for Photonics and Advanced Sensing (IPAS), The University of Adelaide, Adelaide, South Australia 5005, Australia

[§]ARC Centre of Excellence for Nanoscale BioPhotonics (CNBP), The University of Adelaide, Adelaide, South Australia 5005, Australia

[∥]School of Agriculture Food and Wine, The University of Adelaide, Adelaide, South Australia 5064, Australia

[⊥]CSIRO Land and Water, Adelaide, South Australia 5064, Australia

[#]Department of Chemistry, The University of Adelaide, Adelaide, South Australia 5005, Australia

⑤ *Supporting Information*

ABSTRACT: In this study, we explore for the first time the capabilities of nanoporous anodic alumina gradient-index filters (NAA-GIFs) functionalized with titanium dioxide (TiO_2) photoactive layers to enhance photon-to-electron conversion rates and improve the efficiency of photocatalytic reactions by "slow photon" effect. A set of NAA-GIFs was fabricated by sinusoidal pulse anodization, in which a systematic modification of various anodization parameters (i.e., pore widening time, anodization period, and anodization time) enables the fine-tuning of the photonic stopband (PSB) of these nanoporous photonic crystals (PCs) across the spectral regions. The surface of NAA-GIFs was chemically modified with photoactive layers of TiO_2 to create a composite photoactive material with precisely engineered optical properties. The photocatalytic performance of TiO_2-functionalized NAA-GIFs was assessed by studying the photodegradation of three model organic dyes (i.e., methyl orange, Rhodamine B, and methylene blue) with well-defined absorption bands across different spectral regions under simulated irradiation conditions. Our study demonstrates that when the edges of characteristic PSB of TiO_2-modified NAA-GIFs are completely or partially aligned with the absorption band of the organic dyes, the photodegradation rate is enhanced due to "slow photon" effect. A rational design of the photocatalyst material with respect to the organic dye is demonstrated to be optimal to speed up photocatalytic reactions by an efficient management of photons from high-irradiance spectral regions. This provides new opportunities to develop high-performing photocatalytic materials for efficient photocatalysis with broad applicability.

KEYWORDS: *nanoporous anodic alumina, photonic crystals, slow photon effect, surface-modification, photocatalysis*

Utilization of the Slow Photon Effect. Transmission Spectrum of Photoactive NAA-GIFs
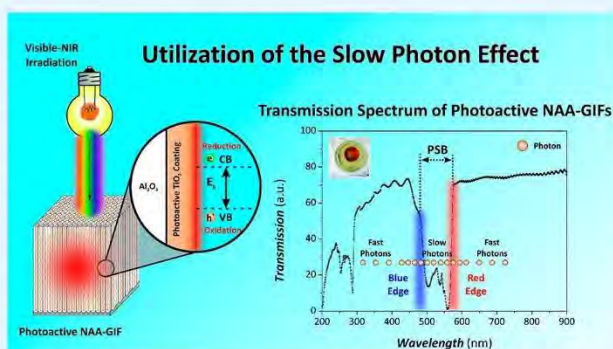
1. INTRODUCTION

Heterogeneous photocatalysis (henceforth "photocatalysis") is a light-driven process in which photons (light−electromagnetic waves) interact with atoms (matter−semiconductors) to generate electron−hole (e^-/h^+) pairs that can subsequently produce free radicals able to undergo secondary reactions.[1] Among other applications, photocatalysis enables the production of clean hydrogen energy,[2] sanitation of water,[3] air purification,[4] ammonia (NH_3) generation,[5] and carbon dioxide (CO_2) reduction.[6] However, most semiconductor materials have a relatively large energy band gap ($\sim$3−5 eV), which constrains their photocatalytic activity to the UV region (only

$\sim$5% of the solar spectrum), preventing the efficient utilization of sunlight for practical photocatalytic applications.

Photonic crystals (PCs) are periodic optical micro-/ nanostructures with forbidden photonic bands that alter the motion of photons when light travels across the PC's structure. The photonic band structure of PCs predicts the propagation of photons with reduced group velocity (v_g) at those directions close to the blue and red edges of the PCs' photonic stopband (PSB), where the band becomes almost flat ("slow photons"

24124
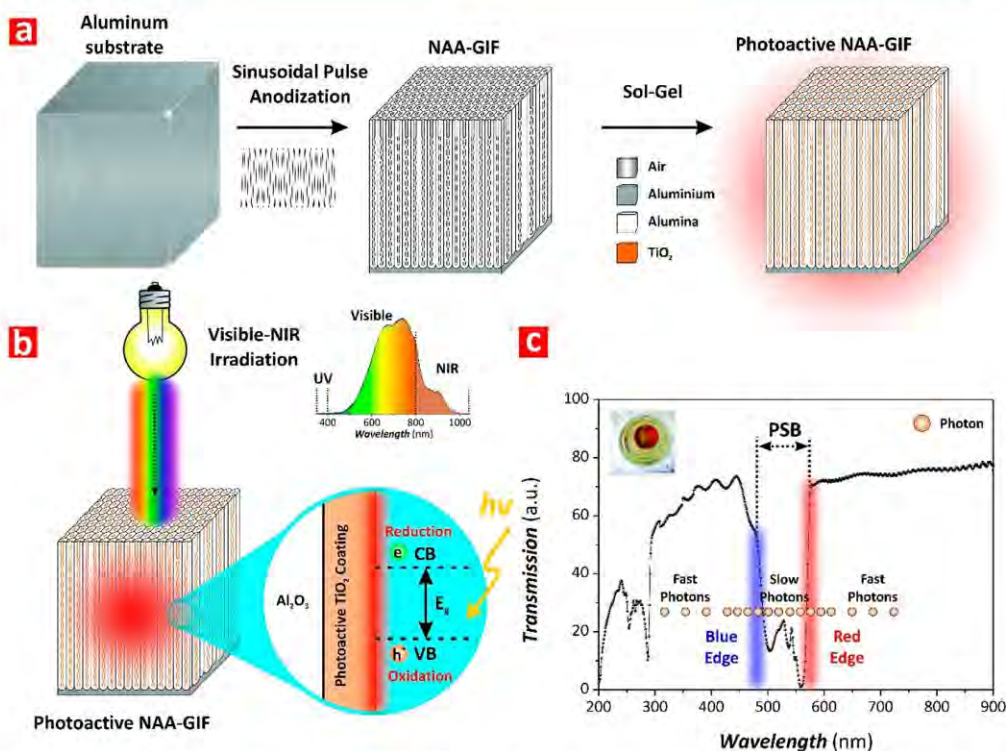
Figure 1. Conceptual illustration of the development and applicability of photoactive NAA-GIFs for photocatalysis. (a) Schematic representing the fabrication process of photoactive NAA-GIFs by sinusoidal pulse anodization (SPA) (left) and deposition of photoactive TiO$_2$ layers by sol−gel method (right). (b) Schematic showing the utilization of TiO$_2$-functionalized NAA-GIFs in photocatalysis under controlled vis−NIR irradiation conditions with details showing the chemical and electronic band structures of these composite photocatalysts, where CB = conduction band, VB = valence band, E_g = band gap energy level, and $h\nu$ = excitation energy. (c) Transmission spectrum of a TiO$_2$-functionalized NAA-GIF showing the blue and red edges of the photonic stopband (PSB) where photons slow down their group velocity after interacting with the PC structure (inset: digital image of that NAA-GIF structure produced with T_P = 650 s, A_J = 0.420 mA cm^{-2}, J_{offset} = 0.280 mA cm^{-2}, t_{an} = 20 h, and t_{pw} = 6 min).

with $\nu_g \sim 0$).[7] In semiconductor PCs, light absorption enhancement by slow photon effect is precisely engineered by the PCs' structure to generate extra e$^-$/h$^+$ pairs at those spectral regions where the semiconductor absorbs light poorly (e.g., TiO$_2$ in the visible/infrared) to enhance photon-to-electron conversion rates.[8−11] Nanoporous semiconductor PCs are of particular importance since these nanostructures offer (i) light-trapping capabilities to collect photons at high-irradiance spectral regions (e.g., visible), (ii) efficient percolation pathways for vectoral transfer of photopromoted electrons, (iii) high specific surface area that increases the number of photoactive centers for redox reactions, and (iv) nanoporous structure that facilitates mass transport of molecular species involved in redox reactions. Some proof-of-concept studies have identified "slow photon" effects in inverted opal PCs. However, these nanostructures have limited versatility to tune the features of the PSB, are restricted to 3D nanostructures, feature defects that act as light scattering centers, require long synthesis processes, and are constrained to small areas.[12]

Some studies to date have demonstrated the fabrication of nanotubular TiO$_2$-based PCs by electrochemical oxidation (i.e., anodization) of titanium substrates.[13,14] However, anodization of titanium does not allow sufficient control of the nanotubular structure of TiO$_2$ to create PC structures with versatile PSB since the hydrofluoric-acid-based (HF-based) electrolytes used progressively etch the nanotubes' walls during the anodization process.[15] Alternative nanoporous materials, such as nanoporous anodic alumina (NAA), can address these

limitations. NAA produced by anodization of aluminum in fact provides an excellent platform to develop PC structures due to its highly controllable and flexible nanoporous geometry, which can be precisely modulated in-depth to engineer its effective medium and create multidimensional (1D, 2D, and 3D) NAA-PCs with versatile PSB across the spectral regions.[16−23] NAA-PCs such as gradient-index filters,[16] optical microcavities,[22] and distributed Bragg reflectors[23] present as ideal platforms to utilize the "slow photon" effect for enhanced photocatalytic reactions. However, the wide energy band gap of NAA (i.e., 7.0−9.5 eV, deep UV region)[24,25] prevents the direct use of NAA-PCs for photocatalysis. Despite this intrinsic limitation, the chemical-modification of NAA-PCs with photoactive materials such as TiO$_2$ does provide an opportunity to develop new platform materials as highly efficient photocatalysts by a rational management of photons at the nanoscale.

Herein, we present the first rationally designed photocatalyst material based on a TiO$_2$-functionalized nanoporous anodic alumina gradient-index filter (NAA-GIF) as a platform to achieve enhanced photocatalytic performances. NAA-GIFs are synthesized by sinusoidal pulse anodization (SPA) approach and subsequently functionalized with photoactive layers of TiO$_2$ through sol−gel method (Figure 1a). We perform a systematic study on the effect of the PSB's features of photoactive NAA-GIFs, controlled by the anodization parameters (i.e., anodization period, anodization time, and pore widening time), on the photocatalytic performance of

151
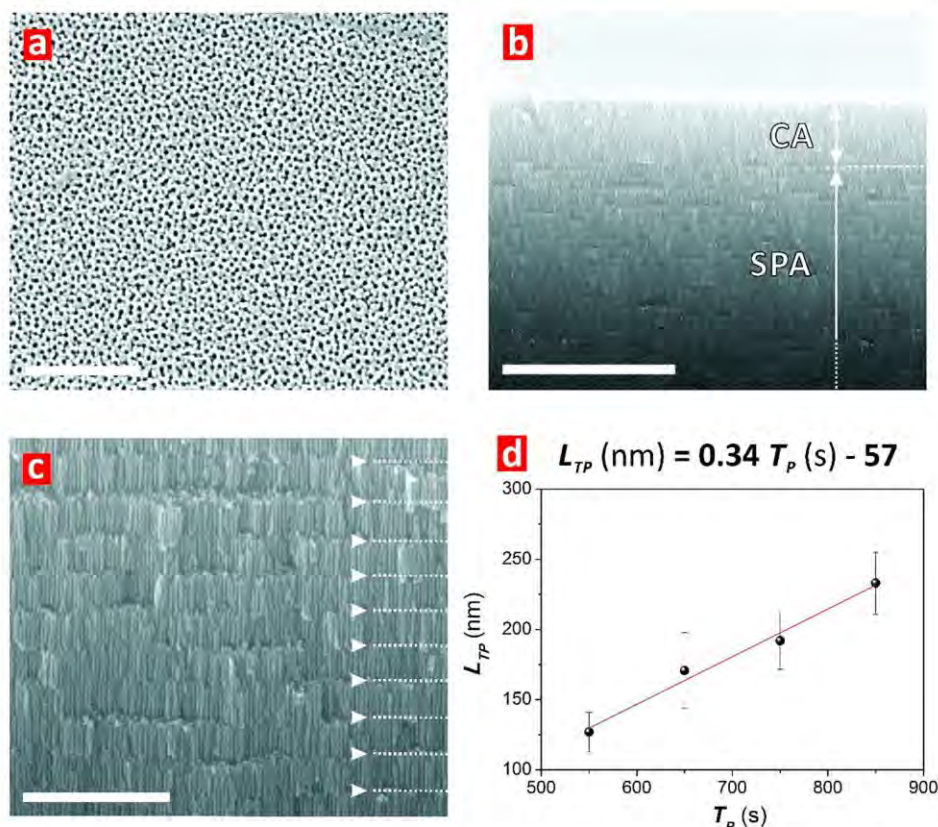
Figure 2. Representative FEG-SEM images of NAA-GIFs produced by the sinusoidal pulse anodization (SPA). (a) Top view FEG-SEM image of a NAA-GIF produced with T_P = 850 s, A_J = 0.420 mA cm^{-2}, J_{offset} = 0.280 mA cm^{-2}, t_{an} = 20 h, and t_{pw} = 6 min (scale bar = 500 nm). (b) General cross-sectional view FEG-SEM image of a NAA-GIF, where CA and SPA represent the constant (CA) and sinusoidal pulse (SPA) modes (scale bar = 5 μm). (c) Magnified view of part b showing details of the nanoporous structure of NAA-GIFs (scale bar = 1 μm) (Note: the layers between each consecutive white arrowhead denote the period length, L_{TP}). (d) Linear relationship between the period length (L_{TP}) and anodization period (T_P) in NAA-GIFs.

these PC structures (Figure 1b,c). Photocatalytic degradation of three model organic dyes (i.e., methyl orange, MO; methylene blue, MB; and Rhodamine B, RhoB) in these photoactive NAA-PCs provides a reference to identify and quantify slow photon effects for enhanced photocatalytic performances.

2. EXPERIMENTAL SECTION

2.1. Materials. High-purity (99.9997%) aluminum (Al) foils 0.32 mm thick were purchased from Goodfellow Cambridge Ltd. and used to produce NAA-GIFs by SPA. Sulfuric acid (H_2SO_4), phosphoric acid (H_3PO_4), hydrochloric acid (HCl), copper(II) chloride ($CuCl_2$), ethanol (EtOH, C_2H_5OH), titanium(IV) butoxide ($Ti(OBu)_4$), hydrogen peroxide (H_2O_2), methyl orange (MO), methylene blue (MB), and Rhodamine B (RhoB) were supplied by Sigma-Aldrich and used as received, without additional purification steps. Ultrapure Milli-Q water (18.2 MΩ cm) was used for the preparation of all the aqueous solutions in this study.

2.2. Fabrication of NAA-GIFs. NAA-GIFs were produced by sinusoidal pulse anodization (SPA) approach under current density control conditions.[16] The 1.5 × 1.5 cm^2 Al square chips were cleaned in EtOH and water under sonication for 15 min each and dried under air stream to remove any organic residues. These Al substrates were subsequently electropolished in a mixture of EtOH and HClO$_4$ 4:1 (v:v) at 20 V and 5 °C for 3 min. After electropolishing, the Al substrates were anodized at −1 °C in a 1.1 M H_2SO_4 aqueous solution with 25 vol % of EtOH to prevent it from freezing at temperatures below 0 °C.[26,27] The anodization process started with a

constant current density of 1.120 mA cm^{-2} for 1 h to achieve a homogeneous pore growth prior to SPA. The anodization profile was subsequently switched to sinusoidal pulse mode, where the anodization current density was pulsed between high (J_{max} = 1.120 mA cm^{-2}) and low (J_{min} = 0.280 mA cm^{-2}) current density values following eq 1:

$$J(t) = A_J\left[\sin\left(\frac{2\pi}{T_P}t\right) + 1\right] + J_{offset} \tag{1}$$

where $J(t)$ is the current density at a given time t, A_J is the current density amplitude, T_P is the anodization period, and J_{offset} is the current density offset.

NAA-GIFs provide an excellent platform to study "slow photon" effects due to their versatile PSB, the features of which (i.e., position of central wavelength and bandwidth) can be precisely engineered across the spectral regions by SPA. To investigate the effect of the anodization period (T_P) and the anodization time (t_{an}) on the photocatalytic performance of TiO$_2$-modified NAA-GIFs, we fabricated a set of NAA-GIFs with fixed A_J and J_{offset} at 0.420 and 0.280 mA cm^{-2}, respectively. In the first set of NAA-GIFs, T_P was systematically modified from 550 to 850 s, with ΔT_P = 100 s at fixed t_{an} = 20 h. The second set of NAA-GIFs was fabricated with varying t_{an} from 5 to 20 h, with Δt_{an} = 5 h and fixed T_P = 850 s. Note that NAA-GIFs were pore widened in an aqueous solution of 5 wt % H_3PO_4 at 35 °C. The pore widening time (t_{pw}) was modified from 0 to 6 min with Δt_{pw} = 2 min.

2.3. Surface Functionalization of NAA-GIFs with TiO$_2$. The surface of NAA-GIFs produced with different T_P (i.e., 550, 650, 750,

and 850 s) and t_{an} (i.e., 5, 10, 15, and 20 h) at t_{pw} = 6 min was chemically functionalized with photoactive layers of TiO_2 through sol−gel method.[28] TiO_2 sol was prepared in a beaker by magnetically mixing a mixture of titanium(IV) butoxide (3 mol %) and EtOH (97 mol %) for 10 min. NAA-GIFs were then dip-coated in the TiO_2 sol for 24 h. The surface-modified NAA-GIFs were subsequently washed with EtOH to remove any excess TiO_2 sol and titanium(IV) butoxide from the inner surface of these nanoporous PCs. After washing, the composite TiO_2−NAA-GIFs were dried in an oven at 50 °C for 10 min to evaporate any residual EtOH.

2.4. Optical Characterization. Prior to optical characterization, NAA-GIFs were chemically etched in a saturated solution of HCl/$CuCl_2$ using a 5 mm diameter circular window etching mask to dissolve the remaining Al substrate from the backside. Transmission spectra of chemically etched and pore widened NAA-GIFs, fabricated with different anodization parameters, were obtained in air and water from 200 to 800 nm at normal incidence (i.e., $\theta = 0°$) using a UV−vis spectrophotometer (Cary 300, Agilent, USA). The absorption spectra of 5 mg L^{-1} organic dyes solution in a polystyrene cuvette of 10 mm path length were acquired from 200 to 800 nm to determine the absorption band of organic dyes (i.e., MO, MB, and RhoB). To characterize the interferometric color of NAA-GIFs, digital pictures with a black background were acquired using a Canon EOS 700D digital camera, which was equipped with a Tamron 90 mm F2.8 VC USD macromount lens with autofocus function under natural light illumination.

2.5. Photocatalytic Degradation of Organic Dyes. The photocatalytic performance of TiO_2-modified NAA-GIFs produced with different T_P and t_{an} was assessed by monitoring the photocatalytic degradation of three different organic dyes with well-defined absorption bands (i.e., MO, λ_{abs-MO} = 464 nm; RhoB, $\lambda_{abs-RhoB}$ = 554 nm; and MB, λ_{abs-MB} = 664 nm) under simulated solar light irradiation conditions. A 2 mL portion of a mixture of 5 mg L^{-1} of dye and 0.1 M H_2O_2 solution was pipetted into a transparent cuvette. The TiO_2-functionalized NAA-GIFs, which had an effective area of 1 cm^2, were then placed in the cuvette filled with the dye mixture. The solution was magnetically stirred in a dark vessel (solar simulator) for 30 min to achieve the adsorption−desorption equilibrium prior to irradiation. This was then illuminated with simulated solar light irradiation using a 150 W (~3000 lm) halogen lamp (HL250-A, Amscope) at room temperature. To determine the concentration of dye at specific time intervals, the absorbance of the absorption band of the solution at each illumination time interval (i.e., 30 min) was analyzed by a UV−vis spectrophotometer. Calibration lines establishing the relationship between the solution absorbance and the concentration of each dye were used to determine the photocatalytic conversion ratio (C_t/C_o), where C_o is the concentration of solution after stirring in the dark for 30 min, and C_t is the concentration at illumination time t (Figure S1, Supporting Information). This parameter was evaluated to determine the kinetic model for this photocatalytic system as a function of the TiO_2−NAA-GIFs and the model dye molecule. Note that these experiments were also performed with nonfunctionalized NAA-GIFs (i.e., NAA-GIFs without TiO_2 functional layer), which were used as control samples.

2.6. Chemical and Structural Characterization. The morphology and geometric features of NAA-GIFs were characterized using field emission gun scanning electron microscopy (FEG-SEM FEI Quanta 450). FEG-SEM images acquired were analyzed by ImageJ software (public domain program developed at the RSB of the NIH).[29] The chemical compositions of NAA-GIFs before and after surface functionalization with TiO_2 were analyzed by energy dispersive X-ray (EDX) spectroscopy during FEG-SEM characterization. The chemical structure of NAA-GIFs was further characterized by Fourier transform infrared (FTIR Nicolet 6700) spectroscopy and X-ray diffraction (XRD Rigaku MiniFlex 600).

3. RESULTS AND DISCUSSION

3.1. Structural Characterization of NAA-GIFs. Figure 2 presents a set of representative FEG-SEM images of the NAA-

GIFs produced in this study. A top view FEG-SEM image is shown in Figure 2a to reveal evenly and randomly distributed nanopores of NAA-GIFs across the surface, where the average pore diameter (d_p) was measured to be 17 ± 3 nm after a pore widening treatment of 6 min. The cross-sectional view FEG-SEM images (Figure 2b,c) show the in-depth modulation of porosity of NAA-GIFs following the sinusoidal current density profile applied during SPA. The distances between adjacent layers with sinusoidally modulated porosity, defined as the period length (L_{TP}), correspond to each pulse in the SPA profile, and it is visually indicated by the white arrowheads shown in Figure 2c. The image analysis revealed a linear correlation between the anodization period (T_p) and L_{TP}, where L_{TP} increases at a rate of 0.34 nm s^{-1} with increasing T_P (Figure 2d).

3.2. Effect of the Anodization Parameters on the Optical Properties of NAA-GIFs. Figure S2 (Supporting Information) shows the intrinsic relationship between the fabrication parameters [i.e., anodization period (T_P), pore widening time (t_{pw}), and anodization time (t_{an}) or number of anodization pulses ($N_P = t_{an}/T_P$)] with the optical properties [i.e., central wavelength (λ_C) of the PSB and interferometric color] of NAA-GIFs. The combined effect of T_P and t_{pw} on the position of the characteristic PSB of NAA-GIFs was systematically studied by modifying T_P from 550 to 850 s with ΔT_P = 100 s, and t_{pw} from 0 to 6 min with Δt_{pw} = 2 min, at a fixed t_{an} of 20 h (Figure S2a). Linear fittings demonstrate the correlation between T_P and λ_C, of which the slopes of the linear fittings were found to be 0.79 ± 0.09, 0.81 ± 0.12, 0.65 ± 0.16, and 0.78 ± 0.16 nm s^{-1} for t_{pw} = 0, 2, 4, and 6 min, respectively. The position of the PSB of these NAA-GIFs can be tuned from 415 ± 1 nm (T_P = 550 s and t_{pw} = 6 min) to 715 ± 1 nm (T_P = 850 s and t_{pw} = 0 min) within the range of fabrication parameters studied. This analysis demonstrates that λ_C red-shifts with T_P, where the optical characteristic of NAA-GIFs shows the strongest dependence on T_P at t_{pw} = 2 min (i.e., sharpest slope −0.81 ± 0.12 nm s^{-1}). As per previous studies,[16] λ_C blue-shifts its position with t_{pw}. Figure S2b illustrates the combined effect of t_{an} (or N_P) and t_{pw} on the λ_C of NAA-GIFs, where t_{an} was systematically modified from 5 to 20 h (i.e., from 22 to 85 pulses) with an interval of 5 h (i.e., 21 pulses), and t_{pw} from 0 to 6 min with an interval of 2 min, while T_P was fixed at 850 s. This graph denotes that λ_C fluctuates around an average value with t_{an} (N_P) and blue-shifts its position with t_{pw}.[16] Figure S2c,d compiles digital pictures of NAA-GIFs produced with different T_P and t_{an} as a function of t_{pw}, respectively. The digital images shown in Figure S2c reveal that as-produced NAA-GIFs (i.e., t_{pw} = 0 min) display vivid colors such as blue and red−orange for T_P = 550 and 650 s, respectively. However, these NAA-GIFs are transparent (i.e., black background, NIR region) for T_P = 750 and 850 s at t_{pw} = 0 min. Note that the interferometric color correlates with the position of the characteristic PSB within the UV−vis−NIR spectrum. As t_{pw} increases, the interferometric color of NAA-GIFs is blue-shifted, becoming blue, cyan, chartreuse, and yellow at t_{pw} = 6 min for NAA-GIFs produced at T_P = 550, 650, 750, and 850 s, respectively. This effect is also observed for NAA-GIFs produced at different anodization times. Figure S2d shows digital pictures of NAA-GIFs produced at t_{an} = 5, 10, 15, and 20 h. At t_{pw} = 0 min, all the NAA-GIFs have located their PSB in the NIR range of the spectrum (i.e., transparent). As t_{pw} increases, the PSB is blue-shifted to the visible range, and interferometric colors rise. NAA-GIFs
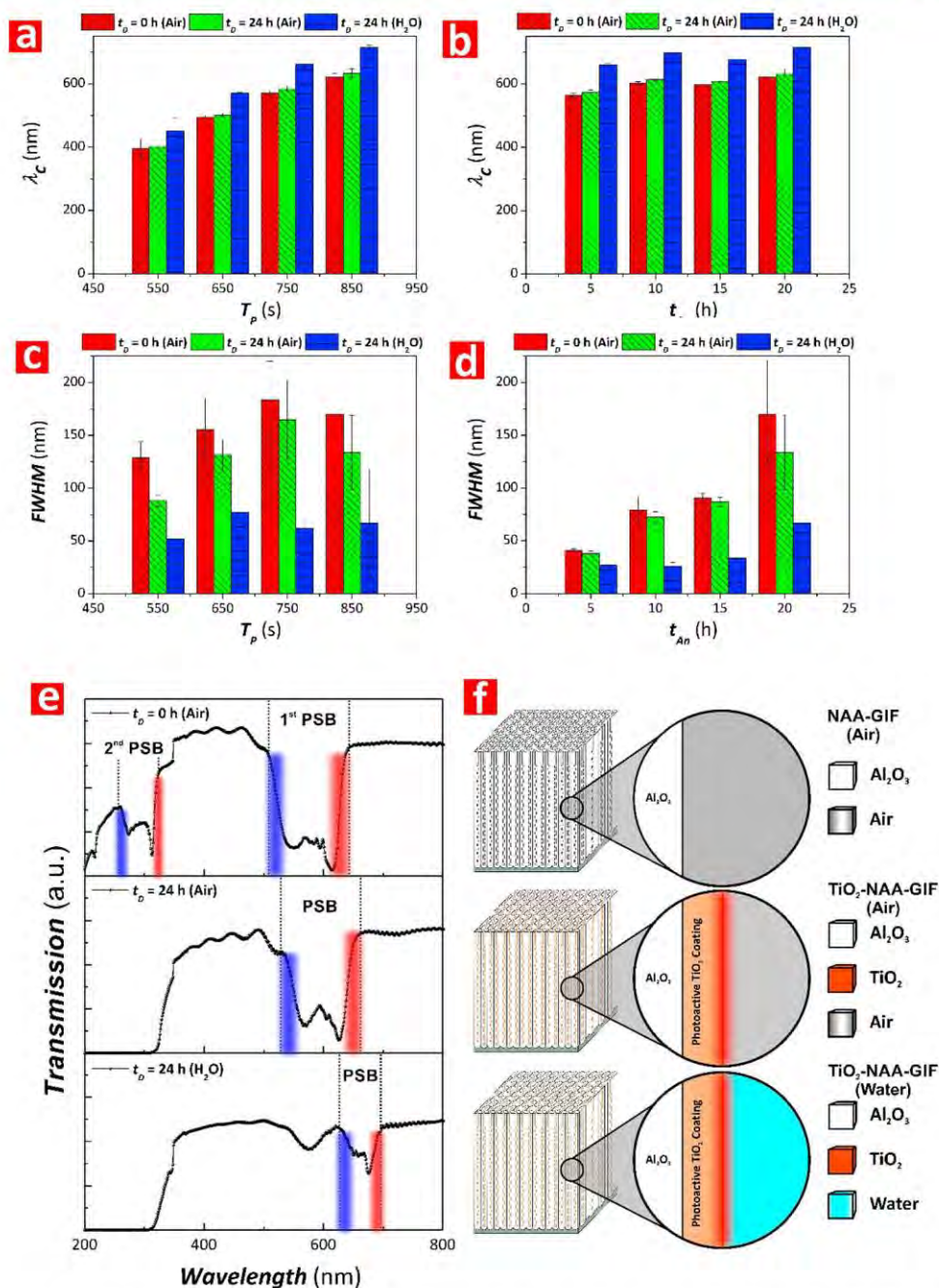
Figure 3. Assessment of optical properties of NAA-GIFs in different media after surface functionalization with TiO_2 layers. (a, b) Bar charts showing the effect of surface-modification parameters on the position of the central wavelength (λ_C) of NAA-GIFs fabricated with t_{pw} = 6 min and varying T_P (i.e., 550, 650, 750, and 850 s) and t_{an} (i.e., 5, 10, 15, and 20 h), respectively. (c, d) Bar charts showing the effect of surface functionalization on the full width at half-maximum (fwhm) of NAA-GIFs fabricated with t_{pw} = 6 min and varying T_P (i.e., 550, 650, 750, and 850 s) and t_{an} (i.e., 5, 10, 15, and 20 h), respectively. (e) Representative transmission spectra of a NAA-GIF produced with T_P = 750 s, A_J = 0.420 mA cm^{-2}, J_{offset} = 0.280 mA cm^{-2}, t_{an} = 20 h, and t_{pw} = 6 min showing the evolution of the PSB with the deposition time and the media filling the nanopores (from top to bottom: NAA-GIF in air, TiO_2-functionalized NAA-GIF in air, and TiO_2-functionalized NAA-GIF in water). (f) Schematic illustration showing the chemical composition and the media filling the nanopores in the scenarios shown in part e.

produced at t_{an} = 5, 10, 15, and 20 h display vivid green, orange, chartreuse, and yellow color at t_{pw} = 6 min. To summarize, the anodization parameters T_P, t_{an}, and t_{pw} can be used to engineer the optical properties (i.e., λ_C and interferometric color) of NAA-GIFs. All the anodization parameters allow the precise tuning of the position of

characteristic PSB of NAA-GIFs across the entire UV−vis−NIR spectrum.

3.3. Chemical Analysis of TiO_2-Functionalized NAA-GIFs. Photoactive NAA-GIFs were produced by modifying the inner surface of NAA-GIFs with photoactive layers of TiO_2 deposited by sol−gel method. Figure S3 (Supporting

Information) shows energy dispersive X-ray (EDX), Fourier transform infrared (FTIR), and X-ray diffraction (XRD) spectra of NAA-GIFs before and after surface functionalization. These analyses demonstrate successful TiO_2-modification of the inner surface of NAA-GIFs after 24 h. Figure S3a shows the EDX spectrum of as-produced NAA-GIFs, which shows the characteristic peaks of O (12%), Al (79%), P (4%), and S (5%). These elements correspond to the alumina structure (Al_2O_3) contaminated by sulfur and phosphorus atoms incorporated into the Al_2O_3 structure during the anodization and pore widening steps, respectively. EDX spectrum of TiO_2-functionalized NAA-GIFs shows characteristic peaks of Ti and an increment of the percentage of O atoms, which denote the presence of TiO_2 in the composite structure. The relative percentage of elements in TiO_2-modified NAA-GIFs was found to be O (23%), Al (64%), P (4%), S (5%), and Ti (4%). The confirmation of the successful deposition of TiO_2 onto the inner surfaces of NAA-GIFs is also demonstrated in FTIR analysis (Figure S3b), which shows three main transmission peaks related to TiO_2 after surface functionalization (i.e., 1530, 1622, and 3263 nm). These transmission peaks are in good agreement with those reported in previous studies for TiO_2 nanoparticles.[30,31] XRD spectra of as-produced and TiO_2-functionalized NAA-GIFs are shown in Figure S3c. As-produced NAA-GIFs present three characteristic peaks in their XRD spectra located at 45°, 65°, and 78°, which correspond to an amorphous alumina (Al_2O_3) phase. The deposition of the TiO_2 functional layer does not generate any additional peak in the XRD spectra, indicating that the TiO_2 layer is crystallographically amorphous. However, the position of these peaks undergoes a slight shift and decrease their intensity. Thus, our chemical analysis confirms the successful deposition of photoactive layers of TiO_2 onto the inner surface of NAA-GIFs to endow these PC structures with photocatalytic activity.

3.4. Effect of TiO_2 Modification on the Optical Properties of NAA-GIFs.

The characteristics of the PSB of photoactive PC structures enable the design and engineering of materials that can make an optimal utilization of the "slow photon" effect for photocatalysis. The effect of surface functionalization on the optical properties of TiO_2-modified NAA-GIFs was studied by varying the deposition time (t_D) of TiO_2 layers from 0 to 24 h and characterized the position of the PSB (λ_C) and its full width at half-maximum (fwhm) in different media (i.e., air and water) filling the nanoporous network of NAA-GIFs. Figure 3 shows the effect of TiO_2 surface functionalization of NAA-GIFs produced with different T_P (i.e., 550, 650, 750, and 850 s) and t_{an} (5, 10, 15, and 20 h) at t_{pw} = 6 min and t_D = 0 and 24 h on the features of the PSB of NAA-GIFs. Figure 3a,b summarizes the dependency of λ_C on t_D and the medium filling the nanopores for the NAA-GIFs assessed in our study. These bar charts demonstrate that, after functionalization with TiO_2 for 24 h, the position of characteristic PSB of NAA-GIFs in air is red-shifted at a rate of 8.9 ± 3.5 nm s^{-1} and 10.5 ± 0.9 nm h^{-1} for T_P and t_{an}, respectively. Modification of the inner surface of NAA-GIFs, with a thin layer of TiO_2, red-shifts progressively the PSB due to the higher refractive index of TiO_2 with respect to Al_2O_3 (i.e., $n_{Al_2O_3}$ = 1.70 RIU and n_{TiO_2} = 2.40 RIU) and the physical reduction of the nanopore diameter of NAA-GIFs. Figure S4 (Supporting Information) shows the effect of the deposition time of TiO_2 on the PSB of NAA-GIFs. This slight red-shift

denotes that the deposited photoactive layer of TiO_2 is thin. In contrast, λ_C undergoes a more significant red-shift when the nanoporous network of surface-modified NAA-GIFs is filled with water (i.e., media in which the photocatalytic reactions occur). Infiltration of these nanoporous PCs with a medium of a higher refractive index than that of air (i.e., n_{air} = 1.00 RIU and n_{water} = 1.33 RIU) leads to a red-shift in the position of the characteristic PSB, 69.2 ± 14.7 nm s^{-1} and 80.5 ± 7.6 nm h^{-1} for T_P and t_{an}, respectively. Figure 3c,d shows the effect of the TiO_2 functionalization and the water infiltration on the fwhm of the PSB of NAA-GIFs produced with various T_P and t_{an}. It is apparent from these figures that fwhm is narrowed at a rate of 29.8 ± 10.3 nm s^{-1} and 12.1 ± 15.8 nm h^{-1} for T_P and t_{an}, respectively, after modifying the inner surface of NAA-GIFs with photoactive TiO_2 layers. Infiltration of the nanopores of TiO_2-functionalized NAA-GIFs with water produces a more significant narrowing of the fwhm. Thus, fwhm narrows its width after infiltration at 65.1 ± 28.2 nm s^{-1} and 44.4 ± 23.9 nm h^{-1} for T_P and t_{an}, respectively. The narrowing of the fwhm of the PSB is associated with the light absorption[16,32] by the deposited layer of TiO_2 and the medium filling the nanopores of NAA-GIFs. A comparative analysis of the effect of both factors reveals that the latter (i.e., water infiltration) produces a more significant effect in the narrowing of the fwhm due to the absorption of incoming light by the water molecules. Figure 3e,f shows representative transmission spectra and schematic illustrations of a NAA-GIF produced with T_P = 750 s and t_{pw} = 6 min at t_D = 0 and 24 h in air and water. This reveals that the position of the characteristic PSB red-shifts while the bandwidth of the PSB is narrowed after surface functionalization with TiO_2 layers and water infiltration. With reference to air, the second-order PSB of the NAA-GIF is located at 288 ± 1 nm before surface-modification with TiO_2 layers. However, the second-order PSB vanishes after the NAA-GIF is modified with TiO_2 layers, which can be associated with the strong light absorption by the TiO_2 layer in the UV region (<380 nm).[33] This further confirms successful modification of the inner surface of NAA-GIFs with photoactive TiO_2 layers, which is in good agreement with the results obtained by EDX and FTIR analyses (Figure S3, Supporting Information).

To summarize, the position and bandwidth of the PSB of NAA-GIFs are precisely tuned across the spectral regions by the manipulation of T_P, t_{an}, and t_D. The relationship between fabrication parameters and features of the PSB of photoactive NAA-GIFs provide an optimal platform to study and engineer the "slow photon" effect for photocatalytic applications. TiO_2 functional layers cannot use photons from the visible and NIR spectral regions for photocatalysis due to its electronic band gap. However, TiO_2-functionalized NAA-GIFs with PSB positioned at the visible and NIR regions can enable the utilization of these high-irradiance sunlight regions to speed up photocatalytic reactions.

3.5. Understanding the "Slow Photon" Effect in TiO_2-Functionalized NAA-GIFs.

The photocatalytic performances of TiO_2-modified NAA-GIFs fabricated at t_{pw} = 6 min and different T_P (i.e., 550, 650, 750, and 850 s) and t_{an} (i.e., 5, 10, 15, and 20 h) were assessed by studying the photocatalytic degradation of three model organic dyes (i.e., MO, RhoB, and MB) under simulated solar light irradiation. Figure S5 (Supporting Information) presents absorption spectra of MO, RhoB, and MB with the corresponding absorption bands at 464, 554, and 664 nm, respectively. Figure S6 (Supporting Information) displays the spectral properties of
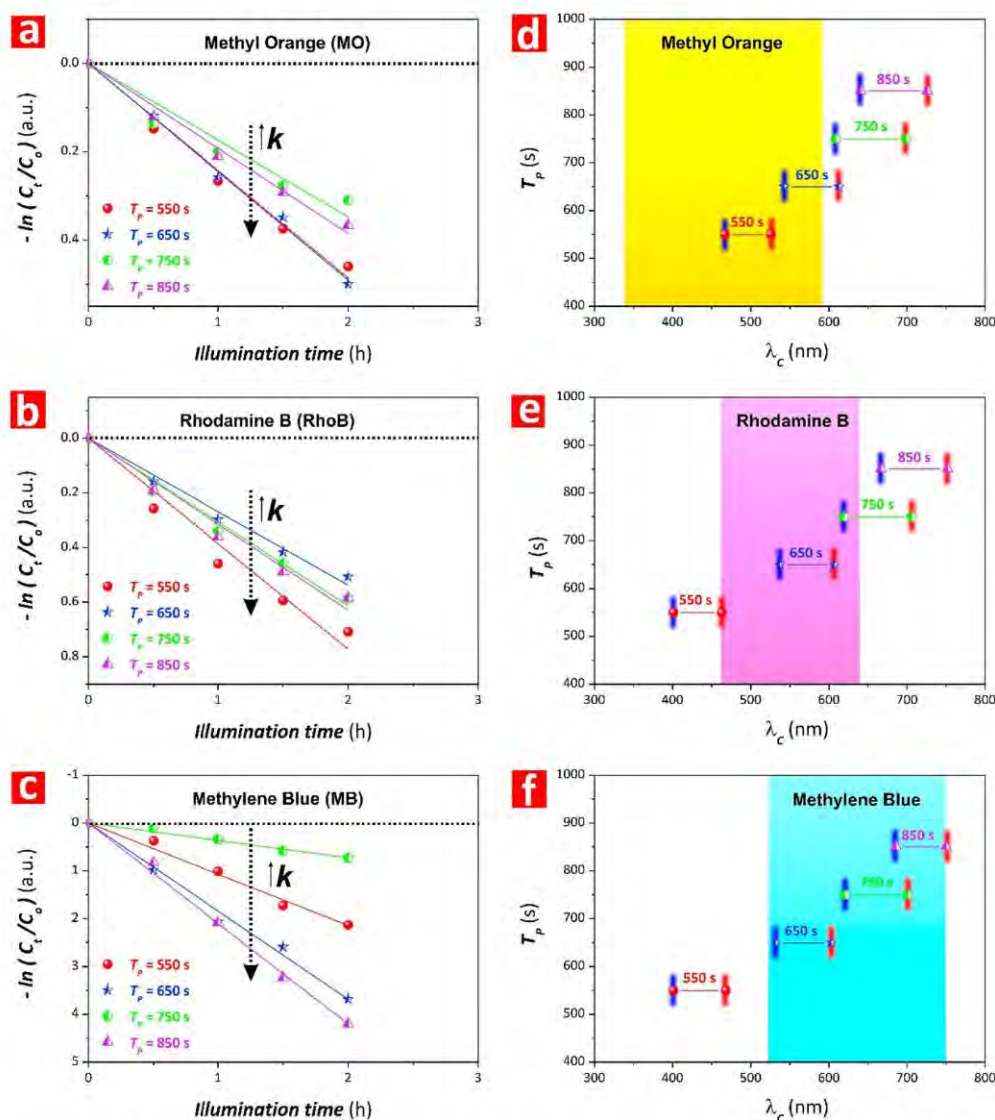
Figure 4. Tuning the blue and red edges of the PSB of TiO_2-functionalized NAA-GIFs produced with different T_P to utilize the "slow photon" effect for the photocatalytic degradation of model organic dyes. (a−c) Photocatalytic degradation kinetics of MO, RhoB, and MB by TiO_2-modified NAA-GIFs fabricated with different T_P = 550, 650, 750, and 850 s under controlled irradiation conditions, respectively (note: black dotted lines denote the photodegradation of the corresponding dye in control NAA-GIFs without functional TiO_2 layer). (d−f) Relative position of the blue and red edges of the characteristic PSB of TiO_2-functionalized NAA-GIFs produced with T_P = 550, 650, 750, and 850 s and the absorption band of MO, RhoB, and MB, respectively (note: blue and red vertical lines on the PSB of NAA-GIFs correspond to the position of the blue and red edges of the PSB).

the artificial illumination used in our study to simulate sunlight irradiation. This graph reveals the spectral distribution to be 0.12% for UV (350−400 nm), 82.60% for visible (400−800 nm), and 17.28% for NIR (800−1025 nm), which is essentially within the visible region. Therefore, liquid-phase photocatalytic degradation of the model organic dyes in our study is mostly driven by visible light irradiation. Note that these reactions were performed with the addition of 0.1 M H_2O_2 solution to aid in the photogeneration of charge carriers in the TiO_2 photoactive layers. The photocatalytic performances of TiO_2-modified NAA-GIFs were measured and fitted to the pseudo-first-order kinetics model shown in eq 2:

$$-\ln\left(\frac{C_t}{C_o}\right) = kt \qquad (2)$$

where C_o is the adsorption−desorption equilibrium concentration of model dye, C_t is the reaction concentration of model dye at time t, and k is the kinetic constant.

The residual concentration of each dye after 2 h of photocatalytic reaction (C_R) was estimated using the calibration lines shown in Figure S1, and the obtained results are summarized in Tables S1 and S2 (Supporting Information).

3.5.1. Effect of Anodization Period on the Photocatalytic Performance of TiO_2−NAA-GIFs. The origin of the "slow photon" effect in photoactive NAA-GIFs is

Table 1. Values of the Kinetic Constant (k) for the Photodegradation of MO, RhoB, and MB Molecules in TiO$_2$-Functionalized NAA-GIFs Produced with T_P = 550, 650, 750, and 850 s

	anodization period			
organic dye	550 s	650 s	750 s	850 s
MO	0.24 ± 0.01 h^{-1}	0.25 ± 0.01 h^{-1}	0.17 ± 0.01 h^{-1}	0.19 ± 0.01 h^{-1}
RhoB	0.39 ± 0.02 h^{-1}	0.27 ± 0.01 h^{-1}	0.30 ± 0.01 h^{-1}	0.31 ± 0.01 h^{-1}
MB	1.07 ± 0.04 h^{-1}	1.84 ± 0.09 h^{-1}	0.36 ± 0.01 h^{-1}	2.10 ± 0.07 h^{-1}

associated with the features of the PC's PSB, where photons from the incoming light reduce group velocity at the wavelengths of the blue and red edges of the PSB. As demonstrated, NAA-GIFs are a perfect platform to study this light–matter interaction since the PSB can be engineered with precision and versatility across the spectral regions by SPA. This provides a unique opportunity to control the interaction between photons and the nanoporous PC structure to generate extra e$^-$/h$^+$ at those spectral regions where the photocatalyst material is intrinsically limited (i.e., visible and NIR for TiO$_2$). Figure 4 and Table 1 summarize the photocatalytic degradation performances of MO, RhoB, and MB in TiO$_2$-functionalized NAA-GIFs with varying T_P, from 550 to 850 s under controlled illumination conditions. Figure 4a−c shows the linearized pseudo-first-order kinetics for these photocatalytic processes, and Figure 4d−f shows the relationship between the blue and red edges of the characteristic PSB of TiO$_2$-modified NAA-GIFs and the absorption band of MO, RhoB, and MB.

The kinetic constant (k) for the photocatalytic degradation of MO by TiO$_2$-functionalized NAA-GIFs with T_P = 550, 650, 750, and 850 s were 0.24 ± 0.01, 0.25 ± 0.01, 0.17 ± 0.01, and 0.19 ± 0.01 h^{-1}, respectively (Figure 4a and Table 1). k values were higher for TiO$_2$-modified NAA-GIFs produced with shorter T_P (i.e., 550 and 650 s) than for those fabricated with longer T_P (i.e., 750 and 850 s), indicating that NAA-GIFs produced with shorter anodization period can photodegrade MO at faster rates than their counterparts produced with longer T_P. For instance, the photodegradation of MO in TiO$_2$-modified NAA-GIFs fabricated with T_P = 550 s is 29% and 21% faster than that in TiO$_2$-functionalized NAA-GIFs produced with T_P = 750 and 850 s, respectively. In the case of TiO$_2$-modified NAA-GIFs fabricated with T_P = 650 s, the photodegradation efficiency difference increases to 32% and 24% as compared to their counterparts fabricated with T_P = 750 and 850 s, respectively.

This enhancement in photodegradation performance is associated with the "slow photon" effect in these PC structures. Figure 4d reveals that the PSB of TiO$_2$-modified NAA-GIFs produced with T_P = 550 and 650 s overlaps completely and partially with the absorption band of MO, respectively. The blue (i.e., blue vertical line) and red (i.e., red vertical line) edges of the PSB of TiO$_2$-functionalized NAA-GIFs with T_P = 550 and 650 s are located within the absorption band of MO (i.e., $\lambda_{\text{blue-550s}}$ = 466 nm, $\lambda_{\text{red-550s}}$ = 527 nm, $\lambda_{\text{blue-650s}}$ = 543 nm, $\lambda_{\text{red-650s}}$ = 613 nm, and $\lambda_{\text{abs-MO}}$ = 464 nm). Under illumination, groups of incoming photons propagate with strongly reduced group velocity at the vicinity of the PC's PSB and localize in high (i.e., photocatalysts) and low (i.e., dye and pores) dielectric parts of the red and blue edge of the PC's PSB, respectively.[34] Photocatalytic degradation of MO would thus be expected to be significantly enhanced in those spectral regions where the edges of the PSB are located in the proximity of the absorption band of MO due to enhancement

in the photon-to-electron conversion rate.[34−36] Our results and analysis confirm this hypothesis since the PSB of TiO$_2$-modified NAA-GIFs produced with T_P = 550 and 650 s are within the absorption band of MO. The slightly higher performance shown by TiO$_2$−NAA-GIFs produced with T_P = 650 s could be associated with the wider PSB of these PC structures (Figure 3c, fwhm$_{550s}$ = 52 ± 18 nm and fwhm$_{650s}$ = 77 ± 25 nm) and its relative position with respect to the absorption band of MO (i.e., $\lambda_{\text{C-550s}}$ = 450 ± 4 nm, $\lambda_{\text{C-650s}}$ = 571 ± 2 nm, and $\lambda_{\text{abs-MO}}$ = 464 nm). In contrast, the characteristic PSB of TiO$_2$-modified NAA-GIFs produced with T_P = 750 and 850 s is located completely outside the absorption band of MO, as shown in Figure 4d, where the latter is located the furthest away. In this region, the photocatalytic performance of these photoactive PC structures is independent of the "slow photon" effect, relying exclusively on the geometric features of the nanoporous PC structure and the irradiation conditions. The better photocatalytic performance shown by NAA-GIFs produced with T_P = 850 s is likely attributable to the enhanced mass transfer and light utilization efficiency by the photoactive TiO$_2$ layers at those spectral regions of higher irradiance due to the increment in T_P that results in longer L_{TP}.

Figure 4b shows the fitting lines for the photocatalytic degradation of RhoB by TiO$_2$-modified NAA-GIFs produced with T_P = 550, 650, 750, and 850 s, the k values of which were found to be 0.39 ± 0.02, 0.27 ± 0.01, 0.30 ± 0.01, and 0.31 ± 0.01 h^{-1}, respectively (Table 1). The best photocatalytic performance was achieved by TiO$_2$-modified NAA-GIFs produced with T_P = 550 s, which is ∼21−31% higher than that shown by NAA-GIFs produced with longer anodization periods (i.e., 650, 750, and 850 s). As Figure 4e shows, the red edge of the PSB of TiO$_2$-functionalized NAA-GIFs fabricated with T_P = 550 s is positioned within the absorption band of RhoB, while the blue edge falls outside of the absorption region (i.e., $\lambda_{\text{blue-550s}}$ = 466 nm, $\lambda_{\text{red-550s}}$ = 527 nm, and $\lambda_{\text{abs-RhoB}}$ = 554 nm). Similarly, the blue edge of the PSB of NAA-GIFs fabricated with T_P = 750 s is partially within the absorption range of RhoB (i.e., $\lambda_{\text{blue-650s}}$ = 543 nm). The red edge of the PSB of NAA-GIFs that are produced with T_P = 550 s is within the absorption band of RhoB, leading to an enhanced absorption of light that results in the highest degradation rate for RhoB ($k_{\text{RhoB-550s}}$ = 0.39 ± 0.02 h^{-1}) due to the generation of extra e$^-$/h$^+$ pairs at these spectral regions. This phenomenon is confirmed in the case of the blue edge of the PSB of NAA-GIFs fabricated with T_P = 750 s, although the photocatalytic performance of this configuration is less photocatalytically efficient ($k_{\text{RhoB-750s}}$ = 0.30 ± 0.01 h^{-1}). The PSB of TiO$_2$-modified NAA-GIFs produced with T_P = 650 s is approximately at the center of the absorption band of RhoB. However, these PCs achieved the worst photocatalytic degradation performance for RhoB molecules ($k_{\text{RhoB-650s}}$ = 0.27 ± 0.01 h^{-1}). As Figure S5 reveals, the intensity of the absorption band of RhoB (i.e., ∼3.6 au) is significantly higher

157

than that of MO (i.e., ~1.5 au) at its central position ($\lambda_{\text{abs-RhoB}}$ = 554 nm). At these spectral regions, RhoB molecules absorb most of the incoming light that propagates through the aqueous organic dye before it reaches the surface of the TiO$_2$–NAA-GIFs, reducing the photocatalytic performance of the material due to light screening effect. The PSB of TiO$_2$-modified NAA-GIFs produced with T_P = 850 s is completely outside the absorption band of RhoB (Figure 4e), although the photocatalytic performance shown by these photoactive PCs to degrade RhoB was found to be comparable to that achieved by NAA-GIFs fabricated with T_P = 750 s ($k_{\text{RhoB-850s}}$ = 0.31 ± 0.01 h^{-1}). In this scenario, photocatalytic performance is exclusively dependent on the geometric features of the PC and on the irradiation conditions than on the "slow photon" effect. These NAA-GIFs have the longest period length (L_{TP}), which facilitates the mass transfer of reactive species along the nanoporous structure and increases the number of photoactive sites, leading to enhanced photodegradation rates. Our analysis clearly demonstrates that the most effective approach to utilize "slow photon" effect in TiO$_2$-modified NAA-GIFs to degrade RhoB molecules is to match the red edge of the PSB of these PCs with the blue and red edges of the absorption band of RhoB.

Figure 4c presents the photocatalytic degradation of MB by TiO$_2$-functionalized NAA-GIFs produced with T_P = 550, 650, 750, and 850 s. The degradation rates achieved by these photoactive PCs were found to be k = 1.07 ± 0.04, 1.84 ± 0.09, 0.36 ± 0.01, and 2.10 ± 0.07 h^{-1}, respectively (Table 1). The highest photodegradation rate of MB was performed by TiO$_2$-modified NAA-GIF fabricated with T_P = 850 s, which was from ~11% to 83% better than NAA-GIF counterparts produced with shorter anodization periods. As Figure 4f shows, the red edge of the PSB of these PCs matches the red edge of the absorption band of MB (i.e., $\lambda_{\text{blue-850s}}$ = 685 nm, $\lambda_{\text{red-850s}}$ = 750 nm, and $\lambda_{\text{abs-MB}}$ = 664 nm). On the other hand, TiO$_2$-modified NAA-GIFs produced with T_P = 750 s displayed the worst performing photocatalytic performance to degrade MB (i.e., $k_{\text{MB-750s}}$ = 0.36 ± 0.01 h^{-1}), which was approximately 6 times slower rate than that of NAA-GIFs produced with T_P = 850 s. According to Figure 4f, the PSB of TiO$_2$-modified NAA-GIFs fabricated with T_P = 750 s is entirely within the absorption band of MB (i.e., $\lambda_{\text{blue-750s}}$ = 621 nm, $\lambda_{\text{red-750s}}$ = 702 nm, and $\lambda_{\text{abs-MB}}$ = 664 nm). Likewise in the photocatalytic degradation of RhoB, the poor photocatalytic performance shown by these PCs can be ascribed to the high absorbance intensity of MB (i.e., ~2.9 au) (Figure S5, Supporting Information), which hinders the incoming photons from reaching the surface of TiO$_2$-modified NAA-GIFs to generate e$^-$/h$^+$ pairs to photodegrade MB molecules absorbed onto the inner surfaces. As Figure 4c shows, TiO$_2$-functionalized NAA-GIFs produced with T_P = 650 s achieved the second-best performance to degrade MB molecules, with $k_{\text{MB-650s}}$ = 1.84 ± 0.09 h^{-1}. An analysis of the relative position of the blue and red edges of the PSB of these photoactive PC structures with respect to the absorption band of MB (Figure 4f) reveals that the PSB's blue edge is well-matched with the blue edge of the absorption band of MB (i.e., $\lambda_{\text{blue-650s}}$ = 531 nm, $\lambda_{\text{red-650s}}$ = 602 nm, and $\lambda_{\text{abs-MB}}$ = 664 nm). This configuration results in enhancement of the photodegradation of these molecules due to "slow photon" effect. However, these TiO$_2$-modified NAA-GIFs undergo photodegradation at a rate ~11% slower than those produced at T_P = 850 s. Finally, Figure 4c shows that the PSB of TiO$_2$-functionalized NAA-GIFs produced with T_P =

550 s is located completely away from the absorption band of MB. Therefore, the photocatalytic performance to degrade the MB molecules by these PCs is associated with the geometric features of the NAA-GIF structure and the irradiation conditions, without contribution from "slow photon" effects. These PC structures showed the second-worst degradation rate of this set of NAA-GIFs, with a $k_{\text{MB-550s}}$ = 1.07 ± 0.04 h^{-1}.

To summarize, a systematic analysis on the effect of T_P on the photocatalytic degradation of three model organic dye molecules (MO, RhoB, and MB) by TiO$_2$-functionalized NAA-GIFs is presented. Our study establishes that the maximum degradation rates for MO, RhoB, and MB were $k_{\text{MO-650s}}$ = 0.25 ± 0.01 h^{-1}, $k_{\text{RhoB-550s}}$ = 0.39 ± 0.02 h^{-1}, and $k_{\text{MB-850s}}$ = 2.10 ± 0.07 h^{-1}, which is achieved by TiO$_2$-functionalized NAA-GIFs produced with T_P = 650, 550, and 850 s, respectively. Our results demonstrate that a rational design of the PSB of these PCs with respect to the absorption band of these dyes can lead to a significant enhancement of the photodegradation rate. Optimal design of these composite photocatalysts requires careful consideration of the position of the blue and red edges of the PSB with respect to the absorption band of the dye molecule to be degraded. However, the pairing between maximum of the absorption band of the dye molecules and the PSB worsens significantly the overall photocatalytic performance due to light screening effect. When the characteristic PSB falls completely outside of the absorption band of the organic dyes, the photocatalytic performance of TiO$_2$-modified NAA-GIFs is solely associated with the geometric features of the nanoporous matrix, and it enhances with increasing T_P due to enhanced mass transfer, increasing number of photoactive sites and light irradiation utilization. The nature of the dye molecules and their interaction with the photocatalyst surface is also a critical contributing factor for the correct interpretation of the obtained photodegradation rates.

For instance, our study established that the average degradation rates for RhoB and MB (i.e., 0.32 ± 0.02 and 1.34 ± 0.04 h^{-1}) were faster than that of MO (i.e., 0.21 ± 0.04 h^{-1}). RhoB and MB are positively charged molecules, whereas the surface of the photoactive TiO$_2$ layer is negatively charged at the pH conditions in which our study was performed (pH = 5.5).[37]

This results in a strong electrostatic attraction between the organic dye molecules and the functional TiO$_2$ layer. The higher number of adsorbed molecules onto the photoactive surface leads to an enhancement of the overall photodegradation rate. In contrast, MO is an anionic organic dye with negative charge that is electrostatically repulsed by the negatively charged surface of TiO$_2$. This reduces the amount of MO molecules absorbed onto the photofunctional surface, worsening the overall photocatalytic degradation performance of the system.[38]

3.5.2. Effect of Anodization Time on the Photocatalytic Performance of TiO$_2$–NAA-GIFs.
The effect of the anodization time (or number of anodization pulses in SPA) on the photocatalytic performance associated with the degradation of two model dyes (i.e., RhoB and MB) was also studied to further define the capabilities of TiO$_2$-functionalized NAA-GIFs as photocatalyst platforms. A set of NAA-GIFs were fabricated by systematically modifying the anodization time (t_{an}) from 5 to 20 h (or from 22 to 85 pulses) with Δt_{an} = 5 h (or ΔN_P = 22 pulses), while other anodization parameters were kept constant (i.e., T_P = 850 s, A_J = 0.420 mA cm^{-2}, J_{offset} = 0.280 mA cm^{-2}, and t_{pw} = 6 min). The surface of

these NAA-GIFs was functionalized with photoactive layers of TiO_2 following the above-mentioned sol−gel protocol. Figure 5 and Table 2 summarize the photocatalytic degradation
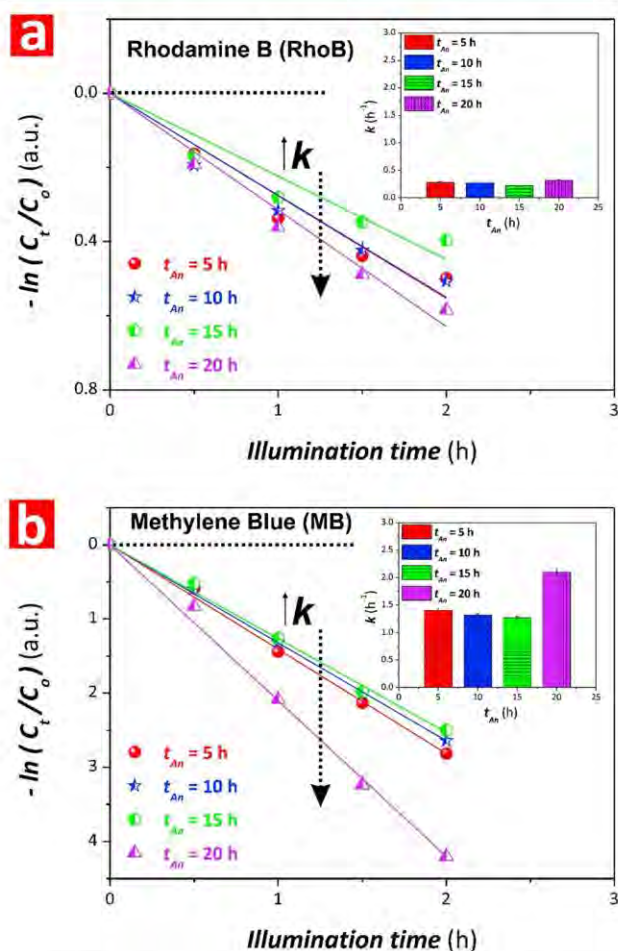
performance of TiO_2-modified NAA-GIFs produced with t_{an} = 5, 10, 15, and 20 h for RhoB and MB with linearized pseudo-first-order kinetics, where the insets represent the degradation rates (k) (i.e., slopes of fitting lines) for each system. Figure 5a displays photocatalytic performance of TiO_2-functionalized NAA-GIFs as a function of t_{an} for RhoB. Our results reveal that

these photoactive PCs degrade RhoB molecules at a rate of 0.28 ± 0.02, 0.27 ± 0.02, 0.22 ± 0.02, and 0.31 ± 0.02 h^{-1} for t_{an} = 5, 10, 15, and 20 h, respectively. In general, the photocatalytic performance shown by these TiO_2-funtionalized NAA-GIFs is comparable, with an average degradation rate of 0.27 ± 0.02 h^{-1}. However, it is apparent that the most optimal platforms are those fabricated with t_{an} = 20 h (i.e., 85 pulses), which provided the best performance as compared to their counterparts produced with shorter anodization time (i.e., 10−29% enhancement). The total thickness of NAA-GIFs is directly proportional to the anodization time (i.e., number of anodization pulses).[39] This thickness increment leads to an enhancement of the total light absorption by the composite PC structure,[40] enabling the generation of extra e$^-$/h$^+$ pairs that can be employed to increase the photodegradation rate of RhoB molecules. The performance of TiO_2-functionalized NAA-GIFs for the photocatalytic degradation of MB is shown in Figure 5b. These results confirm the same trend in the photodegradation rates as a function of the anodization time than that observed for RhoB molecules, where the k values were found to be 1.41 ± 0.04, 1.32 ± 0.02, 1.26 ± 0.03, and 2.10 ± 0.07 h^{-1} for TiO_2-functionalized NAA-GIFs produced with t_{an} = 5, 10, 15, and 20 h, respectively. The rates of photodegradation for TiO_2−NAA-GIFs produced with t_{an} = 5, 10, and 15 h are comparable. However, the fastest degradation rate was achieved by those photoactive PCs produced with t_{an} = 20 h (i.e., 85 pulses), which provided ~33−46% enhancement as compared to their counterparts produced with shorter anodization time.

This analysis demonstrates that TiO_2-modified NAA-GIFs produced with t_{an} = 20 h are the optimal composite PC platforms for the photocatalytic degradation of RhoB and MB dyes. However, the photodegradation of MB molecules was found to be more dependent on t_{an} than RhoB, as demonstrated by the enhancement in degradation rates (i.e., up to 29% and 46% for RhoB and MB, respectively). Our study also reveals that the average k value for the photodegradation of MB is larger than that of RhoB by ~6 times (i.e., 1.52 ± 0.39 and 0.27 ± 0.04 h^{-1}, respectively), where this difference is in good agreement with the results obtained for the photocatalytic degradation of these organic dyes by TiO_2-modified NAA-GIFs produced with different T_p.

3.6. Photocatalytic Degradation Mechanism. A possible photocatalytic degradation mechanism using TiO_2-modified NAA-GIFs with the aid of H_2O_2 under vis−NIR light irradiation ($400 < \lambda < 1000$ nm) is proposed based on the above results. Under light irradiation, e$^-$/h$^+$ pairs in the photoactive TiO_2 layer deposited onto the inner surface of NAA-GIFs are generated in the conduction and valence bands, respectively. Oxidation of H_2O induced by photogenerated holes forms •OH radicals that degrade the model organic dye molecules, decomposing these organic compounds into CO_2 and H_2O. H_2O_2 is added as a primary electron acceptor to form •OH radicals and OH$^-$ ions, which are oxidized by the

Figure 5. Effect of the anodization time (t_{an}) of TiO_2-functionalized NAA-GIFs on the photocatalytic degradation of model organic dyes. (a, b) Photocatalytic degradation kinetics of RhoB and MB in TiO_2-modified NAA-GIFs produced with t_{an} = 5, 10, 15, and 20 h under controlled light irradiation, respectively (insets compile the values of the kinetic constant (k) for the photocatalytic degradation of these model organic dyes) (note: black dotted lines denote the photodegradation of the corresponding dye in control NAA-GIFs without functional TiO_2 layer).

Table 2. Values of the Kinetic Constant (k) for the Photodegradation of RhoB and MB Molecules in TiO_2-Functionalized NAA-GIFs Produced with t_{an} = 5, 10, 15, and 20 h

organic dye	anodization time			
	5 h	10 h	15 h	20 h
RhoB	0.28 ± 0.02 h^{-1}	0.27 ± 0.02 h^{-1}	0.22 ± 0.02 h^{-1}	0.31 ± 0.01 h^{-1}
MB	1.41 ± 0.04 h^{-1}	1.32 ± 0.02 h^{-1}	1.26 ± 0.03 h^{-1}	2.10 ± 0.07 h^{-1}

159

photogenerated holes to $^\bullet$OH radicals. The enhanced photo-degradation rates observed in our study can be associated with the "slow photon" effect, which further facilitates the lifetime and photogeneration of charge carriers, and with the mass transfer and photoactive sites in the nanoporous photonic structure of NAA-GIFs.

Photons from high-irradiance regions (i.e., visible and NIR) are collected by the underlying NAA-based PC structure and utilized by the photoactive TiO_2 functional layer to generate e^-/h^+ pairs. Photocatalytic enhancement is due to the presence of photons with reduced group velocity localized at frequencies of high irradiance that match with the edges of the characteristic PSB of NAA-GIFs. This enhancement was found to be maximum when the blue and red edges of the PSB are located at the proximity of the blue and red sides of the absorbance band of the model dye molecules. However, the high absorption of light of organic dyes at the center of their absorbance band minimizes the amount of light that reaches the photoactive layer of TiO_2-functionalized NAA-GIFs, reducing significantly the overall photodegradation rate. This effect is particularly significant for organic dyes with high absorption bands, such as RhoB and MB. Therefore, the absorption intensity and position of the absorbance band of organic dyes and the relative positioning of the edges of the PSB are critical factors to consider in order to make an optimal utilization of the "slow photon" effect for enhanced photo-catalytic applications by a rational management of photons at the nanoscale.

To date, some proof-of-concept studies have identified and utilized the "slow photon" effect in different photonic crystal structures (Table 3). For instance, Zheng et al. developed 3D

Table 3. Compilation of Representative Values of the Kinetic Constant (k) for the Photodegradation of MO, RhoB, and MB Molecules in Different TiO_2-Based Photocatalyst Systems

TiO_2-based material	organic dye	k (h^{-1})	ref
3D inverted opal PCs	MO	0.01	38
	RhoB	0.47	38
	MB	1.32	38
anodic nanotubular PCs	MO	0.045	42
	RhoB	0.195	41
	MB	2.00	43
P25 nanoparticles	MO	0.24	44
	RhoB	0.47	38
	MB	1.50	43
NAA-GIFs	MO	0.25	this study
	RhoB	0.39	this study
	MB	2.10	this study

TiO_2 inverted opal PCs featuring different pore sizes (i.e., from 270 to 460 nm) and assessed the photodegradation of RhoB, MO, and MB under controlled illumination conditions.[38] The performance of the system to degrade these dyes was assessed under visible light irradiation conditions. The photocatalytic performance of 3D TiO_2 inverted opal PCs was found to be k_{RhoB} = 0.47 h^{-1}, k_{MO} = 0.01h^{-1}, and k_{MB} = 1.32 h^{-1}, respectively. Although the degradation rate for RhoB molecules was slightly higher than that achieved by our system (i.e., ~17% enhancement), TiO_2-functionalized NAA-GIFs showed a much superior performance to photodegrade MO

and MB molecules (i.e., ~96% and ~37% enhancement, respectively).

Fabrication of nanotubular TiO_2 structures by direct anodization of titanium substrates enables the development of TiO_2-based photocatalyst PCs. However, the controllability and versatility of this method to engineer the effective medium of these PCs are limited. To date, several studies have explored the potential applicability of this material for photocatalysis. 1D nanotubular TiO_2 PCs provided degradation rates of k_{RhoB} = 0.195 h^{-1}, k_{MO} = 0.045 h^{-1}, and k_{MB} = 2.00 h^{-1} under visible light irradiation.[41−43] Under the conditions used in our study (vis−NIR irradiation), TiO_2-modified NAA-GIFs outperform significantly 1D nanotubular TiO_2 PCs, with a performance enhancement of ~50%, ~82%, and ~21% to degrade RhoB, MO, and MB molecules, respectively.

Semiconductor nanoparticles are the benchmark and most widely investigated photocatalyst platforms in photocatalysis. Several studies have reported photodegradation of RhoB, MO, and MB using P25 TiO_2 nanoparticles under controlled visible illumination conditions. The best performances achieved by this system were k_{RhoB} = 0.47 h^{-1}, k_{MO} = 0.24 h^{-1}, and k_{MB} = 1.5 h^{-1}.[38,43,44] Photodegradation performance of P25 TiO_2 nanoparticles for RhoB was ~17% superior than that of TiO_2-functionalized NAA-GIFs. However, our system outperformed this photocatalyst benchmark material in the degradation of MO and MB, with an enhancement of ~4% and ~29%, respectively.

These results demonstrate the potential of TiO_2-modified NAA-GIFs as a photocatalyst platform, where optoelectronic properties can be precisely engineered to achieve unprece-dented performances in photocatalysis applications.

4. CONCLUSIONS

To summarize, we have performed a first study assessing the capability of photoactive NAA-based PC structures function-alized with TiO_2 layers to enhance the performance of photocatalytic reactions by "slow photon" effect. Manipulation of various anodization parameters (i.e., pore widening time, anodization period, and anodization time) during the fabrication of these PC structures enables precise engineering of features (i.e., position and bandwidth) of their PSB across the spectral regions. The photon-to-electron conversion rate in TiO_2-modified NAA-GIFs was found to be dependent on the position of edges of the characteristic PSB as well as on the absorption range, absorbance intensity, and properties of model organic dyes under simulated solar light irradiation. A careful design of the position of the edges of the PSB of photoactive NAA-GIFs with respect to the absorption band of organic dyes was found to enhance the photodegradation rate of these molecules significantly by "slow photon" effect. This approach enables the utilization of photons from high-irradiance regions (i.e., visible and NIR) to generate extra e^-/h^+ pairs, overcoming the intrinsic limitation of the photoactive material (i.e., TiO_2, constricted to the UV range). Our study reveals that TiO_2-functionalized NAA-GIFs produced with T_p values of 550, 650, and 850 s show the best photocatalytic performances to degrade Rhodamine B, methyl orange, and methylene blue, respectively (i.e., $k_{RhoB-550s}$ = 0.39 ± 0.02 h^{-1}, $k_{MO-650s}$ = 0.25 ± 0.01 h^{-1}, and $k_{MB-850s}$ = 2.10 ± 0.07 h^{-1}, respectively). In many cases, our system outperformed other photocatalyst platforms in the photo-degradation of these model molecules, demonstrating a promising potential in photocatalysis applications.

Pairing between the absorption band of the organic dye with the edges of the PSB of photoactive NAA-GIFs was found to be optimal to enhance the photodegradation of methyl orange molecules due to the low absorption intensity. However, in the case of highly absorbing dye molecules (i.e., Rhodamine B and methylene blue), optimal utilization of the "slow photon" effect requires alignment of the blue or red edges of the PSB with the edges of the absorption band of the dye to avoid light screening effects. When the characteristic PSB of photoactive NAA-GIFs falls completely outside of the absorption band of the organic dyes, the photocatalytic performance is solely associated with the geometric features of the PC structure. In such a scenario, NAA-GIFs produced with longer anodization period achieve better degradation rates due to the longer period length within the NAA-GIF structure, which enhances the mass transfer of reactive species and increases the number of photoactive sites. Our study also reveals that the optimal anodization time (i.e., number of anodization pulses) for the efficient photocatalytic degradation of organic dyes is 20 h (i.e., 85 pulses at $T_p = 850$ s), independently on the type of organic dye to be degraded. The properties of the model organic dye (i.e., charge and photosensitivity) play a critical role to dictate the overall photocatalytic performance of TiO$_2$-functionalized NAA-GIFs, where positively charged and more photosensitive molecules (i.e., RhoB and MB) degrade at faster rates.

Our comprehensive study demonstrates that the development of photoactive NAA-GIFs with rationally engineered optical and photocatalytic properties can enhance photon-to-electron conversion rates significantly, providing new opportunities for the development of environmentally friendly, economical, and high-performance photocatalysts with broad applicability in environmental remediation and clean energy generation.

ASSOCIATED CONTENT

Ⓢ Supporting Information

The Supporting Information is available free of charge on the ACS Publications website at DOI: 10.1021/acsami.8b05946.

> Further information on the calibration lines correlating dye concentration and absorbance; transmission spectra and digital pictures of NAA-GIFs; chemical analysis confirming the deposition of TiO$_2$ on the surface of NAA-GIFs through EDX, FTIR, and XRD spectra; PSB of NAA-GIFs at different TiO$_2$ deposition time; absorption spectra of methyl orange, methylene blue, and Rhodamine B as well as the spectrum for the simulated solar light irradiation used to assess the photocatalytic performance of TiO$_2$-functionalized NAA-GIFs; information about the residual concentration of each dye after 2 h of photocatalytic reaction in TiO$_2$-functionalized NAA-GIFs (PDF)

AUTHOR INFORMATION

Corresponding Authors

*Phone: +61 8 8313 5652. E-mail: andrew.abell@adelaide.edu.au.

*Phone: +61 8 8313 1535. E-mail: abel.santos@adelaide.edu.au.

ORCID ●

Andrew D. Abell: 0000-0002-0604-2629
Abel Santos: 0000-0002-5081-5684

REFERENCES

(1) Fox, M. A.; Dulay, M. T. Heterogeneous Photocatalysis. *Chem. Rev.* **1993**, *93*, 341–357.

(2) Liu, M.; Chen, Y.; Su, J.; Shi, J.; Wang, X.; Guo, L. Photocatalytic Hydrogen Production Using Twinned Nanocrystals and an Unanchored NiSx Co-Catalyst. *Nat. Energy* **2016**, *1*, 16151.

(3) Mushtaq, F.; Asani, A.; Hoop, M.; Chen, X.-Z.; Ahmed, D.; Nelson, B. J.; Pané, S. Highly Efficient Coaxial TiO$_2$-PtPd Tubular Nanomachines for Photocatalytic Water Purification with Multiple Locomotion Strategies. *Adv. Funct. Mater.* **2016**, *26*, 6995–7002.

(4) Ren, H.; Koshy, P.; Chen, W.-F.; Qi, S.; Sorrell, C. C. Photocatalytic Materials and Technologies for Air Purification. *J. Hazard. Mater.* **2017**, *325*, 340–366.

(5) Hirakawa, H.; Hashimoto, M.; Shiraishi, Y.; Hirai, T. Photocatalytic Conversion of Nitrogen to Ammonia with Water on Surface Oxygen Vacancies of Titanium Dioxide. *J. Am. Chem. Soc.* **2017**, *139*, 10929–10936.

(6) Tu, W.; Zhou, Y.; Zou, Z. Photocatalytic Conversion of CO$_2$ into Renewable Hydrocarbon Fuels: State-of-the-Art Accomplishment, Challenges, and Prospects. *Adv. Mater.* **2014**, *26*, 4607–4626.

(7) Liu, J.; Zhao, H.; Wu, M.; Van der Schueren, B.; Li, Y.; Deparis, O.; Ye, J.; Ozin, G. A.; Hasan, T.; Su, B.-L. Slow Photons for Photocatalysis and Photovoltaics. *Adv. Mater.* **2017**, *29*, 1605349.

(8) Baba, T. Slow Light in Photonic Crystals. *Nat. Photonics* **2008**, *2*, 465–473.

(9) Noda, S.; Chutinan, A.; Imada, M. Trapping and Emission of Photons by a Single Defect in a Photonic Bandgap Structure. *Nature* **2000**, *407*, 608–610.

(10) Noda, S.; Tomoda, K.; Yamamoto, N.; Chutinan, A. Full Three-Dimensional Photonic Bandgap Crystals at Near-Infrared Wavelengths. *Science* **2000**, *289*, 604–606.

(11) Akahane, Y.; Asano, T.; Song, B.-S.; Noda, S. High Q-Photonic Nanocavity in a Two-Dimensional Photonic Crystal. *Nature* **2003**, *425*, 944–947.

(12) Curti, M.; Schneider, J.; Bahnemann, D. W.; Mendive, C. B. Inverse Opal Photonic Crystals as a Strategy to Improve Photocatalysis: Underexplored Questions. *J. Phys. Chem. Lett.* **2015**, *6*, 3903–3910.

(13) Wang, C.; Chen, D.; Ping, G. X.; Liu, S.; Huang, X. N.; Huang, Y. X.; Shu, K. Y.; Li, J. H. Controllable Synthesis of Well-Ordered TiO$_2$ Nanotubes in a Mixed Organic Electrolyte for High-Efficiency Photocatalysis. *Sci. China: Chem.* **2012**, *55*, 2373–2380.

(14) Qin, L.; Chen, Q.; Lan, R.; Jiang, R.; Quan, X.; Xu, B.; Zhang, F.; Jia, Y. Effect of Anodization Parameters on Morphology and Photocatalysis Properties of TiO$_2$ Nanotube Arrays. *J. Mater. Sci. Technol.* **2015**, *31*, 1059–1064.

(15) Lee, K.; Mazare, A.; Schmuki, P. One-Dimensional Titanium Dioxide Nanomaterials: Nanotubes. *Chem. Rev.* **2014**, *114*, 9385–9454.

(16) Santos, A.; Yoo, J. H.; Rohatgi, C. V.; Kumeria, T.; Wang, Y.; Losic, D. Realisation an Advanced Engineering of True Optical Rugate Filters Based on Nanoporous Anodic Alumina by Sinusoidal Pulse Anodisation. *Nanoscale* **2016**, *8*, 1360–1373.

(17) Kumeria, T.; Santos, A.; Rahman, M. M.; Ferré-Borrull, J.; Marsal, L. F.; Losic, D. Advanced Structural Engineering of Nanoporous Photonic Structures: Tailoring Nanopore Architecture to Enhanced Sensing Properties. *ACS Photonics* **2014**, *1*, 1298–1306.

(18) Santos, A. Nanoporous Anodic Alumina Photonic Crystals: Fundamentals, Developments and Perspectives. *J. Mater. Chem. C* **2017**, *5*, 5581–5599.

(19) Santos, A.; Kumeria, T.; Losic, D. Nanoporous Anodic Alumina: A Versatile Platform for Optical Biosensors. *Materials* **2014**, *7*, 4297–4320.

(20) Law, C. S.; Santos, A.; Nemati, M.; Losic, D. Structural Engineering of Nanoporous Anodic Alumina Photonic Crystals by Sawtooth-like Pulse Anodization. *ACS Appl. Mater. Interfaces* **2016**, *8*, 13542–13554.

(21) Law, C. S.; Sylvia, G. M.; Nemati, M.; Yu, J.; Losic, D.; Abell, A. D.; Santos, A. Engineering of Surface Chemistry for Enhanced Sensitivity in Nanoporous Interferometric Sensing Platforms. *ACS Appl. Mater. Interfaces* **2017**, *9*, 8929–8940.

(22) Wang, Y.; Chen, Y.; Kumeria, T.; Ding, F.; Evdokiou, A.; Losic, D.; Santos, A. Facile Synthesis of Optical Microcavities by a Rationally Designed Anodization Approach: Tailoring Photonic Signals by Nanopore Structure. *ACS Appl. Mater. Interfaces* **2015**, *7*, 9879–9888.

(23) Chen, Y.; Santos, A.; Ho, D.; Wang, Y.; Kumeria, T.; Li, J.; Wang, C.; Losic, D. On the Generation of Interferometric Colors in High Purity and Technical Grade Aluminum: An Alternative Green Process for Metal Finishing Industry. *Electrochim. Acta* **2015**, *174*, 672–681.

(24) Lee, C.-Y.; Schmuki, P. Engineering of Self-Organizing Electrochemistry: Porous Alumina and Titania Nanotubes. In *Electrochemical Engineering Across Scales: From Molecules to Proceses*; Alkire, R. C., Bartlett, P. N., Lipkowski, J., Eds.; John Wiley & Sons: Weinheim, 2015; Vol. *15*, pp 145–192.

(25) Wu, J.; Liu, B.; Ren, Z.; Ni, M.; Li, C.; Gong, Y.; Qin, W.; Huang, Y.; Sun, C. Q.; Liu, X. CuS/RGO Hybrid Photocatalyst for Full Solar Spectrum Photoreduction from UV/Vis to Near-Infrared Light. *J. Colloid Interface Sci.* **2018**, *517*, 80–85.

(26) Wang, Y.; Santos, A.; Evdokiou, A.; Losic, D. Rational Design of Ultra-Short Anodic Alumina Nanotubes by Short-Time Pulse Anodizaion. *Electrochim. Acta* **2015**, *154*, 379–386.

(27) Santos, A.; Formentin, P.; Ferré-Borrull, J.; Pallarès, J.; Marsal, L. F. Nanoporous Anodic Alumina Obtained Without Protective Oxide Layer by Hard Anodization. *Mater. Lett.* **2012**, *67*, 296–299.

(28) Massard, C.; Pairis, S.; Raspal, V.; Sibaud, Y.; Awitor, K. Fabrication of TiO_2 Nanotanks Embedded in a Nanoporous Alumina Template. *J. Nanomater.* **2015**, *2015*, 452148.

(29) Abràmoff, M. D.; Magalhães, P. J.; Ram, S. J. Image Processing with ImageJ. *Biophotonics Inter.* **2004**, *11*, 36–42.

(30) León, A.; Reuquen, P.; Garín, C.; Segura, R.; Vargas, P.; Zapata, P.; Orihuela, P. A. FTIR and Raman Characterization of TiO_2 Nanoparticles Coated with Polyethylene Glycol as Carrier for 2-Methoxyestradiol. *Appl. Sci.* **2017**, *7*, 49.

(31) Chellappa, M.; Anjaneyulu, U.; Manivasagam, G.; Vijayalakshmi, U. Preparation and Evaluation of the Cytotoxic Nature of TiO_2 Nanoparticles by Direct Contact Method. *Int. J. Nanomed.* **2015**, *10*, 31–41.

(32) Kumeria, T.; Rahman, M. M.; Santos, A.; Ferré-Borrull, J.; Marsal, L. F.; Losic, D. Structural and Optical Nanoengineering of Nanoporous Anodic Alumina Rugate Filters for Real-Time and Label-Free Biosensing Applications. *Anal. Chem.* **2014**, *86*, 1837–1844.

(33) Zhang, Z.; Wu, H. Multiple Band Light Trapping in Ultraviolet, Visible and Near Infrared Regions with TiO_2 Based Photonic Materials. *Chem. Commun.* **2014**, *50*, 14179–14182.

(34) Nishimura, S.; Abrams, N.; Lewis, B. A.; Halaoui, L. I.; Malluok, T. E.; Benkstein, K. D.; van de Lagemaat, J.; Frank, A. J. Standing Wave Enhancement of Red Absorbance and Photocurrent in Dye-Sensitized Titanium Dioxide Photoelectrodes Coupled To Photonic Crystals. *J. Am. Chem. Soc.* **2003**, *125*, 6306–6310.

(35) Deparis, O.; Mouchet, S. R.; Su, B.-L. Light Harvesting in Photonic Crystals Revisited: Why do Slow Photons at the Blue Edge Enhance Absorption? *Phys. Chem. Chem. Phys.* **2015**, *17*, 30525–30532.

(36) Li, Y.; Kunitake, T.; Fujikawa, S. Efficient Fabrication and Enhanced Photocatalytic Activities of 3D-Ordered Films of Titania Hollow Spheres. *J. Phys. Chem. B* **2006**, *110*, 13000–13004.

(37) *Design of Advanced Photocatalytic Materials for Energy and Environmental Applications*; Coronado, J. M., Fresno, F., Hernández-Alonso, M. D., Portela, R., Eds.; Springer: London, 2013.

(38) Zheng, X.; Meng, S.; Chen, J.; Wang, J.; Xian, J.; Shao, Y.; Fu, X.; Li, D. Titanium Dioxide Photonic Crystals with Enhanced Photocatalytic Activity: Matching Photonic Band Gaps of TiO_2 to the Absorption Peaks of Dyes. *J. Phys. Chem. C* **2013**, *117*, 21263–21273.

(39) Santos, A.; Balderrama, V. S.; Alba, M.; Formentín, P.; Ferré-Borrull, J.; Pallarès, J.; Marsal, L. F. Nanoporous Anodic Alumina Barcodes: Toward Smart Optical Biosensors. *Adv. Mater.* **2012**, *24*, 1050–1054.

(40) Brzózka, A.; Brudzisz, A.; Hnida, K.; Sulka, G. D. Chemical and Structural Modifications of Nanoporous Alumina and Its Optical Properties. In *Electrochemically Engineered Nanoporous Materials: Methods, Properties and Applications*; Losic, D., Santos, A., Eds.; Springer International Publishing: Cham, 2015; Vol. *220*, pp 219–288.

(41) Geng, Z.; Zhang, Y.; Yuan, X.; Huo, M.; Zhao, Y.; Lu, Y.; Qiu, Y. Incorporation of Cu_2O nanocrystals into TiO_2 Photonic Crystal for Enhanced UV-Visible Light Driven Photocalalysis. *J. Alloys Compd.* **2015**, *644*, 734–741.

(42) Lu, Y.; Yu, H.; Chen, S.; Quan, X.; Zhao, H. Integrating Plasmonic Nanoparticles with TiO_2 Photonic Crystal for Enhancement of Visible-Light Driven Photocatalysis. *Environ. Sci. Technol.* **2012**, *46*, 1724–1730.

(43) Sheng, X.; Liu, J.; Coronel, N.; Agarwal, A. M.; Michel, J.; Kimerling, L. C. Integration of Self-Assembled Porous Alumina and Distributed Bragg Reflector for Light Trapping in Si Photovoltaic Devices. *IEEE Photonics Technol. Lett.* **2010**, *22*, 1394–1396.

(44) Guo, M.; Xie, K.; Wang, Y.; Zhou, L.; Huang, H. Aperiodic TiO_2 Nanotube Photonic Crystal: Full-Visible-Spectrum Solar Light Harvesting in Photovoltaic Devices. *Sci. Rep.* **2015**, *4*, 6442.

162

Supporting Information

Engineering the Slow Photon Effect in Photoactive Nanoporous Anodic Alumina Gradient-Index Filters for Photocatalysis

Siew Yee Lim[1,2,3], Cheryl Suwen Law[1,2,3], Marijana Markovic[4,5], Jason K. Kirby[5], Andrew D. Abell[2,3,6] and Abel Santos[1,2,3*]

[1]School of Chemical Engineering, The University of Adelaide, Adelaide, SA 5005, Australia
[2]Institute for Photonics and Advanced Sensing (IPAS), The University of Adelaide, 5005 Adelaide, Australia
[3]ARC Centre of Excellence for Nanoscale BioPhotonics (CNBP), The University of Adelaide, 5005 Adelaide, Australia
[4]School of Agriculture Food and Wine, The University of Adelaide, SA 5064 Adelaide, Australia.
[5]CSIRO Land and Water, SA 5064 Adelaide, Australia.
[6]Department of Chemistry, The University of Adelaide, SA 5005 Adelaide, Australia.

*E-Mails: andrew.abell@adelaide.edu.au ; abel.santos@adelaide.edu.au
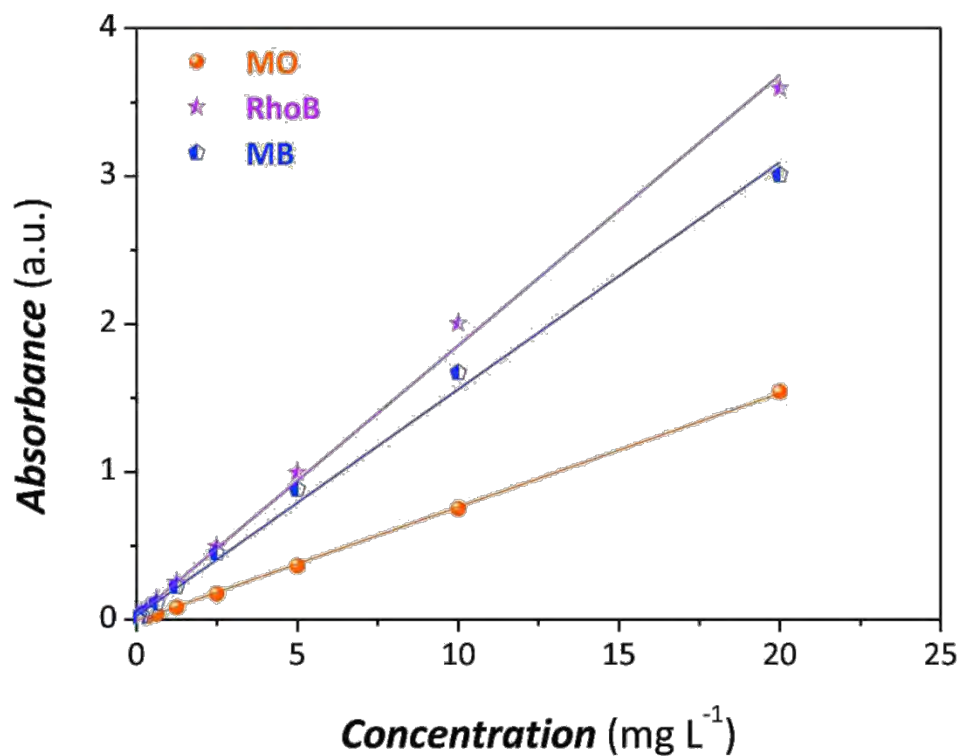
Figure S1. Calibration fitting lines correlating the concentration of each dye (MO, RhoB and MB) with the level of absorbance (note: range of concentrations from 0.00244 to 20 mg L^{-1}). The fitting lines were: Abs_{MO} (a.u.) = 0.07691 [MO] (mg L^{-1}) - 0.00603 with R^2 = 0.99965, Abs_{RhoB} (a.u.) = 0.1828 [RhoB] (mg L^{-1}) + 0.02609 with R^2 = 0.99732 and Abs_{MB} (a.u.) = 0.15335 [MB] (mg L^{-1}) + 0.02479 with R^2 = 0.99635.
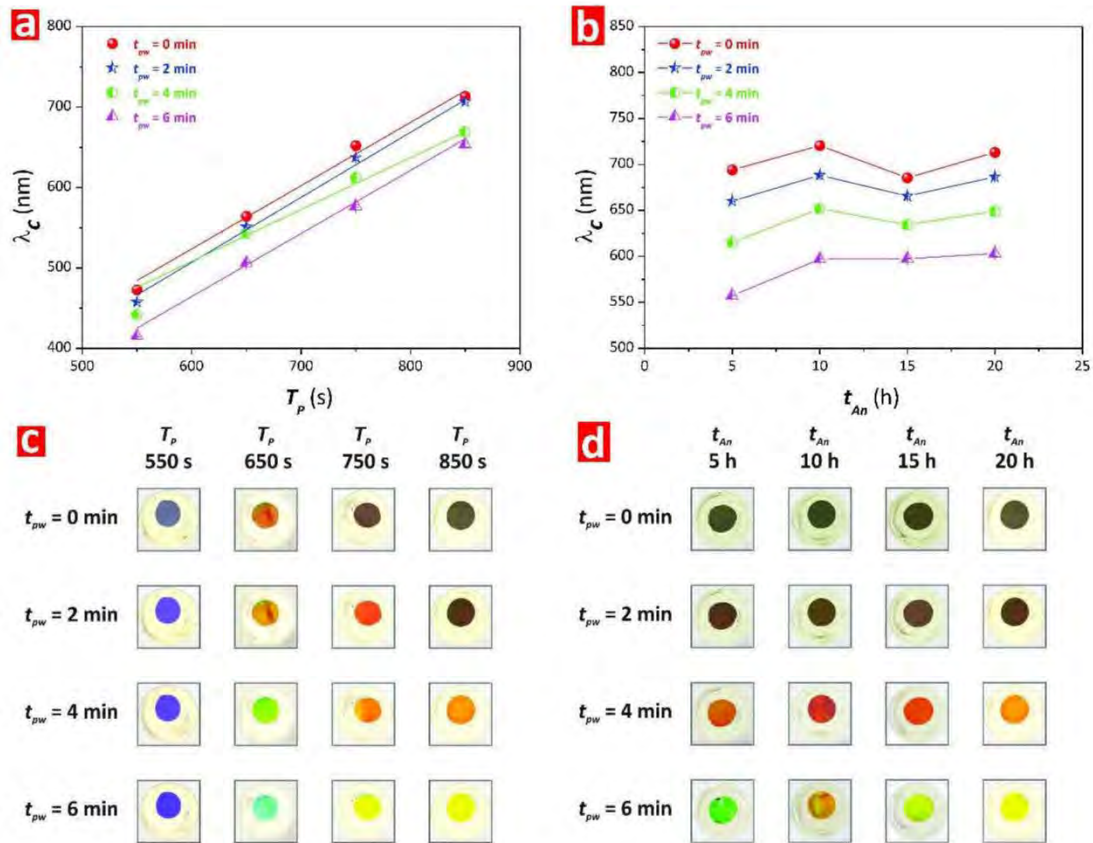
Figure S2. Tunability of the optical properties of NAA-GIFs by modifying the anodization period (T_P) and anodization time of sinusoidal pulse anodization (t_{An}). a) Position of the characteristic photonic stopband (λ_c – PSB) of NAA-GIFs as a function of pore widening time (t_{pw}) and T_P. b) Position of the characteristic photonic stopband (λ_c – PSB) of NAA-GIFs as a function of t_{pw} and t_{An}. c) Interferometric color of NAA-GIFs as a function of t_{pw} and T_P. d) Interferometric color of NAA-GIFs as a function of t_{pw} and t_{An}.

S3
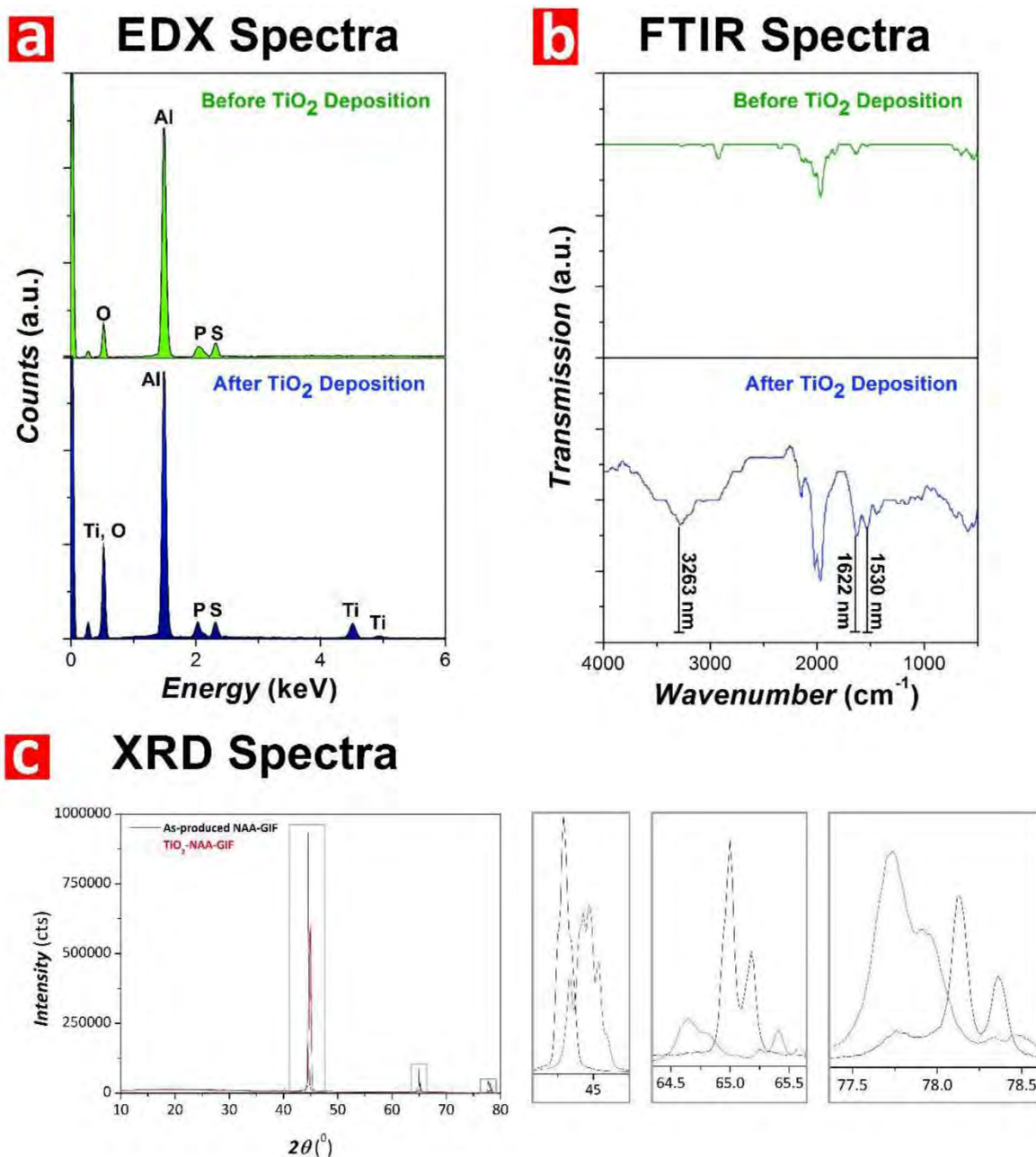
Figure S3. Chemical characterization of a representative NAA-GIF (i.e. T_P = 850 s, A_J = 0.420 mA cm^{-2}, J_{Offset} = 0.280 mA cm^{-2}, t_{An} = 20 h and t_{pw} = 6 min) before and after surface functionalization with titanium dioxide (TiO$_2$) for 24 h. a) Energy dispersive X-ray (EDX) spectra of a representative NAA-GIF with and without deposition of photoactive TiO$_2$ layers. b) Fourier transform infrared (FTIR) spectra of a representative NAA-GIF before and after surface-functionalization with TiO$_2$. c) X-ray diffraction (XRD) spectra of a representative NAA-GIF before and after surface-functionalization with TiO$_2$.
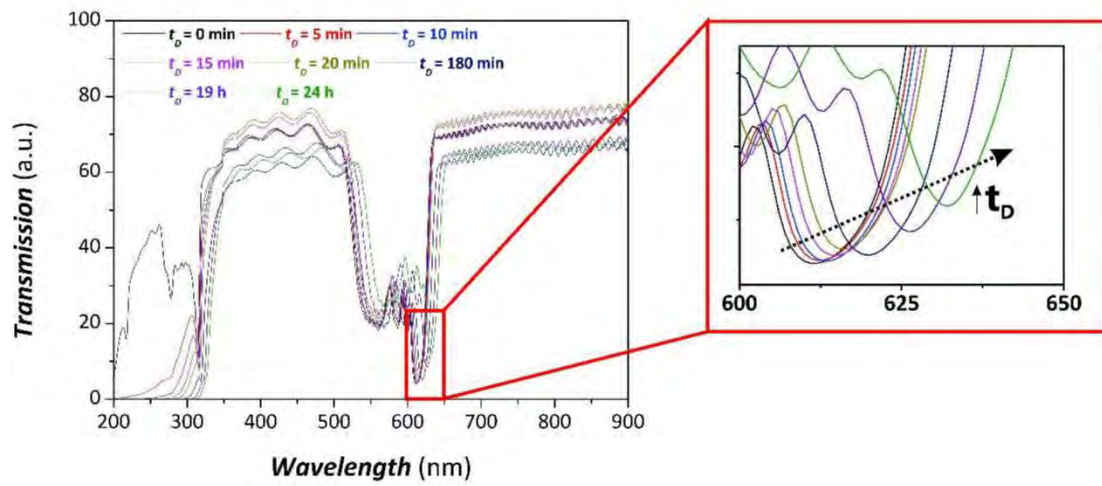
Figure S5. Transmission spectra of a representative NAA-GIF produced with T_P = 750 s at t_D = 0 min, 10 min, 15 min, 20 min, 180 min, 19 h and 24 h.
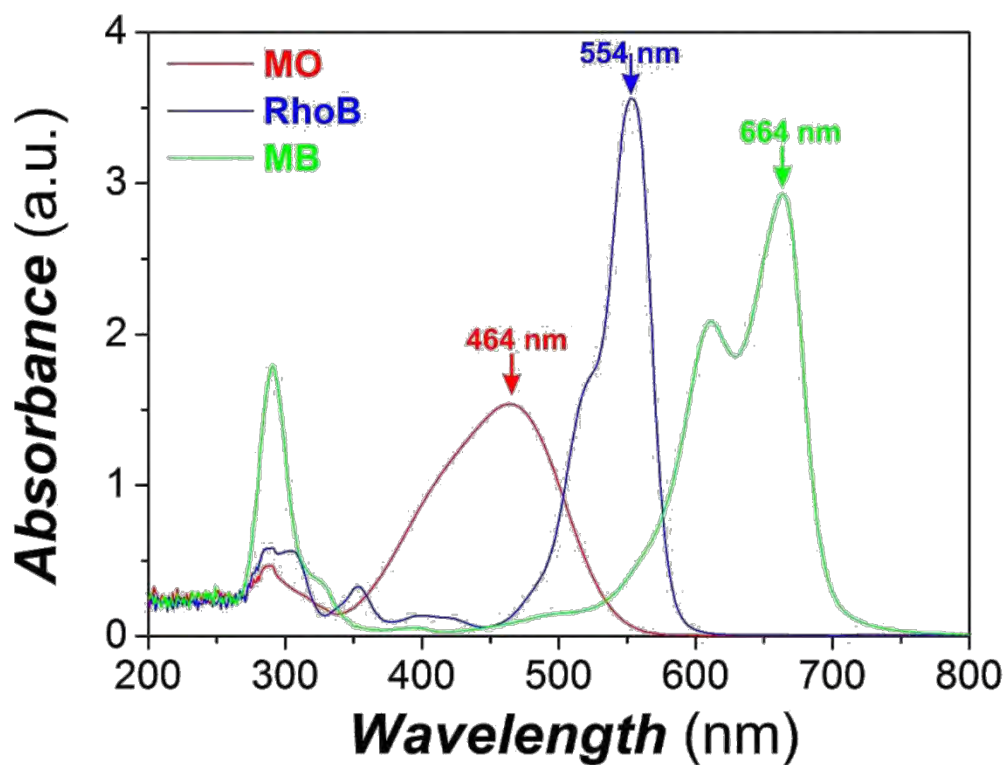
Figure S5. Absorption spectra of methyl orange (MO), rhodamine B (RhoB) and methylene blue (MB) used for assessment of the photocatalytic performance of TiO$_2$-modified NAA-GIFs.
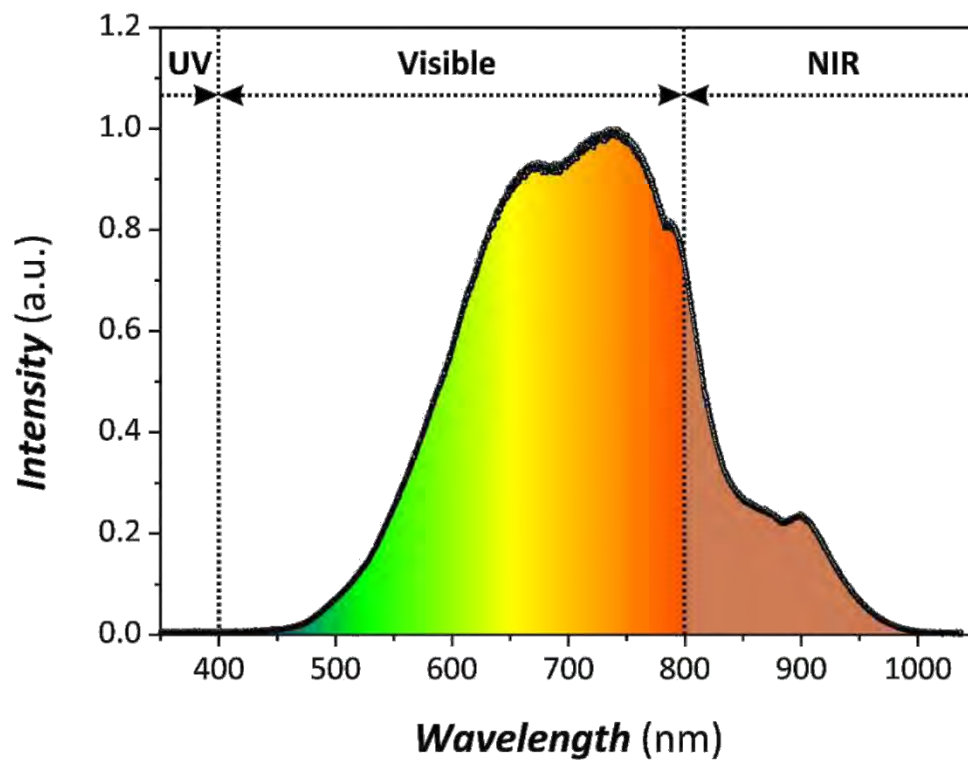
Figure S6. Spectral signature of the simulated solar light irradiation source used for the photocatalytic degradation of the organic dyes (0.12% UV, 82.60% visible and 17.28% NIR).

Table S1. Values of the residual concentration (C_R) for the photodegradation of MO, RhoB and MB molecules in TiO$_2$-functionalized NAA-GIFs produced with T_P = 550, 650, 750 and 850 s after 2 h of photocatalytic reaction.

Organic Dye	Anodization Period			
	550 s	650 s	750 s	850 s
MO	4.30 ± 0.01 mg L^{-1}	3.99 ± 0.05 mg L^{-1}	3.68 ± 0.03 mg L^{-1}	3.41 ± 0.03 mg L^{-1}
RhoB	2.69 ± 0.07 mg L^{-1}	3.37 ± 0.01 mg L^{-1}	3.04 ± 0.04 mg L^{-1}	3.06 ± 0.02 mg L^{-1}
MB	0.75 ± 0.01 mg L^{-1}	0.30 ± 0.02 mg L^{-1}	0.35 ± 0.04 mg L^{-1}	0.13 ± 0.01 mg L^{-1}

Table S2. Values of the residual concentration (C_R) for the photodegradation of RhoB and MB molecules in TiO$_2$-functionalized NAA-GIFs produced with t_{An} = 5, 10, 15 and 20 h after 2 h of photocatalytic reaction.

Organic Dye	Anodization Time			
	5 h	10 h	15 h	20 h
RhoB	3.63 ± 0.01 mg L^{-1}	3.62 ± 0.03 mg L^{-1}	3.06 ± 0.03 mg L^{-1}	3.06 ± 0.02 mg L^{-1}
MB	0.37 ± 0.01 mg L^{-1}	0.40 ± 0.03 mg L^{-1}	0.40 ± 0.01 mg L^{-1}	0.13 ± 0.01 mg L^{-1}

Chapter 6

RATIONAL MANAGEMENT OF PHOTONS
FOR ENHANCED PHOTOCATALYSIS IN
STRUCTURALLY-COLORED
NANOPOROUS ANODIC ALUMINA
PHOTONIC CRYSTALS

6. Rational Management of Photons for Enhanced Photocatalysis in Structurally-Colored Nanoporous Anodic Alumina Photonic Crystals

6.1 Introduction, Significance and Commentary

Chapter 5 has introduced the capability of TiO_2-NAA-GIFs in improving efficiency of photocatalytic reactions by "slow photon" effect. This has led to an innovative approach to produce these photocatalytic systems with another TiO_2-functionalised NAA-PC structures such as TiO_2-NAA-DBRs produced by stepwise pulse anodisation and sol-gel method. This study reveals that photocatalytic performance of these composite PC structures is enhanced by "slow photon" effect when the edges of the PC's PSB fall within the absorbance band of the organic dyes. The photocatalytic degradation of a model pesticide in environmental matrices as well as reusability of TiO_2-NAA-DBRs as efficient photocatalyst platforms were also demonstrated. TiO_2-NAA-DBRs were found to be superior to TiO_2-NAA-GIFs and benchmark photocatalyst materials for the photodegradation of model organics, providing new insights into the development of rationally engineered, high-performing and sustainable photocatalyst systems.

6.2 Publication

This chapter is presented as published journal article by **S.Y. Lim**, C.S. Law, M. Markovic, L.F. Marsal, N.H. Voelcker, A.D. Abell, and A. Santos, *Rational management of photons for enhanced photocatalysis in structurally-colored nanoporous anodic alumina photonic crystals*. ACS Applied Energy Materials, 2019. **2**(2): p. 1169-1184.

Statement of Authorship

Title of Paper	Rational Management of Photons for Enhanced Photocatalysis in Structurally-Colored Nanoporous Anodic Alumina Photonic Crystals
Publication Status	☑ Published ☐ Accepted for Publication ☐ Submitted for Publication ☐ Unpublished and Unsubmitted work written in manuscript style
Publication Details	S.Y. Lim, C.S. Law, M. Markovic, L.F. Marsal, N.H. Voelcker, A.D. Abell, and A. Santos, *Rational management of photons for enhanced photocatalysis in structurally-colored nanoporous anodic alumina photonic crystals.* ACS Applied Energy Materials, 2019. **2**(2): p. 1169-1184.

Principal Author

Name of Principal Author (Candidate)	Siew Yee Lim		
Contribution to the Paper	Performed the experiment, processed and analysed the data and wrote the manuscript under the supervisions of Abel Santos and Andrew D. Abell.		
Overall percentage (%)	70		
Certification:	This paper reports on original research I conducted during the period of my Higher Degree by Research candidature and is not subject to any obligations or contractual agreements with a third party that would constrain its inclusion in this thesis. I am the primary author of this paper.		
Signature		Date	10/06/2020

Co-Author Contributions

By signing the Statement of Authorship, each author certifies that:

i.   the candidate's stated contribution to the publication is accurate (as detailed above);

ii. permission is granted for the candidate in include the publication in the thesis; and

iii. the sum of all co-author contributions is equal to 100% less the candidate's stated contribution.

Name of Co-Author	Cheryl Suwen Law		
Contribution to the Paper	Aided in performing the experiment. Give consent to Siew Yee Lim to present this paper for examination towards the Doctorate of Philosophy.		
Signature		Date	15/06/2020

Name of Co-Author	Marijana Markovic		
Contribution to the Paper	Aided in the evaluation of final version of manuscript. Give consent to Siew Yee Lim to present this paper for examination towards the Doctorate of Philosophy.		
Signature		Date	11/06/20

Name of Co-Author	Lluís F. Marsal		
Contribution to the Paper	Aided in the evaluation of final version of manuscript. Give consent to Siew Yee Lim to present this paper for examination towards the Doctorate of Philosophy.		
Signature		Date	10/06/2020

Name of Co-Author	Nicolas H. Voelcker		
Contribution to the Paper	Aided in the evaluation of final version of manuscript. Give consent to Siew Yee Lim to present this paper for examination towards the Doctorate of Philosophy.		
Signature		Date	10/06/2020

Name of Co-Author	Andrew D. Abell		
Contribution to the Paper	Acted as a co-supervisor for the candidate, and aided in revising and evaluating the manuscript for submission. Give consent to Siew Yee Lim to present this paper for examination towards the Doctorate of Philosophy.		
Signature		Date	10/06/2020

Name of Co-Author	Abel Santos		
Contribution to the Paper	Acted as a primary supervisor for the candidate, and aided in developing, revising and evaluating the manuscript for submission. Give consent to Siew Yee Lim to present this paper for examination towards the Doctorate of Philosophy.		
Signature		Date	11/06/2020

174

Rational Management of Photons for Enhanced Photocatalysis in Structurally-Colored Nanoporous Anodic Alumina Photonic Crystals

Siew Yee Lim,[†,‡,§] Cheryl Suwen Law,[†,‡,§] Marijana Markovic,[‖,⊥] Lluís F. Marsal,[*,#] Nicolas H. Voelcker,[*,∇,○,◆,¶] Andrew D. Abell,[*,‡,§,□] and Abel Santos[*,†,‡,§]

[†]School of Chemical Engineering, The University of Adelaide, Adelaide, South Australia 5005, Australia

[‡]Institute for Photonics and Advanced Sensing (IPAS), The University of Adelaide, Adelaide 5005, South Australia, Australia

[§]ARC Centre of Excellence for Nanoscale BioPhotonics (CNBP), The University of Adelaide, Adelaide 5005, South Australia, Australia

[‖]School of Agriculture Food and Wine, The University of Adelaide, Adelaide 5064, South Australia, Australia

[⊥]Center of Chemistry, Institute of Chemistry, Technology and Metallurgy, University of Belgrade, Belgrade 11000, Serbia

[#]Department of Electronic, Electric, and Automatics Engineering, Universitat Rovira i Virgili, Tarragona, Tarragona 43007, Spain

[∇]Melbourne Centre for Nanofabrication, Victorian Node of the Australian National Fabrication Facility, Monash University, Melbourne, Victoria 3168, Australia

[○]Monash Institute of Pharmaceutical Sciences, Monash University, Melbourne, Victoria 3052, Australia

[◆]Commonwealth Scientific and Industrial Research Organisation (CSIRO), Melbourne, Victoria 3168, Australia

[¶]INM-Leibniz Institute for New Materials, Campus D2 2, Saarbrücken 66123, Germany

[□]Department of Chemistry, The University of Adelaide, Adelaide 5005, South Australia, Australia

S *Supporting Information*

ABSTRACT: A comprehensive study on the engineering of titanium dioxide-functionalized nanoporous anodic alumina distributed Bragg reflectors (TiO₂−NAA-DBRs) for photocatalysis enhanced by the "slow photon" effect is presented. The photocatalytic performance of these composite photonic crystals (PCs) is assessed by monitoring photodegradation of a variety of organic molecules with absorbance bands across the spectral regions. This study demonstrates that photocatalytic performance of TiO₂−NAA-DBRs is enhanced by the "slow photon" effect when the edges of the PC's photonic stopband (PSB) fall within the absorbance band of the organic molecules. The photocatalytic performance is significantly enhanced when the PSB's red edge is in close

proximity to the absorbance band of the organic molecules. Overall photocatalytic degradation is also dependent on the total pore length of the PC structure, charge of the organic molecules, percentage of vis−near-IR irradiation, and matrix complexity (i.e., interfering ions and molecules) when the PC's PSB is partially or entirely misaligned with respect to the absorbance band of the organic molecules. Finally, the real-life application of TiO₂−NAA-DBRs to degrade pollutants such as pesticides in environmental matrices is demonstrated. This study provides new insights into the development of rationally engineered, high-performing, safe, and reusable photocatalyst systems.

KEYWORDS: *photocatalysis, photonic crystals, slow photons, stopband, pulse anodization*
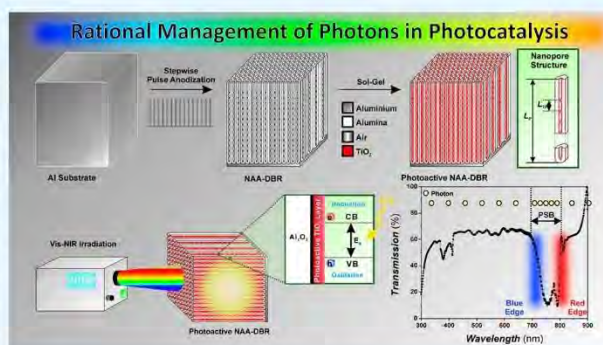
1. INTRODUCTION

Photonic crystals (PCs) are micro-/nanostructures that play important roles in light-driven applications, including photocatalysis,[1−5] photovoltaics,[6−8] optics, and biosensing.[9] The rational design of the PC's structure amplifies light−matter interactions by controlling, modulating, and trapping the propagation of electromagnetic waves across its structure via Bragg diffraction, multiple scattering, and the "slow photon" effect.[10−12] Bragg diffraction forbids light from propagating

across the PC's structure due to its characteristic photonic stopband (PSB). Multiple scattering reduces light loss due to reflection and increases the optical path length of the flowing light at spectral regions that are away from the PC's PSB. As a result, light is internally trapped within the PC, enhancing its
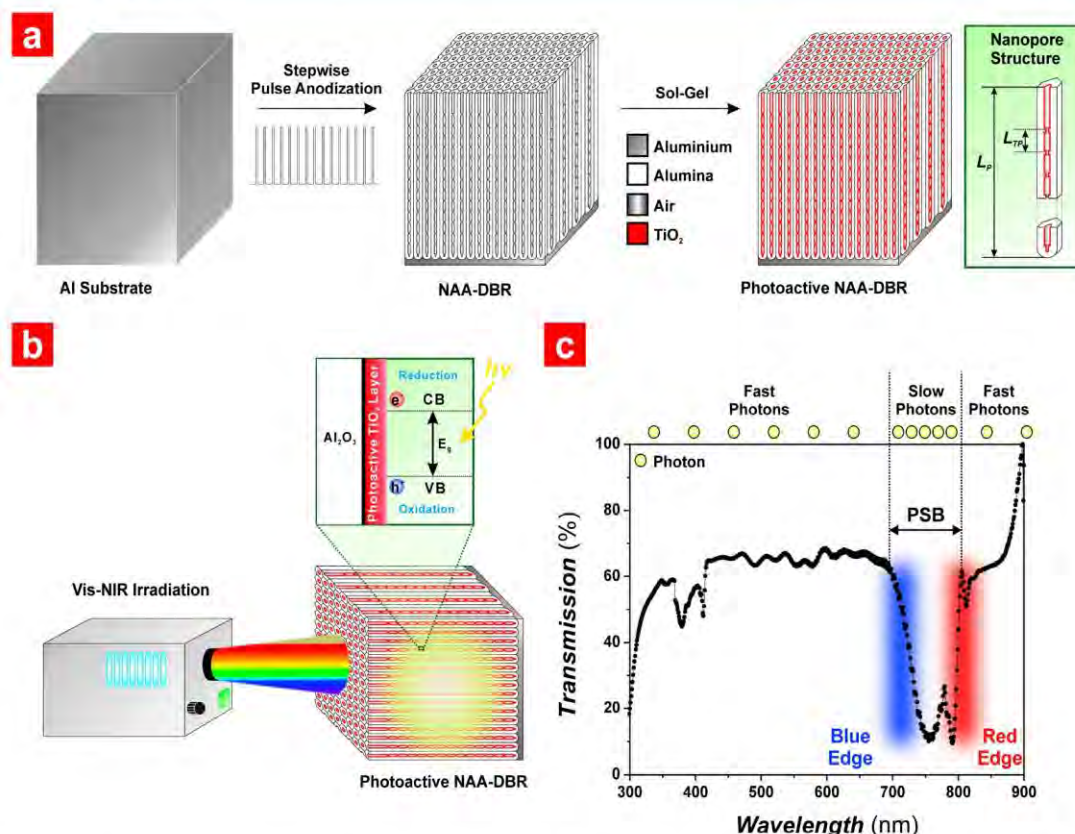
Figure 1. Fabrication and photocatalytic assessment of titania-functionalized structurally-colored nanoporous anodic alumina distributed Bragg reflectors (TiO$_2$–NAA-DBRs). (a) Schematic illustrating the combination of stepwise pulse anodization (STPA) and sol–gel functionalization method used to fabricate TiO$_2$–NAA-DBRs with a visual description of the nanoporous structure of these photonic crystals (i.e., pore length—L_p and period length—L_{TP}). (b) Schematic design of the photocatalytic assessment of TiO$_2$–NAA-DBRs under simulated visible–near-IR irradiation conditions with details showing the chemical and electronic band structures of the composite photonic structures (note: E_g = energy bandgap; hv = excitation energy; CB = conduction and VB = valence bands). (c) Representative transmission spectrum of a reference NAA-DBRs showing the effect of the photonic stopband (PSB) and its blue and red edges on the group velocity of photons across the spectral regions (note: NAA-DBR produced with anodization period, T_p = 1400 s; number of anodization pulses, N_p = 150 pulses; and pore widening time, t_{pw} = 0 min, where the medium filling the nanopores is water).

light-confining properties. Furthermore, photons propagate with strongly reduced group velocity (slow photons) at the frequency edges of the PC's PSB, giving rise to the so-called slow photon effect. Slow photons are strongly localized in different dielectric parts of the PC's structure (i.e., sections of high and low refractive index) at the edges of the PC's PSB (i.e., red and blue edges), enabling a longer lifetime of photons at these spectral regions. This leads to an enhancement in the overall optical absorbance of the material. Besides the enhanced light–matter interactions attributed to the PC effect, nanoporous semiconductor PCs provide high specific surface area that increases the number of functional sites available for reactions. The nanoporous structure facilitates mass transport of ionic and molecular species involved in these photochemical processes and light harvesting capabilities for efficient management of photons at high-irradiance spectral regions (i.e., visible and IR).[1,4]

Nanoporous semiconductor PC structures are superior to their nanoparticle-based counterparts in light-driven applications. Particulate systems have a propensity to aggregate[13] and are also difficult to recover after use,[14,15] becoming potentially toxic to the environment.[16] Furthermore, most semiconductor nanoparticles only absorb light in the UV region (i.e., ~5% of

the solar spectrum) due to a high energy bandgap and the rapid recombination of photogenerated charge carriers at their surface.[17–20] These factors limit the capability of nanoparticle-based systems to attain efficient and practical photon-to-electron conversion rates for real-life light-driven processes. Films of nanoporous semiconductor PCs can overcome these limitations due to their robust structure and unique set of physical and chemical properties, which allows rational management of photons at the nanoscale to speed up redox reactions. The advantages of photocatalyst semiconductor PC structures make them desirable for a broad range of applications, including generation of hydrogen energy,[21–24] purification of air and water,[1–5,25] production of chemicals such as ammonia (NH_3),[26] and carbon dioxide (CO_2) reduction for environmental remediation.[27,28] Nanoporous semiconductor PCs enable control of light–matter (i.e., photons–semiconductor) interactions at the nanoscale in order to generate extra electron/hole (e^-/h^+) pairs and produce strongly oxidizing and nonselective radicals for redox reactions.[29] Pure semiconductor PCs with inverted opal structures have been widely employed for photocatalysis, particularly in water purification.[1,30–32] These semiconductor PC structures show enhanced performances in the photo-

degradation of organic dye molecules under visible light irradiation when compared to nanoparticle and non-porous film counterparts.

Photocatalytic enhancement in these systems is associated with the overall PC effect, particularly with the slow photon effect when the edges of the PC's PSB are tuned with respect to the absorbance band of the organic dye or to the electronic bandgap of the material. However, Zheng et al.[1] and Meng et al.[30] demonstrated that the performance of inverted opal PC structures to degrade organic molecules can be inhibited when the absorbance band of these molecules is located in the UV spectral region. These studies indicate that the photocatalytic capability of these PC structures is limited to organic molecules with absorbance bands within the visible spectral region under visible light irradiation. Furthermore, inverted opal PCs have other intrinsic limitations, including limited versatility in tuning the PSB across the spectral regions, restriction to 3D nanostructures, formation of structural defects (i.e., scattering centers), limitation to small domain areas, and requirement of a long synthesis process (>24 h).[4,33−36] Significant effort has been devoted to developing alternative nanoporous semiconductor PC structures capable of addressing these limitations to achieve enhanced performances for photocatalysis. Among these, nanoporous PCs produced by electrochemical anodization of valve metals have shown promising results in photocatalysis, including titanium dioxide nanotubes[37−40] and nanoporous anodic alumina (NAA).[4] Anodization is an industrially scalable, ecofriendly, highly controllable, and low-cost electrochemical process broadly used in metal finishing industry to modify the properties of metals such as color, brightness, wettability, and corrosion protection. The generation of nanoporous PCs by anodization is a versatile approach that enables the development of PC systems with precisely engineered optical properties for different applications, including optical sensing and biosensing,[41−44] light filtering,[45,46] energy harvesting,[6−8] and photocatalysis.[4,37−40] NAA produced by anodization of aluminum is an excellent platform material to develop PC structures due to its highly versatile and controllable nanoporous structure. However, NAA has a wide energy bandgap (i.e., 7.0−9.5 eV) that prevents the direct use of NAA-PCs in photocatalysis. Despite this intrinsic limitation, we have recently demonstrated that the chemical modification of NAA-PCs with layers of semiconductor materials with narrower energy bandgap such as titanium dioxide (TiO₂, 3.20−3.35 eV) does enable the production of high-performing composite photocatalysts that outperform conventional photocatalyst platforms.[4] NAA-PCs have distinctive PSBs, the features of which can be readily tuned across the spectral regions by engineering the effective medium of NAA in a multidimensional fashion, through various anodization approaches.[45,47−52] These NAA-PC platforms include optical microcavities,[47,48] distributed Bragg reflectors (DBR),[45,49] linear variable bandpass filters,[50] gradient-index filters,[51] and hybrid PCs.[52] These PC structures provide new opportunities to rationally utilize the slow photon effect to attain an efficient management of photons at the nanoscale for photocatalytic applications.

Herein, we develop and study photoactive TiO₂-functionalized structurally-colored NAA-DBRs as photoactive PC platforms for enhanced photocatalytic degradation of organic molecules. NAA-DBRs are fabricated by stepwise pulse anodization (STPA) and subsequently functionalized with photoactive layers of TiO₂ by sol−gel method (Figure 1). Photocatalytic performance of TiO₂−NAA-DBRs is assessed under controlled visible−near-IR irradiation conditions by a systematic modification of several parameters, including the anodization period (i.e., features of PSB), concentration of hydrogen peroxide, characteristics of model organic molecules, and complexity of liquid matrix. This approach enables the identification of photocatalytic enhancements by the slow photon effect, using TiO₂−NAA-DBRs as model photocatalyst platforms under controlled irradiation conditions. Furthermore, other critical factors for real-life applications such as reusability and photodegradation of model pesticides by TiO₂−NAA-DBRs are demonstrated.

2. EXPERIMENTAL SECTION

2.1. Materials. High-purity (99.9997%) aluminum (Al) foils 0.32 mm thick were purchased from Goodfellow Cambridge Ltd. (U.K.). Hydrochloric acid (HCl), copper(II) chloride (CuCl₂), perchloric acid (HClO₄), sodium chloride (NaCl), titanium(IV) butoxide (Ti(OBu)₄), hydrogen peroxide (H₂O₂), methyl orange (MO), methylene blue (MB), rhodamine B (RhoB), and 4-chlorophenol (4-CP) were supplied by Sigma-Aldrich (Australia). Ethanol (EtOH,-C₂H₅OH) and sulfuric acid (H₂SO₄) were purchased from ChemSupply (Australia). Ultrapure Milli-Q water (18.2 MΩ cm) was used in the preparation of all the aqueous solutions used in this study.

2.2. Fabrication of NAA-DBRs. NAA-DBRs were produced by stepwise pulse anodization (STPA) under current density control conditions.[49] Prior to anodization, 1.5 × 1.5 cm² square chips were sonicated in ethanol and water for 15 min each, dried under air stream, and electropolished in a 4:1 mixture of EtOH and HClO₄ (v:v) at 20 V and 5 °C for 3 min. The electropolished Al chips were anodized in an aqueous solution of 1.1 M H₂SO₄ with 25 vol. % EtOH at 1 °C. The anodization process started with a constant current density of 1.120 mA cm⁻² for 1 h to achieve a homogeneous pore growth rate prior to stepwise pulse anodization. The anodization profile was subsequently switched to stepwise pulse mode, where the current density was pulsed between high (J_{max} = 1.120 mA cm⁻²) and low (J_{min} = 0.280 mA cm⁻²) current density values following a stepwise modulation for a total of 150 anodization pulses (N_P). The anodization period (T_P) (i.e., time between consecutive pulses) was modified from 900 to 1600 s with an interval (ΔT_P) of 100 s. Note that T_P is given by eq 1:

$$T_P = t_{max} + t_{min} \tag{1}$$

where t_{max} and t_{min} are the times for maximum and minimum current density pulses (i.e., J_{max} = 1.120 mA cm⁻² and J_{min} = 0.280 mA cm⁻²), respectively, and the time ratio for t_{max} and t_{min} ($t_{max}:t_{min}$) was set to 1:4 for T_P = 900−1600 s.

2.3. Surface Functionalization of NAA-DBRs with Photoactive Layers of TiO₂. The inner surface of NAA-DBRs was chemically functionalized with TiO₂ photoactive layers through the sol−gel method. The TiO₂ sol was prepared by magnetically stirring a mixture of titanium(IV) butoxide (3 vol. %) and EtOH (97 vol. %) for 10 min. NAA-DBRs were subsequently soaked in the TiO₂ sol for 24 h. The surface-functionalized NAA-DBRs were washed with EtOH to remove any excess of TiO₂ sol and titanium(IV) butoxide. The TiO₂−NAA-DBRs were then dried in an oven at 50 °C for 10 min to evaporate any remaining EtOH residues.

2.4. Optical Characterization. Prior to transmission spectra acquisition, NAA-DBRs were chemically etched in a saturated solution of HCl/CuCl₂ using a 5 mm diameter circular window etching mask to selectively dissolve the underlying Al substrate at the backside. Transmission spectra of chemically etched NAA-DBRs fabricated with different anodization periods were obtained in air and water from 200 to 800 nm at normal incidence (i.e., θ = 0°), using a UV−visible spectrophotometer (Cary 300, Agilent, USA). The absorbance spectra of 5 mg L⁻¹ organics (i.e., MO, RhoB, MB, and
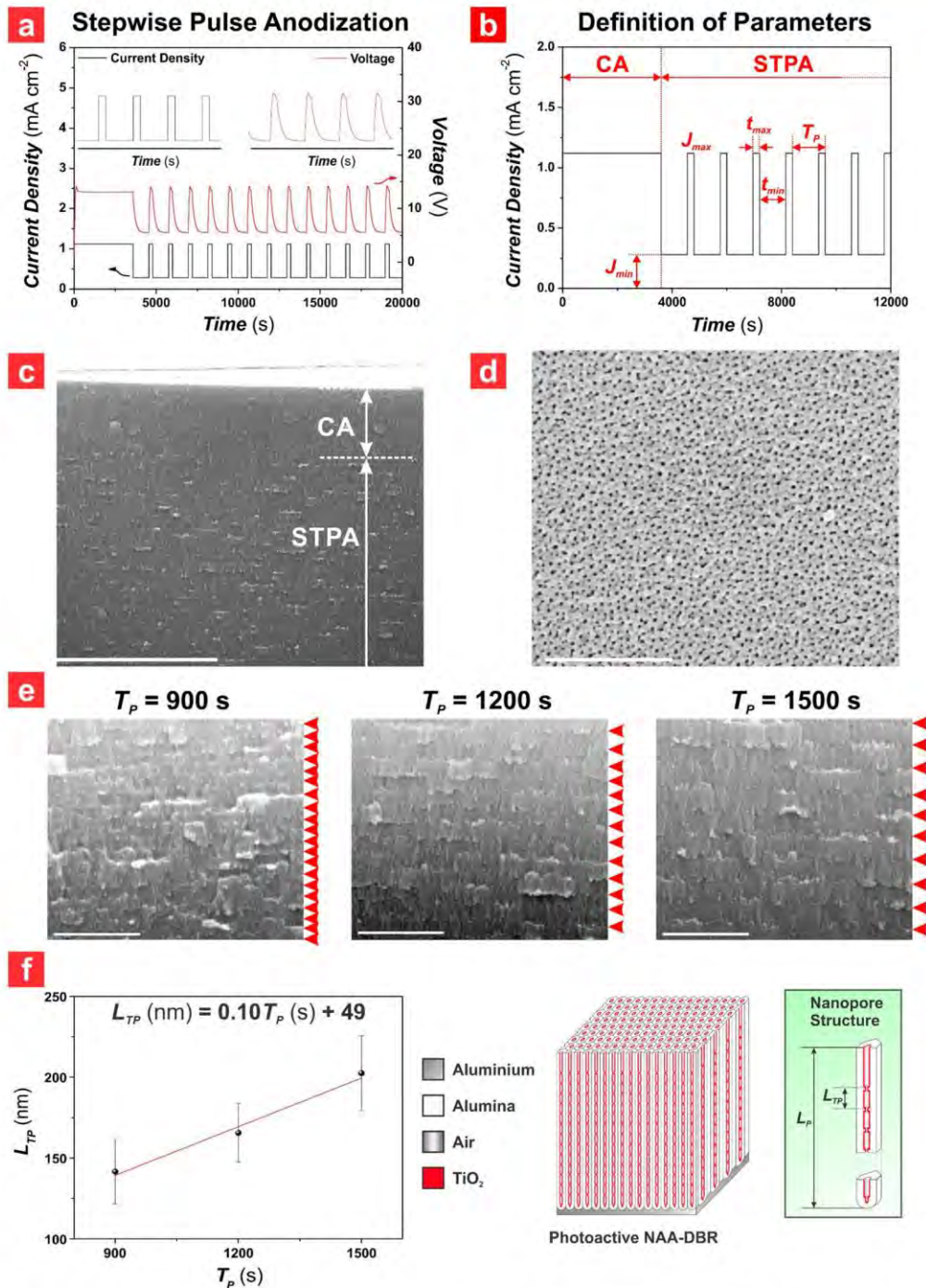
Figure 2. Fabrication and structural characterization of the nanoporous structure of NAA-DBRs fabricated by stepwise pulse anodization (STPA). (a) Representative anodization profile used to produce NAA-DBRs with anodization period (T_P) of 1200 s and 150 anodization pulses (N_P) by STPA approach. (b) Graphical definition of the anodization parameters (i.e., J_{min}, J_{max}, t_{min}, t_{max}, and T_P) used to generate the STPA profiles (note: CA = constant current anodization step). (c) General cross-sectional FEG-SEM image view of a NAA-DBR (scale bar = 4 μm). (d) Top view FEG-SEM image of a NAA-DBR fabricated with T_P = 900 s and N_P = 150 pulses (scale bar = 500 nm). e) FEG-SEM images showing cross-sectional views of NAA-DBRs fabricated with T_P = 900 s (left), T_P = 1200 s (center) and T_P = 1500 s (right) (scale bar = 1 μm) (note: red arrowheads denote the interfaces between anodization periods, L_{TP}). (f) Linear correlation between L_{TP} and T_P (left) with schematic description of L_{TP} in the nanoporous photonic crystal structure (right) (note: error bars denote standard deviation from average measurements obtained from n = 3 independent NAA-DBRs).

4-CP) in a quartz cuvette of 10 mm path length were acquired from 200 to 800 nm to determine the absorbance bands of the organics. The interferometric color of NAA-DBRs in air and water was characterized by digital pictures, using a Canon EOS 700D digital camera equipped with a Tamron 90 mm F2.8 VC USD macromount lens with autofocus function under natural light illumination.

178
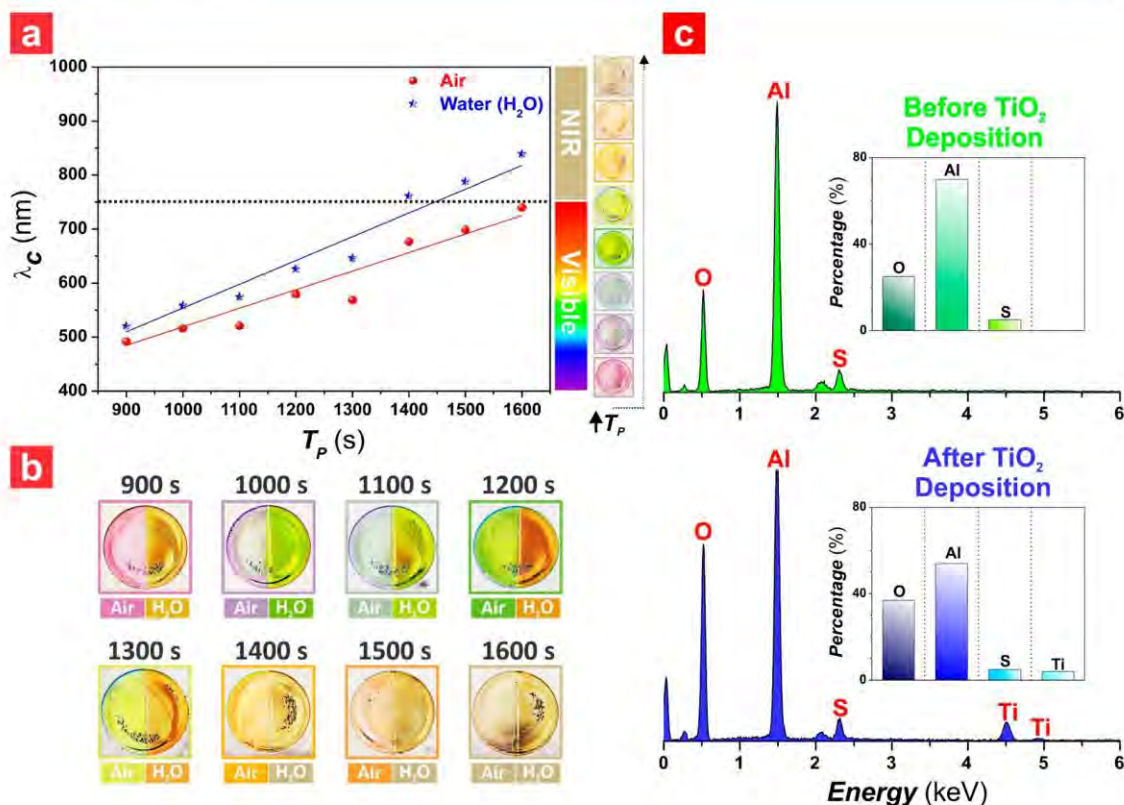
Figure 3. Optical tunability of the PSB of NAA-DBRs by varying anodization period (T_P) and chemical analysis of the composite photonic structures after surface functionalization with photoactive layers of TiO_2. (a) Position of the characteristic photonic stopband (PSB—λ_C) as a function of media (left) and digital images displaying the interferometric color of NAA-DBRs from T_P = 900 to 1600 s with ΔT_P = 100 s in air (right) (note: error bars correspond to standard deviation from n = 3 independent measurements). (b) Interferometric color of NAA-DBRs as a function of T_P and media (note: sample diameter, 1 cm). (c) Energy dispersive X-ray (EDX) spectra of a representative NAA-DBR with insets showing the percentage of main elements present before and after surface functionalization with TiO_2 (note: NAA-DBR produced with T_P = 1200 s and N_P = 150 pulses).

2.5. Photocatalytic Degradation of Organics under Controlled Irradiation Conditions.

Photocatalytic performance of TiO_2−NAA-DBRs fabricated with various T_P was assessed under simulated solar light irradiation conditions, using the degradation of a model organic dye, methylene blue (MB), with well-defined absorbance band within the visible spectral range (i.e., MB − λ_{Abs-MB} = 664 nm) as an efficiency indicator. A 2 mL mixture of 5 mg L^{-1} of MB and 100 mM H_2O_2 solution was pipetted into a transparent cuvette. The TiO_2−NAA-DBRs, which had an effective area of 1 cm², were then submerged inside the organic mixture. The solution was magnetically stirred in a dark vessel (i.e., solar simulator) for 30 min to achieve the adsorption−desorption equilibrium prior to irradiation. The system was subsequently illuminated with simulated solar light irradiation using a 150 W (~3000 lm) halogen lamp (HL250-A, Amscope, Australia) at room temperature. To determine the concentration of MB at specific time intervals, the absorbance of the MB solution at λ_{Abs-MB} = 664 nm for each illumination time interval (i.e., 15 min) was analyzed by UV−visible spectroscopy. The relationship between the absorbance intensity and the concentration of MB was established by a calibration line to obtain the photocatalytic conversion ratio (C_t/C_o), where C_o is the concentration of organic after stirring in the dark for 30 min and C_t is the concentration at illumination time t (Figure S1, Supporting Information). This parameter was used in determining the kinetic model for this photocatalytic system. The effect of the type of organic dye and the concentration of H_2O_2 on the photocatalytic performance of TiO_2−NAA-DBRs fabricated with T_P = 1200 s was systematically assessed by modifying the organic molecule model (i.e., MB, MO, and RhoB; MO − λ_{Abs-MO} = 464 nm and RhoB − $\lambda_{Abs-RhoB}$ = 554 nm) and

the concentration of H_2O_2 solution (i.e., 12.5, 50.0, 100, and 200 mM), respectively. The reusability of TiO_2−NAA-DBRs fabricated with T_P = 1200 s was assessed under simulated solar light irradiation by repeating the photocatalytic degradation of MB molecules five times using the same photocatalyst platform. TiO_2−NAA-DBR was washed in EtOH and water under sonication for 15 min each and dried under air stream before each photocatalytic cycle. To demonstrate the photocatalytic capability of TiO_2−NAA-DBRs for real-life applications, the photodegradation of 4-CP (i.e., $\lambda_{Abs-4-CP}$ = 225 nm), a model pesticide, by TiO_2−NAA-DBRs was investigated. Two main parameters were assessed: (i) the effect of the anodization period (i.e., T_P = 900, 1200, and 1600 s) and (ii) the composition of the aqueous matrix of 4-CP (i.e., Milli-Q water, tap water, filtered Torrens river water, and 10 g L^{-1} NaCl aqueous solution).

2.6. Chemical and Structural Characterization.

The structural features of NAA-DBRs were characterized using a field emission gun scanning electron microscope (FEG-SEM FEI Quanta 450). FEG-SEM images were analyzed by ImageJ.[53] The chemical composition of NAA-DBRs before and after surface functionalization with TiO_2 was analyzed by energy dispersive X-ray (EDX) spectroscopy during FEG-SEM characterization.

3. RESULTS AND DISCUSSION

3.1. Fabrication and Structural Characterization of NAA-DBRs.

Figure 2 shows a representative STPA profile with a graphical description of the different anodization parameters and a set of representative FEG-SEM images of NAA-DBRs produced by STPA process. The anodization profile reveals

that the anodization voltage (i.e., output) follows closely the anodization current density (i.e., input) applied during the STPA process. Thus, the anodization conditions used in our study enable the efficient translation of the anodization current density profiles into changes in the porosity of NAA in depth (Figure 2a). The anodization process begins with a constant current anodization step (CA; Figure 2b), which produces a layer of NAA with straight nanopores. This process is followed by the STPA stage, during which stacked layers of NAA with stepwise porosity are generated, as depicted in the FEG-SEM image shown in Figure 2c. A top view FEG-SEM image reveals that the nanopores are evenly and randomly distributed across the surface of NAA-DBRs, with an average nanopore diameter (d_{pore}) measured to be 10 ± 3 nm (Figure 2d).

A visual analysis of NAA-DBRs fabricated with different anodization periods (i.e., T_P = 900, 1200, and 1600 s) demonstrates that the period length (L_{TP}) of the stacked layers of NAA (graphic illustration in Figure 1a), as indicated by the red arrowheads shown in the cross-sectional FEG-SEM images in Figure 2e, increases with T_P. The correlation between L_{TP} and T_P follows a linear relationship, where L_{TP} increases at a rate of 0.10 nm s^{-1} with increasing T_P (Figure 2f).

3.2. Effect of Anodization Period and Surface Functionalization on the Optical Properties of NAA-DBRs.

Figure 3 depicts the dependence of the optical properties of NAA-DBRs on the anodization period (T_P) in air and water as well as the chemical composition analysis of the NAA-DBRs before and after surface functionalization with photoactive layers of TiO$_2$. The combined effect of T_P and media filling the nanoporous network of NAA-DBRs on the position of the characteristic photonic stopband were systematically studied by modifying T_P from 900 to 1600 s with ΔT_P = 100 s in air and water (H$_2$O) (Figure 3a). It is noteworthy that the photocatalytic reactions assessed in our study were performed in aqueous media. Therefore, establishing the photonic characteristics of NAA-DBRs in water is critical to understand the system's performance and identify photocatalytic performance enhancements associated with the slow photon effect. An analysis of the correlation between T_P and the central wavelength (λ_C) of the characteristic PSB establishes a linear relationship between these two parameters in both air and H$_2$O, with slopes 0.34 ± 0.03 and 0.44 ± 0.04 nm s^{-1}, respectively. In air, the position of the PSB can be tuned from 492 ± 1 to 740 ± 1 nm on varying T_P from 900 to 1600 s. This demonstrates that the position of characteristic PSB red shifts with T_P. This result is further supported by the interferometric color displayed by these NAA-PCs, as indicated by the digital images shown in Figure 3a, and the transmission spectra of NAA-DBRs shown in Figure S2 (Supporting Information). Structurally-colored NAA-DBRs display vivid colors in air, varying from purple (T_P = 900 s), periwinkle (T_P = 1000 s), blue (T_P = 1100 s), green (T_P = 1200 s), yellow (T_P = 1300 s), chartreuse (T_P = 1400 s), orange (T_P = 1500 s), to light brown (T_P = 1600 s). This phenomenon is attributable to a more efficient reflection of light by the PC structure at those spectral regions where the PSB is located.[49] Similarly, the position of the characteristic PSB also red shifts from 521 ± 1 to 839 ± 2 nm with T_P from 900 to 1600 s when the nanopores of NAA-DBRs are infiltrated with H$_2$O. The position of the characteristic PSB is red-shifted at an average rate of 65 ± 26 nm s^{-1} on changing the media within the nanoporous network of NAA-DBRs from air to H$_2$O. This red shift is due to the infiltration of nanopores with a medium of

higher refractive index than that of air (i.e., n_{air} = 1.00 RIU and n_{H_2O} = 1.33 RIU).

Figure 3b compiles a set of digital pictures of NAA-DBRs partially covered with transparent tape displaying interferometric colors as a function of T_P and the media infiltrating the nanopores (i.e., air and water). The left part of the photograph in each digital image corresponds to the interferometric color displayed by NAA-DBRs in air, while the right part corresponds to that in H$_2$O. As commented above, NAA-DBRs display vivid interferometric colors in air (i.e., purple, T_P = 900 s; periwinkle, T_P = 1000 s; blue, T_P = 1100 s; green, T_P = 1200 s; yellow, T_P = 1300 s; chartreuse, T_P = 1400 s; orange, T_P = 1500 s; light brown, T_P = 1600 s), which red shift with T_P. Similarly, the interferometric color also red shifts with T_P when the nanopores of NAA-DBRs are filled with H$_2$O. Furthermore, these images indicate that when the nanopores are filled with H$_2$O, the interferometric color is also red-shifted for all T_P, except for T_P = 1600 s, which displays light brown interferometric color at both parts of the digital picture. Note that the interferometric color relies upon the position of the characteristic PSB within UV–visible–near-IR spectrum. As such, NAA-DBRs featuring the characteristic PSB within the visible spectrum display interferometric color, from purple to orange, while those NAA-DBRs with PSB in the near-IR spectral range are light brown, which is the characteristic color of NAA produced under the fabrication conditions used in this study.

The inner surface of NAA-DBRs was coated with photoactive layers of TiO$_2$ by means of the sol–gel method. Figure 3c shows the energy dispersive X-ray spectra with insets depicting the percentage of the elements present in as-produced (before sol–gel deposition) and TiO$_2$-functionalized (after sol–gel deposition) NAA-DBRs. The EDX spectra reveal that while the intensity of Al and S atoms are constant after the functional TiO$_2$ layers are deposited onto the NAA-DBRs, the intensities of O and Ti atoms increase. For instance, the relative percentage of O, Al, S, and Ti atoms in as-produced NAA-DBRs was 25, 70, 5, and 0%, respectively. Note that for this EDX spectrum, Al and O atoms correspond to alumina (Al$_2$O$_3$), while S atoms were incorporated into the structure of NAA from the acid electrolyte during anodization. After chemical modification of NAA-DBRs with TiO$_2$, the relative percentages of O, Al, S, and Ti atoms were determined to be 37, 54, 5, and 4%, respectively. This analysis demonstrates the successful deposition of TiO$_2$ layers onto the inner surface of NAA-DBRs. The crystallographic phase of the TiO$_2$ layers under the synthesis conditions used in our study was amorphous (Figure S3, Supporting Information).

To summarize, modification of the anodization period can be used to precisely tune the optical properties (i.e., position of the PSB and interferometric color) of NAA-DBRs across the entire visible–near-IR spectrum. Furthermore, the inner surface of NAA-DBRs can be functionalized with photoactive layers of TiO$_2$ through sol–gel method to create composite semiconductor PC structures for photocatalysis.

3.3. Assessment of Photocatalytic Degradation of Model Organic Molecules by TiO$_2$–NAA-DBRs.

The photocatalytic performance of TiO$_2$–NAA-DBRs produced with varied T_P (i.e., from 900 to 1600 s with ΔT_P = 100 s) was assessed by investigating the photocatalytic degradation of three model pollutants (i.e., methyl orange, MO; rhodamine B, RhoB; and methylene blue, MB) under simulated solar light
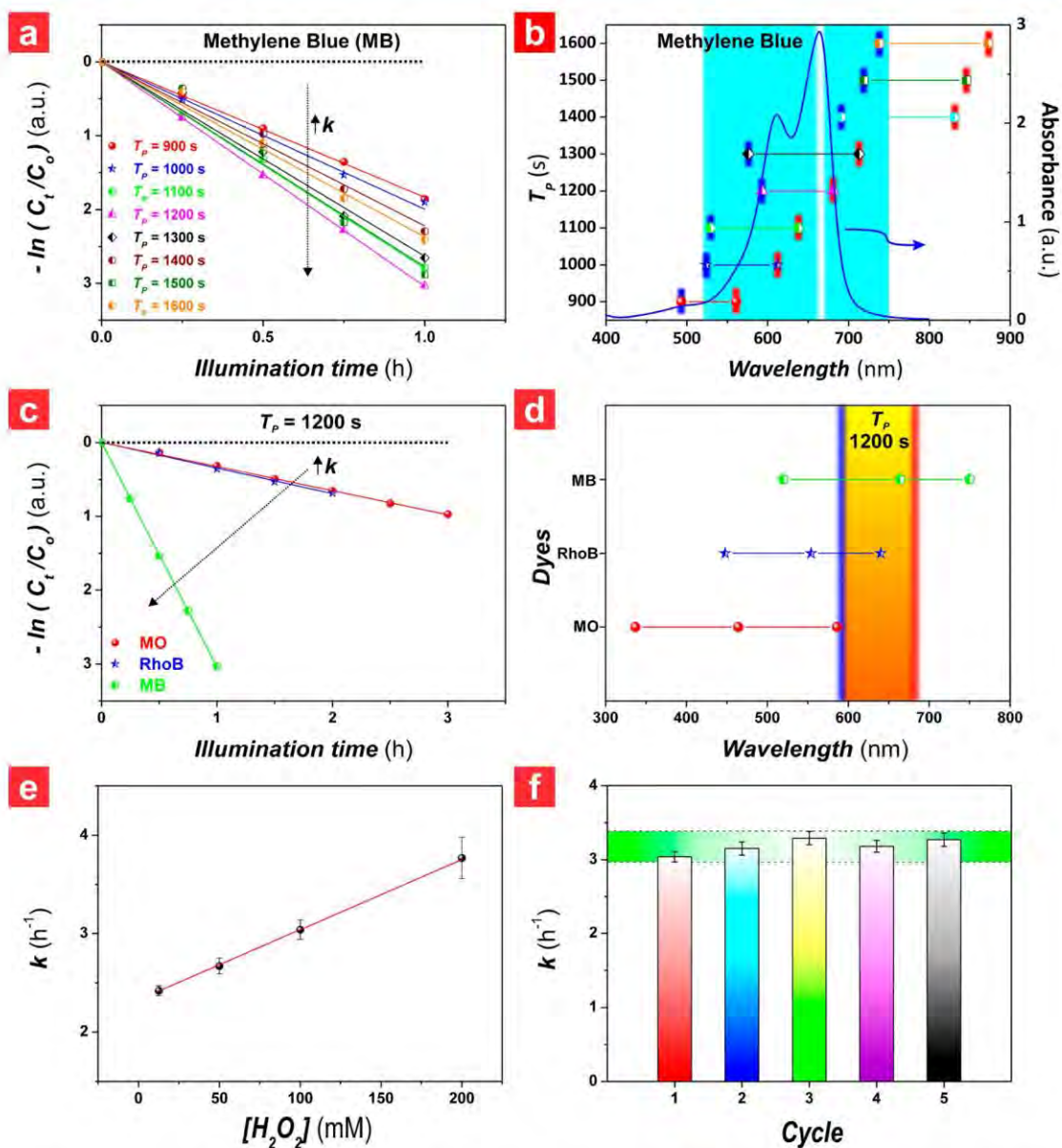
Figure 4. Photocatalytic assessment of TiO$_2$−NAA-DBRs as a function of anodization period (T_P), type of organic molecule, concentration of hydrogen peroxide (H$_2$O$_2$) solution, and recyclability (note: error bars in panels a, c, e, and f correspond to standard deviation from $n = 3$ independent experiments). (a) Photocatalytic degradation kinetics of methylene blue (MB) by TiO$_2$−NAA-DBRs produced with T_P from 900 to 1600 s with $\Delta T_P = 100$ s under controlled irradiation conditions (note: black dotted line denotes the photodegradation of the corresponding organic in a control NAA-DBR fabricated without photoactive TiO$_2$ layers). (b) Relative position of the blue and red edges of the characteristic photonic stopband (PSB) of TiO$_2$−NAA-DBRs from panel a with respect to the absorbance band of MB (note: white gap inside the absorbance band of MB denotes the band maximum of MB, $\lambda_{abs-MB} = 664$ nm, while blue and red vertical lines on the PSB correspond to the position of the blue and red edges of the PSB, respectively). (c) Photocatalytic degradation kinetics of methyl orange (MO), rhodamine B (RhoB), and methylene blue (MB) by TiO$_2$−NAA-DBRs produced with $T_P = 1200$ s under controlled irradiation conditions (note: black dotted line denotes the photodegradation of the corresponding organic in a control NAA-DBR fabricated without photoactive TiO$_2$ layers). (d) Relative position of absorbance bands of model organics from panel c with the characteristic PSB of TiO$_2$−NAA-DBRs produced with $T_P = 1200$ s (note: the blue and red vertical lines on the PSB correspond to the position of the blue and red edges of the PSB, respectively). (e) Linear correlation between the kinetic constant (k) and the concentration of H$_2$O$_2$ ([H$_2$O$_2$]) used in this study. (f) Reusability test of TiO$_2$−NAA-DBRs produced with $T_P = 1200$ s on the photodegradation of MB under simulated solar light irradiation (note: horizontal bar corresponds to the standard deviation between the lowest and highest values of k).

irradiation. Figure S4 (Supporting Information) displays the absorbance spectra of these organic molecules with the corresponding absorbance bands at 464, 554, and 664 nm, respectively. Figure S5 (Supporting Information) illustrates the simulated solar spectrum used in this study. Analysis of this

spectrum reveals a spectral distribution of 0.12% UV (350−400 nm), 64.60% visible (400−750 nm), and 35.28% near-IR (800−1025 nm). The photocatalytic reactions performed in this study are thus driven by visible−near-IR light irradiation (i.e., 400−1025 nm), which is far from the characteristic

Table 1. Effect of the Relative Position of the Blue and Red Edges of the Characteristic PSB and the Total Anodization Time of TiO$_2$−NAA-DBRs Fabricated with Various T_P on the Kinetic Constant (k) for the Photodegradation of MB Molecules (Note: Error Values Correspond to Standard Deviation from n = 3 Independent Experiments)

	anodization period							
	900 s	1000 s	1100 s	1200 s	1300 s	1400 s	1500 s	1600 s
k (h^{-1})	1.83 ± 0.01	2.00 ± 0.06	2.80 ± 0.04	3.04 ± 0.01	2.63 ± 0.10	2.22 ± 0.09	2.77 ± 0.15	2.37 ± 0.08
edge nearest to the peak	red	red	red	red	red	blue	blue	blue
distance of nearest edge to the peak (nm)	103	52	26	17	49	27	55	74
total anodization time (h)	38.5	42.7	46.8	51.0	55.2	59.3	63.5	67.7

energy bandgap of TiO$_2$ (i.e., 3.20−3.35 eV = 370−387 nm). Note that 100 mM of H$_2$O$_2$ was added to the reaction solution to aid the photogeneration of charge carriers (e$^-$/h$^+$) in the photoactive TiO$_2$ layers deposited onto the inner surface of NAA-DBRs. The concentration of organic molecules with time in the reaction solution during the photodriven degradation process (C_t) was estimated from the calibration lines shown in Figure S1. The photocatalytic performance of TiO$_2$−NAA-DBRs was fitted and calculated through the linearized pseudo-first-order kinetics model shown in eq 2:

$$-\ln(C_t/C_o) = kt \tag{2}$$

where C_o is the concentration after stirring in the dark for 30 min, C_t is the concentration at illumination time t, and k is the characteristic kinetic constant.

3.4. Effect of Anodization Period on Photocatalytic Degradation of MB.
Slow photons are photons with reduced group velocity near the vicinity of the PSB of PCs. This effect increases the overall absorbance of the PC material, enhancing light−matter interactions for light harvesting since photons spend longer time within the photocatalytic material (i.e., generation of extra e$^-$/h$^+$ pairs for photocatalysis).[12,54] The well-defined and spectrally controllable PSB of TiO$_2$−NAA-DBRs make these PC structures excellent candidates to study and utilize these light−matter interactions at the nanoscale. Photocatalytic degradation of MB under simulated sunlight irradiation conditions was used as a model reaction to identify slow photon effects in TiO$_2$−NAA-DBRs fabricated with varying T_P from 900 to 1600 s, with ΔT_P = 100 s. Panels a and b of Figure 4 and Table 1 show the effect of T_P as a function of the relative position of the edges of the PSB of TiO$_2$−NAA-DBRs and the absorbance band of MB, using its photocatalytic degradation under simulated solar light irradiation as an indicator of slow photon enhancements. The kinetic constants (k) for TiO$_2$−NAA-DBRs with T_P = 900, 1000, 1100, 1200, 1300, 1400, 1500, and 1600 s were 1.83 ± 0.01, 2.00 ± 0.06, 2.80 ± 0.04, 3.04 ± 0.01, 2.63 ± 0.10, 2.22 ± 0.09, 2.77 ± 0.15, and 2.37 ± 0.08 h^{-1}, respectively (Figure 4a and Table 1). The highest k value was achieved by TiO$_2$−NAA-DBRs produced with T_P = 1200 s, indicating that these composite semiconductor PCs provide the fastest and most efficient platform to photodegrade MB, with a 8−40% superior performance than that achieved by their counterparts produced with shorter or longer T_P. Figure 4b and Table 1 indicate that the position of the red edge of the PSB of TiO$_2$−NAA-DBRs fabricated with T_P = 1200 s is the closest to the absorbance band of MB (i.e., λ_{Abs-MB} = 664 nm) (i.e., ~17 nm away from the absorbance band maximum of MB). Upon irradiation, slow photons are strongly localized in the high (i.e., photoactive layer of TiO$_2$) and low (i.e., organic solution) dielectric parts of the red and blue edges of the characteristic

PSB, respectively.[54] This phenomenon results in a longer lifetime of photons that increases the effective optical path length of the light waves when photons travel across the TiO$_2$−NAA-DBRs' structure. This enhanced light−matter interaction promotes the photon-to-electron conversion rate in these composite PC structures, speeding up the photo-catalytic degradation of MB significantly when the edges of the PSB are located close to the absorbance band maximum of MB.[54−56] The slow photon effect is even more apparent when the red edge of the PSB is in the proximity of the absorbance band of MB. Here slow photons in that spectral region are strongly localized in the high refractive index region of the PC (i.e., semiconductor, TiO$_2$).[12,54] Our results confirm this hypothesis since this model photodegradation reaction is enhanced when the red edge of the PSB of TiO$_2$−NAA-DBRs is at its closest to the absorbance band maximum of MB.

The red edge of the PSB of TiO$_2$−NAA-DBRs produced with T_P = 1100 s is the second closest to the absorbance band maximum of MB (i.e., ~26 nm away). These PC structures are the second best performing type of TiO$_2$−NAA-DBR (i.e., k = 2.80 ± 0.04 h^{-1}). This further confirms the hypothesis that the relative position of the red edge of the PSB with respect to the absorbance band of the organic model molecule plays a more significant role than that of the blue edge in enhancing the photocatalytic degradation of MB through slow photon effect. Although the red edge of the PSB of TiO$_2$−NAA-DBRs produced with T_P = 1300 s is the third closest to the absorbance band maximum of MB (i.e., ~49 nm away), these PC platforms are slightly outperformed by TiO$_2$−NAA-DBRs fabricated with T_P = 1500 s, which achieve approximately 5% superior performance. Figure 4b shows that the characteristic PSB of TiO$_2$−NAA-DBRs produced with T_P = 1500 s partially overlaps with the absorbance band of MB, where the blue edge is 55 nm removed from the absorbance band maximum of MB. The red edge of the PSB of these PCs falls completely outside of the absorbance band. Since the blue edge of the PSB of these TiO$_2$−NAA-DBRs is located inside the absorbance band of MB, a partial enhancement of the photocatalytic perform-ance due to slow photon effect is expected. However, since the PSB is practically located outside of the absorbance range of MB, photocatalytic enhancement under such a configuration relies strongly on other factors such as the geometric features of the overall PC structure. As indicated in Table 1, TiO$_2$−NAA-DBRs fabricated with T_P = 1500 s are produced with the second longest anodization time (i.e., t_{An} = 63.5 h), which is calculated from the number of anodization pulses (N_P = 150 pulses) and the anodization period (T_P = 1500 s) by eq 3:

$$t_{An} = N_P/T_P \tag{3}$$

The total thicknesses or pore length (L_P; Figure 1a) of TiO$_2$−NAA-DBRs is directly proportional to the anodization time.

182

An increase in total thicknesses of the PC platform enhances its overall light absorption, since more semiconductor matter is available for light−matter interactions.[41,57] This leads to the photogeneration of extra charge carriers (e^-/h^+) and thus to an enhancement of the photocatalytic activities achieved by those TiO$_2$−NAA-DBRs featuring thicker structure. The unexpectedly higher performance shown by TiO$_2$−NAA-DBRs produced with T_P = 1500 s is thus attributed to two contributing factors, a partial alignment of the blue edge of the PSB with respect to the absorbance band of MB and the total thickness of the PC platform. The fifth best performing TiO$_2$−NAA-DBRs platforms are those produced with T_P = 1600 s. These semiconductor PCs feature a PSB located almost entirely outside of the absorbance range of MB. Despite having the longest t_{An} (i.e., 67.7 h), the photocatalytic performance shown by these TiO$_2$−NAA-DBRs is less efficient than that achieved by TiO$_2$−NAA-DBRs fabricated with T_P = 1500 s by ∼14%. This result is attributable to the negligible contribution by slow photon effect to the photocatalytic performance since the blue edge of the PSB of these PCs is very far away from the absorbance band of MB (i.e., ∼74 nm).

The blue edge of the PSB of TiO$_2$−NAA-DBRs fabricated with T_P = 1400 s is relatively close to the absorbance band maximum of MB (i.e., ∼55 nm). However, these composite photonic structures provide the sixth best performance in degrading the model organic molecule (i.e., k = 2.22 ± 0.09 h^{-1}). TiO$_2$−NAA-DBRs produced with T_P = 1400 s feature a thinner structure (i.e., t_{An} = 59.3 h) than that of those TiO$_2$−NAA-DBRs produced with T_P = 1500 and 1600 s (i.e., t_{An} = 63.5 and 67.7 h, respectively). This result is attributable to an inefficient combination of both slow photon effect and overall thickness of the PC structure, with a partial alignment of the PSB's blue edge and shorter pore length in the PC structure. The worst performing TiO$_2$−NAA-DBR structures have T_P = 900 and 1000 s, with degradation rates k = 2.00 ± 0.06 and 1.83 ± 0.01 h^{-1}, respectively. TiO$_2$−NAA-DBRs produced with T_P = 900 and 1000 s feature PSBs that are partially and entirely located within the absorbance range of MB, respectively. However, the red edge of the PSBs of these PCs is removed from the absorbance band maximum of MB (i.e., ∼52 and 103 nm). Furthermore, these PCs have the thinnest structures (i.e., t_{An} = 38.5 and 42.7 h, respectively). Thus, a combination of a relative misalignment between the PSB's red edge and the thinnest PC structure has a significant detrimental effect on the overall photodegradation performance of these semiconductor PCs. This analysis establishes that the photocatalytic performance of TiO$_2$−NAA-DBRs with various T_P follows the order 1200 > 1100 > 1500 > 1300 > 1600 > 1400 > 1000 > 900 s. Changes in the characteristic color of the MB solution upon degradation by TiO$_2$−NAA-DBRs under simulated irradiation conditions, from 0 to 60 min with an interval of 15 min (Figure S6, Supporting Information) also confirm the photocatalytic degradation efficiency of TiO$_2$−NAA-DBRs by visual analysis. This result further demonstrates that MB molecules are efficiently photodegraded by TiO$_2$−NAA-DBRs after 1 h.

To summarize, the photocatalytic performance of TiO$_2$−NAA-DBRs is enhanced by the slow photon effect when the edges of the PSB fall within the absorbance range of MB. This enhancement is more significant when the red edge of the PSB of TiO$_2$−NAA-DBRs is at its closest to the absorbance band maximum of MB. Nevertheless, the thickness of the PC platform does play a more significant role in enhancing the

photocatalytic properties of TiO$_2$−NAA-DBRs when the PSB is misaligned with the absorbance band of the model organic molecule. An optimum combination of relative position between the red edge of the PC's PSB and the thickness of the PC platform boosts photocatalytic reactions, making an efficient and rational utilization of the slow photon effect and the physical properties of these photocatalysts.

3.5. Effect of Type of Organic Molecule on the Photocatalytic Performance of TiO$_2$−NAA-DBRs.

The effect of the type and characteristics of organic molecules on the photocatalytic performance of TiO$_2$−NAA-DBRs was investigated by assessing the photocatalytic degradation of three model organics with well-defined absorbance bands across the visible spectral range (i.e., MO, RhoB, and MB). TiO$_2$−NAA-DBRs produced with T_P = 1200 s were used as photocatalyst platforms to study and identify slow photon effects associated with the relative position between the edges

Table 2. Values of the Kinetic Constant (k) for the Photodegradation of Three Organics (i.e., MO, RhoB, and MB) by TiO$_2$−NAA-DBR with T_P = 1200 s (Note: Error Values Correspond to Standard Deviation from n = 3 Independent Experiments)

	organic molecule		
	MO	RhoB	MB
k (h^{-1})	0.32 ± 0.01	0.35 ± 0.01	3.04 ± 0.01

of the PC's PSB and the absorbance and characteristics of the model organic molecules. Panels c and d of Figure 4 and Table 2 summarize the effect of the spectral arrangement between the absorbance bands of these model organic molecules and the position of the edges of the PSB of TiO$_2$−NAA-DBRs, using their respective photodegradation rate as an indicator of enhancements by slow photon effect. The k values for the photodegradation of MO, RhoB, and MB by TiO$_2$−NAA-DBRs produced with T_P = 1200 s were 0.32 ± 0.01, 0.35 ± 0.01, and 3.04 ± 0.01 h^{-1}, respectively (Figure 4c). The highest k value was achieved by the photodegradation of MB, which was degraded at a ∼88 and 89% faster rate than RhoB and MO, respectively. As Figure 4d and Table 2 indicate, the characteristic PSB of TiO$_2$−NAA-DBRs fabricated with T_P = 1200 s falls completely inside the absorbance range of MB. However, only the blue part of the PSB partially overlaps with the absorbance band of RhoB, and it is practically misaligned with the MO's absorbance range. The red edge of the PSB of these TiO$_2$−NAA-DBRs is located near the absorbance band of MB (i.e., ∼17 nm away), while its blue edge is located within the range of the absorbance band of RhoB (i.e., ∼39 nm away) and well-removed from the absorbance band of MO (i.e., ∼129 nm away). As demonstrated in the previous section, the red edge of the PSB is more significant than the blue edge in enhancing photocatalytic reactions by slow photon effect. Our results confirm this hypothesis as indicated by the analysis of the relative positions of the red edge of the PC's PSB and the absorbance band of these model molecules.

It is worth noting that the charge of the organic molecule and its interaction with the surface charge of TiO$_2$−NAA-DBRs are also important contributing factors that impact the overall photodegradation rates achieved by these photocatalyst platforms. Table S1 (Supporting Information) collates the charge of the model organic molecules used in this study, where MO, RhoB, and MB are negatively, positively, and

positively charged, respectively. The surface of the photoactive TiO_2 layer deposited onto the inner surface of NAA-DBRs is negatively charged at pH 5.5, the pH of the aqueous solution at which these photochemical reactions were performed. The negatively charged surface of TiO_2 would have high affinity for positively charged RhoB and MB molecules.[1,4] This would increase the total number of molecules adsorbed onto the surface of TiO_2, boosting the overall photocatalytic degradation rate of the system. Conversely, interaction between the negatively charged surface of the photoactive TiO_2 layers and negatively charged MO molecules is poor due to electrostatic repulsion. The reduced amount of MO molecules present within the vicinity of the photoactive layer would lead to a significant reduction of the system's performance. Another factor to consider is the intensity of the absorption bands of MO, RhoB, and MB. As Figure S4 indicates, the absolute absorption intensity of MO, RhoB and MB at their central position maxima ($\lambda_{abs\text{-}MO}$ = 464 nm, $\lambda_{abs\text{-}RhoB}$ = 554 nm, and $\lambda_{abs\text{-}MB}$ = 664 nm) are ~1.5, 3.6, and 2.8 au, respectively. RhoB (~3.6 au) and MO (~2.8 au) molecules absorb incoming light more efficiently than that of MB (~1.5 au). At these spectral regions, RhoB and MO molecules absorb most of the incoming light that propagates through the aqueous organic solutions before it reaches the surface of the TiO_2−NAA-DBRs. This screening effect reduces the overall photocatalytic performance of the material due to an inefficient use of photons in the semiconductor band. Therefore, overall photocatalytic degradation rates provided by TiO_2−NAA-DBRs are also dependent on the nature of the organic molecule, the electrostatic interactions surface−molecule, and the relative positioning between the edges of the PSB and the absorbance band of the organics. These observations are in good agreement with our previous study using NAA gradient-index filters as model photonic crystal platforms,[4] which is further evidence to support our conclusions.

3.6. Effect of Additive Concentration and Assessment of Reusability on the Photocatalytic Performance of TiO_2−NAA-DBRs.

The relationship between the concentration of H_2O_2 ([H_2O_2]) and the photocatalytic degradation performance of TiO_2−NAA-DBRs was studied by assessing the photocatalytic degradation of MB by TiO_2−NAA-DBRs produced with T_p = 1200 s. In this experiment, the concentration of H_2O_2 was varied from 12.5, 50, 100 to 200 mM (Figure 4e). The kinetic constants for this photocatalytic reaction as a function of [H_2O_2] were determined to be 2.42 ± 0.05, 2.67 ± 0.08, 3.04 ± 0.10, and 3.77 ± 0.21 h^{-1}, respectively. A linear fitting between the k values and [H_2O_2] indicates that the former parameter increases with the latter at a rate of 0.01 ± 0.00 mM h^{-1}. This correlation can be associated with the higher number of $^\bullet$OH radicals photogenerated in the inner surface of TiO_2−NAA-DBRs with increasing [H_2O_2], which speed up the degradation of MB molecules. Reusability is another aspect of paramount importance to minimize the technological translation costs associated with the bench-to-field translation of photocatalyst materials. Reusability of TiO_2−NAA-DBRs was tested using the same TiO_2−NAA-DBR platform (i.e., T_p = 1200 s) in all five consecutive cycles of photodegradation, in which fresh MB solutions were photodegraded under simulated solar light irradiation for 1 h per cycle. The results summarized in Figure 4f show that k fluctuates from 3.04 ± 0.07 to 3.29 ± 0.09 h^{-1} between the first and fifth photodegradation cycle, demonstrating that TiO_2−NAA-DBRs provide a relatively similar

performance after several cycles of use. The average k value for the five photodegradation cycles is 3.18 ± 0.29 h^{-1}, where the photocatalytic conversion ratio of TiO_2−NAA-DBRs in the photodegradation of MB is ~96% under simulated solar light irradiation (Table S2, Supporting Information). These results demonstrate that TiO_2−NAA-DBRs possess high photocatalytic activity, stability, and reusability, which are required properties for real-life photocatalysis applications.

3.7. Assessment of Photocatalytic Degradation of 4-Chlorophenol by TiO_2−NAA-DBRs.

Organic dyes are widely used model organics to assess the photocatalytic degradation performance of photocatalyst PC structures under visible light irradiation.[1,4,5,37] However, resilient organic pollutants such as pesticides have absorbance bands in the UV spectral region. This factor limits substantially the photocatalytic performance of PC structures with PSB in the visible range to degrade these chemicals under visible−near-IR light irradiation. The ability of TiO_2−NAA-DBRs to degrade real-life resilient organic pollutants was assessed by studying the photodegradation of 4-chlorophenol (4-CP) under controlled visible−near-IR irradiations conditions. 4-CP is used as intermediate in the production of pharmaceuticals, agricultural products, biocides, and paints, and it is classified as a dangerous substance that can lead to irreversible changes in aquatic ecosystems. 4-CP has a distinctive and well-resolved absorbance band located at 225 nm (Figure S4, Supporting Information). A direct relationship between its absorbance at 225 nm and the concentration of 4-CP in solution as determined by the calibration line is shown in Figure S7 (Supporting Information). The effect of relative position of the blue and red edges of the PSB with the absorbance band of 4-CP on the photodegradation of 4-CP by TiO_2−NAA-DBRs was first studied using a set of TiO_2−NAA-DBRs fabricated with T_p = 900, 1200, and 1600 s as model PC platforms. Figure 5a shows dynamic photodegradation of 4-CP by these semiconductor PCs, while Table 3 summarizes the kinetic constants estimated for TiO_2−NAA-DBRs produced with T_p = 900, 1200, and 1600 s calculated from linear fittings, which were 0.15 ± 0.01, 0.14 ± 0.01, and 0.03 ± 0.00 h^{-1}, respectively. These results indicate that TiO_2−NAA-DBRs produced with T_p = 900 and 1200 s provide the best photocatalytic performances, where the former model PCs showed a ~7% higher performance than that achieved by their equivalents produced with longer anodization period. In contrast, TiO_2−NAA-DBRs produced with T_p = 1600 s showed the worst photocatalytic performance, which was ~79 to ~80% worse than that of their 1200 and 900 s counterparts, respectively. Figure 5b shows the relative position of the edges of characteristic PSB of these semiconductor PCs with the absorbance band of 4-CP as a function of T_p. The PSB of all these TiO_2−NAA-DBRs falls completely outside of the absorbance range of 4-CP (Figure S3). Under such a configuration, the photocatalytic degradation of 4-CP by TiO_2−NAA-DBRs should not depend on the slow photon effect but rely solely upon the total thicknesses of TiO_2−NAA-DBR platforms. Therefore, the thicker the TiO_2−NAA-DBR platform the better the photocatalytic performance. However, the obtained k values indicate that the closer the PSB of TiO_2−NAA-DBRs is to the UV absorbance band of the model pesticide the faster the degradation rate achieved by this photocatalyst system (i.e., higher k value).

This result is demonstrated to be independent of the thickness of the TiO_2−NAA-DBR platform (i.e., T_p = 900 s
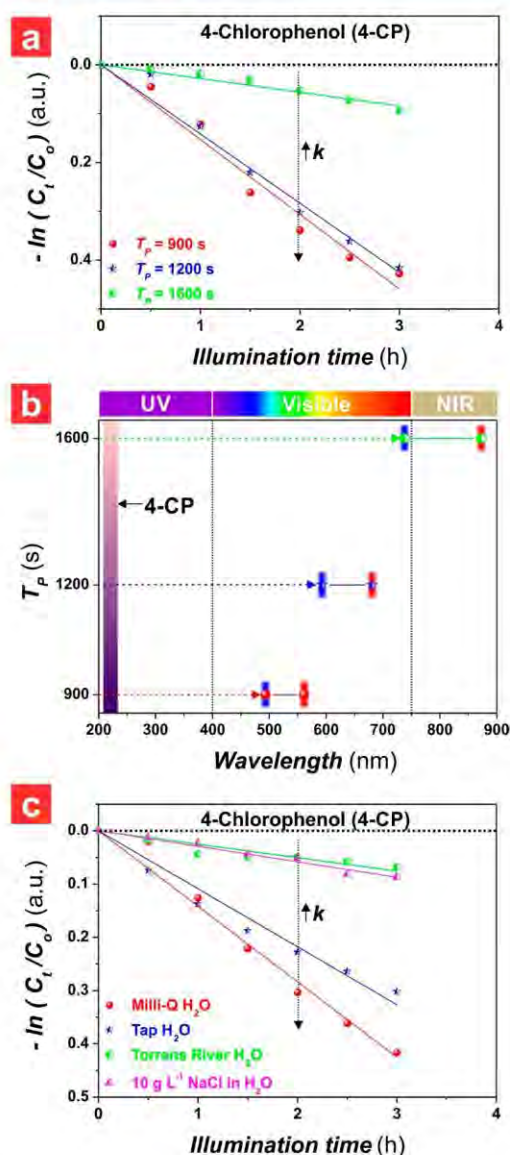
Figure 5. Photocatalytic assessment of TiO$_2$–NAA-DBRs on the photodegradation of 4-chlorophenol (4-CP) as a function of anodization period (T_P) and aqueous matrix composition (note: error bars in panels a and c correspond to standard deviation from n = 3 independent experiments). (a) Photocatalytic degradation kinetics of 4-CP by TiO$_2$–NAA-DBRs produced with T_P = 900, 1200, and 1600 s under controlled irradiation conditions (note: black dotted line denotes the photodegradation of the 4-CP in a control NAA-DBR fabricated without photoactive TiO$_2$ layers). (b) Relative position of the blue and red edges of the characteristic photonic stopband (PSB) of TiO$_2$–NAA-DBRs from panel a with the absorbance band of 4-CP (note: the blue and red vertical lines on the PSB correspond to the position of the blue and red edges of the PSB, respectively). (c) Photocatalytic degradation kinetics of 4-CP in different aqueous matrices by TiO$_2$–NAA-DBRs produced with T_P = 1200 s under controlled irradiation conditions (note: black dotted line denotes the photodegradation of 4-CP in a control NAA-DBR fabricated without photoactive TiO$_2$ layers).

and t_{An} = 38.5 h; T_P = 1200 s and t_{An} = 51.0 h; T_P = 1600 s and t_{An} = 67.7 h). We hypothesize that this effect can be attributable to slow photon effect-driven enhancement of the photocatalysis performance achieved by these TiO$_2$–NAA-

Table 3. Values of the Kinetic Constant (k) for the Photodegradation of 4-CP by TiO$_2$–NAA-DBRs Produced with T_P = 900, 1200, and 1600 s (Note: Error Values Correspond to Standard Deviation from n = 3 Independent Experiments)

	for given anodization period		
	900 s	1200 s	1600 s
k (h^{-1})	0.15 ± 0.01	0.14 ± 0.01	0.03 ± 0.00

DBRs. Figure 5b further supports this hypothesis since the PSB of TiO$_2$–NAA-DBRs produced with T_P = 900 and 1200 s falls completely under the visible spectral region, while the PSB of TiO$_2$–NAA-DBRs fabricated with T_P = 1600 s is almost entirely located within the near-IR region of the spectrum.

Figure S5 shows that ∼65% of the artificial illumination used in our study corresponds to visible light, while the remaining ∼35% of illumination is near-IR light. Therefore, it is inferred that TiO$_2$–NAA-DBRs with PSB within the visible spectral region can collect and utilize more efficiently photons from the high-irradiance visible region to generate carriers for photocatalytic degradation of 4-CP. This also contributes to the superior performance achieved by TiO$_2$–NAA-DBRs produced with shorter T_P, since the PSB of these PCs is located in the visible spectral range. Note that the overall photocatalytic degradation of 4-CP molecules is low as compared to that achieved for MO, RhoB, and MB. However, 4-CP is a chemically resilient and negatively charged molecule (Table S1) that is electrostatically repulsed by the negatively charged inner surface of TiO$_2$–NAA-DBRs. This minimizes the number of 4-CP molecules that are absorbed onto the photocatalyst platform surface, reducing the overall photodegradation performance of the system. Kim and Choi[58] studied the visible-light-induced degradation reaction of 4-CP in aqueous suspension, using pure TiO$_2$ powder as photocatalyst platform material. Their observations indicate that the surface complexation between phenolic compounds and TiO$_2$ appears to be responsible for the visible light reactivity. According to this photodegradation mechanism, a direct electron transfer from surface-complexed phenol groups to the conduction band of the TiO$_2$ coating upon absorbing visible light is the responsible factor to initiate the oxidative degradation of 4-CP.

The performances of photocatalyst materials are typically assessed using ultrapure water-based aqueous solutions. However, the effect of the composition and complexity of the aqueous matrix on the performance of photocatalysts is a critical aspect to consider for real-life applications and for the translation of fundamental advances in photocatalysis into practical systems that can address real-world problems. Therefore, the effect of the media composition on the photocatalytic performance of a set of TiO$_2$–NAA-DBRs produced with T_P = 1200 s was assessed by studying the degradation of 4-CP in various matrices (i.e., Milli-Q H$_2$O, tap H$_2$O, Torrens river H$_2$O, and 10 g L^{-1} NaCl aqueous solution).

Figure 5c shows dynamic photodegradation of 4-CP in these matrices and Table 4 summarizes the obtained k values, which were estimated to be 0.14 ± 0.01, 0.11 ± 0.01, 0.025 ± 0.001, and 0.029 ± 0.002 h^{-1}, respectively. These results indicate that this photochemical reaction achieves its best performance when the aqueous matrix is Milli-Q H$_2$O (k = 0.14 ± 0.01 h^{-1}). This result is expected since this matrix does not have

185

Table 4. Values of the Kinetic Constant (k) for the Photodegradation of 4-CP in Four Different Matrices (i.e., Milli-Q H_2O, tap H_2O, Torrens River H_2O, and 10 g L^{-1} NaCl Aqueous Solution) by TiO_2−NAA-DBRs Produced with T_P = 1200 s (Note: Error Values Correspond to Standard Deviation from n = 3 Independent Experiments)

	matrix			
	Milli-Q H_2O	tap H_2O	Torrens river H_2O	10 g L^{-1} NaCl
k (h^{-1})	0.14 ± 0.01	0.11 ± 0.00	0.025 ± 0.001	0.029 ± 0.002

interfering molecules that can potentially hinder the interaction between 4-CP molecules and the inner functional surface of TiO_2−NAA-DBRs. The k value for the photodegradation of 4-CP in tap H_2O is the second highest, and it was found to perform ~21% less efficiently than in Milli-Q H_2O under simulated solar light irradiation (k = 0.11 ± 0.01 h^{-1}). When the photocatalytic degradation of 4-CP is performed in environmental water from the Torrens river (Adelaide, Australia) and a Milli-Q H_2O-based 10 g L^{-1} NaCl solution, the k values were found to be ~73 and 81% lower than those obtained in less complex matrices (i.e., k = 0.025 ± 0.001 and 0.029 ± 0.002 h^{-1}, respectively). This result indicates that this photochemical reaction is hindered when it is conducted in complex matrices. This significant difference in photocatalytic degradation of 4-CP by TiO_2−NAA-DBRs can be attributable to interfering ions and molecules present in these complex solutions.

Milli-Q H_2O and tap H_2O matrices are relatively free from ions and molecules, although the latter contains some small concentration of ions such as Ca^{2+}, Na^+, K^+, Mg^{2+}, Fe^{2+}, and Cl^- that slightly interfere with the photodegradation of 4-CP, as indicated by the k values. When this light-driven reaction is performed in a saline aqueous solution (i.e., 10 g L^{-1} NaCl), salt molecules dissociate in water to form Na^+ and Cl^- ions. A high concentration of these ions inside the nanopores of TiO_2−NAA-DBRs is demonstrated to slow down this reaction by hindering interactions between the inner surface of TiO_2−NAA-DBRs and water molecules to form •OH radicals that subsequently oxidize absorbed 4-CP molecules into by-products. Furthermore, the presence of these ions also reduces the total amount of 4-CP molecules absorbed onto the negatively charged inner surface of TiO_2−NAA-DBRs, decreasing significantly the overall performance of the system. As the k values indicate, the photocatalytic degradation of 4-CP in Torrens river H_2O is slightly worse than that obtained in the 10 g L^{-1} NaCl aqueous solution, due to the presence of ions and organic molecules that interfere with the formation of •OH radicals and compete with the absorption of 4-CP molecules onto the inner surface of TiO_2−NAA-DBRs. This analysis reveals that the photocatalytic performance of TiO_2−NAA-DBRs in degrading 4-CP molecules is thus highly affected by the presence of interfering ions and organic molecules. However, TiO_2−NAA-DBRs are still efficient enough to degrade a highly resilient environmental pollutant in complex aqueous matrices. This is a clear demonstration of the potential of these semiconductor PC structures for real-life applications.

3.8. Photocatalytic Degradation Mechanism. The experimental results obtained in this study allow us to propose a photocatalytic degradation mechanism that explains the performance of TiO_2−NAA-DBRs. These NAA-based PC structures collect photons from a high-irradiance spectral region (i.e., visible and near-IR), which are efficiently utilized by the photoactive TiO_2 layers to speed up photocatalytic reaction rates, as indicated by the degradation of model

organic molecules. In this process, charge carriers (e^-/h^+) are generated and separated upon light irradiation to the conduction band and valence band of TiO_2, respectively. These charge carriers are subsequently transferred to the surroundings of the nanopores' surface and react with redox species to produce reactive oxidation species (i.e., •OH radicals), which decompose organic molecules absorbed onto or close to the inner surface of the nanopores.[59] When H_2O_2 molecules are added to the matrix solution, electrons at the conduction band react with H_2O_2 to form •OH radicals and $^-$OH ions, which can be further oxidized to •OH radicals by the photogenerated holes at the valence band of TiO_2. Photogenerated holes also oxidize H_2O molecules to form •OH radicals, which decompose organic molecules into CO_2 and H_2O, which are harmless to the environment. Our results demonstrate that the photocatalytic decomposition rate at the TiO_2 layers can be significantly enhanced by rationally engineering the underlying NAA-DBR structure to increase photon-to-electron conversion rates at the TiO_2 functional layers. Photons absorbed by the structure of NAA-DBRs propagate with reduced group velocity and localize near the PSB's edges, resulting in longer lifespan of photons at these spectral regions. These photons can be subsequently utilized by the photoactive TiO_2 layers to generate extra carriers and accelerate light-driven redox reactions occurring within the nanopores of TiO_2−NAA-DBRs. The slow photon effect is strongly dependent on the relative position of the PSB's edges with respect to the absorbance band of model organic molecules. For instance, the photocatalytic enhancement was found to be maximum when the PSB's red edge falls completely within the absorbance band maximum of the organic molecules. Our results also indicate that positioning the blue edge of the PSB toward the absorbance band maximum of these organic molecules can enhance photo-catalytic reactions by slow photon effect too, although in a less efficient manner than that achieved by the red edge due to the higher localization of slow photons at the high refractive index section of the PC structure (i.e., semiconductor—red edge).

The slow photon enhancement is dramatically reduced when the distance between the PSB's edges and the absorbance band of organic molecules is increased. Under this arrangement (i.e., partial overlapping between the PC's PSB and the absorbance band of the organic molecule), the contribution of the slow photon effect to the overall photocatalytic enhancement is weak and other factors such as the total pore length of the composite PC structure are found to have a more significant contribution toward the photocatalytic performance of the PC structure. However, the assessment on the photodegradation of 4-CP molecules (i.e., absorbance band in the UV range) indicates that when the configuration of the system is such that the PSB falls completely outside the absorbance band of the organic molecule, the closer the PSB is from the absorbance band the more efficient the photocatalytic PC system is, independently of its overall thickness. However, other factors such as percentage of high-irradiance spectral regions also

contribute significantly to the overall performance of these semiconductor PCs. Our study also establishes that the nature of the organic molecule is another important contributing factor to the efficiency of these light-driven reactions.

Table 5. Compilation of Representative Kinetic Constant (k) Values for the Photodegradation of MO, RhoB, MB, and 4-CP Molecules by Various Photocatalysts

	k (h^{-1})				
photocatalyst	MO	RhoB	MB	4-CP	ref
P25 TiO$_2$ nanoparticles	0.00	0.17	0.64	0.037	1, 60
TiO$_2$ inverse opal	0.01	0.47	1.32		1
ZnO inverse opal	0.01	0.13	1.49	0.00	30
TiO$_2$–NAA-GIFs	0.25	0.39	2.10		4
TiO$_2$–NAA-DBRs	0.32	0.35	3.04	0.15	this study

3.9. Comparative Analysis with Benchmark Photocatalyst Platforms. Table 5 compiles a summary of representative studies using benchmark photocatalyst materials with and without PC structure, the performance of which was assessed under visible-light-irradiation conditions. Multiple studies reported on the photocatalytic performance of P25 TiO$_2$ nanoparticles to photodegrade MO, RhoB, MB, and 4-CP under visible-light-irradiation conditions.[1,60] P25 TiO$_2$ is a benchmark photocatalyst material that features anatase crystallographic phase and only absorbs light in the UV spectral region. The photocatalytic degradation rates reported for P25 TiO$_2$ nanoparticles when photodegrading these model organics were $k_{MO} = 0.00$ h^{-1}, $k_{RhoB} = 0.17$ h^{-1}, $k_{MB} = 0.64$ h^{-1}, and $k_{4-CP} = 0.0037$ h^{-1}. These values indicate that TiO$_2$–NAA-DBRs substantially outperform P25 TiO$_2$ nanoparticles in the degradation of these organic molecules under visible light irradiation, with a photocatalytic enhancement of 100, 51, 79, and 75%, respectively. Though a direct comparison could not be entirely correct due to differences in experimental conditions (e.g., irradiation spectral distribution, power density, and catalyst loading, etc.), this comparison indicates the potential of TiO$_2$–NAA-DBRs as efficient photocatalyst platforms.

TiO$_2$ inverse opals feature a 3D PC structure and have been devised as promising photocatalyst platforms due to their well-defined and relatively controllable characteristic PSB. The PC structure of semiconductor inverse opals enables the utilization of the slow photon effect to enhance photocatalytic reactions. Zheng et al.[1] fabricated a set of TiO$_2$-based inverted opal structures featuring various pore sizes (i.e., from 270 to 550 nm) and assessed the photodegradation of three model organic dyes (i.e., RhoB, MO, and MB) under visible light irradiation. The photocatalytic performance achieved by this system was $k_{MO} = 0.01$ h^{-1}, $k_{RhoB} = 0.47$ h^{-1}, and $k_{MB} = 1.32$ h^{-1}, respectively. Although these TiO$_2$ inverse opal structures outperform TiO$_2$–NAA-DBRs by ~34% in the photodegradation of RhoB, TiO$_2$–NAA-DBRs show enhanced photocatalytic performances in the photodegradation of MO and MB (i.e., ~97 and ~57% superior performance, respectively). Other types of inverse opal PC structures have been explored for enhanced photon-to-electron conversion rates through the slow photon effect. For instance, ZnO-based inverse opals with PSB positioned in the visible range (i.e., 510, 600, and 720 nm) were fabricated by systematically modifying the pore size of the semiconductor structure from 260 to 320 nm. The photocatalytic performance of these PCs was assessed

by the degradation of MO, RhoB, MB, and 4-CP under visible light irradiation.[30] These ZnO inverse opal structures achieved photocatalytic degradation rates of $k_{MO} = 0.01$ h^{-1}, $k_{RhoB} = 0.13$ h^{-1}, $k_{MB} = 1.49$ h^{-1}, and $k_{4-CP} = 0.00$ h^{-1} for MO, RhoB, MB, and 4-CP molecules, respectively. A comparison with our results (Table 5) indicates that TiO$_2$–NAA-DBR structures provide properties superior to those of ZnO inverse opals to photodegrade these organic molecules, with an enhancement of 97, 63, 51, and 100%, respectively.

Our group developed NAA-based gradient-index filters (NAA-GIFs) PC structures with deposited photoactive layers of TiO$_2$.[4] TiO$_2$–NAA-GIFs were produced with varying anodization period (i.e., from 650 to 850 s) and used as photocatalyst platforms to degrade MO, RhoB, and MB under visible–near-IR irradiation. The photocatalytic decomposition rates achieved for MO, RhoB, and MB were $k_{MO} = 0.25$ h^{-1}, $k_{RhoB} = 0.39$ h^{-1}, and $k_{MB} = 2.10$ h^{-1}, respectively. Although the photocatalytic performance of TiO$_2$–NAA-GIFs for RhoB was 11% better than that achieved by TiO$_2$–NAA-DBRs, TiO$_2$–NAA-DBRs show more efficient performance for MO and MB, with an enhancement of 22 and 31%, respectively. In general, TiO$_2$–NAA-DBRs perform more efficiently than TiO$_2$–NAA-GIFs under visible–near-IR irradiation. This enhancement may be attributable to the more efficient light collection associated with the broader and intenser characteristic PSB of NAA-DBR structures.

To summarize, this comparison demonstrates that the photocatalytic performance of TiO$_2$–NAA-DBRs is generally superior to that of existing photocatalyst systems. The optical and optoelectronic properties of these semiconductor composite PC structures can be precisely tuned across the spectral regions to achieve enhanced performances in photocatalysis by rationally managing photons at the nanoscale.

4. CONCLUSIONS

This study provides new insights into the capability of NAA-based composite semiconductor photonic crystal structures to enhance and accelerate photocatalytic reactions by the "slow photon" effect. NAA-DBRs with varying anodization period were fabricated by stepwise pulse anodization and subsequently functionalized with photoactive TiO$_2$ layers. The optical properties of these model nanoporous semiconductor PCs can be precisely tuned across the spectral regions to identify light–matter interactions that lead to unprecedented enhancements in photocatalytic reactions. Slow photon effects in TiO$_2$–NAA-DBRs were investigated by model photochemical reactions, using the photodegradation of methyl orange, rhodamine B, methylene blue, and 4-chlorophenol under controlled visible–near-IR light irradiation. Our study demonstrates that TiO$_2$–NAA-DBRs degrade these organic molecules efficiently with high photocatalytic performances (i.e., $k_{MO} = 0.32 \pm 0.01$ h^{-1}, $k_{RhoB} = 0.35 \pm 0.01$ h^{-1}, $k_{MB} = 3.04 \pm 0.01$ h^{-1}, and $k_{4-CP} = 0.15 \pm 0.01$ h^{-1}). TiO$_2$–NAA-DBRs demonstrate outstanding photocatalytic performances as compared to other benchmark photocatalyst platforms such as P25 TiO$_2$ nanoparticles and TiO$_2$ and ZnO inverted opal PCs.

Enhancement of photodegradation rates in TiO$_2$–NAA-DBRs is found to be optimal when the red edge of the PSB is in close proximity to or falls entirely within the absorbance band of the model organic molecules. However, the photocatalytic enhancement by the slow photon effect becomes weaker with increasing distance between the edges of the PSB and the absorbance band of the organic molecules. When the

PSB partially overlaps with the absorbance band of the organic compound, a compromise between the total pore length of the PC structure and the slow photon effect in the photocatalytic enhancement can provide photocatalytic enhancements by an optimal combination of these factors. Our study also indicates that, in the case of organics with absorbance bands in the UV spectral region, when the PC's PSB is in the visible or near-IR region, the photocatalytic performance of TiO_2−NAA-DBRs is only associated with the relative distance between the absorbance band and the PC's PSB and the percentage of visible−near-IR irradiation, and independent of the total pore length of the PC structure. Furthermore, our study demonstrates that interferences from ions and molecules present in the aqueous matrix strongly decrease the overall photocatalytic degradation rate of TiO_2−NAA-DBRs. However, these PC structures are still able to photodegrade resilient pesticide molecules such as 4-chlorophenol in complex aqueous matrices. The charge of the organic molecules and the concentration of hydrogen peroxide solution are also contributing factors in dictating the overall photocatalytic performance of TiO_2−NAA-DBRs, where positively charged molecules (i.e., rhodamine B and methylene blue) and higher concentration of hydrogen peroxide result in enhanced photocatalytic performances. TiO_2−NAA-DBRs also provide high photostability and reusability in the photocatalytic degradation of organic molecules and can maintain their outstanding performance after five cycles.

In summary, this study provides new opportunities to develop sustainable and high-performing photocatalyst platforms based on surface-functionalized nanoporous anodic alumina photonic crystals fabricated with a rational design of optical properties to attain an efficient management of photons for photocatalysis.

ASSOCIATED CONTENT

Ⓢ Supporting Information

The Supporting Information is available free of charge on the ACS Publications website at DOI: 10.1021/acsaem.8b01721.

> Further information on the fabrication, surface functionalization and photocatalytic performance of TiO_2−NAA-DBRs; calibration lines correlating organic molecules concentration and absorbance; transmission spectra of NAA-DBRs; absorbance spectra of organic molecules; spectrum for the simulated solar light irradiation; digital pictures of photodegraded MB solution; properties of organic molecules; results of reusability (PDF)

AUTHOR INFORMATION

Corresponding Authors

*(L.F.M.) Phone: + 34 977559625. E-mail: lluis.marsal@urv.cat. Web page: http://www.urv.cat/html/docencia-per-centre/general-94602760.php.
*(N.H.V.) Phone: + 61 03 9902 9097. E-mail: nicolas.voelcker@monash.edu. Web page: https://research.monash.edu/en/persons/nicolas-voelcker.
*(A.D.A.) Phone: + 61 8 8313 5652. E-mail: andrew.abell@adelaide.edu.au. Web page: http://researchers.adelaide.edu.au/profile/andrew.abell#contact-details.
*(A.S.) Phone: +61 8 8313 1535. E-mail: abel.santos@adelaide.edu.au. Web page: http://www.adelaide.edu.au/directory/abel.santos.

ORCID

Lluís F. Marsal: 0000-0002-5976-1408
Nicolas H. Voelcker: 0000-0002-1536-7804
Andrew D. Abell: 0000-0002-0604-2629
Abel Santos: 0000-0002-5081-5684

Notes

The authors declare no competing financial interest.

REFERENCES

(1) Zheng, X.; Meng, S.; Chen, J.; Wang, J.; Xian, J.; Shao, Y.; Fu, X.; Li, D. Titanium Dioxide Photonic Crystals with Enhanced Photocatalytic Activity: Matching Photonic Band Gaps of TiO_2 to the Absorption Peaks of Dyes. *J. Phys. Chem. C* **2013**, *117*, 21263−21273.
(2) Geng, Z.; Zhang, Y.; Yuan, X.; Huo, M.; Zhao, Y.; Lu, Y.; Qiu, Y. Incorporation of Cu_2O nanocrystals into TiO_2 Photonic Crystal for Enhanced UV-Visible Light Driven Photocatalysis. *J. Alloys Compd.* **2015**, *644*, 734−741.
(3) Lu, Y.; Yu, H.; Chen, S.; Quan, X.; Zhao, H. Integrating Plasmonic Nanoparticles with TiO_2 Photonic Crystal for Enhancement of Visible-Light Driven Photocatalysis. *Environ. Sci. Technol.* **2012**, *46*, 1724−1730.
(4) Lim, S. Y.; Law, C. S.; Markovic, M.; Kirby, J. K.; Abell, A. D.; Santos, A. Engineering the Slow Photon Effect in Photoactive Nanoporous Anodic Alumina Gradient-Index Filters for Photocatalysis. *ACS Appl. Mater. Interfaces* **2018**, *10*, 24124−24136.
(5) Toumazatou, A.; Arfanis, M. K.; Pantazopoulos, P.-A.; Kontos, A. G.; Falaras, P.; Stefanou, N.; Likodimos, V. Slow-Photon Enhancement of Dye Sensitized TiO_2 Photocatalysis. *Mater. Lett.* **2017**, *197*, 123−126.
(6) Sheng, X.; Liu, J.; Coronel, N.; Agarwal, A. M.; Michel, J.; Kimerling, L. C. Integration of Self-Assembled Porous Alumina and Distributed Bragg Reflector for Light Trapping in Si Photovoltaic Devices. *IEEE Photonics Technol. Lett.* **2010**, *22*, 1394−1396.
(7) Guo, M.; Xie, K.; Wang, Y.; Zhou, L.; Huang, H. Aperiodic TiO_2 Nanotube Photonic Crystal: Full-Visible-Spectrum Solar Light Harvesting in Photovoltaic Devices. *Sci. Rep.* **2015**, *4*, 6442.
(8) Guo, M.; Su, H.; Zhang, J.; Liu, L.; Fu, N.; Yong, Z.; Huang, H.; Xie, K. Broadband and Omnidirectional Light Harvesting Enhancement in Photovoltaic Devices with Aperiodic TiO_2 Nanotube Photonic Crystal. *J. Power Sources* **2017**, *345*, 12−20.
(9) Dronov, R.; Jane, A.; Shapter, J. G.; Hodges, A.; Voelcker, N. H. Nanoporous Alumina-Based Interferometric Transducers Ennobled. *Nanoscale* **2011**, *3*, 3109−3114.
(10) Wijnhoven, J. E. G. J.; Vos, W. L. Preparation of Photonic Crystals Made of Air Sphers in Titania. *Science* **1998**, *281*, 802−804.
(11) Yablonovitch, E. Inhibited Spontaneous Emission in Solid-State Physics and Electronics. *Phys. Rev. Lett.* **1987**, *58*, 2059.
(12) Liu, J.; Zhao, H.; Wu, M.; Van der Schueren, B.; Li, Y.; Deparis, O.; Ye, J.; Ozin, G. A.; Hasan, T.; Su, B.-L. Slow Photons for Photocatalysis and Photovoltaics. *Adv. Mater.* **2017**, *29*, 1605349.

(13) Guesh, K.; Márquez-Álvarez, C.; Chebude, Y.; Diaz, I. Enhanced Photocatalytic Activity of Supported TiO_2 by Selective Surface Modification of Zeolite Y. *Appl. Surf. Sci.* **2016**, *378*, 473−478.

(14) Wang, C.; Shi, H.; Li, Y. Synthesis and Characteristics of Natural Zeolite Supported Fe^{3+}-TiO_2 Photocatalysts. *Appl. Surf. Sci.* **2011**, *257*, 6873−6877.

(15) Dong, H.; Zeng, G.; Tang, L.; Fan, C.; Zhang, C.; He, X.; He, Y. An Overview on Limitations of TiO_2-Based Particles for Photocatalytic Degradation of Organic Pollutants and the Corresponding Countermeasures. *Water Res.* **2015**, *79*, 128−146.

(16) Zhu, X.; Chang, Y.; Chen, Y. Toxicity and Bioaccumulation of TiO_2 Nanoparticle Aggregates in Daphnia Magna. *Chemosphere* **2010**, *78*, 209−215.

(17) Hoffmann, M. R.; Martin, S. T.; Choi, W.; Bahnemann, D. W. Environmental Applications of Semiconductor Photocatalysis. *Chem. Rev.* **1995**, *95*, 69−96.

(18) Chen, X.; Shen, S.; Guo, L.; Mao, S. S. Semiconductor-based Photocatalytic Hydrogen Generation. *Chem. Rev.* **2010**, *110*, 6503−6570.

(19) Liu, G.; Wang, L.; Yang, H. G.; Cheng, H.-M.; Lu, G. Q. Titania-Based Photocatalysts − Crystal Growth, Doping and Heterostructuring. *J. Mater. Chem.* **2010**, *20*, 831−843.

(20) Ollis, D. F.; Pelizzetti, E.; Serpone, N. Photocatalyzed Destruction of Water Contaminants. *Environ. Sci. Technol.* **1991**, *25*, 1522−1529.

(21) Liu, J.; Liu, G.; Li, M.; Shen, W.; Liu, Z.; Wang, J.; Zhao, J.; Jiang, L.; Song, Y. Enhancement of Photochemical Hydrogen Evolution over Pt-Loaded Hierarchical Titania Photonic Crystal. *Energy Environ. Sci.* **2010**, *3*, 1503−1506.

(22) Kim, K.; Thiyagarajan, P.; Ahn, H.-J.; Kim, S.-I.; Jang, J.-H. Optimization for Visible Light Photocatalytic Water Splitting: Gold-Coated and Surface-Textured TiO_2 Inverse Opal Nano-Networks. *Nanoscale* **2013**, *5*, 6254−6260.

(23) Boppella, R.; Kochuveedu, S. T.; Kim, H.; Jeong, M. J.; Marques Mota, F.; Park, J. H.; Kim, D. H. Plasmon-Sensitized Graphene/TiO_2 Inverse Opal Nanostructures with Enhanced Charge Collection Efficiency for Water Splitting. *ACS Appl. Mater. Interfaces* **2017**, *9*, 7075−7083.

(24) Zhou, M.; Bao, J.; Xu, Y.; Zhang, J.; Xie, J.; Guan, M.; Wang, C.; Wen, L.; Lei, Y.; Xie, Y. Photoelectrodes Based Upon Mo:$BiVO_4$ Inverse Opals for Photoelectrochemical Water Splitting. *ACS Nano* **2014**, *8*, 7088−7098.

(25) Sadakane, M.; Sasaki, K.; Kunioku, H.; Ohtani, B.; Abe, R.; Ueda, W. Preparation of 3-D Ordered Macroporous Tungsten Oxides and Nano-Crystalline Particulate Tungsten Oxides Using a Colloidal Crystal Template Method, and Their Structural Characterization and Application as Photocatalysts under Visible Light Irradiation. *J. Mater. Chem.* **2010**, *20*, 1811−1818.

(26) Hirakawa, H.; Hashimoto, M.; Shiraishi, Y.; Hirai, T. Photocatalytic Conversion of Nitrogen to Ammonia with Water on Surface Oxygen Vacancies of Titanium Dioxide. *J. Am. Chem. Soc.* **2017**, *139*, 10929−10936.

(27) Jiao, J.; Wei, Y.; Chi, K.; Zhao, Z.; Duan, A.; Liu, J.; Jiang, G.; Wang, Y.; Wang, X.; Han, C.; Zheng, P. Platinum Nanoparticles Supported on TiO_2 Photonic Crystals as Highly Active Photocatalyst for the Reduction of CO_2 in the Presence of Water. *Energy Technol.* **2017**, *5*, 877−883.

(28) Ren, M.; Valsaraj, K. Inverse Opal Titania on Optical Fiber for the Photoreduction of CO_2 to CH_3OH. *Int. J. Chem. React. Eng.* **2009**, *7*, A90.

(29) Fox, M. A.; Dulay, M. T. Heterogeneous Photocatalysis. *Chem. Rev.* **1993**, *93*, 341−357.

(30) Meng, S.; Li, D.; Wang, P.; Zheng, X.; Wang, J.; Chen, J.; Fang, J.; Fu, X. Probing Photonic Effect on Photocatalytic Degradation of Dyes Based on 3D Inverse Opal ZnO Photonic Crystal. *RSC Adv.* **2013**, *3*, 17021−17028.

(31) Xie, H.; Li, Y.; Jin, S.; Han, J.; Zhao, X. Facile Fabrication of 3D-Ordered Macroporous Nanocrystalline Iron Oxide Films with Highly Efficient Visible Light Induced Photocatalytic Activity. *J. Phys. Chem. C* **2010**, *114*, 9706−9712.

(32) Li, X.; Chen, Z.; Quan, H.; Shao, Y.; Li, D. Constructing Photocatalyst from β-Bi_2O_3 Photonic Crystals for Enhanced Photocatalytic Performance. *J. Porous Mater.* **2018**, *25*, 677−685.

(33) Curti, M.; Schneider, J.; Bahnemann, D. W.; Mendive, C. B. Inverse Opal Photonic Crystals as a Strategy to Improve Photocatalysis: Underexplored Questions. *J. Phys. Chem. Lett.* **2015**, *6*, 3903−3910.

(34) Stein, A.; Wilson, B. E.; Rudisill, S. G. Design and Functionality of Colloidal-Crystal-Templated Materials − Chemical Applications of Inverse Opals. *Chem. Soc. Rev.* **2013**, *42*, 2763−2803.

(35) Gaillot, D. P.; Summers, C. J. Inverse Opal Photonics. In *Atomic Layer Deposition of Nanostructured Materials*; Pinna, N., Knez, M., Eds.; Wiley-VCH: Weinheim, Germany, 2012; pp 345−371, DOI: 10.1002/9783527639915.ch15.

(36) Likodimos, V. Photonic Crystal-Assisted Visible Light Activated TiO_2 Photocatalysis. *Appl. Catal., B* **2018**, *230*, 269−303.

(37) Zhai, C.; Zhu, M.; Lu, Y.; Ren, F.; Wang, C.; Du, Y.; Yang, P. Reduced Graphene Oxide Modified Highly Ordered TiO_2 Nanotube Arrays Photoelectrode with Enhanced Photoelectrocatalytic Performance under Visible-Light Irradiation. *Phys. Chem. Chem. Phys.* **2014**, *16*, 14800−14807.

(38) Liao, W.; Yang, J.; Zhou, H.; Murugananthan, M.; Zhang, Y. Electrochemically Self-Doped TiO_2 Nanotube Arrays for Efficient Visible Light Photoelectrocatalytic Degradation of Contaminants. *Electrochim. Acta* **2014**, *136*, 310−317.

(39) Wang, C.; Chen, D.; Ping, G. X.; Liu, S.; Huang, X. N.; Huang, Y. X.; Shu, K. Y.; Li, J. H. Controllable Synthesis of Well-Ordered TiO_2 Nanotubes in a Mixed Organic Electrolyte for High-Efficiency Photocatalysis. *Sci. China: Chem.* **2012**, *55*, 2373−2380.

(40) Mehedi, I. M.; Hossain, M. F.; Takahashi, T.; Islam, M. S. Nano-Structural Variation of Highly Aligned Anodic Titania Nanotube Arrays for Gas Phase Photocatalytic Application. *J. Photochem. Photobiol., A* **2017**, *335*, 200−210.

(41) Santos, A.; Balderrama, V. S.; Alba, M.; Formentín, P.; Ferré-Borrull, J.; Pallarès, J.; Marsal, L. F. Nanoporous Anodic Alumina Barcodes: Toward Smart Optical Biosensors. *Adv. Mater.* **2012**, *24*, 1050−1054.

(42) Law, C. S.; Sylvia, G. M.; Nemati, M.; Yu, J.; Losic, D.; Abell, A. D.; Santos, A. Engineering of Surface Chemistry for Enhanced Sensitivity in Nanoporous Interferometric Sensing Platforms. *ACS Appl. Mater. Interfaces* **2017**, *9*, 8929−8940.

(43) Law, C. S.; Lim, S. Y.; Abell, A. D.; Santos, A. Real-Time Binding Monitoring between Human Blood Proteins and Heavy Metal Ions in Nanoporous Anodic Alumina Photonic Crystals. *Anal. Chem.* **2018**, *90*, 10039−10048.

(44) Chen, Y.; Santos, A.; Wang, Y.; Kumeria, T.; Wang, C.; Li, J.; Losic, D. Interferometric Nanoporous Anodic Alumina Photonic Coatings for Optical Sensing. *Nanoscale* **2015**, *7*, 7770−7779.

(45) Law, C. S.; Lim, S. Y.; Santos, A. On the Precise Tuning of Optical Filtering Features in Nanoporous Anodic Alumina Distributed Bragg Reflectors. *Sci. Rep.* **2018**, *8*, 4642.

(46) Santos, A.; Pereira, T.; Law, C. S.; Losic, D. Rational Engineering of Nanoporous Anodic Alumina Optical Bandpass Filters. *Nanoscale* **2016**, *8*, 14846−14857.

(47) Wang, Y.; Chen, Y.; Kumeria, T.; Ding, F.; Evdokiou, A.; Losic, D.; Santos, A. Facile Synthesis of Optical Microcavities by a Rationally Designed Anodization Approach: Tailoring Photonic Signals by Nanopore Structure. *ACS Appl. Mater. Interfaces* **2015**, *7*, 9879−9888.

(48) Law, C. S.; Lim, S. Y.; Abell, A. D.; Marsal, L. F.; Santos, A. Structural Tailoring of Nanoporous Anodic Alumina Optical Microcavities for Enhanced Resonant Recirculation of Light. *Nanoscale* **2018**, *10*, 14139−14152.

(49) Chen, Y.; Santos, A.; Wang, Y.; Kumeria, T.; Ho, D.; Li, J.; Wang, C.; Losic, D. Rational Design of Photonic Dust from Nanoporous Anodic Alumina Films: A Versatile Photonic Nanotool for Visual Sensing. *Sci. Rep.* **2015**, *5*, 12893.

189

(50) Sukarno; Law, C. S.; Santos, A. Realisation and Optical Engineering of Linear Variable Bandpass Filters in Nanoporous Anodic Alumina Photonic Crystals. *Nanoscale* **2017**, *9*, 7541–7550.

(51) Santos, A.; Yoo, J. H.; Rohatgi, C. V.; Kumeria, T.; Wang, Y.; Losic, D. Realisation an Advanced Engineering of True Optical Rugate Filters Based on Nanoporous Anodic Alumina by Sinusoidal Pulse Anodisation. *Nanoscale* **2016**, *8*, 1360–1373.

(52) Lim, S. Y.; Law, C. S.; Marsal, L. F.; Santos, A. Engineering of Hybrid Nanoporous Anodic Alumina Photonic Crystals by Heterogeneous Pulse Anodization. *Sci. Rep.* **2018**, *8*, 9455.

(53) Abràmoff, M. D.; Magalhães, P. J.; Ram, S. J. Image Processing with ImageJ. *Biophotonics Int.* **2004**, *11*, 36–42.

(54) Nishimura, S.; Abrams, N.; Lewis, B. A.; Halaoui, L. I.; Mallouk, T. E.; Benkstein, K. D.; van de Lagemaat, J.; Frank, A. J. Standing Wave Enhancement of Red Absorbance and Photocurrent in Dye-Sensitized Titanium Dioxide Photoelectrodes Coupled To Photonic Crystals. *J. Am. Chem. Soc.* **2003**, *125*, 6306–6310.

(55) Li, Y.; Kunitake, T.; Fujikawa, S. Efficient Fabrication and Enhanced Photocatalytic Activities of 3D-Ordered Films of Titania Hollow Spheres. *J. Phys. Chem. B* **2006**, *110*, 13000–13004.

(56) Deparis, O.; Mouchet, S. R.; Su, B.-L. Light Harvesting in Photonic Crystals Revisited: Why do Slow Photons at the Blue Edge Enhance Absorption? *Phys. Chem. Chem. Phys.* **2015**, *17*, 30525–30532.

(57) Brzózka, A.; Brudzisz, A.; Hnida, K.; Sulka, G. D. Chemical and Structural Modifications of Nanoporous Alumina and Its Optical Properties. In *Electrochemically Engineered Nanoporous Materials: Methods, Properties and Applications*; Losic, D., Santos, A., Eds.; Springer Series in Materials Science, Vol. *220*; Springer International: Cham, Switzerland, 2015; pp 219–288, DOI: 10.1007/978-3-319-20346-1_8.

(58) Kim, S.; Choi, W. Visible-Light-Induced Photocatalytic Degradation of 4-Chlorophenol and Phenolic Compounds in Aqueous Suspension of Pure Titania: Demonstrating the Existence of a Surface-Complex-Mediated Path. *J. Phys. Chem. B* **2005**, *109*, 5143–5149.

(59) Lee, K.; Mazare, A.; Schmuki, P. One-Dimensional Titanium Dioxide Nanomaterials: Nanotubes. *Chem. Rev.* **2014**, *114*, 9385–9454.

(60) Lettmann, C.; Hildenbrand, K.; Kisch, H.; Macyk, W.; Maier, W. F. Visible Light Photodegradation of 4-Chlorophenol with a Coke-Containing Titanium Dioxide Photocatalyst. *Appl. Catal., B* **2001**, *32*, 215–227.

190

Supporting Information

Rational Management of Photons for Enhanced Photocatalysis in Structurally-Colored Nanoporous Anodic Alumina Photonic Crystals

Siew Yee Lim[1,2,3], Cheryl Suwen Law[1,2,3], Marijana Markovic[4,5], Lluís F. Marsal[*6], Nicolas H. Voelcker[*7,8,9,10], Andrew D. Abell[*2,3,11] and Abel Santos[*1,2,3]

[1]School of Chemical Engineering, The University of Adelaide, Adelaide, South Australia 5005, Australia.
[2]Institute for Photonics and Advanced Sensing (IPAS), The University of Adelaide, Adelaide, South Australia 5005, Australia.
[3]ARC Centre of Excellence for Nanoscale BioPhotonics (CNBP), The University of Adelaide, Adelaide, South Australia 5005, Australia.
[4]School of Agriculture Food and Wine, The University of Adelaide, Adelaide, South Australia 5064, Australia.
[5]Center of Chemistry, Institute of Chemistry, Technology and Metallurgy, University of Belgrade, Belgrade 11000, Serbia.
[6]Department of Electronic, Electric, and Automatics Engineering, Universitat Rovira i Virgili, Tarragona, Tarragona 43007, Spain.
[7]Melbourne Centre for Nanofabrication, Victorian Node of the Australian National Fabrication Facility, Monash University, Melbourne, Victoria 3168, Australia.
[8]Monash Institute of Pharmaceutical Sciences, Monash University, Melbourne, Victoria 3052, Australia.
[9]Commonwealth Scientific and Industrial Research Organisation (CSIRO), Melbourne, Victoria 3168, Australia.
[10]INM-Leibniz Institute for New Materials, Campus D2 2, Saarbrücken 66123, Germany.
[11]Department of Chemistry, The University of Adelaide, Adelaide, South Australia 5005, Australia.

*E-Mails: lluis.marsal@urv.cat ; nicolas.voelcker@monash.edu ; andrew.abell@adelaide.edu.au ; abel.santos@adelaide.edu.au
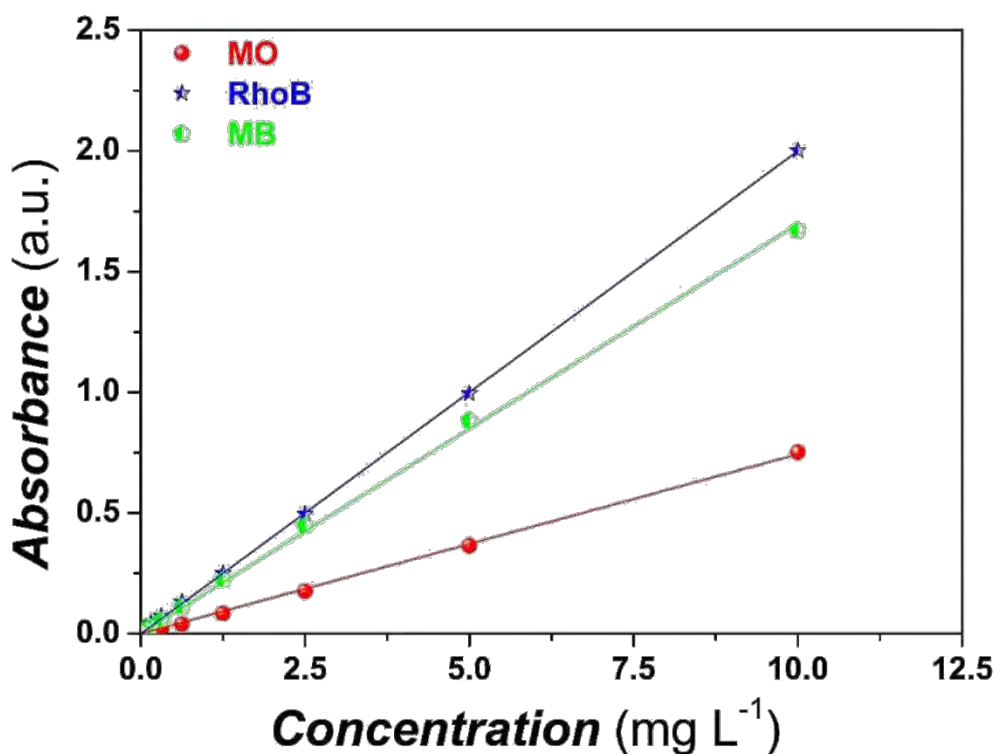
Figure S1. Linear correlation between absorbance and concentration of methyl orange (MO), rhodamine B (RhoB), and methylene blue (MB) (note: concentration range from 0.00244 to 10 mg L^{-1}). The linear correlation for MO, RhoB and MB were: Abs_{MO} (a.u.) = 0.07436 *[MO]* (mg L^{-1}), Abs_{RhoB} (a.u.) = 0.19998 *[RhoB]* (mg L^{-1}) and Abs_{MB} (a.u.) = 0.1697 *[MB]* (mg L^{-1}), respectively. The R^2 values for MO, RhoB and MB were 0.99940, 0.99979, and 0.99923, respectively.
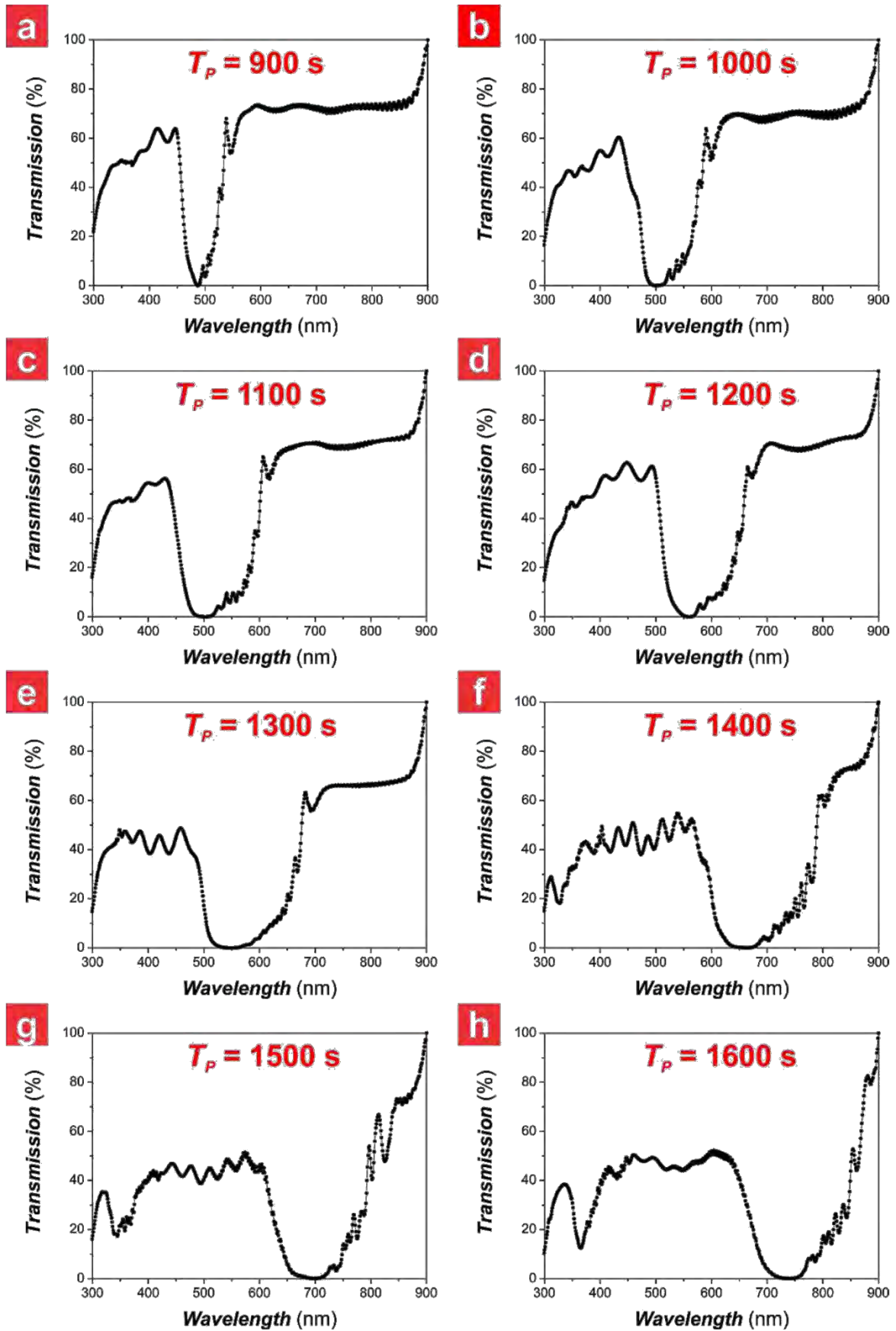
Figure S2. Transmission spectra of NAA-DBRs produced with anodization period (T_P) of: a) 900 s, b) 1000 s, c) 1100 s, d) 1200 s, e) 1300 s, f) 1400 s, g) 1500 s and h) 1600 s (note: media = air).
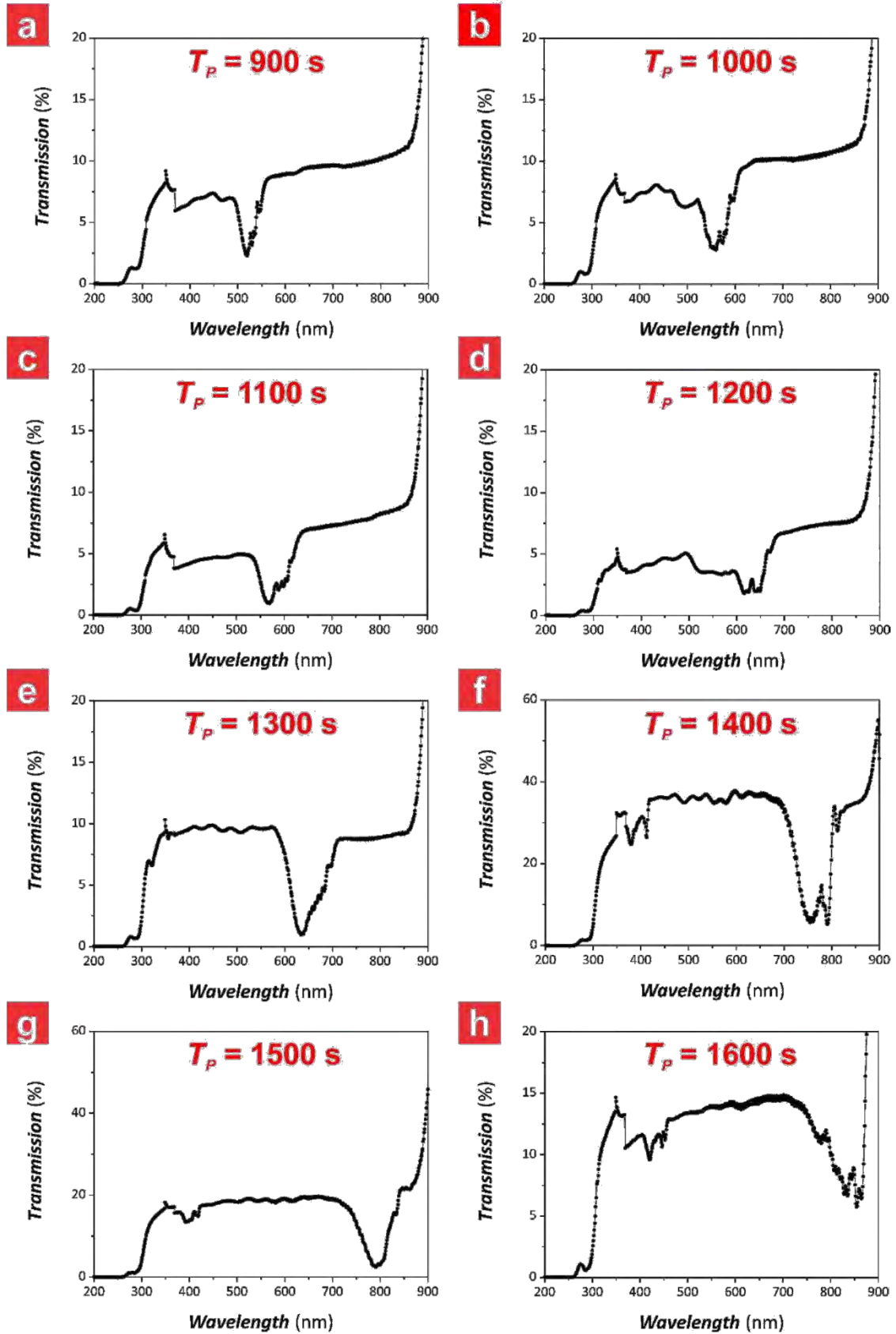
Figure S2 (cont). Transmission spectra of NAA-DBRs produced with anodization period (T_P) of: a) 900 s, b) 1000 s, c) 1100 s, d) 1200 s, e) 1300 s, f) 1400 s, g) 1500 s and h) 1600 s (note: media = water).
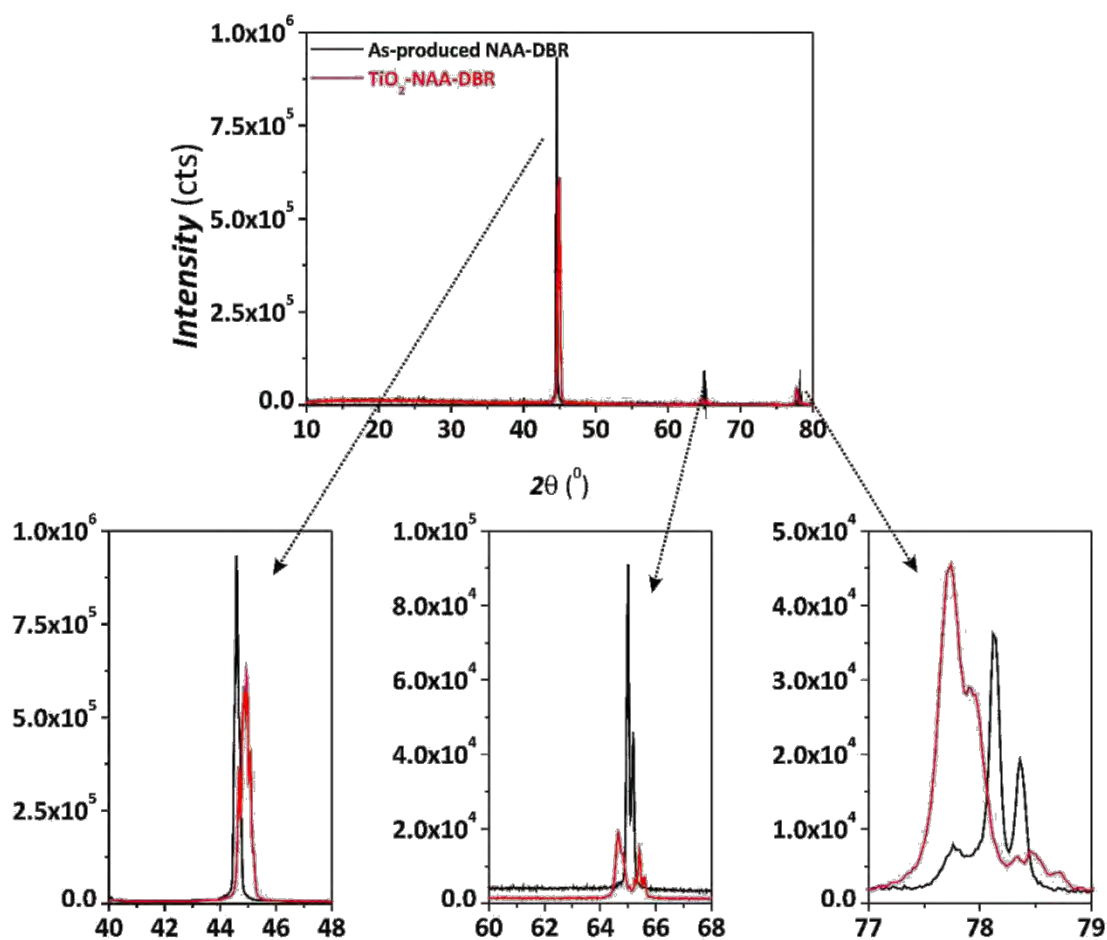
Figure S3. X-ray diffraction (XRD) spectra of a representative NAA-DBR before and after surface-functionalization with TiO_2 (measurements performed in a XRD Rigaku MiniFlex 600). As-produced NAA-DBRs present three characteristic peaks in their XRD spectra located at 45, 65 and 780^0, which correspond to an amorphous alumina (Al_2O_3) phase. The deposition of the TiO_2 functional layer does not generate any additional peak in the XRD spectra, indicating that the TiO_2 layer is crystallographically amorphous. However, the position of these peaks undergoes a slight shift in position and decrease their intensity, confirming the successful deposition of photoactive layers of amorphous TiO_2 onto the inner surface of NAA-DBRs.
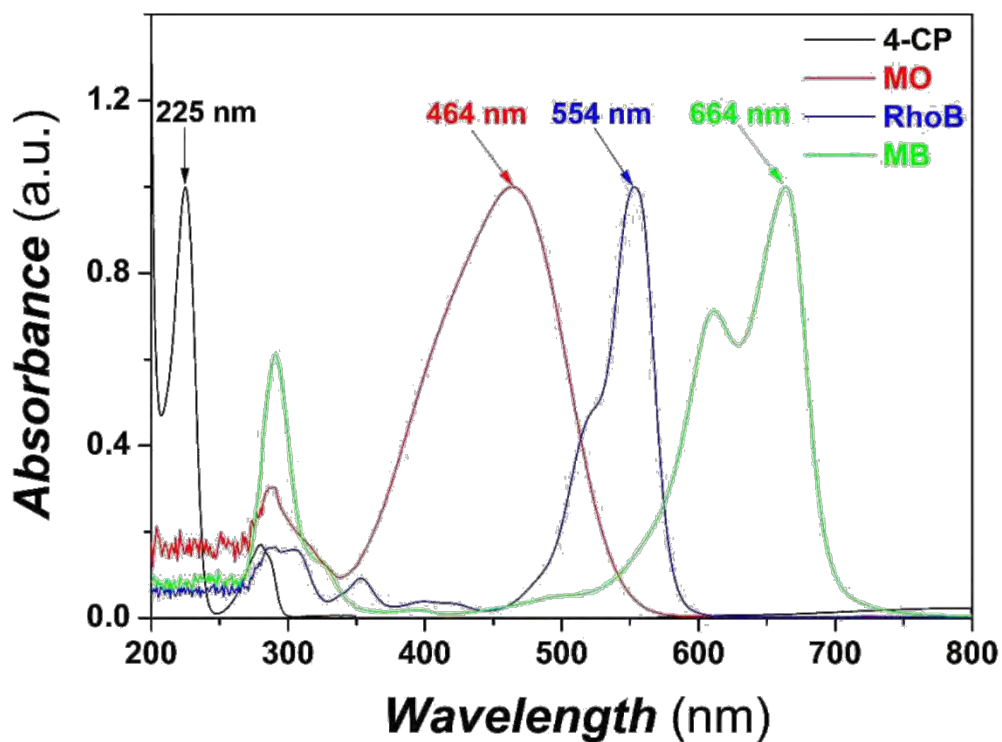
Figure S4. Optical absorbance spectra of 4-chlorophenol (4-CP), methyl orange (MO), rhodamine B (RhoB), and methylene blue (MB) used for photocatalysis in TiO$_2$-NAA-DBRs. The absorption band maxima for 4-CP, MO, RhoB and MB were $\lambda_{\text{abs-4-CP}}$ = 225 nm, $\lambda_{\text{abs-MO}}$ =464 nm, $\lambda_{\text{abs-RhoB}}$ = 554 nm, and $\lambda_{\text{abs-MB}}$ = 664 nm, respectively (note: the absolute absorption intensities of MB, RhoB and MO at the central position were ~2.8, 3.6 and 1.5 a.u., respectively).
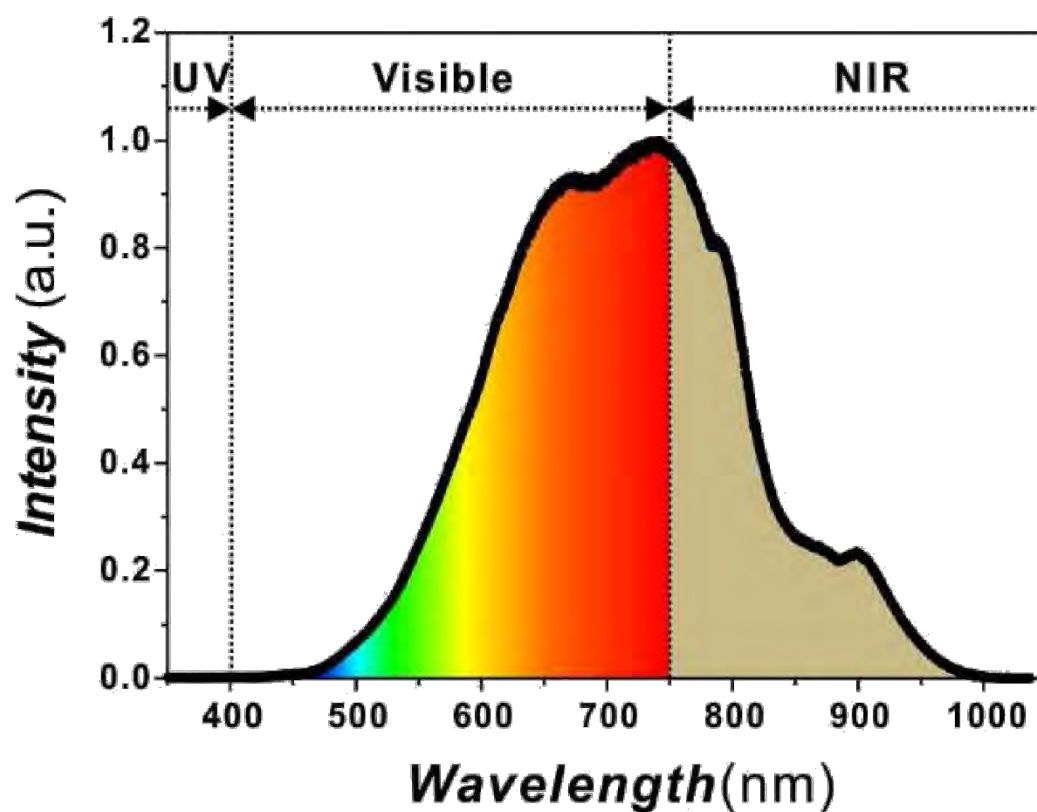
Figure S5. Simulated visible light-near infrared (vis-NIR) irradiation source used for photocatalysis in our study (i.e. 0.12% UV, 64.60% visible and 35.28% NIR). The irradiation spectrum was measured using an optical fiber spectrometer (USB 4000, Ocean Optics, USA).
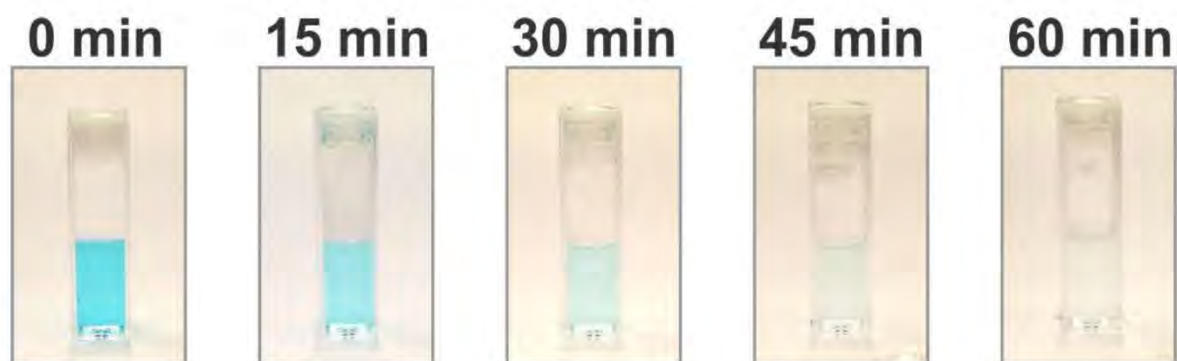
Figure S6. Representative digital images of photodegradation of methylene blue (MB) by TiO$_2$-NAA-DBRs as a function of degradation time from 0 min to 1 h with intervals of 15 min.
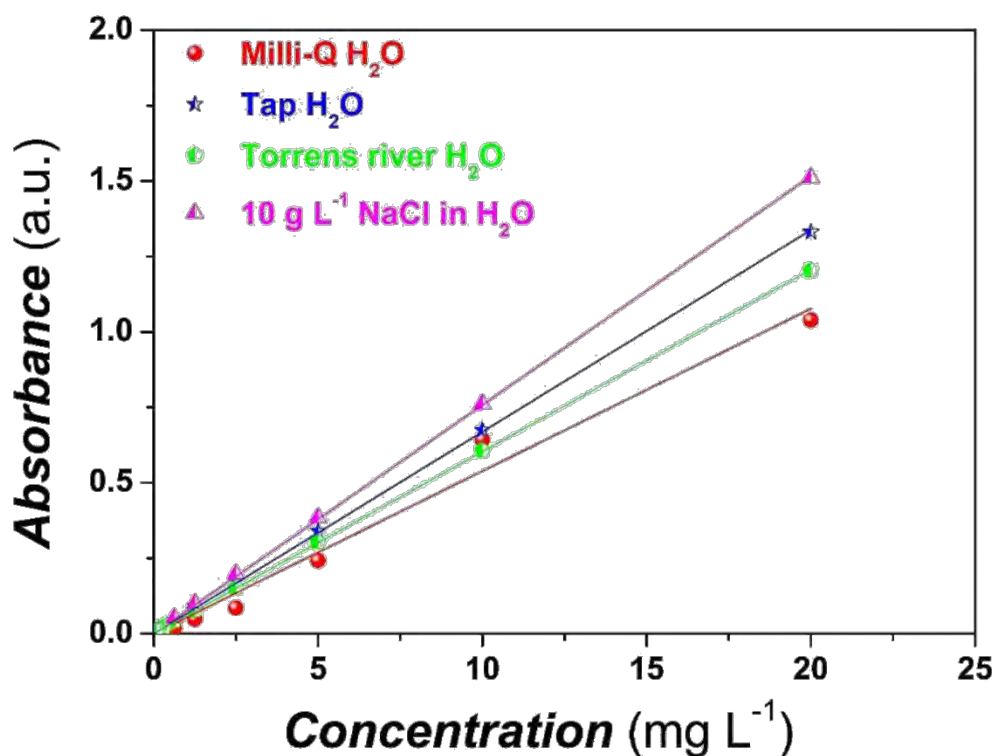
Figure S7. Linear correlation between optical absorbance and concentration of 4-chlorophenol (4-CP) in Milli-Q H_2O, Tap H_2O, Torrens river H_2O, and 10 g L^{-1} NaCl in H_2O (note: concentration range from 0.03906 to 20 mg L^{-1}). The linear correlations were: $Abs_{Milli\text{-}Q\ H2O}$ (a.u.) = 0.05386 *[Milli-Q H_2O]* (mg L^{-1}), $Abs_{Tap\ H2O}$ (a.u.) = 0.06689 *[Tap H_2O]* (mg L^{-1}), $Abs_{Torrens\ river\ H2O}$ (a.u.) = 0.06032 *[Torrens river H_2O]* (mg L^{-1}) and $Abs_{10\ g\ L\text{-}1\ NaCl\ in\ H2O}$ (a.u.) = 0.07580 *[10 g L^{-1} NaCl in H_2O]* (mg L^{-1}) respectively. The R^2 values for were 0.98763, 0.99986, 0.99993, and 0.99993, respectively.

Table S1. Properties of organic molecules used for photocatalytic analysis.
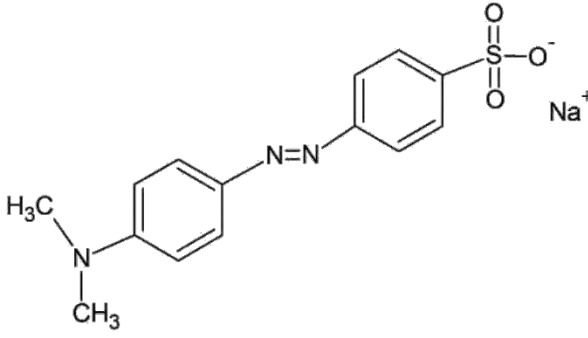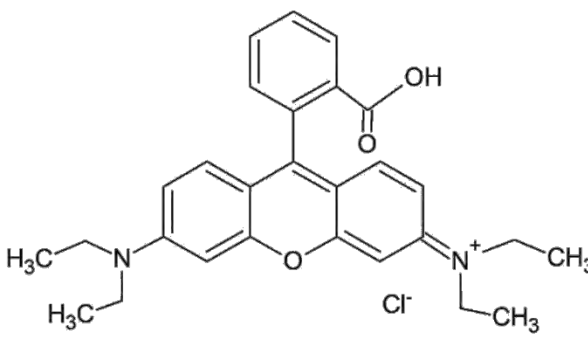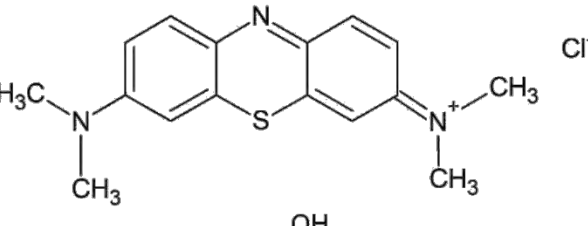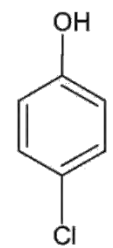
Name of Organic Molecules	Color	Molecular Charge	Molecular Structure
Methyl Orange (MO)	Orange	Anionic	
Rhodamine B (RhoB)	Pink	Cationic	
Methylene Blue (MB)	Blue	Cationic	
4-Chlorophenol (4-CP)	Colorless	Anionic	

Table S2. Residual concentration of methylene blue (MB) after five cycles of photocatalytic degradation by TiO$_2$-NAA-DBRs produced with T_P = 1200 s for 1 h.

Cycle	Residual Concentration (mg L^{-1})
1	0.24 ± 0.07
2	0.21 ± 0.09
3	0.19 ± 0.09
4	0.21 ± 0.08
5	0.19 ± 0.09
Average	0.21 ± 0.02
Photocatalytic Conversion Ratio (%)	96

Chapter 7

INTEGRATING SURFACE PLASMON
RESONANCE AND SLOW PHOTON
EFFECTS IN NANOPOROUS ANODIC
ALUMINA PHOTONIC CRYSTALS FOR
PHOTOCATALYSIS

7. Integrating Surface Plasmon Resonance and Slow Photon Effects in Nanoporous Anodic Alumina Photonic Crystals for Photocatalysis

7.1 Introduction, Significance and Commentary

Chapters 4 and 5 have explored the possibility of TiO_2-functionalised NAA-PCs of different nanoarchitectures for enhanced photocatalysis by "slow photon" effect. This chapter aims to investigate the potential of gold-coated titania-functionalised nanoporous anodic alumina distributed Bragg reflectors (Au-TiO_2-NAA-DBRs) as platforms to enhance photocatalytic reactions by coupling effects between "slow photon" and surface plasmon resonance (SPR). These photocatalyst platforms were synthesised by two-step pulse anodisation and chemically-modified by a sol-gel method and deposition of Au. This study demonstrates that the photocatalytic enhancement in Au-TiO_2-NAA-DBRs is strongly associated with "slow photon" effect, while the contribution of SPR to the overall photocatalytic enhancement is weak due to the localised generation of surface plasmons on the top surface of the composite PC structures. Therefore, a rational and optimal design of these photocatalyst platforms is essential to efficiently utilise and manage the coupling photonic and plasmonic effects to attain maximum photocatalytic activities.

7.2 Publication

This chapter is presented as published journal article by **S.Y. Lim**, C.S. Law, L. Liu, M. Markovic, A.D. Abell, and A. Santos, *Integrating surface plasmon resonance and slow photon effects in nanoporous anodic alumina photonic crystals for photocatalysis*. Catalysis Science & Technology, 2019. **9**(12): p. 3158-3176.

Statement of Authorship

Title of Paper	Integrating Surface Plasmon Resonance and Slow Photon Effects in Nanoporous Anodic Alumina Photonic Crystals for Photocatalysis
Publication Status	☑ Published ☐ Accepted for Publication ☐ Submitted for Publication ☐ Unpublished and Unsubmitted work written in manuscript style
Publication Details	S.Y. Lim, C.S. Law, L. Liu, M. Markovic, A.D. Abell, and A. Santos, *Integrating surface plasmon resonance and slow photon effects in nanoporous anodic alumina photonic crystals for photocatalysis*. Catalysis Science & Technology, 2019. **9**(12): p. 3158-3176.

Principal Author

Name of Principal Author (Candidate)	Siew Yee Lim		
Contribution to the Paper	Performed the experiment, processed and analysed the data and wrote the manuscript under the supervisions of Abel Santos and Andrew D. Abell.		
Overall percentage (%)	70		
Certification:	This paper reports on original research I conducted during the period of my Higher Degree by Research candidature and is not subject to any obligations or contractual agreements with a third party that would constrain its inclusion in this thesis. I am the primary author of this paper.		
Signature		Date	10/06/2020

Co-Author Contributions

By signing the Statement of Authorship, each author certifies that:

i. the candidate's stated contribution to the publication is accurate (as detailed above);

ii. permission is granted for the candidate in include the publication in the thesis; and

iii. the sum of all co-author contributions is equal to 100% less the candidate's stated contribution.

Name of Co-Author	Cheryl Suwen Law		
Contribution to the Paper	Aided in performing the experiment. Give consent to Siew Yee Lim to present this paper for examination towards the Doctorate of Philosophy.		
Signature		Date	15/06/2020

Name of Co-Author	Lina Liu		
Contribution to the Paper	Aided in the evaluation of final version of manuscript. Give consent to Siew Yee Lim to present this paper for examination towards the Doctorate of Philosophy.		
Signature		Date	10/06/2020

Name of Co-Author	Marijana Markovic
Contribution to the Paper	Aided in the evaluation of final version of manuscript. Give consent to Siew Yee Lim to present this paper for examination towards the Doctorate of Philosophy.

Signature		Date	11/06/20

Name of Co-Author	Andrew D. Abell
Contribution to the Paper	Acted as a co-supervisor for the candidate, and aided in revising and evaluating the manuscript for submission. Give consent to Siew Yee Lim to present this paper for examination towards the Doctorate of Philosophy.

Signature		Date	10/06/2020

Name of Co-Author	Abel Santos
Contribution to the Paper	Acted as a primary supervisor for the candidate, and aided in developing, revising and evaluating the manuscript for submission. Give consent to Siew Yee Lim to present this paper for examination towards the Doctorate of Philosophy.

Signature		Date	11/06/2020

Check for updates

Integrating surface plasmon resonance and slow photon effects in nanoporous anodic alumina photonic crystals for photocatalysis†

Siew Yee Lim,[abc] Cheryl Suwen Law,[abc] Lina Liu,[ad] Marijana Markovic,[ae] Andrew D. Abell [ID] *[bcf] and Abel Santos [ID] *[abc]

This study explores the potential of gold-coated titania-functionalized nanoporous anodic alumina distributed Bragg reflectors (Au-TiO$_2$-NAA-DBRs) as platforms to enhance photocatalytic reactions by integrating "slow photons" and surface plasmon resonance (SPR). The photocatalytic degradation rate of methylene blue – a model organic compound with a well-defined absorption band in the visible spectral region – by these composite photonic crystals (PCs) upon visible-NIR light irradiation is used as an indicator to identify coupling effects between the "slow photon" effect and SPR. Our study demonstrates that the photocatalytic enhancement in Au-TiO$_2$-NAA-DBRs is strongly associated with "slow photon" effect, while the contribution of SPR to the overall photocatalytic enhancement is weak due to the localized generation of surface plasmons on the top surface of the composite PC structure. Photocatalytic enhancement is optimal when the characteristic photonic stopband of these PCs partially overlaps with the absorption band of methylene blue, which results in edges being positioned away from the absorption maximum of the organic dye. The overall photocatalytic degradation for methylene blue is also correlated to the type of noble metal coating and the geometric features of the PC structures. These results establish a rationale for further development of noble metal-coated NAA-based hybrid plasmonic–photonic crystal photocatalyst platforms to optimally integrate "slow photons" and SPR for enhancing the efficiency of photocatalytic reactions and other light harvesting applications.

Introduction

Semiconductor photocatalysts harvest the energy of incoming photons to drive chemical reactions for solar-to-fuel conversion and environmental remediation, including hydrogen (H$_2$) energy generation,[1–3] water treatment,[4–11] air purification,[12,13] ammonia (NH$_3$) synthesis,[14,15] carbon dioxide (CO$_2$) reduction[16,17] and warfare agent destruction.[18,19] In landmark studies, Fujishima[20] and Carey[21] reported production of clean H$_2$ energy and degradation of organic pollutants by semiconducting titanium dioxide (TiO$_2$) under UV light irradi-

ation, respectively. TiO$_2$ remains a benchmark semiconducting material for photocatalysis applications due to its strong oxidizing capability, remarkable stability against photo- and chemical corrosion, non-toxicity and low cost.[22] However, the high recombination rate of electron/hole (e$^-$/h$^+$) pairs (*i.e.* ~90%) and the large energy bandgap (*i.e.* ~3.0–3.2 eV) of TiO$_2$ only enable efficient absorption of UV light (*i.e.* ~4% of the solar spectrum), limiting the practical capability of this material for sunlight-driven photocatalysis applications.[23]

Various approaches have been devised to overcome the intrinsic limitations of TiO$_2$, including doping,[24,25] coupling with other semiconducting metal oxides,[26,27] surface modification,[28,29] engineering of mesoporous structures[30,31] and incorporation of noble metals.[7–9,32] Enhanced photocatalytic performance of hybrid noble metal/TiO$_2$ composite structures is associated with localized surface plasmon resonances (SPR), which are collective oscillations of the conducting electrons in the noble metal driven by the electromagnetic field generated by incident photons.[33,34] For instance, Lu *et al.* (2012)[5] demonstrated that hybrid Au nanoparticle-decorated TiO$_2$ nanocrystalline platforms have ~52% superior performance compared to uncoated TiO$_2$ nanocrystalline particles in the photocatalytic degradation of 2,4-

[a] School of Chemical Engineering, The University of Adelaide, 5005 Adelaide, Australia. E-mail: abel.santos@adelaide.edu.au

[b] Institute for Photonics and Advanced Sensing (IPAS), The University of Adelaide, 5005 Adelaide, Australia. E-mail: andrew.abell@adelaide.edu.au

[c] ARC Centre of Excellence for Nanoscale BioPhotonics (CNBP), The University of Adelaide, 5005 Adelaide, Australia

[d] School of Chemistry and Chemical Engineering, Ningxia University, 7520021 Yinchuan, P.R. China

[e] Center of Chemistry, Institute of Chemistry, Technology and Metallurgy, University of Belgrade, 11000 Belgrade, Serbia

[f] Department of Chemistry, The University of Adelaide, 5005 Adelaide, Australia

† Electronic supplementary information (ESI) available. See DOI: 10.1039/c9cy00627c

3158 | *Catal. Sci. Technol.*, 2019, **9**, 3158–3176

This journal is © The Royal Society of Chemistry 2019

dichlorophenol under visible light irradiation. This photocatalytic enhancement is associated with SPR, which can extend absorption of the semiconductor material to a longer wavelength range (*i.e.* visible spectrum), while also reducing the recombination rate of e^-/h^+ pairs by forming a heterojunction between the semiconductor and the noble metal. Photocatalytic reactions can be further enhanced by engineering the structure of hybrid noble metal–TiO$_2$ photocatalyst materials in the form of photonic crystals (PCs), including nanotubes,[35] inverse opals[5,36] and bio-inspired PC structures.[37] For instance, hybrid Au nanoparticle-decorated TiO$_2$ inverse opal PC structures outperform Au nanoparticle-decorated TiO$_2$ nanocrystalline counterparts, with ~56% enhancement in the photodegradation of the same organic pollutant.[5] PC structures can enhance light–matter interactions for photocatalysis *via* Bragg diffraction, multiple scattering and the "slow photon" effect.[9,38–40] Bragg diffraction inhibits propagation of light within the spectral range of the PC's photonic stopband (PSB). However, multiple scattering increases the confinement of light at those wavelengths away from the PSB so the light trapped within the PC's structure can be used by the semiconductor to speed up photocatalytic reactions. The "slow photon" effect occurs at the frequency edges of the PSB, where slow photons (*i.e.* photons with strongly reduced group velocity) are primarily localized in the high (*i.e.* red edge of the PSB) and low (*i.e.* blue edge of the PSB) dielectric parts of the PC's structure. This effect significantly increases the lifetime of photons and the overall light absorption of the semiconductor. Coupling of SPR and PC effects in hybrid noble metal–TiO$_2$ PC photocatalyst structures can thus significantly enhance the overall photon-to-electron conversion rate by rational management of photons at the nanoscale. However, the fabrication of TiO$_2$-based PCs presents intrinsic limitations and technical challenges, including limited spectral controllability of the PC's PSB features, restriction to small areas and long processing times (*i.e.* TiO$_2$-based inverted opal PCs), and light scattering due to the over-etching of the PC structure in hydrofluoric acid (HF)-based electrolytes (*i.e.* TiO$_2$-based nanotubular PCs produced by anodization). These drawbacks limit practical utilization of TiO$_2$-based PCs for efficient and large-scale photocatalytic applications.[41–46]

Significant effort has been devoted to large scale production of alternative materials that can be engineered into high-performance TiO$_2$-based PC photocatalyst platforms for real-life applications. We have recently demonstrated that TiO$_2$-functionalized nanoporous anodic alumina photonic crystals (NAA-PCs), with rationally engineered optical properties, provide superior performance to conventional photocatalyst platforms in the photodegradation of a variety of organic pollutants.[10,11] NAA is an ideal platform to develop PC structures due to its highly controllable and versatile nanoporous structure composed of cylindrical nanopores. The optical features of the characteristic PSB in NAA-PCs can be modulated with precision by engineering their nanoporous structure in the form of different PC architectures, including

distributed Bragg reflectors (DBRs),[11,47] bandpass filters,[48,49] Fabry–Pérot interferometers,[50,51] gradient-index filters,[10,52–54] hybrid photonic crystals,[55] and optical microcavities.[56–58] NAA-PCs have been used in optical chemo- and biosensing,[50,51] light filtering,[47] optical encoding[54] and photocatalysis.[10,11] The nanoporous structure of NAA-PCs facilitates mass transfer of ionic and molecular species involved in photocatalytic reactions and efficient management of photons by controlled light–matter interactions to increase photon-to-electron conversion rates for high-performance photocatalytic applications.[4,10,11]

In this study, we analyze the photocatalytic performance of hybrid Au-TiO$_2$-NAA-DBRs by monitoring the photodegradation of a model organic compound. Au-TiO$_2$-NAA-DBRs are fabricated by two-step pulse anodization and chemically modified by a sol–gel method and deposition of Au (Fig. 1). The effect of various fabrication parameters (*i.e.* anodization period, pore widening time, noble metal deposition time, starting anodization voltage and type of noble metal coating) on the photocatalytic performance of these hybrid PCs under controlled visible-NIR irradiation is systematically investigated. The photocatalytic degradation of methylene blue by Au-TiO$_2$-NAA-DBRs allows the identification and quantification of photocatalytic performance enhancements associated with coupling effects between slow photons and SPR.

Experimental section

Materials

High purity (99.9997%) aluminum (Al) foil, 0.32 mm thick, was supplied by Goodfellow Cambridge Ltd. (UK). Oxalic acid (H$_2$C$_2$O$_4$), perchloric acid (HClO$_4$), copper(II) chloride (CuCl$_2$), hydrochloric acid (HCl), chromic acid (H$_2$CrO$_4$), titanium(IV) butoxide (Ti(OBu)$_4$), hydrogen peroxide (H$_2$O$_2$) and methylene blue (C$_{16}$H$_{18}$ClN$_3$S, MB) were purchased from Sigma-Aldrich (Australia). Ethanol (C$_2$H$_5$OH, EtOH) and phosphoric acid (H$_3$PO$_4$) were supplied by ChemSupply (Australia). Aqueous solutions used in this study were prepared with ultrapure Milli-Q® water (18.2 mΩ cm).

Fabrication of NAA-DBRs

NAA-DBRs were synthesized by two-step pulse anodization under voltage control conditions.[56,59] 1.5 × 1.5 cm^2 Al square chips were sonicated in EtOH and ultrapure water for 15 min each, dried under air stream and electropolished in a mixture of EtOH and HClO$_4$ 4:1 ($v:v$) at 20 V and 5 °C for 3 min. Anodization was performed in an electrochemical reactor with a circular window of 1 cm in diameter. The first anodization step was performed in 0.3 M H$_2$C$_2$O$_4$ at 40 V and 6 °C for 20 h. The resulting NAA layer was removed by wet chemical etching in a mixture of 0.2 M H$_2$CrO$_4$ and 0.4 M H$_3$PO$_4$ at 70 °C for 3 h. The second anodization step was carried out using the same acid electrolyte and temperature as in the first anodization step. The anodization process started with a constant voltage step of 40 V for 10 min. The anodization
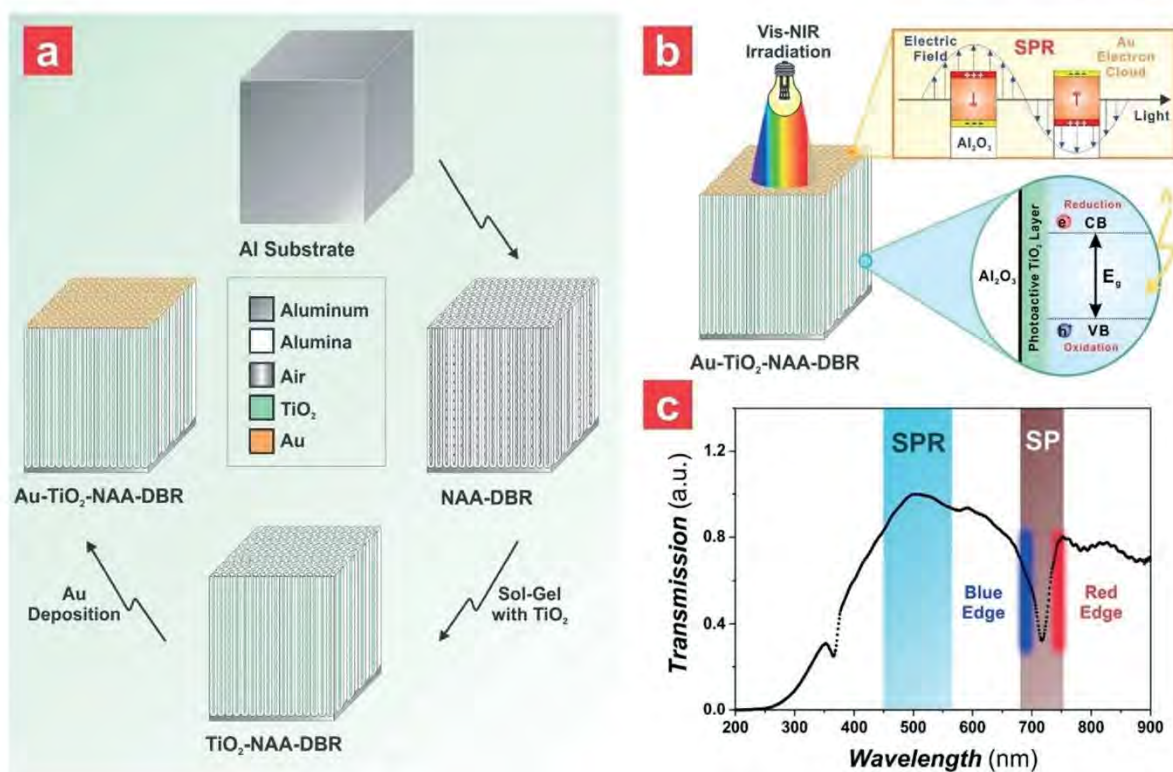
Fig. 1 Fabrication of gold-coated titania-functionalized nanoporous anodic alumina distributed Bragg reflectors (Au-TiO$_2$-NAA-DBRs) by two-step pulse anodization for their application in photocatalysis. a) Schematic showing the fabrication of Au-TiO$_2$-NAA-DBRs by two-step pulse anodization, surface functionalization with photoactive TiO$_2$ and deposition of metallic Au. b) Schematic illustrating the photocatalytic assessment of Au-TiO$_2$-NAA-DBRs under controlled visible-NIR irradiation conditions, with details showing the surface plasmon resonance (SPR) (top) and the chemical and electronic band structures (bottom) of the composite PC structures (note: E_g = energy bandgap, hv = excitation energy, CB = conduction band and VB = valence band). c) Transmission spectrum of a reference Au-TiO$_2$-NAA-DBR showing the region of the "slow photon" (SP) effect induced by the blue and red edges of the photonic stopband (PSB) and the SPR effect associated with the metallic Au film on the top of the PC structure (note: Au-TiO$_2$-NAA-DBR produced with anodization period – T_P = 985 s, pore widening time – t_{pw} = 24 min, Au deposition time – τ_D = 30 s and medium = air).

profile was subsequently switched to a pulse mode, in which each asymmetric stepwise pulse consisted of three stages: (i) a high voltage (HV) stage at a constant voltage of 50 V, (ii) a decreasing voltage ramp at a rate of 0.078 V s^{-1} from 50 V to 20 V, and (iii) a low voltage (LV) stage at a constant voltage of 20 V. The anodization period (T_P) – total time for each pulse – was calculated using eqn (1) as the contribution of each pulse stage (i.e. time at the HV stage – t_{HV}, time at the decreasing ramp stage – $t_{LV–HV}$, and time at the LV stage – t_{LV}). While the number of pulses, $t_{LV–HV}$ and t_{LV} was fixed at 60 pulses, ~385 s and 8 min, respectively, t_{HV} was systematically modified from 30 to 120 s, with Δt_{HV} = 30 s.

$$T_P = t_{HV} + t_{LV–HV} + t_{LV} \qquad (1)$$

The anodization period (T_P) and pore widening time (t_{pw}) were systematically manipulated from 895 to 985 s with ΔT_P = 30 s and from 0 to 24 min with Δt_{pw} = 12 min, respectively. Note that NAA-DBRs were pore widened in an aqueous solution of 5 wt% H$_3$PO$_4$ at 35 °C after fabrication.

The effect of the pore diameter and interpore distance (or lattice constant) on the top surface of NAA-DBRs on the

photocatalytic performance of these composite photocatalyst platforms was assessed. The geometric features of NAA-DBRs were systematically modified by a three-step pulse anodization approach, using different starting anodization voltages (V_o) ranging from 60 to 100 V with ΔV_o = 20 V. The first and second anodization steps were performed at V_o using the same acid electrolyte, though the duration of the latter was set to 45, 30 and 15 min for V_o = 60, 80 and 100 V, respectively. After the second anodization step, a pore widening treatment was carried out for 20, 20 and 35 min, respectively, to thin the oxide barrier layer located at the nanopore bottom tips and allow the effective flow of electrolytic species and the translation of anodization voltage modifications into porosity changes. The third anodization step was performed in pulse anodization mode at fixed t_{HV} = 120 s (i.e. T_P = 985 s) (vide supra).

Surface functionalization and top coating of NAA-DBRs

The surface of NAA-DBRs was chemically functionalized with layers of photoactive TiO$_2$ through a sol–gel method. EtOH (97 v%) and titanium(IV) butoxide (3 v%) were mixed under

208

magnetic stirring for 10 min to prepare a TiO₂ sol. NAA-DBRs were then immersed in the TiO₂ sol for 24 h to functionalize the inner surface of NAA-DBRs. Surface-functionalized NAA-DBRs were then washed with EtOH to remove any excess of TiO₂ sol and titanium(IV) butoxide. After washing, TiO₂-NAA-DBRs were dried in an oven at 50 °C for 10 min to evaporate residual EtOH. The top surface of TiO₂-NAA-DBRs was subsequently coated with an ultrathin layer of noble metal (*i.e.* Au or Ag) using a sputter coater equipped with a film thickness monitor (sputter coater 108auto, Cressington, USA). To investigate the effect of surface plasmon resonance (SPR) on the photocatalytic performance of noble metal-TiO₂-NAA-DBRs, the deposition time (τ_D) of the noble metal was systematically varied from 0 to 60 s with an interval of $\Delta\tau_D = 30$ s. The effect of different noble metal coatings (*i.e.* Au and Ag) was also studied.

Optical characterization

Prior to optical characterization, the remaining Al substrate was selectively dissolved from the backside of NAA-DBRs by wet chemical etching in a saturated solution of HCl/CuCl₂, using an etching cell with a Viton® mask featuring a circular window of 5 mm in diameter. The absorption and transmission spectra of NAA-DBRs fabricated under various conditions were obtained in air and water at normal incidence (*i.e.* $\theta = 0°$) from 200 to 900 nm with a resolution of 1 nm using a UV-visible-NIR spectrophotometer (Cary 60, Agilent, USA). The absorption spectrum of 5 mg L⁻¹ MB in a 10 mm path length polystyrene cuvette was acquired from 200 to 800 nm to determine the absorption band of MB (Fig. S1 – ESI†). The reflection spectra of NAA-DBRs produced under various fabrication conditions at normal incidence were obtained in air and water. The surface of NAA-DBRs was illuminated with white light from a tungsten source (LS-1LL, Ocean Optics, USA) using a bifurcated optical probe. The collection fiber in the optical probe collected and transferred the light reflected from the illumination spot (~2 mm in diameter) to a miniature spectrometer (USB 4000+VIS-NIR-ES, Ocean Optics, USA). The interferometric color displayed by NAA-DBRs as a function of various fabrication parameters was characterized through digital pictures, using a Canon EOS 700D digital camera equipped with a Tamron 90 mm F2.8 VC USD macro mount lens with an autofocus function under natural light illumination. The position of the central wavelength of the photonic stopband of NAA-DBRs was estimated by Gaussian fittings using OriginPro 8.5®.

Photocatalytic degradation of the model organic dye

The photocatalytic performance of noble metal-TiO₂-NAA-DBRs produced with different T_P, t_{pw}, τ_D, V_o and noble metal coatings was assessed under simulated solar light irradiation conditions using photocatalytic degradation of methylene blue (MB) as an indicator, which is a model organic dye with a well-defined absorption band within the

visible spectral range (*i.e.* MB – $\lambda_{\text{Abs-MB}} = 664$ nm). Photocatalytic reactions were performed in a transparent reactor, in which noble metal-TiO₂-NAA-DBRs with an effective area of 1 cm² were immersed in a 2 mL solution mixture of 5 mg L⁻¹ MB and 100 mM H₂O₂. The solution was stirred magnetically in a dark vessel (*i.e.* solar simulator) for 30 min to ensure an adsorption and desorption equilibrium prior to irradiation. The system was then illuminated with a 150 W (~3000 lumens) halogen lamp (HL250-A, Amscope, Australia) at room temperature to simulate solar light. The absorbance of the solution mixture at $\lambda_{\text{Abs-MB}} = 664$ nm was analyzed for each illumination time interval (*i.e.* 15 min) using a UV-visible spectrophotometer in order to determine the concentration of MB throughout time. A calibration line establishing the correlation between the absorbance and the concentration of MB was used to obtain the photocatalytic conversion ratio (C_t/C_o), where C_o is the concentration of MB after stirring in the dark for 30 min and C_t is the concentration at a given illumination time t (Fig. S2 – ESI†). This parameter was used to establish the kinetic model for this photocatalytic system. The average photocatalytic degradation rates were summarized in contour maps generated using OriginPro 8.5®, using a triangulation algorithm in which the coordinates of the intersection point were computed with linear interpolation.

Chemical and structural characterization

The nanoporous structure of NAA-DBRs produced under various conditions was characterized using a field emission gun scanning electron microscope (FEG-SEM FEI Quanta 450). FEG-SEM images were analyzed with ImageJ to establish the geometric features of NAA-DBRs.[60] The chemical composition of NAA-DBRs before and after surface functionalization with TiO₂ was analyzed by energy dispersive X-ray (EDX) spectroscopy during FEG-SEM characterization.

Results and discussion

Structural characterization of NAA-DBRs

Fig. 2 depicts the representative FEG-SEM images and a schematic definition of the structural features of NAA-DBRs produced by pulse anodization. NAA-DBRs feature an organized nanoporous geometry in two planar directions: (i) honeycomb-like distribution of nanopores across the top plane and (ii) periodically modulated nanopore diameter in depth along the normal plane (Fig. 2a). The main structural parameters of Au-NAA-DBRs include the total pore length (L_p), interpore distance (d_{int}), pore diameter (d_p), period length (L_{TP}) and noble metal thickness (L_D). Fig. 2b shows arrays of homogeneously distributed, hexagonally arranged nanopores across the top surface NAA-DBRs, where the average d_p is 31 ± 4 nm with no pore widening treatment. The cross-sectional view FEG-SEM image displays the constant voltage anodization (CA) step, during which straight cylindrical nanopores are produced (Fig. 2c).
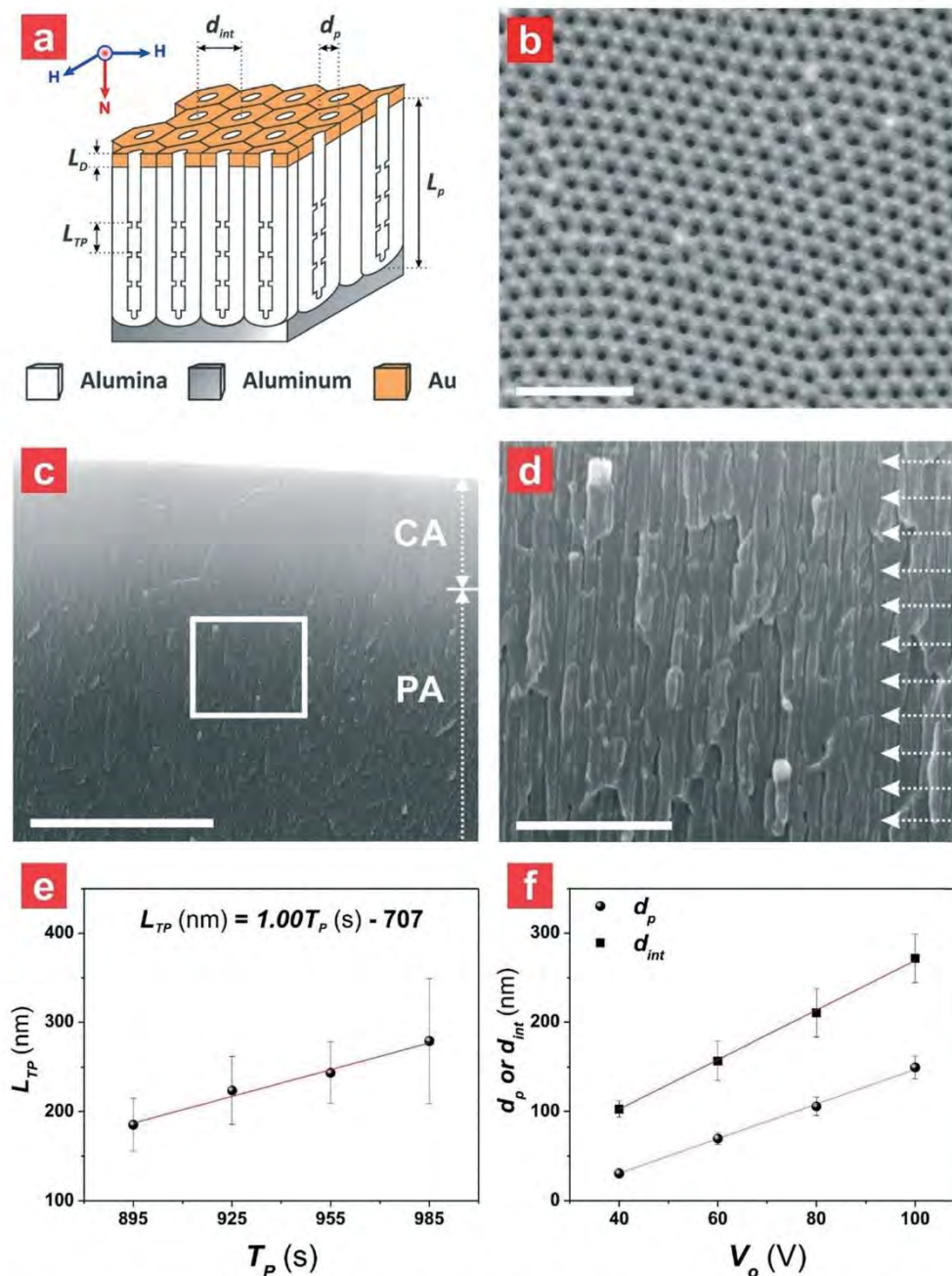
Fig. 2 Nanoporous structure of NAA-DBRs produced by pulse anodization. a) Illustration describing the geometric features of gold-coated NAA-DBRs including the total pore length (L_p), interpore distance (d_{int}), pore diameter (d_p), period length (L_{TP}) and Au thickness (L_D) (note: H = top horizontal plane and N = vertical normal plane). b) Representative top view FEG-SEM image of a NAA-DBR produced by two-step pulse anodization with anodization period T_P = 985 s, number of anodization pulses N_p = 60 pulses and pore widening time t_{pw} = 0 min (scale bar = 500 nm). c) General cross-sectional view FEG-SEM image of a NAA-DBR, where CA and PA represent the constant (CA) and pulse voltage anodization (PA) steps (scale bar = 5 μm). d) Magnified view of the white square shown in c) (scale bar = 1 μm). e) Linear correlation establishing the dependency of L_{TP} and T_P from 895 to 985 s. f) Linear dependence of d_{int} and d_p on the voltage during the constant anodization step (V_o).

Alternating stacked layers of NAA with periodic modulation of nanopore diameter are produced during the pulse anodization (PA) stage, as indicated by L_{TP} in the schematic in Fig. 2a and the white arrowheads shown in Fig. 2d. These periodic layers feature straight cylindrical pores with branched tips that form during high and low voltage anodization stages, respectively. Nanopore branching is associ-

ated with the growth of nanopores under non-steady conditions (*i.e.* low voltage anodization), which is characterized by a current recovery stage in the anodization profile.[53] Fig. 2e shows the linear dependence of L_{TP} on T_P, where L_{TP} increases at a rate of 1.00 ± 0.10 nm s^{-1} with T_p. The geometric features (*i.e.* d_p and d_{int}) of NAA-DBRs also follow a linear trend with V_o, where d_p and d_{int} increase at a rate of 1.94 ±

3162 | *Catal. Sci. Technol.*, 2019, **9**, 3158–3176

This journal is © The Royal Society of Chemistry 2019

210

0.04 and 2.78 ± 0.05 nm s^{-1} with increasing V_o, respectively (Fig. 2f).

Effect of anodization parameters on the optical properties of NAA-DBRs

Fig. 3 presents a representative two-step pulse anodization profile used to produce NAA-DBRs as well as the combined effect of T_P and t_{pw} on the central position of the characteristic photonic stopband (λ_C) of NAA-DBRs in air and water.

The anodization profile demonstrates that the current density (*i.e.* output) follows the pulse anodization voltage (*i.e.* input) applied during the second anodization step (Fig. 3a). However, a slight current recovery period was observed as compared to NAA-DBRs fabricated in H_2SO_4 electrolyte.[11,47] This is due to the thicker oxide barrier layer located at the nanopore bottom tips under these fabrication conditions.[61] To understand the effect of T_P and t_{pw} on the optical properties of NAA-DBRs, a set of NAA-DBRs was produced by systematically modifying T_P from 895 to 985 s with $\Delta T_P = 30$ s and t_{pw} from 0 to 24 min with $\Delta t_{pw} = 12$ min. Fig. 3b depicts the interferometric color displayed by these photonic crystal structures in air, where some NAA-DBRs display vivid color from purplish blue to red, while others display transparent

color (*i.e.* black background). The position of the characteristic PSB dictates the interferometric color displayed by the NAA-DBRs. As such, these PCs feature transparent and vivid colors when the characteristic photonic stopband (PSB) falls within the NIR and visible regions of the spectrum, respectively (Fig. S3 – ESI†). The intensity of the characteristic PSB also plays a major role in the intensity of the interferometric color of NAA-DBRs. For instance, NAA-DBRs produced with $T_P = 895$ and 955 s at $t_{pw} = 0$ min display weak green and red colors, respectively, as compared to the vivid colors shown by their analogue NAA-DBRs produced at $t_{pw} = 12$ min (*i.e.* intense blue and red, respectively). The digital images also demonstrate that the interferometric color of NAA-DBRs red-shifts with increasing T_P. For example, NAA-DBRs produced with $T_P = 895$, 925, 955 and 985 s at $t_{pw} = 24$ min show vivid blue, green, orange and red color, respectively. In contrast to the effect of T_P, the interferometric color of NAA-DBRs blue-shifts with t_{pw}, as revealed by the red, gold and green vivid colors observed for NAA-DBRs fabricated at $T_P = 925$ s with increasing t_{pw}, from 0 to 24 min with $\Delta t_{pw} = 12$ min, respectively. The correlation between T_P and λ_C establishes a linear relationship with t_{pw} from 0 to 24 min, where the slopes of the linear fittings were 3.59 ± 0.09, 3.54 ± 0.03 and 3.22 ± 0.09 nm s^{-1}, respectively (Fig. 3c). λ_C can be tuned from $421 \pm$
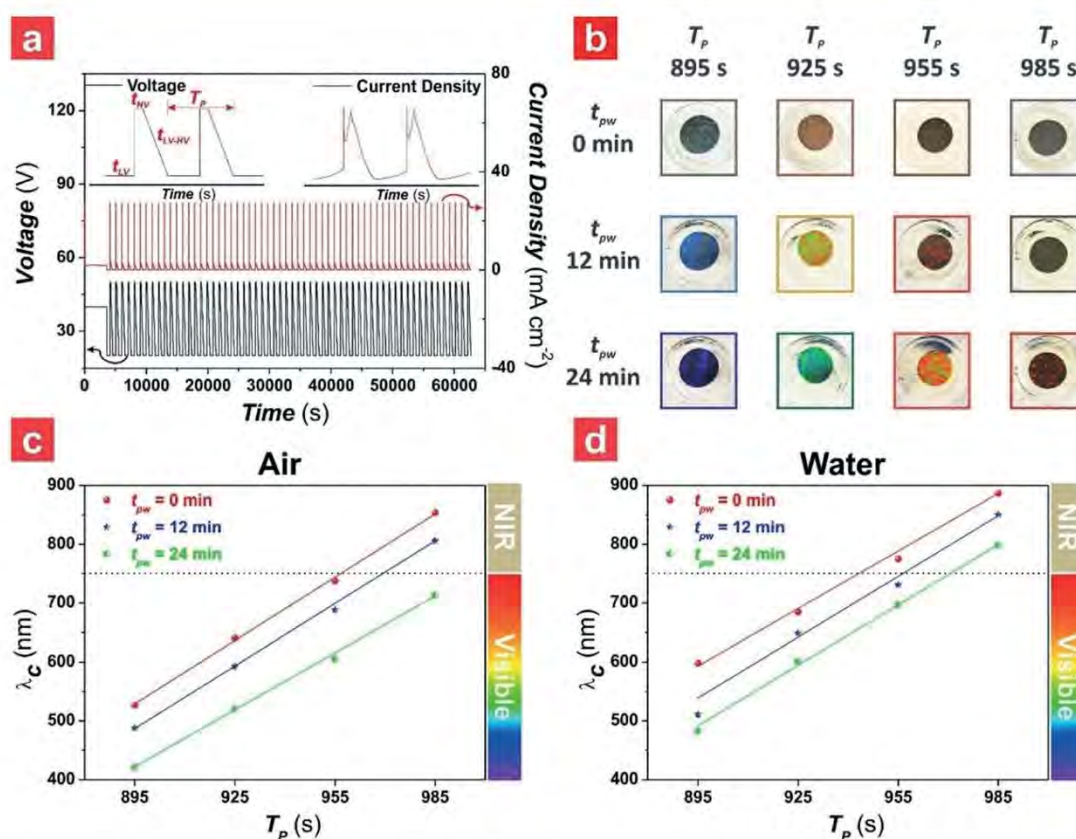
Fig. 3 Effect of anodization period (T_P) and pore widening time (t_{pw}) on the optical properties of NAA-DBRs. a) Representative anodization profile of NAA-DBRs produced by pulse anodization with $T_P = 985$ s and $N_p = 60$ pulses. b) Digital pictures of NAA-DBRs produced with different T_P and t_{pw} values. c) and d) Central position of the characteristic photonic stopband (PSB – λ_C) as a function of T_P and t_{pw}, where the medium filling the nanoporous structure of NAA-DBRs is air and water, respectively.

This journal is © The Royal Society of Chemistry 2019

Catal. Sci. Technol., 2019, **9**, 3158–3176 | **3163**

211

1 nm (T_P = 895 s and t_{pw} = 6 min) to 854 ± 1 nm (T_P = 985 s and t_{pw} = 0 min) for the range of anodization parameters studied, demonstrating that λ_C red-shifts with increasing T_P and blue-shifts with increasing t_{pw}. The optical properties of NAA-DBRs were characterized in water to identify photocatalytic enhancements associated with the "slow photon" effect, since the photocatalytic degradation of MB was performed in aqueous solution. Fig. 3d shows the linear dependence of λ_C on T_P in water, in which the former parameter red-shifts at a rate of 3.26 ± 0.08, 3.44 ± 0.23 and 3.42 ± 0.10 nm s^{-1} with the latter parameter for t_{pw} = 0, 12 and 24 min, respectively. These results also demonstrate that λ_C blue-shifts with increasing t_{pw}. The position of the characteristic PSB of NAA-DBRs in water can be tuned from 483 ± 1 nm (T_P = 895 s and t_{pw} = 6 min) to 887 ± 1 nm (T_P = 985 s and t_{pw} = 0 min), as denoted in the transmission spectra shown in Fig. S4 (ESI†). When the medium filling the nanoporous structures of NAA-DBRs is changed from air to water, the position of the characteristic PSB is red-shifted at an average rate of 46 ± 17, 42 ± 14 and 80 ± 13 nm s^{-1} for t_{pw} = 0, 12 and 24 min, respectively (Fig. 3c and d). These red-shifts are associated with the filling of the nanoporous network of NAA-DBRs with a medium of higher refractive index than air (*i.e.* n_{air} = 1.00 RIU and n_{water} = 1.33 RIU). These results demonstrate that the optical characteristics of NAA-DBRs can be precisely tuned across the visible-NIR spectrum by systematically manipulating the fabrication parameters (*i.e.* T_P and t_{pw}).

Effect of surface functionalization of TiO$_2$ and noble metal coating on the properties of NAA-DBRs

Fig. 4 depicts the effect of the deposition of TiO$_2$ layers and noble metal (*i.e.* Au) on the chemical and optical characteristics of NAA-DBRs. Photoactive layers of TiO$_2$ were deposited onto the inner surface of NAA-DBRs by the sol–gel method to develop a photoactive composite photonic crystal structure for photocatalysis.

Fig. 4a shows the energy dispersive X-ray (EDX) spectra, including insets of graphical illustration of NAA-DBRs (left) and percentage of main elements (right), before and after depositing TiO$_2$ onto the inner surface of NAA-DBRs. The EDX spectrum for the as-produced NAA-DBRs indicates that the
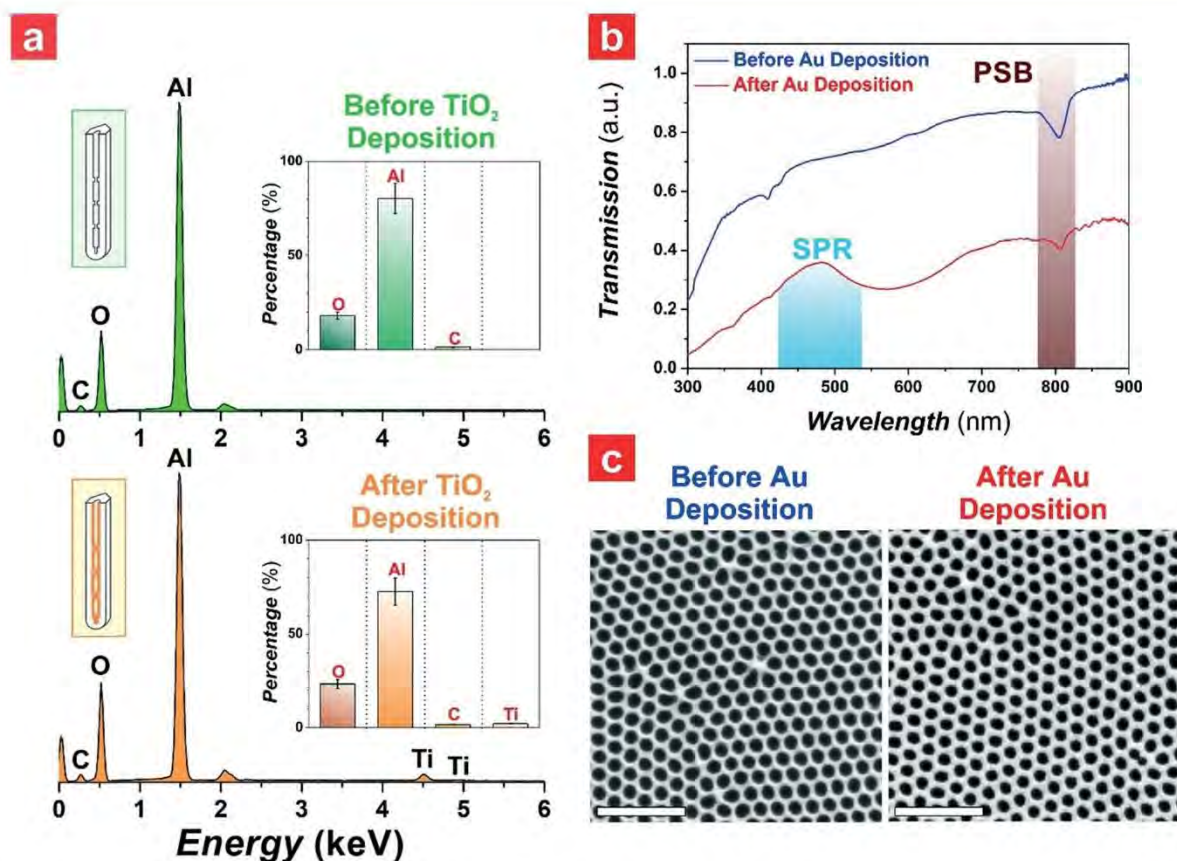
Fig. 4 Chemical and optical characterization of Au-TiO$_2$-NAA-DBRs after surface functionalization with photoactive layers of TiO$_2$ and top coating with metallic Au. a) Energy dispersive X-ray (EDX) spectra of a representative NAA-DBR with insets showing the schematic composition of NAA-DBRs (left) and the percentage of main elements present (right) before and after surface functionalization with TiO$_2$ (note: NAA-DBR produced with T_P = 985 s and t_{pw} = 24 min). b) Transmission spectrum of the representative NAA-DBR in water showing the surface plasmon resonance band (SPR) and characteristic photonic stopband (PSB) before and after coating the top surface with Au for a deposition time (τ_D) of 30 s. c) FEG-SEM images of the representative NAA-DBR from (b) before and after Au coating (scale bar = 500 nm).

3164 | *Catal. Sci. Technol.*, 2019, **9**, 3158–3176

This journal is © The Royal Society of Chemistry 2019

212

percentage of elements such as Al, O and C was 80.4 ± 8.0, 18.2 ± 1.8 and $1.4 \pm 0.1\%$, respectively. These atoms correspond to the chemical composition of the photonic structures, where Al and O atoms correspond to alumina (Al_2O_3) and C atoms are associated with contaminants incorporated into the alumina structure from the acid electrolyte (*i.e.* oxalic acid) during anodization. After surface functionalization with TiO_2 layers, the percentages of Al, O, C and Ti were determined to be 72.6 ± 7.3, 23.4 ± 2.3, 1.7 ± 0.2 and $2.3 \pm 0.2\%$, respectively. The relative percentage increment in the characteristic peaks of O and Ti atoms after TiO_2 deposition indicates that photoactive TiO_2 layers were successfully deposited onto the inner surface of NAA-DBRs. The top surface of NAA-DBRs was also coated with thin layers of Au by sputtering to provide the surface plasmon resonance (SPR) in the composite photonic crystal structures. Fig. 4b shows the transmission spectra of a representative NAA-DBR in water before and after coating with a thin film of Au for 30 s. Before coating, the position of the characteristic PSB is located at 804 ± 1 nm. After Au coating for 30 s ($L_D = 5 \pm 1$ nm), a less intense characteristic PSB is observed at 806 ± 1 nm, which is statistically the same as that of the as-produced NAA-DBR. This suggests that incorporation of Au does not shift the PSB of NAA-DBRs and slow photons still exist in these PC structures. This observation is in good agreement with previous studies.[7] However, an extraordinary optical transmission band due to surface plasmon resonance (λ_{SPR}) is observed at 481 ± 1 nm in Au-coated NAA-DBRs, which corresponds to the characteristic SPR band of Au. The successful deposition of a thin film of Au is further supported by the representative top view FEG-SEM images shown in Fig. 4c, in which the pore diameter (d_p) in a NAA-DBR at $t_{pw} = 24$ min is reduced from 81 ± 6 to 70 ± 4 nm after Au deposition. However, Au-TiO_2-NAA-DBRs maintain their original morphology after Au deposition (Fig. S5 – ESI†). The XRD spectra also successfully demonstrate the deposition of TiO_2 and Au, where the three characteristic peaks corresponding to an amorphous alumina (Al_2O_3) phase in the XRD spectra of the as-produced NAA-DBRs (*i.e.* 45°, 65° and 78°) undergo a slight shift and decrease in intensity after surface functionalization of TiO_2 followed by Au coating (Fig. S6 – ESI†). A weak characteristic peak corresponding to polycrystalline Au in the XRD spectrum of Au-TiO_2-NAA-DBRs (*i.e.* 39°) is also observed. This indicates that while TiO_2 layers are crystallographically amorphous, the deposited Au film is polycrystalline. The successful deposition of Au and TiO_2 layers on NAA-DBRs was further characterized by FEG-SEM image analysis, contact angle measurement and EDX spectroscopy (Fig. S7 – ESI†).

As these results demonstrate, Au-TiO_2-NAA-DBRs are ideal model platforms to integrate and engineer slow photons and surface plasmon resonances. SPR modes are characterized by an extraordinary transmission band (λ_{SPR}) that can be controlled by modifying the geometric features of nanopores (*i.e.* d_p, d_{int} and L_D) at the top plane of NAA-DBRs (horizontal plane). The Bragg modes (*i.e.* slow photons), characterized by the PSB, can be tuned by modifying the period length (L_{TP})

along the normal plane of the NAA-DBR structure. These versatile hybrid plasmonic–photonic crystal structures enable the engineering of photocatalytic enhancements by coupling between slow photon and SPR effects.

Assessment of photocatalytic degradation of MB by Au-TiO_2-NAA-DBRs

The photocatalytic performance of Au-TiO_2-NAA-DBRs was analyzed by monitoring the degradation of MB molecules under visible-NIR irradiation. The absorption maximum of MB (λ_{Abs-MB}) is located at 664 nm (Fig. S1 – ESI†). The concentration of this organic dye at a given illumination time t (C_t) was estimated from a previously established calibration line (Fig. S2 – ESI†). The photocatalytic performance of the hybrid plasmonic–photonic crystal structures was fitted to the linearized pseudo-first order kinetics model shown in eqn (2):

$$-\ln(C_t/C_o) = kt \qquad (2)$$

where C_o is the concentration at adsorption and desorption equilibrium and k is the kinetic constant.

Photocatalytic degradation of MB was carried out with 100 mM H_2O_2 solution to provide photogeneration of additional charge carriers from the relatively thin photoactive TiO_2 layer in Au-TiO_2-NAA-DBRs. The simulated solar light irradiation used in our study has a spectral distribution of 0.12% UV (350–400 nm), 64.60% visible (400–750 nm) and 35.28% NIR (800–1025 nm). Therefore, these photocatalytic reactions were mostly driven by visible-NIR irradiation (Fig. S8 – ESI†).

Effect of fabrication parameters of Au-TiO_2-NAA-DBRs on the photocatalytic degradation of MB

NAA-DBRs are 1D photonic crystals with a well-defined PSB that can be precisely tuned across the spectral regions by modifying the anodization parameters. Functionalization of the inner surface of NAA-DBRs with TiO_2 layers provides these nanoporous PCs with essential photocatalytic activity to photodegrade organic molecules. However, these composite semiconductor PCs also provide opportunities to further enhance the efficiency of photocatalytic reactions by the engineered "slow photon" effect. Slow photons have reduced group velocity at those spectral regions near the blue and red edges of the characteristic PSB.[62] This effect enhances the photon-to-electron conversion rate since photons have a longer lifespan within the composite photonic structures. The top surface of TiO_2-NAA-DBRs can also be coated with thin films of noble metals to further enhance the photocatalytic performance of the composite platform by SPR, which minimizes the recombination rate of electron/hole pairs at the hybrid heterojunction Au-TiO_2-NAA-DBRs, and extends the absorption of visible light by the hybrid plasmonic–photonic crystal structure.[5] Photocatalytic degradation of methylene blue was analyzed under simulated solar light irradiation as an indicator to identify photocatalytic enhancements associated with coupling effects between slow photons and SPR in

This journal is © The Royal Society of Chemistry 2019

Catal. Sci. Technol., 2019, **9**, 3158–3176 | **3165**

Au-TiO$_2$-NAA-DBRs. The anodization period (T_P), pore widening time (t_{pw}) and Au deposition time (τ_D) of Au-TiO$_2$-NAA-DBRs were systematically modified from T_P = 895 to 985 s with ΔT_P = 30 s, from t_{pw} = 0 to 24 min with Δt_{pw} = 12 min, and from τ_D = 0 to 60 s with $\Delta \tau_D$ = 30 s, respectively. Fig. 5 depicts the linearized pseudo-first order kinetics for the photocatalytic degradation of MB by Au-TiO$_2$-NAA-DBRs (t_{pw} = 0 min) with different T_P and τ_D values, where the slope corresponds to the kinetic constant (k) or the photocatalytic performance of Au-TiO$_2$-NAA-DBRs. The obtained results for Au-TiO$_2$-NAA-DBRs with t_{pw} = 12 and 24 min are provided in Fig. S9 and S10 (ESI†), respectively. A summary of the k values obtained from linear fittings of these linearized pseudo-first order photodegradation kinetics of MB is provided in Table S1 (ESI†) and Fig. 6. Fig. 6a–c illustrate the contour maps summarizing the effect of T_P and τ_D on the k values for Au-TiO$_2$-NAA-DBRs produced with t_{pw} = 0, 12 and 24 min, respectively, and Fig. 6d–f depict the correlation between the absorption band of MB and the position of the blue and red edges of the characteristic PSB of Au-TiO$_2$-NAA-DBRs fabricated with t_{pw} = 0, 12 and 24 min, respectively.

Fig. 6a shows a homogeneous bimodal dependency of k on T_P and τ_D, as indicated by the equidistant color field lines with T_P and τ_D and the two local maxima of k at T_P = 895 s

and τ_D = 0 s and at T_P = 955 s and τ_D = 0 s. When τ_D is fixed at 0 s (*i.e.* no SPR in the composite PC structures), k decreases from T_P = 895 to 925 s (*i.e.* from k = 1.83 ± 0.06 to 1.26 ± 0.04 h^{-1}), increases to a maximum of kinetic constant at T_P = 955 s (*i.e.* k_{max} = 2.22 ± 0.08 h^{-1}), and decreases again to a lower k value at T_P = 985 s (*i.e.* k = 1.57 ± 0.05 h^{-1}). These results denote that at τ_D = 0 s, Au-TiO$_2$-NAA-DBRs produced with T_P = 955 s photodegrade MB molecules more efficiently than their counterparts produced at different anodization periods. This result can be correlated with the relative position of the edges of the characteristic PSB and the absorption band of MB (Fig. 6b). Au-TiO$_2$-NAA-DBRs produced with T_P = 955 s achieve the highest k value since the characteristic PSB of these PCs partially overlaps with the absorption band of MB, with the PSB's blue edge located ~89 nm away from the absorption maximum of MB (*i.e.* λ_{Abs-MB} = 664 nm). On the other hand, Au-TiO$_2$-NAA-DBRs fabricated with T_P = 925 s show the lowest k value, where the distance between the PSB's blue edge and the absorption maximum of MB is the shortest (*i.e.* ~22 nm). The relative position between the red and blue edges of the characteristic PSB and the absorption band of the model organic compound are critical in enhancing light–matter interactions and boosting photon-to-electron conversion rates. The photocatalytic performance of Au-TiO$_2$-NAA-DBRs is significantly enhanced
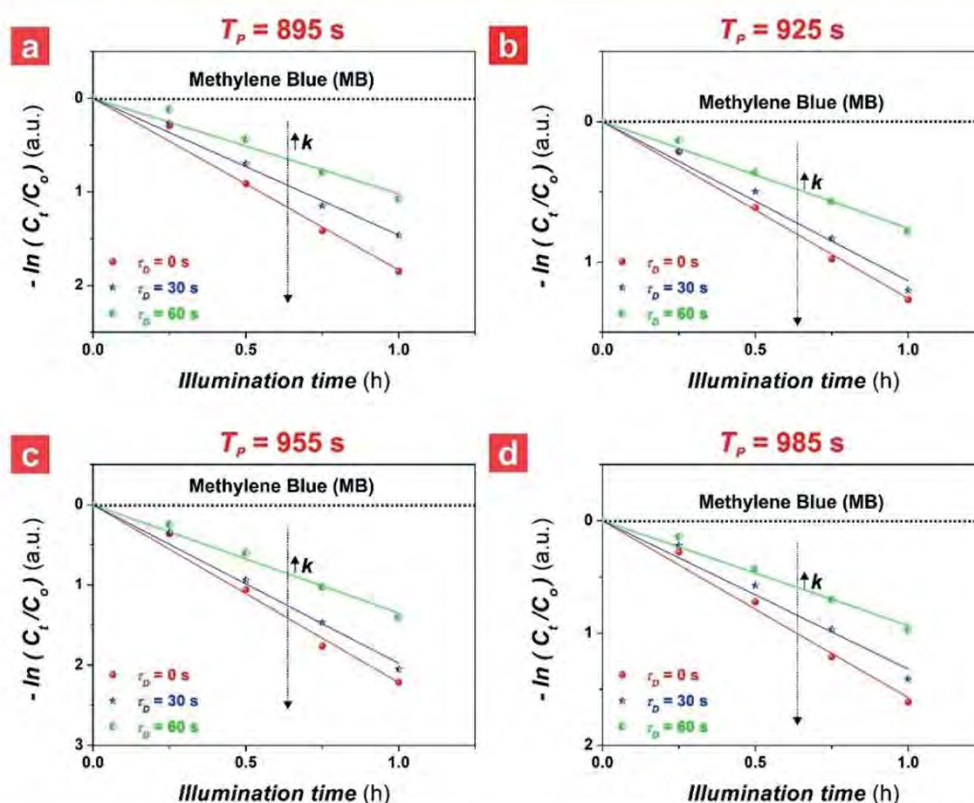
Fig. 5 Photocatalytic degradation kinetics of methylene blue (MB) by Au-TiO$_2$-NAA-DBRs fabricated by two-step pulse anodization at fixed pore widening time (t_{pw} = 0 min), and variable Au deposition time (τ_D = 0, 30 and 60 s) and anodization period (T_P = a) 895 s, b) 925 s, c) 955 s and d) 985 s) under controlled irradiation conditions (note: black dotted lines correspond to the photodegradation of MB in control NAA-DBRs without photoactive TiO$_2$ layers).

214
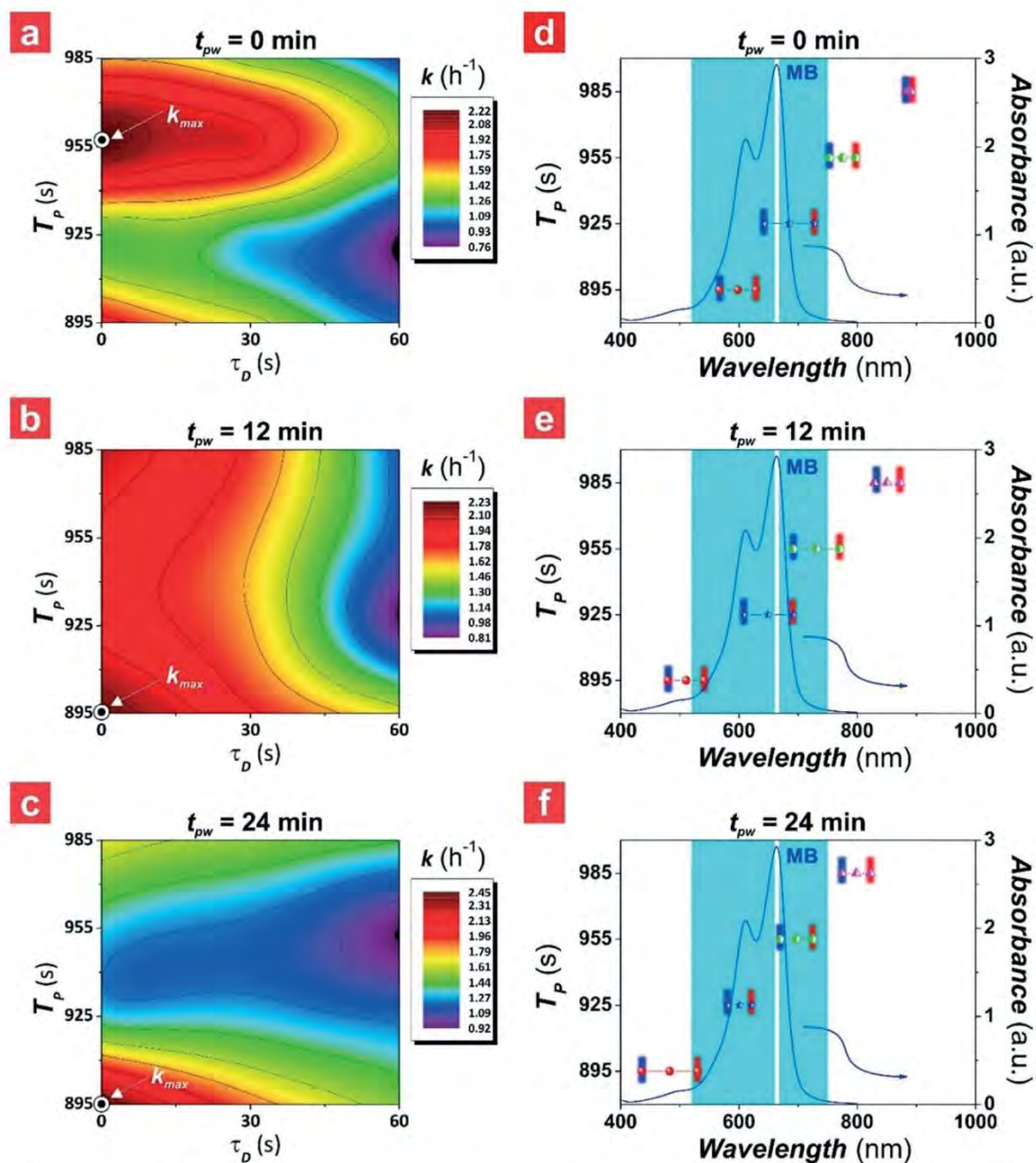
Fig. 6 Combinational effect of the anodization period (T_P), pore widening time (t_{pw}), Au deposition time (τ_D) and position of the blue and red edges of the characteristic stopband (PSB) of Au-TiO$_2$-NAA-DBRs on the photocatalytic degradation rates (k) of methylene blue (MB). a–c) Contour plots showing the combined effect of T_P and τ_D on k values for the photodegradation of MB by Au-TiO$_2$-NAA-DBRs with t_{pw} = 0, 12 and 24 min, respectively. d–f) Relative position of the blue and red edges of the characteristic PSB of Au-TiO$_2$-NAA-DBRs produced with varying T_P from 895 to 985 s with ΔT_P = 30 s with respect to the absorption band of MB for t_{pw} = 0, 12 and 24 min, respectively (note: the white gap inside the absorption band of MB denotes the absorption maximum of MB – $\lambda_{abs\text{-}MB}$ = 664 nm, while the blue and red vertical lines on the PSB correspond to the blue and red edges of the PSB).

when the edges of the characteristic PSB partially overlap with the absorption band of MB.[10,62–65] However, when the edges of the PSB fall within the absorption maximum of MB or are too far from the absorption band of MB (T_P = 925 and 985 s), the photocatalytic performance is reduced significantly. The poor photocatalytic performance observed

for Au-TiO$_2$-NAA-DBRs produced with T_P = 925 s is attributed to the screening effect by MB molecules at their absorption maximum (*i.e.* $\lambda_{Abs\text{-}MB}$ = 664 nm; ~2.9 a.u.). Under such a configuration, most of the irradiated light is absorbed by MB molecules before it reaches the inner surface of the composite PC structures. This dramatically

reduces the photocatalytic efficiency of Au-TiO$_2$-NAA-DBRs due to the poor utilization of incoming photons by the photoactive TiO$_2$ layer. This observation is in good agreement with previous studies.[10] It is worth noting that the characteristic PSB of the second best performing Au-TiO$_2$-NAA-DBR structure (T_P = 895 s) is also partially overlapped with the absorption band of MB, though with a reasonable distance between the PSB's red edge and the absorption maximum of MB (*i.e.* ~36 nm). When a characteristic PSB is completely outside the absorption band of MB, the photocatalytic degradation rate of Au-TiO$_2$-NAA-DBR is strongly dependent on the geometric features of the nanoporous PC structures and independent on the "slow photon" effect. The main geometric factor affecting the photocatalytic performance of Au-TiO$_2$-NAA-DBRs in this situation is the total pore length (L_P), which is directly proportional to the anodization time.[10,66,67] The overall light absorption of the composite PC structure enhances with increasing L_P, leading to an increase in the photogeneration of charge carriers and the overall photodegradation rate achieved by Au-TiO$_2$-NAA-DBRs. Au-TiO$_2$-NAA-DBRs produced with T_P = 985 s have the longest pore length (*i.e.* total anodization time = 17.4 h) as compared to their analogues fabricated with shorter T_P (*i.e.* from 15.9 to 16.9 h). In summary, this analysis reveals that the photocatalytic performance of Au-TiO$_2$-NAA-DBRs produced with t_{pw} = 0 min, τ_D = 0 s and varying T_P follows the order 955 > 895 > 985 > 925 s.

Fig. 6a shows that this trend is consistent with increasing thickness of the Au coating (from τ_D = 0 to 60 s) in Au-TiO$_2$-NAA-DBRs produced at t_{pw} = 0 min. However, these hybrid plasmonic–photonic crystal structures achieve lower k values in general, as indicated by the color field distribution with increasing τ_D. The minimum kinetic constant (k_{min}) of 0.76 ± 0.02 h^{-1} is achieved by those Au-TiO$_2$-NAA-DBRs fabricated with T_P = 925 s and τ_D = 60 s (*i.e.* black region of the contour map), denoting that the k values decrease with increasing τ_D. This phenomenon can be explained by analyzing the optical characteristics of Au-TiO$_2$-NAA-DBRs as a function of τ_D. The optical behavior of Au-TiO$_2$-NAA-DBRs is equivalent to the sum of their transmission, absorption and reflection. To gain further insight into the effect of τ_D on the photocatalytic behavior of Au-TiO$_2$-NAA-DBRs, we analyzed the optical transmission, absorption and reflection of a representative Au-TiO$_2$-NAA-DBR produced with T_P = 925 s, t_{pw} = 24 min and medium = air (Fig. 7). The transmission spectra of these hybrid plasmonic–photonic crystal structures show a characteristic SPR band at 491 ± 1 nm for Au-TiO$_2$-NAA-DBRs synthesized with τ_D = 30 and 60 s (Fig. 7a). This SPR band results from an extraordinary transmission of light and can be controlled by modifying the geometric features of the nanopores on the top surface of the hybrid plasmonic–photonic crystal structures. However, as the orange shaded region in the transmission spectra indicates, the deposition of a thin layer of gold on the top surface of the TiO$_2$-NAA-DBR reduces the intensity of the characteristic PSB with increasing τ_D, and also red-shifts slightly its posi-

tion from 612 ± 1 to 615 ± 1 nm when τ_D is increased from 0 to 60 s. The absorption spectra at different τ_D values (Fig. 7b) confirm that the position of the characteristic PSB is slightly red-shifted with increasing τ_D. Though the intensity of the characteristic PSB is similar in all the cases, the overall light absorption by the composite PC structure increases significantly with increasing τ_D. Fig. 7c demonstrates that the intensity of the characteristic PSB in the reflection spectrum decreases with increasing τ_D, while its position remains practically constant (only a slight red shift is observed, from 612 ± 1 to 613 ± 1 nm when τ_D is increased from 0 to 60 s). The effect of the deposition of the thin Au layer can also be observed in the interferometric color of the Au-TiO$_2$-NAA-DBR, which switches from red to gold color with increasing τ_D. This analysis indicates that the transmission and reflection of Au-TiO$_2$-NAA-DBRs decrease with increasing τ_D, while their optical absorption increases. As the k values reveal, Au-TiO$_2$-NAA-DBRs have a poorer photocatalytic performance with increasing τ_D. This observation is attributable to the light screening effect by the thin Au layer deposited on the top surface of TiO$_2$-NAA-DBRs, which reduces the amount of incident photons that travel across the bulk photocatalyst platforms. The localized position of the Au thin film on the top surface of Au-TiO$_2$-NAA-DBRs implies that no effective Schottky barrier is formed between the Au nanostructure and the functional TiO$_2$ layer deposited onto the inner surface of TiO$_2$-NAA-DBRs. The absence of an effective hybrid heterojunction between Au and TiO$_2$ and the absorption of light by the Au film prevent the effective transfer of photo-excited electrons from the Au layer to the semiconductor layers and the photogenerated carriers are mainly recombined in the Au layer, worsening the overall photocatalytic degradation of MB molecules by Au-TiO$_2$-NAA-DBRs.

Fig. 6b shows a k maximum of 2.23 ± 0.08 h^{-1} at T_P = 895 s and τ_D = 0 s, and a minimum of 0.82 ± 0.03 h^{-1} at T_P = 925 s and τ_D = 60 s for Au-TiO$_2$-NAA-DBRs fabricated with t_{pw} = 12 min. The contour map reveals a smooth variation of k with T_P and τ_D, as indicated by the homogeneous distribution of color fields. However, the effect of T_P on the photocatalytic performance of Au-TiO$_2$-NAA-DBRs is less significant than that of τ_D at t_{pw} = 12 min. The dependence of k on τ_D is stronger at longer deposition times, as indicated by the denser distribution of color fields and field lines with increasing τ_D. The photocatalytic performance of Au-TiO$_2$-NAA-DBRs decreases with increasing τ_D, which is in good agreement with the results obtained for Au-TiO$_2$-NAA-DBRs fabricated with t_{pw} = 0 min. The photocatalytic performance of Au-TiO$_2$-NAA-DBRs (t_{pw} = 12 min) is strongly dependent on the relative position between the edges of the characteristic PSB and the absorption band of MB molecules (Fig. 6e). The photocatalytic enhancement associated with the "slow photon" effect is apparent when the characteristic PSB partially overlaps with the absorption band of MB. Au-TiO$_2$-NAA-DBRs produced with T_P = 895 s achieve the k_{max} since more than half of the characteristic PSB is

3168 | *Catal. Sci. Technol.*, 2019, **9**, 3158–3176

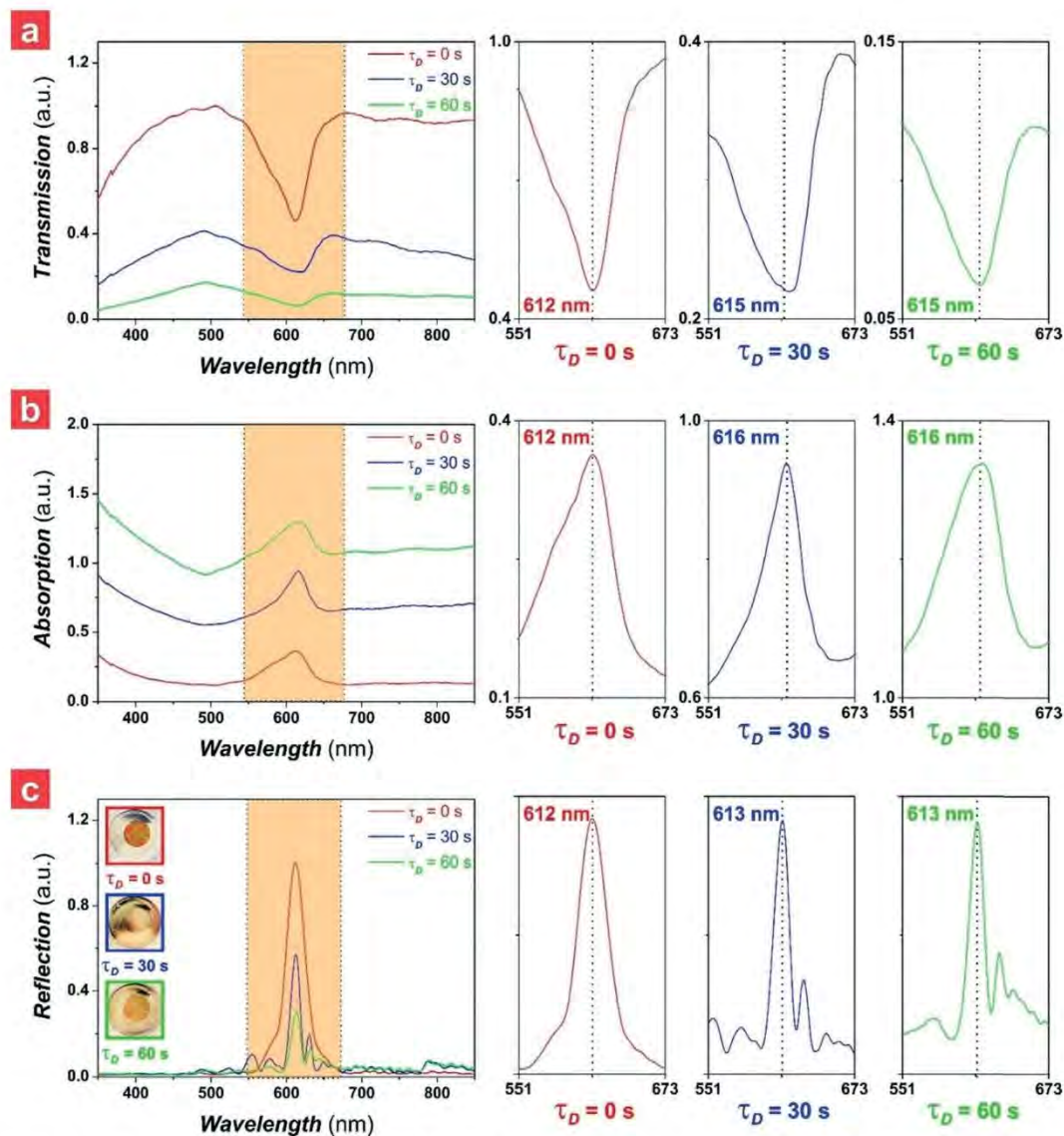This journal is © The Royal Society of Chemistry 2019

216

Fig. 7 Optical characterization of a representative Au-TiO$_2$-NAA-DBR produced with anodization period T_P = 955 s and pore widening time t_{pw} = 24 min in air (note: shaded regions correspond to the magnified views of the photonic stopbands (PSBs) for different τ_D values shown on the right side). a) Transmission spectra of the Au-TiO$_2$-NAA-DBRs as a function of the Au deposition time (τ_D). b) Absorption spectra of the Au-TiO$_2$-NAA-DBRs as a function of τ_D. c) Reflection spectra and digital pictures of the Au-TiO$_2$-NAA-DBRs as a function of τ_D.

located outside the absorption maximum of MB (*i.e.* ~123 nm away). In contrast, Au-TiO$_2$-NAA-DBRs fabricated with T_P = 925 s provide the worst k since the characteristic PSB of PCs is located under the absorption maximum of MB (*i.e.* PSB's blue edge ~27 nm away from λ_{Abs-MB} = 664 nm). The characteristic PSB of Au-TiO$_2$-NAA-DBRs fabricated with T_P = 985 s is entirely outside the absorption band of MB. Under this configuration, the photocatalytic performance of these composite PCs relies exclusively on the total length of the nanopores. These Au-TiO$_2$-NAA-DBRs show slightly superior performance to their counterparts fabricated with T_P = 925 and 955 s at any τ_D = 0, 30 and 60 s, respectively. Hence, the photodegradation rate of MB in Au-TiO$_2$-NAA-DBRs produced with t_{pw} = 12 min follows the order T_P = 895 > 985 > 955 > 925 s.

Fig. 6c summarizes the photocatalytic performance of Au-TiO$_2$-NAA-DBRs fabricated with t_{pw} = 24 min as a function of T_P and τ_D. As the contour map shows, k_{max} (*i.e.* 2.45 ± 0.13 h^{-1}) and k_{min} (*i.e.* 0.92 ± 0.03 h^{-1}) are located at T_P = 895 s and τ_D = 0 s and T_P = 955 s and τ_D = 60 s, respectively. The distribution of color fields and field lines is denser within the area around the local maximum, for T_P < 925 s and τ_D < 30 s, indicating a strong dependence of k on these fabrication conditions. However, at T_P > 925 s, the kinetic constant becomes less dependent on τ_D as indicated by the broad color fields and field lines. The k values decrease with increasing τ_D and the photocatalytic performance of these Au-TiO$_2$-NAA-DBRs follows the order T_P = 895 > 985 > 955 > 925 s. This behavior is analogous to that of Au-TiO$_2$-NAA-DBRs produced at different pore widening times, though the overall

k values are slightly higher than those of their counterparts produced at $t_{pw} = 0$ and 12 min. The photocatalytic performance order of Au-TiO$_2$-NAA-DBRs fabricated at $t_{pw} = 24$ min is dictated by the relative position of the characteristic PSB of these composite PC structures with respect to the absorption band of MB (Fig. 6f). The "slow photon" effect significantly enhances the photodegradation of MB when the characteristic PSB partially falls within the absorption band of MB and its edges are positioned far away from the absorption maximum of MB. As Fig. 6f shows, Au-TiO$_2$-NAA-DBRs fabricated with $T_P = 895$ s achieve $k_{max} = 2.45 \pm 0.13$ h^{-1}, the characteristic PSB of these Au-TiO$_2$-NAA-DBRs is slightly overlapped with the absorption band of MB, with the PSB's red edge located far away from the absorption maximum of MB (i.e. ~134 nm away). When the distance between the absorption maximum of MB and the blue edge of the PSB of these Au-TiO$_2$-NAA-DBRs is the narrowest (i.e. ~5 nm for Au-TiO$_2$-NAA-DBRs produced with $T_P = 955$ s), the photocatalytic performance is the worst as compared to that of Au-TiO$_2$-NAA-DBRs produced with a shorter anodization period (i.e. $T_P = 895$ and 925 s). This result is attributable to the light screening effect by MB molecules at those spectral regions near the absorption maximum of MB. It is noteworthy that Au-TiO$_2$-NAA-DBRs fabricated with $T_P = 985$ s show a photocatalytic behavior that is independent of the "slow photon" effect since the PSB is located far away from the absorption band of MB. Under this configuration, the photocatalytic performance of these Au-TiO$_2$-NAA-DBRs relies strongly on the total pore length, achieving the second best performance at any τ_D.

To summarize, Fig. 6a–c show that Au-TiO$_2$-NAA-DBRs fabricated with $t_{pw} = 24$ min provide the highest k_{max} and k_{min} values. These k_{max} and k_{min} were found to be 8–9% and 12–17% higher than those of Au-TiO$_2$-NAA-DBRs produced with shorter t_{pw}. The superior performance achieved by Au-TiO$_2$-NAA-DBRs at $t_{pw} = 24$ min can be associated with the broader and more intense characteristic PSB of these composite PCs, which provides a more efficient collection and utilization of incident photons to photodegrade MB molecules. An enhancement in photocatalytic degradation of MB in Au-TiO$_2$-NAA-DBRs is strongly dependent on the "slow photon" effect. This enhancement is apparent when the edges of the characteristic PSB of these composite PCs partially overlap with the absorption band of MB, though they are positioned far away from the absorption maximum of MB. When the vicinity of the characteristic PSB is near the absorption maximum of MB, the photocatalytic performance of Au-TiO$_2$-NAA-DBRs is significantly reduced due to the light screening effect (i.e. MB molecules absorb light efficiently in these spectral regions so incoming photons cannot reach the photoactive layers within the nanoporous PC structure). When the characteristic PSB of Au-TiO$_2$-NAA-DBRs is located completely outside the absorption band of MB, the photocatalytic performance relies exclusively on the geometric features of the nanoporous PC and is independent of the "slow photon" effect. Our study

also indicates that while incorporation of a nanoporous plasmonic structure enhances the overall collection of incident photons in Au-TiO$_2$-NAA-DBRs, this is not translated into an effective utilization of SPR photons in the photocatalytic reaction. This is due to the isolated position of the Au film on the top surface of the PC structure. Incident light is partially absorbed by the Au film to generate SPR photons, minimizing the amount of incoming photons that travel across the PC structure. SPR photons are localized onto the top surface of the PC structure and cannot be efficiently transferred into the TiO$_2$ photoactive layer on the inner surface of Au-TiO$_2$-NAA-DBRs. As a result, the incorporation of the Au film worsens the photocatalytic performance of Au-TiO$_2$-NAA-DBRs.

Effect of the noble metal coating type on the photodegradation of MB

The SPR effect associated with the type of noble metal coating on the photocatalytic performance of these composite PC structures was studied by coating TiO$_2$-NAA-DBRs fabricated with $T_P = 985$ s and $t_{pw} = 24$ min with thin films of Au and Ag with varying deposition time (τ_D), from 0 to 60 s with $\Delta\tau_D = 30$ s. The optical transmission of these composite PC structures was characterized and analyzed. Table S2 (ESI†) and Fig. 8 summarize the effect of Au and Ag coatings on the kinetic constant and optical transmission of noble metal-coated TiO$_2$-functionalized NAA-DBRs. Fig. 8a and b show the transmission spectra of Au- and Ag–TiO$_2$-NAA-DBRs as a function of τ_D, respectively. In general, the intensity of the characteristic PSB of these noble metal-TiO$_2$-NAA-DBRs decreases with increasing τ_D due to the absorption by the nanoporous metallic layer deposited on the top surface of these composite PCs. These PC structures show 1st and 2nd order characteristic PSBs, which are denoted by the red and purple shaded regions in Fig. 8a and b, and also characteristic SPR bands for Au- and Ag–TiO$_2$-NAA-DBRs located at 497 ± 1 nm and 335 ± 1 nm, respectively. Magnified views of the characteristic PSBs (shaded regions in Fig. 8a and b) for Au- and Ag–TiO$_2$-NAA-DBRs are shown in Fig. 8c and d, respectively. Fig. 8c shows that the change in the position of the 1st and 2nd order PSBs of Au-TiO$_2$-NAA-DBRs with the Au coating is almost negligible, in agreement with our previous observations (Fig. 7). On the other hand, Fig. 8d shows that the features of the 1st and 2nd order PSBs of Ag–TiO$_2$-NAA-DBRs blue-shift their position and broaden their width with increasing τ_D. Fig. 8e and f summarize the photocatalytic performance of Au- and Ag–TiO$_2$-NAA-DBRs as a function of τ_D in terms of linearized pseudo-first order kinetics for the photodegradation of MB, where the insets correspond to the photocatalytic degradation rates (k – slopes of linear fittings) of each system. These results demonstrate that the photocatalytic degradation rate of MB by both Au- and Ag–TiO$_2$-NAA-DBRs worsens with increasing τ_D. The k values achieved by Au-TiO$_2$-NAA-DBRs produced at $\tau_D = 0$, 30 and 60 s were 1.67 ± 0.05, 1.54 ± 0.07 and 1.41 ± 0.06 h^{-1}, respectively.

3170 | Catal. Sci. Technol., 2019, 9, 3158–3176

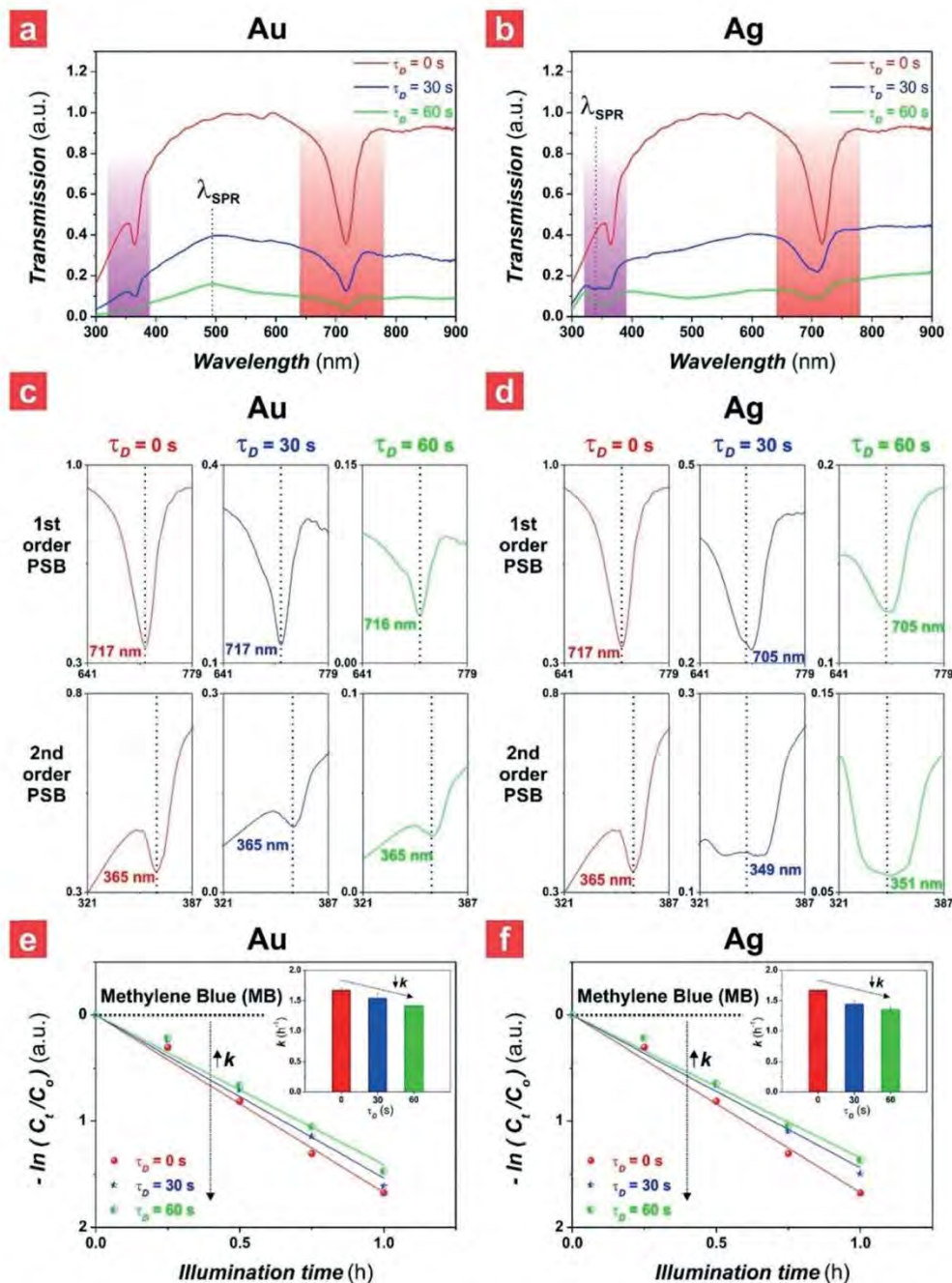This journal is © The Royal Society of Chemistry 2019

218

Fig. 8 Optical characterization and photocatalytic degradation assessment of Au- and Ag–TiO$_2$-NAA-DBRs produced with T_P = 985 s and t_{pw} = 24 min. a and b) Transmission spectra of Au- and Ag–TiO$_2$-NAA-DBRs as a function of the deposition time (τ_D), respectively (note: medium = air). c and d) Magnified views of the photonic stopbands (PSBs) of Au- and Ag–TiO$_2$-NAA-DBRs from the shaded regions shown in (a) and (b) at different τ_D values, respectively. e and f) Photocatalytic degradation kinetics of methylene blue (MB) in Au- and Ag–TiO$_2$-NAA-DBRs, respectively (note: black dotted lines correspond to the photocatalytic degradation of MB in control NAA-DBRs without the photoactive TiO$_2$ layer with insets compiling the values of the kinetic constant (k) for MB).

These results demonstrate that non-coated TiO$_2$-NAA-DBRs outperform their Au-coated counterparts by a 7–16% superior performance in degrading MB. Ag–TiO$_2$-NAA-DBRs synthesized with τ_D = 0 s have the highest k value (*i.e.* 1.67 ± 0.05 h^{-1}) when compared to Ag-coated analogues fabricated with τ_D = 30 and 60 s, which achieve k values of 1.44 ± 0.06 and 1.35 ± 0.05 h^{-1}, respectively. It is thus clear that non-coated

TiO$_2$-NAA-DBRs provide a 14–19% superior performance in degrading MB compared to Ag-coated composite PCs. In summary, Au-TiO$_2$-NAA-DBRs perform more efficiently than Ag–TiO$_2$-NAA-DBRs at any τ_D. Ag nanostructures provide enhanced SPR effects as compared to their Au-based counterparts. However, the chemical stability of Au against surface oxidation and dissolution in aqueous environments makes

This journal is © The Royal Society of Chemistry 2019

Catal. Sci. Technol., 2019, **9**, 3158–3176 | **3171**

Au-TiO$_2$-NAA-DBRs superior platforms to photodegrade MB molecules.

Effect of geometric features of Au-TiO$_2$-NAA-DBRs on the photocatalytic degradation of MB

The position of the SPR band of Au-TiO$_2$-NAA-DBRs (λ_{SPR}) can be readily controlled by modifying the pore diameter (d_p) and interpore distance (d_{int}) of nanopores at the top plane of NAA-DBRs (horizontal plane – Fig. 2a). To demonstrate the tuneability and effect of the position of the SPR band on the photodegradation of MB, the geometric features (i.e. d_p and d_{int}) of Au-TiO$_2$-NAA-DBRs at the top horizontal plane were systematically modified by a three-step anodization approach, in which the starting anodization voltage (V_o) and Au deposition time (τ_D) were modified from V_o = 60 to 100 V with ΔV_o = 20 V, and from τ_D = 0 to 60 s with $\Delta \tau_D$ = 30 s. The fabrication parameters of the third anodization step (i.e. pulse anodization mode) were fixed to T_P = 985 s, number of pulses = 60 pulses, and t_{pw} = 0 min to maintain the position and features of the characteristic PSB, which were established by the period length (L_{TP}) along the normal plane of the NAA-DBR structure. Fig. S11 (ESI†) demonstrates that the PSB of these PCs in the reflection spectrum does not change its position

significantly with varying V_o, both in air and water. The average λ_C in Au-TiO$_2$-NAA-DBRs in air and water was 835 ± 14 and 865 ± 9 nm, respectively. Under such a configuration, the characteristic PSB is located outside the absorption band of MB and therefore the photocatalytic system is independent of the "slow photon" effect. Table S3 (ESI†) and Fig. 9 summarize the correlation of the photocatalytic performance of Au-TiO$_2$-NAA-DBRs with V_o and τ_D.

Fig. 9a presents the photocatalytic degradation kinetics of MB as a function of V_o and τ_D, in which the slope of the fitting lines corresponds to k – an indicator of the photocatalytic performance. As these results demonstrate, in general k decreases with increasing τ_D. This can be attributable to the isolated position of the nanoporous Au layer on the top plane of the composite PC structures. The Au thin film acts as a screen that absorbs the majority of the incoming light and prevents its efficient propagation across the bulk Au-TiO$_2$-NAA-DBR structure, minimizing the overall photocatalytic performance due to a localized generation of SPR-excited photons on the top surface (i.e. photons are not transferred efficiently to the photoactive TiO$_2$ layer). Fig. 9b illustrates the idealized structure of Au-TiO$_2$-NAA-DBRs fabricated by three-step pulse anodization, in which the high starting anodization voltage in the second step is followed by a reduction of the anodization
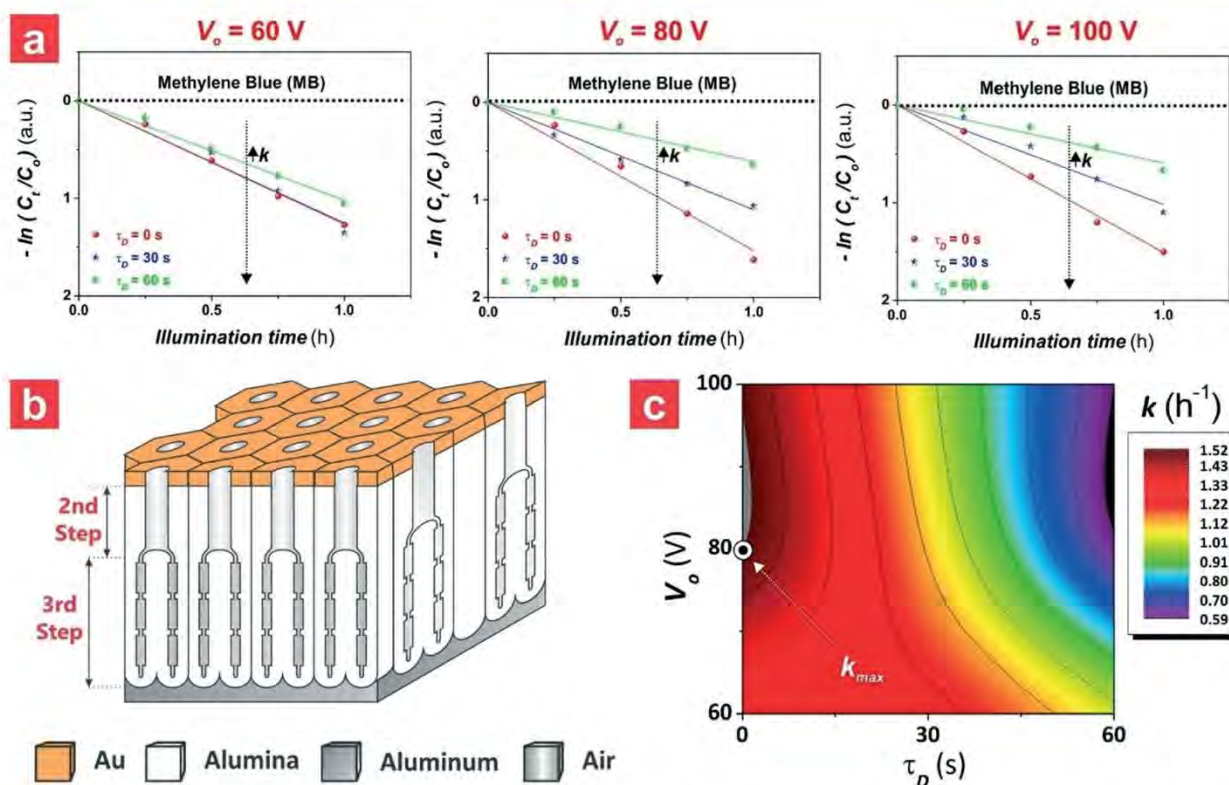
Fig. 9 Combinational effect of starting anodization voltage (V_o) and Au deposition time (τ_D) on the kinetic constant (k) for the photodegradation of methylene blue (MB) by Au-TiO$_2$-NAA-DBRs. a) Photocatalytic degradation kinetics of MB by Au-TiO$_2$-NAA-DBRs fabricated by three-step pulse anodization with τ_D = 0, 30 and 60 s and anodization voltage (V_o) of 60 V (left), 80 V (center) and 100 V (right) (note: black dotted lines correspond to the photodegradation of MB in control NAA-DBRs without the photoactive TiO$_2$ layer). b) Schematic of the nanoporous structures of NAA-DBRs fabricated by three-step pulse anodization. c) Contour map showing the combined effect of V_o and τ_D on k values for the photodegradation of MB by Au-TiO$_2$-NAA-DBRs.

220

voltage during the third step that leads to branching of nanopores. The contour graph shown in Fig. 9c summarizes the dependency of the photocatalytic performance of Au-TiO$_2$-NAA-DBRs on V_o and τ_D. The smooth and homogeneous distribution of color fields and field lines implies a relatively weak dependence of k on these fabrication parameters, though the effect of V_o on k is less significant than that of τ_D. The maximum and minimum k values (1.52 ± 0.07 and 0.59 ± 0.06 h^{-1}) are located at $V_o = 80$ V and $\tau_D = 0$ s, and $V_o = 100$ V and $\tau_D = 60$ s, respectively. The k_{max} (1.51 ± 0.05 h^{-1}) located at $V_o = 100$ V and $\tau_D = 0$ s is statistically the same as the maximum k observed at $V_o = 80$ V and $\tau_D = 0$ s, with only ~1% of difference. In contrast, the k (1.26 ± 0.03 h^{-1}) located at $V_o = 60$ V is ~17% smaller than that achieved by Au-TiO$_2$-NAA-DBRs produced at $V_o = 80$ and 100 V. It is also worth noting that the photocatalytic performance of Au-TiO$_2$-NAA-DBRs produced with $V_o = 60$ V is relatively similar with increasing τ_D as compared to the significant decrease observed in Au-TiO$_2$-NAA-DBRs produced with $V_o = 80$ and 100 V. The average k value of Au-TiO$_2$-NAA-DBRs produced with $V_o = 60$ V at various τ_D values was found to be 1.18 ± 0.14 h^{-1}.

Table 1 summarizes the geometric characteristics – d_p and d_{int} – of Au-TiO$_2$-NAA-DBRs produced at different V_o values and the percentage decrement in k as a function of the fabrication parameters – V_o and τ_D. The d_p and d_{int} of nanopores at the top surface of Au-TiO$_2$-NAA-DBRs ($\tau_D = 0$ s) increase with increasing V_o (*i.e.* from 70 to 150 nm and from 157 to 272 nm, respectively). Larger d_p and d_{int} enhance the absorption of light by the PC structure, increasing the photogeneration of e$^-$/h$^+$ pairs in the photoactive TiO$_2$ layer and improving the photocatalytic performance of Au-TiO$_2$-NAA-DBRs ($\tau_D = 0$ s). This effect is demonstrated by the k values observed for Au-TiO$_2$-NAA-DBRs produced with $V_o = 60$, 80 and 100 V (Fig. 9c). k decreases slightly with increasing τ_D for Au-TiO$_2$-NAA-DBRs produced with $V_o = 60$ V, with an average reduction of photocatalytic performance of ~1% and 19% when τ_D is varied from 0 to 30 s and from 0 to 60 s, respectively. However, Au-TiO$_2$-NAA-DBRs fabricated with $V_o = 80$ and 100 V show a significantly higher reduction in k with τ_D (*i.e.* ~28% and 60% for τ_D from 0 to 30 s, and ~33% and 61% for τ_D from 0 to 60 s, respectively).

Photocatalytic degradation mechanism

Based on these results, we propose a possible photocatalytic degradation mechanism to describe the photocatalytic degradation of the organic dye by Au-TiO$_2$-NAA-DBRs driven under visible-NIR irradiation (400–1025 nm) with the addition of H$_2$O$_2$. Upon light irradiation, charge carriers (*i.e.* electrons and holes) are produced in the conduction and valence bands, respectively, of the photoactive TiO$_2$ layer deposited onto the inner surface of Au-TiO$_2$-NAA-DBRs. Photogenerated holes induce oxidation of H$_2$O in the aqueous organic solution, which is in contact with the photoactive TiO$_2$ layer. This generates OH$^{\cdot}$ radicals, which can degrade the organic dye molecules to liberate CO$_2$ and H$_2$O. Photogenerated electrons also react with H$_2$O$_2$ to produce OH$^{\cdot}$ radicals and OH$^-$ ions, of which the latter are oxidized into OH$^{\cdot}$ radicals by photogenerated holes in the valence band of the photoactive TiO$_2$ layer. Our results indicate that enhancements in the photodegradation of methylene blue are strongly associated with slow photons in Au-TiO$_2$-NAA-DBRs. This light–matter interaction increases the lifespan of incoming photons with specific energies (*i.e.* wavelengths close to the blue and red edges of the PSB), which spend longer time within the structure of Au-TiO$_2$-NAA-DBRs. This can then be exploited more efficiently by the photoactive TiO$_2$ layer to generate extra e$^-$/h$^+$ pairs that speed up the photocatalytic degradation of MB. The photocatalytic enhancement associated with this effect is found to be maximum when the edges of the characteristic PSB of Au-TiO$_2$-NAA-DBRs are in close proximity to the blue and red sides of the absorption band of MB. Overlapping the PSB with the absorption maximum of MB worsens dramatically the performance of Au-TiO$_2$-NAA-DBRs due to the light screening effect, since in this spectral region only a small portion of the incoming light reaches the photoactive TiO$_2$ layer to generate extra e$^-$/h$^+$ pairs that can be utilized by the composite PC structures to photodegrade MB molecules. Deposition of a thin Au layer on the top surface of TiO$_2$-NAA-DBRs provides an additional feature to the system in the form of a surface plasmon resonance band, which extends the overall light absorption of the non-coated TiO$_2$-NAA-DBR structure. However, SPR-excited photons generated by the Au layer deposited on the top surface of Au-TiO$_2$-NAA-DBRs are not fully utilized by the photocatalytic platform due to the isolated configuration between the Au layer and the photoactive TiO$_2$ layer in the inner surface of the composite PC structure. The majority of the incoming light is absorbed by the nanoporous Au layer before it reaches the photoactive surface of TiO$_2$-NAA-DBRs, and the overall photocatalytic performance of Au-TiO$_2$-NAA-DBRs decreases with the thickness of the Au layer (*i.e.* more light is absorbed by the Au layer). Our analysis also demonstrates that though Ag has a better SPR than Au, Au-TiO$_2$-NAA-DBRs perform better than their Ag-coated counterparts. This is due to the higher chemical stability of Au in aqueous solution. The overall photocatalytic performance of Au-TiO$_2$-NAA-DBRs can be enhanced by engineering the geometric features (*i.e.* d_p, d_{int}, L_{TP} and L_p) of these nanoporous composite semiconductor PC structures. The rational design of Au-TiO$_2$-NAA-DBRs enables an efficient management of photons by "slow photon" and SPR effects, tuning the relative position of the edges of the characteristic PSB and SPR with respect to the absorption band of MB.

Table 1 Effect of the starting anodization voltage (V_o) of Au-TiO$_2$-NAA-DBRs produced by three-step pulse anodization on the pore diameter (d_p), interpore distance (d_{int}) and the decrease in percentage of kinetic constant (k) at different Au deposition times (τ_D), from 0 to 60 s

V_o (V)	d_p (nm)	d_{int} (nm)	k decrement from $\tau_D = 0$ to 30 s (%)	k decrement from $\tau_D = 0$ to 60 s (%)
60	70 ± 1	157 ± 1	1	19
80	106 ± 1	211 ± 2	28	60
100	150 ± 1	272 ± 3	33	61

Table 2 Compilation of representative kinetic constants (k) for the photocatalytic degradation of MB molecules by various benchmark TiO_2-based photocatalyst materials

TiO_2-based photocatalyst	k (h^{-1})	Ref
P25 nanoparticles	0.64	4
Inverse opal	1.32	4
NAA-DBRs	2.45	This study
Ag-P25 nanoparticles	1.56	6
Ag-inverse opal	0.64	8
Ag-NAA-DBRs	1.44	This study

Comparison with benchmark Photocatalyst materials

Table 2 compiles the photocatalytic performances of representative benchmark photocatalytic materials with and without noble metal (*i.e.* Ag) and photonic crystal structure (*i.e.* inverse opal and DBR), where the photodegradation of MB molecules was conducted under visible light irradiation conditions.

The photocatalytic degradation rate of MB by as-produced P25 TiO_2 nanoparticles, TiO_2 inverse opals and TiO_2-NAA-DBRs was found to be 0.64, 1.32 and 2.45 h^{-1}, respectively.[4] It is clear that TiO_2-NAA-DBRs perform more efficiently than these reference materials, with a ~74 and 46% superior performance, respectively. Incorporation of SPR effects in noble metal-coated photocatalysts can enhance their performance due to extended light absorption and minimization of charge carrier recombination rates. The k values for Ag-coated P25 TiO_2 nanoparticles, TiO_2 inverse opals and TiO_2-NAA-DBRs were found to be 1.56, 0.64 and 1.44 h^{-1}, respectively.[6,8] This demonstrates that Ag-P25 TiO_2 nanoparticles perform much better than Ag–TiO_2 inverse opals (~59% superior performance), and slightly better than Ag–TiO_2-NAA-DBRs (~8% superior performance) in the photodegradation of MB. This result can be associated with a better interfacial connection between the noble metal coating and the semiconductor material in Ag-P25 TiO_2. However, Ag–TiO_2-NAA-DBRs outperform Ag–TiO_2 inverse opals by ~56% enhancement. A direct comparison with these studies could not be completely correct due to small differences in experimental conditions (*i.e.* loading of catalysts, spectral distribution and power of light illumination, specific area and volume). However, these results demonstrate that TiO_2-NAA-DBRs are promising photocatalyst platforms that provide new opportunities to develop high-performance photocatalyst materials with broad applicability.

Conclusions

This study provides new insights into the design and engineering of high-performance photocatalyst platforms with rationally designed optical properties to harness light–matter interactions for photocatalysis. The photocatalytic capabilities of NAA-based photonic crystals functionalized with photoactive layers of TiO_2 and noble metal coatings have been systematically assessed, using the degradation rate of a model organic dye as an indicator to identify enhancements associated with different optical phenomena. Noble metal-

TiO_2-NAA-DBRs were produced with various fabrication parameters (*i.e.* anodization period, starting anodization voltage, pore widening time, noble metal deposition time and type of noble metal coating) to enable the fine-tuning of the optical properties (*i.e.* position and features of PSB and SPR bands) of these composite PC structures across the spectral regions. Our results indicate that the best photocatalytic degradation rate for methylene blue (*i.e.* $k = 2.45$ h^{-1}) is achieved by Au-TiO_2-NAA-DBRs produced with $V_o = 40$ V, $T_P = 895$ s, $t_{pw} = 24$ min and $\tau_D = 0$ s. Enhancements in the photocatalytic performance are strongly dependent on the "slow photon" effect, being optimal when the edges of the characteristic PSB of Au-TiO_2-NAA-DBRs are partially overlapped with the absorption band of methylene blue, but away from its maximum to avoid the undesired light screening effect. Photodegradation rate enhancements in noble metal-TiO_2-NAA-DBRs are independent of the "slow photon" effect when the characteristic PSB is completely outside the absorption band of MB. Under such a configuration, enhancements are solely dependent on the total pore length of the noble metal-TiO_2-NAA-DBRs, and the thicker the PC structure the more efficient the photocatalytic performance. This study also reveals that enhancements in the photocatalytic performance of noble metal-TiO_2-NAA-DBRs by SPR in the noble metal layer are not significant due to the isolated behavior of the nanoplasmonic structure, which is localized in the top surface of the composite PC structures. As a result, the majority of light is absorbed in the metallic coating before it reaches the bulk PC structure, worsening the overall photocatalytic performance. The type of noble metal coating (*i.e.* Ag and Au) also plays a critical role in the overall photocatalytic performance of noble metal-TiO_2-NAA-DBRs, where Au coatings are demonstrated to provide superior performance compared to Ag coatings due to the higher chemical stability of Au in aqueous solution. This study also demonstrates that the photocatalytic performance of non-coated TiO_2-NAA-DBRs enhances with increasing pore diameter and interpore distance through enhanced light scattering and absorption.

In summary, a rational and optimal design of noble metal-TiO_2-NAA-DBRs is essential to efficiently utilize and manage "slow photon" and SPR effects for photocatalytic reactions. This study provides a strong foundation for improving the design of NAA-based photoactive photonic crystals, generating new opportunities to spread the applicability of these engineered materials across various photocatalytic applications such as sanitation of water, production of clean hydrogen and carbon dioxide reduction.

Conflicts of interest

There are no conflicts to declare.

Acknowledgements

222

References

1 K. Kim, P. Thiyagarajan, H.-J. Ahn, S.-I. Kim and J.-H. Jang, *Nanoscale*, 2013, **5**, 6254–6260.

2 R. Bopella, S. T. Kochuveedu, H. Kim, M. J. Jeong, F. Marques Mota, J. H. Park and D. H. Kim, *ACS Appl. Mater. Interfaces*, 2017, **9**, 7075–7083.

3 M. Zhou, J. Bao, Y. Xu, J. Zhang, J. Xie, M. Guan, C. Wang, L. Wen, Y. Lei and Y. Xie, *ACS Nano*, 2014, **8**, 7088–7098.

4 X. Zheng, S. Meng, J. Chen, J. Wang, J. Xian, Y. Shao, X. Fu and D. Li, *J. Phys. Chem. C*, 2013, **117**, 21263–21273.

5 Y. Lu, H. Yu, S. Chen, X. Quan and H. Zhao, *Environ. Sci. Technol.*, 2012, **46**, 1724–1730.

6 S. Ko, C. K. Banerjee and J. Sankar, *Composites, Part B*, 2011, **42**, 579–583.

7 Z. Cai, Z. Xiong, X. Lu and J. Teng, *J. Mater. Chem. A*, 2014, **2**, 545–553.

8 Z. Chen, L. Fang, W. Dong, F. Zheng, M. Shen and J. Wang, *J. Mater. Chem. A*, 2014, **2**, 824–832.

9 S. Meng, D. Li, L. Fu and X. Fu, *J. Mater. Chem. A*, 2015, **3**, 23501–23511.

10 S. Y. Lim, C. S. Law, M. Markovic, L. F. Marsal, N. H. Voelcker, A. D. Abell and A. Santos, *ACS Appl. Energy Mater.*, 2019, **2**, 1169–1184.

11 S. Y. Lim, C. S. Law, M. Markovic, J. K. Kirby, A. D. Abell and A. Santos, *ACS Appl. Mater. Interfaces*, 2018, **10**, 24124–24136.

12 M. Curti, C. B. Mendive, M. A. Grela and D. W. Bahnemann, *Mater. Res. Bull.*, 2017, **9**, 155–165.

13 S. Zhao, Z. Qu, N. Yan, Z. Li, W. Zhu, J. Pan, J. Xu and M. Li, *RSC Adv.*, 2015, **5**, 30841–30850.

14 H. Hirakawa, M. Hashimoto, Y. Shiraishi and T. Hirai, *J. Am. Chem. Soc.*, 2017, **139**, 10929–10936.

15 J. Yang, Y. Guo, R. Jiang, F. Qin, H. Zhang, W. Lu, J. Wang and J. C. Yu, *J. Am. Chem. Soc.*, 2018, **140**, 8497–8508.

16 W. Hou, W. H. Hung, P. Pavaskar, A. Goeppert, M. Aykol and S. B. Cronin, *ACS Catal.*, 2011, **1**, 929–936.

17 J. Jiao, Y. Wei, K. Chi, Z. Zhao, A. Duan, J. Liu, G. Jiang, Y. Wang, X. Wang, C. Han and P. Zheng, *Energy Technol.*, 2017, **5**, 877–883.

18 V. Štengl, T. M. Grygar, F. Opluštil and T. Němec, *J. Hazard. Mater.*, 2012, **227–228**, 62–67.

19 A. Sengele, D. Robert, N. Keller, V. Keller, A. Herissan and C. Colbeau-Justin, *J. Catal.*, 2016, **334**, 129–141.

20 A. Fujishima and K. Honda, *Nature*, 1972, **238**, 37–38.

21 J. H. Carey, J. Lawrence and H. M. Tosine, *Bull. Environ. Contam. Toxicol.*, 1976, **16**, 697–701.

22 M. Anpo, *Catal. Surv. Jpn.*, 1997, **1**, 169–179.

23 X. Chen and S. S. Mao, *Chem. Rev.*, 2007, **107**, 2891–2959.

24 R. Asahi, T. Morikawa, T. Ohwaki, K. Aoki and Y. Taga, *Science*, 2001, **293**, 269–271.

25 W. Choi, A. Termin and M. R. Hoffmann, *J. Phys. Chem.*, 1994, **98**, 13669–13679.

26 Y. Liu, L. Yu, Y. Hu, C. Guo, F. Zhang and X. W. Lou, *Nanoscale*, 2012, **4**, 183–187.

27 M. Zalfani, B. van der Schueren, Z.-Y. Hu, J. C. Rooke, R. Bourguiga, M. Wu, Y. Li, G. V. Tendeloo and B.-L. Su, *J. Mater. Chem. A*, 2015, **3**, 21244–21256.

28 H. Fu, T. Xu, S. Zhu and Y. Zhu, *Environ. Sci. Technol.*, 2008, **42**, 8064–8069.

29 D. Jian, P.-X. Gao, W. Cai, B. S. Allimi, S. P. Alpay, Y. Ding, Z. L. Wang and C. Brooks, *J. Mater. Chem.*, 2009, **19**, 970–975.

30 J. G. Yu, Y. R. Su and B. Cheng, *Adv. Funct. Mater.*, 2007, **17**, 1984–1990.

31 R. Bleta, P. Alphonse and L. Lorenzato, *J. Phys. Chem. C*, 2010, **114**, 2039–2048.

32 T. Hirakawa and P. V. Kamat, *J. Am. Chem. Soc.*, 2005, **127**, 3928–3934.

33 X. Zhou, G. Liu, J. Yu and W. Fan, *J. Mater. Chem.*, 2012, **22**, 21337–21354.

34 S. K. Ghosh and T. Pal, *Chem. Rev.*, 2007, **107**, 4797–4862.

35 J. E. G. J. Wijnhoven and W. L. Vos, *Science*, 1998, **281**, 802–804.

36 Z. Zhang, L. Zhang, M. N. Hedhili, H. Zhang and P. Wang, *Nano Lett.*, 2013, **13**, 14–20.

37 C.-T. Dinh, H. Yen, F. Kleitz and T.-O. Do, *Angew. Chem., Int. Ed.*, 2014, **53**, 6618–6623.

38 Y. Wang, D.-B. Xiong, W. Zhang, H. Su, Q. Liu, J. Gu, S. Zhu and D. Zhang, *Catal. Today*, 2016, **274**, 15–21.

39 E. Yablonovitch, *Phys. Rev. Lett.*, 1987, **58**, 2059.

40 J. Liu, H. Zhao, M. Wu, B. Van der Schueren, Y. Li, O. Deparis, J. Ye, G. A. Ozin, T. Hasan and B.-L. Su, *Adv. Mater.*, 2017, **29**, 1605349.

41 M. Curti, J. Schneider, D. W. Bahnemann and C. B. Mendive, *J. Phys. Chem. Lett.*, 2015, **6**, 3903–3910.

42 A. Steins, B. E. Wilson and S. G. Rudisill, *Chem. Soc. Rev.*, 2013, **42**, 2763–2803.

43 D. P. Gaillot and C. J. Summers, in *Atomic Layer Deposition of Nanostructured Materials*, ed. N. Pinna and M. Knez, Wiley-VCH, Weinheim, 1st edn, 2012, ch. 15, pp. 345–371.

44 V. Likodimos, *Appl. Catal., A*, 2018, **230**, 269–303.

45 K. Lee, A. Mazare and P. Schmuki, *Chem. Rev.*, 2014, **114**, 9385–9454.

46 J. W. Galusha, C.-K. Tsung, G. D. Stucky and M. H. Bartl, *Chem. Mater.*, 2008, **20**, 4925–4930.

47 C. S. Law, S. Y. Lim and A. Santos, *Sci. Rep.*, 2018, **8**, 4642.

48 A. Santos, T. Peirera, C. S. Law and D. Losic, *Nanoscale*, 2016, **8**, 14846–14857.

49 Sukarno, C. S. Law and A. Santos, *Nanoscale*, 2017, **9**, 7541–7550.

50 C. S. Law, G. M. Sylvia, M. Nemati, J. Yu, D. Losic, A. D. Abell and A. Santos, *ACS Appl. Mater. Interfaces*, 2017, **9**, 8929–8940.

51 C. S. Law, S. Y. Lim, A. D. Abell and A. Santos, *Anal. Chem.*, 2018, **90**, 10039–10048.

This journal is © The Royal Society of Chemistry 2019

Catal. Sci. Technol., 2019, **9**, 3158–3176 | **3175**

223

52 A. Santos, J. H. Yoo, C. V. Rohatgi, T. Kumeria, Y. Wang and D. Losic, *Nanoscale*, 2016, **8**, 1360–1373.

53 A. Santos, C. S. Law, D. W. C. Lei, T. Pereira and D. Losic, *Nanoscale*, 2016, **8**, 18360–18375.

54 A. Santos, C. S. Law, T. Pereira and D. Losic, *Nanoscale*, 2016, **8**, 8091–8100.

55 S. Y. Lim, C. S. Law, L. F. Marsal and A. Santos, *Sci. Rep.*, 2018, **8**, 9455.

56 Y. Wang, Y. Chen, T. Kumeria, F. Ding, A. Evdokiou, D. Losic and A. Santos, *ACS Appl. Mater. Interfaces*, 2015, **7**, 9879–9888.

57 C. S. Law, S. Y. Lim, A. D. Abell, L. F. Marsal and A. Santos, *Nanoscale*, 2018, **10**, 14139–14152.

58 C. S. Law, S. Y. Lim, R. M. Macalincag, A. D. Abell and A. Santos, *ACS Appl. Nano Mater.*, 2018, **1**, 4418–4434.

59 M. M. Rahman, L. F. Marsal, J. Pallarès and J. Ferré-Borrull, *ACS Appl. Mater. Interfaces*, 2013, **5**, 13375–13381.

60 M. D. Abràmoff, P. J. Magalhães and S. J. Ram, *BioPhotonics International*, 2004, **11**, 36–42.

61 A. Santos, *J. Mater. Chem. C*, 2017, **5**, 5581–5599.

62 S. Nishimura, N. Abrams, B. A. Lewis, L. I. Halaoui, T. E. Malluok, K. D. Benkstein, J. van de Lagemaat and A. J. Frank, *J. Am. Chem. Soc.*, 2003, **125**, 6306–6310.

63 Y. Li, T. Kunitake and S. Fujikawa, *J. Phys. Chem. B*, 2006, **110**, 13000–13004.

64 O. Deparis, S. R. Mouchet and B.-L. Su, *Phys. Chem. Chem. Phys.*, 2015, **17**, 30525–30532.

65 H. Zhao, Z. Hui, J. Liu, Y. Li, M. Wu, G. V. Tendeloo and B.-L. Su, *Nano Energy*, 2018, **47**, 266–274.

66 A. Santos, V. S. Balderrama, M. Alba, P. Formentín, J. Ferré-Borrull, J. Pallarès and L. F. Marsal, *Adv. Mater.*, 2012, **24**, 1050–1054.

67 A. Brzózka, A. Brudzisz, K. Hnida and G. D. Sulka, in *Electrochemically Engineered Nanoporous Materials: Methods, Properties and Applications*, ed. D. Losic and A. Santos, Springer International Publishing, Cham, 2015, ch. 8, vol. 220, pp. 219–288.

224

Electronic Supplementary Information

Integrating Surface Plasmon Resonance and Slow Photon Effects in Nanoporous Anodic Alumina Photonic Crystals for Photocatalysis

Siew Yee Lim[a,b,c], Cheryl Suwen Law[a,b,c], Lina Liu[a,d], Marijana Markovic[a,e], Andrew D. Abell[*b,c,f] and Abel Santos[*a,b,c]

[a]School of Chemical Engineering, The University of Adelaide, Adelaide, SA 5005, Australia
[b]Institute for Photonics and Advanced Sensing (IPAS), The University of Adelaide, 5005 Adelaide, Australia
[c]ARC Centre of Excellence for Nanoscale BioPhotonics (CNBP), The University of Adelaide, 5005 Adelaide, Australia
[d]School of Chemistry and Chemical Engineering, Ningxia University, 750021 Yinchuan, P.R. China
[e]Center of Chemistry, Institute of Chemistry, Technology and Metallurgy, University of Belgrade, 11000 Belgrade, Serbia
[f]Department of Chemistry, The University of Adelaide, Engineering North Building, 5005 Adelaide, Australia.

*E-Mails: andrew.abell@adelaide.edu.au ; abel.santos@adelaide.edu.au
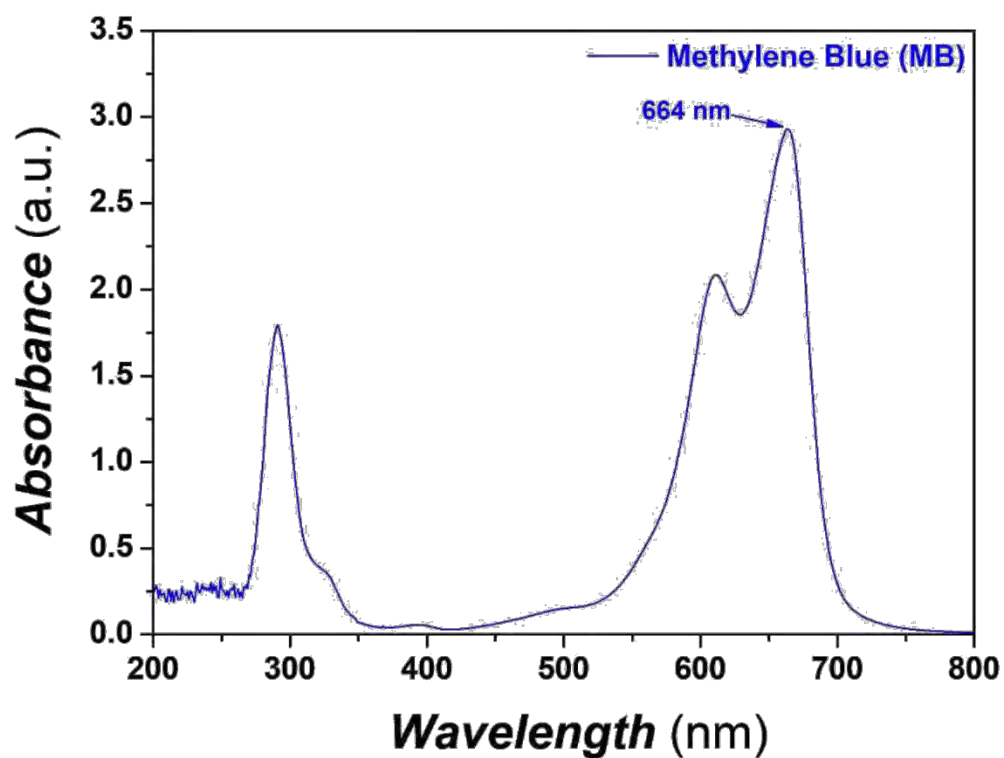
Figure S1. Absorbance spectrum of methylene blue (MB). Absorbance band maximum located at $\lambda_{abs\text{-}MB}$ = 664 nm, with an absolute absorbance intensity of ~2.9 a.u.
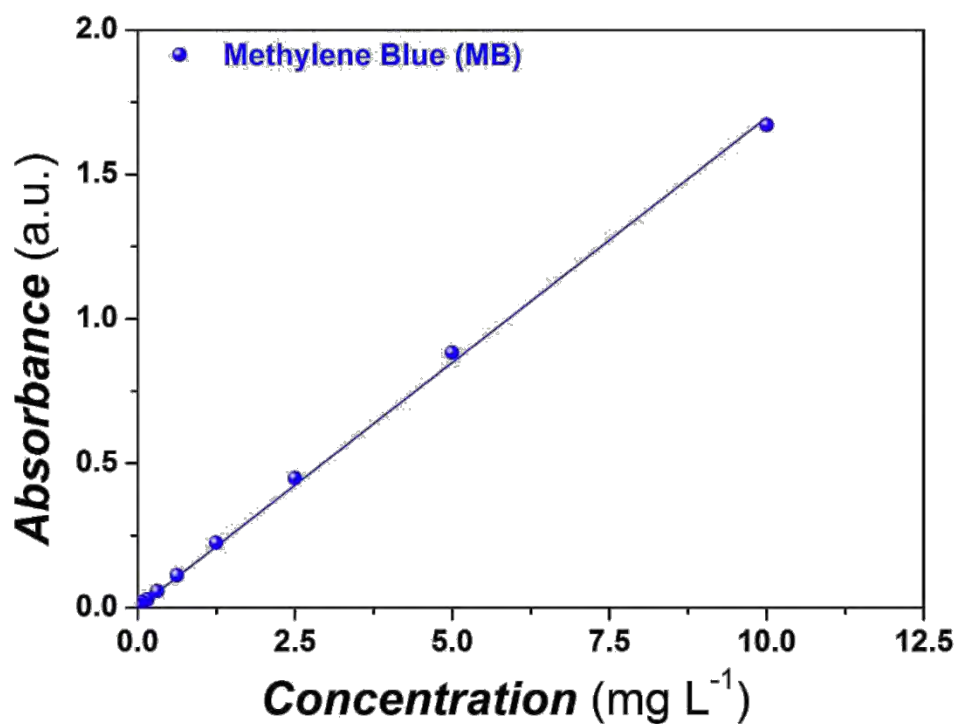
Figure S2. Linear correlation between optical absorbance and concentration of methylene blue (MB) (note: concentration range from 0.00244 to 10 mg L^{-1}). The fitting line for MB was Abs_{MB} (a.u.) = 0.1697 $[MB]$ (mg L^{-1}) with R^2 = 0.99923.
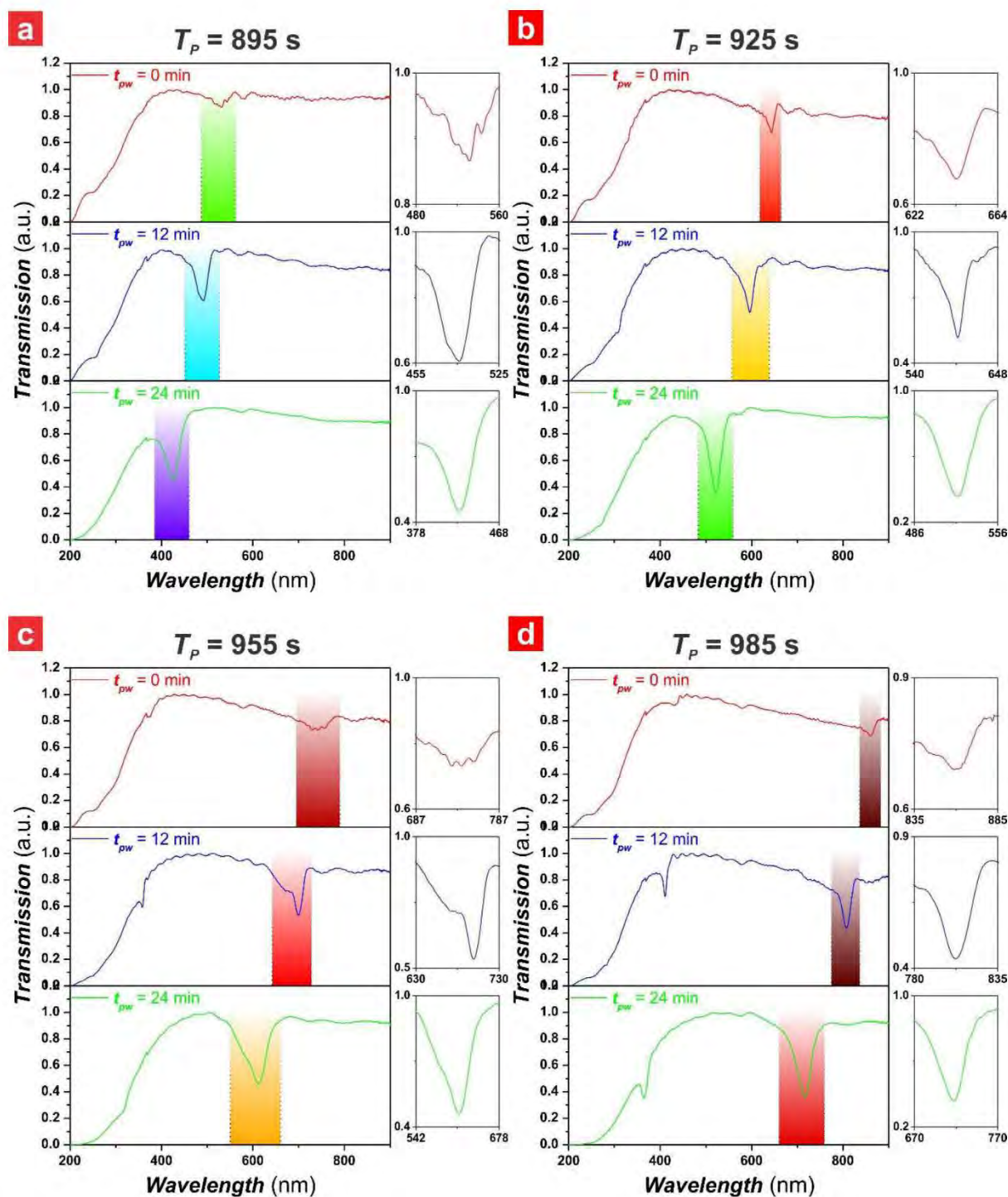
Figure S3. Transmission spectra of NAA-DBRs produced by two-step pulse anodization with anodization period (T_P) of a) 895 s, b) 925 s, c) 955 s and d) 985 s, where the medium filling the nanopores is air (note: shaded region corresponds to the magnified view of the photonic stopband displayed on the right).
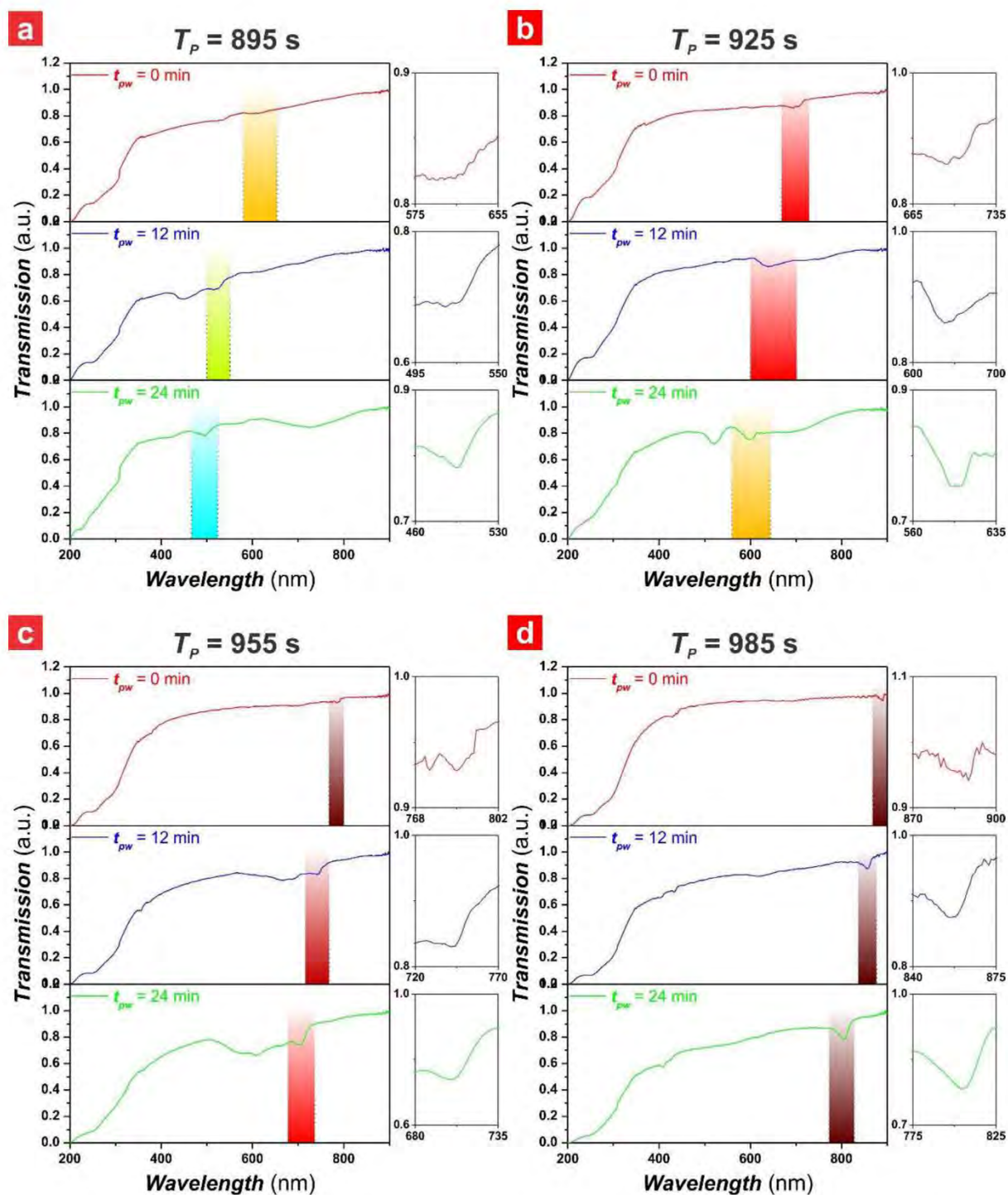
Figure S4. Transmission spectra of NAA-DBRs produced by two-step pulse anodization with anodization period (T_P) of a) 895 s, b) 925 s, c) 955 s and d) 985 s, where the medium filling the nanopores is water (note: shaded region corresponds to the magnified view of the photonic stopband displayed on the right).
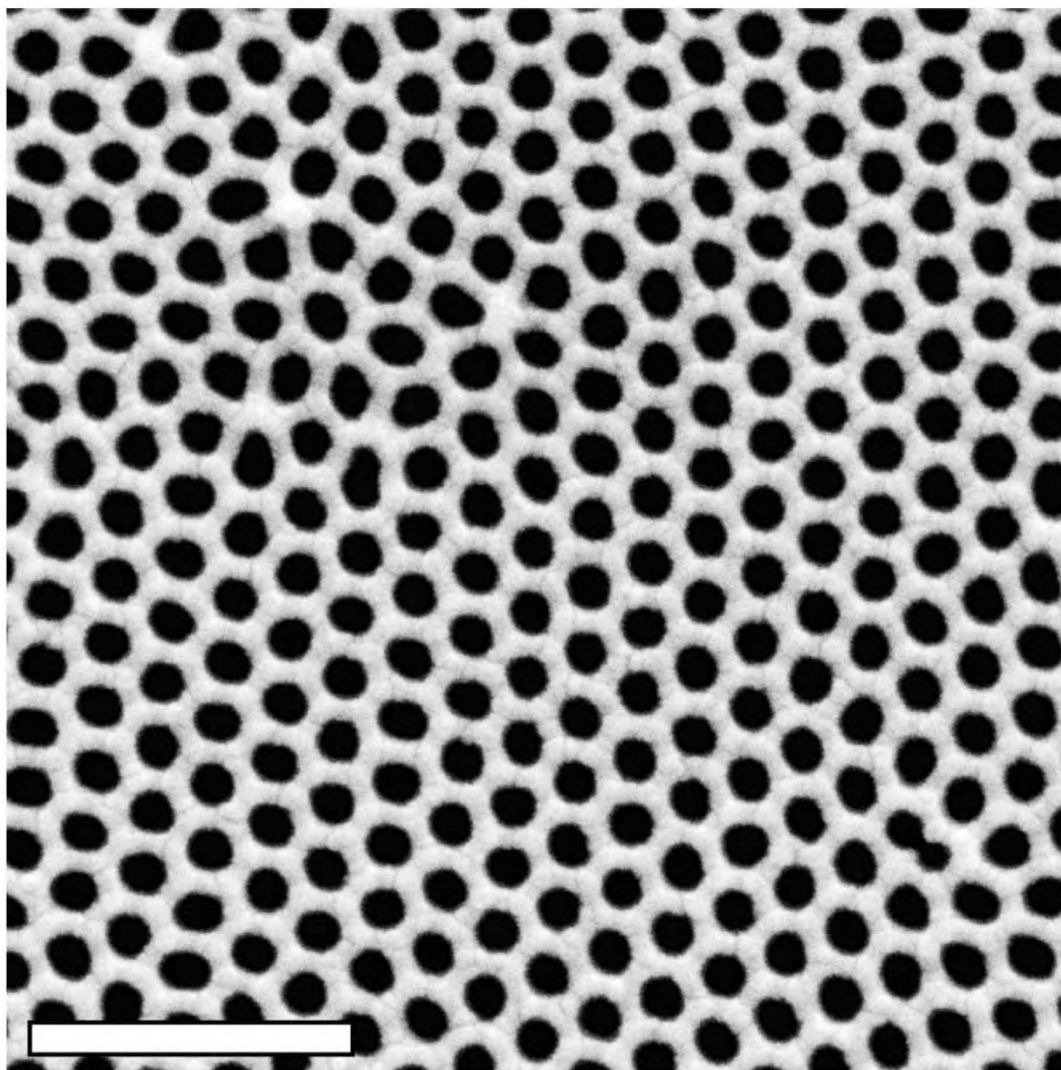
Figure S5. FEG-SEM image of a representative NAA-DBR after 30 s of Au coating (scale bar = 500 nm) (note: NAA-DBR produced with T_P = 985 s and t_{pw} = 24 min).
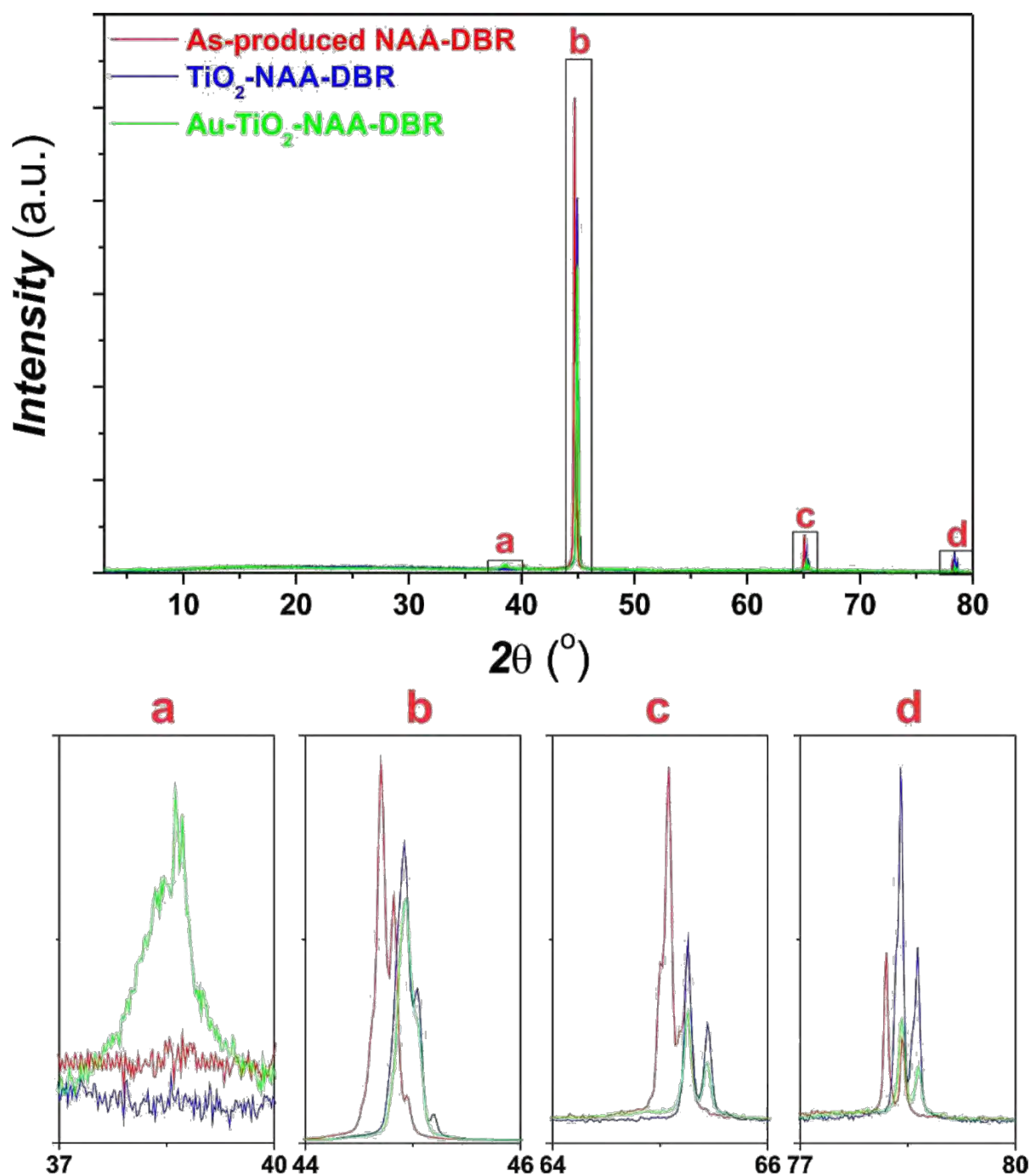
Figure S6. X-ray diffraction (XRD) spectra of a representative NAA-DBR before and after surface functionalization of TiO_2 and 30 s of Au coating (note: NAA-DBR produced with T_P = 985 s and t_{pw} = 24 min).
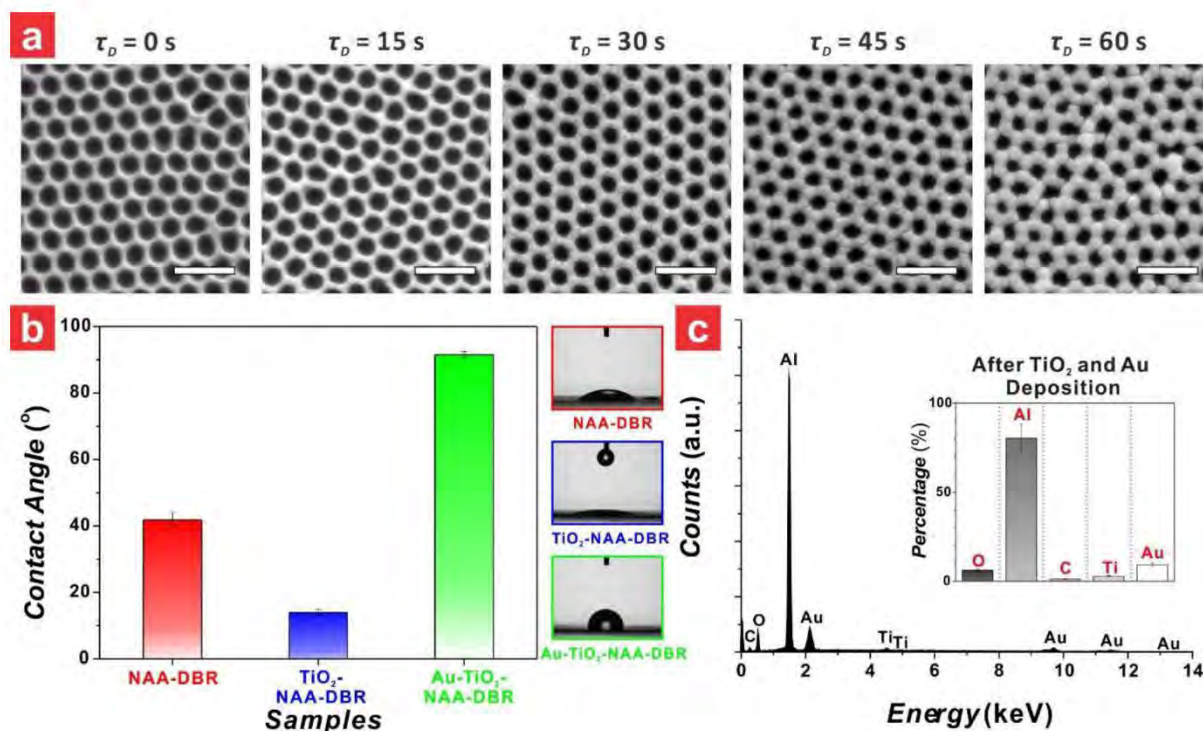
Figure S7. Structural, contact angle and chemical characterization of a representative NAA-DBR before and after surface functionalization with TiO_2 and coating with Au (note: NAA-DBR produced with T_P = 985 s and t_{pw} = 24 min). a) Top view FEG-SEM images of the NAA-DBR as a function of Au deposition time (τ_D). b) Influence of deposition of TiO_2 followed by Au coating on the contact angle (left) and digital image (right) of the as-produced NAA-DBR. c) Energy dispersive X-ray (EDX) spectrum of the representative NAA-DBR deposited with TiO_2 and 30 s Au with inset showing the percentage of main elements present in the photonic crystal structure (right).

Figure S7 - Discussion

Figure S7 provides a set of characterizations of a representative NAA-DBR produced with T_P = 985 s and t_{pw} = 24 min that demonstrate the successful deposition of TiO_2 and Au onto the inner and top surface of the nanoporous PC structure:

- <u>FEG-SEM:</u> Figure S7a compiles a set of top view FEG-SEM images of the TiO_2-modified NAA-DBR at different deposition time (τ_D), from τ_D = 0 to 60 s (i.e. 0, 15, 30, 45 and 60 s). Image analysis of these images reveals that the pore diameter (d_p) of the TiO_2-NAA-DBR is reduced with increasing Au deposition time, from d_p = 81 ± 6 nm at τ_D = 0 s to d_p = 50 ± 6 nm at τ_D = 60 s.
- <u>Contact Angle:</u> The successful functionalization of TiO_2 and deposition of Au were further validated and analyzed by contact angle measurements (Figure S7b). The contact angle for the NAA-DBR platform at different fabrication stages (i.e. as-produced, TiO_2 coating, and Au deposition) was measured by a tensiometer (Attension Theta optical tensiometer), using the sensile drop method. A water droplet was formed on the end of a syringe, which descended until the water droplet touched the surface of the NAA-DBR. After contact, the syringe was withdrawn from the surface of the NAA-DBR. Image analysis (i.e. Figure S7b – right) was used to establish the contact angle on the surface of the NAA-DBR platform before and after deposition of TiO_2 and Au (i.e. Figure S7b – left). After functionalizing the surface of the NAA-DBRs with TiO_2, the contact angle was found to decrease from 41 ± 2 to 14 ± 1°. This indicates that TiO_2-NAA-DBRs are more hydrophilic than as-produced NAA-DBRs, and the change observed in the contact angle further demonstrates the successful functionalization of the NAA-DBR by TiO_2. A significant increase in the contact angle (i.e. 78 ± 1°) of TiO_2-NAA-DBRs was observed after coating with the Au coating, indicating that Au-TiO_2-NAA-DBRs are significantly more hydrophobic than their TiO_2-NAA-DBR counterparts. This analysis implies that Au layers were successfully deposited onto the top surface of TiO_2-NAA-DBRs.
- <u>Energy dispersive X-Ray Analysis (EDX):</u> Figure S7c shows EDX spectra of a representative Au-TiO_2-NAA-DBR. The percentage of elements such as Al, Au, O, Ti and C were 80.4 ± 8.0, 9.3 ± 0.9, 6.3 ± 0.6, 2.9 ± 0.3 and 1.2 ± 0.1 %, respectively. These atoms correspond to the chemical composition of the composite photonic structure, where Al, Ti and O atoms correspond to alumina (Al_2O_3) and titania (TiO_2), C atoms correspond to contaminants incorporated into the alumina structure from the acid electrolyte (i.e. oxalic acid) during anodization, and Au atoms correspond to the Au layer deposited onto the top surface of the composite PC structure.
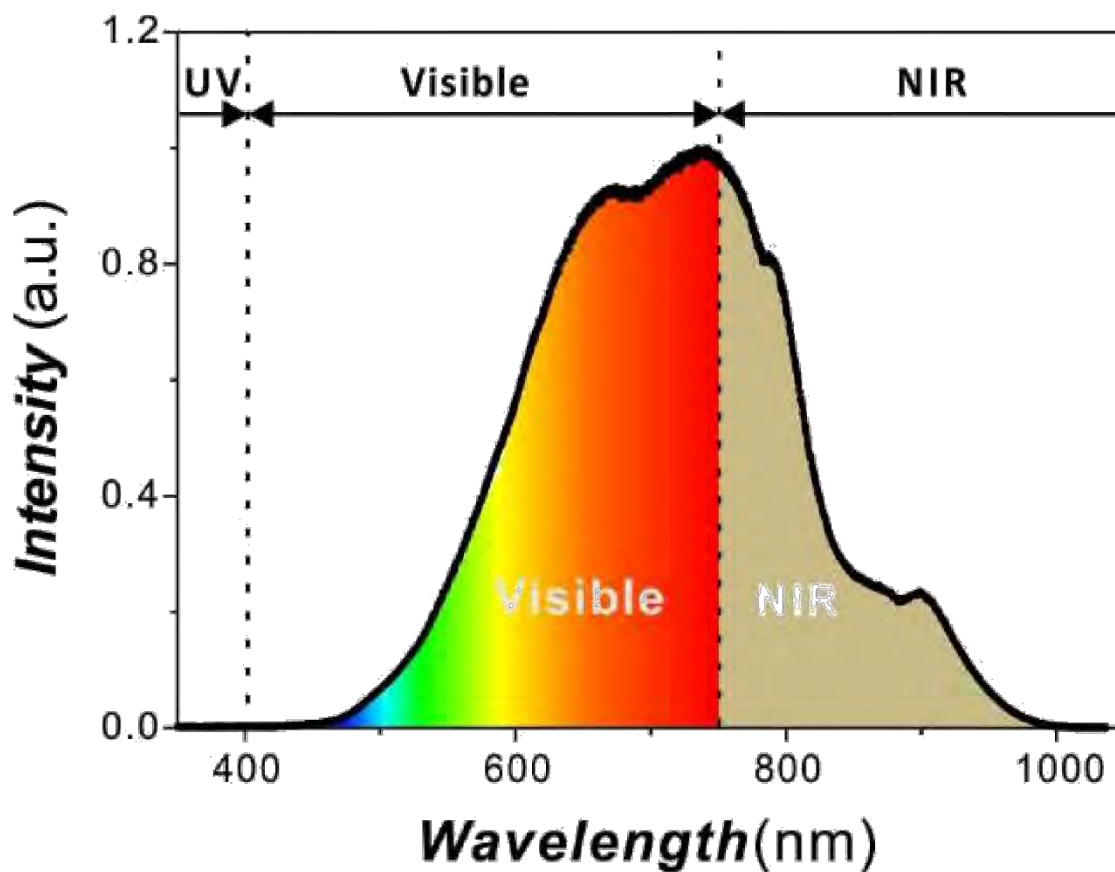
Figure S8. Spectrum of a simulated solar light irradiation source (i.e. 0.12% UV, 64.60% visible and 35.28% NIR) used for the photocatalytic degradation of methylene blue (note: the spectrum was measured using an optical fiber spectrophotometer – USB 4000, Ocean Optics, USA).
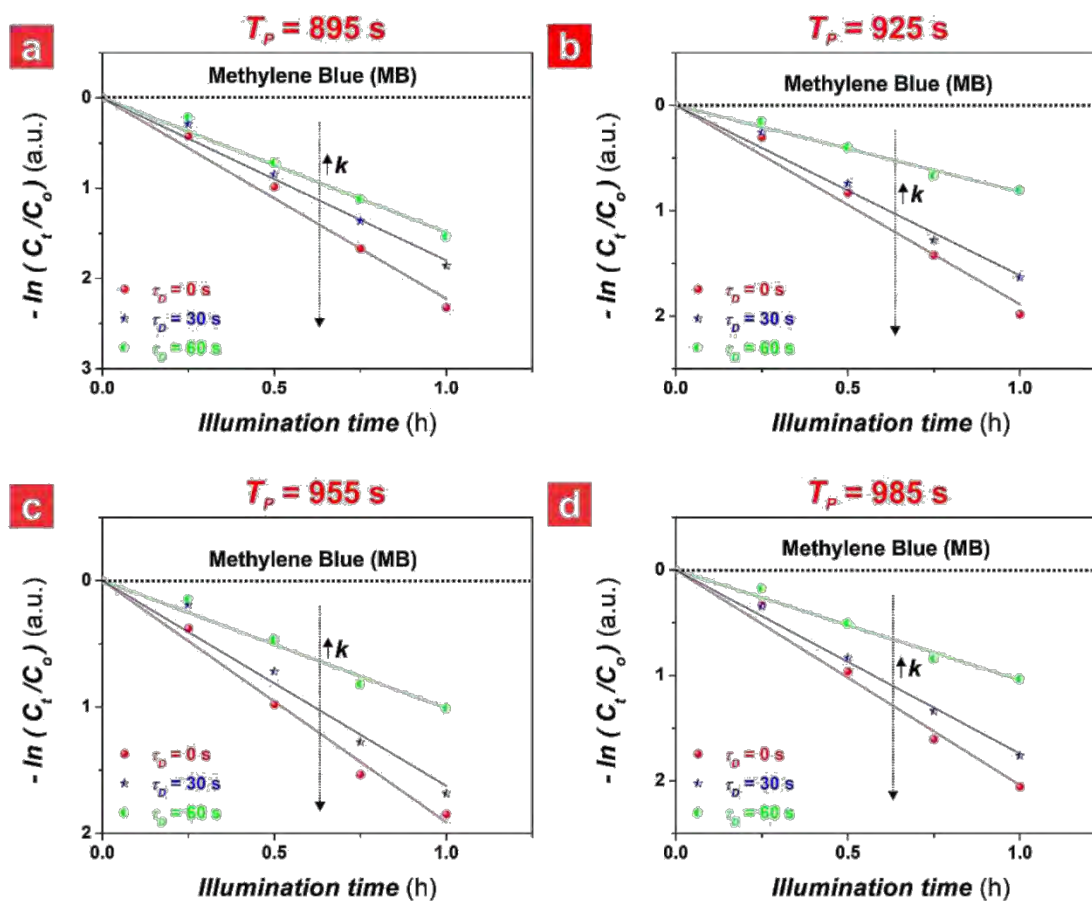
Figure S9. Photocatalytic degradation kinetics of methylene blue (MB) by Au-TiO$_2$-NAA-DBRs fabricated by two-step pulse anodization with t_{pw} = 12 min, Au deposition time from τ_D = 0, 30 and 60 s and anodization period T_P = a) 895 s, b) 925 s, c) 955 s and d) 985 s (note: black dotted lines correspond to the photodegradation of MB in control NAA-DBRs without the photoactive TiO$_2$ layer).
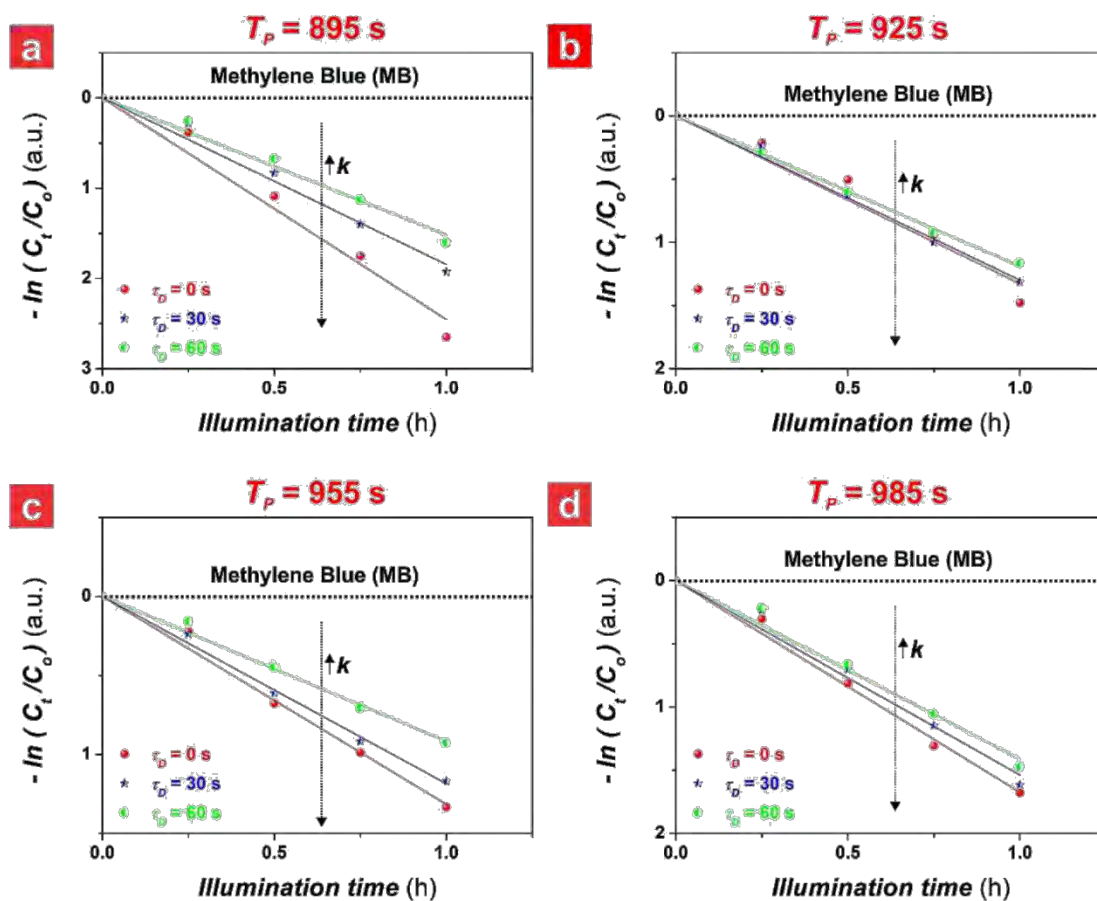
Figure S10. Photocatalytic degradation kinetics of methylene blue (MB) by Au-TiO$_2$-NAA-DBRs fabricated by two-step pulse anodization with t_{pw} = 24 min, Au deposition time from τ_D = 0, 30 and 60 s and anodization period T_P = a) 895 s, b) 925 s, c) 955 s and d) 985 s (note: black dotted lines correspond to the photodegradation of MB in control NAA-DBRs without the photoactive TiO$_2$ layer).
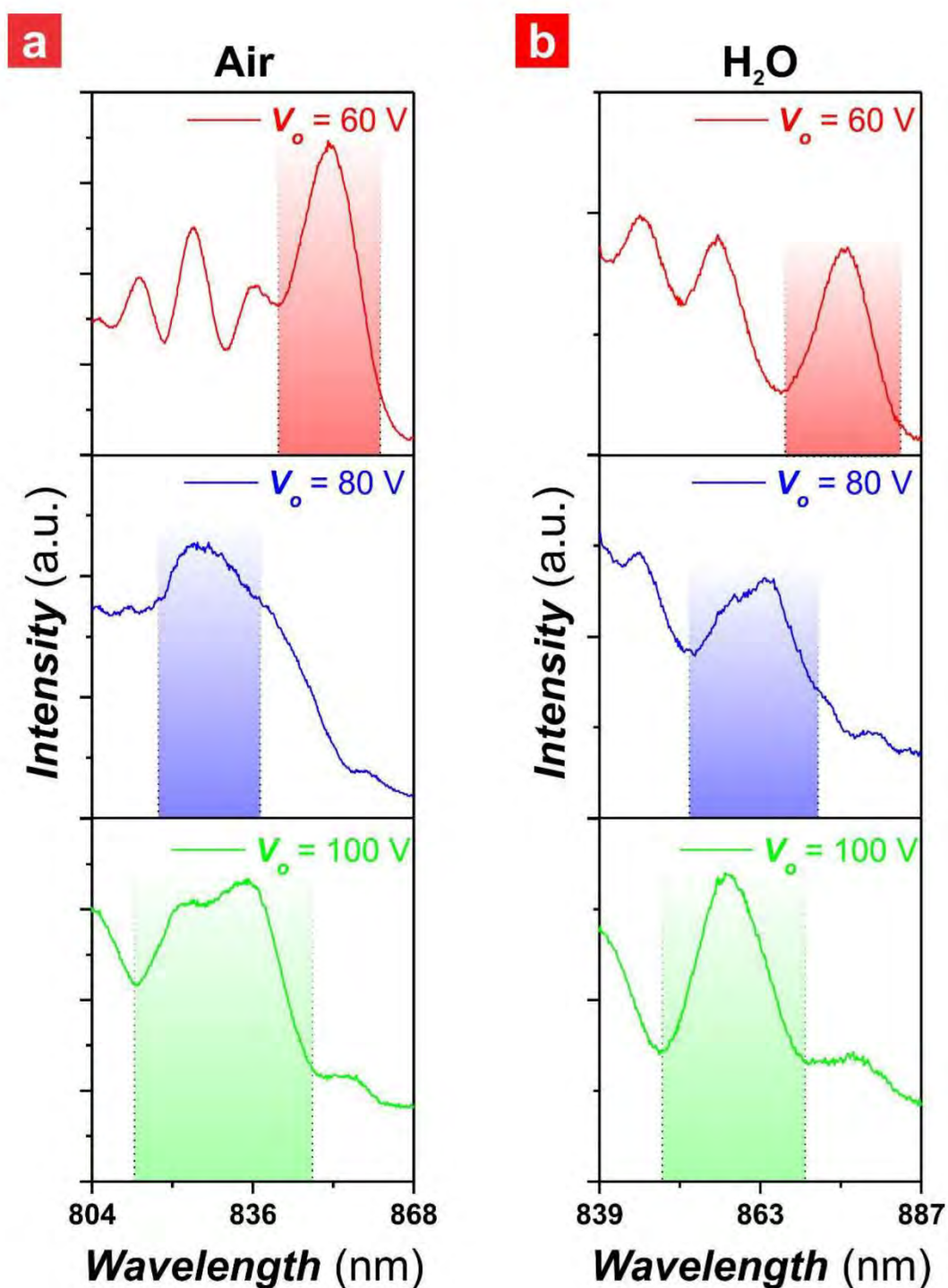
Figure S11. Reflection spectra of NAA-DBRs fabricated by three-step pulse anodization with different starting anodization voltage V_o = 60, 80 and 100 V, where the media filling the photonic structures are a) air and b) water (H_2O), respectively (note: shaded region denotes the position of the photonic stop band).

Table S1. Values of the kinetic constant (k) for the photodegradation of MB molecules by Au-TiO$_2$-NAA-DBRs produced by two-step pulse anodization with various pore widening time (t_{pw}), Au deposition time (τ_D) and anodization period (T_P).

t_{pw} (min)	τ_D (s)	T_P (s)	k (h^{-1})
0	0	895	1.83 ± 0.06
		925	1.26 ± 0.04
		955	2.22 ± 0.08
		985	1.57 ± 0.05
	30	895	1.46 ± 0.04
		925	1.13 ± 0.04
		955	1.98 ± 0.07
		985	1.32 ± 0.06
	60	895	1.02 ± 0.06
		925	0.76 ± 0.02
		955	1.35 ± 0.05
		985	0.93 ± 0.04
12	0	895	2.23 ± 0.08
		925	1.89 ± 0.08
		955	1.91 ± 0.06
		985	2.04 ± 0.07
	30	895	1.80 ± 0.07
		925	1.61 ± 0.06
		955	1.62 ± 0.09
		985	1.74 ± 0.04
	60	895	1.49 ± 0.06
		925	0.82 ± 0.03
		955	1.01 ± 0.05
		985	1.04 ± 0.04
24	0	895	2.45 ± 0.13
		925	1.33 ± 0.09
		955	1.32 ± 0.04
		985	1.67 ± 0.05
	30	895	1.85 ± 0.08
		925	1.30 ± 0.04
		955	1.19 ± 0.03
		985	1.54 ± 0.07
	60	895	1.52 ± 0.06
		925	1.19 ± 0.02
		955	0.92 ± 0.03
		985	1.41 ± 0.06

Table S2. Values of the kinetic constant (k) for the photodegradation of MB molecules by TiO_2-NAA-DBRs produced with T_P = 985 s and t_{pw} = 24 min, and different top coatings (i.e. Au and Ag) and deposition time (τ_D).

Top Coating	τ_D (s)	k (h^{-1})
Au	0	1.67 ± 0.05
	30	1.54 ± 0.07
	60	1.41 ± 0.06
Ag	0	1.67 ± 0.05
	30	1.44 ± 0.06
	60	1.35 ± 0.05

Table S3. Values of the kinetic constant (k) for the photodegradation of MB molecules by Au-TiO_2-NAA-DBRs produced by three-step pulse anodization with different starting anodization voltage (V_o) and Au deposition time (τ_D).

V_o (V)	τ_D (s)	k (h^{-1})
60	0	1.26 ± 0.03
	30	1.25 ± 0.07
	60	1.02 ± 0.03
80	0	1.52 ± 0.07
	30	1.10 ± 0.03
	60	0.61 ± 0.03
100	0	1.51 ± 0.05
	30	1.02 ± 0.06
	60	0.59 ± 0.06

Chapter 8

TAILOR-ENGINEERED PLASMONIC SINGLE-LATTICES: HARNESSING LOCALIZED SURFACE PLASMON RESONANCES FOR VISIBLE-NIR-ENHANCED PHOTOCATALYSIS

8. Tailor-Engineered Plasmonic Single-Lattices: Harnessing Localized Surface Plasmon Resonances for Visible-NIR-Enhanced Photocatalysis

8.1 Introduction, Significance and Commentary

Chapter 7 has introduced the concept of SPR effect from noble metal layers deposited onto the top surface of Au-TiO$_2$-NAA-DBRs. However, further understanding of plasmonic effects of individual components in noble metal structures is essential for optimal integration with NAA-PC structures for enhanced photocatalytic efficiencies. This chapter aims to explore a better understanding of localised surface plasmon resonance (LSPR) effects for visible-NIR light-driven photocatalysis by developing a photocatalytic platform material composed of 2D gold nanodot plasmonic single-lattices (Au-nD-PSLs). Au-nD-PSLs were produced by a straightforward, industrially scalable template-assisted approach, using nanopatterned aluminium substrates fabricated from anodisation as templates. This study reveals that Au-nD-PSLs provide outstanding photocatalytic performances due to strongly localised electromagnetic fields around these metallic structures, as demonstrated by finite-difference time-domain (FDTD) simulations and experimental observations. The photocatalytic performance of Au-nD-PSLs can also be further enhanced by coupling LSPR effects with the electronic bandgap of semiconductor substrates. Au-nD-PSLs also show remarkable photocatalytic performances in photodegradation of methylene blue when compared to conventional nanoparticle-based plasmonic photocatalysts (i.e. ~82 to 91% superior performance), providing new opportunities to rationally design efficient photocatalyst platform materials that harvest visible-NIR spectrum for a broad range of plasmonic, photonic and photocatalytic applications.

8.2 Publication

This chapter is presented as published journal article by **S.Y. Lim**, C.S. Law, F. Bertó-Roselló, L. Liu, M. Markovic, J. Ferré-Borrull, A.D. Abell, N.H. Voelcker, L.F. Marsal, and A. Santos, *Tailor-engineered plasmonic single-lattices: harnessing localized surface plasmon resonances for visible–NIR light-enhanced photocatalysis*. Catalysis Science & Technology, 2020. **10**(10): p. 3195–3211.

Statement of Authorship

Title of Paper	Tailor-Engineered Plasmonic Single-Lattices: Harnessing Localized Surface Plasmon Resonances for Visible–NIR Light-Enhanced Photocatalysis
Publication Status	☑ Published ☐ Accepted for Publication ☐ Submitted for Publication ☐ Unpublished and Unsubmitted work written in manuscript style
Publication Details	S.Y. Lim, C.S. Law, F. Bertó-Roselló, L. Liu, M. Markovic, J. Ferré-Borrull, A.D. Abell, N.H. Voelcker, L.F. Marsal, and A. Santos, *Tailor-engineered plasmonic single-lattices: harnessing localized surface plasmon resonances for visible–NIR light-enhanced photocatalysis.* Catalysis Science & Technology, 2020. **10**(10): p. 3195–3211.

Principal Author

Name of Principal Author (Candidate)	Siew Yee Lim		
Contribution to the Paper	Performed the photocatalytic experiment, processed and analysed the data, and wrote the manuscript except for fabrication and simulation part under the supervisions of Abel Santos and Andrew D. Abell. Equal contribution with Cheryl Suwen Law and Francesc Bertó-Roselló.		
Overall percentage (%)	30		
Certification:	This paper reports on original research I conducted during the period of my Higher Degree by Research candidature and is not subject to any obligations or contractual agreements with a third party that would constrain its inclusion in this thesis. I am the primary author of this paper.		
Signature		Date	10/06/2020

Co-Author Contributions

By signing the Statement of Authorship, each author certifies that:

    i.   the candidate's stated contribution to the publication is accurate (as detailed above);

    ii.   permission is granted for the candidate in include the publication in the thesis; and

    iii.   the sum of all co-author contributions is equal to 100% less the candidate's stated contribution.

Name of Co-Author	Cheryl Suwen Law		
Contribution to the Paper	Performed the fabrication part of the experiment, processed and analysed the data, and wrote the manuscript. Equal contribution with Siew Yee Lim and give consent to her to present this paper for examination towards the Doctorate of Philosophy.		
Signature		Date	15/06/2020

Name of Co-Author	Francesc Bertó-Roselló		
Contribution to the Paper	Performed the simulation part of the experiment, processed and analysed the data, and wrote the manuscript. Equal contribution with Siew Yee Lim and give consent to her to present this paper for examination towards the Doctorate of Philosophy.		
Signature		Date	11 June 2020

Name of Co-Author	Lina Liu		
Contribution to the Paper	Aided in the evaluation of final version of manuscript. Give consent to Siew Yee Lim to present this paper for examination towards the Doctorate of Philosophy.		
Signature		Date	10/06/2020

Name of Co-Author	Marijana Markovic		
Contribution to the Paper	Aided in the evaluation of final version of manuscript. Give consent to Siew Yee Lim to present this paper for examination towards the Doctorate of Philosophy.		
Signature		Date	11/06/20

Name of Co-Author	Josep Ferré-Borrull		
Contribution to the Paper	Aided in the evaluation of final version of manuscript. Give consent to Siew Yee Lim to present this paper for examination towards the Doctorate of Philosophy.		
Signature		Date	June 10th, 2020

Name of Co-Author	Andrew D. Abell		
Contribution to the Paper	Acted as a co-supervisor for the candidate, and aided in revising and evaluating the manuscript for submission. Give consent to Siew Yee Lim to present this paper for examination towards the Doctorate of Philosophy.		
Signature		Date	10/06/2020

Name of Co-Author	Nicolas H. Voelcker		
Contribution to the Paper	Aided in the evaluation of final version of manuscript. Give consent to Siew Yee Lim to present this paper for examination towards the Doctorate of Philosophy.		
Signature		Date	10/06/2020

Name of Co-Author	Lluís F. Marsal		
Contribution to the Paper	Aided in the evaluation of final version of manuscript. Give consent to Siew Yee Lim to present this paper for examination towards the Doctorate of Philosophy.		
Signature		Date	10/06/2020

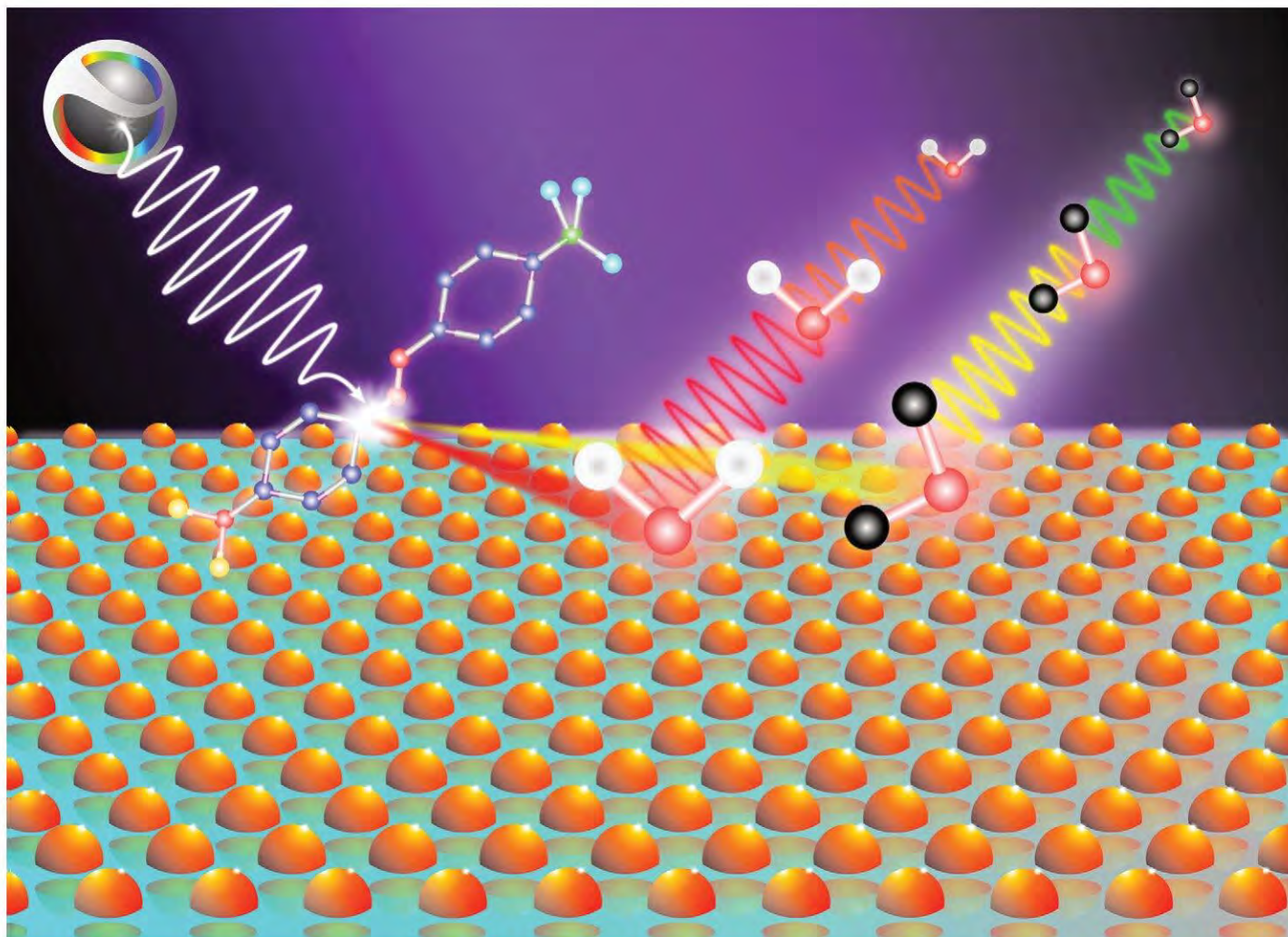| Name of Co-Author	Abel Santos		
Contribution to the Paper	Acted as a primary supervisor for the candidate, and aided in developing, revising and evaluating the manuscript for submission. Give consent to Siew Yee Lim to present this paper for examination towards the Doctorate of Philosophy.		
Signature		Date	11/06/2020

244

Showcasing research from Josep Ferré-Borrull, Andrew D. Abell, Nicolas H. Voelcker, Lluís F. Marsal and Abel Santos's Laboratories at Rovira i Virgili University, Monash University and The University of Adelaide.

Tailor-engineered plasmonic single-lattices: harnessing localized surface plasmon resonances for visible-NIR light-enhanced photocatalysis

2D gold (Au) nanodot plasmonic single-lattices (Au-nD-PSLs) featuring tailor-engineered geometric features are demonstrated for visible-NIR light-driven enhanced photocatalysis. Rational engineering of LSPR effects in Au-nD-PSLs provides exciting opportunities to develop high-performing and reusable photocatalysts that harvest the visible-NIR spectrum for photocatalysis applications.

As featured in:

See Josep Ferré-Borrull, Andrew D. Abell, Nicolas H. Voelcker, Lluís F. Marsal, Abel Santos *et al.*, *Catal. Sci. Technol.*, 2020, **10**, 3195.

ROYAL SOCIETY OF **CHEMISTRY**

rsc.li/catalysis

PAPER

Tailor-engineered plasmonic single-lattices: harnessing localized surface plasmon resonances for visible-NIR light-enhanced photocatalysis†
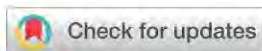
Siew Yee Lim,‡[abc] Cheryl Suwen Law,‡[abc] Francesc Bertó-Roselló,‡[d] Lina Liu,[aef] Marijana Markovic,[ag] Josep Ferré-Borrull,*[d] Andrew D. Abell, [iD] *[bch] Nicolas H. Voelcker, [iD] *[ijkl] Lluís F. Marsal [iD] *[d] and Abel Santos [iD] *[abc]

A platform material composed of 2D gold (Au) nanodot plasmonic single-lattices (Au-nD-PSLs) featuring tailor-engineered geometric features for visible-NIR light-driven enhanced photocatalysis is presented. Au-nD-PSLs efficiently harness incident visible-NIR electromagnetic waves to accelerate photo-chemical reactions by localized surface plasmon resonance (LSPR) effects. Au-nD-PSLs are fabricated by a straightforward, industrially scalable template-assisted approach, using nanopatterned aluminum substrates as templates. The method overcomes the constraints of direct writing lithography and allows Au-nD-PSLs to be transferred to arbitrary functional flexible substrates. Triangular lattice Au-nD-PSLs feature tunable and controllable characteristic LSPR bands across the visible spectrum. Strongly localized electromagnetic fields around Au-nD-PSLs are responsible for the outstanding photocatalytic performance of these plasmonic nanostructures, as demonstrated by finite-difference time-domain simulations and experimental observations. Our approach of rational engineering of LSPR effects in Au-nD-PSLs provides exciting opportunities to develop high-performing and reusable photocatalysts that harvest the visible-NIR spectrum for a broad range of optoelectronic and plasmonic applications.

[a] *School of Chemical Engineering and Advanced Materials, The University of Adelaide, Adelaide, South Australia 5005, Australia.*
E-mail: abel.santos@adelaide.edu.au
[b] *Institute for Photonics and Advanced Sensing, The University of Adelaide, Adelaide, South Australia 5005, Australia. E-mail: andrew.abell@adelaide.edu.au*
[c] *ARC Centre of Excellence for Nanoscale BioPhotonics, The University of Adelaide, Adelaide, South Australia 5005, Australia*
[d] *Department of Electronic, Electric, and Automatics Engineering, University Rovira i Virgili, Tarragona 43007, Spain. E-mail: lluis.marsal@urv.cat*
[e] *State Key Laboratory of High-efficiency Utilization of Coal and Green Chemical Engineering, Ningxia University, Yinchuan 750021, P.R. China*
[f] *College of Chemistry and Chemical Engineering, Ningxia University, Yinchuan 750021, P. R. China*
[g] *School of Agriculture Food and Wine, The University of Adelaide, South Australia 5064, Australia*
[h] *Department of Chemistry, The University of Adelaide, South Australia 5005 Adelaide, Australia*
[i] *Melbourne Centre for Nanofabrication, Victorian Node of the Australian National Fabrication Facility, Monash University, Victoria 3168, Australia.*
E-mail: nicolas.voelcker@monash.edu
[j] *Monash Institute of Pharmaceutical Sciences, Monash University, Victoria 3052, Australia*
[k] *Commonwealth Scientific and Industrial Research Organisation (CSIRO), Victoria 3168, Australia*
[l] *INM-Leibniz Institute for New Materials, Campus D2 2, Saarbrücken 66123, Germany*
† Electronic supplementary information (ESI) available. See DOI:10.1039/c9cy02561h
‡ Equal contribution.

Introduction

Photocatalysis is a light-guided photo-chemical process where incident natural or artificial light is transformed into chemical energy to drive a broad range of reactions.[1] For practical applications, photocatalyst materials should have excellent capability to harvest high irradiance sections of the solar spectrum, particularly the abundant visible and NIR light spectral regions, which account for ~47 and ~51% of the incoming solar energy, respectively.[2] Photocatalyst platforms interact with incoming electromagnetic waves and convert photons to heat and charge carriers (*i.e.* electrons and holes – e^-/h^+), which are capable of undergoing secondary reactions for a variety of applications including water purification,[3–8] air treatment,[9] hydrogen (H_2) energy production,[10–12] ammonia (NH_3) generation,[13] carbon dioxide (CO_2) reduction,[14,15] oxidation of aromatic alcohols[16,17] and reduction of nitroaromatic compounds.[18] Noble metal-based nanoparticles provide efficient platforms capable of harvesting visible light energy for photocatalysis through localized surface plasmon resonance (LSPR) effects.[7,8,16–18] Upon visible light illumination, noble metal nanoparticles concentrate and confine light on their structure in the form of strongly and locally enhanced electromagnetic fields – so-called plasmonic 'hot spots' – which act as reaction sites to

This journal is © The Royal Society of Chemistry 2020

Catal. Sci. Technol., 2020, **10**, 3195–3211 | **3195**

246

drive photocatalytic reactions.[19–23] LSPR-based enhancements in noble metal nanoparticles rely strongly on their shape, size and spatial arrangement. Therefore, the smart design of the geometric features and spatial distribution of noble metal nanoparticles can provide new opportunities to harness LSPR interactions for boosting photon-to-electron conversion rates in photocatalysis.[24–27] However, practical use of nanoparticulate systems in photocatalysis faces technical challenges (e.g. heterogeneous distribution in size and shape, strong tendency to agglomerate), and environmental and health regulatory constraints (i.e. uncertainty about the fate and toxicity of nanomaterials), which prevent the bench-to-field translation of this technology.[28] These drawbacks can be overcome by transferring noble metal-based nanoparticle systems onto flexible and mechanically robust substrates in the form of 2D plasmonic single- and super-lattices.[29] Single- and super-lattice LSPR modes can be tuned over a broad frequency range by modifying the geometric features of the lattice unit and have been reported to yield remarkably strong resonance bands in the visible spectrum.[30–32] The use of direct writing techniques such as electron beam lithography and focused ion beam lithography, allows the fabrication of noble metal-based single- and super-lattices with precisely controlled nanometric features. However, these techniques are time-consuming (~12–24 h), non-scalable (limited to mm^2) and costly (~$2M capital investment).[33–38]

Alternatively, noble metal nanoparticle lattices can be fabricated by self-assembly and template-assisted methods.[39,40] 2D nanoplasmonic lattices produced by these cost-competitive approaches have been demonstrated to provide enhanced electromagnetic field performances for SERS applications, by coupling hybrid plasmonic and photonic resonances through tailored structural designs.[41] Despite these advances, there remain fundamental and applied questions concerning nanofabrication approaches that can produce 2D plasmonic lattices with optimal homogeneity over nano and macroscopic areas to operate at the visible-NIR spectral region. Model metal-based nanoparticle lattices with optimal designs and features integrated into functional substrates will be a key advance to fully understand and use complex hybrid plasmonic resonance modes for photocatalysis. However, these advances will also require nanofabrication approaches that are fully scalable, cost-competitive, environment-friendly, and compatible with existing industrial processes to facilitate the bench-to-field translation and minimize technological translation costs. Self-organized nanoporous anodic alumina (NAA) produced by electrochemical oxidation of aluminum – anodization – provides an ideal template material for a broad range of photonic and plasmonic applications due to its versatile and well-defined geometric features at the nanoscale.[42] NAA features arrays of self-organized hemispherical nanocaps at its bottom side, which are hexagonally arranged with a lattice constant or interpore distance that can be precisely tuned from ~60 to 700 nm by the anodization voltage.[43]

During anodization, an inverse replica of NAA's hemispherical nanocaps is transferred onto the underlying aluminum substrate by a self-organization, mechano-electrochemical growth process, in which the oxide layer formed at the oxide–metal interface undergoes volume expansion (i.e. Pilling–Bedworth ratio ~1.23[42]) and patterns the aluminum substrate. Selective removal of the NAA layer by wet chemical etching, results in a nanopatterned aluminum substrate featuring triangular lattice arrays of hemispherical nanoconcavities.[44] Recently, Ikeda and co-workers demonstrated the fabrication of highly ordered arrays of Au nanodots on nanopatterned aluminum substrates by combining anodization, metal coating and thermal sintering.[45] Here, we report a straightforward, versatile and cost-effective non-lithographic nanofabrication approach to produce 2D gold (Au) nanodot plasmonic single-lattices (Au-nD-PSLs) with precisely designed and engineered optical properties for visible-NIR light-driven photocatalysis (Fig. 1). Nanopatterned aluminum substrates featuring triangular lattice arrays of hemispherical nanoconcavities with varied geometry (i.e. lattice constant ~60–550 nm and nanoconcavity diameter ~40–512 nm) were engineered by modifying the anodization voltage from 25 to 195 V (Fig. 1a). Gold nanodot arrays were produced by metal sputtering and thermal sintering using nanopatterned aluminum substrates as templates. Single-lattice gold nanodot arrays with controlled geometric features (i.e. diameter ~40–430 nm, lattice constant ~60–550 nm and height ~20–215 nm) were transferred onto polydimethylsiloxane (PDMS) and titanium dioxide functional films by selective dissolution of the aluminum substrate. The features of the LSPR bands of Au-nD-PSLs (i.e. position of central wavelength, full width at half-maximum and intensity) were tuned across the visible spectral range by structural engineering of the Au nanodot arrays (Fig. 1b). Au-nD-PSLs function as highly performing broadband photocatalyst platforms that can drive photo-chemical transformation of model organics under visible-NIR light irradiation by engineered LSPR modes.

Experimental section

Materials

High purity (99.9997%) aluminum (Al) foils 0.32 mm thick supplied by Goodfellow Cambridge Ltd. (UK) were used to produce nanopatterned aluminum templates via anodization. Hydrochloric acid (HCl), copper(II) chloride (CuCl$_2$), perchloric acid (HClO$_4$), oxalic acid (H$_2$C$_2$O$_4$), chromic acid (H$_2$CrO$_4$), titanium(IV) butoxide (Ti(OBu)$_4$), hydrogen peroxide (H$_2$O$_2$), methyl orange (C$_{14}$H$_{14}$N$_3$NaO$_3$S, MO), rhodamine B (C$_{28}$H$_{31}$ClN$_2$O$_3$, RhoB) and methylene blue (C$_{16}$H$_{18}$ClN$_3$S, MB) were supplied by Sigma-Aldrich (Australia). Ethanol (C$_2$H$_5$OH, EtOH), phosphoric acid (H$_3$PO$_4$) and sulfuric acid (H$_2$SO$_4$) were purchased from ChemSupply (Australia). SYLGARD 184 Silicone Elastomer kits were purchased from The Dow
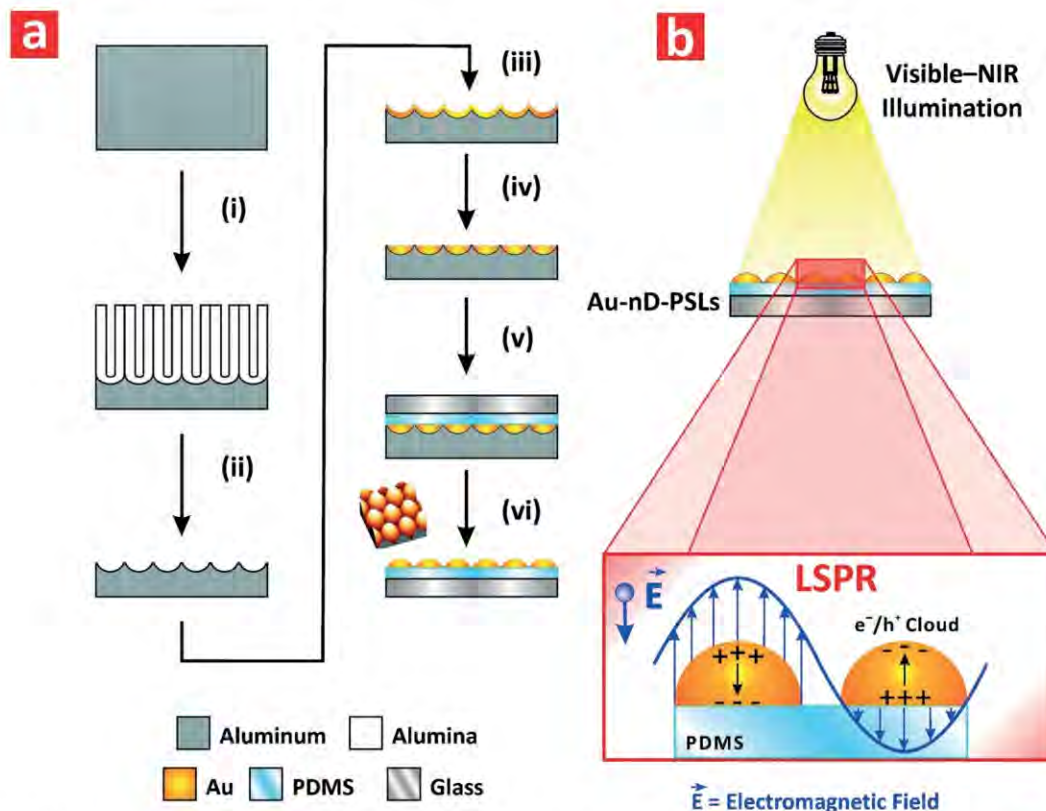
247

Fig. 1 Fabrication of 2D gold (Au) nanodot plasmonic single-lattices (Au-nD-PSLs) and their application in photocatalysis. a) Schematic diagram describing the fabrication process of Au-nD-PSLs by template-assisted approach and their transfer to polydimethylsiloxane (PDMS)-coated glass substrates: (i) anodization of aluminum (Al), (ii) removal of nanoporous anodic alumina layer, (iii) deposition of a thin layer of Au on nanopatterned Al substrate, (iv) annealing and sintering, (v) transfer to PDMS-coated glass substrate, (vi) selective removal of Al template. b) Application of Au-nD-PSLs in photocatalysis under visible-NIR illumination conditions (top), and illustration showing details of the generation of localized surface plasmon resonances (LSPR) around these Au nanostructures upon illumination (bottom).

Chemical Company (Australia). Aqueous solutions used in this study were prepared with Milli-Q® water (18.2 MΩ) (Australia).

Fabrication of nanopatterned aluminum templates

2.25 cm^2 square Al substrates were first cleaned under sonication in EtOH and ultrapure water for 15 min each, and dried under an air stream. Al substrates were then electropolished in a mixture of 4:1 (v:v) EtOH:HClO$_4$ at 20 V and 5 °C for 3 min. To obtain nanopatterned Al substrates with varied geometric features, electropolished Al substrates were anodized in an electrochemical reactor under various conditions (Table S1 – ESI†). After anodization, NAA films were removed by selective wet chemical etching in a mixture of 0.2 M H$_2$CrO$_4$ and 0.4 M H$_3$PO$_4$ at 40 °C overnight.

Sintering of noble-metal nanodot arrays

Nanopatterned Al substrates were coated with a thin layer of gold (or silver) in a sputter coater (Cressington 108, USA). Thin films were deposited from 99.99% purity gold and silver targets under 99.997% purity argon gas atmosphere. Noble metal-coated nanopatterned Al substrates were annealed in a

muffle furnace (LABEC, Australia) at 400 °C for 1 h under air atmosphere.

Fabrication of Au-nD-PSLs

Au nanodot arrays generated on the surface of annealed Al substrates were transferred to polydimethylsiloxane (PDMS)-coated glass slides. PDMS was prepared by thorough mixing of base agent and curing agent at a ratio of 10:1 (wt:wt), and then degassed under vacuum for 1 h to ensure complete removal of air bubbles. Glass slides were coated with PDMS by spin coating at ~2000 rpm, using a custom-made spin coater system. Al templates were sandwiched with PDMS-coated glass slides and placed in a vacuum chamber to expel trapped air bubbles. Samples were then placed in oven at 100 °C for 1 h. The remaining Al substrate was removed by selective wet chemical etching in a saturated solution of HCl–CuCl$_2$. PDMS-coated glass substrates were chemically functionalized with TiO$_2$ through sol–gel method. A mixture of EtOH (97 v%) and titanium(IV) butoxide (3 v%) was magnetically stirred for 10 min to prepare TiO$_2$ sol. These substrates were then immersed in the TiO$_2$ sol for 24 h, washed with EtOH and dried in an oven at 50 °C for 10 min.

This journal is © The Royal Society of Chemistry 2020

Catal. Sci. Technol., 2020, **10**, 3195–3211 | **3197**

248

Numerical simulations

Numerical calculations were performed using Lumerical FDTD Solutions® (www.lumerical.com). The geometric features of Au-nD-PSLs used for modelling were set according to nanodot sizes measured by FEG-SEM (Table S1†). The dispersion model of gold was provided by Lumerical and a PDMS-coated glass substrate was considered as underlying substrate, with $n_{PDMS} = 1.40$ RIU, $n_{glass} = 1.52$ RIU and $n_{air} = 1.00$ RIU. An unpolarized plane wave source impinging at normal incidence to different Au-nD-PSLs was modeled with a wavelength ranging from 400 to 1000 nm. A non-uniform FDTD mesh method was adapted to optimize computation resources and calculation time.

Optical characterization

Optical absorption and transmission spectra of Au-nD-PSLs were acquired in air and water at normal incidence (i.e. $\theta = 0°$) from 200 to 900 nm with a resolution of 1 nm using a UV-visible spectrophotometer (Cary 300, Agilent, USA). Optical features of the characteristic LSPR bands (i.e. central wavelength – λ_{LSPR}, full width at half maximum – $FWHM_{LSPR}$ and intensity – I_{LSPR}) were estimated by Gaussian fittings in OriginPro 8.5®. Absorbance spectra of 5 mg L^{-1} solution of organics in a 10 mm path length polystyrene cuvette were acquired from 200 to 800 nm to determine the absorbance band of MO, RhoB and MB. Plasmonic color of Au-nD-PSLs was characterized by digital images acquired with a Canon EOS 700D equipped with a Tamron 90 mm F2.8 VC USD macro mount lens with autofocus function under natural light illumination.

Structural characterization

Morphological features of Au-nD-PSLs at different fabrication stages were characterized by field emission gun scanning electron microscopy (FEG-SEM FEI Quanta 450). ImageJ was used to estimate the geometric features of Au-nD-PSLs.

Photocatalytic assessment

The photocatalytic performance of Au-nD-PSLs was assessed by monitoring the degradation of three model organics under simulated solar light conditions. Photocatalytic reactions were performed in a transparent reactor, in which photocatalyst platforms with an effective area of 1 cm^2 were immersed in a 4 mL reactant solution mixture containing 5 mg L^{-1} of organic and 100 mM H$_2$O$_2$. The solution was continuously stirred in a dark vessel (i.e. solar simulator) for 30 min to ensure adsorption–desorption equilibrium prior to illumination. A 150 W ($\sim$3000 lumen) halogen lamp (HL250-A, Amscope, Australia) at room temperature was used to simulate solar light (i.e. average optical power of incident light 150 W cm^{-2}). Reusability of Au-nD-PSLs was assessed by photocatalytic degradation of RhoB molecules for five times, using the same photocatalyst platform. The Au-nD-PSL platform was washed with water and dried under air stream before each cycle.

Results and discussion

Fabrication of Au-nD-PSLs

Fig. 1a illustrates the fabrication process used to prepare Au-nD-PSLs. In brief, an aluminum (Al) substrate was anodized under potentiostatic conditions to generate a nanoporous anodic alumina (NAA) film. Nanopores in the NAA film self-organized during anodization, patterning the underlying aluminum substrate with hemispherical nanoconcavities by volume expansion mechanism.[42] The NAA film was selectively removed by wet chemical etching, leaving a nanopatterned aluminum substrate. The surface of the nanopatterned aluminum was coated with a thin layer of gold via sputtering. The Au film was sintered upon thermal annealing at 400 °C for 1 h, forming ordered arrays of Au nanodots. In this process, hemispherical nanoconcavities on the aluminum substrate act as nanoscale crucibles, shaping the sintered Au film into hemispherical shapes. Au nanodot arrays were transferred to a PDMS-coated glass substrate to form a mechanically robust 2D plasmonic single-lattice structure. Finally, the Al template was removed by selective wet chemical etching. The versatility of this non-lithographic nanofabrication process was demonstrated by producing Au nanodot arrays of varying size and lattice constant through systematic modification of the anodization conditions and Au deposition time. Au-nD-PSLs with tunable geometric features act as LSPR-based photocatalytic platforms under controlled visible-NIR illumination conditions (Fig. 1b).

Structural and optical characterization of Au-nD-PSLs

Fig. 2 shows a set of top view FEG-SEM images of Au-nD-PSLs produced with varied geometrical features at different fabrication stages (i.e. nanopatterned Al substrate, Au-coated Al template, Au nanodots after thermal sintering, and Au-nD-PSLs transferred to PDMS-coated glass substrate). The geometric features of Au-nD-PSLs were varied by engineering the nanopore features in the NAA films (i.e. nanodot diameter $\sim$40–430 nm, interdot distance or lattice constant $\sim$60–550 nm and nanodot height $\sim$20–215 nm), by applying one of the following four anodization conditions: i) mild anodization in 0.3 M sulfuric acid at 25 V (MA-NAA$_{Su}$), ii) mild anodization in 0.3 M in oxalic acid at 40 V (MA-NAA$_{Ox}$), hard anodization in 0.3 M oxalic acid at 140 V (HA-NAA$_{Ox}$), and mild anodization in 0.1 M phosphoric acid at 195 V (MA-NAA$_{Ph}$) (Table S1 – ESI†). Fig. 2a shows FEG-SEM images of arrays of hemispherical nanoconcavities formed on the surface of aluminum substrates after selective chemical dissolution of the NAA films. The hexagonal arrangement of these nanoconcavities is determined by the pattern at the backside of the NAA film. Fig. 2b shows top view FEG-SEM images of these NAA films after Au sputtering. These images reveal that both the surface and edges of nanopatterned aluminum substrates are homogenously coated with gold
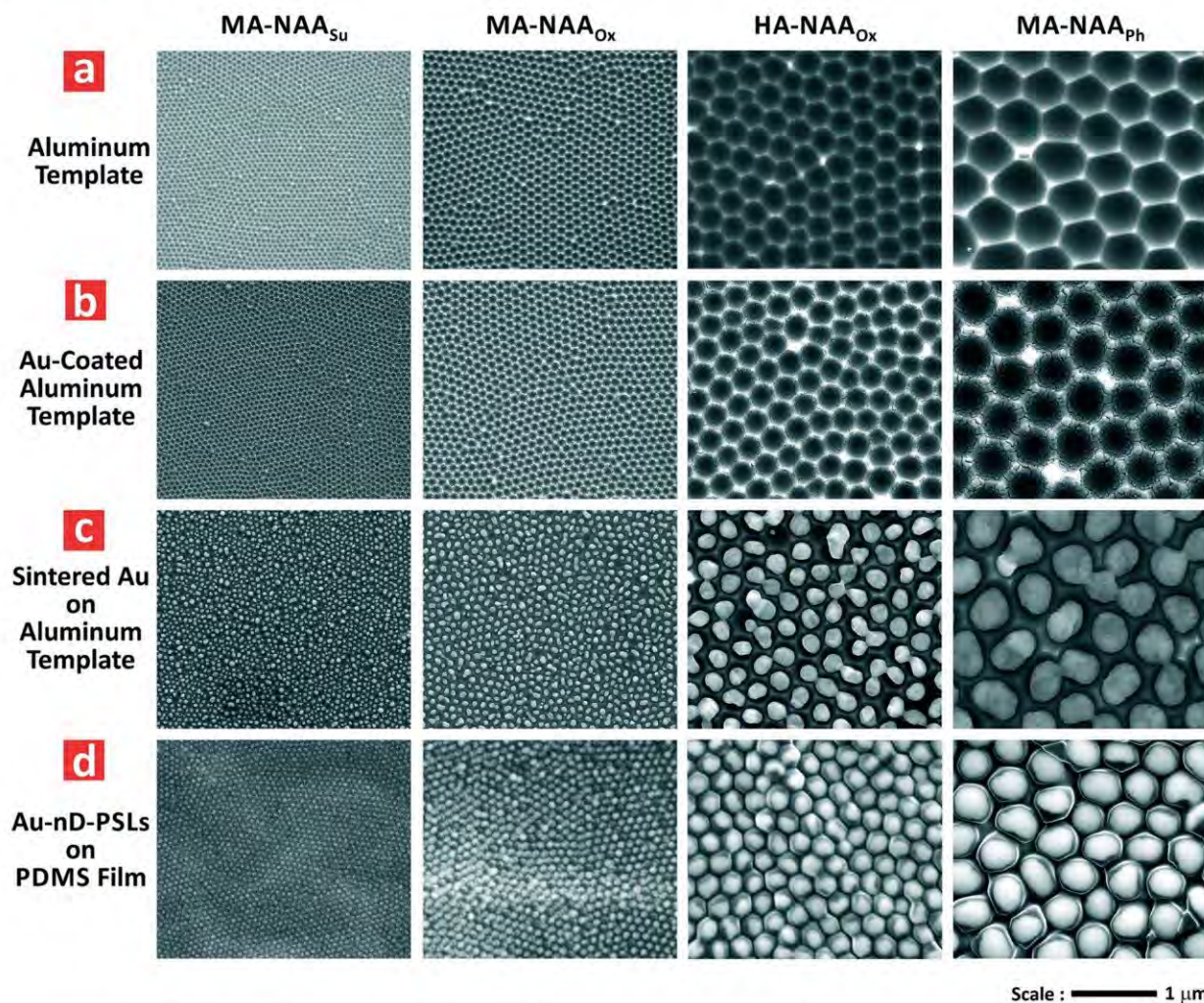
3198 | Catal. Sci. Technol., 2020, 10, 3195–3211

This journal is © The Royal Society of Chemistry 2020

Fig. 2 Top-view FEG-SEM images characterizing the different fabrication stages to produce Au-nD-PSLs with varying geometric features (scale bar = 1 μm). (a) Aluminum templates produced under mild anodization in sulfuric acid at 25 V (MA-NAA$_{Su}$), mild anodization in oxalic acid at 40 V (MA-NAA$_{Ox}$), hard anodization in oxalic acid at 140 V (HA-NAA$_{Ox}$) and mild anodization in phosphoric acid at 195 V (MA-NAA$_{Ph}$). (b) Au-coated aluminum templates produced from MA-NAA$_{Su}$, MA-NAA$_{Ox}$, HA-NAA$_{Ox}$, and MA-NAA$_{Ph}$ templates. (c) Sintered gold on aluminum templates produced from MA-NAA$_{Su}$, MA-NAA$_{Ox}$, HA-NAA$_{Ox}$, and MA-NAA$_{Ph}$ templates after annealing at 400 °C for 1 h. (d) Au-nD-PSLs transferred to PDMS films after selective dissolution of the aluminum templates.

after this process. Note that the deposition time ($\tau_{D\text{-}Au}$) was adjusted for each geometric pattern in preliminary experiments, with optimal $\tau_{D\text{-}Au}$ = 7, 15, 30 and 70 s for MA-NAA$_{Su}$, MA-NAA$_{Ox}$, HA-NAA$_{Ox}$, and MA-NAA$_{Ph}$ templates, respectively. Fig. 2c depicts top view FEG-SEM images of the structure of Au-coated nanopatterned Al templates after thermal annealing at 400 °C for 1 h. These images demonstrate that the Au films undergo thermal sintering under these conditions. The nanoconcavities generated on the surface of the Al templates act as crucibles and melted gold replicates the hemispherical shape of the nanoconcavities to minimize its energy state and reduce surface tension.[45,46] The morphology and shape of Au nanodots is almost circular from top-view, with some degree of deformation attributable to incomplete transformation, uneven Au coating or excessive surface diffusion. Fig. 2d shows the structure of Au-nD-PSLs transferred to PDMS-

coated glass slides after selective wet chemical etching of aluminum templates. These images reveal arrays of hemispherical Au nanodots in a distribution that approximates the hexagonal packing of the corresponding nanopatterned aluminum substrates. This result demonstrates that the geometric features of Au-nD-PSLs can be precisely engineered and tuned by the aluminum template features. As such gold nanodots in Au-nD-PSLs increase in size with increasing size of nanoconcavities in the aluminum template.

Formation of ordered Au nanodots also depends on the thickness of the Au film so the bigger the hemispherical nanoconcavities on the aluminum substrate the thicker the Au film have to be to avoid incomplete template filling. This process can be finely controlled by adjusting the deposition time (*i.e.* $\tau_{D\text{-}Au}$ = 7, 15, 30 and 70 s for MA-NAA$_{Su}$, MA-NAA$_{Ox}$, HA-NAA$_{Ox}$, and MA-NAA$_{Ph}$, respectively). The temperature

and time of thermal annealing were found to be critical in controlling the geometric features of Au-nD-PSLs. A too low annealing temperature (<400 °C) was ineffective in sintering the Au film due to insufficient energy to drive the diffusion of Au on the Al template surface. Conversely, an excessive annealing temperature and prolonged annealing time led to the formation of Au nanodot agglomerates with non-uniform distribution. These findings indicate that the optimal annealing conditions are 400 °C and 1 h. Fig. 3a illustrates the geometric characteristics defining the structure of Au-nD-PSLs, which include nanodot diameter (d_{dot}), interdot distance or lattice constant (d_{int}) and nanodot height (H_{dot}). Fig. 3b indicates a strong linear correlation (*i.e.* average $R^2 \sim 0.95$) between the geometric features of Au nanodot arrays and τ_{D-Au}, in which d_{int}, d_{dot} and H_{dot} increase at a rate of 8.1

± 1.6, 6.7 ± 0.6 and 3.4 ± 0.3 nm s^{-1} with increasing τ_{D-Au}, respectively. The geometric features of nanoconcavities generated on the surface of aluminum substrates during anodization are established by the anodization voltage (V_{an}).[42] As such d_{dot}, d_{int} and H_{dot} increase linearly with V_{an} at a rate of 0.6 ± 0.2, 2.5 ± 0.3 and 0.8 ± 0.1 nm s^{-1}, respectively, with average $R^2 \sim 0.96$ (Fig. S1 – ESI†). Au deposition was performed at a rate of ~0.033 nm s^{-1}, so the estimated optimal Au film thicknesses for MA-NAA$_{Su}$, MA-NAA$_{Ox}$, HA-NAA$_{Ox}$, and MA-NAA$_{Ph}$ templates are ~0.23, 0.49, 0.99 and 2.31 nm, respectively. Table S2 (ESI†) summarizes the relationship between the geometric features of Au-nD-PSLs, anodization voltage and τ_{D-Au} obtained from FEG-SEM image analysis. Values for d_{dot}, d_{int} and H_{dot} for MA-NAA$_{Su}$, MA-NAA$_{Ox}$, HA-NAA$_{Ox}$, and MA-NAA$_{Ph}$ templates were found to
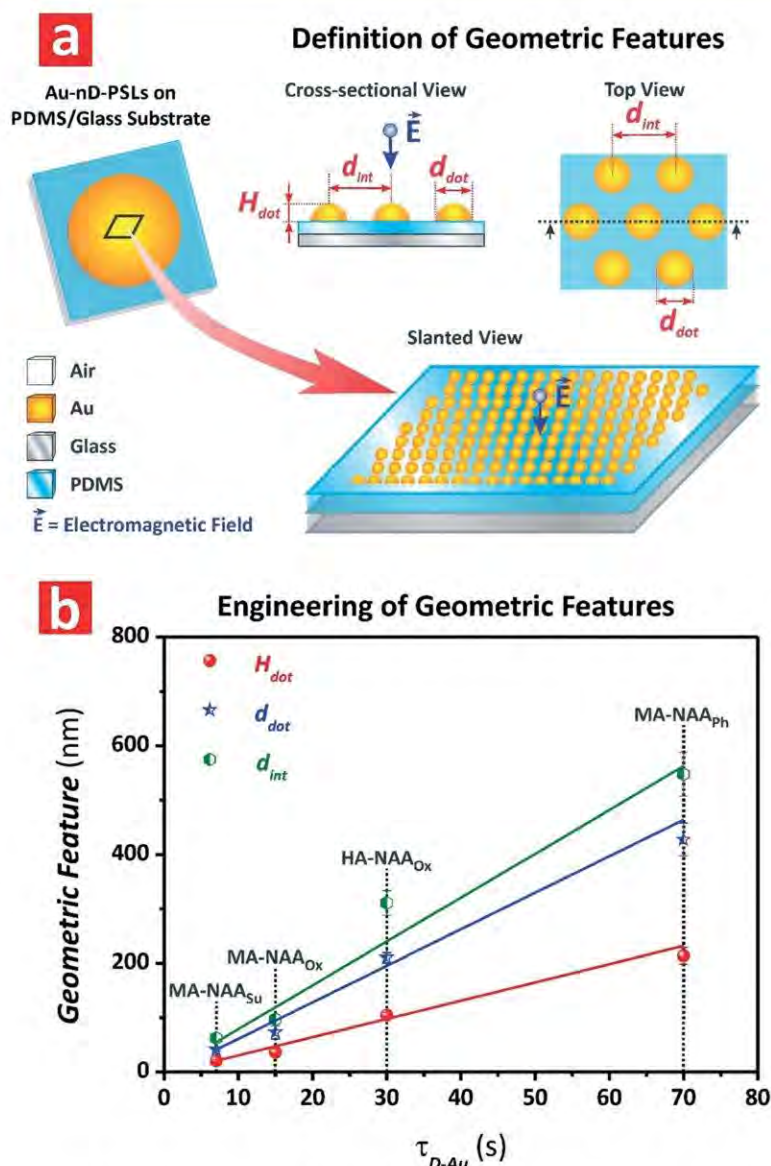

Fig. 3 Definition and characterization of geometric features of Au-nD-PSLs. (a) Schematic describing the geometric characteristics of Au-nD-PSLs, including nanodot diameter (d_{dot}), interdot distance (d_{int}) and nanodot height (H_{Au}). (b) Linear correlation between the geometric features of Au-nD-PSLs (d_{int}, d_{dot} and H_{dot}) and Au deposition time (τ_{D-Au} = 7, 15, 30 and 70 s).

3200 | *Catal. Sci. Technol.*, 2020, **10**, 3195–3211

This journal is © The Royal Society of Chemistry 2020

251

vary between ~40–430 nm, ~60–550 nm and ~20–215 nm, respectively. These results demonstrate the versatility of this non-lithographic nanofabrication approach to generate Au-nD-PSLs with well-resolved geometric features within a wide dimensional range.

The geometric characteristics of metal-based plasmonic single-lattices determine the features of the characteristic LSPR band of these nanoplasmonic structures.[29] To demonstrate the optical tunability of Au-nD-PSLs produced by this non-lithographic approach, the effect of the structural characteristics of Au-nD-PSLs (i.e. d_{int}, d_{dot} and H_{Au}) on the features of the LSPR band of these plasmonic single-lattices (i.e. position of the central wavelength – λ_{LSPR}, full width at half-maximum – $FWHM_{LSPR}$, and intensity – I_{LSPR}) was investigated. Table 1 summarizes the experimental and simulated values of the optical features of the LSPR band in the optical absorption and transmission spectra of Au-nD-PSLs produced with MA-NAA$_{Su}$, MA-NAA$_{Ox}$, HA-NAA$_{Ox}$, and MA-NAA$_{Ph}$ templates. Experimental optical transmission and absorption spectra of these plasmonic structures are depicted in Fig. 4a and b. It is apparent that the fabricated Au-nD-PSLs show a characteristically broad LSPR band, which is located within the visible spectral region, with λ_{LSPR} ranging from 561 ± 1 to 627 ± 1 nm for Au-nD-PSLs replicated from MA-NAA$_{Su}$ and HA-NAA$_{Ox}$ templates, respectively (Table 1). The central wavelength of the LSPR band has the same position in the absorption and transmission spectra of Au-nD-PSLs (Fig. 4a and b). Theoretical simulations using a geometrically tailored FDTD model were used to validate the experimental results (Fig. 4c). The central wavelength of the LSPR band in the experimental transmission spectra of Au-nD-PSLs fabricated with MA-NAA$_{Su}$, MA-NAA$_{Ox}$, HA-NAA$_{Ox}$, and MA-NAA$_{Ph}$ templates only deviates ~2.9, 1.2, 1.7 and 9.6% from values of the λ_{LSPR} predicted by FDTD simulations, respectively (Table 1). The FDTD model used in these simulations considers perfectly organized, defect-free Au-nD-PSLs but actual Au-nD-PSLs have small defects in the

structure of Au-nD-PSLs, resulting in the small deviation observed. Therefore, this excellent agreement between experimental and simulated results demonstrates that this non-lithographic approach provides excellent control over the geometric features of Au-nD-PSLs at the nanoscale. Fig. 4d shows the relationship between λ_{LSPR} and τ_{D-Au} in air and water for Au-nD-PSLs replicated from MA-NAA$_{Su}$, MA-NAA$_{Ox}$, HA-NAA$_{Ox}$, and MA-NAA$_{Ph}$ templates. It is apparent that λ_{LSPR} varies linearly with τ_{D-Au} following a double linear regime, one from τ_{D-Au} = 7 to 30 s and another one from τ_{D-Au} = 30 to 70 s. Within the first regime, λ_{LSPR} red-shifts with τ_{D-Au} at linear rates of 2.91 ± 0.24 and 3.13 ± 0.50 nm s^{-1} in air and water, respectively. However, within the second linear regime, λ_{LSPR} undergoes a slight blue shift in air (−0.23 ± 0.02 nm s^{-1}) and a moderate red shift in water (0.90 ± 0.09 nm s^{-1}). This graph also reveals that λ_{LSPR} red-shifts its position with an average $\Delta\lambda_{LSPR}$ of 19 ± 25 nm, when the refractive index of the medium surrounding the Au-nD-PSLs increases from n_{air} = 1.00 RIU to n_{water} = 1.33 RIU. Another interesting optical characteristic of Au-nD-PSLs is that these plasmonic structures display colors, as digital pictures of Au-nD-PSLs shown in Fig. 4d (inset) demonstrate. This property arises from collective plasmonic resonances at visible light frequencies influenced by the Wood's anomaly and Bloch wave surface plasmon polaritons, which are mutually coupled.[47] For instance, Au-nD-PSLs produced from MA-NAA$_{Su}$ templates feature Au nanodots with the smallest size and have their LSPR band located in the green section of the visible spectrum (i.e. λ_{LSPR} = 561 ± 1 nm). These Au-nD-PSLs display a weak pinkish color, which results from a combination of absorption and reflection of incident green–red light, respectively.[48] It is also apparent that the intensity of the LSPR absorption band of Au-nD-PSLs plays a major role in determining the intensity of the plasmonic color displayed by these structures. As Fig. 4b and Table 1 indicate, the overall light absorption of Au-nD-PSLs increases with the size of Au nanodots. Au-nD-PSLs produced with MA-NAA$_{Su}$ templates (I_{LSPR} = 0.2 ± 0.1 a.u.) display weak color, while those Au-nD-PSLs replicated from HA-NAA$_{Ox}$ and MA-NAA$_{Ph}$ templates feature the most intense colors (I_{LSPR} = 0.6 ± 0.1 and 0.4 ± 0.1 a.u., respectively). Fig. 4e compiles a summary of the optical features of the characteristic LSPR band in the absorption and transmission (experimental and simulated) spectra of Au-nD-PSLs (i.e. λ_{LSPR}, $FWHM_{LSPR}$ and I_{LSPR}) as a function of τ_{D-Au}. These graphs demonstrate that the LSPR band red-shifts its position with the size of the Au nanodots and the lattice constant, from τ_{D-Au} = 7 to 30 s. However, a slight blue shift is observed when the feature size increases from d_{dot} = 210 ± 10 (HA-NAA$_{Ox}$) to 428 ± 30 nm (HA-NAA$_{Ph}$). λ_{LSPR} values in the absorption and transmission spectra of Au-nD-PSLs are perfectly correlated and the results obtained from FDTD simulations can predict with good accuracy the position of the LSPR band of these plasmonic single-lattices, with a ~1–10% deviation between experimental and simulated results. The Au-nD-PSLs fabricated show a characteristically broad LSPR band, with an average

Table 1 Experimental and simulated tunability of optical features (i.e. position of the central wavelength – λ_{LSPR}, full width at half-maximum – $FWHM_{LSPR}$, and intensity – I_{LSPR}) in the absorption and transmission spectra of Au-nD-PSLs in air as a function of aluminum template (MA-NAA$_{Su}$, MA-NAA$_{Ox}$, HA-NAA$_{Ox}$, and MA-NAA$_{Ph}$) and deposition time (τ_{D-Au})

Optical property	τ_{D-Au} (s)	Template	λ_{LSPR} (nm)	$FWHM_{LSPR}$ (nm)	I_{LSPR} (a.u.)
Absorption (experimental)	7	MA-NAA$_{Su}$	561 ± 1	113 ± 11	0.2 ± 0.1
	15	MA-NAA$_{Ox}$	574 ± 1	105 ± 10	0.4 ± 0.1
	30	HA-NAA$_{Ox}$	627 ± 1	168 ± 17	0.6 ± 0.1
	70	MA-NAA$_{Ph}$	620 ± 1	157 ± 16	0.4 ± 0.1
Transmission (experimental)	7	MA-NAA$_{Su}$	561 ± 1	141 ± 14	36 ± 4
	15	MA-NAA$_{Ox}$	579 ± 1	131 ± 13	37 ± 4
	30	HA-NAA$_{Ox}$	627 ± 1	194 ± 19	21 ± 2
	70	MA-NAA$_{Ph}$	618 ± 1	166 ± 17	16 ± 2
Transmission (simulated)	—	MA-NAA$_{Su}$	578 ± 1	83 ± 7	48 ± 4
	—	MA-NAA$_{Ox}$	572 ± 1	82 ± 7	42 ± 4
	—	HA-NAA$_{Ox}$	638 ± 1	126 ± 8	38 ± 2
	—	MA-NAA$_{Ph}$	564 ± 1	84 ± 6	15 ± 2

This journal is © The Royal Society of Chemistry 2020

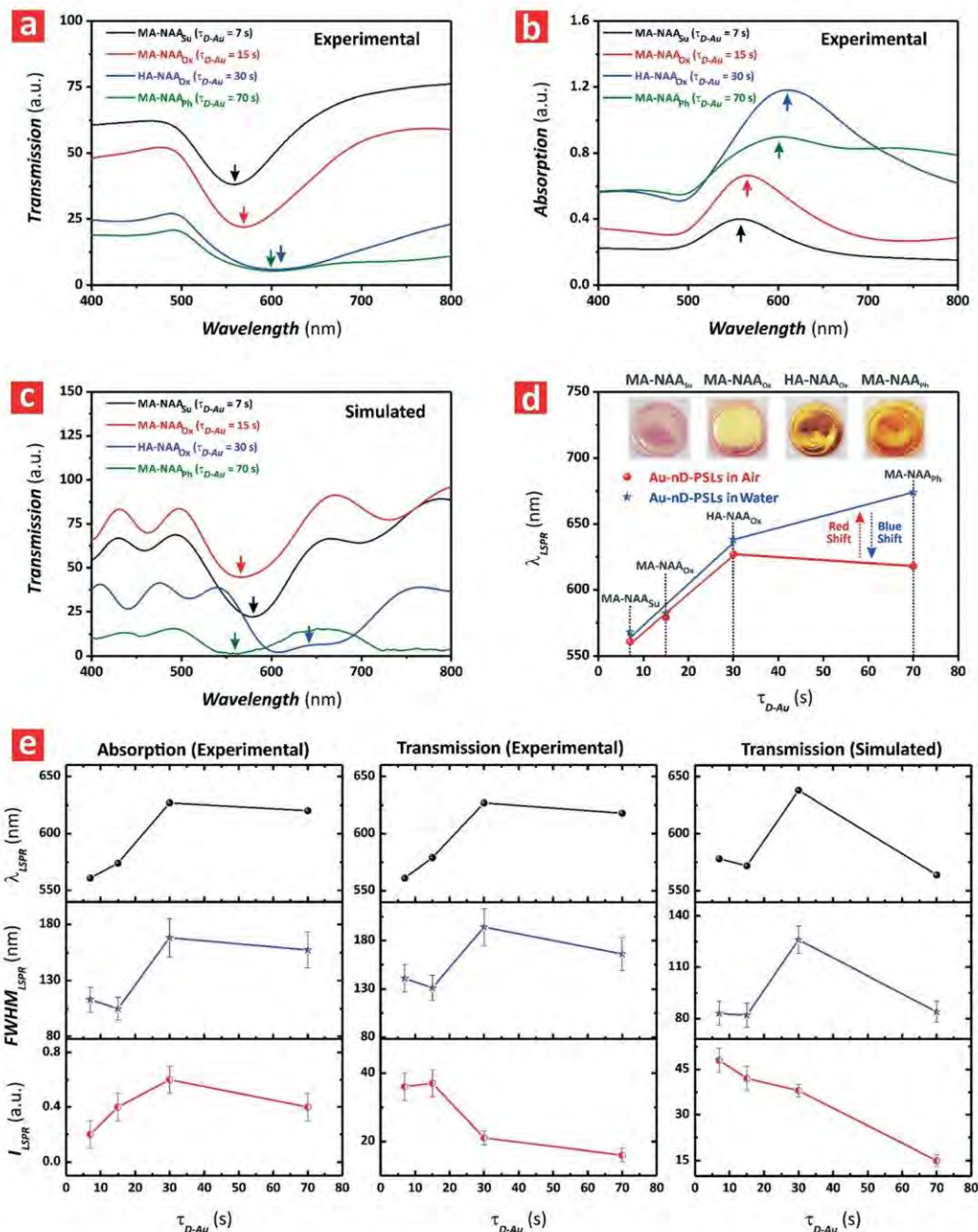Catal. Sci. Technol., 2020, **10**, 3195–3211 | **3201**

252

Fig. 4 Engineering and tunability of optical features in Au-nD-PSLs. (a) and (b) Experimental transmission and absorption spectra of Au-nD-PSLs produced with MA-NAA$_{Su}$, MA-NAA$_{Ox}$, HA-NAA$_{Ox}$, and MA-NAA$_{Ph}$ templates (NB: color arrows denote the approximate position of the central wavelength of LSPR bands). (c) Simulated transmission spectra of Au-nD-PSLs (NB: color arrows denote the approximate position of the central wavelength of LSPR bands). (d) λ_{LSPR} as a function of τ_{D-Au} estimated from the experimental transmission spectra of Au-nD-PSLs in air and water (NB: inset contains digital images of these plasmonic structures displaying plasmonic colors). (e) Dependence of optical features (λ_{LSPR}, FWHM$_{LSPR}$ and I_{LSPR}) on τ_{D-Au} estimated from experimental absorption (left) and transmission (center), and simulated transmission (right) spectra of Au-nD-PSLs.

FWHM$_{LSPR}$ of 136 ± 31 and 158 ± 28 nm in the absorption and transmission spectra, respectively.

The LSPR bands in the simulated transmission spectra are slightly narrower than those obtained from experimental results, with an average FWHM$_{LSPR}$ of 94 ± 22 nm. The FDTD model used in our study describes LSPR interactions in Au-nD-PSLs featuring a defect-free structure of perfectly

distributed Au nanodots. However, actual Au-nD-PSLs have small structural imperfections and spatial distortions associated with the grain boundaries in the aluminum template.[42] Therefore, this slight discrepancy between experimental and simulated results might be attributable to small imperfections in the structure of Au-nD-PSLs. However, defect-free and perfectly organized Au-nD-PSL structures

3202 | *Catal. Sci. Technol.*, 2020, **10**, 3195–3211

This journal is © The Royal Society of Chemistry 2020

could be produced by a combination of nanolithography and anodization.[49] The intensity of the LSPR bands in the absorption spectra of Au-nD-PSLs increases with d_{dot} from 41 ± 3 to 210 ± 10 nm, and decreases slightly from d_{dot} = 210 ± 10 to 428 ± 30 nm.

Conversely, I_{LSPR} in the transmission spectra of Au-nD-PSLs decreases with d_{dot}, achieving a minimum of 16 ± 2 a.u. at d_{dot} = 428 ± 30 nm. It is worthwhile noting that the overall transmission intensity of these plasmonic structures decreases dramatically with the feature size, since the larger Au-nD-PSLs scatter visible light more efficiently than their counterparts produced with small feature size. This analysis also reveals that the I_{LSPR} in simulated Au-nD-PSL structures has an excellent correlation with the experimental results, demonstrating that this is a suitable model to describe these light–matter interactions.

Assessment of photocatalytic performance of Au-nD-PSLs

LSPR interactions in noble metal-based plasmonic nanostructures can drive photocatalytic reactions through a combination of different optical phenomena, including intense light absorption, far-field light scattering, generation of hot carriers and plasmonic heating effects.[50,51] We have shown that structural engineering of Au-nD-PSLs can allow rational harvesting of incident electromagnetic waves at specific spectral regions to maximize photocatalytic reaction rates. Motivated by these results, we explored the potential applicability of Au-nD-PSLs as advanced platform material for photocatalysis. The photodegradation rate of three model organic molecules with absorbance bands in the visible spectrum (i.e. methylene blue, MB, λ_{Abs-MB} = 664 nm; rhodamine B, RhoB, $\lambda_{Abs-RhoB}$ = 554 nm; methyl orange, MO, λ_{Abs-MO} = 464 nm) was used as a reference parameter to identify photocatalytic enhancements associated with LSPR effects in Au-nD-PSLs (Fig. S2 – ESI†). The concentration of these model organics at a given illumination time (C_t) was estimated from calibration lines correlating organic concentration with optical absorbance intensity (Fig. S3 – ESI†). The photocatalytic performance of Au-nD-PSLs was estimated by the slope of the linearized pseudo-first order kinetics model shown in eqn (1):
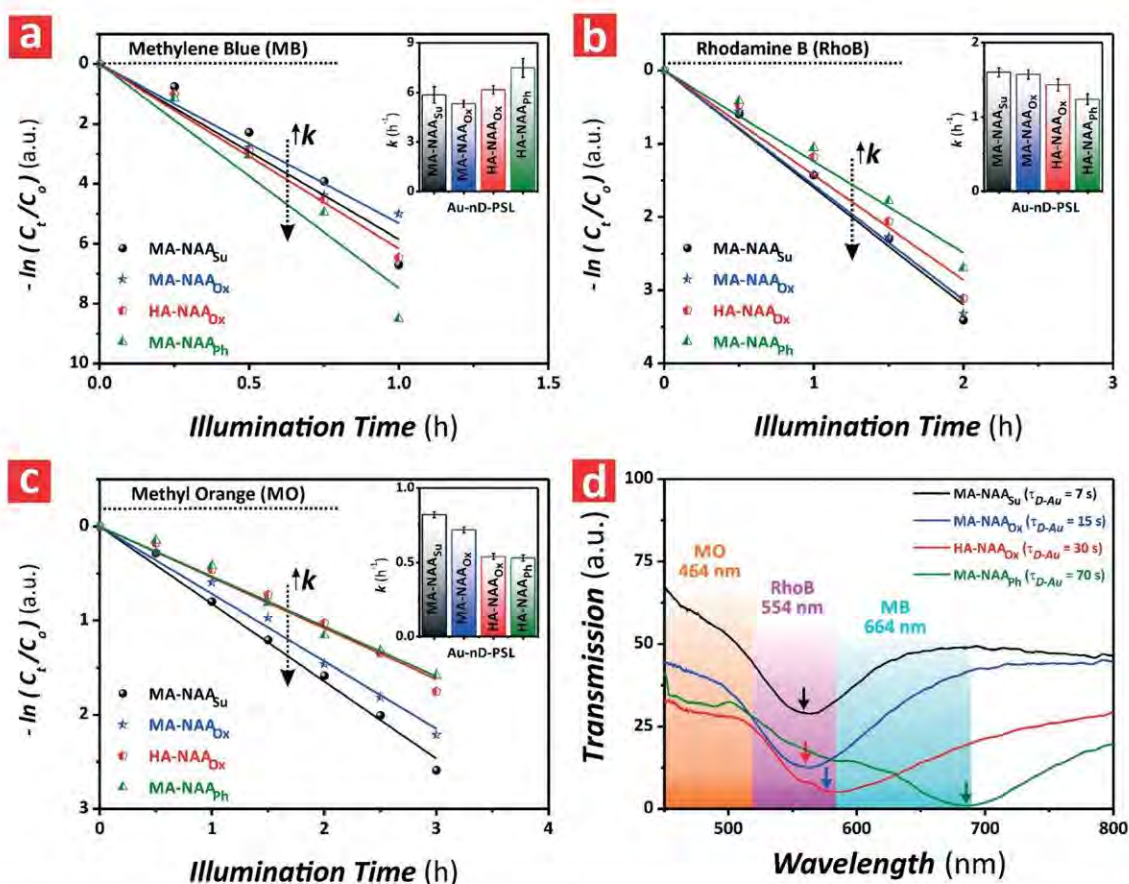

Fig. 5 Effect of geometric features on the photocatalytic performance of Au-nD-PSLs. (a–c) Photocatalytic degradation kinetics of MB, RhoB and MO by Au-nD-PSLs produced with MA-NAA_Su, MA-NAA_Ox, HA-NAA_Ox and MA-NAA_Ph templates under controlled visible-NIR illumination conditions, with bar charts (insets) summarizing the kinetic constant values (k) (NB: horizontal black dotted lines denote control experiments performed with PDMS-coated glass substrates without Au-nD-PSLs and error bars denote standard deviation from average measurements obtained from n = 3 independent Au-nD-PSLs). (d) Relative position of absorbance band of model organics (shaded color bands) and LSPR band in the transmission spectra of Au-nD-PSLs in water (NB: color arrows denote the approximate position of the central wavelength of LSPR bands).

254

$$-\ln(C_t/C_o) = kt \qquad (1)$$

where C_o is the concentration at the adsorption–desorption equilibrium, and k is the photodegradation kinetic constant.

These experiments were performed under controlled visible-NIR light irradiation conditions, with a spectral distribution of 0.12% UV (350–400 nm), 64.60% visible (400–750 nm) and 35.28% near IR (800–1025 nm) (Fig. S4 – ESI†).

Effect of geometric features on photocatalytic performance of Au-nD-PSLs

Fig. 5a–c depict the effect of the geometric features of Au-nD-PSLs on the photocatalytic degradation rate (k) of MB, RhoB and MO under visible-NIR illumination conditions. The k values summarized in bar charts (insets in Fig. 5a–c) and Table 2 correspond to the slope of the linear fittings shown in these graphs. Control experiments performed with PDMS-coated glass substrates without Au-nD-PSL platforms (i.e. dotted black lines in Fig. 5a–c) reveal that there is no photocatalytic activity in the absence of the Au nanodots. Therefore, these photocatalytic reactions are entirely associated with LSPR effects in Au-nD-PSLs. Fig. 5a denotes that Au-nD-PSLs produced with MA-NAA$_{Su}$, MA-NAA$_{Ox}$ and HA-NAA$_{Ox}$ provide comparable photocatalytic performance to degrade MB molecules, with an average k value of 5.77 ± 0.43 h^{-1}. Au-nD-PSL platforms replicated from MA-NAA$_{Ph}$ templates provide the best performing photocatalyst system (i.e. k = 7.48 ± 0.57 h^{-1}), with a ~18–29% superior performance than that of their analogues of smaller geometric features. Photocatalytic rates achieved by Au-nD-PSLs to degrade RhoB molecules are summarized in Fig. 5b. This graph indicates that k decreases with increasing Au nanodot size in Au-nD-PSLs, with k = 1.60 ± 0.06, 1.57 ± 0.06, 1.43 ± 0.08 and 1.24 ± 0.07 h^{-1} for Au-nD-PSLs produced with d_{dot} = 41 ± 3, 73 ± 12, 210 ± 10 and 428 ± 30 nm, respectively. The best performing photocatalyst platforms (i.e. Au-nD-PSLs fabricated from MA-NAA$_{Su}$ templates) provide a ~2–23% superior performance than that achieved by their counterparts featuring bigger Au nanodot size. Fig. 5c shows the photocatalytic degradation rate of MO molecules by Au-nD-PSLs, which also decreases with the Au nanodot size. Au-

nD-PSLs featuring d_{dot} = 41 ± 3, 73 ± 12, 210 ± 10 and 428 ± 30 nm achieve photodegradation rates of 0.82 ± 0.02, 0.72 ± 0.02, 0.54 ± 0.02 and 0.53 ± 0.02 h^{-1}, respectively. Au-nD-PSLs produced with MA-NAA$_{Su}$ templates outperform their equivalent photocatalyst platforms with larger Au nanodot size, with a ~12–35% enhancement.

Optical arrangement between the absorbance band of organic molecules and the LSPR band of plasmonic nanostructures is key to tailor LSPR effects for enhanced photocatalysis by maximized utilization of incident light. Fig. 5d depicts the relative position between the absorbance band of MB, RhoB and MO and the characteristic LSPR band in the transmission spectra of Au-nD-PSLs produced with d_{dot} = 41 ± 3, 73 ± 12, 210 ± 10 and 428 ± 30 nm. This graph reveals that the λ_{LSPR} of Au-nD-PSLs featuring bigger Au nanodot size (i.e. HA-NAA$_{Ox}$ and MA-NAA$_{Ph}$) covers a broader range of optical absorbance of MB. Analysis of degradation rates indicates that this reaction is driven more efficiently by Au-nD-PSLs of larger Au nanodot size. Under such optical configuration, LSPR effects are more effective with increasing Au nanodot size since incoming visible photons in that spectral regions are concentrated more efficiently by the plasmonic structure, boosting the generation of charge carriers and thus the photocatalytic rate. Conversely, the LSPR band of Au-nD-PSLs replicated from MA-NAA$_{Su}$, MA-NAA$_{Ox}$ and HA-NAA$_{Ox}$ templates entirely overlaps the absorbance band of RhoB. This optical configuration maximizes LSPR effects in Au-nD-PSLs featuring smaller Au nanodot size since incoming visible photons are more efficiently used by the nanoplamonic structure, increasing the photocatalytic degradation rate. The LSPR band of Au-nD-PSLs replicated from MA-NAA$_{Su}$, MA-NAA$_{Ox}$ and HA-NAA$_{Ox}$ templates is slightly misaligned with the absorbance band of MO. Photodegradation rates of in this system indicate that Au-nD-PSLs featuring smaller Au nanodot size and blue-shifted LSPR band outperform their counterparts with larger feature size and red-shifted λ_{LSPR}.

In summary, structural engineering of Au-nD-PSLs makes it possible to tune and maximize LSPR interactions to speed up photocatalytic reactions. Enhancement of these light–matter interactions is found to be maximum when the characteristic LSPR band of Au-nD-PSLs is aligned with the absorbance band of model organics. Photocatalytic degradation rates rely strongly on this optical arrangement. This analysis also reveals that the chemical nature of model organics is another critical factor affecting the overall photocatalytic performance of Au-nD-PSLs. Table 2 summarizes the average k value for photodegradation of MB, RhoB and MO molecules by Au-nD-PSLs, which follow the order MB > RhoB > MO (i.e. k = 6.20 ± 0.92, 1.46 ± 0.16 and 0.65 ± 0.14 h^{-1}, respectively). These results demonstrate that Au-nD-PSLs achieve fastest photodegradation rates for MB molecules, with a ~76 and 90% superior efficiency than that achieved for RhoB and MO molecules, respectively. This difference is attributable to the molecular steric structure of these organics, which in turn determines how these

Table 2 Position of central wavelength of LSPR band (λ_{LSPR}) in water and values of the kinetic constant (k) for the photodegradation of MB, RhoB and MO molecules in Au-nD-PSLs replicated from MA-NAA$_{Su}$, MA-NAA$_{Ox}$, HA-NAA$_{Ox}$ and MA-NAA$_{Ph}$ templates under controlled visible-NIR illumination conditions (NB: errors denote standard deviation from average measurements obtained from n = 3 independent Au-nD-PSLs)

Template	λ_{LSPR} (nm)	k (h^{-1}) MB	RhoB	MO
MA-NAA$_{Su}$	568 ± 1	5.85 ± 0.50	1.60 ± 0.06	0.82 ± 0.02
MA-NAA$_{Ox}$	582 ± 1	5.32 ± 0.21	1.57 ± 0.06	0.72 ± 0.02
HA-NAA$_{Ox}$	638 ± 1	6.16 ± 0.24	1.43 ± 0.08	0.54 ± 0.02
MA-NAA$_{Ph}$	674 ± 1	7.48 ± 0.57	1.24 ± 0.07	0.53 ± 0.02
	Average	6.20 ± 0.92	1.46 ± 0.16	0.65 ± 0.14

3204 | *Catal. Sci. Technol.*, 2020, **10**, 3195–3211

This journal is © The Royal Society of Chemistry 2020

255

molecules interact with the surface of Au nanodots in Au-nD-PSLs. Both RhoB and MB are positively (cationic) charged molecules, while MO is negatively (anionic) charged. Surface Au nanodots are negatively charged at the pH conditions in which these reactions were performed (pH = 5.5).[52,53] Therefore, positively charged RhoB and MB molecules have high affinity toward Au-nD-PSLs. Strong electrostatic attraction increases the number of molecules absorbed onto the surface of Au nanodots, thus enhancing the overall photocatalytic degradation rate of the system. The close proximity of molecules and the surface enables an efficient utilization of photo-generated charge carriers in the photocatalyst platforms. However, MB exhibits a higher photodegradation rate than RhoB, which is attributable to a partially inhibited adsorption by steric repulsion associated with carboxylate anions in RhoB molecules.[54] In contrast, strong steric repulsion between negatively charged MO and the negatively charged surface of Au nanodots limits the effective adsorption of MO molecules, minimizing the utilization of charge carriers and significantly reducing the rate of this photodegradation reaction.

Understanding LSPR effects in Au-nD-PSLs

Further insight into the physical origin of photocatalytic enhancements associated with LSPR lattice resonances can be gained from analyzing FDTD simulations of distributions of electric field intensity at resonant and non-resonant wavelengths ($|E^2|$), and the optical absorption density in Au-nD-PSLs. Fig. 6a–d and Movies S1–S4 (ESI†) show the simulated $|E|^2$ profiles at resonant wavelengths in Au-nD-PSLs replicated from MA-NAA$_{Su}$, MA-NAA$_{Ox}$, HA-NAA$_{Ox}$ and MA-NAA$_{Ph}$ templates. Fig. 6a reveals that Au nanodots in Au-nD-PSLs produced from MA-NAA$_{Su}$ templates displays two $|E|^2$ maxima at the junction interface Au nanodot–surrounding medium–PDMS substrate. The electric field extends its distribution along the lateral side of the Au nanodots and the surface of the underlying PDMS substrate. Photocatalytic platforms under such arrangement can minimize charge recombination and maximize the use of photo-generated charge carriers due to the electronically insulating nature of the PDMS substrate. Au-nD-PSLs produced with MA-NAA$_{Ox}$ and HA-NAA$_{Ox}$ templates display
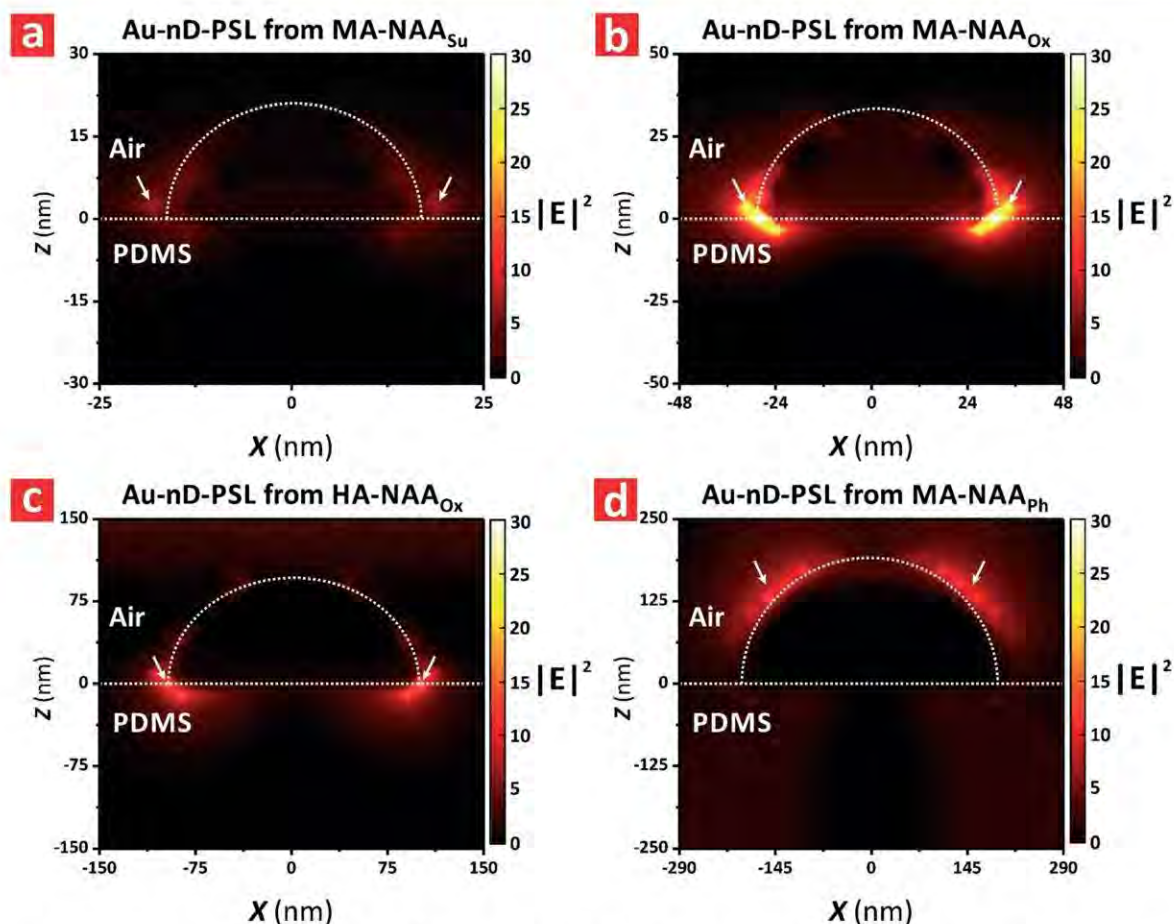

Fig. 6 Cross-sectional FDTD electric field intensity ($|E^2|$) distribution profiles at resonant wavelengths in Au-nD-PSLs produced with: (a) MA-NAA$_{Su}$ (λ_{LSPR} = 561 nm), (b) MA-NAA$_{Ox}$ (λ_{LSPR} = 579 nm), (c) HA-NAA$_{Ox}$ (λ_{LSPR} = 627 nm), and (d) MA-NAA$_{Ph}$ (λ_{LSPR} = 618 nm) templates (NB: FDTD simulations were performed considering a PDMS substrate at the bottom of the Au nanodots and air as surrounding medium; white arrows denote sections of maximum field tensity around these plasmonic nanostructures).

This journal is © The Royal Society of Chemistry 2020

Catal. Sci. Technol., 2020, **10**, 3195–3211 | **3205**

qualitatively comparable $|E|^2$ distributions, although the magnitude of $|E|^2$ in the latter plasmonic structures is higher than that of the former ones (Fig. 6b and c). The magnitude of electric field intensity in these Au-nD-PSLs is higher than that shown by their analogs produced with MA-NAA$_{Su}$ templates. However, the electric field maxima are partially embedded into the PDMS substrate, minimizing the efficient utilization of photo-generated charge carriers due to electronic screening effect by the PDMS substrate. Fig. 6d shows the $|E|^2$ distribution in Au-nD-PSLs replicated from MA-NAA$_{Ph}$ templates. This simulation reveals two broad maxima of moderate magnitude located at the lateral top side of the Au nanodots. Distribution of field intensity is most suitable for charge generation and utilization when the LSPR band is aligned with the absorbance band of the organic. Further mechanistic information about these light–matter interactions can be obtained from analyzing the $|E|^2$ profiles at non-resonant wavelengths and the optical absorption density distribution in Au-nD-PSLs. Fig. S5 (ESI†) reveals that Au-nD-PSLs do not show significant concentration of $|E|^2$ at non-resonant wavelengths. Therefore, the contribution of incident photons at non-resonance wavelengths to the photocatalytic performance of Au-nD-PSLs is almost negligible. However, experimental observations are further supported by analyzing the optical absorption density distribution in Au-nD-PSLs (Fig. S6 – ESI†). FDTD simulations show that Au-nD-PSLs featuring $d_{dot} = 41 \pm 3$, 73 ± 12, 210 ± 10 and 428 ± 30 nm achieve optical absorption density maxima of ~5500, 2200, 550 and 60 W μm^{-3}, respectively.

So, smaller Au nanodots in Au-nD-PSLs can harvest incident photons more efficiently to drive photocatalytic reactions. To summarize, FDTD simulations demonstrate that, upon visible-NIR illumination, Au-nD-PSLs featuring $d_{dot} = 41 \pm 3$, 73 ± 12 and 210 ± 10 nm can strongly concentrate electric field intensity at the interface Au nanodot–surrounding medium–PDMS substrate. In general, nanoplasmonic structures with smaller Au nanodot size outperform their counterparts with bigger feature size. However, Au-nD-PSLs with $d_{dot} = 428 \pm 30$ nm are found to be the best performing plasmonic nanostructures when the characteristic LSPR band of these plasmonic structures is aligned with the absorbance band of the model organic (Table 2). Analysis of electric field intensity distributions reveals that Au-nD-PSLs replicated from MA-NAA$_{Ph}$ templates strongly localize electric fields on the upper side of Au nanodots. MB molecules have high affinity toward the surface of Au nanodots.[55] So, it is inferred that strongly absorbed MB molecules can be degraded efficiently by hot electrons generated on the surface of Au nanodots. Conversely, RhoB and MO molecules have less electrostatic affinity toward Au surfaces due to their molecular electrostatic potential. Under such conditions, highly concentrated electric fields at the joint interface between Au nanodots and substrate are found to drive these photodegradation reactions more efficiently.

Effect of opto-electronic properties of underlying substrate in Au-nD-PSLs

Functional substrates can provide Au-nD-PSLs with mechanical stability to prevent release of nanoparticles to the environment for practical applications. Electronically insulating or semiconducting substrates can also minimize fast recombination and transferring of charge carriers by tuning the electronic bandgap of the underlying substrate.[56,57] Different forms of titanium dioxide (TiO$_2$) nanostructures have been widely used for heterogeneous photocatalysis due to its low cost, chemical stability, abundancy and high photocatalytic activity. However, TiO$_2$ cannot utilize incoming visible-NIR light due to its characteristic energy bandgap in the UV spectral region (i.e. 3.20–3.35 eV = 370–387 nm). Hybrid noble metal–semiconductor photocatalysts can overcome this limitation and enable efficient utilization of visible-NIR light by coupling LSPR effects with the electronic bandgap of semiconductor materials. Upon visible-NIR irradiation, conduction electrons in the noble metal nanostructure are excited by LSPR effect. Energized conduction electrons are then transferred to the conduction band of the semiconductor, leaving positive hole carriers on the noble metal.[51]

Positive holes can receive electrons from an electron donor species to boost redox reactions by enabling rapid transfer of charge carriers between the noble metal and semiconductor. This approach extends the light absorption range of the semiconductor beyond its electronic bandgap by the formation of a hybrid heterojunction, enhancing photon-to-electron conversion rates in the photocatalyst systems. The versatility of the non-lithographic approach used in this study allow us to combine Au-nD-PSLs with arbitrary functional substrates. Motivated by this rationale, we decided to integrate Au-nD-PSLs into TiO$_2$-based functional substrates to further enhance the photocatalytic performance of this system by coupling LSPR effects with the electronic bandgap of the underlying substrate. A set of Au-nD-PSLs replicated from MA-NAA$_{Su}$, MA-NAA$_{Ox}$, HA-NAA$_{Ox}$ and MA-NAA$_{Ph}$ templates were fabricated on TiO$_2$-coated PDMS substrates. Photodegradation of RhoB molecules was used as a model photocatalytic reaction to identify and quantify enhancements associated with coupling LSPR–semiconductor effects in these hybrid plasmonic–semiconductor structures. TiO$_2$–Au-nD-PSLs feature a top–down structure consisting of arrays of Au nanodots (plasmonic layer), TiO$_2$ film (semiconductor layer), PDMS film (electronic insulating layer) and glass substrate (optically transparent and mechanical support) (Fig. 7a). Fig. 7b depicts transmission spectra in air and water of Au-nD-PSLs and TiO$_2$–Au-nD-PSLs produced from MA-NAA$_{Ox}$ templates, and Fig. S7 (ESI†) compiles all the transmission spectra of the TiO$_2$–Au-nD-PSLs produced in this study. Analysis of the characteristic LSPR band of Au-nD-PSLs and TiO$_2$–Au-nD-PSLs produced from MA-NAA$_{Ox}$ templates indicates that the combination of Au-nD-PSLs with
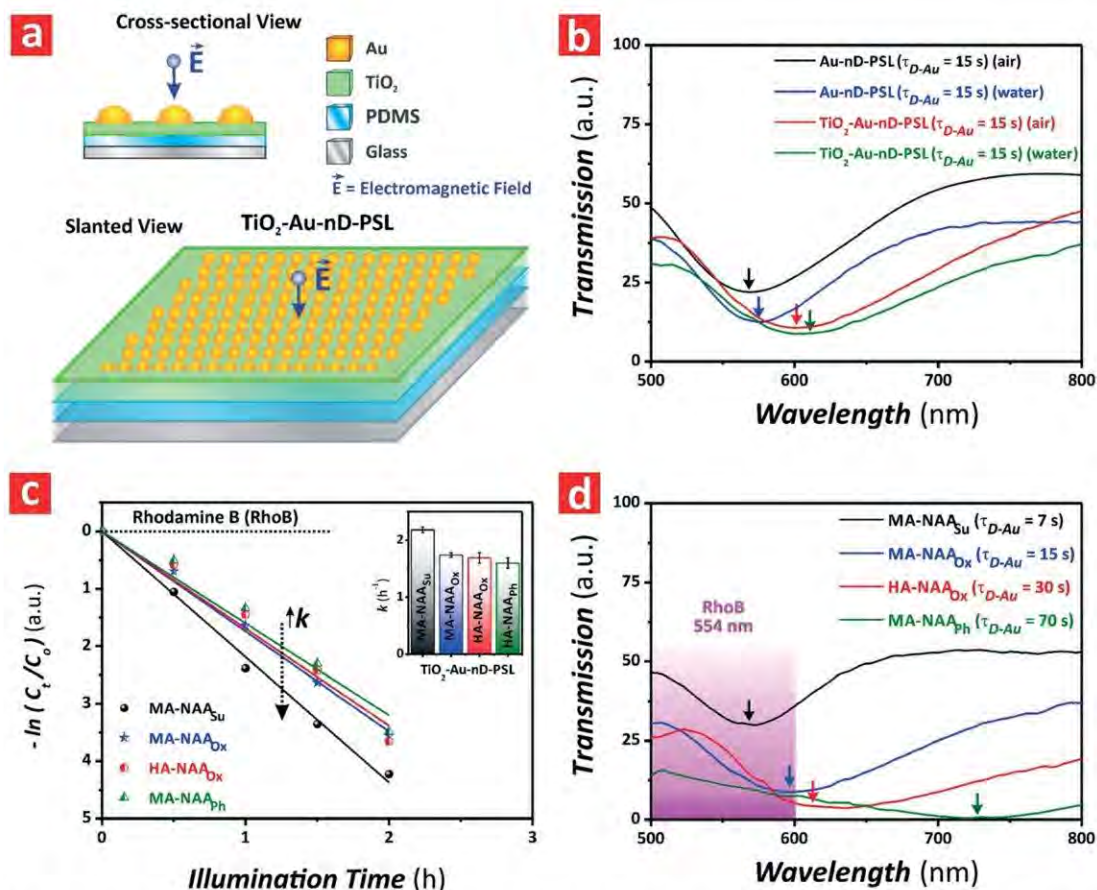
3206 | Catal. Sci. Technol., 2020, 10, 3195–3211

This journal is © The Royal Society of Chemistry 2020

257

Fig. 7 Optical characterization and photocatalytic assessment of TiO_2–Au–nD-PSLs replicated from MA-NAA$_{Su}$, MA-NAA$_{Ox}$, HA-NAA$_{Ox}$ and MA-NAA$_{Ph}$ templates. (a) Schematic showing the structural architecture of TiO_2–Au–nD-PSLs with arrays of Au nanodots (plasmonic layer), TiO_2 film (semiconductor layer), PDMS film (electronic insulating layer) and glass substrate (mechanical support). (b) Transmission spectra of Au-nD-PSLs and TiO_2–Au–nD-PSLs produced with MA-NAA$_{Ox}$ templates in air and water (NB: color arrows denote the approximate position of the central wavelength of the LSPR band). (c) Photocatalytic degradation kinetics of RhoB by TiO_2–Au–nD-PSLs produced with MA-NAA$_{Su}$, MA-NAA$_{Ox}$, HA-NAA$_{Ox}$ and MA-NAA$_{Ph}$ templates under visible-NIR illumination, with bar chart (inset) summarizing the kinetic constant values (k) of this photocatalyst system (NB: horizontal black dotted lines denote control experiments performed with a PDMS-coated glass substrate without TiO_2–Au–nD-PSLs platform and error bars denote standard deviation from average measurements obtained from $n = 3$ independent TiO_2–Au–nD-PSLs). (d) Relative position of the absorbance band of RhoB (shaded pink band) and LSPR band in the transmission spectra of TiO_2–Au–nD-PSLs in water (NB: color arrows denote the approximate position of the central wavelength of the LSPR bands).

a functional TiO_2 layer red-shifts λ_{LSPR} from 579 ± 1 to 614 ± 1 nm, broadens FWHM from 131 ± 13 to 148 ± 15 nm, and reduces I_{LSPR} from 37 ± 4 to 33 ± 3 a.u. in air. Both the red spectral shift and decrease in I_{LSPR} observed in TiO_2–Au–nD-PSLs are attributable to an increase in the refractive index of the underlying substrate (*i.e.* $n_{PDMS} = 1.40$ RIU and $n_{TiO_2} = 2.40$ RIU). The FWHM broadening denotes an extension of the light absorption range of the TiO_2–Au–nD-PSLs system, which is in good agreement with previous studies.[58,59] Upon infiltration with water, λ_{LSPR} red-shifts its position from 614 ± 1 to 616 ± 1 nm, but I_{LSPR} and FWHM remain constant at 33 ± 3 a.u. and 148 ± 15 nm, respectively. Red shifts in the characteristic LSPR band of TiO_2–Au–nD-PSLs are associated with changes in the refractive index of the surrounding medium, from air to water (*i.e.* $n_{air} = 1.00$ RIU and $n_{water} = 1.33$ RIU). Characterization of the optical properties of TiO_2–Au–nD-PSLs in water is critical to understand photocatalytic enhancements in this system since these light-driven

reactions are performed in an aqueous reactant medium. Fig. 7c illustrates the photocatalytic degradation rate of RhoB molecules by TiO_2–Au–nD-PSLs. Photocatalytic rates of these reactions are summarized in the bar chart shown in Fig. 7c (inset) and Table 3. Analysis of these reactions indicates that k decreases with the Au nanodot size. TiO_2–Au–

Table 3 Position of central wavelength of LSPR band (λ_{LSPR}) in water and values of the kinetic constant (k) for the photodegradation of RhoB molecules in TiO_2–Au–nD-PSLs replicated from MA-NAA$_{Su}$, MA-NAA$_{Ox}$, HA-NAA$_{Ox}$ and MA-NAA$_{Ph}$ templates under controlled visible-NIR illumination conditions (NB: errors denote standard deviation from average measurements obtained from $n = 3$ independent Au-nD-PSLs)

Template	λ_{LSPR} (nm)	k_{RhoB} (h^{-1})
MA-NAA$_{Su}$	570 ± 1	2.18 ± 0.05
MA-NAA$_{Ox}$	616 ± 1	1.74 ± 0.04
HA-NAA$_{Ox}$	691 ± 1	1.69 ± 0.09
MA-NAA$_{Ph}$	706 ± 1	1.60 ± 0.09

nD-PSLs featuring d_{dot} = 41 ± 3, 73 ± 12, 210 ± 10 and 428 ± 30 nm achieve photodegradation rates k = 2.18 ± 0.05, 1.74 ± 0.04, 1.69 ± 0.09 and 1.60 ± 0.09 h^{-1}, respectively. So, TiO$_2$–Au-nD-PSLs produced with MA-NAA$_{Su}$ templates achieve ~20–27% photocatalytic enhancement as compared to their counterparts of larger Au nanodot size. The average photocatalytic degradation rate of TiO$_2$-Au-nD-PSLs (k = 1.80 ± 0.26 h^{-1}) is found to be ~19% superior to that achieved by Au-nD-PSLs (k = 1.46 ± 0.16 h^{-1}) for RhoB (Table 2). Fig. 7d illustrates the relative position between the absorbance band of RhoB and the characteristic LSPR band in the transmission spectra of TiO$_2$–Au-nD-PSLs produced with d_{dot} = 41 ± 3, 73 ± 12, 210 ± 10 and 428 ± 30 nm. Analysis of this graph reveals that the λ_{LSPR} of TiO$_2$–Au-nD-PSLs covers more range of the optical absorbance band of RhoB as the Au nanodot size is reduced. As such, TiO$_2$–Au-nD-PSL structures replicated from MA-NAA$_{Su}$ provide a more suitable optical alignment between absorbance band of model organic and LSPR band of photocatalyst platform. Therefore, our results demonstrate that a smart combination of opto-electronic features (i.e. semiconductor properties of the underlying substrate, and relative position between LSPR band and absorbance band of model organic) is an optimal strategy to further enhance photon-to-electron conversion rates in visible-NIR light-driven photocatalysis.

Effect of type of noble metal and reusability assessment of Au-nD-PSLs

A set of silver-based nanodot plasmonic single-lattices (Ag-nD-PSLs) was fabricated to further demonstrate the versatility of this non-lithographic approach, assessing their photocatalytic performance through the visible-NIR light-driven degradation of RhoB molecules. Ag-nD-PSLs were produced from HA-NAA$_{Ox}$ templates following the outlined protocol used to fabricate Au-nD-PSLs (vide supra). A comparison of the photocatalytic rates achieved by Au-nD-PSLs and Ag-nD-PSLs to degrade RhoB molecules is summarized in Fig. 8a and Table 4. These results reveal that Au-nD-PSLs achieve higher k than Ag-nD-PSLs, with a ~34% superior photodegradation rate (i.e. 1.43 ± 0.08 and 0.95 ± 0.06 h^{-1}, respectively). The LSPR band in Ag-nD-PSLs (λ_{LSPR} = 623 ± 1 nm) is blue-shifted with respect to their Au-based counterparts (λ_{LSPR} = 638 ± 1 nm). Fig. 8b depicts the optical arrangement between the characteristic LSPR bands of Au-nD-PSLs and Ag-nD-PSLs and the absorbance band of RhoB. Although the LSPR band of Ag-nD-PSLs is closer to the maximum absorption of RhoB molecules (λ_{RhoB} = 554 nm) and Ag generates stronger LSPR effects than Au, Au-nD-PSLs can degrade RhoB molecules more efficiently. The higher photocatalytic performance of Au-nD-PSLs is attributed to the superior chemical stability of Au over Ag, which protects Au-nD-PSLs against surface oxidation in aqueous environment (i.e. reaction medium).[55] Reusability is also critical in the development of photocatalyst materials for real-life applications. This was assessed by analyzing
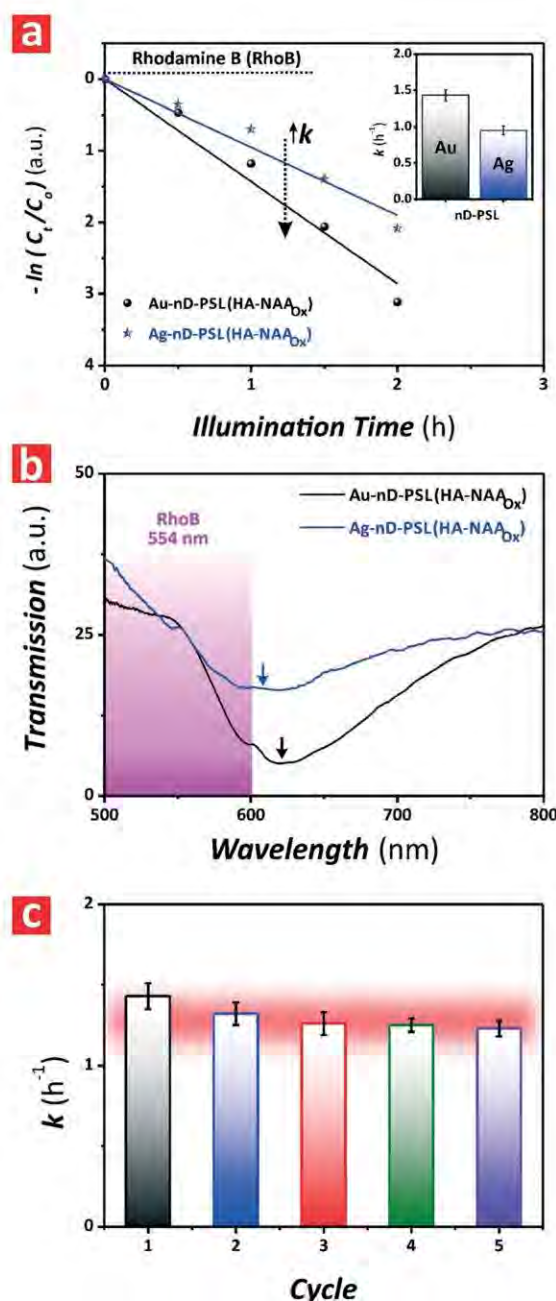
Fig. 8 Effect of type of noble metal and reusability of Au-nD-PSLs. (a) Photocatalytic degradation kinetics of RhoB by Au-nD-PSLs and Ag-nD-PSLs produced with HA-NAA$_{Ox}$ templates under visible-NIR illumination, with bar chart (inset) summarizing the kinetic constant values (k) of these reactions (NB: horizontal black dotted line denotes control experiment performed with a PDMS-coated glass substrate without photocatalyst platform and errors denote standard deviation from average measurements obtained from n = 3 independent Au-nD-PSLs and Ag-nD-PSLs). (b) Relative position of absorbance band of RhoB (shaded pink band) and LSPR band in the transmission spectra of Au-nD-PSLs and Ag-nD-PSLs in water (NB: color arrows denote the approximate position of the central wavelength of the LSPR bands). (c) Assessment of reusability of Au-nD-PSLs produced with HA-NAA$_{Ox}$ templates for photodegradation of RhoB under visible-NIR illumination for five cycles (errors denote standard deviation from average measurements obtained from n = 3 independent Au-nD-PSLs).

3208 | Catal. Sci. Technol., 2020, 10, 3195–3211

This journal is © The Royal Society of Chemistry 2020

259

Table 4 Position of central wavelength of LSPR band (λ_{LSPR}) and values of the kinetic constant (k) for the photodegradation of RhoB molecules in Au-nD-PSLs and Ag-nD-PSLs replicated from HA-NAA$_{Ox}$ templates under controlled visible-NIR illumination conditions (NB: errors denote standard deviation from average measurements obtained from n = 3 independent Au-nD-PSLs and Ag-nD-PSLs)

Template	Single-lattice	λ_{LSPR} (nm)	k_{RhoB} (h^{-1})
HA-NAA$_{Ox}$	Au-nD-PSLs	638 ± 1	1.43 ± 0.08
HA-NAA$_{Ox}$	Ag-nD-PSLs	623 ± 1	0.95 ± 0.06

Table 5 Kinetic constant (k) for the photocatalytic degradation of MB molecules by various benchmark photocatalyst materials

Photocatalyst platform	k_{MB} (h^{-1})	Ref.
P25 TiO$_2$ nanoparticles	0.64	60
Au/P25 TiO$_2$ nanoparticles	0.84	60
Au–TiO$_2$ nanocups	1.33	61
Au–TiO$_2$ nanocrystals	3.00	59
Au-Mesoporous TiO$_2$	1.20	60
Au-nD-PSLs	7.48	This study

photodegradation of RhoB molecules in an Au-nD-PSL produced with d_{dot} = 210 ± 10 nm for five consecutive cycles for 2 h, using fresh organic solution after each photocatalytic cycle. Fig. 8c shows that the photodegradation rate of RhoB by Au-nD-PSLs after five cycles decreases slightly from cycle 1 to cycle 5, with k varying from 1.43 ± 0.08 to 1.23 ± 0.05 h^{-1}, respectively. However, Au-nD-PSLs provide a significantly stable average k of 1.30 ± 0.08 h^{-1}, with a conversion ratio of 93 ± 14% for RhoB molecules (Table S3 – ESI†). These results demonstrate that Au-nD-PSLs possess outstanding photocatalytic activity, chemical stability and ability to be used for several cycles without compromising photocatalytic performance. Reusability of photocatalyst platforms is critical to minimize running costs in real-life processes, and to facilitate the adoption and deployment of this technology in real-life scenarios.

Photocatalytic degradation mechanism in Au-nD-PSLs

A photocatalytic degradation mechanism for visible-NIR light-driven photocatalytic reactions in Au-nD-PSLs would involve concentration of incoming photons into small volumes around Au nanodot structures. Enhanced intensity of the electromagnetic field around their structure in the form of hot spots drives the generation of charge carriers, thermal effects by increasing the temperature of the reactant solution and excited carriers of inter-band transition. Absorbed organic molecules on the surface of Au nanodots are degraded to CO$_2$ and H$_2$O by photo-generated e$^-$/h$^+$ pairs.[55] H$_2$O$_2$ molecules in the reactant solution interact with hot electrons generated on the surface of Au nanodots, producing ˙OH radicals and OH$^-$ ions. OH$^-$ ions are further oxidized into ˙OH radicals by positively charged holes, which can also degrade organic molecules to CO$_2$ and H$_2$O. Our findings indicate that photocatalytic enhancements in Au-nD-PSLs under visible-NIR irradiation rely strongly on the optical alignment between the LSPR band of these plasmonic structures and the absorbance band of model organics. Tailored LSPR effects boost photocatalytic reactions by an efficient utilization of incoming photons from high irradiance spectral regions. The geometric features of Au nanodots, electronic properties of the underlying functional substrate and the nature of the organic molecules all impact on the overall photocatalytic performance of Au-nD-PSL platforms. FDTD simulations and experimental observations

demonstrate that Au nanodots collect and concentrate incident visible-NIR photons efficiently and the performance of Au-nD-PSLs can be further enhanced by coupling LSPR effects with the electronic bandgap of semiconductor substrates. This approach makes it possible to extend the optical absorption range of the semiconductor toward high irradiance spectral regions. Positively charged molecules can be degraded more efficiently by Au-nD-PSLs due to electrostatic affinity with the negatively charged surfaces of Au nanodots. Au nanodot arrays were also found to perform better than their silver-based counterparts due to higher chemical stability against surface oxidation in aqueous medium. Au-nD-PSLs also provide photostability to be used for several cycles without compromising their performance.

Benchmarking of Au-nD-PSLs

Table 5 provides a comparative summary of the photodegradation rates of MB under visible light illumination by several benchmark nanoparticle-based plasmonic photocatalysts. Au-nD-PSLs outperform P25 TiO$_2$ nanoparticles – benchmark photocatalyst material – with a ~91% superior photodegradation rate for MB under visible light illumination conditions. Hybrid systems combining different forms of TiO$_2$ with noble metals have been demonstrated to improve the photocatalyst activity of TiO$_2$. However, this comparison demonstrates that Au-nD-PSLs provide a ~82–89% superior performance than hybrid Au–TiO$_2$ nanoparticulate systems such as Au/P25 TiO$_2$,[60] Au–TiO$_2$ nanocups,[61] Au–TiO$_2$ nanocrystals[59] and Au-mesoporous TiO$_2$.[60] Photocatalytic performance enhancements in Au-nD-PSLs are attributed to efficient collection and strong confinement of incident photons from high irradiance spectral regions, which can be readily tuned to maximize photon-to-electron conversion rates within a broad spectral range.

Conclusions

We have demonstrated a novel and versatile non-lithographic nanofabrication approach to produce noble metal-based plasmonic single-lattice structures with tailor-engineered geometric features (i.e. diameter ~40–430 nm, lattice constant ~60–550 nm and height ~20–215 nm) for visible-NIR light-driven photocatalysis. Au-nD-PSLs exhibited well-resolved localized surface plasmon resonances, which were

shown to be precisely tuned across the visible spectral region through structural engineering. Theoretical modelling and experimental observations demonstrated that LSPR effects in Au-nD-PSLs originate from strongly localized concentrations of electric field on Au nanodots upon visible-NIR illumination. The photocatalytic capability of Au-nD-PSLs was assessed *via* the photodegradation rate of model organics (*i.e.* MB, RhoB and MO), which was used as a reference parameter to identify enhancements associated with LSPR effects. Au-nD-PSLs are demonstrated to be highly efficient photocatalyst platforms, degrading model organic dyes at high rates (*i.e.* k_{MB} = 7.48 h^{-1}, k_{RhoB} = 1.60 h^{-1} and k_{MO} = 0.82 h^{-1}) as compared to other benchmark photocatalysts. Our findings indicate that the geometric features of Au nanodots, the electronic properties of the underlying functional substrate and the nature of the organic molecules are contributing factors to the overall photocatalytic performance of Au-nD-PSL platforms. Theoretical predictions and experimental observations demonstrate that the optical alignment of LSPR bands of Au-nD-PSLs and absorbance bands of model organics is critical to enhance photocatalytic efficiency. Our study also demonstrates that performance of Au-nD-PSLs can be further increased by coupling LSPR effects with the electronic bandgap of semiconductor substrates, which enables extension of the optical absorption range of the semiconductor over high irradiance spectral regions. Au-nD-PSLs degrade more efficiently positively charged molecules due to electrostatic affinity between organic molecules and the surfaces of Au nanodots. This non-lithographic approach has also been shown to readily produce plasmonic single-lattices of distinct noble metals, and Au-nD-PSLs can be reused for several photocatalytic cycles without compromising their performance. This study thus provides new opportunities to rationally design and engineering advanced platform materials for a broad range of plasmonic and photonic applications, using a fully scalable, cost-competitive and reproducible non-lithographic nanofabrication approach.

Conflicts of interest

Authors have no conflict of interest to declare.

Acknowledgements

References

1 M. A. Fox and M. T. Dulay, *Chem. Rev.*, 1993, **93**, 341–357.
2 Z. Zou, J. Ye, K. Sayama and H. Arakawa, *Nature*, 2001, **414**, 625–627.
3 X. Zheng, S. Meng, J. Chen, J. Wang, J. Xian, Y. Shao, X. Fu and D. Li, *J. Phys. Chem. C*, 2013, **117**, 21263–21273.
4 S. Y. Lim, C. S. Law, M. Markovic, J. K. Kirby, A. D. Abell and A. Santos, *ACS Appl. Mater. Interfaces*, 2018, **10**, 24124–24136.
5 S. Y. Lim, C. S. Law, M. Markovic, L. F. Marsal, N. H. Voelcker, A. D. Abell and A. Santos, *ACS Appl. Energy Mater.*, 2019, **2**, 1169–1184.
6 S. Y. Lim, C. S. Law, L. Liu, M. Markovic, A. D. Abell and A. Santos, *Catal. Sci. Technol.*, 2019, **9**, 3158–3176.
7 K.-H. Chen, Y.-C. Pu, K.-D. Chang, Y.-F. Liang, C.-M. Liu, J.-W. Yeh, H.-C. Shih and Y.-J. Hsu, *J. Phys. Chem. C*, 2012, **116**, 19039–19045.
8 Z.-C. Wu, Y. Zhang, T.-X. Tao, L. Zhang and H. Fong, *Appl. Surf. Sci.*, 2010, **257**, 1092–1097.
9 S. Zhao, Z. Qu, N. Yan, Z. Li, W. Zhu, J. Pan, J. Xu and M. Li, *RSC Adv.*, 2015, **5**, 30841–30845.
10 H. J. Kim, S. H. Lee, A. A. Upadhye, I. Ro, M. I. Tejedor-Tejedor, M. A. Anderson, W. B. Kim and G. W. Huber, *ACS Nano*, 2014, **8**, 10756–10765.
11 M. Zhou, J. Bao, Y. Xu, J. Zhang, J. Xie, M. Guan, C. Wang, L. Wen, Y. Lei and Y. Xie, *ACS Nano*, 2014, **8**, 7088–7098.
12 K. Kim, P. Thiyagarajan, H.-J. Ahn, S.-I. Kim and J.-H. Jang, *Nanoscale*, 2013, **5**, 6254–6260.
13 J. Yang, Y. Guo, R. Jiang, F. Qin, H. Zhang, W. Lu, J. Wang and J. C. Yu, *J. Am. Chem. Soc.*, 2018, **140**, 8497–8508.
14 W. Hou, W. H. Hung, P. Pavaskar, A. Goeppert, M. Aykol and S. B. Cronin, *ACS Catal.*, 2011, **1**, 929–936.
15 J. Jiao, Y. Wei, K. Chi, Z. Zhao, A. Duan, J. Liu, G. Jiang, Y. Wang, X. Wang, C. Han and P. Zheng, *Energy Technol.*, 2017, **5**, 877–883.
16 G. L. Hallett-Tapley, M. J. Silvero, M. González-Béjar, M. Grenier, J. C. Netto-Ferreira and J. C. Scaiano, *J. Phys. Chem. C*, 2011, **115**, 10784–10790.
17 X. G. Zhang, Z. B. Ke and H. Y. Zhu, *Chem. – Eur. J.*, 2012, **18**, 8048–8056.
18 H. Y. Zhu, X. B. Ke, X. Z. Yang, S. Sarina and H. W. Liu, *Angew. Chem., Int. Ed.*, 2010, **49**, 9657–9661.
19 T. Jensen, L. Kelly, A. Lazarides and G. C. Schatz, *J. Cluster Sci.*, 1999, **10**, 295–317.
20 K. L. Kelly, E. Coronado, L. L. Zhao and G. C. Schatz, *J. Phys. Chem. B*, 2003, **107**, 668–677.
21 S. A. Maier, *Plasmonics: Fundamentals and Applications*, Springer Science+Business Media LLC, Spring Street, NY, USA 2007.
22 M. Pelton and G. Bryant, *Introduction to Metal-Nanoparticle Plasmonics*, John Wiley & Sons, Hoboken, NJ, USA 2013.
23 G. V. Hartland, L. V. Besteiro, P. Johns and A. O. Govorov, *ACS Energy Lett.*, 2017, **2**, 1641–1653.

3210 | *Catal. Sci. Technol.*, 2020, **10**, 3195–3211

This journal is © The Royal Society of Chemistry 2020

24 P. K. Jain, K. S. Lee, I. H. El-Sayed and M. A. El-Sayed, *J. Phys. Chem. B*, 2006, **110**, 7238–7248.

25 H. J. Chen, X. S. Kou, Z. Yang, W. H. Ni and J. F. Wang, *Langmuir*, 2008, **24**, 5233–5237.

26 K. L. Kelly, E. Coronado, L. L. Zhao and G. C. Schatz, *J. Phys. Chem. B*, 2003, **107**, 668–677.

27 T. D. Phuc, M. Yoshino, A. Yamanaka and T. Yamamoto, *Int. J. Autom. Technol.*, 2014, **8**, 74–82.

28 M. Bundschuh, J. Filser, S. Lüderwald, M. S. McKee, G. Metreveli, G. E. Schaumann, R. Schulz and S. Wagner, *Environ. Sci. Eur.*, 2018, **30**, 6.

29 D. Wang, A. Yang, W. Wang, Y. Hua, R. D. Schaller, G. C. Schatz and T. W. Odom, *Nat. Nanotechnol.*, 2017, **12**, 889–894.

30 K. Volk, J. P. S. Fitzgerald, P. Ruckdeschel, M. Retsch, T. A. F. König and M. Karg, *Adv. Opt. Mater.*, 2017, **5**, 1600971.

31 C. Hanske, M. Tebbe, C. Kuttner, V. Bieber, V. V. Tsukruk, M. Chanana, T. A. F. König and A. Fery, *Nano Lett.*, 2014, **14**, 6863–6871.

32 H. Cha, J. H. Yoon and S. Yoon, *ACS Nano*, 2014, **8**, 8554–8563.

33 A. Yang, T. B. Hoang, M. Dridi, C. Deeb, M. H. Mikkelsen, G. C. Schatz and T. W. Odom, *Nat. Commun.*, 2015, **6**, 6939.

34 C. L. Haynes and R. P. Van Duyne, *J. Phys. Chem. B*, 2001, **105**, 5599–5611.

35 T. R. Jensen, M. D. Malinsky, C. L. Haynes and R. P. Van Duyne, *J. Phys. Chem. B*, 2000, **104**, 10549–10556.

36 J. C. Hulteen, D. A. Treichel, M. T. Smith, M. L. Duval, T. R. Jensen and R. P. Van Duyne, *J. Phys. Chem. B*, 1999, **103**, 3854–3863.

37 S. Y. Chou, P. R. Krauss and P. J. Renstrom, *Appl. Phys. Lett.*, 1995, **67**, 3114–3116.

38 C. H. Yao, H. Y. Hsiung and C. K. Sung, *Microelectron. Eng.*, 2009, **86**, 665–668.

39 T. Akahane, M. Huda, T. Tamura, Y. Yin and S. Hosaka, *Jpn. J. Appl. Phys.*, 2011, **50**, 06GG04-1.

40 S. Strobel, C. Kirkendall, J. B. Chang and K. K. Berggren, *Nanotechnology*, 2010, **21**, 505301.

41 C. Matricardi, C. Hanske, J. L. Garcia-Pomar, J. Langer, A. Mihi and L. M. Liz-Marzán, *ACS Nano*, 2018, **12**, 8531–8539.

42 W. Lee and S.-J. Park, *Chem. Rev.*, 2014, **114**, 7487–7556.

43 A. Santos, *J. Mater. Chem. C*, 2017, **5**, 5581–5599.

44 H. Masuda and K. Fukuda, *Science*, 1995, **268**, 1466–1468.

45 H. Ikeda, M. Iwai, D. Nakajima, T. Kikuchi, S. Natsui, N. Sakaguchi and R. O. Suzuki, *Appl. Surf. Sci.*, 2019, **465**, 747–753.

46 X. Shi, K. Ueno, N. Takayabashi and H. Misawa, *J. Phys. Chem. C*, 2012, **117**, 2494–2499.

47 T. Lee, J. Jang, H. Jeong and J. Rho, *Nano Convergence*, 2018, **5**, 1.

48 E. C. Dreaden, A. M. Alkilany, X. Huang, C. J. Murphy and M. A. El-Sayed, *Chem. Soc. Rev.*, 2012, **41**, 2740–2779.

49 H. Masuda, M. Ohya, H. Asoh, M. Nakao, M. Nohtomi and T. Tamamura, *Jpn. J. Appl. Phys.*, 1999, **38**, L1403.

50 N. Wu, *Nanoscale*, 2018, **10**, 2679–2696.

51 S. Sarina, E. R. Waclawik and H. Zhu, *Green Chem.*, 2013, **15**, 1814–1833.

52 E. Csapó, D. Sebők, J. M. Babić, F. Šupljika, G. Bohus, I. Dékány, N. Kallay and T. Preočanin, *J. Dispersion Sci. Technol.*, 2014, **35**, 815–825.

53 M. F. Cuddy, A. R. Poda and L. N. Brantley, *ACS Appl. Mater. Interfaces*, 2013, **5**, 3514–3518.

54 Y.-H. Chiu, T.-F. M. Chang, C.-Y. Chen, M. Sone and Y.-J. Hsu, *Catalysts*, 2019, **9**, 430.

55 C. Wang and D. Astruc, *Chem. Soc. Rev.*, 2014, **43**, 7188–7216.

56 X. Chen, H. Y. Zhu, J. C. Zhao, Z. F. Zheng and X. P. Gao, *Angew. Chem., Int. Ed.*, 2008, **47**, 5353–5356.

57 X. Chen, Z. F. Zheng, X. B. Ke, E. Jaatinen, T. F. Xie, D. J. Wang, C. Guo, J. C. Zhao and H. Y. Zhu, *Green Chem.*, 2010, **12**, 414–419.

58 Y. Lu, H. Yu, S. Chen, X. Quan and H. Zhao, *Environ. Sci. Technol.*, 2012, **46**, 1724–1730.

59 S. Zhu, S. Liang, Q. Gu, L. Xie, J. Wang, Z. Ding and P. Liu, *Appl. Catal., B*, 2012, **119**, 146–155.

60 Z. Bian, T. Tachikawa, P. Zhang, M. Fujitsuka and T. Majima, *J. Am. Chem. Soc.*, 2014, **136**, 458–465.

61 J. Lu, P. Zhang, A. Li, F. Su, T. Wang, Y. Liu and J. Gong, *Chem. Commun.*, 2013, **49**, 5817–5819.

This journal is © The Royal Society of Chemistry 2020

Catal. Sci. Technol., 2020, **10**, 3195–3211 | **3211**

Electronic Supplementary Information

Tailor-Engineered Plasmonic Single-Lattices: Harnessing Localized Surface Plasmon Resonances for Visible–NIR Light-Enhanced Photocatalysis

Siew Yee Lim[1,2,3], Cheryl Suwen Law[1,2,3], Francesc Bertó-Roselló[4], Lina Liu[1,5,6], Marijana Markovic[1,7], Josep Ferré-Borrull[*4], Andrew D. Abell[*2,3,8], Nicolas H. Voelcker[*9,10,11,12], Lluís F. Marsal[*4] and Abel Santos[*1,2,3]

[1]School of Chemical Engineering and Advanced Materials, The University of Adelaide, Adelaide, South Australia 5005, Australia
[2]Institute for Photonics and Advanced Sensing, The University of Adelaide, Adelaide, South Australia 5005, Australia
[3]ARC Centre of Excellence for Nanoscale BioPhotonics, The University of Adelaide, Adelaide, South Australia 5005, Australia
[4]Department of Electronic, Electric, and Automatics Engineering, University Rovira i Virgili, Tarragona 43007, Spain
[5]State Key Laboratory of High-efficiency Utilization of Coal and Green Chemical Engineering, Ningxia University, Yinchuan 750021, P.R. China
[6]College of Chemistry and Chemical Engineering, Ningxia University, Yinchuan 750021, P. R. China
[7]School of Agriculture Food and Wine, The University of Adelaide, South Australia 5064, Australia
[8]Department of Chemistry, The University of Adelaide, South Australia 5005 Adelaide, Australia
[9]Melbourne Centre for Nanofabrication, Victorian Node of the Australian National Fabrication Facility, Monash University, Victoria 3168, Australia
[10]Monash Institute of Pharmaceutical Sciences, Monash University, Victoria 3052, Australia
[11]Commonwealth Scientific and Industrial Research Organisation (CSIRO), Victoria 3168, Australia
[12]INM-Leibniz Institute for New Materials, Campus D2 2, Saarbrücken 66123, Germany

*E-Mails: andrew.abell@adelaide.edu.au ; nicolas.voelcker@monash.edu ; lluis.marsal@urv.cat ; abel.santos@adelaide.edu.au

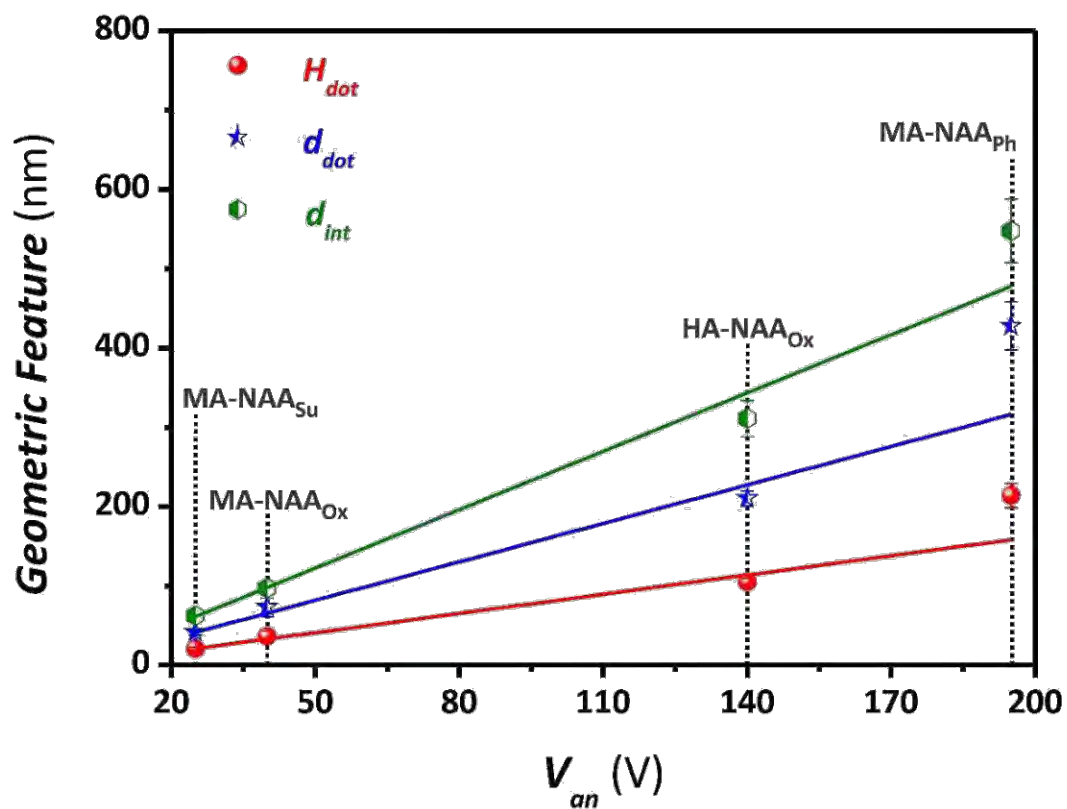**Figure S1.** Linear correlation between Au-nD-PSLs geometric features (d_{int}, d_{dot} and H_{dot}) and anodization voltage (V_{an} = 25, 40, 140 and 195 V).
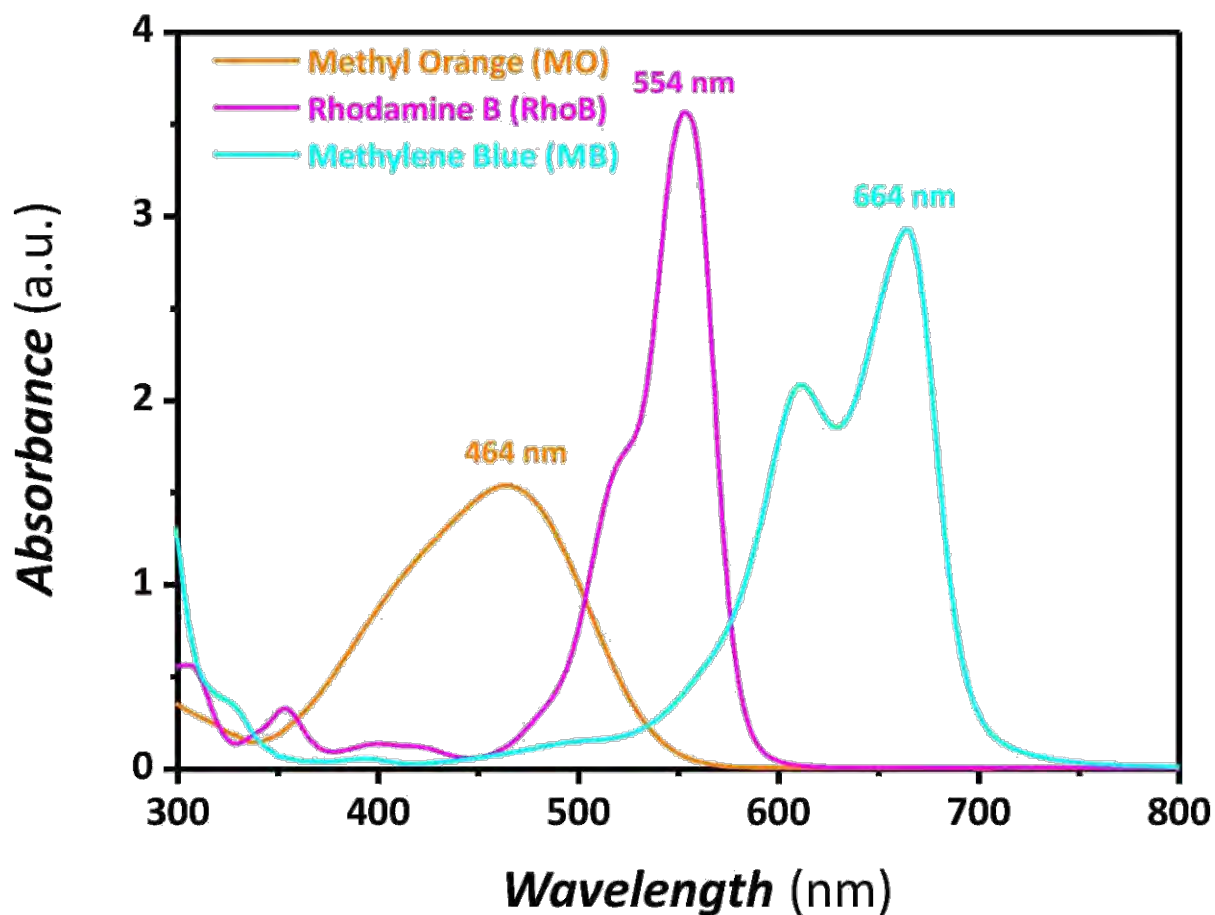
Figure S2. Absorption spectra of methylene blue (MB), rhodamine B (RhoB) and methyl orange (MO), with absorption band maxima at $\lambda_{Abs\text{-}MO}$ = 464 nm, $\lambda_{Abs\text{-}RhoB}$ = 554 nm and $\lambda_{Abs\text{-}MB}$ = 664 nm, respectively (NB: [organic] = 5 mg L^{-1}).
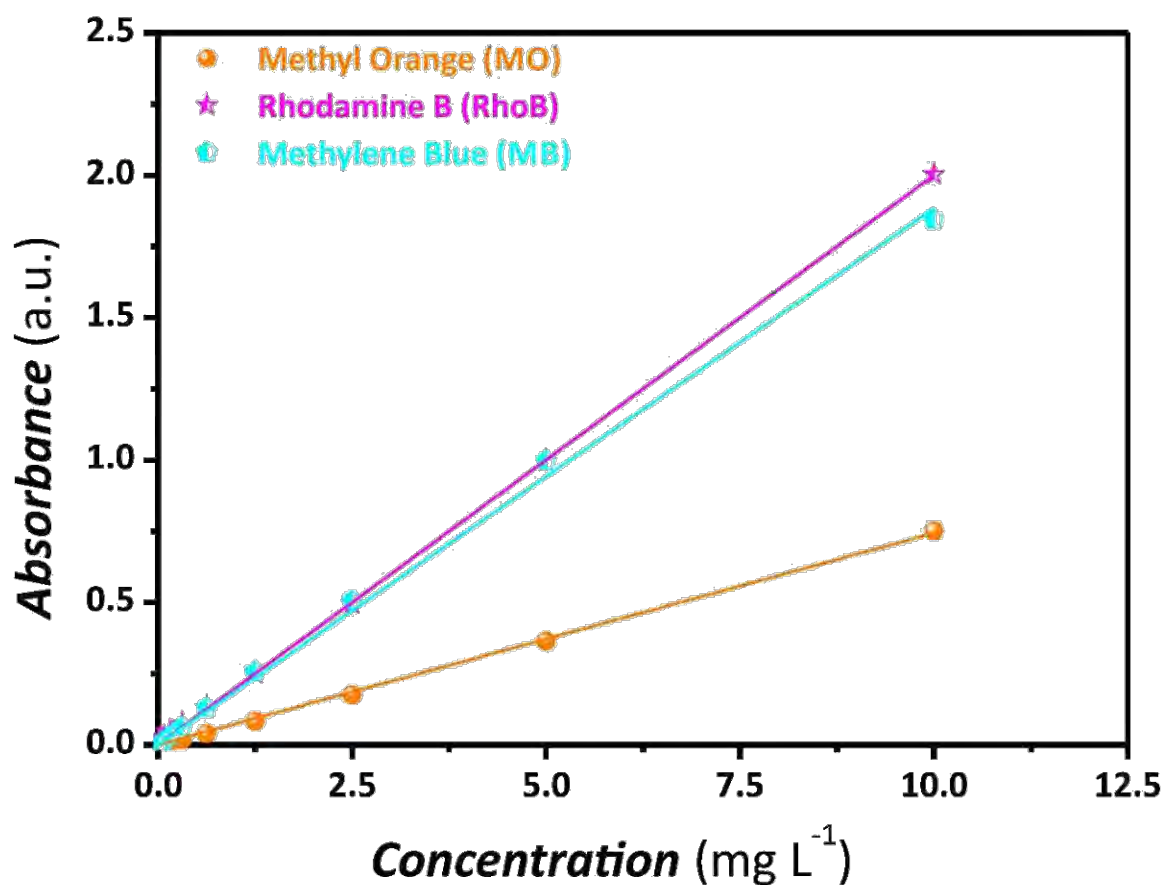
Figure S3. Linear correlation between optical absorbance and concentration of methylene blue (MB), rhodamine B (RhoB) and methyl orange (MO) (NB: concentration range from 0.00244 to 10 mg L^{-1}). The fitting lines for MB, RhoB and MO were: Abs_{MB} (a.u.) = 0.18832 $[MB]$ (mg L^{-1}), Abs_{RhoB} (a.u.) = 0.19998 $[RhoB]$ (mg L^{-1}) and Abs_{MO} (a.u.) = 0.07436 $[MO]$ (mg L^{-1}), respectively. R^2 values for MB, RhoB and MO were 0.99852, 0.99979 and 0.99940, respectively.
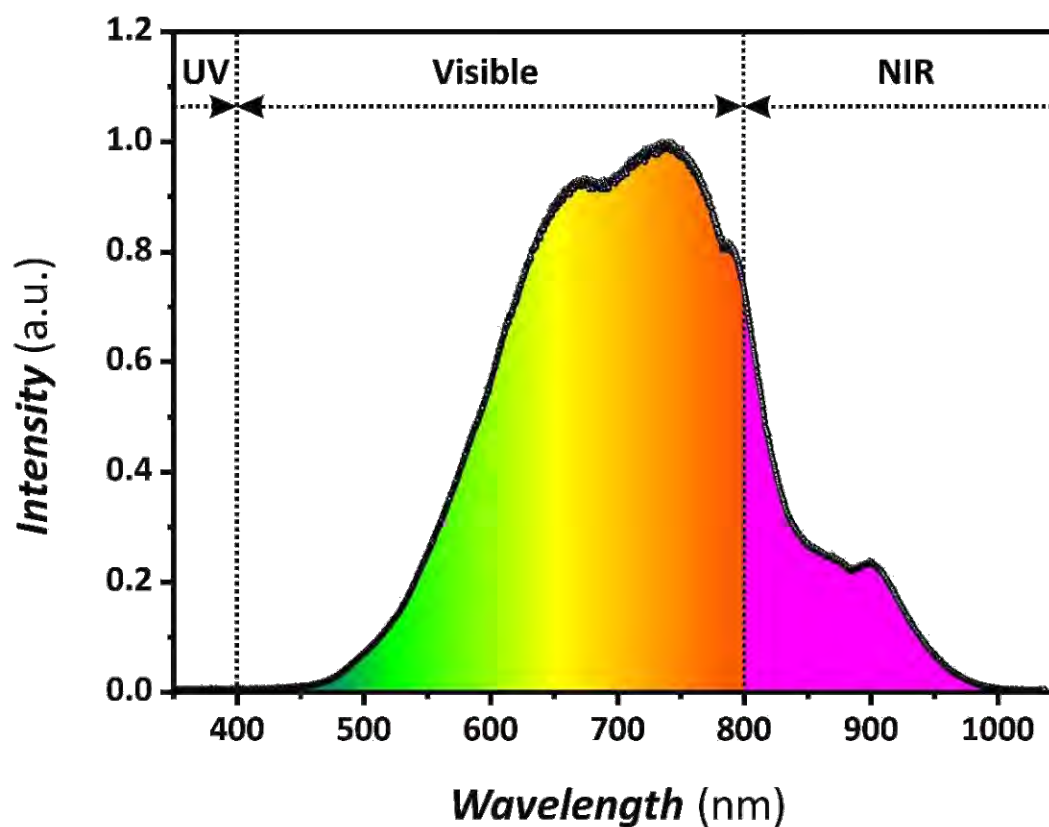
Figure S4. Irradiation spectrum of the simulated solar light irradiation source used in our study (i.e. 0.12% UV, 64.60% visible and 35.28% NIR) for the assessment of the photocatalytic degradation of model organics (NB: spectrum acquired using an optical fiber spectrophotometer USB 4000, Ocean Optics, USA).
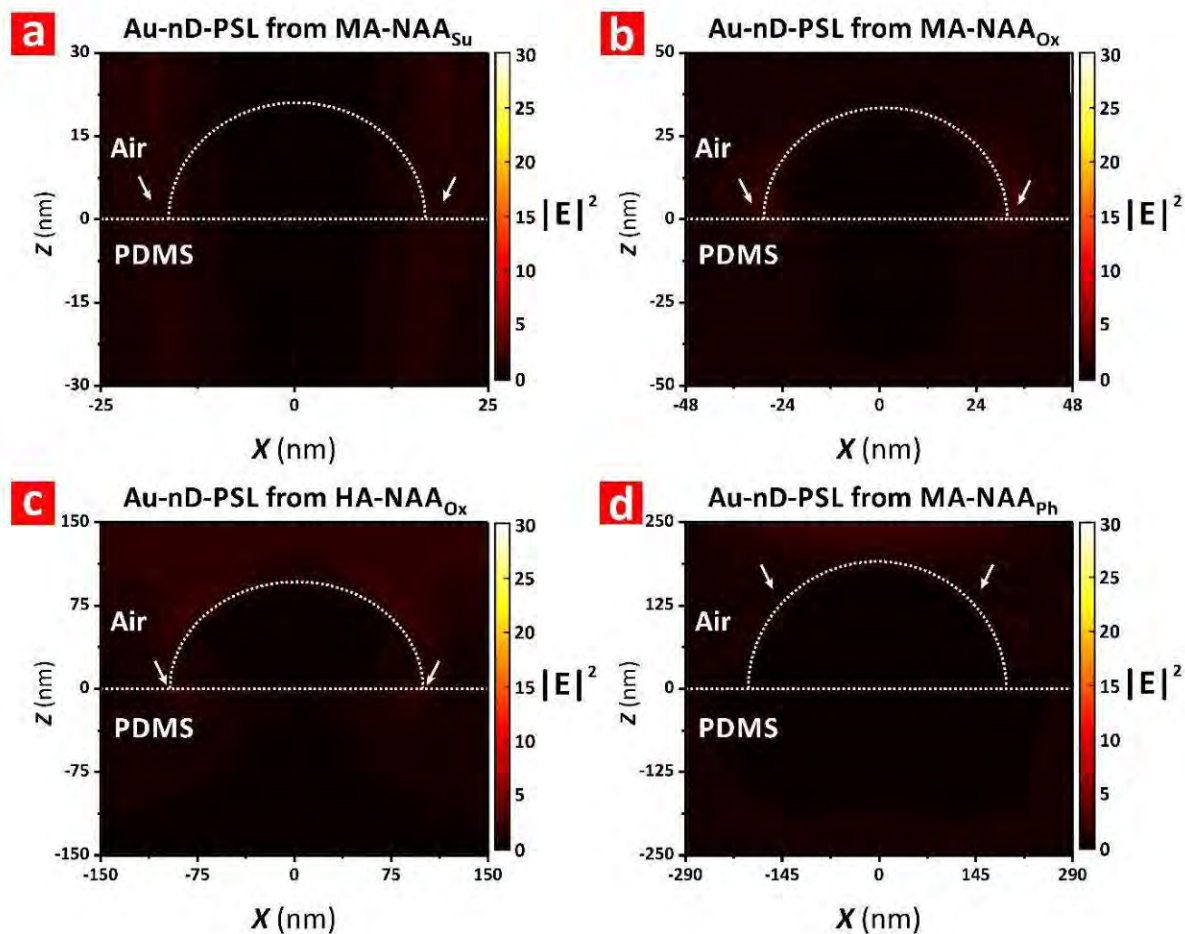
Figure S5. Cross-sectional FDTD electric field intensity ($|E^2|$) distribution profiles at non-resonant wavelengths in Au-nD-PSLs produced with: (a) MA-NAA$_{Su}$, (b) MA-NAA$_{Ox}$, (c) HA-NAA$_{Ox}$ and (d) MA-NAA$_{Ph}$ templates (NB: FDTD simulations were performed considering a PDMS substrate at the bottom of the Au nanodots and air as surrounding medium; white arrows denote sections of maximum field intensity around these plasmonic nanostructures).
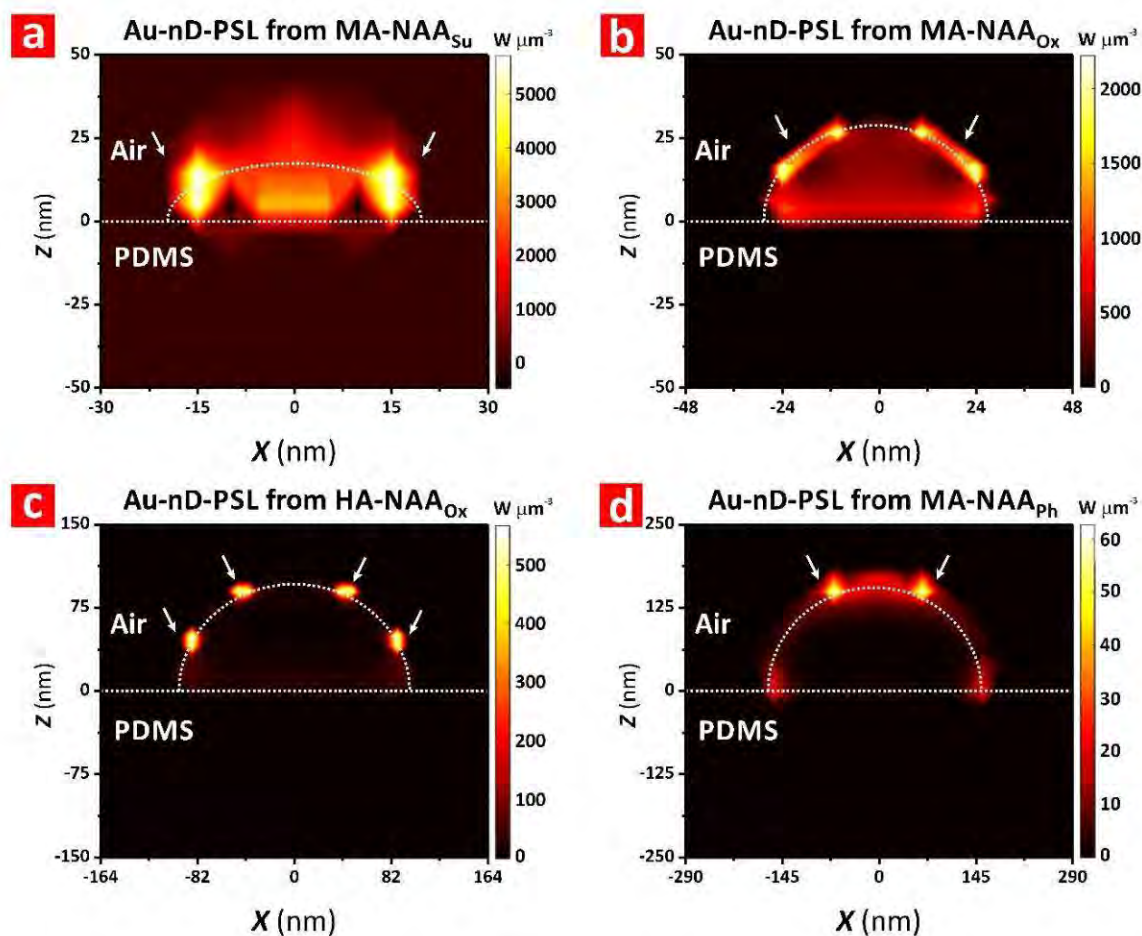
Figure S6. Cross-sectional FDTD optical absorption density distribution profiles in Au-nD-PSLs produced with: (a) MA-NAA$_{Su}$ (λ_{LSPR} = 561 nm), (b) MA-NAA$_{Ox}$ (λ_{LSPR} = 579 nm), (c) HA-NAA$_{Ox}$ (λ_{LSPR} = 627 nm) and (d) MA-NAA$_{Ph}$ (λ_{LSPR} = 618 nm) templates (NB: FDTD simulations were performed considering a PDMS substrate at the bottom of the Au nanodots and air as surrounding medium; white arrows denote sections of maximum field intensity around these plasmonic nanostructures).
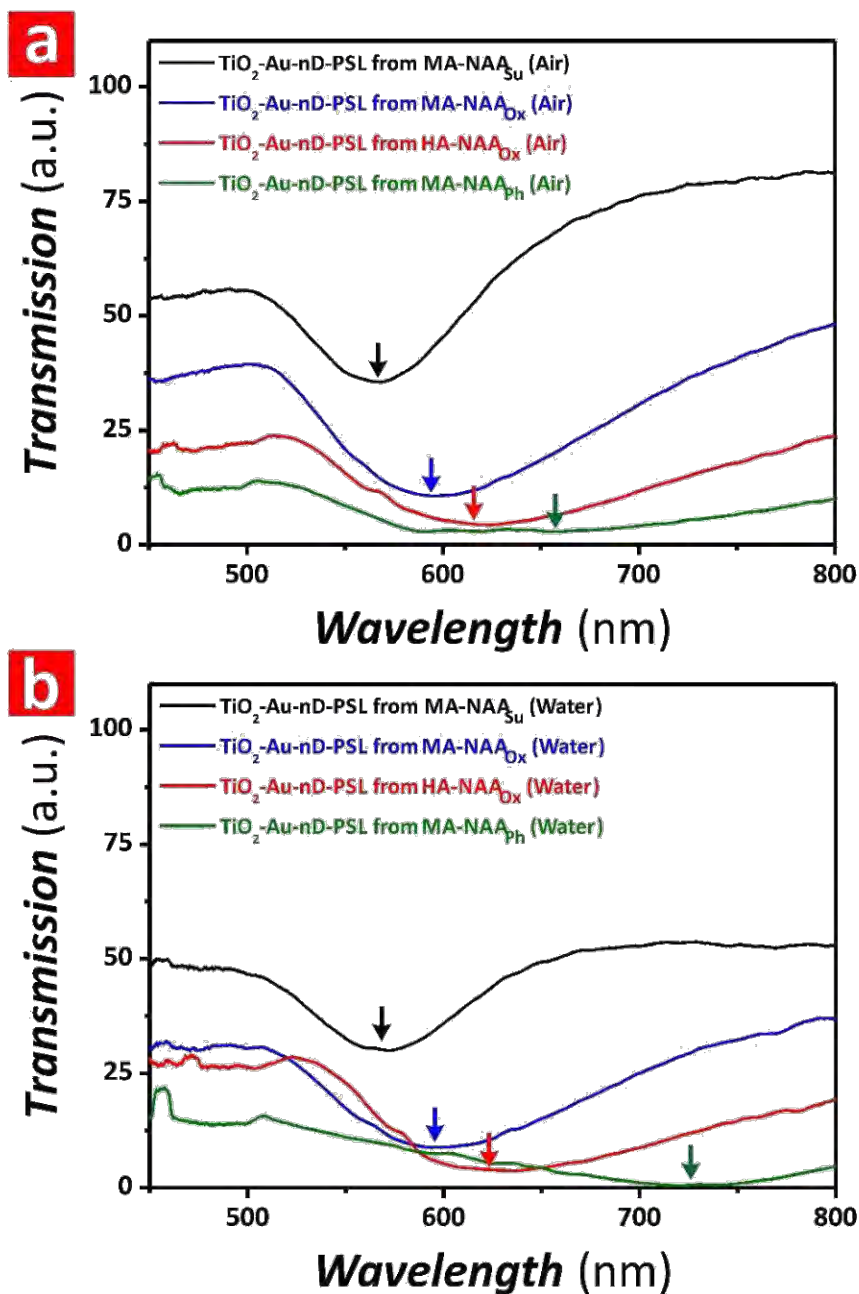
Figure S7. LSPR bands in the transmission spectra of TiO_2-Au-nD-PSLs produced with MA-NAA$_{Su}$, MA-NAA$_{Ox}$, HA-NAA$_{Ox}$ and MA-NAA$_{Ph}$ templates in air (a) and water (b) (NB: color arrows denote the approximate position of the central wavelength of the LSPR bands).

Lumerical Simulations

The modelling and simulations were performed by using a FDTD 3D Electromagnetic Simulator from Lumerical Inc. The optical constants of the specific material components were provided by Lumerical's material database. **Figure S8** illustrates both the computational domain and the unit cell used for the simulations. The computational domain was defined as pictured in **Figure S8a**. The dimensions were d_{int} in the X direction, $\sqrt{3} \cdot d_{int}$ in the Y direction and 106 μm in the Z direction. The plasmonic structure corresponds to a hexagonal unit cell of nanodots in an PDMS matrix, placed at the center of the computational domain reproducing the hexagonal nanodot arrangement (**Figure S8b**). An auto-nonuniform mesh was selected and automatically generated by Lumerical. Subsequently, an additional mesh refinement was incorporated in order to increase the accuracy for the simulation overriding the regions of the nanodots. The size mesh employed for these override regions was of dx = dy = dz = 3.5 nm. The plasmonic structure is periodic in X and Y directions, therefore, in order to increase computational efficiency and optimize memory requirements and computation time, periodic boundary conditions were applied in these directions. For the Z direction, in order to prevent undesirable reflections, perfectly matched layers were implemented. The optical source was an incident plane wave perpendicular to the surface of the structure (XY plane) propagating in the negative Z direction. The range of wavelengths for the optical source was from 400 to 800 nm. The reflection and transmission data were obtained by using two monitors located above and below the structure as depicted in **Figure S8a**.
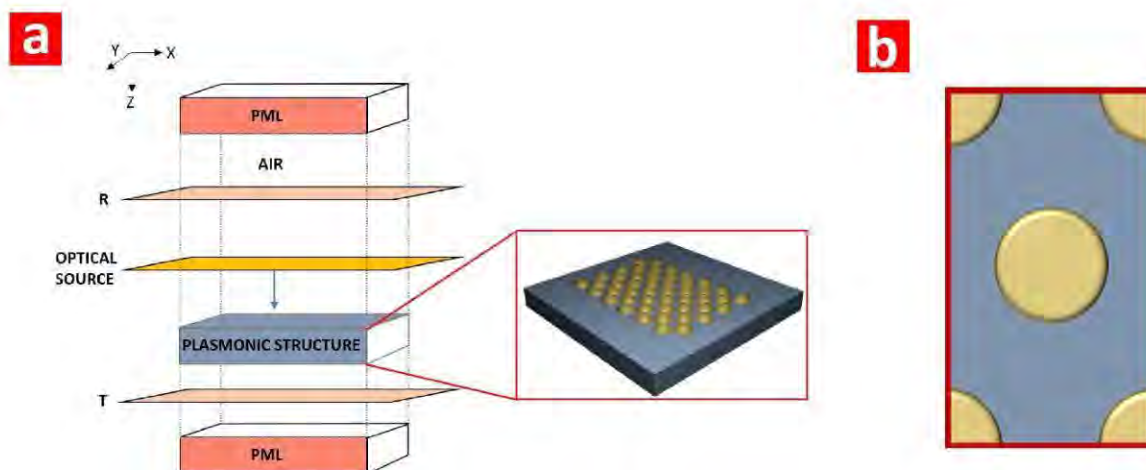

Figure S8. Illustration of the FDTD computational domain used in our study. a) Illustrative view of the computational domain where R designates the reflectance monitor, PML are perfectly matched layers, the plasmonic structure and the source re explicitly indicated. b) XY view of the FDTD unit cell: the red square designates the unit cell in the XY plane and the golden circles denote the Au nanodots.

Table S1. Anodization conditions used to produce MA-NAA$_{Su}$, MA-NAA$_{Ox}$, HA-NAA$_{Ox}$, and MA-NAA$_{Ph}$ templates.

Template	Electrolyte	Anodization Regime	Concentration (M)	Temperature (°C)	Voltage (V)	Time (h)
MA-NAA$_{Su}$	H_2SO_4	MA	0.3	6	25	20
MA-NAA$_{Ox}$	$C_2H_2O_4$	MA	0.3	6	40	20
HA-NAA$_{Ox}$	$C_2H_2O_4$	HA	0.3	0	140	1
MA-NAA$_{Ph}$	H_3PO_4	MA	0.1	−1	195	20

Table S2. Structural tunability of geometric features in Au-nD-PSLs (i.e. nanodot diameter $-d_{dot}$, interdot distance or lattice constant $- d_{int}$ and nanodot height $- H_{dot}$) as a function of the aluminum template and the deposition time (τ_{D-Au} = 7, 15, 30 and 70 s).

Template	τ_{D-Au} (s)	d_{dot} (nm)	d_{int} (nm)	H_{dot} (nm)
MA-NAA$_{Su}$	7	41 ± 3	62 ± 6	21 ± 2
MA-NAA$_{Ox}$	15	73 ± 12	97 ± 8	36 ± 6
HA-NAA$_{Ox}$	30	210 ± 10	311 ± 23	105 ± 5
MA-NAA$_{Ph}$	70	428 ± 30	547 ± 40	214 ± 15

Table S3. Residual concentration from the photodegradation of 5 mg L^{-1} of RhoB molecules by Au-nD-PSLs produced with HA-NAA$_{Ox}$ templates for 2 h after five photocatalytic cycles.

Photocatalytic Cycle	Residual Concentration (mg L^{-1})
1	0.29 ± 0.08
2	0.36 ± 0.07
3	0.40 ± 0.07
4	0.41 ± 0.04
5	0.43 ± 0.05
Average	0.38 ± 0.06
Conversion Ratio (%)	93 ± 14

Movie S1. FDTD electric field intensity ($|E^2|$) distribution profile at resonant wavelengths in Au-nD-PSLs produced with MA-NAA$_{Su}$ (λ_{LSPR} = 561 nm).

Movie S2. FDTD electric field intensity ($|E^2|$) distribution profile at resonant wavelengths in Au-nD-PSLs produced with MA-NAA$_{Ox}$ (λ_{LSPR} = 579 nm).

Movie S3. FDTD electric field intensity ($|E^2|$) distribution profile at resonant wavelengths in Au-nD-PSLs produced with HA-NAA$_{Ox}$ (λ_{LSPR} = 627 nm).

Movie S4. FDTD electric field intensity ($|E^2|$) distribution profile at resonant wavelengths in Au-nD-PSLs produced with MA-NAA$_{Ph}$ (λ_{LSPR} = 618 nm).

Chapter 9

CONCLUSIONS

9. Conclusions

9.1 Conclusions

This thesis presents studies on advancing fundamental and applied knowledge in the structural and optical engineering, chemical functionalisation and application of NAA-PCs for use as inexpensive, highly efficient and sustainable light-harnessing platforms for various photocatalytic applications. Engineering of NAA-PCs with desirable structural, optical and chemical properties is critical to achieve enhanced performances in photocatalytic reactions. The photonic stopbands of these PC structures can be precisely tuned across the spectral regions by structural engineering, while chemical functionalisation with semiconducting oxides or noble metal structures enables the integration and harnessing of distinct forms of light–matter interactions to speed up photocatalytic reactions. This combination of strategies provides new venues for attaining optimal performances by a rational management of photons at the nanoscale. The individual and combined effects of photochemically functional layers on these model composite PC structures allow us to better understand how photocatalytic enhancements can be maximised by efficient utilisation of light–matter interactions. The following sections outline specific conclusions drawn from work presented in this thesis, based on its delivered objectives.

9.1.1. Objective 1

Various anodisation profiles were employed to produce a complete palette of NAA-PC structures with unique optical properties. In Chapter 3, heterogeneous pulse anodisation was explored to fabricate hybrid NAA-PCs (Hy-NAA-PCs) composed of different combinations of distributed Bragg reflectors (DBRs) and apodised gradient-index filters (APO-GIFs) in a single PC structure. Manipulation of anodisation parameters was demonstrated as an effective approach to finely tune the optical properties of Hy-NAA-PCs across the UV–visible–NIR spectrum. In Chapter 4, sinusoidal pulse anodisation under mild conditions was used to produce NAA-GIFs. The selective addition of alcohol type and concentration into the anodising acid electrolyte maximises optical signal intensity and minimises spectral bandwidth of the

characteristic PSB of these PC structures. These are desirable characteristics for many applications including optical sensing, photonics and photocatalysis.

9.1.2. Objectives 2, 3, 4

Light-trapping capabilities of chemically-modified NAA-PCs in enhancing photocatalysis by "slow photon" effect was explored. Well-established fabrication protocols were used to develop a broad palette of NAA-PCs by anodisation of aluminium substrates, including: (i) NAA-GIFs by sinusoidal pulse anodisation (Chapter 5), (ii) NAA-DBR by stepwise pulse anodisation (Chapter 6), and (iii) NAA-DBR by two-step anodisation (Chapter 7). These PC structures were subsequently modified with photoactive layers of titanium dioxide (TiO_2) using the sol-gel method to provide the composite PC structures with essential photocatalytic properties. Enhancements in photocatalytic performance in TiO_2-functionalised NAA-PCs by "slow photon" effect were monitored by studying the photodegradation of model organics with well-defined absorbance bands across different spectral regions, under simulated solar light irradiation conditions. Our studies demonstrate that, when the edges of the characteristic PSB of TiO_2-functionalised NAA-PCs are completely or partially aligned with the absorbance bands of organics, photocatalytic performance is enhanced due to "slow photon" effects. Overall photocatalytic degradation rate is also dependent on the geometric features of the PC structures, charge and photosensitivity of the organic molecules, percentage of visible–NIR irradiation, additive concentrations, matrix complexity and reusability cycles. Chapter 7 presents studies on modification of the top surface of TiO_2-NAA-DBRs with a thin layer of noble metal (i.e. gold – Au) to integrate surface plasmon resonance (SPR) effects with the "slow photon" effect for enhanced photocatalysis. This lead to the conclusion that contribution of SPR to the overall photocatalytic enhancement is weak due to the localised generation of surface plasmons on the top surface of the composite PC structures. Despite this, the overall photocatalytic degradation rate still correlates to the deposition time and type of noble metal coating. In many cases, TiO_2-functionalised NAA-PCs, with and without noble metal coating, show superior performance to benchmark photocatalyst materials. They thus present as promising platforms for many photocatalytic applications. This thesis paves the way for creating

a new generation of photocatalyst platforms with high performance, scalability, versatility and sustainability.

9.1.3. Objective 4

In Chapter 8, a platform material composed of 2D Au nanodot plasmonic single-lattices (Au-nD-PSLs) featuring tailor-engineered geometric features for visible-NIR light-driven enhanced photocatalysis was reported. A strongly localised electromagnetic field around these reusable platform materials was demonstrated to provide outstanding photocatalytic performances, as revealed by finite-difference time-domain (FDTD) simulations and experimental observations. These performances can be significantly enhanced by coupling localised surface plasmon resonance (LSPR) effects with the electronic bandgap of semiconducting oxides such as TiO_2. Au-nD-PSLs also show remarkable photocatalytic degradation rates for model organics when compared to those of conventional nanoparticle-based plasmonic photocatalysts, creating new opportunities to rationally design light-harnessing platforms with maximised utilisation of solar energy for high performance in photocatalytic devices.

9.2 Recommendations for Future Work

The works presented in this thesis advance the development of rationally designed photocatalyst platforms by providing extensive fundamental research on structural optimisation, chemical modification and photocatalytic assessment of chemically modified NAA-PCs. Future work would involve translating these platforms into safe, cost-competitive, scalable and efficient photocatalytic devices for a broad range of applications addressing global energy and environmental issues should focus on the following possible directions:

1. Although we have explored several NAA-PC structures produced by anodisation of aluminium substrates, the optical properties of these NAA-PCs have not been fully exploited as a means to enhance photocatalytic reactions by "slow photon" effect. Further experimental optimisation to align photonic stopbands with electronic bandgaps of functional layers should be performed

to ensure that photocatalytic efficiencies can be maximised for specific reactions.

2. These NAA-PCs developed focus on the chemical modification with titanium dioxide through sol-gel method. More fundamental research assessing the capabilities and limitations of the proposed chemically-modified photocatalytic platforms, with different photoactive materials, is still required due to varying quantum efficiency, electron mobility, electrochemical properties, energy bandgap and chemical stability. Such studies should evaluate aspects such as photon-to-electron conversion rate, photosensitivity, reproducibility, stability, abrasion resistance and residual stress. In addition, more precise chemical modification techniques to fine control the thicknesses of the photo-active layers will make it possible to finely align photonic and electronic structures.

3. 2D gold nanodot plasmonic single-lattices reveal LSPR bands with plasmonic bands in the visible spectral region, which accounts for ~43% of the solar spectrum, have shown outstanding performances. Our study suggests that rational design and integration of these nanostructures, with light-trapping NAA-PCs, could maximise photocatalytic reactions due to efficient utilisation of solar energy at high-irradiance spectral regions, harnessing photonic and plasmonic light–matter interactions.

4. The use of chemically-functionalised NAA-PCs in our studies focus on photocatalytic degradation of single type of organics within a small effective area. To translate these chemically-functionalised NAA-PCs into fully functional prototypes for real-life multiplexed photocatalytic applications, large-scale anodisation of aluminium, chemical functionalisation with photoactive materials, and application of the decontamination of a wide range of organic pollutants and their resultant by-products in real-life samples such as wastewater, groundwater, drinking water and contaminated soil, are neccessary.

5. Chemically-modified NAA-PCs developed in our studies focus on the photocatalytic water purification. The versatility of these chemically-modified NAA-PCs can be further demonstrated by extensive research of using these platforms for other types of photocatalytic applications, including clean hydrogen fuel generation, carbon dioxide reduction, and ammonia production, which could be one of the major sources in solving global energy and environmental issues.

Appendix I

SURFACE MODIFICATION OF NANOPOROUS ANODIC ALUMINA PHOTONIC CRYSTALS FOR PHOTOCATALYTIC APPLICATIONS

S.Y. Lim, C.S. Law, and A. Santos, *Surface modification of nanoporous anodic alumina photonic crystals for photocatalytic applications*. in *Nanophotonics Australasia 2017*. 2018. International Society for Optics and Photonics.

Statement of Authorship

Title of Paper	Surface Modification of Nanoporous Anodic Alumina Photonic Crystals for Photocatalytic Applications
Publication Status	☑ Published ☐ Accepted for Publication ☐ Submitted for Publication ☐ Unpublished and Unsubmitted work written in manuscript style
Publication Details	S.Y. Lim, C.S. Law, and A. Santos, *Surface modification of nanoporous anodic alumina photonic crystals for photocatalytic applications*. in *Nanophotonics Australasia 2017*. 2018. International Society for Optics and Photonics.

Principal Author

Name of Principal Author (Candidate)	Siew Yee Lim		
Contribution to the Paper	Performed the experiment, processed and analysed the data and wrote the manuscript under the supervision of Abel Santos.		
Overall percentage (%)	70		
Certification:	This paper reports on original research I conducted during the period of my Higher Degree by Research candidature and is not subject to any obligations or contractual agreements with a third party that would constrain its inclusion in this thesis. I am the primary author of this paper.		
Signature		Date	10/06/2020

Co-Author Contributions

By signing the Statement of Authorship, each author certifies that:

    i.   the candidate's stated contribution to the publication is accurate (as detailed above);

    ii.   permission is granted for the candidate in include the publication in the thesis; and

    iii.   the sum of all co-author contributions is equal to 100% less the candidate's stated contribution.

Name of Co-Author	Cheryl Suwen Law		
Contribution to the Paper	Aided in performing the experiment. Give consent to Siew Yee Lim to present this paper for examination towards the Doctorate of Philosophy.		
Signature		Date	15/06/2020

Name of Co-Author	Abel Santos		
Contribution to the Paper	Acted as a primary supervisor for the candidate, and aided in developing, revising and evaluating the manuscript for submission. Give consent to Siew Yee Lim to present this paper for examination towards the Doctorate of Philosophy.		
Signature		Date	11/06/2020

Surface Modification of Nanoporous Anodic Alumina Photonic Crystals for Photocatalytic Applications

Siew Yee Lim[a,b,c], Cheryl Suwen Law[a,b,c], Abel Santos[a,b,c*]

[a] School of Chemical Engineering, The University of Adelaide, Australia; [b] Institute for Photonics and Advanced Sensing (IPAS), The University of Adelaide, Australia; [c] ARC Centre of Excellence for Nanoscale Biophotonics (CNBP), The University of Adelaide, Australia
*abel.santos@adelaide.edu.au

ABSTRACT

Herein, we report on the development of a rationally designed composite photocatalyst material by combining nanoporous anodic alumina-rugate filters (NAA-RFs) with photo-active layers of titanium dioxide (TiO_2). NAA-RFs are synthesised by sinusoidal pulse anodisation and subsequently functionalised with TiO_2 by sol-gel method to provide the photonic structures with photocatalytic properties. We demonstrate that the characteristic photonic stopband (PSB) of the surface-modified NAA-RFs can be precisely tuned across the UV-visible-NIR spectrum to enhance the photon-to-electron conversion of TiO_2 by 'slow photon effect'. We systematically investigate the effect of the anodisation parameters (i.e. anodisation period and pore widening time) on the position of the PSB of NAA-RFs as well as the photocatalytic performances displayed by these photonic crystal structures. When the edges of the PSB of surface-modified NAA-RFs are positioned closely to the absorption peak of the model organic dye (i.e. methyl orange – MO), the photocatalytic performance of the system to degrade these molecules is enhanced under simulated solar light irradiation due to slow photon effect. Our investigation also reveals that the photocatalytic activity of surface-modified NAA-RFs is independent of slow photon effect and enhances with increasing period length (i.e. increasing anodisation period) of the photonic structures when there is no overlap between the PSB and the absorption peak of MO. This study therefore provides a rationale towards the photocatalytic enhancement of photonic crystals by a rational design of the PSB, creating new opportunities for the future development of high-performance photocatalysts.

Keywords: Photocatalysis, nanoporous anodic alumina, photonic stopband, photonic crystal, anodisation, solar light, photolysis

1. INTRODUCTION

Organic dyes are commonly discharged to water sources or ecosystems from various industries, including textile, cosmetic, pharmaceutical, food, paper, plastic and printing[1-2]. These untreated dyes may be highly reactive and persistent when released to the environment, preventing the absorption of solar light required by the aquatic plants for photosynthesis, deteriorating the aquatic ecosystems and the quality of water sources[3-6]. Conventional chemical and biological water treatment processes (coagulation, flocculation, clarification, filtration, and disinfection) cannot effectively remove these emerging pollutants to meet the stringent water quality standards. Therefore, cost-competitive, eco-friendly wastewater treatments are urgently needed. Among the different alternatives, heterogeneous photocatalysis (henceforth "photocatalysis") is a light-driven process that harnesses solar energy to generate strong, oxidising and non-selective radicals (i.e. ·OH radicals) on the surface of semiconductor materials to mineralise organic pollutants to harmless compounds for the environment and humans[7].

An example of a key photo-active material for photocatalysis is titanium dioxide (TiO_2). This semiconductor has excellent photochemical stability and well-balanced electrochemical properties for good photocatalytic activities[7-8]. However, its intrinsic limitations in light absorption (i.e. constrained to UV light, which is only ~5% of the solar

spectrum) and high recombination rate of photogenerated charge carriers constrain the efficient solar-to-energy conversion in TiO_2-based photocatalysts[9-11]. In addition, the practical use of TiO_2 as nanoparticles presents difficulties in the recovery of the nanoparticles[12-14], including low adsorption capacity[13-15], high aggregation tendency[16] and potential toxicity when released to the environment[17]. Therefore, enhancement of solar-to-energy conversion and immobilisation of TiO_2 are required to address these problems.

The macroscopic optoelectronic properties of semiconductors are strongly dependent on the interaction between photons (light) and atoms (matter) at the nanoscale. In light-driven processes, every photon is precious and, as such, a rational management of photons can lead to efficient photon-to-electron conversions for enhanced optoelectronic applications. Smart designs of materials at the nanoscale can lead to high-performance photocatalyst materials by efficient solar-to-energy (photon-to-electron) conversions. Photonic crystal (PC) structures are periodic optical nanostructures that can control the propagation of light when incoming photons travel across the PCs' structures[18-22]. In particular, nanoporous PC structures possess unique structural and optical properties to facilitate mass transfer and light utilisation[23-24] through their large surface area to volume ratio and slow photon (SP) effects[25]. The rational utilisation of SP effects can improve the photocatalytic activities of photocatalyst materials by tuning the PC's photonic stopband (PSB) and overlap it with the absorption of organic dyes[25-26]. The structural engineering of the PSB of nanoporous PCs [27] can slow down incoming photons at its edges and localise them in the photo-active material to increase the photogeneration of charge carriers[26].

Nanoporous anodic alumina (NAA) produced by anodisation of aluminium is envisaged as a platform to develop PC structures due to its highly controllable and flexible nanopore geometry, chemical resistance, thermal stability, mechanical robustness and optoelectronic properties[28-29]. Some examples of PC structures of NAA include optical microcavities, Fabry-Perot interferometers, bandpass filters, distributed Bragg reflectors, gradient-index filters[27] and rugate filters (RFs)[30]. Among these, NAA-RFs feature a well-resolved intense characteristic PSB, which can be readily tuned across the spectral regions to match the absorption bands of environmental pollutants. Another advantage of NAA-RFs is that the inner surface of these PCs can be modified with layers of photo-active materials to endow NAA-RFs with photocatalyst properties[31].

In this context, this study aims to use NAA-RFs as a platform material to enhance the photocatalytic performances of TiO_2. NAA-RFs are produced by galvanostatic sinusoidal pulse anodisation and subsequently functionalised with photo-active layers of TiO_2 through sol-gel method (Fig. 1). We demonstrate that the position of the characteristic PSB of the NAA-RFs can be precisely engineered by systematically modifying the anodisation period and pore widening time. The effect of these anodisation parameters on the PSB of the photonic structures as well as the photocatalytic degradation of a model dye (i.e. methyl orange – MO) are systematically evaluated.
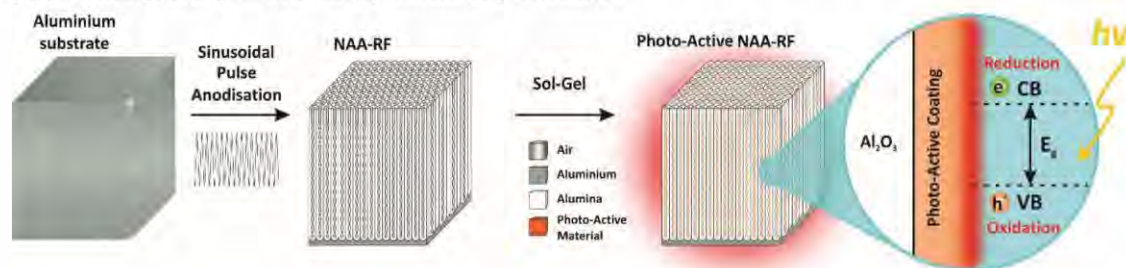

Figure 1. Scheme describing the fabrication of photo-active NAA-RF from its precursor (aluminium substrate) by sinusoidal pulse anodisation (left) and sol-gel method (right).

2. EXPERIMENTAL

2.1 Fabrication of NAA-RFs by sinusoidal pulse anodisation

NAA-RFs were synthesised by galvanostatic sinusoidal pulse anodisation (SPA) approach using and aqueous sulphuric acid (H_2SO_4) electrolyte (Fig. 2) as described by Santos et al.[30]. Briefly, 1.5 x 1.5 cm^2 aluminium (Al) substrates were

sonicated in ethanol (EtOH) and water each for 15 min to remove organic residues. These Al substrates were electropolished in a mixture of EtOH and perchloric acid ($HClO_4$) 4:1 (v:v) at 20 V and 5 °C for 3 min. The electropolished Al substrates were anodised using a 1.1 M aqueous H_2SO_4 solution, in which 25 v% EtOH was added to prevent it from freezing at temperatures below 0 °C[32-33]. The anodisation process was started for 1 h at -1 °C with a constant current density of 1.12 mA cm^{-2} to produce a thin layer of nanoporous oxide that acts as a shuttle to achieve homogeneous pore growth before SPA. The anodisation profile was subsequently set to sinusoidal pulse mode, where the current density was sinusoidally pulsed between high (J_{Max} = 1.12 mA cm^{-2}) and low (J_{Min} = 0.28 mA cm^{-2}) current density values, according to equation (1):

$$J(t) = A_J \left[\sin\left(\frac{2\Pi}{T_P} t \right) + 1 \right] + J_{Offset} \tag{1}$$

For this equation, $J(t)$ is the current density at a given time t, A_J is the current density amplitude, T_P is the anodisation period and J_{Offset} is the current density offset (Fig. 2).
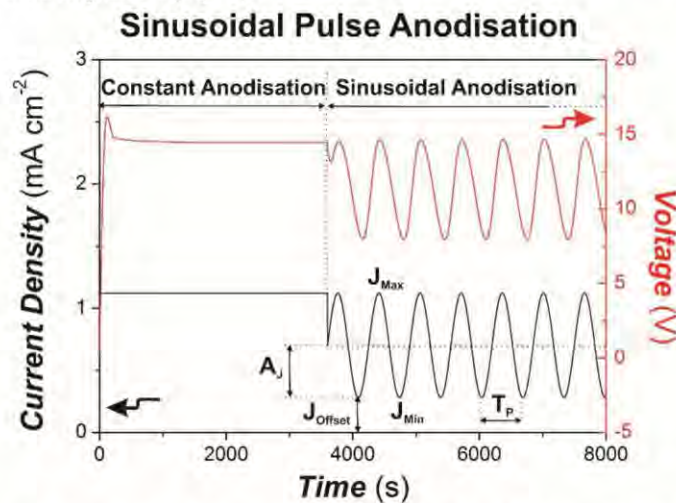

Figure 2. Representative anodisation profile used to produce NAA-RFs including a graphical description of the main anodisation parameters (i.e. T_P, J_{Min}, J_{Max}, J_{Offset} and A_J).

Certain anodisation parameters were fixed for SPA as follows: the current density amplitude (A_J = 0.420 mA cm^{-2}), current density offset (J_{Offset} = 0.28 mA cm^{-2}) and total anodisation time (t_{An} = 20 h). To engineer the photonic features of NAA-RFs (i.e. characteristic transmission peaks or PSB), the anodisation period (T_P) and pore widening time (t_{pw}) were systematically modified from 650 to 850s (ΔT_P = 100 s) and from 0 to 6 min (Δt_{pw} = 2 min), respectively.

Before pore widening was carried out, the remaining aluminium substrate from the backside of NAA-RFs was removed by wet chemical etching in a saturated solution of hydrochloric acid-copper (II) chloride (HCl–CuCl$_2$), using a 5 mm diameter circular window etching mask. Subsequently, the nanopores of NAA-RFs were widened in an aqueous phosphoric acid (H$_3$PO$_4$ 5 wt %) solution by wet chemical etching at 35 °C for the pore widening time specified (from 0 to 6 min with Δt_{pw} = 2 min).

2.2 Surface modification of NAA-RFs with TiO₂

The inner surface of NAA-RFs produced with different T_p (650, 750 and 850 s) at fixed t_{pw} (6 min) was modified with photo-active layers of TiO$_2$ through sol-gel method[34]. TiO$_2$ sol was prepared by magnetically stirring a mixture of titanium (IV) butoxide (3 mol %) and EtOH (97 mol %) in a beaker for 10 min. NAA-RFs were subsequently dip coated by immersing them into TiO$_2$ sol for 24 h. The surface-modified NAA-RFs were washed with EtOH to remove any excess sol and titanium (IV) butoxide on the surface. These samples were dried in an oven at 50 °C for 10 min to evaporate any residual EtOH.

2.3 Optical characterisation

The transmission spectra of NAA-RFs in air were obtained across the UV-visible spectrum (i.e. from 200 to 800 nm) at normal incidence (i.e. $\theta = 0°$) using a UV-visible spectrophotometer (Cary 300, Agilent, USA). The transmission spectra of the surface-modified NAA-RFs in air and 5 mg L^{-1} of MO were also collected under the same conditions. Digital images of NAA-RFs displaying interferometric colours were acquired by using a Canon EOS 700D digital camera equipped with a Tamron 90 mm F2.8 VC USD macro mount lens with autofocus feature under natural light illumination.

2.4 Photocatalytic degradation of methyl orange

MO was photocatalytically degraded with TiO$_2$-NAA-RFs composites of different T_p in a transparent cuvette under simulated solar light irradiation. The TiO$_2$-NAA-RFs composites, which had an effective area of 1 cm^2, were placed in a cuvette containing a mixture of 2 mL of 5 mg L^{-1} MO and 0.1 M hydrogen peroxide (H$_2$O$_2$) solution. The solution was stirred magnetically in a dark vessel (solar simulator) for 30 min to reach the adsorption–desorption equilibrium. After this, simulated solar light irradiation was shined using a 150 W halogen lamp (HL250–A, Amscope, Australia). The absorbance of the absorption peak of MO for each illumination time interval (i.e. 30 min) was analysed by UV-visible spectroscopy to determine the concentration of MO at specific time intervals. The photocatalytic conversion ratio (C_t/C_o), where C_o is the concentration of solution after stirring in the dark for 30 min and C_t is the concentration at illumination time t, was evaluated to determine the kinetic model for this photocatalytic system.

3.   RESULTS AND DISCUSSION

3.1   Effect of anodisation parameters on the optical properties of NAA-RFs

The effect of T_P on the characteristic transmission PSB (i.e. 1st order) of NAA-RFs produced by SPA was studied by manipulating T_P from 650 to 850 s with an interval (ΔT_P) of 100 s. Fig. 3a demonstrates that the central wavelength (λ_C) is linearly dependent on T_P at fixed t_{pw} as shown by the slopes of the fitting lines (i.e. 0.55 ± 0.03, 0.49 ± 0.00, 0.44 ± 0.03 and 0.43 ± 0.07 nm s^{-1} for t_{pw} of 0, 2, 4 and 6 min, respectively). Furthermore, the position of the characteristic transmission PSB of NAA-RFs is red-shifted with T_P, in which this effect is also displayed in the interferometric colours of NAA-RFs (Fig. 3b). This phenomenon is due to the relationship between T_P and the period length (L_{TP}) of NAA-RFs[27]. When T_P increases, L_{TP} (i.e. the length of NAA layers between the consecutive sinusoidal pulses)[30] in the photonic structure also increases. As a result, NAA-RFs reflect light more efficiently at longer wavelengths, which is in good agreement with the Bragg's law[27] and previous studies[30]. Therefore, T_P can be manipulated to precisely tune the position of the PSB of NAA-RFs across the entire UV-visible-NIR spectrum and display various interferometric colours of NAA-RFs.

To study the effect of t_{pw} on the position of characteristic transmission peak of NAA-RFs, t_{pw} was varied from 0 to 6 min with an interval of 2 min. As indicated in Fig. 3a, an increase in t_{pw} is accompanied by a decrease in λ_C, implying that the position of the 1st order PSB of NAA-RFs is blue-shifted with t_{pw}, which is in good agreement with previous studies on NAA-RFs[30]. This blue-shift is also featured in the interferometric colours of NAA-RFs as shown in Fig. 3b. The blue-shift observed is associated with the modification of the nanoporous structure of NAA-RFs by wet chemical etching. This process widens the pores of NAA-RFs, which in turn modifies the effective medium of NAA-RFs and alters the PSB. Thus, a pore widening treatment allows the precise tuning of the position of characteristic transmission PSB of NAA-RFs across the spectral regions with various interferometric colours showcased.
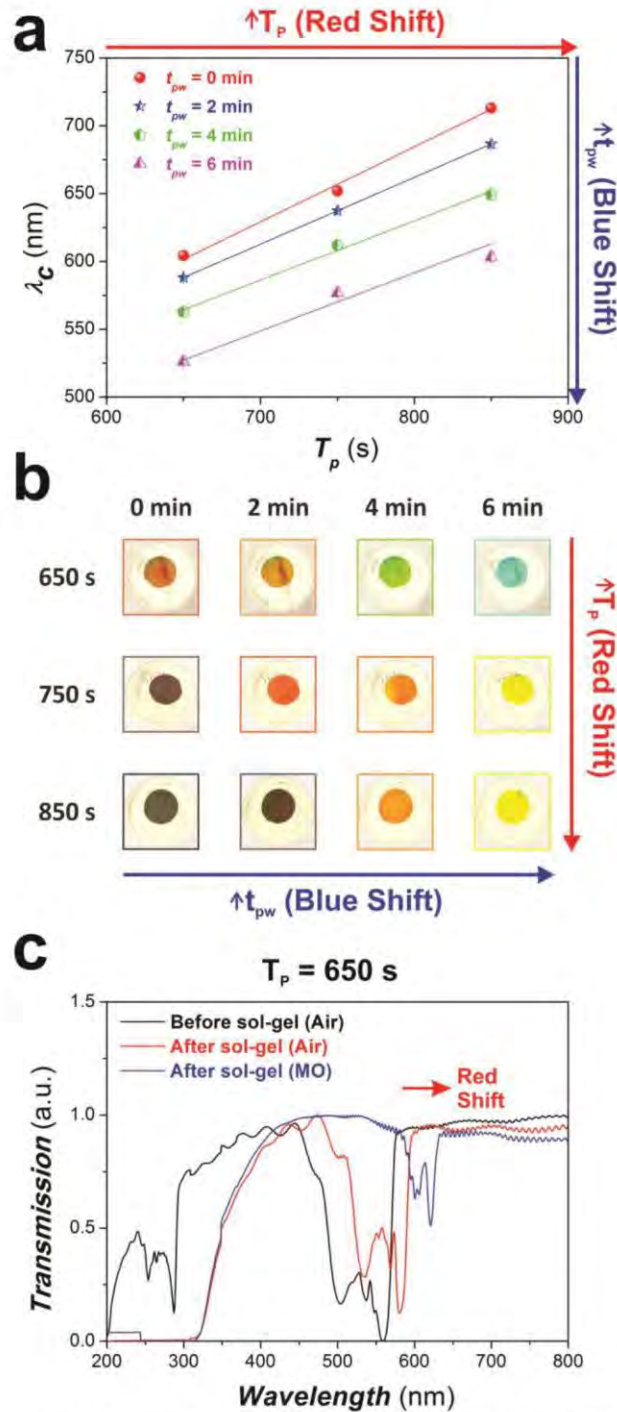
Figure 3. Tunability of the characteristic transmission PSBs and interferometric colours of NAA-RFs by the anodisation and sol-gel parameters. (a) Position of the first characteristic transmission PSB of NAA-RFs as a function of T_P and t_{pw}. (b) Interferometric colour of NAA-RFs as a function of T_P and t_{pw}. (c) Representative transmission spectrum of a reference NAA-RF (i.e. T_P = 650 s, A_J = 0.420 mA cm^{-2}, J_{Offset} = 0.280 mA cm^{-2}, J_{Min} = 0.280 mA cm^{-2}, J_{Max} = 1.12 mA cm^{-2}, t_{An} = 20 h and t_{pw} = 6 min) in air and 5 mg L^{-1} of MO before and after sol-gel modification with TiO$_2$ for 24 h.

285

3.2 Effect of surface modification of NAA-RFs with TiO₂

The effect of the surface functionalisation of NAA-RFs (i.e. $T_P = 650$ s, $t_{pw} = 6$ min) with TiO$_2$ layers on the position of the characteristic transmission PSB was studied after the photonic structures was dip-coated with TiO$_2$ sol for 24 h by sol-gel method. As demonstrated in Fig. 3c, the position of the 1st order PSB with reference to air is red shifted from 526 ± 1 to 556 ± 1 nm after sol-gel modification. A more significant red shift in the position of PSB (i.e. 612 ± 1 nm) is observed when the surface-modified NAA-RF is filled with 5 mg L^{-1} of MO. These red-shift phenomena are observed due to the increase of the refractive index of the medium filling the nanopores of NAA-RFs, including photo-active layers of TiO$_2$ and MO solution, which both have larger refractive index than that of air. It should also be noted that the full width at half maximum (FWHM) of the PSB decreases after filling the nanopores with TiO$_2$ and MO solution. This reduction is caused by the light absorption of TiO$_2$ and MO solution, which filled the nanopores of the NAA-RFs[30, 35]. Besides that, the 2nd order transmission PSB disappears after sol-gel method. This is because the 2nd order PSB is located at positions <300 nm, which corresponds to the strong UV absorption range of TiO$_2$ (<380 nm)[36]. This indicates that TiO$_2$ is successfully deposited onto the inner surface of NAA-RFs. Surface-modified NAA-RFs of different T_P (750 and 850 s) with the same t_{pw} (6 min) also showed similar red shifts, reduction in FWHM and disappearance of 2nd order PSB. Therefore, NAA-RFs are proved to be surface-modified with photo-active layers of TiO$_2$ and their PSB demonstrated to be tunable across the UV-visible-NIR spectrum by manipulating the filling fractions of the medium.

3.3 Photocatalytic degradation of methyl orange with surface-modified NAA-RFs

Photocatalytic degradation of MO as model dye was studied to evaluate the photocatalytic performances of the surface-modified NAA-RFs ($T_P = 650$, 750 and 850 s; $t_{pw} = 6$ min) under simulated solar light irradiation. The photocatalytic activity of these NAA-RFs for liquid-phase degradation was carried out with the addition of 0.1 M H$_2$O$_2$ solution to aid in the photogeneration of charge carriers in TiO$_2$. After addition of H$_2$O$_2$, the performances of the surface-modified NAA-RFs were measured as displayed in Fig. 4a, where the photocatalytic degradation process is fit for pseudo-first order kinetics by linearising the formula into equation (2):

$$-\ln\left(\frac{C_t}{C_o}\right) = kt \tag{2}$$

In this equation, C_o is the adsorption-desorption equilibrium concentration, C_t is the concentration at time t and k is the apparent rate constant.

The values of k for the MO degradation using surface-modified NAA-RFs with T_P values of 650, 750 and 850 s were 0.31 ± 0.01, 0.36 ± 0.01 and 0.34 ± 0.00 h^{-1}, respectively. These k values are all larger than that for commercial P25 TiO$_2$ nanoparticles treated with aqueous H$_2$O$_2$ solution (i.e. $k = 0.24$ h^{-1})[37], demonstrating that the surface-modified NAA-RFs perform better than the commercial P25 TiO$_2$ nanoparticles in the photocatalytic degradation of MO under simulated solar light irradiation (~23–33% enhancement). Besides that, the surface-modified NAA-RF with $T_P = 750$ s was the most efficient photo-active PC platform to degrade MO. This result can be ascribed to the slow photon (SP) effects, which enhances the photocatalytic degradation of MO. According to Nishimura et al.[26], the light propagated at the vicinity of the PSB will slow down and localise in different parts of the PC structure. The SP will localise in the high dielectric part of the photonic crystal (i.e. photocatalyst) at the red edge of PSB and in the low dielectric part (i.e. dye or voids) at the blue edge of PSB. Therefore, when the edges of the PSB are matched with the absorption peak of the dye, the photocatalytic degradation of the dye can be significantly enhanced. To validate if the increase in the photocatalytic performance of surface-modified NAA-RF (i.e. $T_P = 750$ s) is due to SP effects, the characteristic transmission PSB of surface-modified NAA-RFs ($T_P = 650$, 750 and 850 s) with the absorption peak of MO are displayed in Fig.4 (b, c and d respectively). According to this analysis, the blue edge of the PSB of the surface-modified NAA-RF with $T_P = 750$ s is the nearest to the absorption peak of MO, which corresponds to the best photocatalytic activity observed for MO degradation. This demonstrates that SP effects play a major role in improving the photocatalytic degradation of MO for this type of surface-modified NAA-RF.

Besides that, when the position of the characteristic transmission PSB of surface-modified NAA-RFs is far away from the absorption peak of MO, the photocatalytic degradation of MO should be independent of the PSB[25] and only related to the changes of the overall photonic structures. For instance, with increasing T_P, mass transfer and light utilisation efficiency may have enhanced for light absorption of TiO$_2$ due to the enlargement of L_{TP} in the NAA-RFs. Consequently,

286

TiO$_2$ can generate more ·OH radicals to mineralise MO, increasing the photocatalytic degradation rate. Therefore, since the PSB of the surface-modified NAA-RFs with T_P of 650 and 850 s are far away from the absorption peak of MO (Figs. 4b and d, respectively), it is observed that the photocatalytic performances of the surface-modified NAA-RFs increases with increasing T_P (Fig. 4a). Moreover, the increased light absorption by TiO$_2$ may also be influenced by the light scattering occurring within the structure of the surface-modified of NAA-RFs with TiO$_2$. Hence, the changes in the surface-modified NAA-RFs can be significant for the photocatalytic degradation of MO and investigation on the effects of other anodisation and sol-gel parameters should be carried out.
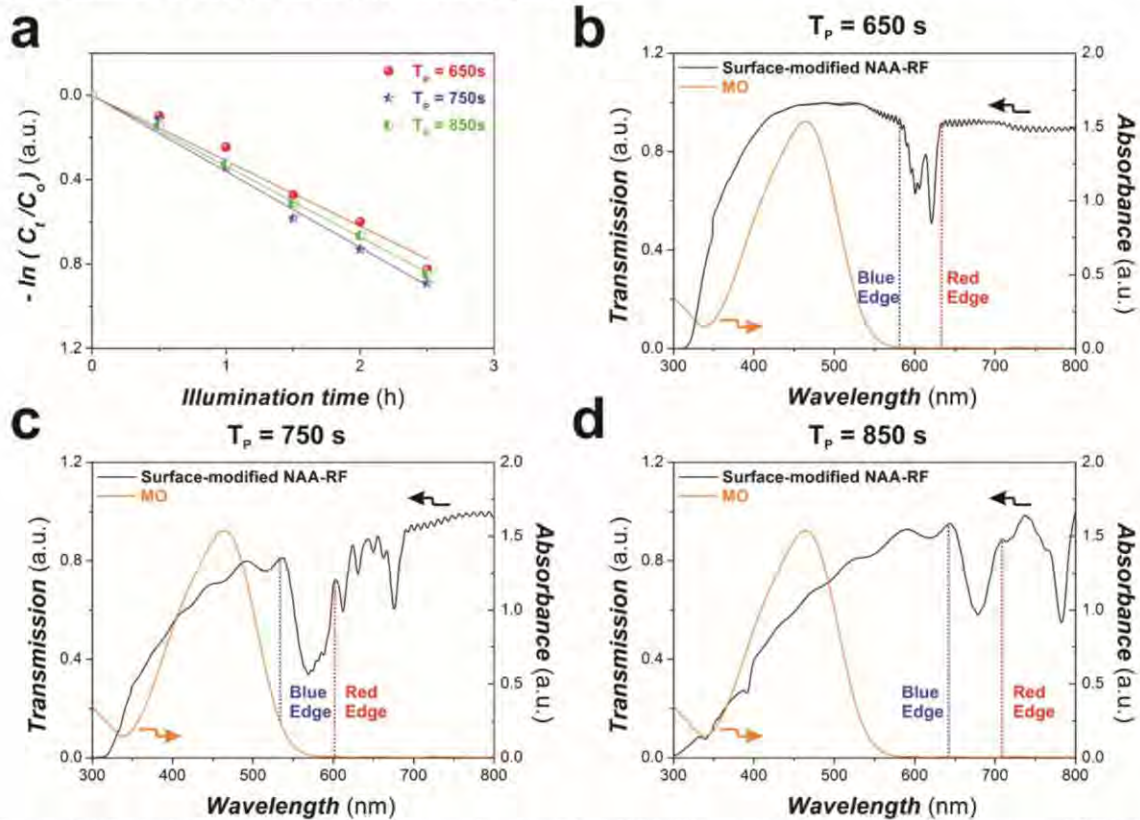

Figure 4. Effect of slow photon effects of the surface-modified NAA-RFs on the photocatalytic degradation of MO. (a) Kinetic linear simulation curve of photocatalytic degradation of MO under simulated solar light irradiation. Optical absorption peak of MO and transmission spectra of TiO$_2$-NAA-RF composites with an anodisation period of (b) 650 s, (c) 750 s and (d) 850 s.

3.4 Kinetics

A photocatalytic degradation mechanism for the surface-modified NAA-RFs with the addition of H$_2$O$_2$ solution is deduced based on the above experiment. When TiO$_2$ is irradiated with simulated solar light, electron/hole pairs are generated in the conduction and valence band of TiO$_2$, respectively. Nevertheless, fewer ·OH radicals are produced for the decomposition of organic dye since the photogenerated charge carriers may readily recombine due to short lifetime in the electronic bands. This will result in a slow photocatalytic kinetics. Hence, TiO$_2$ is deposited on the surfaces of NAA-RFs to utilise the SP effects of the photonic structures to increase the lifetime and photogeneration of the charge carriers. This increase is possible since the photons at the frequency edges of the PSB will propagate with strongly reduced group velocity, being trapped within the photonic structure. Since the slow photons are localised in the edges of PSB, matching these edges with the absorption peak of the organic dye (i.e. localised region of the organic dye) can increase the efficiency of the photocatalytic degradation of TiO$_2$ in the PC structures to mineralise the organic dye into carbon dioxide and water. Furthermore, H$_2$O$_2$ is also added as a primary electron acceptor to facilitate the electron-charge transfer and promote the generation of the ·OH radicals, improving the photocatalytic performances of the surface-

modified NAA-RFs. Thus, the addition of H_2O_2 and the surface modification of NAA-RFs with TiO_2 can enhance the photocatalytic degradation of MO under simulated solar light irradiation.

4. CONCLUSION

In summary, this study has presented an approach to synthesise photonic crystal structures based on NAA and TiO_2 for improving the photocatalytic degradation performances. The optical properties of NAA-RFs (i.e. characteristic PSB) synthesised by sinusoidal pulse anodisation was carried out by systematically modifying two anodisation parameters (i.e. anodisation period and pore widening time) for precise tuning of the PSB across the UV-visible-NIR spectrum. The surfaces of NAA-RFs with different anodisation period (i.e. 650, 750 and 850 s) at fixed pore widening time (i.e. 6 min) were subsequently modified with photo-active layers of TiO_2 by sol-gel method to provide these PCs with photocatalytic properties. When the edges of the PSB of the surface-modified NAA-RF (T_P = 750 s) are matched closely to the absorption peak of the model dye (i.e. MO), the photocatalytic activity of the system is significantly improved due to SP effects in the PC structures. Nevertheless, when the position of PSB of surface-modified NAA-RFs are located away from the absorption peak of dye, the photocatalytic degradation of MO is independent of the PSB and becomes dependent on the period length of the photonic structures since mass transfer and light utilisation enhance with increasing period length (i.e. increasing anodisation period). Therefore, the rationale generated using TiO_2-NAA-RFs PC structures as model composite photocatalyst material may provide new opportunities to develop cost-competitive, simple and sustainable photocatalysts for the photodegradation of persistent organic dyes and pollutants.

REFERENCES

[1] Vaghela, S. S., Jethva, A. D., Mehta, B. B., Dave, S. P., Adimurthy, S. and Ramachandraiah, G., "Laboratory studies of electrochemical treatment of industrial azo dye effluent," Environ. Sci. Technol. 39(8), 2848-2855 (2005).

[2] Prasad, A. R. and Joseph, A., "Synthesis, characterization and investigation of methyl orange dye removal from aqueous solutions using waterborne poly vinyl pyrrolidone (PVP) stabilized poly aniline (PANI) core-shell nanoparticles," RSC Adv. 7(34), 20960-20968 (2017).

[3] Garg, V. K., Amita, M., Kumar, R. and Gupta, R., "Basic dye (methylene blue) removal from simulated wastewater by adsorption using Indian Rosewood sawdust: a timber industry waste," Dyes Pigm. 63(3), 243-250 (2004).

[4] Sun, H., Cao, L. and Lu, L., "Magnetite/reduced graphene oxide nanocomposites: One step solvothermal synthesis and use as a novel platform for removal of dye pollutants," Nano Res. 4(6), 550-562 (2011).

[5] Hai, F. I., Yamamoto, K. and Fukushi, K., "Hybrid treatment systems for dye wastewater," Crit. Rev. Environ. Sci. Technol. 37(4), 315-377 (2007).

[6] Husain, Q., "Potential applications of the oxidoreductive enzymes in the decolorization and detoxification of textile and other synthetic dyes from polluted water: A review," Crit. Rev. Biotechnol. 26(4), 201-221 (2006).

[7] Lee, K., Mazare, A. and Schmuki, P., "One-dimensional titanium dioxide nanomaterials: nanotubes," Chem. Rev. 114(19), 9385-9454 (2014).

[8] Coronado, J. M., Fresno, F., Hernández-Alonso, M. D. and Portela, R., [Design of Advanced Photocatalytic Materials for Energy and Environmental Applications], Springer, London, 85-102 (2013).

[9] Ollis, D. F., Pelizzetti, E. and Serpone, N., "Photocatalyzed destruction of water contaminants," Environ. Sci. Technol. 25(9), 1522-1529 (1991).

[10] Choi, S. K., Kim, S., Lim, S. K. and Park, H., "Photocatalytic comparison of TiO_2 nanoparticles and electrospun TiO_2 nanofibers: Effects of mesoporosity and interparticle charge transfer," J. Phys. Chem. C 114(39), 16475-16480 (2010).

[11] Fox, M. A. and Dulay, M. T., "Heterogeneous photocatalysis," Chem. Rev. 93(1), 341-357 (1993).

[12] Li, F., Jiang, Y., Yu, L., Yang, Z., Hou, T. and Sun, S., "Surface effect of natural zeolite (clinoptilolite) on the photocatalytic activity of TiO_2," Appl. Surf. Sci. 252(5), 1410-1416 (2005).

[13] Wang, C., Shi, H. and Li, Y., "Synthesis and characteristics of natural zeolite supported Fe^{3+}-TiO_2 photocatalysts," Appl. Surf. Sci. 257(15), 6873-6877 (2011).

[14] Dong, H., Zeng, G., Tang, L., Fan, C., Zhang, C., He, X. and He, Y., "An overview on limitations of TiO_2-based particles for photocatalytic degradation of organic pollutants and the corresponding countermeasures," Water Res. 79, 128-146 (2015).

[15] Wang, C., Shi, H. and Li, Y., "Synthesis and characterization of natural zeolite supported Cr-doped TiO_2 photocatalysts," Appl. Surf. Sci. 258(10), 4328-4333 (2012).

[16] Guesh, K., Márquez-Álvarez, C., Chebude, Y. and Diaz, I., "Enhanced photocatalytic activity of supported TiO_2 by selective surface modification of zeolite Y," Appl. Surf. Sci. 378, 473-478 (2016).

[17] Zhu, X., Chang, Y. and Chen, Y., "Toxicity and bioaccumulation of TiO_2 nanoparticles aggregates in Daphnia magna," Chemosphere, 78(3), 209-215 (2010).

[18] Song, B.-S., Noda, S., Asano, T. and Akahane, Y., "Ultra-high-Q photonic double-heterostructure nanocavity," Nat. Mater. 4(3), 207-210 (2005).

[19] Noda, S., Chutinan, A. and Imada, M., "Trapping and emission of photons by a single defect in a photonic bandgap structure," Nature 407(6804), 608-610 (2000).

[20] Akahane, Y., Asano, T., Song, B.-S. and Noda, S., "High-Q photonic nanocavity in a two-dimensional photonic crystal," Nature 425(6961), 944-947 (2003).

[21] Noda, S., Tomoda, K., Yamamoto, N. and Chutinan, A., "Full three-dimensional photonic bandgap crystals at near-infrared wavelengths," Science 289(5479), 604-606 (2000).

[22] López, C., "Materials aspects of photonic crystals," Adv. Mater. 15(20), 1679-1704 (2003).

[23] Raccis, R., Nikoubashman, A., Retsch, M., Jonas, U., Koynov, K., Butt, H.-J., Likos, C. N. and Fytas, G., "Confined diffusion in periodic porous nanostructures," ACS Nano 5(6), 4607-4616 (2011).

[24] Nykypanchuk, D., Strey, H. H. and Hoagland, D. A., "Brownian motion of DNA confined within a two-dimensional array," Science 297(5583), 987-990 (2002).

[25] Zheng, X., Meng, S., Chen, J., Wang, J., Xian, J., Shao, Y., Fu, X. and Li, D., "Titanium dioxide photonic crystals with enhanced photocatalytic activity: Matching photonic band gaps of TiO_2 to the absorption peaks of dyes," J. Phys. Chem. C 117(41), 21263-21273 (2013).

[26] Nishimura, S., Abrams, N., Lewis, B. A., Halaoui, L. I., Mallouk, T. E., Benkstein, K. D., van de Lagemaat, J. and Frank, A. J., "Standing wave enhancement of red absorbance and photocurrent in dye-sensitized titanium dioxide photoelectrodes coupled to photonic crystals," J. Am. Chem. Soc. 125(20), 6306-6310 (2003).

[27] Santos, A., "Nanoporous anodic alumina photonic crystals: fundamentals, developments and perspectives," J. Mater. Chem. C 5(23), 5581-5599 (2017).

[28] Eftekhari, A., [Nanostructured Materials in Electrochemistry], Wiley-VCH, Weinheim, 1-116 (2008).

[29] Lee, W. and Park, S.-J., "Porous anodic aluminum oxide: Anodisation and templated synthesis of functional nanostructures," Chem. Rev. 114(15), 7487-7556 (2014).

[30] Santos, A., Yoo, J. H., Rohatgi, C. V., Kumeria, T., Wang, Y. and Losic, D., "Realisation and advanced engineering of true optical rugate filters based on nanoporous anodic alumina by sinusoidal pulse anodization," Nanoscale 8(3), 1360-1373 (2016).

[31] Kumeria, T., Santos, A. and Losic, D., "Nanoporous anodic alumina platforms: Engineered surface chemistry and structure for optical sensing applications," Sensors 14(7), 11878-11918 (2014).

[32] Wang, Y., Santos, A., Evdokiou, A. and Losic, D., "Rational design of ultra-short anodic alumina nanotubes by short-time pulse anodization," Electrochim. Acta 154, 379-386 (2015).

[33] Santos, A., Formentin, P. Ferré-Borrull, J., Pallarès, J. and Marsal, L. F., "Nanoporous anodic alumina obtained without protective oxide layer by hard anodization," Mater. Lett. 67(1), 296-299 (2012).

[34] Massard, C., Pairis, S., Raspal, V., Sibaud, Y. and Awitor, K., "Fabrication of TiO_2 nanotanks embedded in a nanoporous alumina template," J. Nanomater. 2015, 1-7 (2015).

[35] Kumeria, T., Rahman, M. M., Santos, A., Ferré-Borrull, J., Marsal, L. F. and Losic, D., "Structural and optical nanoengineering of nanoporous anodic alumina rugate filters for real-time and label-free biosensing applications," Anal. Chem. 86(3), 1837-1844 (2014).

[36] Zhang, Z. and Wu, H., "Multiple band light trapping in ultraviolet, visible and near infrared regions with TiO_2 based photonic materials," Chem. Commun. 50(91), 14179-14182 (2014).

[37] Zou, J., Gao, J. and Wang, Y., "Synthesis of highly active H_2O_2-sensitized sulfated titania nanoparticles with a response to visible light," J. Photochem. Photobiol. 202(2-3), 128-135 (2009).

Appendix II

ENHANCED VISIBLE LIGHT PHOTOCATALYSIS IN TITANIUM DIOXIDE-FUNCTIONALIZED NANOPOROUS ANODIC ALUMINA PHOTONIC CRYSTALS

S.Y. Lim, C.S. Law, and A. Santos, *Enhanced visible light photocatalysis in titanium dioxide-functionalized nanoporous anodic alumina photonic crystals*. in *Solid-State Lighting 2018*. 2018. Optical Society of America.

Statement of Authorship

Title of Paper	Enhanced Visible Light Photocatalysis in Titanium Dioxide-Functionalized Nanoporous Anodic Alumina Photonic Crystals
Publication Status	☑ Published ☐ Accepted for Publication ☐ Submitted for Publication ☐ Unpublished and Unsubmitted work written in manuscript style
Publication Details	S.Y. Lim, C.S. Law, and A. Santos, *Enhanced visible light photocatalysis in titanium dioxide-functionalized nanoporous anodic alumina photonic crystals.* in *Solid-State Lighting 2018*. 2018. Optical Society of America.

Principal Author

Name of Principal Author (Candidate)	Siew Yee Lim
Contribution to the Paper	Performed the experiment, processed and analysed the data and wrote the manuscript under the supervision of Abel Santos.
Overall percentage (%)	70
Certification:	This paper reports on original research I conducted during the period of my Higher Degree by Research candidature and is not subject to any obligations or contractual agreements with a third party that would constrain its inclusion in this thesis. I am the primary author of this paper.
Signature	Date 10/06/2020

Co-Author Contributions

By signing the Statement of Authorship, each author certifies that:

    i.   the candidate's stated contribution to the publication is accurate (as detailed above);

    ii.   permission is granted for the candidate in include the publication in the thesis; and

    iii.   the sum of all co-author contributions is equal to 100% less the candidate's stated contribution.

Name of Co-Author	Cheryl Suwen Law
Contribution to the Paper	Aided in performing the experiment. Give consent to Siew Yee Lim to present this paper for examination towards the Doctorate of Philosophy.
Signature	Date 15/06/2020

Name of Co-Author	Abel Santos
Contribution to the Paper	Acted as a primary supervisor for the candidate, and aided in developing, revising and evaluating the manuscript for submission. Give consent to Siew Yee Lim to present this paper for examination towards the Doctorate of Philosophy.
Signature	Date 11/06/2020

Enhanced Visible Light Photocatalysis in Titanium Dioxide-Functionalized Nanoporous Anodic Alumina Photonic Crystals

Siew Yee Lim[1,2,3]*, Cheryl Suwen Law[1,2,3], Abel Santos[1,2,3±]

[1]School of Chemical Engineering, The University of Adelaide, SA 5005 Adelaide, Australia.
[2]Institute for Photonics and Advanced Sensing (IPAS), The University of Adelaide, SA 5005 Adelaide, Australia.
[3]ARC Centre of Excellence for Nanoscale BioPhotonics (CNBP), The University of Adelaide, SA 5005 Adelaide, Australia.
*siew.lim@adelaide.edu.au; ±abel.santos@adelaide.edu.au

Abstract: Herein, we demonstrate the enhanced photocatalytic performance of a rationally designed nanoporous anodic alumina gradient-index filters functionalized with photoactive titanium dioxide. The photonic efficiency of this composite material improves photocatalytic reactions by 'slow photon' effect. © 2018 The Author(s)
OCIS codes: (050.5298) Photonic Crystals; (160.5293) Photonic Bandgap Materials; (350.6050) Solar Energy.

1. Introduction

Photonic crystals (PCs) are periodic optical nanostructures that can confine, control and mold photons at the micro/nanoscale. They forbid the propagation of light of certain wavelengths when photons travel across the PC's structure through photonic stopbands (PSB). Photons of energies near the frequencies of the blue and red edges of the PC's PSB propagate with reduced or approximately zero group velocity [1]. This phenomenon, known as 'slow photons' (SP), makes these photons to have longer lifespan at these spectral regions, enhancing the interaction between light and material. This light harvesting enhancement is exploited particularly for photocatalysis [2], but the difficulties in the fabrication process and tuning of the features of PSB of titanium dioxide (TiO_2) PCs limit their potential use for real-life photocatalytic applications [3]. Nanoporous anodic alumina (NAA) can address these limitations since this platform PC material provides highly controllable and flexible nanoporous geometry, simple fabrication process for PC structures and template platform for TiO_2. These PCs can provide composite structures with outstanding photocatalytic capabilities [4]. This study reports on the photocatalytic applicability of TiO_2-functionalized nanoporous anodic alumina gradient-index filter (TiO_2-NAA-GIFs) produced by sinusoidal pulse anodization and sol-gel method (Fig. 1(a)).
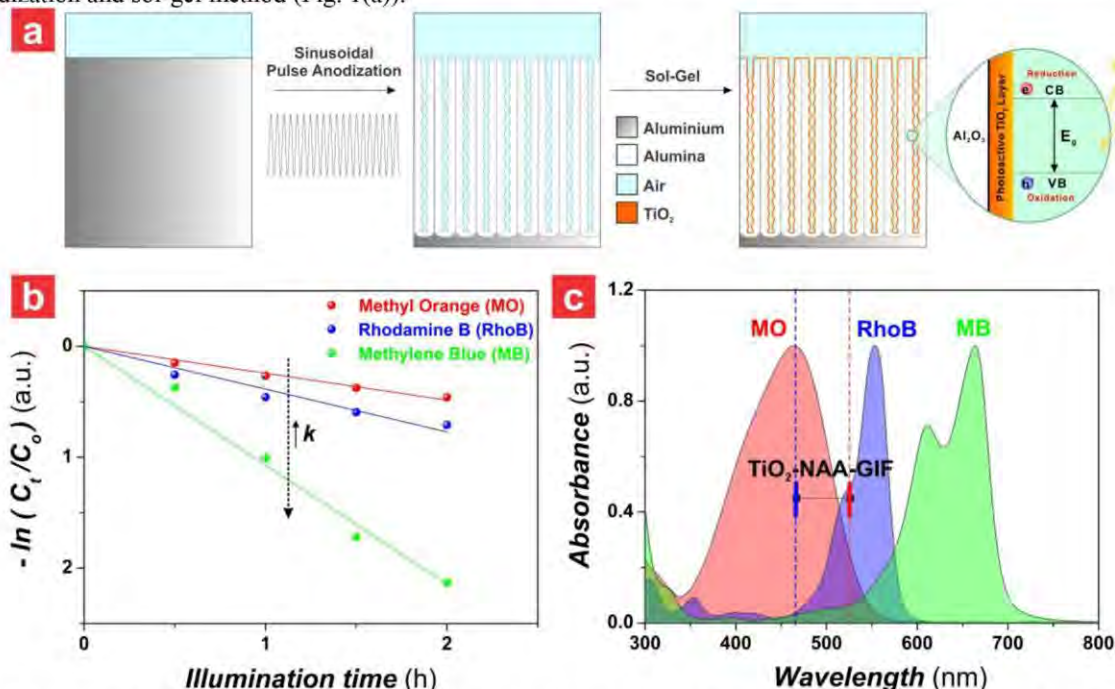

Fig. 1. Summary of the fabrication of TiO_2-NAA-GIF and its photocatalytic performance on three different types of organic dyes using the slow photon effect. (a) Schematic illustration of the fabrication of photoactive NAA-GIF from aluminium by sinusoidal pulse anodization (left) and

sol-gel process (right). (b) Kinetic linear line of photocatalytic degradation of three type of organic dyes (MO, RhoB and MB). (c) Relative position of the blue and red edges of the characteristic PSB of TiO_2-NAA-GIF and the optical absorption bands of MO, RhoB and MB.

2. Methods

NAA-GIFs with an anodization period (T_P) of 550 s and 6 min pore widening time (t_{pw}) were fabricated following the protocol [5]. NAA-GIFs were functionalized with photoactive TiO_2 layers with a deposition time of 24 h through sol-gel method. The transmission spectrum of TiO_2-NAA-GIFs in water were obtained across the UV-visible spectrum at normal incidence (i.e. $\theta = 0$ °C) using a UV-visible spectrophotometer.

The photocatalytic degradation of three types of organic dyes (methyl orange – MO, rhodamine B – RhoB and methylene blue – MB) was carried out under simulated solar light irradiation. Briefly, TiO_2-NAA-GIFs were placed inside a cuvette of 2 mL mixture of 5 mg/L of dye and 0.1 M hydrogen peroxide solution. The solution mixture was stirred magnetically in a solar simulator for 30 min in the dark and subsequently shined for 2 h using a 150 W halogen lamp. The photocatalytic conversion ratio (C_t/C_o), where C_o is the concentration after stirring in the dark for 30 min and C_t is the concentration at illumination time t, was calculated and fit into the linearized pseudo-first order kinetics in equation (1) to determine k (i.e. the apparent rate constant).

$$- \ln\left(\frac{C_t}{C_o}\right) = kt \qquad (1)$$

3. Results and Discussion

The photocatalytic performance of TiO_2-NAA-GIFs on the degradation of three type of organic dyes (i.e. MO, RhoB and MB) was studied and the results are displayed in Fig.1b, where the performance is measured as the slope or the apparent kinetic constant (k) value. The increment of k value from MO, RhoB to MB demonstrate that the charge of the dye molecules (i.e. negative, positive and positive, respectively) significantly affects the photocatalytic performance of TiO_2-NAA-GIFs since the surface of TiO_2 is negatively charged (Table 1). The k values for the photocatalytic degradation of MB, RhoB and MO under visible light irradiation onto TiO_2-NAA-GIFs were enhanced by approximately 40, 56 and 58% respectively when compared to that with Degussa P25 nanoparticles, a benchmark photocatalytic material. These enhancements are associated with SP effect, where the light propagated at the vicinity (i.e. blue and red edges) of the PCs' PSB slow downs and localizes in different parts of the PC structures [1,6]. Therefore, matching the edges of the PCs' PSB within the absorption range of the organic dyes can significantly enhance the photocatalytic degradation of these model organic molecules, particularly when the edges of the PSB match with the absorption peak of the dye (i.e. localized region of the dye). This SP effect is demonstrated in Fig. 1c, where the blue edge of the PSB matches the absorption peak of MO, the red edge of the PSB is near the absorption peak of RhoB and both the edges of the PSB are located away from the absorption peak but still within the absorption range of MB.

Table 1. k values for the photocatalytic degradation of MO, RhoB and MB under visible light irradiation.

Material	Kinetic Constant, k (h^{-1})			Reference
	MO	RhoB	MB	
Degussa P25 Nanoparticles	0.10	0.17	0.64	[2]
TiO_2-NAA-GIF	0.24 ± 0.01	0.39 ± 0.02	1.07 ± 0.04	This Study

4. Conclusion

In summary, this study demonstrates that TiO_2-NAA-GIFs improve and speed up the efficiency of photocatalytic reactions by utilizing an efficient utilization of the slow photon effect in semiconductor PCs. This rationally designed composite material can provide sustainable photocatalysts for water and wastewater treatment applications.

5. References

[1] S. Nishimura, N. Abrams, B.A. Lewis, L.I. Halaoui, T.E. Malluok, K.D. Benkstein, J. van de Lagemaat, and A.J. Frank, "Standing wave enhancement of red absorbance and photocurrent in dye-sensitized titanium dioxide photoelectrodes coupled to photonic crystals," J. Am. Chem. Soc. **125**, 6306-6310 (2003).
[2] X. Zheng, S. Meng, J. Chen, J. Wang, J. Xian, Y. Shao, X. Fu, and D. Li, "Titanium dioxide photonic crystals with enhanced photocatalytic activity: Matching photonic band gaps of TiO_2 to the absorption peaks of dyes," J. Phys. Chem. C **117**, 21263-21273 (2013).
[3] M. Curti, J. Schneider, D.W. Bahnemann, and C.B. Mendive, "Inverse opal photonic crystals as a strategy to improve photocatalysis: Underexplored questions," J. Phys. Chem. Lett. **6**, 3903-3910 (2015).
[4] A. Santos, "Nanoporous anodic alumina photonic crystals: Fundamentals, developments and perspectives," J. Mater. Chem. C **5**, 5581-5599 (2017).
[5] S.Y. Lim, C.S. Law, and A. Santos, "Surface modification of nanoporous anodic alumina photonic crystals for photocatalytic applications," in Nanophotonics Australasia 2017, (SPIE, Melbourne, 2017).
[6] O. Deparis, S.R. Mouchet, and B.-L. Su, "Light harvesting in photonic crystals revisited: Why do slow photons at the blue edge enhance absorption?" Phys. Chem. Chem. Phys. **17**, 30525-30532 (2015).